SUMMER FACULTY RESEARCH PROGRAM

LEVEL II

Research Reports

Volume II of II

UNCLASSIFIED

SECURITY CLASSIFICATION OF THIS PAGE (When Data Entered)

REPORT DOCUMENTATION PAGE	READ INSTRUCTIONS BEFORE COMPLETING FORM
1. REPORT NUMBER: AFOSR-TR-79-0235	2. GOVT ACCESSION NO. / 3. RECIPIENT'S CATALOG NUMBER
4. TITLE (and Subtitle): 1978 USAF-ASEE Summer Faculty Research Program (Volume II)	5. TYPE OF REPORT & PERIOD COVERED: Final report, 1 Jan 76-30 Sep 78
	6. PERFORMING ORG. REPORT NUMBER
7. AUTHOR(s): J. Fred O'Brien	8. CONTRACT OR GRANT NUMBER(s): F44620-75-C-0031
9. PERFORMING ORGANIZATION NAME AND ADDRESS: Auburn University, Auburn Alabama	10. PROGRAM ELEMENT, PROJECT, TASK AREA & WORK UNIT NUMBERS: 61102F, 2307/D1
11. CONTROLLING OFFICE NAME AND ADDRESS: Air Force Office of Scientific Research/XOP, Bldg. 410, Bolling AFB, Washington D.C. 20332	12. REPORT DATE: September 1978 / 13. NUMBER OF PAGES: 306
14. MONITORING AGENCY NAME & ADDRESS (if different from Controlling Office)	15. SECURITY CLASS. (of this report): UNCLASSIFIED / 15a. DECLASSIFICATION/DOWNGRADING SCHEDULE

16. DISTRIBUTION STATEMENT (of this Report)

Approved for public release; distribution unlimited.

17. DISTRIBUTION STATEMENT (of the abstract entered in Block 20, if different from Report)

18. SUPPLEMENTARY NOTES

19. KEY WORDS (Continue on reverse side if necessary and identify by block number)

20. ABSTRACT (Continue on reverse side if necessary and identify by block number)

The USAF-ASEE Summer Faculty Research Program was begun in 1975 with 22 members of engineering and science faculties from colleges and universities throughout the country. These professors were assigned to various USAF research laboratories at Wright-Patterson AFB and Eglin AFB for a ten-week period of concentrated research in their selected field and of mutual interest and benefit to the participant (and his university) and the USAF. In 1976, this program was expanded to a total of 53 faculty participants assigned to all Air Force Systems Command laboratories. In 1977, the number of participants was expanded to

DD FORM 1 JAN 73 1473 390 276 UNCLASSIFIED

70 professors and continued at that level in 1978.

LEVEL II

2

1978 USAF/ASEE SUMMER FACULTY RESEARCH PROGRAM (NON-WPAFB)

Conducted by

Auburn University

with Assistance from

Ohio State University

and

Other Installations

under

USAF Contract Number F 44620-75-C-0031

PARTICIPANTS' RESEARCH REPORTS

Volume II of II

Submitted to

Air Force Office of Scientific Research

Bolling Air Force Base

Washington, D.C.

by

J. Fred O'Brien, Jr., University Project Director
Associate Director, Engineering Extension Service
Auburn University

September 1978

1978 USAF/ASEE SUMMER FACULTY RESEARCH PROGRAM

LIST OF PARTICIPANTS

NAME/ADDRESS	DEGREE, SPECIALTY & LABORATORY ASSIGNMENT
Dr. S. Reza Ahsan Professor of Cartography & Remote Sensing Department of Geography & Geology Western Kentucky University Bowling Green, KY 42101 (502)745-4555 Ext. [redacted]	Degree: Ph.D., Geography, 1963 Specialty: Cartography & Remote Sensing, Landuse & Env. Impact Assigned: CEEDO (Tyndall) [redacted]
Dr. Jon S. Bailey Associate Professor, Psychology Dept. Florida State University Tallahassee, FL 32306 (904)644-6443 [redacted]	Degree: Ph.D., Psychology, 1970 Specialty: Developmental Psycholo & Behavior Analysis Assigned: AFHRL (Williams) [redacted]
Professor Nicola Berardi Electrical Engineering Technology Dept. MGL Building Purdue University West Lafayette, IN 47907 (317) 493-2593 [redacted]	Degree: M.S., Electrical Engineering, 1974 Specialty: Control Systems & Digital Design Assigned: RADC (Griffiss) [redacted]
Dr. Theodore S. Boilis Assistant Professor of Mathematics Dept. of Mathematical Sciences SUNY College at Oneonta Oneonta, NY 13820 (607)431-3384 [redacted]	Degree: Ph.D., Mathematics, 1971 Specialty: Analysis, Algebra, Statistics Assigned: RADC (Griffiss) [redacted]
Dr. R. Leonard Brown, Jr. Assistant Professor Applied Math/Computer Science Thornton Hall University of Virginia Charlottesville, VA 22903 (804)924-7201 [redacted]	Degree: Ph.D., Computer Science, 1975 Specialty: Numerical Methods for Digital Computers Assigned: AEDC (Arnold) [redacted]
Dr. Roger K. Bunting Associate Professor, Chemistry Dept. Illinois State University Normal, IL 61761 (309)438-7659 [redacted]	Degree: Ph.D., Chemistry, 1965 Specialty: Inorganic Chemistry Assigned: FJSRL (AF Academy) [redacted]
Dr. Paul R. Caron Professor of Electrical Engineering Southern Massachusetts University North Dartmouth, MA 02747 (617)997-9321 Ext. 355 [redacted]	Degree: Ph.D., Engineering, 1963 Specialty: Antennas, Plasmas Assigned: RADC (Hanscom) [redacted]

NAME/ADDRESS	DEGREE, SPECIALTY & LABORATORY ASSIGNMENT
Dr. Robert L. Carroll Assistant Professor Dept. of Electrical & Computer Engineering University of South Carolina Columbia, SC 29208 (803)777-4195 [redacted]	Degree: Ph.D., Electrical Engineering, 1973 Specialty: Systems Theory Control & Identification Assigned: AFATL (Eglin) [redacted]
Dr. Shyhming Chang Associate Professor of Mechanical Eng. School of Engineering California State University - Fresno Fresno, CA 93740 (209)487-2566 [redacted]	Degree: Ph.D., Solid Mechanics, 1972 Specialty: Composite Material Analysis, Structural Dynamics Assigned: AFRPL (Edwards) [redacted]
Dr. Irvin M. Citron Professor of Chemistry Fairleigh Dickinson University Rutherford, NJ 07070 (201)933-5000 Ext. 255 [redacted]	Degree: Ph.D., Chemical Education, 1969 Specialty: Analytical Chemistry (Instrumental Analysis) Assigned: AFRPL (Edwards) [redacted]
Dr. Henry D'Angelo Professor, Dept. of Mathematical Sciences Memphis State University Memphis, TN 38152 (901)454-2762 [redacted]	Degree: Ph.D., Electrical Engineering, 1964 Specialty: Modeling, Systems Theory, Microcomputer Structures Assigned: EDS (Hanscom) [redacted]
Dr. Louis A. DeAcetis Professor of Physics Bronx Community College/CUNY 181st St. & University Ave. Bronx, NY 10453 (212)367-7300 Ext. 433 [redacted]	Degree: Ph.D., Physics, 1969 Specialty: Electromagnetic Diffraction & Microwave Optics Assigned: AFATL (Eglin) [redacted]
Dr. Alan A. Desrochers Assistant Professor Dept. of Systems & Computer Engineering Boston University 110 Cummington St. Boston, MA 02215 (617)353-2808 [redacted]	Degree: Ph.D., Electrical Engineering, 1977 Specialty: Automatic Control Assigned: AFATL (Eglin) [redacted]
Dr. Richard Dobrin Professor of Physics Sarah Lawrence College Bronxville, NY 10708	Degree: Ph.D., Physics, 1971 Specialty: Radiological, Atomic, & Solid State Physics Assigned: RADC (Hanscom) [redacted]

NAME/ADDRESS	DEGREE, SPECIALTY & LABORATORY ASSIGNMENT
Dr. Philip J. Feinsilver Assistant Professor Department of Mathematics Southern Illinois University Carbondale, Il 62901 (618)453-5302	Degree: Ph.D., Mathematics, 1975 Specialty: Probability Assigned: AFRPL (Edwards) [redacted]
Dr. Robert H. Foulkes, Jr. Associate Professor Electrical Engineering Youngstown State University Youngstown, OH 44555 (216)746-1851 Ext. 423 [redacted]	Degree: Ph. D., Systems Engineering, 1970 Specialty: Control, Communication & General Systems Theories Assigned: RADC (Griffiss) [redacted]
Dr. Albert J. Frasca Associate Professor of Physics Wittenberg University Springfield, OH 45501 (513)327-7827 [redacted]	Degree: Ph.D., Nuclear Physics, 1966 Specialty: Applied Nuclear Physics/Accelerators & Dosimetry Assigned: AFWL (Kirtland) [redacted]
Dr. Robert B. Green Assistant Professor, Dept. of Chemistry West Virginia University Morgantown, WV 26506 (304)293-5220 [redacted]	Degree: Ph.D., Chemistry, 1974 Specialty: Analytical Chemistry, Spectroscopy Assigned: AFWL (Kirtland) [redacted]
Dr. Robert L. Gutmann Assistant Professor Electrical & Computer Engineering Dept. University of Massachusetts Amherst, MA 01003 (413)545-0714 [redacted]	Degree: Ph.D., Electrical Engineering, 1976 Specialty: Control Systems Assigned: AFWL (Kirtland) [redacted]
Dr. Michael Hankamer Assistant Professor Department of Electrical Engineering Texas A & I University Kingsville, TX 78363 (512)595-2001	Degree: Ph.D., Electrical Engineering, 1978 Specialty: Information Theory & Coding; Communication Systems Assigned: SAM (Brooks) [redacted]
Dr. Donald C. Haueisen Assistant Professor of Physics Pacific Lutheran University Tacoma, WA 98447 (206)531-6900 Ext. 281 [redacted]	Degree: Ph.D., Experimental Physics, 1972 Specialty: Laser Systems, Nonlinear Optics Assigned: AFWL (Kirtland) [redacted]

NAME/ADDRESS	DEGREE, SPECIALTY & LABORATORY ASSIGNMENT
Dr. William A. Hornfeck Assistant Professor of Electrical Eng. Gannon College Perry Square Erie, PA 16501 (814)456-7523 [redacted]	Degree: Ph.D., Electrical Eng. Digital Systems, 1971 Specialty: Computer Architecture/ Digital Simulation/Microprocessors Assigned: AFATL (Eglin) [redacted]
Dr. James W. Jeter, Jr. Associate Professor, Mechanical Eng. Virginia Military Institute Lexington, VA 24450 (703)463-6308 [redacted]	Degree: Ph.D., Applied Mechanics, 1972 Specialty: Dynamic Loads, Finite Elements, Structural Analysis Assigned: AFWL (Kirtland) [redacted]
Dr. Robert A. Kadlec Assistant Professor Aerospace Engineering Sciences Engineering Center, ECOT 6-16 University of Colorado Boulder, CO 80302 (303)492-7880 [redacted]	Degree: Ph.D., Aeronautics & Astronautics, 1973 Specialty: Fluid Mechanics & Plasma Physics Assigned: FJSRL (Af Academy) [redacted]
Dr. James C. Lauffenberger Associate Professor of Physics Canisius College 2001 Main Street Buffalo, NY 14208 (716)883-7000 [redacted]	Degree: Ph.D., Solid State (Surface Physics), 1965 Specialty: Optics, X-Ray Diffraction Assigned: AFRPL (Edwards) [redacted]
Dr. June K. Lee Assistant Professor Dept. of Engineering Mechanics Ohio State University 155 West Woodruff Columbus, OH 43210 (614)422-7371 [redacted]	Degree: Ph.D., Engineering Mechanics, 1976 Specialty: Continuum Mechanics, Finite Element Methods Assigned: AFATL (Eglin) [redacted]
Dr. Gordon A. Lewandowski Assistant Professor Dept. of Chemical Engineering New Jersey Institute of Technology 323 High Street Newark, NJ 07102 (201)645-5402 [redacted]	Degree: D. Eng. Sci., Chemical Engineering, 1970 Specialty: Air Pollution Control Assigned: CEEDO (Tyndall) [redacted]
Dr. James A. Liburdy Assistant Professor of Mechanical Eng. Memphis State University Memphis, TN 38152 (901) 454-2173 [redacted]	Degree: Ph.D., Mechanical Engineering, 1976 Specialty: Turbulence, Fluid Mechanics, Heat Transfer Assigned: AEDC (Arnold) [redacted]

NAME/ADDRESS	DEGREE, SPECIALTY & LABORATORY ASSIGNMENT
Dr. Robert E. Lovell Associate Professor of Engineering Industrial & Management Systems Engineering Arizona State University Tempe, AZ 85281 (602)965-2700 [redacted]	Degree: Ph.D., Systems Engineering, 1975 Specialty: Systems Engineering (Simulation by Computer) Assigned: ESD (Hanscom) [redacted]
Dr. James D. Lowther Professor, Dept. of Mechanical Engineering Louisiana Tech University Box 4875 Ruston, LA 71272 (318)256-4436 [redacted]	Degree: Ph.D., Mechanical Engineering, 1968 Specialty: Thermodynamics, Mechanical Reliability Assigned: CEEDO (Tyndall) [redacted]
Dr. John L. Lowther Associate Professor of Computer Science Dept. of Mathematics & Computer Science Michigan Technological University Houghton, MI 49931 (906)487-2183 [redacted]	Degree: Ph.D., Computer Science, 1975 Specialty: Computer Science, Mathematics, Physics Assigned: CEEDO (Tyndall) [redacted]
Dr. Robert W. McLaren Associate Professor Dept. of Electrical Engineering University of Missouri Columbia, MO 65201 (314)882-3553 [redacted]	Degree: Ph.D., Electrical Engineering, 1966 Specialty: Artificial Intelligence; Computer Engineering Assigned: RADC (Griffiss) [redacted]
Dr. Owen W. Miller Associate Professor, Industrial Eng. Room 111 University of Missouri Columbia, MO 65201 (314)882-2691 [redacted]	Degree: D.Sc., Industrial Engineering, 1966 Specialty: IE Apps., Human Factors Engr., Productivity Assigned: AFHRL (Luke) [redacted]
Professor Dean E. Nold Chairman, Dept. of Electrical Eng. Tech. Purdue University 2101 Coliseum Blvd., East Fort Wayne, IN 46805 (219)482-5738 [redacted]	Degree: M.S., Electrical Engineering, 1963 Specialty: Aviation & Fuze Systems Assigned: AFHRL (Luke) [redacted]
Dr. Russell E. Petersen Professor, Aerospace & Mechanical Eng. Aero. Bldg. 16 University of Arizona Tucson, AZ 85721 (602)884-1265 [redacted]	Degree: Ph.D., Eng. Science & Applied Physics, 1958 Specialty: Combustion/Propulsion Assigned: AFRPL (Edwards) [redacted]

NAME/ADDRESS	DEGREE, SPECIALTY & LABORATORY ASSIGNMENT
Dr. Robert Premus Associate Professor of Economics Wright State University Dayton, OH 45435 (513)873-3165 [redacted]	Degree: Ph.D., Economics, 1974 Specialty: Economic Theory, Quantitative Meth. & Reg'l Econ. Assigned: AFCEC (Tyndall) [redacted]
Dr. John E. Reissner Assistant Professor, Physical Sciences Pembroke State University Pembroke, NC 28372 (919)521-4214 Ext. 247 [redacted]	Degree: Ph.D., Chemistry, 1972 Specialty: Physical Chemistry Assigned: AEDC (Arnold) [redacted]
Dr. Charles W. Sanders Assistant Professor, Electrical Eng. University of Houston Cullen Blvd. Houston, TX 77004 (713)749-2782 [redacted]	Degree: Ph.D., Electrical Engineering, 1973 Specialty: Parameter & State Est., Optimal & Stochastic Control Assigned: ADTC (Eglin) [redacted]
Dr. Jay R. Sculley Associate Professor, Dept. of Civil Eng. Virginia Military Institute Lexington, VA 24450 (703)463-6331 [redacted]	Degree: Ph.D., Env. Engr. & Oper. Research Specialty: Operations Research, Computer Sci., Env. Engr. Assigned: AFCEC (Tyndall) [redacted]
Dr. Marvin S. Seppanen Assistant Professor, Industrial Eng. University of Alabama P. O. Box 6316 University, AL 35486 (205)348-7160 [redacted]	Degree: Ph.D., Operations Research, 1975 Specialty: Industrial Engr., Oper. Research, Computer Sci. Assigned: FJSRL (AF Academy) [redacted]
Dr. Wesley W. Shelton, Jr. Assistant Professor, Dept. Electrical Eng. Florida Institute of Technology Melbourne, FL 32901 (305)723-3201 Ext. 215 [redacted]	Degree: Ph.D., Electrical Engineering, 1974 Specialty: Electrical/Biomedical Eng. & Biophysics Assigned: SAM (Brooks) [redacted]
Dr. Rex D. Stith Associate Professor Dept. of Physiology & Biophysics Health Sciences Center University of Oklahoma P. O. Box 26901 Oklahoma City, OK 73190 (405)271-2243 [redacted]	Degree: Ph.D., Physiology, 1971 Specialty: Endocrinology, Neuroendocrinology Assigned: SAM (Brooks) [redacted]

NAME/ADDRESS	DEGREE, SPECIALTY & LABORATORY ASSIGNMENT
Dr. Timothy F. Thomas Associate Professor, Dept. of Chemistry University of Missouri-Kansas City Kansas City, MO 64110 (816)276-1555 [redacted]	Degree: Ph.D., Chemistry, 1964 Specialty: Physical Chemistry (Photochemistry & Chem. Kinetics) Assigned: AFGL (Hanscom) [redacted]
Dr. Kenneth W. Wegner Associate Professor, Education 305 McGuinn Hall Boston College Chestnut Hill, MA 01267 (617)969-0100 Ext. 4079 [redacted]	Degree: Ed.D., Counseling Psych. (Educ. Psych.), 1961 Specialty: Psychological Testing, Behavioral Analysis, Training Assigned: AFISC (Norton) [redacted]
Dr. Thomas A. Williamson Assistant Professor College of Engineering & Technology Northern Arizona University Flagstaff, AZ 86011 (602)523-3589 [redacted]	Degree: Ph.D., Electrical Eng. & Computer Science Specialty: Nuclear Electronics Assigned: AFWL (Kirtland) [redacted]

PARTICIPANT LABORATORY ASSIGNMENT

1978 USAF/ASEE SUMMER FACULTY RESEARCH PROGRAM

AFCEC AIR FORCE CIVIL ENGINEERING CENTER (TYNDALL AIR FORCE BASE)
1. Dr. Robert Premus - Wright State University
2. Dr. Jay Raymond Sculley - Virginia Military Institute

CEEDO DET 1 (CIVIL & ENVIRONMENTAL ENGINEERING DEV. OFFICE), HQ ADTC(AFSC) (TYNDALL AIR FORCE BASE)
1. Dr. S. Reza Ahsan - Western Kentucky University
2. Dr. Gordon Lewandowski - New Jersey Institute of Technology
3. Dr. James David Lowther - Louisiana Tech University
4. Dr. John L. Lowther - Michigan Technological University

ADTC AIR FORCE ARMAMENT LABORATORY (ELGIN AIR FORCE BASE)
1. Dr. Robert L. Carroll - University of South Carolina
2. Dr. Louis Anthony DeAcetis - Bronx Community College/Cuny
3. Dr. Alan Alfred Desrochers - Boston University
4. Dr. William Alfred Hornfeck - Gannon College
5. Dr. June K. Lee - Ohio State University
6. Dr. Charles Woodford Sanders - University of Houston

RADC/ET ROME AIR DEVELOPMENT LABORATORY (HANSCOM AIR FORCE BASE)
1. Dr. Paul R. Caron - Southern Massachusetts University
2. Dr. Richard Dobrin - Long Island University

ESD ELECTRONICS SYSTEMS DIVISION (HANSCOM AIR FORCE BASE)
1. Dr. Henry D'Angelo - Memphis State University
2. Dr. Robert E. Lovell - Arizona State University

AFGL AIR FORCE GEOPHYSICS LABORATORY (HANSCOM AIR FORCE BASE)
1. Dr. Timothy F. Thomas - University of Missouri-Kansas City

FJSRL FRANK J. SEILER RESEARCH LABORATORY (AIR FORCE ACADEMY)
1. Dr. Robert A. Kadlec - University of Colorado
2. Dr. Roger K. Bunting - Illinois State University
3. Dr. Marvin S. Seppanen - University of Alabama

AEDC ARNOLD ENGINEERING DEVELOPMENT CENTER (ARNOLD AIR FORCE BASE)
1. Dr. R. Leonard Brown, Jr. - University of Virginia
2. Dr. James A. Liburdy - Memphis State University
3. Dr. John Eric Reissner - Pembroke State University

AFRPL AIR FORCE ROCKET PROPULSION LABORATORY (EDWARDS AIR FORCE BASE)
1. Dr. Philip J. Feinsilver - University of Utah
2. Dr. James C. Lauffenburger - Canisius College
3. Dr. Irvin M. Citron - Fairleigh Dickinson University
4. Dr. Shyhming Chang - California State University
5. Dr. Russell E. Petersen - University of Arizona

PARTICIPANT LABORATORY ASSIGNMENT Continued

RADC .ROME AIR DEVELOPMENT CENTER (GRIFFISS AIR FORCE BASE)
1. Robert H. Foulkes, Jr. - Youngstown State University
2. Dr. Theodore S. Bolis - Syny College at Oneonta
3. Dr. Robert W. McLaren - University of Missouri
4. Nicola Berardi - Purdue University

SAM SCHOOL OF AEROSPACE MEDICINE (BROOKS AIR FORCE BASE)
1. Dr. Michael Hankamer - New Mexico State University
2. Dr. Wesley W. Shelton - Florida Institute of Technology
3. Dr. Rex D. Stith - University of Oklahoma

AFHRL-FT AIR FORCE HUMAN RESOURCES LABORATORY (WILLIAMS AIR FORCE BASE)
1. Jon S. Bailey - Florida State University

AFHRL-FT AIR FORCE HUMAN RESOURCES LABORATORY (LUKE AIR FORCE BASE)
1. Dr. Owen W. Miller - University of Missouri
2. Dean E. Nold - Purdue University

AFWL AIR FORCE WEAPONS LABORATORY (KIRTLAND AIR FORCE BASE)
1. Dr. Albert J. Frasca - Wittenberg University
2. Dr. Robert B. Green - West Virginia University
3. Dr. Robert L. Gutmann - University of Massachusetts
4. Dr. Donald C. Haueisen - Pacific Lutheran University
5. Dr. James W. Jeter, Jr. - Virginia Military Institute
6. Dr. Thomas A. Williamson - Northern Arizona University

AFISC HQ,USAF INSPECTION AND SAFETY CENTER (NORTON AIR FORCE BASE)
1. Dr. Kenneth W. Wegner - Boston College

RESEARCH REPORTS

1978 USAF/ASEE SUMMER FACULTY RESEARCH PROGRAM

VOLUME I

Report No.	Title	Research Associates
1	Environmental Remote Sensing for Air Force Resource Management	Dr. S. Reza Ahsan
2	Control of JP-4 Emissions from Underground Storage Tanks	Dr. Gordon A. Lewandowski
3	Forestry Lands Allocated for Managing Energy (Flame) Feasibility Study	Dr. James D. Lowther
4	Sensitivity Analysis of Air Quality Assessment Model Predictions for Air Force Operations	Dr. John L. Lowther
5	A Comprehensive Socioeconomic Impace Assessment Model	Dr. Robert Premus
6	The Environmental Technical Information System for Air Force Use	Dr. Jay R. Sculley
7	Adaptively-predictive Linear Optimal Guidance: Target Seeking	Dr. Robert L. Carroll
8	Wide-Band Radome Research in Refractive Error Correction	Dr. Louis A. DeAcetis
9	Analysis of a Zoom Chain Optical System	Dr. Alan A. Desrochers
10	Data System Architectures for Stores Management Systems	Dr. William A. Hornfeck
11	A Three-dimensional Elastic-Plastic Analysis of High Velocity Impace Problems By a Finite Element Method	Dr. June K. Lee
12	On-Line Spectral Estimation Via Maximum Entropy Processing	Dr. Charles W. Sanders
13	Advanced Acquisition/Strike System Guidance Techniques	Robert H. Foulkes, Jr.
14	Application of Bayesian Techniques to Reliability Demonstration Estimation and Updating of the Prior Distribution	Dr. Theodore S. Bolis

RESEARCH REPORTS (Continued)

Report No.	Title	Research Associates
15	Digital Image Processing: Design Considerations for Future Systems	Dr. Robert W. McLaren
16	Clutter Suppression Through Radar Polarization Processing	Nicola Berardi
17	Measuremnet of Photodissociation Cross Sections of Water Cluster Ions	Dr. Timothy F. Thomas
18	A Quantitative Approach to Aggregation in the Modeling of Tactical Command and Control Systems	Dr. Henry D'Angelo
19	Specialized Stimulation Concepts for Command-Control-Communications-Intelligence (C^3I) Systems	Dr. Robert E. Lovell
20	Overlapped Sub-Array Techniques for Use in a Space Radar	Dr. Paul R. Caron
21	Design of an Imaging System to Conduct Human Thermal Signature Analysis with a 256 Element Schottky Barrier IRCCD Detector	Dr. Richard Dobrin
VOLUME II		
22	Investigation of the Computational Aspects of the Numerical Solution of Flow on a Core	Dr. R. Leonard Brown
23	Numerical Investigations of Natural Convection Inside of a Finite Horizontal Cylinder	Dr. James A. Liburdy
24	Gas Sampling Probe Computer Program	Dr. John Eric Reissner
25	The Application of Laser Doppler Velocimetry to the Study of Vortex Formation and Propagation in Unsteady Separated Flows	Dr. Robert A. Kadlec
26	Physical Properties of Molten Chloroaluminate Salt Systems	Dr. Roger K. Bunting
27	Technical Planning for the USAF Standard Base Supply System (SBSS); Rimstop and Beyond	Dr. Marvin S. Seppanen
28	Engineering Equations Verification Study: X-Ray Deposition Analysis	Dr. Philip Feinsilver
29	Target Materials for Low Energy X-Ray Sources	Dr. James C. Lauffenburger

RESEARCH REPORTS (Continued)

Report No.	Title	Research Associates
30	The Quantitative Determination of Trace Levels of Titanium in Hydrazine	Dr. Irvin M. Citron
31	Evaluation of Current Research in Fracture and Failure Behavior of Solid Propellant	Dr. Shyhming Chang
32	An Investigation of Critical Erosion Analysis Deficiencies	Dr. Russell E. Petersen
33	Adaptive/Predictive Data Compression for Electrocardiagrams	Dr. Michael Hankamer
34	In Vitro Study of Microwave Effects on Calcium Efflux in Rat Brain Tissue	Dr. Wesley W. Shelton, Jr.
35	Effect of Microwave Exposure on Certain Neuro-endocrine Parameters in Various Regions of the Rat Brain	Dr. Rex D. Stith
36	Applied Behavior Analysis in Flying Training Research	Dr. Jon S. Bailey
37	A Proposed Model System: Production Planning and Control for a Research and Development Function	Dr. Owen W. Miller
38	Using Fourier Coefficients as a Proposed Indicator of ACM Pilot Tracking Skills (Terminal Phase) for the Simulator for Air-to-Air Combat (SAAC)	Dean E. Nold
39	Neutron Production from Collective Ion Acceleration and Plasma Heating Experimentation Using a 6MeV 150 Kiloampere Field Emission Generator	Dr. Albert J. Frasca
40	Laser-Induced Fluorescence Studies of SnO and PbF	Dr. Robert B. Green
41	Adaptive Identification and Control of a Gimbaled Laser Pointing and Tracking System	Dr. Robert L. Gutmann
42	Nonlinear Adaptive Optics	Dr. Donald C. Haueisen
43	Inelastic Dynamic Response of Reinforced Concrete	Dr. James W. Jeter
44	Optimized Procedures for Radiation Testing of LSI Circuit Technology	Dr. Thomas A. Williamson
45	Relationship of Fighter Pilot-Operator Age and Flying Experience to Selected Unsafe Acts and Psychophysiological and Environmental Variables in Major/Class A Mishaps	Dr. Kenneth W. Wegner

1978 USAF-ASEE SUMMER FACULTY RESEARCH PROGRAM
sponsored by
THE AIR FORCE OFFICE SCIENTIFIC RESEARCH
conducted by
AUBURN UNIVERSITY AND OHIO STATE UNIVERSITY

PARTICIPANT'S FINAL REPORT

INVESTIGATION OF THE COMPUTATIONAL ASPECTS OF THE NUMERICAL SOLUTION OF FLOW ON A CONE

Prepared by:	R. Leonard Brown, Ph.D.
Academic Rank:	Assistant Professor
Department and University:	Dept. of Applied Mathematics and Computer Science School of Engineering and Applied Science University of Virginia
Assignment:	
(Air Force Base)	Arnold Air Force Station
(Laboratory)	Arnold Engineering Development Center
(Facility)	von Karman Gas Dynamics Facility
(Branch)	Aerodynamic Projects
Research Colleague:	John C. Adams, Ph.D. (ARO, Inc.)
Date:	August 18, 1978
Contract No:	F44620-75-C-0031

INVESTIGATION OF THE COMPUTATIONAL ASPECTS OF THE NUMERICAL SOLUTION OF FLOW ON A CONE

by
R. Leonard Brown

ABSTRACT

The incompressible fluid flow around a cone at hypersonic speed and high angle of attack is modelled by a parabolic system of nonlinear partial differential equations expressing conservation of mass, momentum, and energy, and an algebraic equation of state. Typical flow variables are functions of density, velocity, and energy with respect to position in a body centered coordinate system. In such a system, x is distance along the cone generator, η is normal to the cone surface and relative to the shock stand off distance computed by other means, and ϕ is a circumferential coordinate going from 0° at the windward side to 180° at leeward.

By stating the equation as a boundary value partial differential system in η and ϕ and an initial value problem in x, a numerical marching technique in x from a point near the cone tip onward along the cone can be used. An implicit formula is used to insure a stable numerical process. A computer implementation due to Lubard and Helliwell (RDA-TR-150, R&D Associates, Santa Monica, CA) is used at AEDC to model behavior of high speed, high angle of attack cones, and requires large amounts of computer time.

The most time consuming portion of this code involves solving block tridiagonal systems of equations. The cost of the block method based on tridiagonal systems with scalar elements is proportional to $7n\ m^3/3$ where there are n blocks of m by m matrices.

Profile Gaussian elimination was found to cost $10n\ m^3/3$. A method based on iterative residual correction was found to reduce the cost of running certain problems, depending on what percentage of iterations converged. The method was programmed with heuristic devices to determine whether or not to use residual correction.

ACKNOWLEDGEMENT

The author appreciates the support of this summer research by the Air Force Systems Command. The efforts of Mr. Fred O'Brien, who administered the program in behalf of Auburn and the American Society for Engineering Education, contributed greatly to making this a productive summer and a smoothly running program.

The efforts of Dr. J. C. Adams of the Aerodynamics Project Branch of the von Karman Gas Dynamics Facility at AEDC to introduce an interesting problem and provide the researcher with a simple starting model contributed much to the author's productivity. The sample problems provided by Dr. A. W. Mayne also advanced the work. The author is grateful to all the staff members with whom he interacted in discussions of many topics, and thanks them for making him at home in their research community.

INTRODUCTION

The incompressible fluid flow around a cone at hypersonic speed and angle of attack $\alpha \geq 0$ is modelled by a parabolic system of non-linear partial differential equations expressing conservation of energy, mass, and momentum, plus an algebraic equation of state. Typical flow variables are functions of density, velocity and energy. The asymptotic (steady-state) solution in three dimensions is sought. A suitable coordinate system for a cone shaped object uses the variables x, the length from the tip along the cone generator; η the normal to the surface relative to the bow shock stand-off distance ($\eta = y/d(x,\phi)$ where y is perpendicular to x and d is the bow shock stand-off distance computed from theory); and ϕ, the circumferential angle from $\phi = 0°$ at the windward side to $\phi = 180°$ at the leeward side, see Fig. 1. Flow Separation is likely to occur at the leeward side at significant angle of attack $\alpha > 0$, and standard numerical methods have proven inadequate to model this case, so special computer methods have been developed for it.

Beam and Warming (Ref. 1) have treated this problem as a parabolic boundary value problem in ϕ and η since theoretical results are available on the behavior of the bow shock, and as an initial value problem in x which allows a marching type numerical solution to be generated given an initial condition away from the point x = 0. They treated the more general hyperbolic system

$$\frac{\partial U}{\partial x} + \frac{\partial F(U)}{\partial \eta} + \frac{\partial G(U)}{\partial \phi} = \frac{\partial V(U,\ \partial U/\partial \eta,\ \partial U/\partial \phi)}{\partial \eta} + \frac{\partial W(U,\ \partial U/\partial \eta,\ \partial U/\partial \phi)}{\partial \phi} \qquad (1)$$

Where U is the m-dimensional state vector, F and U are given vector functions of U, and V and W are vector functions of U. Steady state Navier-Stokes equations are a special case of (1). For the purpose of illustration, let the right hand side of (1) be 0, giving the equation for inviscid flow. A discussion of boundary and inital condiitons can be found in (ref. 2). By using a finite difference scheme in η and ϕ for the boundary value problem, a one-step implicit integration scheme in x can be employed to solve the initial value problem. For the implementation of Lubard and Helliwell (Ref. 2), central differences

$$\frac{\partial U}{\partial \eta} = \frac{1}{2\Delta\eta}\left(U(\eta_{j+1},\ \phi_k) - U(\eta_{j-1},\ \phi_k)\right) \qquad (2)$$

$$\frac{\partial^2 U}{\partial \phi^2} = \frac{1}{\Delta\phi^2}\left(U(\eta_j,\ \phi_{k-1}) - 2U(\eta_j,\ \phi_k) + U(\eta_j,\ \phi_{k+1})\right) \qquad (3)$$

are used with the Backward Euler implicit formula

$$U(x_{i+1},\ \eta_j,\ \phi_k) = U(x_i,\ \eta_j,\ \phi_k) + \Delta x\ \partial U(x_{i+1},\ \eta_j,\ \phi_k)/\partial x \qquad (4)$$

Stability considerations derived from considering the numerical solution of an associated linearized system of equations leads to both lower and upper bounds on Δx as a function of $\Delta\eta$ and $\Delta\phi$ (Ref. 2).

To understand the implementation, consider the linearized problem for $A = \partial F/\partial U$ and $B = \partial G/\partial U$ given as

$$\frac{\partial U}{\partial x} + A\frac{\partial U}{\partial \eta} + B\frac{\partial U}{\partial \phi} = 0 \tag{5}$$

Applying the trapexoidal rule $U(x_{i+1}) = U(x_i) + \frac{\Delta x}{2}\left(\frac{\partial U(x_{i+1})}{\partial x} + \frac{\partial U(x_i)}{\partial x}\right)$, a more accurate implicit scheme than Backward Euler, and using a truncated Taylor Series for F(U) and G(U) given by

$$F^{i+1} = F^i + A^i\,(U(x_{i+1}) - U(x_i)) + o(\Delta x^2)$$

$$G^{i+1} = G^i + B^i\,(U(x_{i+1}) - U(x_i)) + o(\Delta x^2)$$

yields the system of linear equations

$$\left[I + \frac{\Delta x}{2}\left(\frac{\partial A^i}{\partial \eta} + \frac{\partial B^i}{\partial \phi}\right)\right] U^{i+1} = \left[I + \frac{\Delta x}{2}\left(\frac{\partial A^i}{\partial \eta} + \frac{\partial B^i}{\partial \phi}\right)\right] U^i - \Delta x\left(\frac{\partial F}{\partial \eta} + \frac{\partial G}{\partial \phi}\right) \tag{6}$$

This large, sparse system can be solved by methods such as alternating direction implicit (ADI) method of Douglas (Ref. 3) which solves only the equation in η first, then the equations in ϕ. Beam and Warming introduce an error of $(\Delta x)^3$ in an approximate factorization scheme based on Peaceman and Rachford (Ref. 4) by replacing (6) with

$$\left(I + \frac{\Delta x}{2}\frac{\partial A^i}{\partial \eta}\right)\left(I + \frac{\Delta x}{2}\frac{\partial B^i}{\partial \phi}\right) U^{i+1} = \left(I + \frac{\Delta x}{2}\frac{\partial A^i}{\partial \eta}\right)\left(I + \frac{\Delta x}{2}\frac{\partial B^i}{\partial \phi}\right) U^i - \Delta x\left(\frac{\partial F}{\partial \eta} + \frac{\partial G}{\partial \phi}\right) + o(\Delta x^3) \tag{7}$$

Since the error introduced is of the same order Δx^3 as the error in the trapezoidal rule, stability is not affected. This equation can then be solved in two levels

$$\left(I + \frac{\Delta x}{2}\frac{\partial A^i}{\partial \eta}\right)\Delta U^* = -\Delta x\left(\frac{\partial F}{\partial \eta} + \frac{\partial G}{\partial \phi}\right),$$

$$\left(I + \frac{\Delta x}{2}\frac{\partial B^i}{\partial \phi}\right)\Delta U^i = \Delta U^*,$$

$$U^{i+1} = U^i + \Delta U^i.$$

This method has several disadvantages. If used with a more accurate difference method, the error introduced in the factorization will lower the error order of the method; however, if used with a lower order method such as the Backward Euler, good results could be expected. However, Lubard and Helliwell note that the difference in ϕ near $\eta = 0$ has a singularity there, and use instead a method that uses the factorization (7) in η but solves for each set of solutions at each ϕ_k in sequence $\phi_o = 0°$ to $\phi_k = 180°$ in steps of $\Delta\phi$. This is done iteratively until the computation converges. At each ϕ_k, the resulting system of linear equations is an n by n block tridiagonal matrix of block size m by m where i=1,...,n for η_i and m = 6, the number of states at each point. The method is comparable to a Gauss-Seidel iteration with each element of the solution replaced by a $(n*m)^2$ size linear equation.

OBJECTIVES

The method of Lubard and Helliwell (Ref. 2) has been programmed as a production code and is used at AEDC in several areas, including turbulent flow and flow separation determinations. The major computational effort involves solving, for each ϕ_k, k = 1, K, the tridiagonal system of n blocks of 6 by 6 matrices. Currently, a method due to Isaacson and Keller (Ref. 5) is used based on a scalar tridiagonal factorization scheme which requires the inversion (factorization) of only the blocks on the diagonal. The cost of this block tridiagonal effort was computed in terms of machine operations (multiplications and divisions, which use much more execution time than other arithmetic operations) and this cost was compared to that of numerical techniques based on existing technology. Conditions under which these methods might perform faster than the current method were found, and tests on several problems were carried out to determine if the predicted cost reductions were realized. For these test cases, total computation time on the IBM 370/165 was used as the cost. Thus, any increase in overhead of the proposed new method over the original method, which might cancel the expected decrease in cost, could be identified.

The objective of the research program of Summer, 1978, was to provide a production FORTRAN code of an improved block tridiagonal linear system solver that could be used directly by the Lubard-Helliwell code and that regularly reduces computation costs on some production problems, and otherwise recognizes when no savings are possible and reverts to the original method.

BLOCK TRIDIAGONAL FACTORIZATION

Each of the k systems of equations

$$Z_k \, \Delta U = \begin{bmatrix} B_2 & C_2 & & & \\ A_3 & B_3 & C_3 & & \\ & \ddots & \ddots & & \\ & & A_{n-1} & B_{n-1} & C_{n-1} \\ & & & A_n & B_n \end{bmatrix} \Delta U = \begin{bmatrix} d_2 \\ d_3 \\ \vdots \\ d_{n-1} \\ d_n \end{bmatrix} \tag{8}$$

is solved for the update vector ΔU of $U^{i+1} = U^i + \Delta U$. The current solution algorithm from (Ref. 2) is

(decomposition)

$$\hat{B}_2 \leftarrow B_2$$

$$G_2 \leftarrow B_2^{-1} C_2$$

$$\left.\begin{aligned} \hat{B}_i &\leftarrow B_i - A_i G_{i-1} \\ G_i &\leftarrow \hat{B}_i^{-1} C_i \end{aligned}\right\} \quad i=3,4,\ldots,n$$

(forward substitution)

$$Y_2 \leftarrow \hat{B}_2^{-1} d_2$$

$$Y_i \leftarrow \hat{B}_i^{-1} (d_i - A_i Y_{i-1}) \quad i=3,4,\ldots,n$$

(back substitution)

$$U_n \leftarrow Y_n$$

$$U_i \leftarrow Y_i - G_i Y_{i+1} \quad i=n-1,\ldots,2$$

Here $G_i \leftarrow \hat{B}^{-1} C_i$ is actually solved by performing LU decomposition of the m by m matrix $\hat{B}_i$ and solving for each column of G_i using the corresponding column of C_i as the right hand side. It was noted that the code decomposed each $\hat{B}_i$ twice, once in the decomposition step and again in back substitution. The code was reordered and subroutine LEQ was replaced by DECOMP and SOLVE (Ref. 6) which stores the decomposition for reuse. The new code is

(decomposition; forward substitution)

$$\hat{B}_2 \leftarrow B_2$$

$$G_2 \leftarrow \hat{B}_2^{-1} C_2$$

$$Y_2 \leftarrow \hat{B}_2^{-1} d_2$$

$$\left.\begin{aligned} \hat{B}_i &\leftarrow B_i - A_i G_{i-1} \\ G_i &\leftarrow \hat{B}_i^{-1} C_i \\ Y_i &\leftarrow \hat{B}_i^{-1} (d_i - A_i Y_{i-1}) \end{aligned}\right\} \quad i=2,3,\ldots,n$$

(back substitution)

$$U_n \leftarrow Y_n$$

$$U_i \leftarrow Y_i - G_i Y_{i+1} \quad i = n-1, \ldots,2$$

This method requires $8nm^3/3 + 4nm^2 + o(n)$ machine operations. An improvement over this value is sought. The reordered method requires $7nm^3/3 + 4nm^2$ operations.

First, profile Gaussian Elimination without pivoting, which would not change the block tridiagonal structure of the matrix Z, was studied. In this case, the cost can be computed for each m rows of the matrix. For the first row, the multiplier $m_{i1} = a_{i1}/a_{11}$ must be formed for m-1 rows, then each element of the remaining (2m-1) columns must be formed as $\hat{a}_{ij} = a_{ij} - m_{i1} a_{1j}$. For the next (m-1) rows, (m-k) multipliers $m_{ik} = a_{ik}/a_{kk}$, $k = 2,\ldots,m$ must be formed, and (2m-k) values of column elements modified. For the next m rows, a multiplier must be found and (3m-k+1) elements modified. This gives (m-k)(2m-k) + m(3m-k+1) operations for each of k=1,...,m, since on completion of each block, the next block is of the same form. See Fig. 2 for a diagram of the reduction. The cost is thus $n(\frac{10}{3} m^3 + o(m^2))$ which is twice the number of operations used by the block tridiagonal scheme, with no expected reduction in overhead. It can be concluded that, of all direct methods for solving a block tridiagonal system, the block tridiagonal scheme is nearly optimal since only the blocks on the diagonal must be decomposed ($m^3/3$ operations) and, since any decomposition is equivalent to Gaussian Elimination, $o(m^3)$ operations are required. Thus, the 7/3 coefficient of the cost of the reordered block tridiagonal method is quite low.

As an alternative, an iterative method that takes advantage of the physical problem can be considered. Due to the use of a finite difference scheme, the matrix Z_k will vary slowly with x and with ϕk, and thus a previous decomposition $LU = Z_{k-p}$ can be considered as a decomposition of Z_k with a large error. This is the basis for the method of residual correction of the system Ax = b, where A has been decomposed as A = LU, and y^o is the initial approximation of the solution.

step 0) $i \leftarrow 0$; $y^i \leftarrow y^o$

step 1) $r^i \leftarrow b - Ay^i$

step 2) $LU\,\Delta y^i = r^i$

step 3) $y^{i+1} = y^i + \Delta y^i$

} $i = 1,\max$

for max = maximum iterations allowed. Of course, any time $||\Delta y^i||$ becomes small, the iteration can stop. The method is guaranteed to converge monotonically for <u>any</u> y^o, if $||I-(LU)^{-1}A|| < 1$ in some norm, even if LU was computed independently of A.

Since Z_k is slowly varying, rather than using the block tridiagonal scheme for each k, one can use $\hat{B}_i$ and G_i from Z_p, $p<k$, and A_k from the current Z_k and use residual correction. This is equivalent to $Z_k \doteq L_k U_p$.

If this does not converge, the Block Tridiagonal decomposition can be updated. Additional storage is required for at least the $\hat{B}_i$, G_i computed in the decomposition, or an additional $2nm^2$ storage locations for each decomposition. If a full decomposition is stored for each value of ϕ, this becomes very large. However, since Z_k also varies slowly with ϕ_k usually only one to three decompositions, evenly spaced between 0° and 180°, need be stored. This was verified experimentally. The algorithm is

Step 0) find $L_o U_o = Z_o$,

$y_o \leftarrow (L_o U_o)^{-1} d_o$,

$k \leftarrow 0$,

$p \leftarrow 0$;

Step 1) $k \leftarrow k + 1$,

compute Z_k, d_k,

$y_k \leftarrow 0$

$r^o \leftarrow d_k$,

$i \leftarrow 0$;

Step 2) $\Delta y_k^i \leftarrow (L_k U_p)^{-1} r^i$

$y_k^{i+1} \leftarrow y_k^i + \Delta y_k^i$;

if $||\Delta y_k^i|| < EPS$, to to step 1;

if $i < \max$, $i \leftarrow i + 1$, $r^i \leftarrow d_k - Z_k y_k^i$,

go to step 2;

Step 3) else set $p \leftarrow k$, $L_p U_p = Z_k$,

$y_k = (L_k U_k)^{-1} d_k$,

go to step 1.

The test for convergence, $||\Delta y|| < EPS$, should be a relative error test due to the different orders of magnitude of the state vectors. Since the tridiagonal system actually computes ΔU, an update to U, these values from the previous step can be saved and $EPS_j = .01 * \Delta U_j$ has be verified experimentally to be an accurate error limit.

Figure 3 is a structured flow chart of a subroutine SOLVEQ which implements this algorithm.

The cost of this algorithm is dependent on R, the fraction of cases when the residual correction converges, and q, the average number of steps per convergent iteration. The cost of each residual correction is $3nm^2$ plus calculation of the residual; for $q \leq 2$, this can be ignored since the initial residual is taken to be d, the right hand side, corresponding to a zero solution. For the improved method to be better than the original method,

$$n(Rq3m^2 + (1-R)(max * 3m^2 + 7m^3/3 + 4\ m^2) < 8nm^3/3 + 4nm^2 \qquad (9)$$

is required. R depends on max and EPS, being larger for larger max and for larger EPS. Experiments verify this and provided justification for a method which automatically picks max after a number of iterations are sampled.

NUMERICAL RESULTS

A one dimensional time-dependent flow of an inviscid perfect gas through a converging-diverging nozzle was programmed using the SOLVEQ subroutine from the Lubard-Helliwell code. There are m=3 dependent variables, and a spacing in the x dimension of 51 units from 0.0 to 1.0 in a relative coordinate system. The minimum nozzle diameter occurs at .26, where the velocity should be 1 (Mach number). The example is from (Ref. 7). The problem was run with the residual correction algorithm for 200 steps at constant Δt, and the solutions with relative error EPS = 0.001, max = 3, gave results identical to the Lubard-Helliwell answers to three decimal places. Data were collected to determine R, the fraction of residual correction steps that converged, and q, the number of steps per successful iteration. R was found to be .995 $\doteq$ 1., and q = 2.63. Thus, the cost for residual correction was dependent on qn * 3 m^2 = 3621, while the original was dependent on 7n $m^3/3$ = 3213. Thus, it is expected that execution time (8.5 sec) for the original method be smaller than execution time (9.9 sec) for residual correction. In fact, whenever max = q $\geq$ 5m/9, no increase in performance can be expected. Values of max should normally be at least 2, so this case is representative.

However, this example proved the accuracy of the basic residual correction code imbedded in SOLVEQ, and also verified the formula for predicting cost.

The actual Lubard-Helliwell code was tested on three real problems. On the first one, using turbulence and zero angle of attack, and only three values of ϕ (0°, 90°, 180°), various combinations of max and EPS were used to determine their effect on R and q. These data used to implement a heuristic to determine max dynamically during execution, and to determine when the residual correction method is inappropriate.

For the turbulence case, one extra storage array is needed for $\hat{B}_i$ and G_i, i = 1, ..., n, to store the previous decomposition U_p of $Z_k = L_k\ U_p$. Each is dimensioned (6, 6, 50) so 3600extra single precision storage elements are required. Since the actual value of the state vector U is not passed to SOLVEQ, the relative error is based on the $||\Delta U_i||_\infty$ computed in the previous step, and requires only 6 storage elements to keep the largest ΔU_i computed in the previous step. Table I summarizes the test results as EPS and max were varied.

TABLE I

COST VS PARAMETERS TO SOLVEQ

CASE	EPS	MAX	R(%)	q	T(SEC)
1	0.001	3	31	2.10	359
2	0.01	2	28	1.99	325
3	0.001	2	22	1.99	340
4	0.001	6	32	2.68	384
5	0.01	3	33	2.44	328

Comparison of the results of the residual correction computation with those of the original code showed agreement to five decimal places and no tendency to instability, even for EPS = 0.01. The original method ran 597 sec. On the basis of this chart, a number of experiments were made on this problem and on a second problem using 19 values of ϕ from 0° to 180° in increments of 10° for laminar flow and α = 5°. The following conclusions were drawn.

Only one set $\hat{B}_i$, G_i need be stored since for small $\Delta\phi$, the variation from ϕ_i to ϕ_{i+1} on the same pass is smaller than the variation from one pass to the next for the same value of ϕ. Thus, only 3600 single precision words of extra space is needed. Setting max = $\lceil q \rceil$, the next integer larger than r, causes little decrease in R but can effectively reduce cost compared to a larger max. Also, a good estimate of R and q is available after about 200 systems are solved.

These results, together with (9), can be implemented in a heuristic method to calculate max and to cut off use of the residual correction method if it will not be cost effective. The method initialize max to 10, then whenever the residual correction method converges max is changed to the largest of max -1, 2, $\hat{q}$; whenever it does converge max is set to the smallest of max + 1, 10, and $\hat{q}$, where $\hat{q}$ is the average number of iterations in each successful residual correction calculation. If, after 200 systems are solved, the expected cost of residual correction is more than for the original method, residual correction will no longer be used. By setting q = max, the asymptotic value of max under the heuristic, a cost saving will occur when

$$Rq3m^2 + (1-R)(q\ 3m^2 + 7m^3/3 + 4m^2) < 8m^3/3 + 4m^2 \qquad (10)$$

which reduces to $(q-m/9)/R < 7m/9 + 4/3$.

Table II gives the computation times for the original and improved SOLVEQ for three problems; turbulence at α = 0°, laminar flow at α =5°, and a biconic restart problem. In the last two cases, residual correction is shut off after 200 systems are solved.

TABLE II

STATISTICS FROM 3 TEST RUNS

	R	q	t(sec)	t(sec)-Original Method
Turbulence	0.93	2.00	221	597
Laminar, $\alpha = 5$	0.76	4.97	1478	1021
Biconic Restart	0.54	4.55	1505	977

CONCLUSIONS AND RECOMMENDATIONS

It can be concluded that, of all deterministic algorithms for solving a block tridiagonal system of equations, the currently used one is of minimum order nm^3 and has the lowest known coefficient, 7/3. It is also now known that an iterative method based on residual correction of an inexact decomposition of the matrix can sometimes be used to find such solutions faster; the cases for which this happens can be determined by gathering statistics R and q early in the run and discontinuing the iterative procedure if it is found inappropriate. A computer code implementing this is being provided to AEDC.

Further research into techniques to reduce computation time is recommended. Areas that may prove fruitful are listed here. Changing from finite differences to finite elements may give greater accuracy in representing the boundary value problems in η and ϕ; proper numbering of the nodes can minimize the bandwidth of the resulting linear systems. Multistep methods such as Backward Differentiation Formulas (Ref. 8) may allow larger step sizes to be taken. For a fixed step size Δx, a stability analysis for both minimum and maximum Δx in terms of $\Delta\eta$ and $\Delta\phi$ must be made; since this is more complicated than for one step methods, it should be done using computer assisted character manipulation. However, there exists several multipurpose codes which change both the method order and the step size dynamically, and implementation of the model using one of these should be attempted. Also, the existing limits on Δx are derived from a linearized model. The stability of the actual nonlinear system should be investigated using computational methods currently being developed by the author and others.

REFERENCES

1. Beam, R. M. and R. F. Warming, "An Implicit Finite-Difference Algorithm for Hyperbolic Systems in Conservation Law Forum," Journal Computational Physics, 22, pp. 87-110 (1976).

2. Lubard, S. C. and W. S. Helliwell "Calculation of the Flow on a Cone at High Angle of Attack," RDA-TR-150, R&D Associates, Santa Monica, CA. (1973).

3. Douglas, J. and G. E. Gunn "A General Formulation of Alternating Direction Methods," Num. Math., 6, pp. 428-253 (1964)

4. Peacemen, D. W. and H. H. Rachford "The Numerical Solution of Parabolic and Elliptical Differential Equations," SIAM Journal, 3, pp. 28-41, (1955).

5. Isaacson, E. and H. B. Keller "Analysis of Numerical Methods, John Wiley and Sons, New York (1966).

6. Forsythe, G. E., M. A. Malcolm, and C. B. Moler, Computer Methods for Mathematical Computations, Prentice-Hall, Englewood Cliffs, N. J. (1977).

7. Beam, R. M. and R. F. Warming, "An Implicit Factored Scheme for the Compressible Navier-Stokes Equations," AIAA Journal, 16, pp. 393-402 (1978).

8. Gear, C. W., Numerical Initial Value Problems in Ordinary Differential Equations, Prentice-Hall, Englewood Cliffs, N. J. (1971).

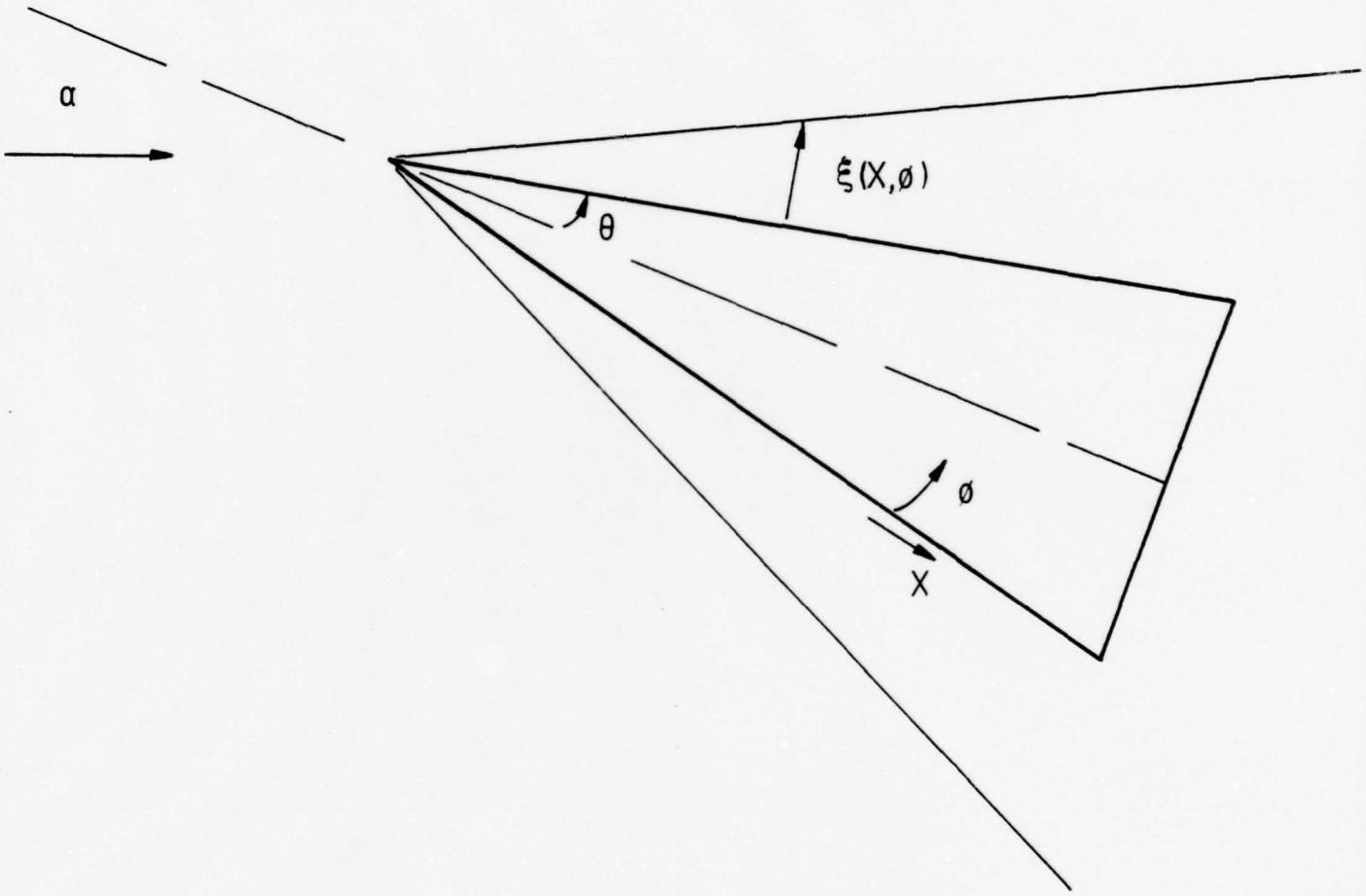

Fig. 1 Coordinate System

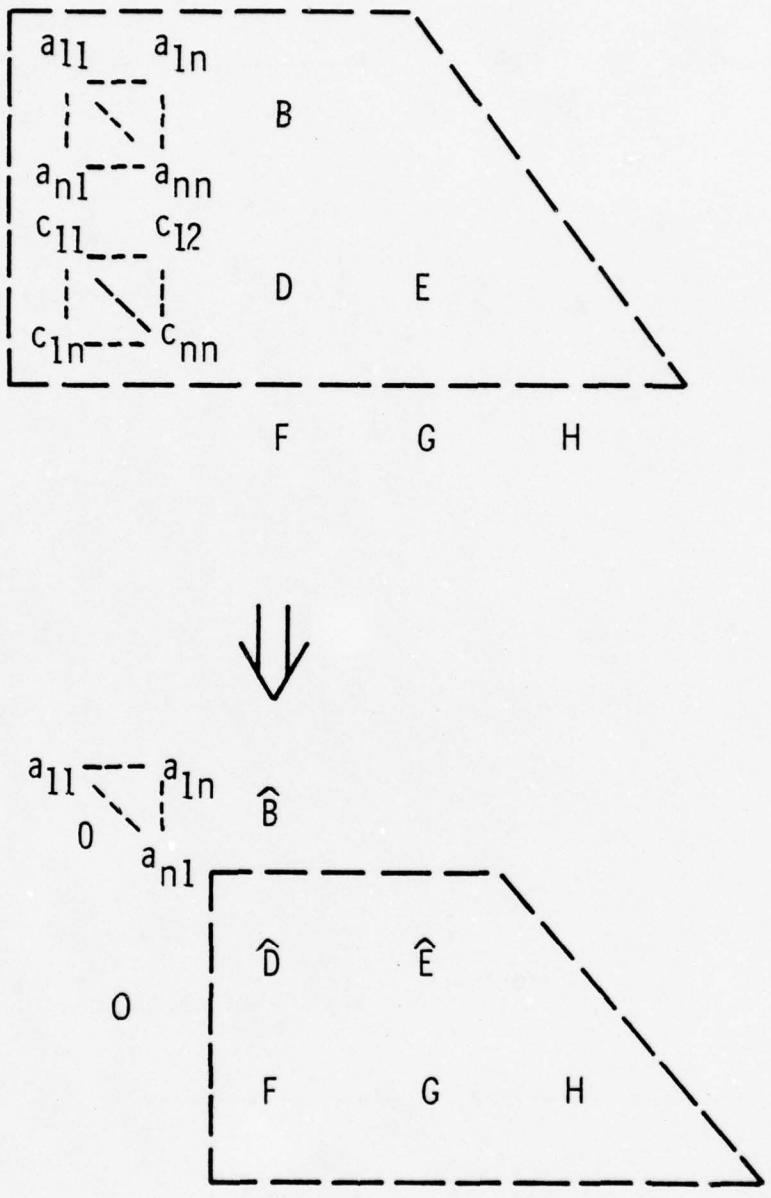

Fig. 2 Diagram of Block Matrix Reduction Using Profile Gaussian Elimination

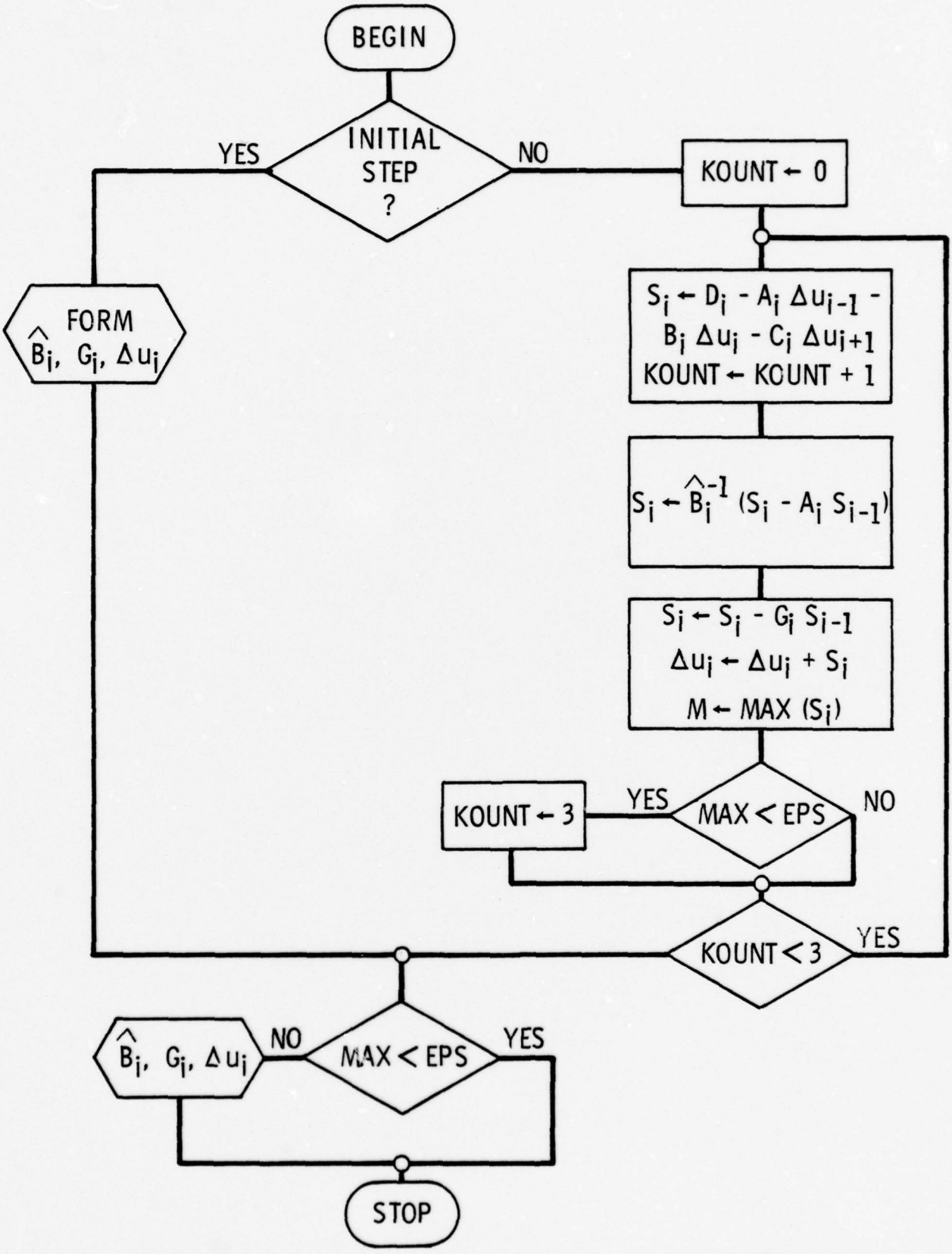

Fig. 3 Structured Flowchart of Basic Subroutine SOLVEQ

1978 USAF-ASEE SUMMER FACULTY RESEARCH PROGRAM
sponsored by
THE AIR FORCE OFFICE SCIENTIFIC RESEARCH
conducted by
AUBURN UNIVERSITY AND OHIO STATE UNIVERSITY

Participant's Final Report

NUMERICAL INVESTIGATIONS OF NATURAL CONVECTION INSIDE OF A FINITE HORIZONTAL CYLINDER

Prepared by:	James A. Liburdy
Academic Rank:	Assistant Professor
Department and University:	Department of Mechanical Engineering Memphis State University
Assignment:	
(Air Force Base) (Laboratory)	Arnold Air Station TSD
Research Colleague:	H. LeRoy Henderson
Date:	August 11, 1978
Contract No.:	F44620-75-0031

NUMERICAL INVESTIGATIONS OF NATURAL CONVECTION INSIDE OF A FINITE HORIZONTAL CYLINDER

by

J. A. Liburdy

Abstract

Natural convection currents may exist inside high temperature air supply systems and significantly influence the heat transfer characteristics which determine the wall temperatures. The present study is designed to provide convective film coefficients which can be incorporated in an overall radiation and conduction heat transfer model for a horizontal-finite length cylinder. The primary purpose is then to determine the thermal stresses that develop in the cylinder wall.

A three dimensional model is presented. A finite difference approximation to the vorticity and energy equations are solved by means of introducing a vector potential. The velocities and temperatures are determined and the convective film coefficient then calculated. The boundary conditions consist of an outside wall heat flux to stagnant ambient air with one closed end. The other end is exposed to a high temperature source.

Results indicate a Nu-Ra correlation similar to two dimensional results with possibly slightly higher Nu values (~10-20%). The highest Nu values occur at the sides of the cylinder where the velocities are greater than either the top or bottom.

NOMENCLATURE

A - representative nondimensional dependent variable, Equation (10)
B - term in finite difference approximation
C - constant, Equation (10)
Cp - specific heat at constant pressure
f - specified function of the independent variables
F - nondimensional function of the independent variable
g - acceleration due to gravity, directed down
Gr - Grashoff number = $g\beta(2r_o)^3\Delta T/\nu^2$
h - convective film coefficient
i,j,b - subscripts in the finite difference approximations
k - thermal conductivity
L - length of cylinder
n - time step
Nu - Nusselts number = $q/h\Delta T = h(2ro)/k$
P - pressure
Pr - Prandth number = ν/α
$q_,$ - heat flux at a solid surface
Q - temperature gradient at a solid surface
Q - nondimensional temperature gradient at a solid surface
r - radial coordinate
r_o - cylinder radius
R - nondimensional radial coordinate = r/ro
Ra - Rayleigh number = P_r Gr
S - representative nondimensional dependent variable, Equation (13)
t - time variable
T - temperature
T_o - initial temperature
ΔT - prescribed temperature difference
T_r - reference temperature
U - $\emptyset$ velocity component
v - r velocity component
$\bar{v}$ - velocity vector
V - nondimensional velocity vector = $\bar{v}r_c/\nu$
w - velocity component
ζ - longitudinal coordinate
Z - nondimensional longitudinal coordinate = ζ/r_c
α - thermal diffusivity
β - volumetric expansion coefficient with temperature
δ - finite difference operator
Δ - finite difference
Δ_1 - factor in Equation (13) = $2/(\Delta\zeta^2 r\Delta r^2 + r_c^2\Delta\varphi^2)$
Θ - nondimensional temperature $(T_o-T)/T_o$
μ - dynamic viscosity
ν - kinematic viscosity
ρ - density
τ - nondimensional time = $t\nu/r_c$
φ - angular coordinate
$\bar{\psi}$ - nondimensional vector potential, Equation (9)
$\bar{\omega}$ - nondimensional vorticity, Equation (8)

INTRODUCTION

It is the purpose of this study to provide both heat transfer analyses and develop an analytical tool for examining an enclosed three dimensional cylindrical natural convection flow field. This entails a numerical solution of the basic conservation equations. The analysis is designed to provide the transient velocity and temperature profiles within the enclosure as determined by the imposed boundary conditions. Also, the heat transfer coefficient by means of the Nusselts number, is correlated with the nondimensional Rayleigh number and compared to existing experimental and numerical investigations. Novel boundary conditions are also examined which are indicative of an insulated horizontal right circular cylinder open at one end. This situation is of interest to high temperature and pressure air supply systems used for wind tunnel testing (1).

Figure (1) shows the geometry of the modelled system and the coordinate system used. The open end boundary condition presents some difficulty with respect to modelling in order to closely resemble the actual physical conditions desired. The real situation occurring in the air supply systems mentioned consists of a cylindrical extension arm projecting horizontally from a hot pebble bed heater housing. It is this extension arm that is to be modelled. The arm contains an exit nozzle in the radial direction from which the hot air is exhausted to be used in a particular test section. The refractory brick lining used in the arm has experienced stress failures in the past due to excessively large thermal gradients. It is desired to know the effects of natural convection when high temperature gases exist in the arm. This then will later be coupled with radiation and conduction heat transfer to fully analyze the thermal characteristics during operation.

The boundary conditions imposed on the periphery and the closed end is determined by the composite wall structure. That is, heat is allowed to be transferred through a refractory lining and pressure vessel. To complete this condition an external convective heat transfer coefficient is imposed based on the recommendation of McAdams (2) for horizontal cylinders in a quiescent environment. If the housing, which contains hot gases, is stagnant the open end boundary condition is modelled as a constant temperature surface with zero velocity. More realistically natural convection currents will exist in the housing itself. To simulate this condition a prescribed velocity and temperature distribution is imposed. Lastly, to approximate a stratified stagnant gas in the housing a linear temperature distribution and zero velocity are used. It should be noted that each of these conditions does not allow mixing of the gases in the arm and housing.

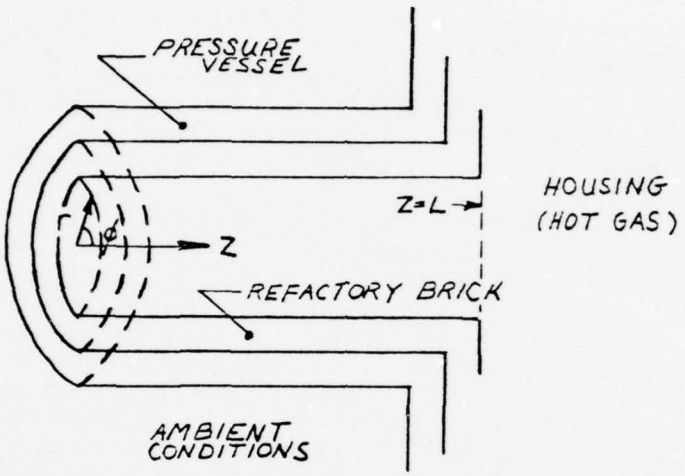

FIGURE 1. Modelled Configuration and Coordinate System

REVIEW OF PREVIOUS WORK

A wealth of correlated information exists for naturla convection from a horizontal cylinder (external flow). Also, the problem of combined forced and natural convection in cylinders has received considerable attention for obvious reasions (3, 4, and others). The two dimensional case of transient natural convection in a horizontal cylinder has been examined both numerically (5) and experimentally (6). Numerous other studies have been made for a rectangular three dimensional geometry (7, 8 and others). The boundary conditions normally imposed in these studies are either constant wall temperature or heat flux or step changes in the wall temperature. Consequently, direct comparison with the present investigation is not strictly valid. However, these previous studies will provide the means for qualitative comparisons of the boundary condition effects, in particular the open end condition, upon the heat transfer coefficient.

An experimental study by Evans and Stefany {9} examined the heat transfer correlations for transient heat transfer (both heating and cooling) for liquids in a cylindrical enclosure. They obtained bulk fluid temperatures as a function of time for step changes in the wall temperature. Their results were correlated in the following form:

$$Nu = 0.55(Ra)^{0.25} \tag{1}$$

where the Nusselt's number, Nu, is based on the instantaneous temperature change with time to determine the heat flux from the cylinder. The temperature difference used to define h is equal to the constant wall value minus the instantaneous bulk fluid temperature. The Rayleigh number, Ra, is defined in terms of the initial temperature difference between the wall and fluid. They observed an initially high h value, due to conduction, followed by an approximately constant value until the system neared equilibrium.

Empirical results for heat transfer correlations in various enclosures and orientation are very similar to Equation (1), see McAdams (2). The use of a logarithmic plot of Nu vs. Ra apparently is quite convenient for most practical purposes but has the disadvantage of absorbing most of the subtities associated with the existing temperature and velocity profiles.

MATHEMATICAL MODEL

The governing differential equations for the conservation of mass, momentum and energy, written in vector notation, become respectively:

$$\frac{D\rho}{Dt} + \rho(\nabla \cdot \bar{v}) = 0 \tag{2}$$

$$\rho \frac{D\bar{v}}{Dt} = -\nabla P + \mu \nabla^2 \bar{v} + \bar{g}(\rho - \rho\beta(T - T_r)) \tag{3}$$

$$\rho C_p \frac{DT}{Dt} = k\nabla^2 T \tag{4}$$

where the following basic assumptions have been introduced:

(i) Newtonian fluid with μ and k constant,
(ii) Boussinesq approximation where density variations are only introduced into the body force terms in the momentum equation,
(iii) viscous dissipation in the energy equation is negligible,
(iv) the density-temperature relationship is linear through the use of B.

The latter assumption (iv) can be modified in the case of large temperature differences by specifying a $\rho(T)$ function for the particular fluid under question.

The boundary conditions previously described can be formulated to coexist with Equations (2) - (4)

$$\begin{aligned}
r = 1: \quad & \bar{V} = 0 \\
& \frac{\partial T}{\partial r} = Q_1' \\
\phi = 0^\circ, 180^\circ: \quad & \frac{\partial \bar{V}}{\partial \phi} = 0 \\
& \frac{\partial T}{\partial \phi} = 0 \\
Z = 0: \quad & \bar{V} = 0 \\
& \frac{\partial T}{\partial Z} = Q_2'
\end{aligned} \tag{5}$$

$Z = L$: (1) $\bar{V} = 0$
$T = f_1(r, \phi, Z)$ (STAGNANT-STRATIFIED) CONDITION

(2) $\bar{V} = f_2(r, \phi, Z)$
$T = f_3(r, \phi, Z)$ (CONVECTIVE-STRATIFIED) CONDITION

The values of the temperature gradients at r=1 and Z=0 were imposed by specifying an overall resistance to heat transfer through the composite material and specifying an ambient temperature to be used with the calculated outside convective film coefficient using Equation (1). The functions f_1, f_2 and f_3 are taken to be linear with respect to the vertical, that is in the (Z-ϕ=0°) plane.

Rather than attempt to solve the conservation Equations (2)-(4) directly they were manipulated to formulate the more tractable vorticity transport and energy equations given as:

$$\frac{D\omega}{D\tau} = \bar{\omega} \cdot \nabla \bar{V} + \nabla^2 \bar{\omega} - Gr \begin{bmatrix} -\frac{\partial \theta}{\partial Z} \cos\phi \\ -\frac{\partial \theta}{\partial Z} \sin\phi \\ \frac{\partial \theta}{\partial R} \sin\phi + \frac{1}{R} \frac{\partial \theta}{\partial \phi} \cos\phi \end{bmatrix} \quad (6)$$

$$\frac{D\theta}{D\tau} = \frac{1}{Pr} \nabla^2 \theta \quad (7)$$

where the vorticity is defined by:

$$\nabla \times \bar{V} = \bar{\omega} \quad (8)$$

The vector potential was also introduced following the three dimensional cartesian coordinate analysis of Aziz and Helluims (7) and is defined as:

$$\bar{V} = \nabla \times \bar{\Psi} \tag{9}$$

In Equations (6)-(9) and henceforth, unless otherwise stated, the variables are nondimensional as defined in the nomenclature.

The resulting boundary conditions for the set of Equations (6)-(9) become:

R = 1:

$$\omega_R = 0$$

$$\omega_\phi = \frac{\partial W}{\partial R}$$

$$\omega_Z = -\frac{\partial U}{\partial R}$$

$$\frac{\partial \Theta}{\partial R} = Q_1$$

Z = 0:

$$\omega_R = \frac{\partial U}{\partial Z}$$

$$\omega_\phi = -\frac{\partial V}{\partial Z}$$

$$\omega_Z = 0$$

$$\frac{\partial \Theta}{\partial Z} = Q_2$$

Z = L:

(1) $\omega_R = \frac{\partial U}{\partial Z}$

$\omega_\phi = -\frac{\partial V}{\partial Z}$

$\omega_Z = 0$ (STAGNANT-STRATIFIED)

$\Theta = F_1(R, \phi, Z)$

(2) $\bar{\omega} = F_2(R, \phi, Z)$ (CONVECTIVE-STRATIFIED CONDITION)

$\Theta = F_3(R, \phi, Z)$

where the functions F_1, and F_3 represents the assumed nondimensional temperature profiles, and F_2 is the curl of the assumed velocity profile at Z=L.

Numerical Procedure:

The numerical modelling scheme employed to solve the system of governing equations was a modified version of the one presented by AZIZ and Hellums (7) for a rectangular box. The grid arrangement is shown in Figure 2. In order to evaluate the dependent variables at the centerline a cartesian coordinate system was imposed along the line r = o. This eliminated the obvious tendency for the differencing equations to blow up when r = o.

The numerical procedure consisted of three steps. First the parabolic equations were attacked. The set of three equations, solved at each time step can be expressed as:

$$\frac{A^{(1)}_{n+1} - A^{(o)}_n}{\Delta\tau} = C\left[\tfrac{1}{2}S_\phi(A^{(1)}_{n+1} + A^{(o)}_n) + S_R(A^{(o)}_n) + S_Z(A^{(o)}_n)\right]$$

$$\frac{A^{(2)}_{n+1} - A^{(o)}_n}{\Delta\tau} = C\left[\tfrac{1}{2}S_\phi(A^{(1)}_{n+1} + A^{(o)}_n) + \tfrac{1}{2}S_R(A^{(2)}_{n+1} + A^{(o)}_n) + S_Z(A^{(o)}_n)\right] \qquad (10)$$

$$\frac{A^{(3)}_{n+1} - A^{(o)}_n}{\Delta\tau} = C\left[\tfrac{1}{2}S_\phi(A^{(1)}_{n+1} + A^{(o)}_n) + \tfrac{1}{2}S_R(A^{(2)}_{n+1} + A^{(o)}_n) + \tfrac{1}{2}S_Z(A^{(3)}_{n+1} + A^{(o)}_n)\right]$$

The equations are to be solved in the order shown where $A^{(3)}$ represents the approximated value of the variable A at the n+1 time step. $A^{(o)}$ represents the value of A at the previous time step; $A^{(1)}$ the first approximation due to changes in the ϕ direction; $A^{(2)}$ the second approximation which incorporates changes in the r direction. C represents a constant and equals one when solving for the vorticity components and $\frac{1}{Pr}$ for the temperature solution. The delta functions, δ, represent the following combinations of first and second derivatives:

$$S_\phi = \frac{1}{R^2}\frac{\partial^2}{\partial\phi^2} - \frac{V}{R}\frac{\partial}{\partial\phi}$$

$$S_R = \frac{\partial^2}{\partial R^2} - \left(V - \frac{1}{R}\right)\frac{\partial}{\partial R} \qquad (11)$$

$$S_Z = \frac{\partial^2}{\partial Z^2} - W\frac{\partial}{\partial Z}$$

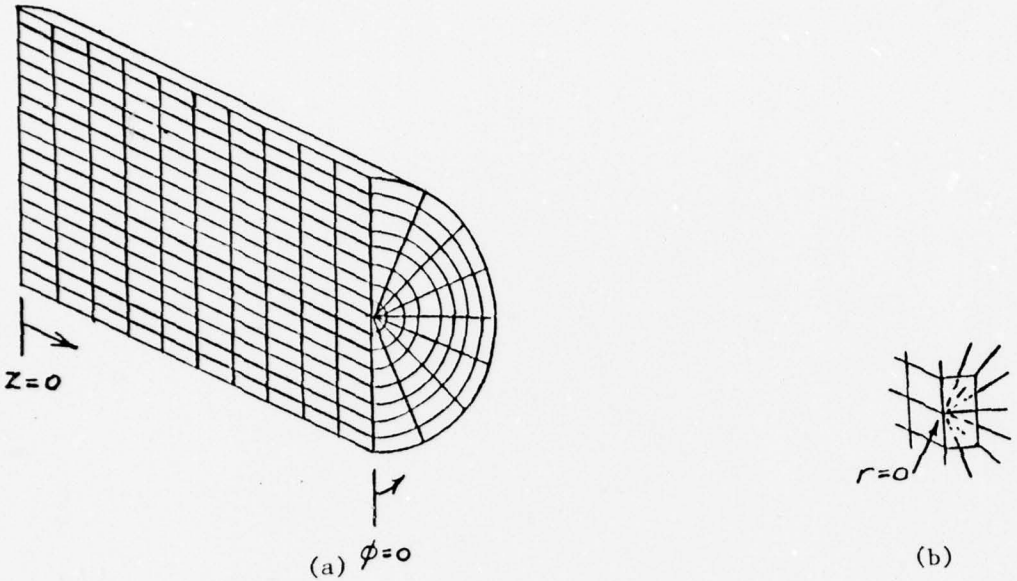

(a) (b)

FIGURE 2 (a) GRID SYSTEM FOR FINITE DIFFERENCE APPROXIMATION
(b) BLOW UP OF GRID ABOUT r = o

The conventional symmetric finite difference forms for first and second derivatives were used to evaluate each δ to assure errors of the order of the grid size squared. As an illustration of how Equations (10) were applied consider the following formulation to evaluate the first approximation of ω_ϕ , the ϕ component of the vorticity at an interior node (i,j,k):

$$\frac{\omega_{\phi,n+1}^{(1)}(i,j,k) - \omega_{\phi,n}^{(c)}(i,j,k)}{\Delta t} = \frac{1}{2}\left\{\left(\frac{\omega_\phi^{(1)}(i+1,j,k) - 2\omega_\phi^{(1)}(i,j,k) + \omega_\phi^{(1)}(i-1,j,k)}{R^2 \Delta\phi^2} - \frac{U(i,j,k)}{R} \frac{\omega_\phi^{(1)}(i+1,j,k) - \omega_\phi^{(1)}(i-1,j,k)}{2\Delta\phi} \right)_{n+1}\right.$$

$$+ \left(\frac{\omega_\phi^{(c)}(i+1,j,k) - 2\omega_\phi^{(c)}(i,j,k) + \omega_\phi^{(c)}(i-1,j,k)}{R^2 \Delta\phi^2} - \frac{U(i,j,k)}{R} \frac{\omega_\phi^{(c)}(i+1,j,k) - \omega_\phi^{(c)}(i-1,j,k)}{2\Delta\phi} \right)_n$$

$$+ \left(\frac{\omega_R^{(c)}(i,j+1,k) - 2\omega_R^{(c)}(i,j,k) + \omega_R^{(c)}(i-1,j,k)}{\Delta R^2} - \left(V(i,j,k) - \frac{1}{R}\right) \frac{\omega_R^{(c)}(i,j+1,k) - \omega_R^{(c)}(i,j-1,k)}{2\Delta R} \right)_n \qquad (12)$$

$$+ \left(\frac{\omega_Z^{(c)}(i,j,k+1) - 2\omega_Z^{(c)}(i,j,k) + \omega_Z^{(c)}(i,j,k-1)}{\Delta Z^2} - W(i,j,k) \frac{\omega_Z^{(c)}(i,j,k+1) - \omega_Z^{(c)}(i,j,k-1)}{2\Delta Z} \right)_n$$

$$+ \left\{ -G \frac{\partial\theta}{\partial Z}\cos\phi + \frac{2}{R^2}\frac{\partial\omega_R}{\partial\phi} \frac{\omega_\phi}{R^2} - \frac{U(i,j,k)\omega_R(i,j,k)}{R} + \omega_\phi \frac{1}{R}\frac{\partial U}{\partial\phi} + \omega_R \frac{\partial U}{\partial R} \right.$$

$$\left. + \omega_Z \frac{\partial U}{\partial R} + \frac{V(i,j,k)\omega_R}{R} \right\}_n$$

The term in square brackets represents the B term in Equation (10). Similar equations result for ω_R , ω_Z and Θ dimensionless temperature). The terms in B can be evaluated at time step n, n + ½ or n+1. Once the above equation is solved for $\omega_{\phi,n+1}^{(1)}$ it is stored and the equation for $\omega_{\phi,n+1}^{(2)}$ (i,j,k) is solved using $\omega_{\phi,n+1}^{(1)}$ in the δ_ϕ operator as indicated in Equations (12).

Then the third approximation was obtained using the first two approximations. The set of equations were then solved for each of the vorticity components and temperature.

It was desired to keep the error of the order of the grid size squared. As such the following approximations for the derivatives at the boundary were used:

$$\left(\frac{\partial A}{\partial R}\right)_{R=1} = \frac{1}{2(\Delta R)}\left[3A(i,j,k) - 4A(i,j-1,k) + A(i,j-2,k)\right]$$

$$\left(\frac{\partial^2 A}{\partial R^2}\right)_{R=1} = \frac{1}{(\Delta R)^2}\left[-2A(i,j,k) + 5A(i,j-1,k) - 4A(i,j-2,k) + A(i,j-3,k)\right]$$

with similar expressions for the derivatives in the Z direction at the closed end.

In order to assure the least error introduced in the finite difference approximation of the time derivatives it is necessary that B and the velocity components be evaluated at n + ½ or n + 1. This requires a two stage iteration scheme. First the vorticity and temperature are evaluated using the old values of B from which the vector potential and velocity components are calculated (this procedure is outlined further on and requires an iteration procedure. These updated values are then reinserted into the parabolic set of equations to reevaluate ω and Θ at the same time step. New values of $\vec{\Psi}$ and $\vec{V}$ are then calculated and again used to update ω and Θ. This is continued until a predetermined convergence criteria is satisfied (that is, the fractional change in the updated and old values is less than some tolerance). Once completed the entire process is repeated at the next time step.

There is the further requirement to specify the vorticity at the solid boundaries, R=1 and Z=0. These are obtained indirectly by examining the boundary conditions for the vector potential. Morean {9} concludes that the normal derivatives of the normal $\vec{\Psi}$ component at a solid surface is identically zero. Further, the tangential component of $\vec{\Psi}$ to the surface also must vanish to satisfy the no-slip conditions. Transforming these conditions into the vorticity components yields the following:

R = 1:
$$\omega_\phi = \frac{\partial W}{\partial R} \cong \frac{1}{2(\Delta R)}\left(4W(i,j-1,k) - W(i,j-2,k)\right)$$

$$\omega_R = C$$

$$\omega_Z = -\frac{\partial U}{\partial R} \cong \frac{-1}{2(\Delta R)}\left(4U(i,j-1,k) - U(i,j-2,k)\right)$$

Z = 0:
$$\omega_\phi = -\frac{\partial V}{\partial Z} \cong \frac{1}{2(\Delta Z)}\left(4V(i,j,k+1) - V(i,j,k+2)\right)$$

$$\omega_R = \frac{\partial U}{\partial R} \cong \frac{-1}{2(\Delta Z)}\left(4U(i,j,k+1) - U(i,j,k+2)\right)$$

$$\omega_Z = C$$

where the finite difference approximations are second-order in space

coordinates. This formulation implies that new, or updated, values of the velocity components are required to evaluate updated vorticity components at the boundaries. Again, this is incorporated into the double iteration scheme at each time step.

We now continue on to the solution scheme for the elliptic equations. A successive overrelaxation method was used to solve the finite difference approximation which can be expressed in the following form:

$$S_n^{(m)}(i,j,k) = \frac{\omega_{opt}}{\Delta_p}\left[\frac{S_n^{(m-1)}(i,j,k+1) + S_n^{(m)}(i,j,k-1)}{\Delta Z^2} + \frac{S_n^{(m-1)}(i,j+1,k) + S_n^{(m)}(i,j-1,k)}{\Delta R^2}\right.$$

$$+ \frac{S_n^{(m-1)}(i,j+1,k) - S_n^{(m)}(i,j-1,k)}{R \cdot 2\Delta R} + \frac{S_n^{(m-1)}(i+1,j,k) + S_n^{(m)}(i-1,j,k)}{R^2 \Delta\phi^2} \left. - \Delta_p S_n^{(m-1)}(i,j,k)\right] \quad (13)$$

$$- \omega_{opt}\Phi + S_n^{(m-1)}(i,j,k)$$

where Δ_p is defined in the nomenclature and the superscripts (m) and (m-1) represent current and previous iteration values respectively. The term Φ is the appropriate component of vorticity to correspond with the particular vector potential component being evaluated. In this expression ω_{opt} represents an acceleration parameter and can take on values typically in the range zero to two. An optimal value can be found which is designed to provide the fastest rate of convergence, see Forsythe and Wason (10). This optimal value was used in the present problem.

Equation (13) was iterated upon until the fractional change in the vector potential component was less than some set tolerance. The convergence was tested at each nodal location in order to assure that the entire system was well behaved.

The grid spacing used was 9 x 9 x 11. That is, the radial increment equaled $r_o/8$, the angle increment $\pi/8$ and the longitudinal increment $L/(10 \times r_o)$. A smaller grid size was not used, however a 9 x 5 x 11 grid was attempted which showed some convergence problems. The aspect ratio was 3.25 (inside length per inside diameter).

The program is designed to run until steady state conditions result. Steady state is determined by evaluating the total heat loss rate from the cylinder. When the heat loss rate no longer varies within one percent steady state was assumed.

In the following section some results are given. It is hoped that further work in this area will develop the program to its full potential. The following is restricted to the stagnant-stratified open end boundary condition.

RESULTS AND DISCUSSION

To date, the computer program to fully explore the convective heat transfer phenomena inside the described horizontal cylinder has not been fully tested. There appears to be some convergence problems in the solution of the elliptic equations particularly at high Rayleigh numbers. As such the results and discussion will be limited to the few cases that did show reasonable results.

Figure 3 shows, qualitatively, a typical flow pattern that results for fairly low values of Ra (below 10^6). A definite downward flowing boundary layer is evident. Either a stagnant or small eddy region occurs near the bottom. The central region flows upward to replace the heavier falling fluid at the outer boundaries.

The Nu correlation with Ra is shown in Figure 4. The Nu values are consistently larger than the correlation for the experimental results of Reference (6). It should be noted that (6) imposed a wall temperature step change as the boundary condition of their two dimensional case. The discrepancy is still rather small and it appears as the Ra power is identical in both cases.

Figure 5 gives the transient nature of the Nusselt's number. Experimental observations by Evans and Stefany (6) show a constant film coefficient for both transient heating and cooling. In the present case the wall heat flux is not a constant and it seems physically reasonable for Nu to decrease as steady state conditions are approached. It was observed that initially high values of Ra resulted in a more rapid decline of Nu. Actually steady state conditions were not reached however because of the convergence problem mentioned earlier. During the time period examined the wall heat flux only varied by a few percent, however the temperature difference (T_b/T_w) decreased more rapidly. Thus, the decline in Nu is largely due to the cooling of the fluid and wall but each at a different rate.

A numerical study by Hellums and Churchill (11) for transient natural convection in a two dimensional horizontal cylinder shows a significant initial drop in Nu with time followed by an increase which is a function of angular position until steady state is reached. The cylinder had two vertical halves each at a different temperature.

Figures 6 and 7 show the longitudinal and angular variations of the film coefficient. Figure 7 also contains the angular variation of wall temperature. Longitudinal variations are slight. The velocities in the Z direction were small compared to the r and Ø components.

This condition is dependent on the boundary condition imposed at the open end.

There is a slight indication that the largest h values will exist near the ends. In particular it was found that the h value at the closed end was approximately 20% to 25% higher than the average value for the entire cylinder. Peripheral variations in h were slight except very near the top and bottom. During the initial period Hellums and Churchill (11) also found Nusselt numbers to be smallest near the top and bottom. This is most likely due to the lower fluid velocity.

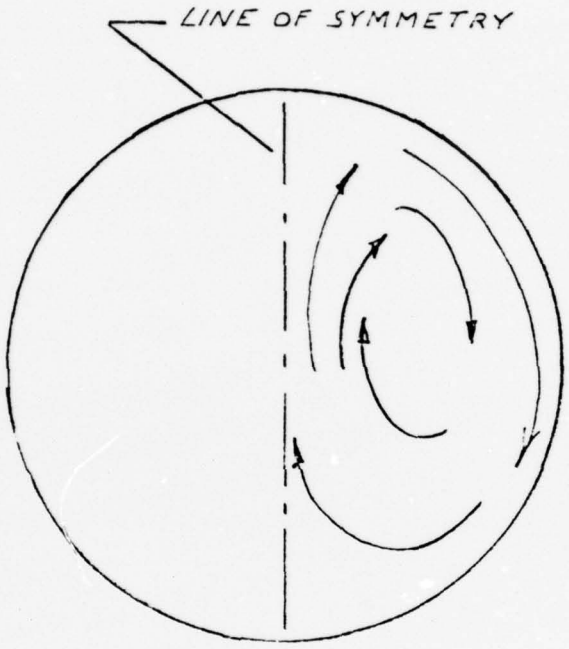

Figure 3. Representative flow field

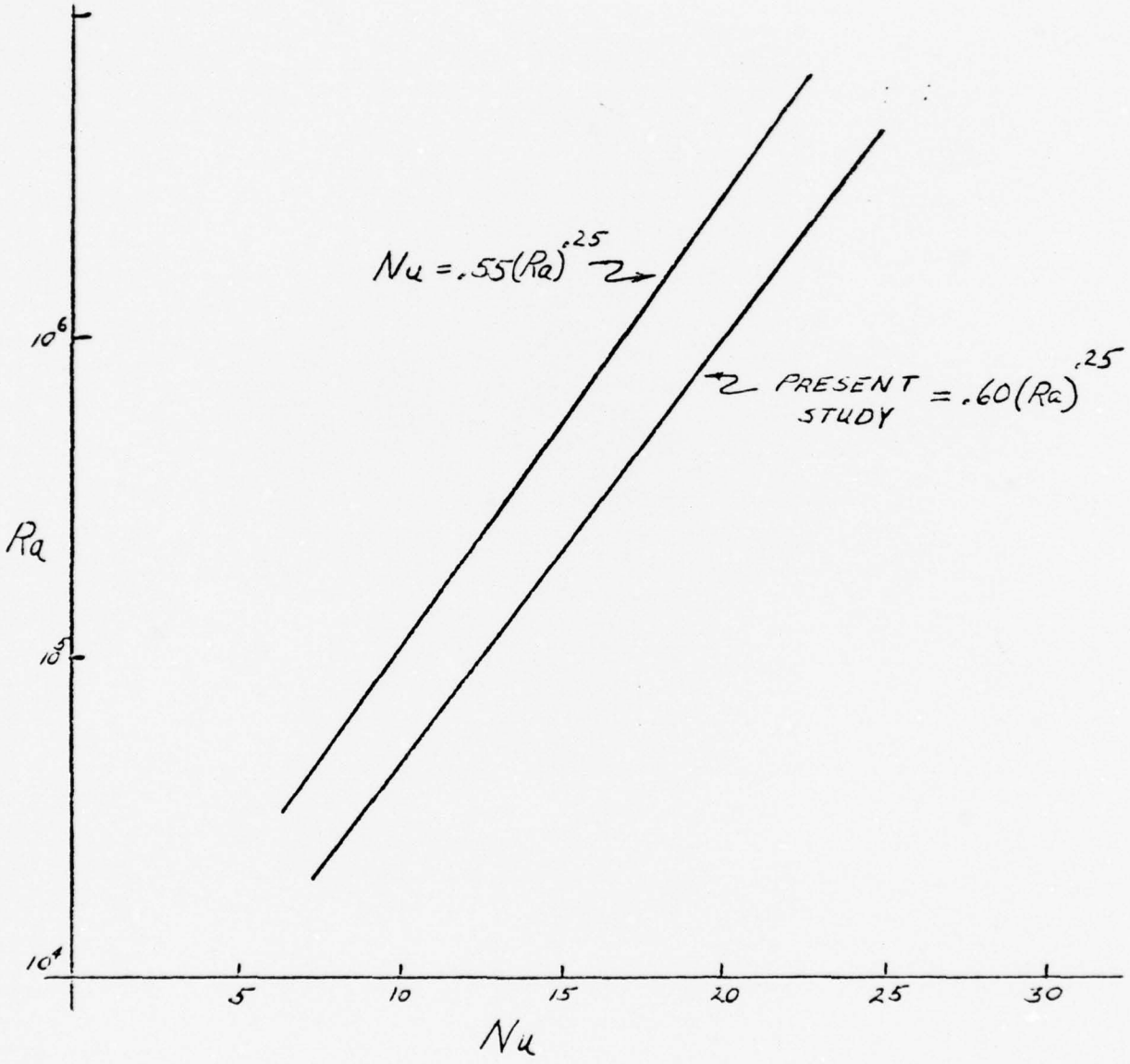

Figure 4. Nu correlation

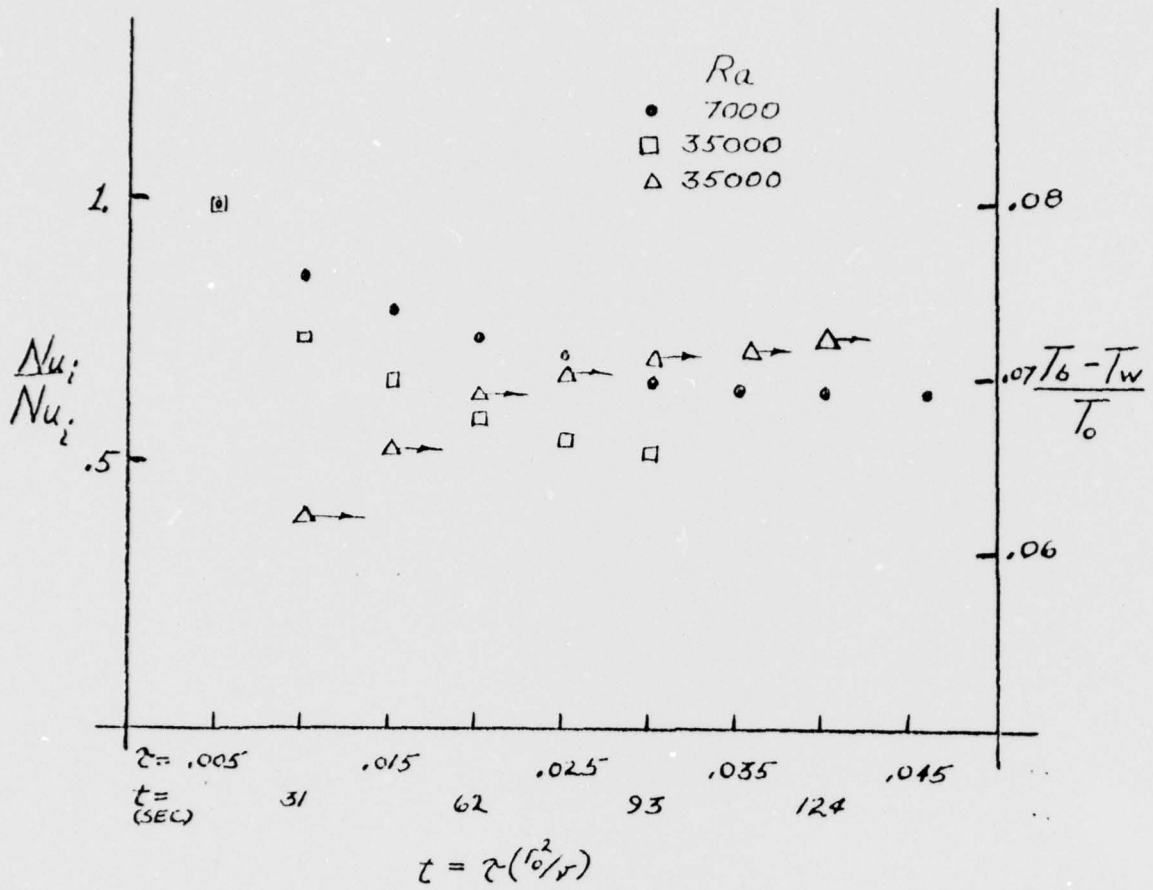

Figure 5 Transient nature of Nu and (T_b T_w)

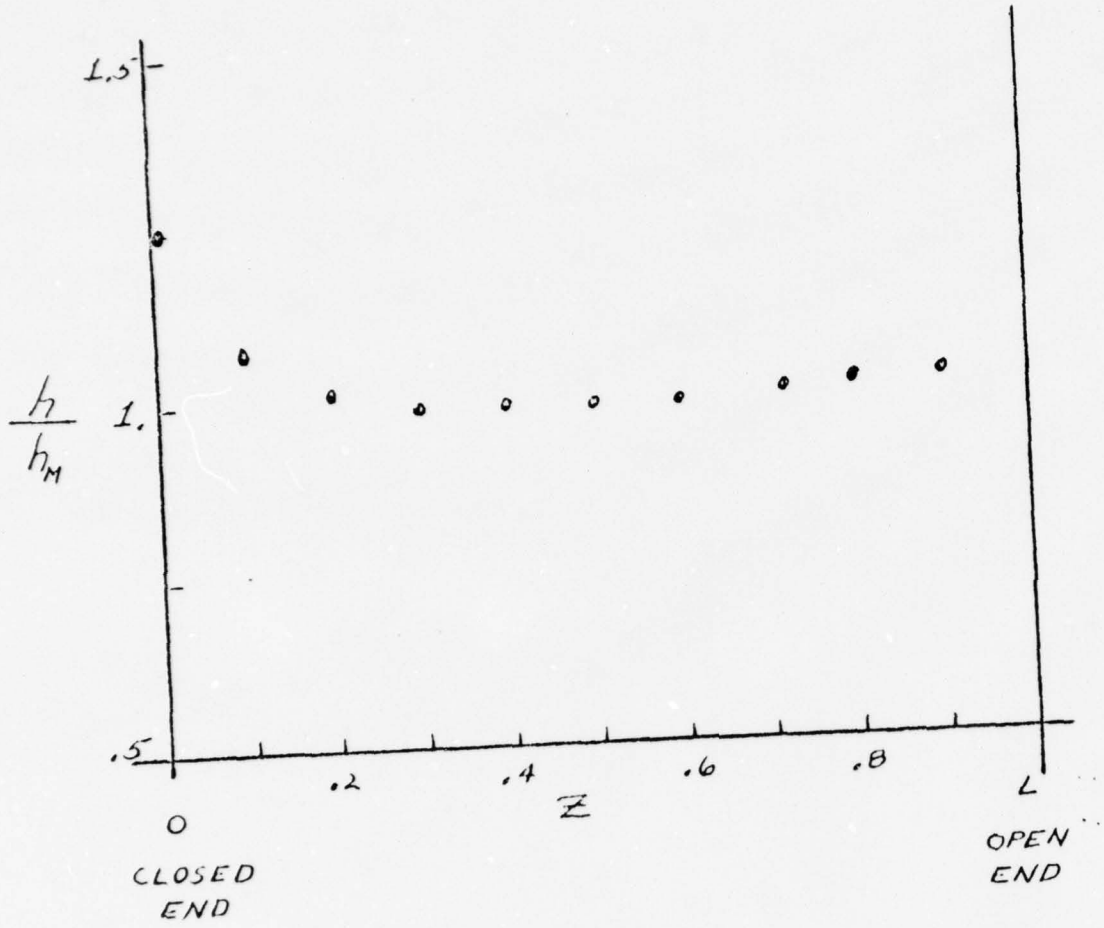

Figure 6 Longitudinal variation of h

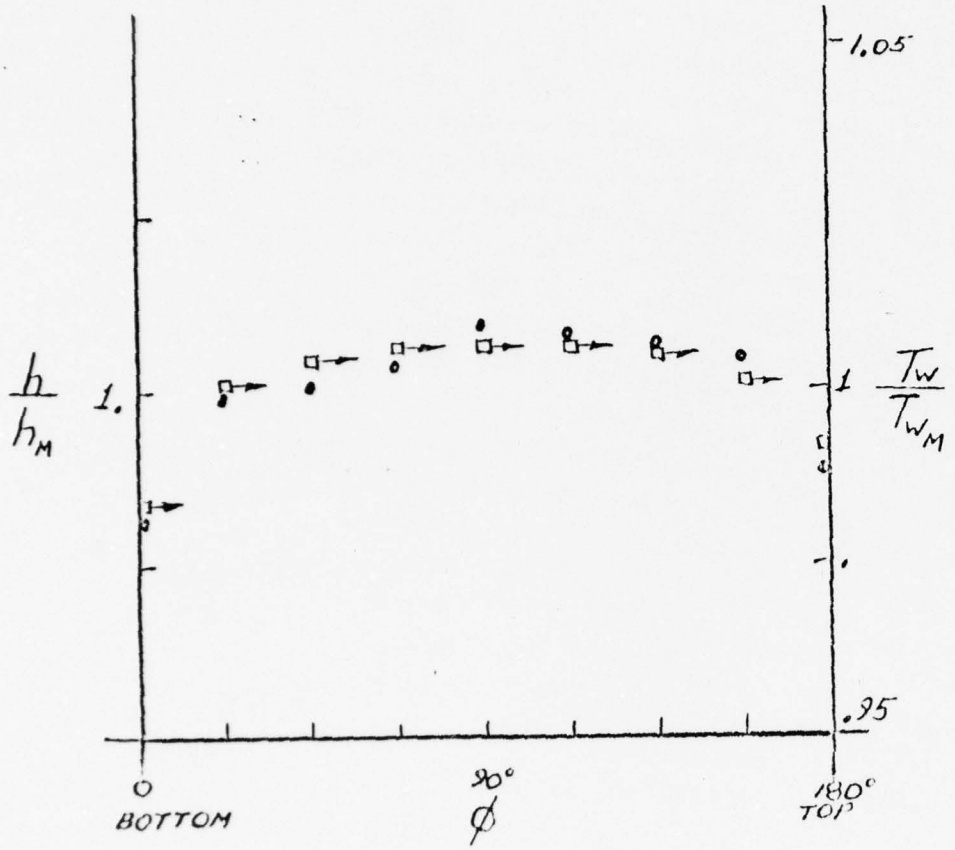

Figure 7 Angular variation of h and T_w

CONCLUSIONS AND RECOMMENDATIONS

The present work has shown, at least in the nitial stages, the Nusselt's number very nearly follows the same correlation found for two dimensional cylinders. However the open end boundary condition has not been fully explored and is likely to cause secondary flows which may enhance the overall convective film coefficient. It is encouraging that preliminary results are consistent with other's works.

The convergence of the inner and outer iterations has yet to be explored. This should present little problem but must be examined before further numerical experiments can reliably be conducted. Naturally, the ultimate test will be experimental verification of the results.

Since this model was developed with the intent of supplying convective film coefficients to the radiative heat transfer effects in a high temperature system, there is the possibility that transition to turbulent flow may result. Should this occur significant modifications-through turbulence modeling-will be required.

REFERENCES

1. Henderson, H. LeRoy, ARO, Inc. AEDC Division, Arnold Air Force Station, TN 37389, Personal Communication.

2. McAdams, W. H., Heat Transmission, McGraw-Hill Book Co., New York, N.Y., 1954.

3. McComas, S. T. and Ecker, E.R.G., "Combined Free and Forced Convection in a Horizontal Circular Tube," J. Heat Transfer, Transactions ASME, Series C, Vol. 88, 1966, pp 147-153.

4. Patankar, S. V., Ramadhyani, S., and Sparrow, E. M., "Effects of Circumferentially Nonuniform Heating on Laminar Combined Convection in a Horizontal Tube," J. Heat Transfer, Transactions ASME, Series C, Vol. 100, 1978, pp 63-70.

5. Maahs, H., "Transient Natural Convection Heat Transfer in a Horizontal Cylinder," Ph.D. Thesis, University of Washington, Seattle, 1964.

6. Evans, L. B., and Stefany, N. E., "An Experimental Study of Transient Heat Transfer to Liquids in Cylindrical Enclosures," Heat Transfer Conference-Los Angeles, AIChE Symposium Series, 1965.

7. Aziz, K. and Hellums, J. D., "Numerical Solution of the Three-Dimensional Equations of Motion for Laminar Natural Convection," Physics of Fluids, Vol. 10, No. 2, 1967, pp 314-324.

8. Ozoe, H., Yamamoto, K. and Sayama, H., "Natural Convection Patterns in a Long Inclined Rectangular Box Heated from Uelow," Int. J. Heat Mass Transfer, Vol. 20, 1977, pp 131-139.

9. See reference (7).

10. Forsythe, G. E. and Wason, W. R., Finite-Difference Methods for Partial Differential Equations, John Wiley and Sons Inc., New York, N.Y., 1967.

11. Hellums, J. D. and Churchill, S. W., "Transient and Steady State, Free and Natural Convection, Numerical Solutions: Part II. The Region Inside a Horizontal Cylinder," AIChE Journal, Vol. 8, No. 5, Nov. 1962, pp 692-719.

1978 USAF-ASEE SUMMER FACULTY RESEARCH PROGRAM

sponsored by

THE AIR FORCE OFFICE SCIENTIFIC RESEARCH

conducted by

AUBURN UNIVERSITY AND OHIO STATE UNIVERSITY

PARTICIPANT'S FINAL REPORT

GAS SAMPLING PROBE COMPUTER PROGRAM

Prepared by:	John E. Reissner, Ph.D
Academic Rank:	Assistant Professor
Department and University:	Department of Physical Science Pembroke State University Pembroke, NC
Assignment:	
(Air Force Base) (Laboratory) (Division) (Branch)	Arnold Air Force Base Arnold Engineering Development Ctr. Engine Test Facility, ARO, Inc. Technology Applications Branch Physics Section
USAF Research Colleague:	LeRoy Brewer, D.Sc.
Date:	August 11, 1978
Contract No:	F44620-75-C-0031

GAS SAMPLING PROBE COMPUTER PROGRAM

by
John E. Reissner

ABSTRACT

Extractive probe sampling of turbojet exhaust effluent may provide a convenient means of characterizing levels of pollutant emission from such devices, but questions exist as to the extent that the sampling process may perturb these concentrations from their pertinent values. As part of the effort to characterize the extent of such perturbations, computer modelling of the reactive gasdynamics processes within such probes was undertaken.

In this work, existing code was generalized to account for homogeneous reactions in one-dimensional flow in probes of non-constant cross-section, including recovery from supersonic flow by a normal shock crossing the probe. The generalizations were implemented through subroutines so as to preserve the flexibility of the program for accommodation of other phenomena, e.g. heterogeneous reactions and frictional effects.

The equations of one-dimensional reactive flow in a non-constant area probe with heat transfer through the walls are briefly reviewed. The method of solution of these flow equations is described, and the organization of the code is outlined. Data from initial runs of the generalized program for two probes, one of constant area and one with convergence and divergence in area, are presented to indicate some of the types of information sought in a study of this type. In particular, post-recovery cooling of flows in the non-constant area ("aerodynamic") probe is shown to be far more modest than would be anticipated from consideration of the supersonic expansion of the flow alone. Some differences in patterns of reactivity between the two probes are noted, for a single set of kinetic parameters used. Further anticipated developments of the program are discussed.

ACKNOWLEDGMENTS

It is more than difficult to either adequately or comprehensively acknowledge the contributions of various kinds to the exceptional experience I have enjoyed in these ten weeks. First of all, to Bob Bryson and Jim Few goes my deep appreciation for their generous sharing of their insight into and experience with the world of phenomena pertaining to flows in probes. To Dr. Chad Limbaugh and Gerald Stacey go my thanks for their patient, friendly, and effective concern and tutelage for my efforts to use the computer productively. A large number of people at this remarkable institution have made comments or asked questions that were particularly helpful in a variety of ways: The ones coming to mind at the late hour this text is prepared include Dr. Charley Fisher, Dr. Burt Krakow, Dr. Wheeler McGregor, Dr. Carroll Peters, Robert Rhodes and Sam Wehofer. I also wish to thank Professor Dave Miller of the University of California at La Jolla for a conversation most helpful in orienting me to the subject area of reactive gasdynamics. Linda Crosslin assisted indispensably in the preparation of materials of various kinds in a variety of unfailingly cheerful ways. To my "dean for the summer", Mr. J. Fred O'Brien, goes my gratitude for his welcome personal interest, and his pains in developing and maintaining such an effective program. Almost finally, I thank my encouraging boss and valued "Research Colleague", Dr. LeRoy Brewer, for preparing the situation and seeing it through in the way he did. But my final thanks must go to my wife, Zollene, who lovingly kept things together while all this went on.

INTRODUCTION

Knowledge of the distribution of chemical species in turbojet exhaust effluent is essential to the evaluation of the environmental impact of such a propulsion device. There are, essentially, two classes of methods of obtaining such knowledge: One, in-situ spectroscopic determination, is in principle non-perturbing and capable of application to the measurement of any chemical species, regardless of stability. The newer of the two classes, it is generally costly and requires highly-trained personnel for operation, notwithstanding providing data whose reduction is an area of continuing research. The other, perhaps more classical, group of methods is extractive probe sampling. The latter group essentially leads to the transfer of a cooled, quiescent sample to instrumentation ostensibly specific to the determination of given chemical species. Interferences of species within a given instrument are by no means unknown, and determination of such effects is also an area of on-going study (Ref. 1). Another area of potential difficulty, that most immediately connected to the present study, is perturbation of the concentrations of species of interest by the extractive sampling process itself. Undoubtedly, unstable intermediates of the combustion process existing in the exhaust stream are lost in the sampling process. It is important to know, for example, the extent to which this change is coupled to changes in concentrations of more stable species of interest, relative to their in-situ values both in the near-jet exhaust stream and in the far-jet wake as they enter the natural chemical cycles of the environment (Ref. 2).

Among specific observations lending weight to concern with these questions are the findings of the Technology Applications Branch of the Engine Test Facility at the Arnold Engineering Development Center, that in-situ spectroscopic determinations of oxides of nitrogen in turbojet and combustor exhaust effluents yield values up to six times those obtained by probe sampling methods (Refs. 3-6). These and another study (Ref. 7) have provided observations consistent with the occurrence of probe-dependent reactions, particularly in high temperature and reducing (e.g. fuel-rich) gas flows, which consume oxides of nitrogen and tend to enhance carbon monoxide levels.

OBJECTIVES

As part of a broadly based effort to resolve the nature and significance of these discrepancies, computer modelling of the reactive gasdynamics processes within the probe was deemed a useful undertaking. At the inception of this project, code existed for the study of finite-rate reactions occurring in one-

dimensional constant area flow, with modelled heat transfer to a constant temperature wall. It was considered desirable to extend the code to account for phenomena associated with varying area and wall temperature towards, as stated in the work assignment for this project, "a realistic prediction of what happens to the pollutant species in a gas sample because of the presence of the sampling probe." In this report, we shall describe briefly the success in meeting these objectives, and the author's conclusions and recommendations. Several matters intended to be later considered are excluded from this report: they include (1) a comprehensive description and thorough documentation of the code used and developed, together with a full derivation of the analysis coded, (2) a thorough discussion of the chemistry of potential interest to this problem, with emphasis on the likely precision and accuracy of the parameters describing the individual rate processes of that material, and (3) a review of the state-of-the-art of sensitivity analysis, pertinent to assessing the impact of imprecisions and inaccuracies of such parameters on the specific predictions of the complex model. Work on at least the first two of these matters necessarily preceded the developments reported here, and represented a substantial effort, given the state of the 1800 line program existing, and the diversity of physico-chemical phenomena relevant to the problem under consideration. Constraints of time within the program necessitate a far briefer report than the value of the experience to the author would justify.

ONE-DIMENSIONAL FLOW

We review very briefly here the familiar equations of one-dimensional flow (Ref. 8), and aspects of their adaptation to reactive systems, primarily to define notation and to lay the groundwork for some discussion to the method of coding the problem.

Consider flow along the x-axis through a channel of area A(x) of a gas of density ρ and velocity u. The flow rate $\dot{M}$ (grams/second) is given by

$$\rho u A = \dot{M}, \tag{1}$$

and in steady flow, $\dot{M}$ = constant reflects the conservation of mass. Conservation of momentum is expressed by the differential form of Euler's equation, which introduces the static pressure, P,

$$dP + \rho u du = 0. \tag{2}$$

With this form of equation (2), we restrict consideration of the system to inviscid flows in the absence of frictional forces. Conservation of energy manifests itself in a relation between local stagnation enthalpy per unit mass, H_T, the corresponding static (chemical-thermodynamic) enthalpy H, and velocity. Stagnation enthalpy changes from its initial value H_0 with the absorption of heat Q from the walls by a flowing parcel of gas, and at any instant is equal to the sum of the static enthalpy and kinetic energy of flow,

$$H_T = H_0 + Q = H + u^2/2. \tag{3}$$

Chemical reactions and temperature changes cause changes of H, which, in balance with changes in Q, mediate variation in the velocity u along the flow.

The heat absorbed, Q, is the integral of $\dot{Q}$, the rate of heat flow per unit mass of flowing gas. The expression for this rate is given in terms of a heat transfer coefficient h, local wall temperature T_W, and, for a probe of circular cross-section, the local probe circumference πD, by the relation

$$\dot{Q} = -h(T-T_W)\pi Du/\dot{M}. \tag{4}$$

The defining equations of the gas dynamic system are completed by specification of the equations of state of the gas. These relations depend upon the gas composition. For an NT component mixture of chemical species i=1, ..., NT, we describe composition by mole-mass ratios B_i, the ratio of mole fraction of species i to the average molecular weight of the mixture. The thermal equation of state we use is that of an ideal gas

$$P = \rho RT \sum_{i=1}^{i=NT} B_i. \tag{5}$$

The gas constant R here is the molar quantity

$$R = 82.0567 \text{ cm}^3 \text{ atm/mole K} = 8.31434 \times 10^7 \text{ ergs/mole K}.$$

The caloric equation of state is

$$H = \sum_{i=1}^{i=NT} H_i B_i, \tag{6}$$

where H_i is the molar enthalpy of species i. That enthalpy, and its temperature derivative, the molar heat capacity of species i, C_{pi}, are provided by coefficients of an expression of temperature dependence, confirmed in this work to provide heat capacities, enthalpies, and free energies of the species considered in essential agreement with those of the 1971 JANNAF table (Ref. 9). Differentiation of equations (1), (3), (5) and (6), and combination with equations (2) and (4), together with the definition of velocity, $u = dx/dt$, provide a system of flow equations that, in steady state, may be solved to follow in time the passage of a fluid particle along the distance, x. The system of equations as used is modified by consideration of conservation of the number of atoms of each of the NE elements present, reducing the number of independent measures of concentration to $N = NT - NE$. This consideration provides expressions for the $N + 1^{st}$ through NT^{th} mole-mass ratios, of the form

$$B_i = \sum_{j=1}^{j=N} A_{ji} B_j + C_i, \quad i = N + 1, \ldots, NT. \tag{7}$$

where the coefficients A_{ji} are determined by the atomic compositions of the molecular species present, and the constants C_i depend also on the initial composition of the system. All the mole-mass ratios change in time as chemical reactions occur, at rates $\dot{B}_i$. We have, then, for the system of rate equations describing overall changes in the system with time

$$\frac{dB_i}{dt} = \dot{B}_i, \quad i = 1, \ldots, N, \tag{8}$$

$$\frac{dT}{dt} = \frac{(\rho - P/u^2)\left(\sum_{i=1}^{i=NT} H_i \dot{B}_i - \dot{Q}\right) + Pu\,(d \ln A/dx) - \rho RT \sum_{i=1}^{i=NT} \dot{B}_i}{P/T - (\rho - P/u^2)C_p} \tag{9}$$

$$\frac{dx}{dt} = u, \tag{10}$$

and

$$\frac{dQ}{dt} = \dot{Q}, \tag{11}$$

i.e., a system of expressions for N + 3 rates dY_i/dt, i = 1, ..., N + 3. Here C_p is the specific heat of the gas,

$$C_p = \sum_{i=1}^{i=NT} B_i C_{pi}. \tag{12}$$

Together with equation (7) for the "dependent" B_i, i = N + 1, ..., NT, the solution of these equations at any instant provides values for all the B_i, and T, x, and Q. The rearrangement of equation (3),

$$u = \sqrt{2(H_o + Q - H)}\ , \tag{13}$$

together with equation (6) for H, gives the velocity. With the conservation of mass, equation (1), we have

$$\rho = \dot{M}/uA, \tag{14}$$

and finally the equation of state (5) gives the pressure. This review of the system of equations of the motion of the system in fact parallels the computation of the quantities in the program code: It may be of some interest that this sequence of operations appears to pass without difficulty from subsonic to supersonic flow, in spite of the existence of a bifurcation of the solution at that point.

SOLUTION OF THE FLOW EQUATIONS

A system of equations of the type given by equations (8) - (11) can be solved in a variety of ways. The method of solution chosen should remain stable for reasonable step sizes. In the situation prevailing here the system is "stiff" on account of the broad spectrum of relaxation times existing in the presence of rapid chemical reaction rates. The method of solution presently implemented, the modified Euler method, appears to provide a simple means to attain such stability under these conditions. In this method, one linearizes the system in time, essentially approximating the linearized rates midway along the increment Δt. The result of this operation is to convert the system of differential equations to a system of algebraic equations

$$\dot{Y}_i = \sum_{j=1}^{j=N+3} \left[\frac{\delta_{ij}}{\Delta t} - \frac{1}{2} \left(\frac{\partial \dot{Y}_i}{\partial Y_j} \right)_{Y_k \neq Y_j} \right] \Delta Y_j \qquad (15)$$

to be solved for the increments ΔY_j. In this expression, δ_{ij} is the Kronecker delta, and the subscript notation on each partial derivative indicates that it be taken with all the Y_k, save Y_j, held fixed. At any instant, the rates $\dot{Y}_i$ and partial derivatives $(\partial Y_i/\partial Y_j)_{Y_k \neq Y_j}$ are given in terms of the levels Y_j, and solution of the system (14), here by Kraut-Cholesky reduction, provides increments ΔY_j associated with a specified time interval Δt. These intervals are determined at each step in the course of testing the solution ΔY_j for acceptability.

ORGANIZATION OF CODE

Figure 1 provides the organization of subroutines as currently implemented in the gas sampling code computer program. In this depiction, calls are indicated by directed solid lines and returns (in all cases here to the point of call) are indicated by dotted lines. The sequence of calls and returns in the first pair of normal execution, excepting iteration with the matrix inversion subroutine between call 30 and return 31, is numbered at the origins of the calls and returns, respectively. The time-marching of the program is by the loop beginning with call 9 and ending upon return 32. However, it is to be emphasized that the constitution of this program is extremely flexible, and the range of phenomena modelled in its operation can be extended with relative ease once the overall structure of the program and its relations is perceived. For example, in the present work it was found that modification of the constant area and constant wall temperature conditions was quite easily obtained by the subroutine WALL (unique to each probe configuration), and that the recovery of conditions in flow becoming supersonic in the course of traversing appropriate probes was fairly straightforwardly implemented through subroutine SHOK, integrating the system of flow equations across the (here, frozen and thin) shock discontinuity. The exact solution of this problem proved unpredictable in the outcome of its iterations when the temperature dependence of the heat capacities were accounted for. An approximate but reliable iteration procedure, exact for temperature intervals across a shock sufficiently moderate that $\gamma = C_p/(C_p-R)$ is linear, exists in the program as described here.

PROBES STUDIED

A diverse variety of extractive composition probe geometries have been developed to sample combustion effluents in a variety of circumstances, always with the intention of obtaining compositions free of probe-induced perturbations. The proceedings of the 14th and 15th AIAA Aerospace Sciences Meetings (Refs. 10 & 11) include reviews and original papers of a timely nature referring to and describing the greater part of this diversity. We confine ourselves to discussion of two probes simulated in the current program, both used in turbojet emissions investigations at AEDC. One, the "Baseline Probe", is a counterflow-cooled straight pipe of inside diameter 0.775 cm; the other, the "Aerodynamic Probe", is a converging-tubular-diverging-tubular sequence of sections of entrant diameter 0.12 cm, designed to cool the effluent sample by aerodynamic, as well as convective, cooling. Figure 2 shows the configurations of these two probes. Figures 3 and 4 describe the rather distinct temperature paths of the flowing gas in its respective trajectories through the two probes as calculated using entrant conditions of P=3 atm, T=2000°K, and u=10^4 cm/sec, corresponding to conditions downstream of a bow shock before the probe orifice. The baseline probe maintains the flow at close to the initial speed through the 30 cm length studied (the time taken for this passage was 3.2 milliseconds), and undergoes little drop in temperature. In the aerodynamic probe, by comparison, after the flow becomes supersonic (at about 0.06 cm, the end of the convergent section) and begins its supersonic acceleration (at 0.21 cm, the start of the divergent section) the static temperature falls at a phenomenal rate, from above 1600°K (at 4.8μsec) to 444°K (at about 9.6μsec). However, at the latter time, recovery occurs through a normal shock crossing the probe. This shock appears in the present version of the program when the recovery static pressure falls below the specified sample line pressure maintained by pumping, here 0.3 atm. (There are many calls to SHOK, but few shocks are chosen.) At recovery, the static temperature rises again, to around 1728°K. However, the process of supersonic expansion is not without effect, for recovery in pressure (Figure 5) is by no means as dramatic as that in temperature and cooling proceeds for the relatively expanded gas with a rate of temperature loss more than 8 times that of the baseline probe on a time basis. (Something on the order of half the magnitude of this factor is attributable to the difference in surface-to-volume ratio between the two probes.)

CHEMICAL EFFECTS

Modelling of the type undertaken here offers the possibility of a detailed study of the evolution of distribution of

chemical species as the gas traverses probe and sample line (Refs. 12, 13, 14). Table 1 presents a list of the reactions occurring in the runs discussed here, together with the kinetic parameters used. Figures (6) and (7) compare the evolution of nitrogeneous compounds included in these preliminary runs in the baseline and aerodynamic probes. One sees, comparing these figures, that the predominant species, N_2 and NO, maintain stable levels. In the case of the less abundant compounds (for the starting conditions of these runs), N_2O, N, and NO_2, probe-dependent differences in reactivity manifest themselves. In the aerodynamic probe, for example, only 1/4 as high a maximum of nitrous oxide, N_2O, is attained as in the baseline probe, the net production being halted at the onset of supersonic expansion at 0.06 cm, while continuing in the baseline probe for 15 times that distance (and 30 times that time). The rapid transient rises in the species N_2O, NO_2, and N each from mole fraction 9.9×10^{-10} as observed for both probes may represent rapid relaxation of hypothetical conditions that are inappropriate to the entrant gas conditions. Further investigation is, however, required to exclude the possibility that they are in greater or lesser part numerical artifacts associated with the behavior of small numbers in the starting procedure of the calculation. Such study must precede any claim for the authenticity of the evolution of concentrations of trace species as presented here. We discuss these concentrations at this time primarily to indicate some of the types of information of interest to a study such as this.

Referring to the behavior of O/H compounds, figures (8) and (9), we see in the baseline probe suggestively lower concentrations of H, OH, O, O_2 and HO_2, the comparison factors at 2 cm being about 10 for H and OH, 100 for O, and 1000 for O_2 and HO_2. Apparently reactions consuming these reactants tend to be "frozen out" by the aerodynamic probe. At the recovery point at 1.07 cm, losses of HO_2 and O_2 are suddenly accelerated. Possibly noteworthy is the tendency of H atoms to remain "free", post-recovery, and the observation that the higher HO_2 levels in the aerodynamic probe are not associated with higher levels of NO_2. (The reaction $NO + HO_2 \rightarrow NO_2 + OH$ has been frequently mentioned as the primary source of NO_2 as a combustion effluent, tending to occur when HO_2 builds up in relatively cool regions of the system.)

CONCLUSIONS AND RECOMMENDATIONS

As discussed in the previous section, the reliability of the chemistry in this program is needful of verification. Indeed, for homogeneous reactions (to which the program as presently implemented is limited) a careful selection of reactions and rate constants should be made. Tests on simple systems will be valuable, to confirm the program's ability to reliably repro-

duce the description of well-understood phenomena. Sensitivity to choice of rate constants should be assessed.

Insofar as extensions of the current program are concerned, for purposes of assessing possible probe effects the inclusion of heterogeneous reactions may be essential. The code of this program appears amenable to incorporating surface reactions into the model subject to phenomenological assumptions concerning the diffusive transport of molecules to the walls (Ref. 12). Typically, wall reactions attain importance at lower temperatures, where homogeneous reactions are quenched (Ref. 15). However, a recent study of Myerson discusses an intermediate temperature (1300 - 1700°K) surface reaction associated with carbonaceous deposits from combustion effluents, forming largely N_2 and CO from the deposit and NO (Ref. 16). This particular reaction, only 75% complete for an 0.1 second residence time of 10^{-3} mole fraction NO (albeit in a 1.9 cm diameter reactor), seems somewhat too slow to be an obvious candidate notwithstanding the similarity of the reaction to gross patterns of "probe effects" previously studied (Refs. 6 and 7). Nonetheless, in light of imperfect but developing knowledge of possible reactions, their rate constants, and pertinent diffusive processes, it may be of interest to inquire as to what ranges of conditions could account for probe effects as observed.

Frictional effects remain to be considered in the model: They can be incorporated phenomenologically into the one-dimensional model (Ref. 6). In the longer term, it will be desirable to extend the calculation to two dimensions. The consistency of hypotheses in the one-dimensional calculation with findings of the multiple-streamline generalization of the system will be of interest.

The range of phenomena operational in probe systems is diverse. The modelling of such systems can provide no less than useful insights into the coupling of these phenomena as a by-product of a necessary part of the effort towards the resolution of an environmentally significant issue.

REFERENCES

1. Matthews, R. D., Sawyer, R. F., and Schefer, R. W. "Interferences in Chemiluminescent Measurement of NO and NO_2 Emissions from Combustion Systems." Env. Sci. Tech. 11, 1092-1096, 1977.

2. Anderson, L. B. and Meyer, J. W. "High Altitude Jet Plume Chemistry." Fourth Int'l. Colloquium on Gasdynamics of Explosions and Reactive Systems, La Jolla, 1973.

3. Davidson, D. L. and Domal, A. F. "Emission Measurements of a J93 Turbojet Engine." AEDC-TR-73-132, 1973.

4. Few, J. D., Bryson, R. J., McGregor, W. K., and Davis, M. G. "Evaluation of Probe Sampling versus an In-Situ Optical Technique for Nitric Oxide Concentration Measurement in Combustion Gas Streams." Int'l. Conference Environmental Sensing and Assessment, 2, 27/6, 1975. Also, Few, J. D., Bryson, R. J., and McGregor, W. K. "Evaluation of Probe Sampling versus Optical In-Situ Measurements of Nitric Oxide Concentrations in a Jet Engine Exhaust." AEDC-TR-76-180, 1977.

5. Few, J. D. "Optical Measurements of NO and NO_2 in the Exhaust of an F101-GE-100 Engine at Simulated Altitudes." AEDC-TR-77-75, 1977.

6. Few, J. D., Bryson, R. J., and Lowry III, H. S. "Evaluation of Optical In-Situ versus Nitric Oxide Concentration as a Function of Axial Positions in a Jet Engine Combustor Exhaust." AEDC-TR-78-32, to appear.

7. Bryson, R. J. and Few, J. D. "Comparisons of Turbine Engine Combustor Exhaust Emissions Using Three Gas-Sampling Probe Designs." AEDC-TR-78-7, to appear.

8. See, for example, Shapiro, A. H. The Dynamics and Thermodynamics of Compressible Fluid Flow, Volume I. (New York: The Ronald Press Company, 1953.), 647pp.

9. Stull, D. R. and Prophet, H., et.al. JANNAF Thermochemical Tables, NSRDS-NBS 37 (Washington: The U. S. Government Printing Office, 1971), 1141pp.

10. ed. Zinn, B. T. Experimental Diagnostics in Gas Phase Combustion Systems (New York: AIAA, 1977), 657pp.

11. ed. Kennedy, L. A. Turbulent Combustion (New York: AIAA, 1978), 485pp.

12. Amin, H. "Effect of Heterogeneous Removal of Oxygen Atoms on Measurement of Nitrogen Dioxide in Combustion Gas Sampling Probes." Combustion Sci. Tech. 15, 31-40, 1977.

13 Krantch, J. C. and Moore, [illegible] "Modelling and Measurement of Sample Probe Effects on Pollutant Gases Drawn from Flame Zones." Combustion Sci. Tech. 18, 81-104, 1978.

14. In this work, we have to date used only a set of 37 reactions and rate constants adopted by I. Osgerby in the development of the program in 1974. These reactions and their rate data as used are given in Table 1. Several of these data are as referenced in Osgerby, I. T., "Literature Review of Turbine Combustor Modelling and Emissions." AIAA J. 12, 743-754, 1974. Subsequent work will include proper emphasis on judicious preparation of such input data.

15 For example, see Wise H. and Frech, M. F. "Kinetics of Decomposition of Nitric Oxide at Elevated Temperatures I. Rate Measurements in a Quartz Vessel" J. Chem. Phys 20, 22-24, 1952, and by the same authors, "... II. The Effect of Reaction Products and the Mechanism of Decomposition," ibid, 20, 1724-1727, 1952. Data provided here will be of good use in "bench-marking" aspects of the program.

16. Myerson, A. L. "New Heterogeneous Mode of Nitric Oxide Reduction by an In-Situ Formed Carbon." Env. Sci. Tech. 12, 212-217, 1978. The author notes that the dependence of conversion on residence indicates the reaction is first order in NO. However, the fact that the extrapolation of his linear fit of log ($[NO]_{initial}/[NO]_{final}$) versus residence time has a zero residence time intercept around 0.45 seems to justify further consideration.

Figure 1

Code Organization

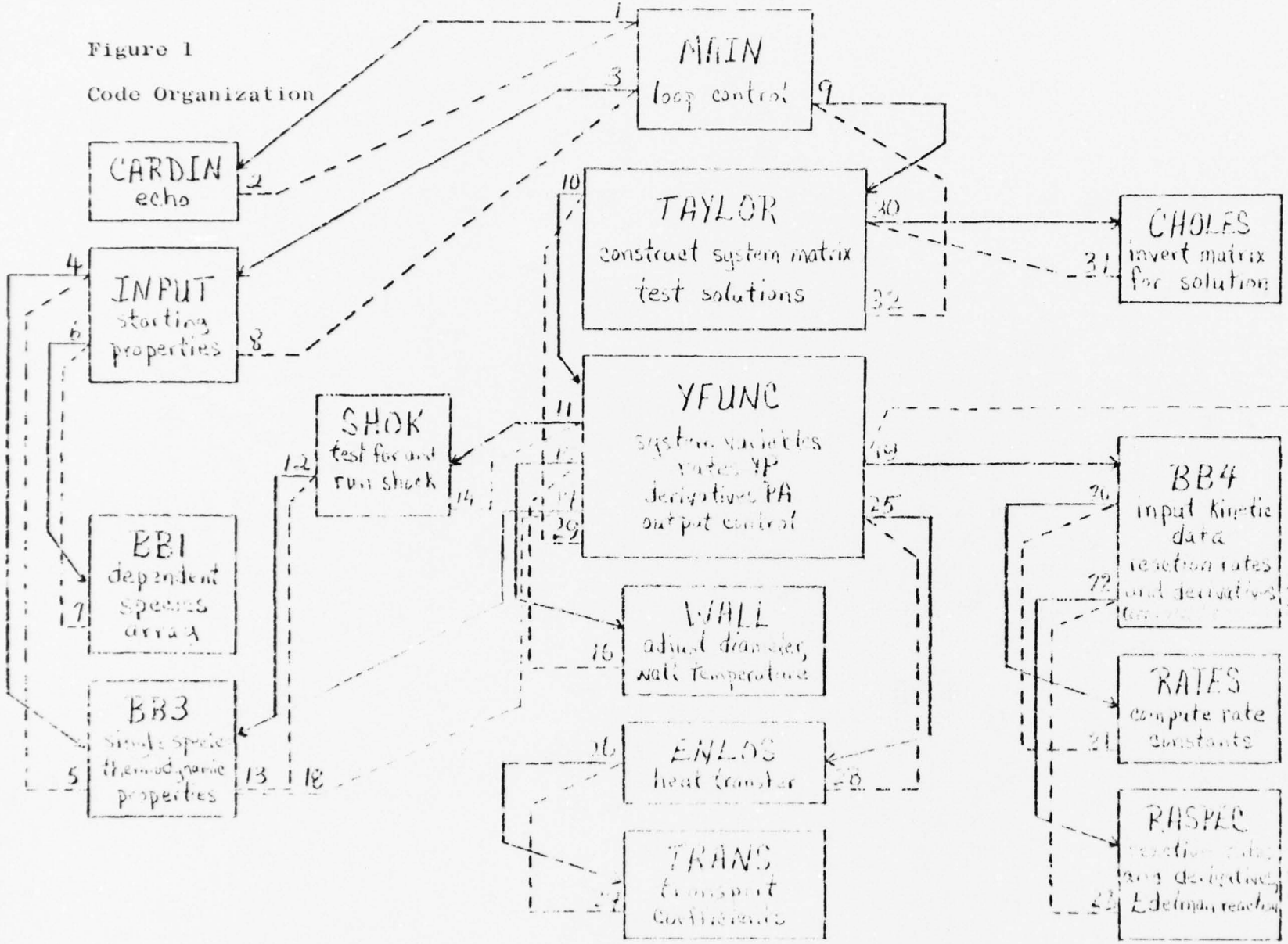

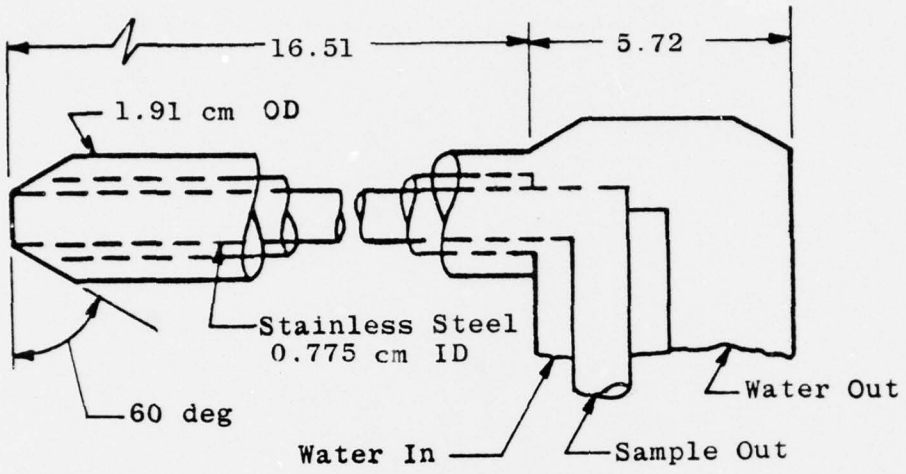

Baseline Probe

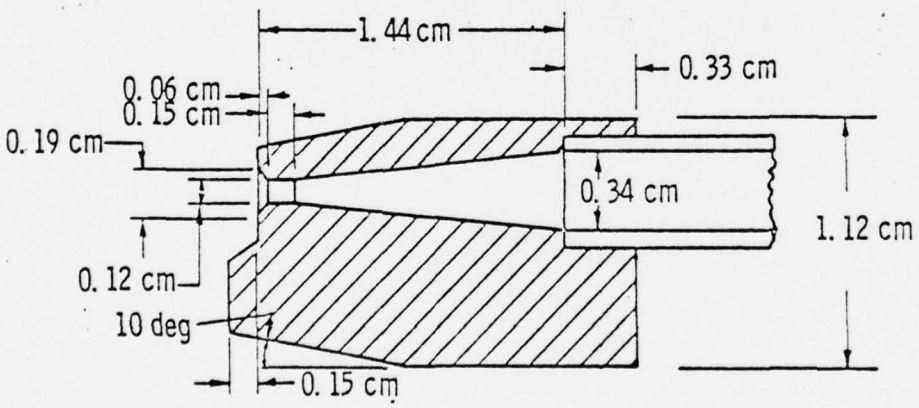

Aerodynamic Probe

Figure 2

Baseline and Aerodynamic Probes

DATE 08-09-78 ARO INC
PROJ-

Figure 3

Static Temperature in Baseline Probe

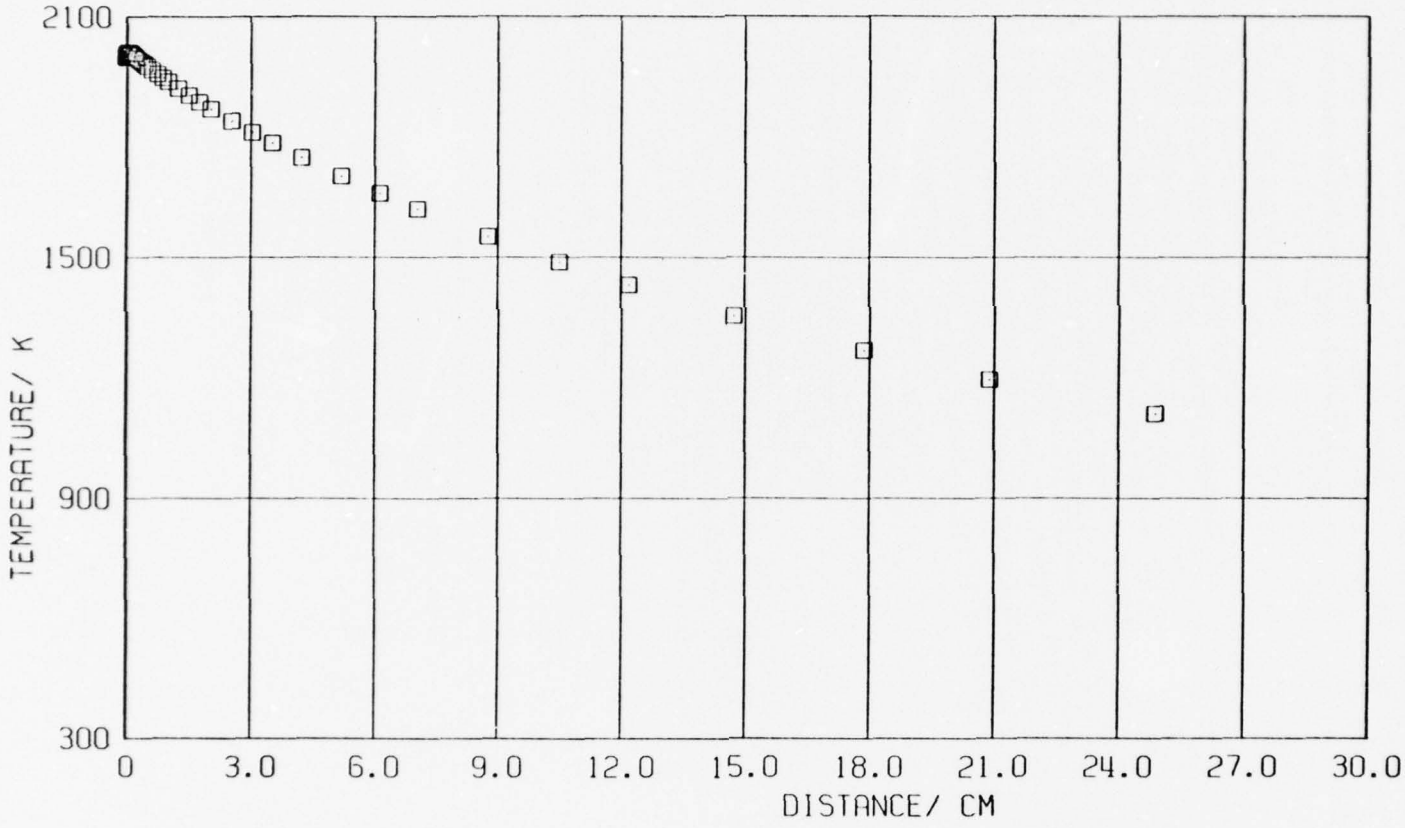

DATE 08-09-78 ARO INC
PROJ-

Figure 4

Static Temperature in Aerodynamic Probe

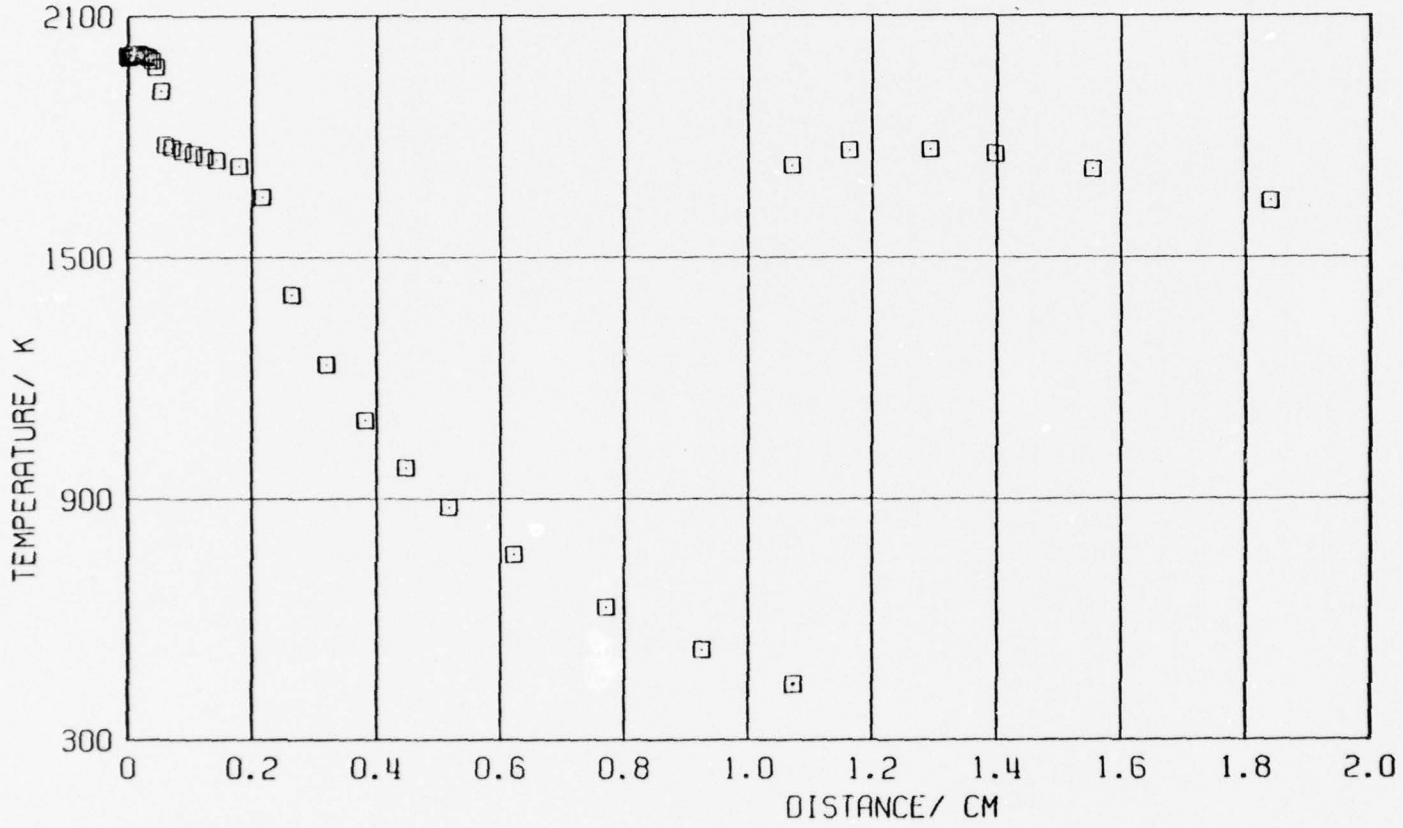

DATE 08-09-78 ARO INC
PROJ-

Figure 5

Static Pressure in Aerodynamic Probe

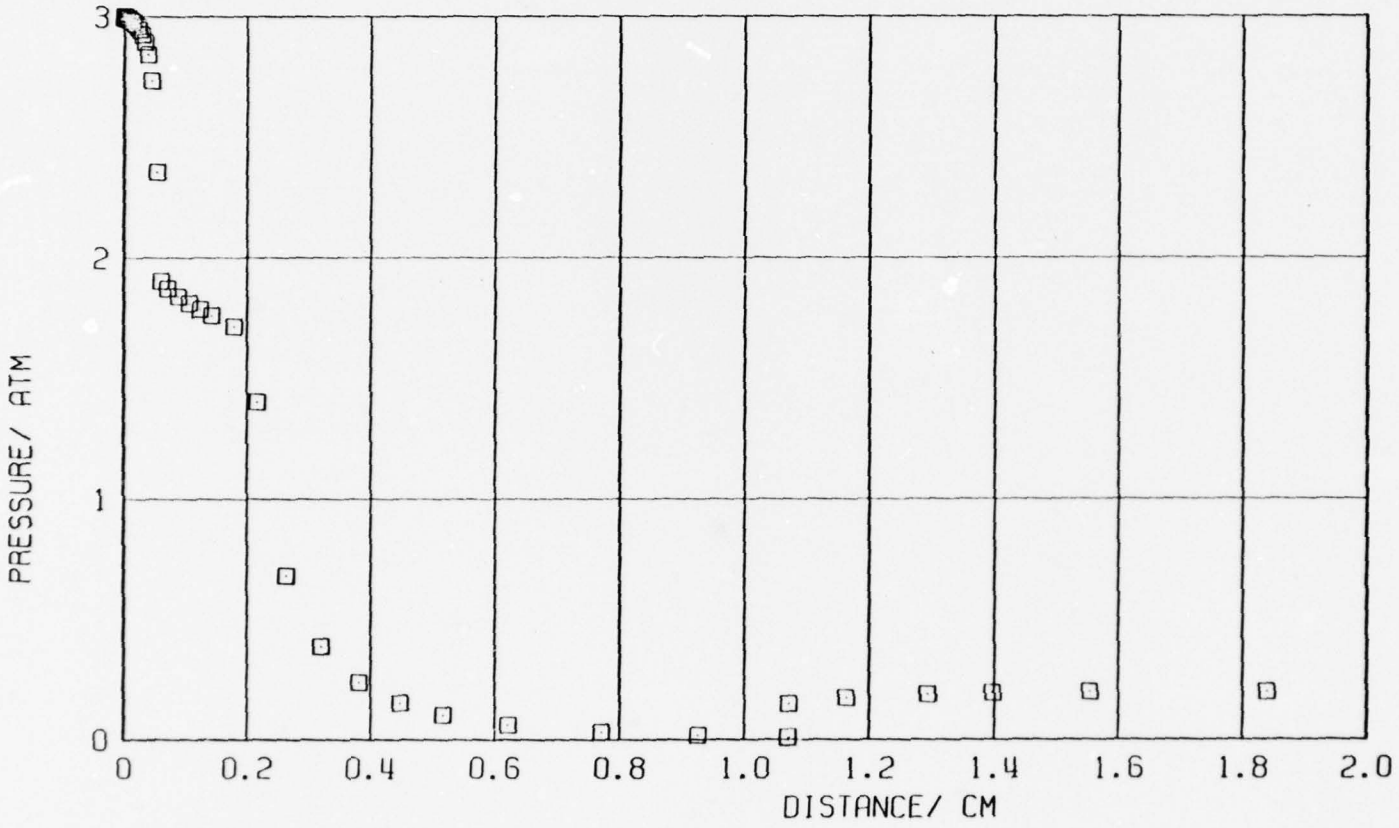

DATE 08-09-78 ARO INC
PROJ-

Figure 6

Compounds of Nitrogen and Oxygen in Baseline Probe (log plot)

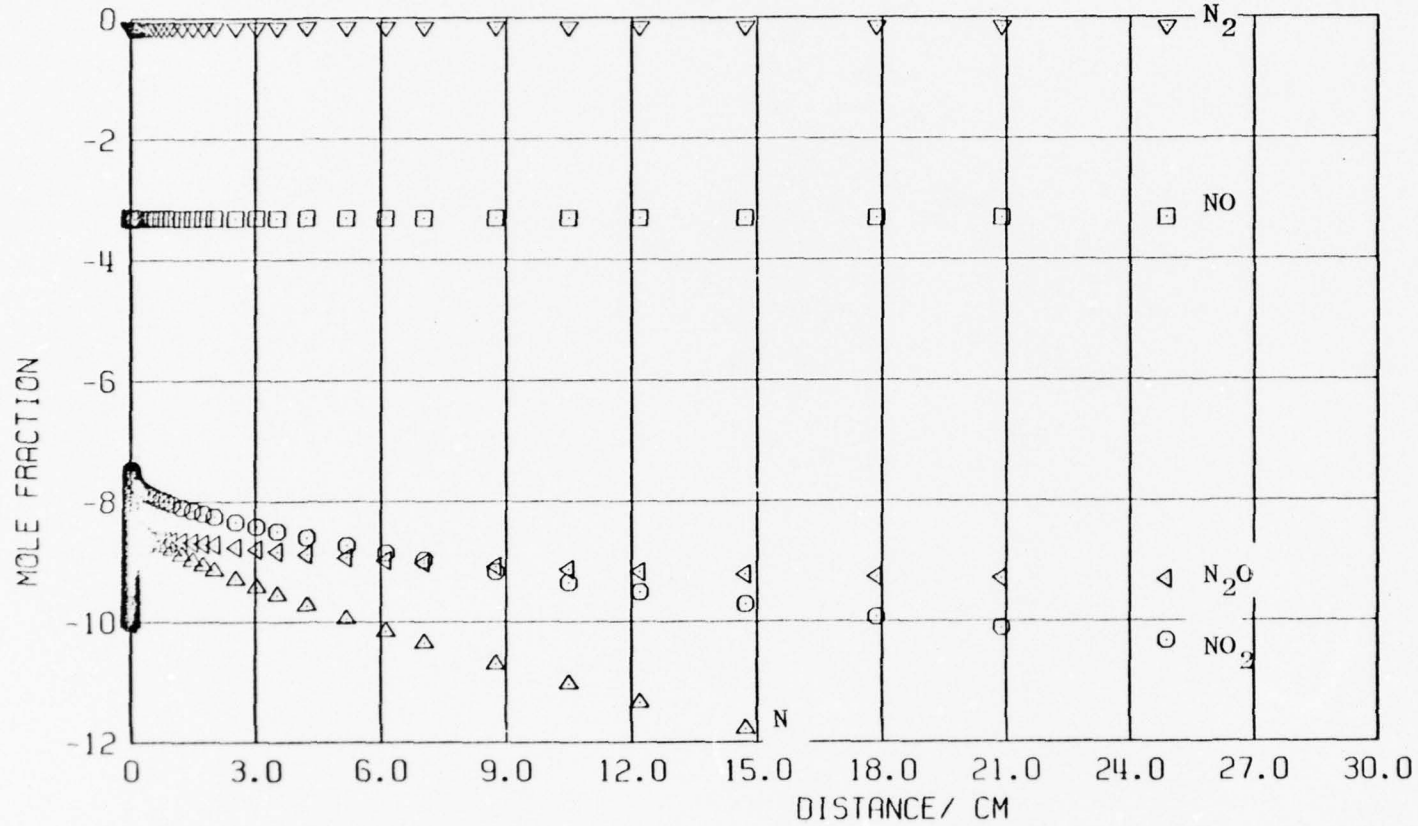

DATE 08-09-78 ARO INC
PROJ-

Figure 7

Compounds of Nitrogen and Oxygen in Aerodynamic Probe (log plot)

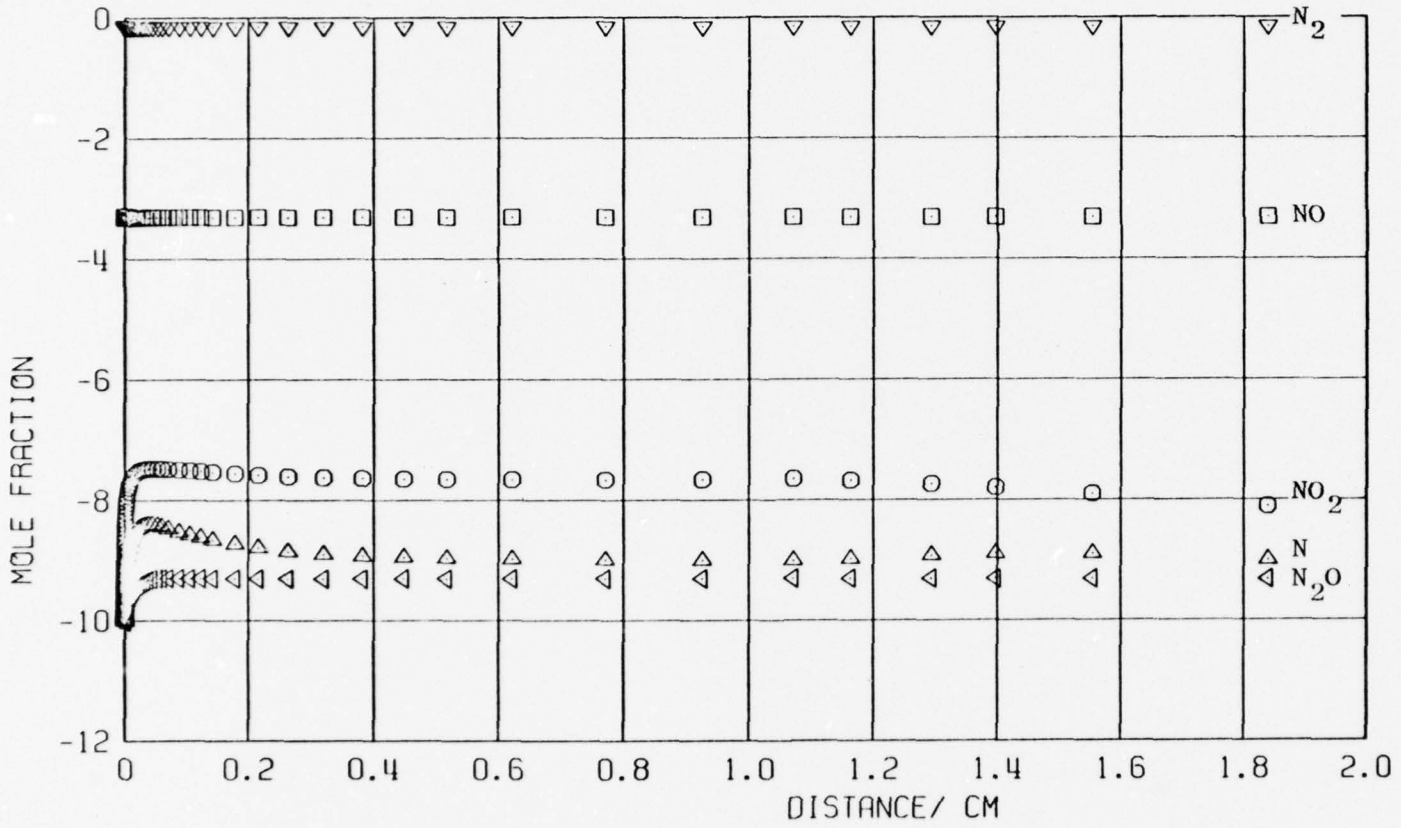

DATE 08-09-78 ARO INC
PROJ-

Figure 8

Compounds of Hydrogen and Oxygen in Baseline Probe (log plot)

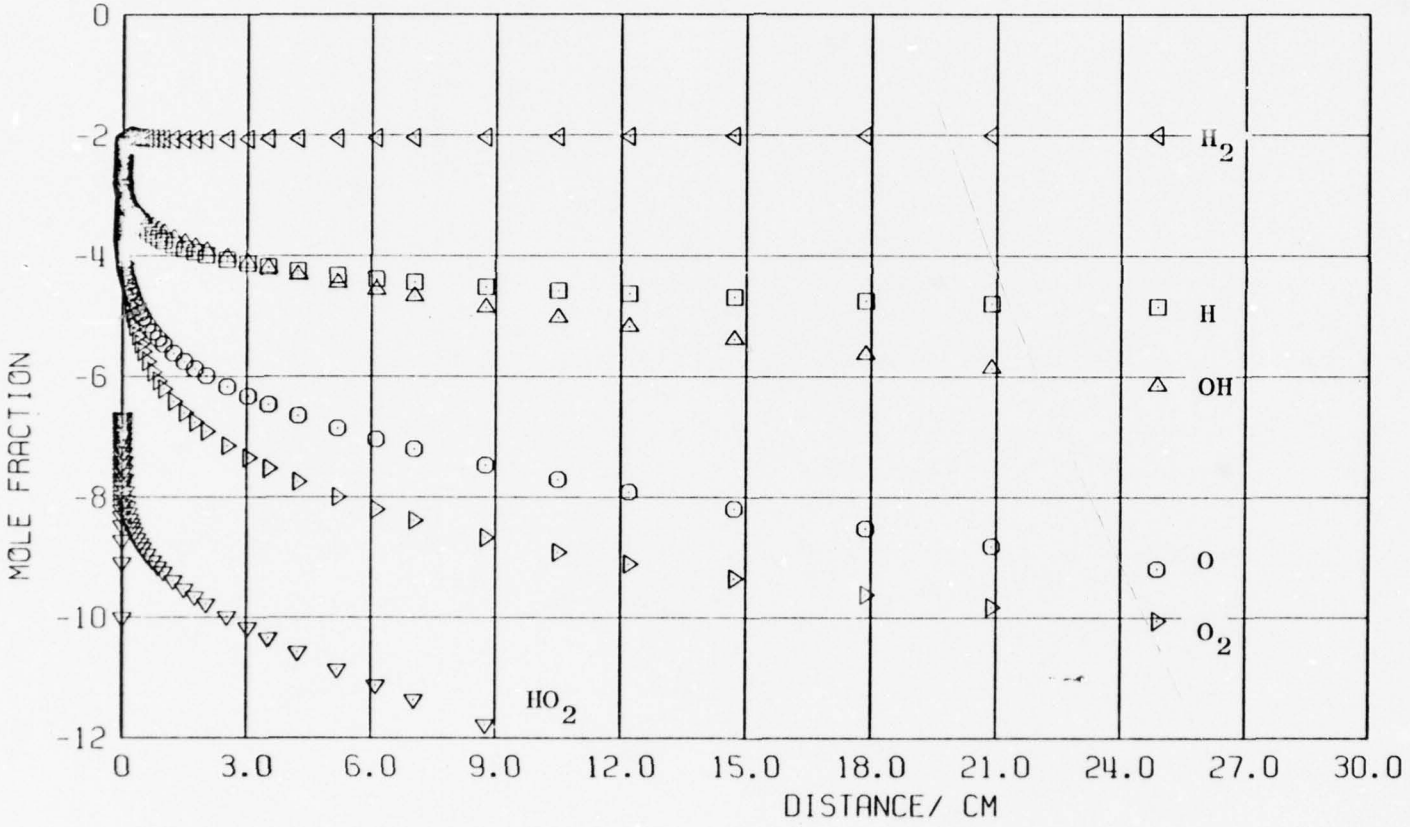

DATE 08-09-78 ARO INC
PROJ-

Figure 9

Compounds of Hydrogen and Oxygen in Aerodynamic Probe (log plot)

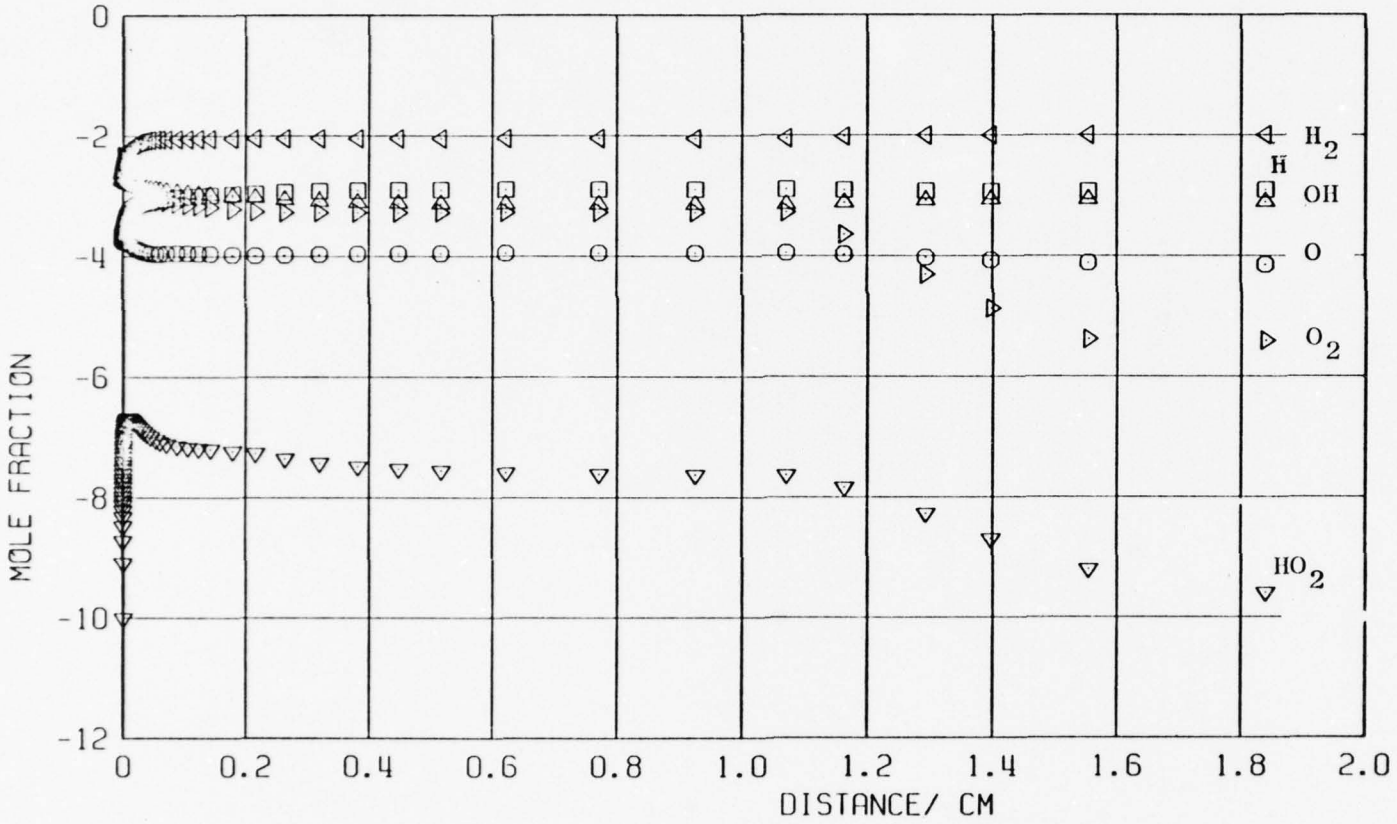

Table 1

Chemical Kinetics Data as Used in Program Runs

Classification of Reaction		Rate Constant[1] $k=AT^n e^{-E/RT}$			
Reaction	Code[2]	A[3,4]	n	E/R[5]	Notes
NO_x conversions					
$O + N_2 = NO + N$	7	1.36 (14)	0	37,750	6
$N + O_2 = NO + O$	33	1.55 (9)	1	19,450	6
$N + OH = NO + H$	2	4.21 (13)	0	0	6,7
$H + N_2O = OH + N_2$	1	3.01 (13)	0	5,435	7
$O + N_2O = O_2 + N_2$	3	3.61 (13)	0	12,077	7
$N_2 + NO_2 = NO + N_2O$	4	1.41 (14)	0	41,766	7
$H + NO_2 = NO + OH$	5	3.00 (13)	0	0	7
$NO + HO_2 = OH + NO_2$	6	6.00 (11)	0	0	7
$NO + O_2 = O + NO_2$	9	1.00 (12)	0	22,900	
$NO + NO = N_2O + O$	10	7.05 (11)	0	32,708	
$N_2 + O_2 = N + NO_2$	30	2.70 (14)	-1	60,600	7
$N_2 + O_2 = NO + NO$	31	9.10 (24)	-5/2	64,600	
$N + NO_2 = NO + NO$	32	1.00 (10)	0	44,300	
$NO + CO = N + CO_2$	35	2.00 (11)	-1/2	4,000	8
$CO + NO_2 = NO + CO_2$	36	2.00 (11)	-1/2	2,500	7
$NO_2 + M = NO + O + M$	8	1.10 (16)	0	33,000	8
$O + N_2 + M = N_2O + M$	11	6.30 (14)	0	28,582	7
$NO_2 + M = O_2 + N + M$	34	6.00 (14)	-3/2	52,600	8
H/O conversions					
$H + O_2 = O + OH$	13	2.20 (14)	0	8,454	
$OH + OH = O + H_2O$	14	5.75 (12)	0	393	7
$O + H_2 = H + OH$	15	1.74 (13)	0	4,750	7
$OH + H_2 = H_2O + H$	16	2.20 (13)	0	2,592	7
$H + HO_2 = OH + OH$	21	2.50 (14)	0	956	7
$OH + HO_2 = H_2O + O_2$	22	1.20 (14)	0	503	
$O + HO_2 = OH + O_2$	23	5.00 (13)	0	0	
$H + HO_2 = H_2 + O_2$	24	2.50 (13)	0	352	7
$H + HO_2 = O + H_2O$	25	1.00 (13)	0	503	7
$H_2 + O_2 = OH + OH$	28	1.70 (13)	0	2,470	
$H + H + M = H_2 + M$	17	5.00 (15)	0	0	
$H + OH + M = H_2O + M$	18	1.00 (17)	0	0	
$O + O + M = O_2 + M$	19	9.38 (14)	0	0	
$H + O_2 + M = HO_2 + M$	20	1.50 (15)	0	-503	7
$O + H + M = OH + M$	29	1.00 (16)	0	0	
C/O conversions					
$CO + OH = H + CO_2$	12	5.60 (11)	0	543	
$CO + O_2 = CO_2 + O$	26	3.00 (12)	0	24,000	
$CO + O + M = CO_2 + M$	27	1.80 (19)	-1	2,000	
$C_8H_{16} + 4O_2 = 8CO + 8H_2$	37		1	12,400	9

Table 1 Continued

Notes

1) "Forward" rate constant, k, for reaction proceding from left to right; reverse rate constant obtained from k and equilibrium constant

2) Sequential position of reaction data in input deck used for test runs in this work

3) Units: cm^3 $mole^{-1}$ sec^{-1} for bimolecular reactions, cm^6 $mole^{-2}$ sec^{-1} for termolecular reactions

4) The expression n(m) is to be read n x 10^m

5) Units: degrees Kelvin

6) Zel'dovich mechanism

7) Parameters as cited in reference (12)

8) This reaction is input in the opposite direction from that listed here; an input parameter causes the program to use the reaction as listed

9) For this reaction (Edelman, R. B. and Fortune, O. F., "A Quasi-Global Chemical Kinetic Model for the Combustion of Hydrocarbon Fuels," AIAA paper 69-86, 1969) $A=5.52 \times 10^8 p^{-0.825}$. This reaction is constrained to occur in the "forward" direction only

1978 USAF-ASEE SUMMER FACULTY RESEARCH PROGRAM
sponsored by
THE AIR FORCE OFFICE SCIENTIFIC RESEARCH
conducted by
AUBURN UNIVERSITY AND OHIO STATE UNIVERSITY

PARTICIPANT'S FINAL REPORT

THE APPLICATION OF LASER DOPPLER VELOCIMETRY TO THE STUDY OF VORTEX FORMATION AND PROPAGATION IN UNSTEADY SEPARATED FLOWS

Prepared by:	Robert A. Kadlec, Ph.D.
Academic Rank:	Assistant Professor
Department and University:	Department of Aerospace Engineering Sciences University of Colorado
Assignment:	
(Air Force Base)	Air Force Academy
(Laboratory)	Frank J. Seiler Research Laboratory
(Division)	Aerospace-Mechanics Sciences
(Branch)	Mechanics
USAF Research Colleague:	Capt Michael S. Francis
Date:	August 11, 1978
Contract No.:	F44620-75-C-0031

THE APPLICATION OF LASER DOPPLER VELOCIMETRY TO THE STUDY OF VORTEX FORMATION AND PROPAGATION IN UNSTEADY SEPARATED FLOWS

by

Robert A. Kadlec

ABSTRACT

The Frank J. Seiler Research Laboratory (FJSRL) at the U.S. Air Force Academy is conducting a comprehensive experimental research program to study unsteady separated flows and, in particular, the dynamic stall of oscillating airfoils. The aim of this study is to achieve a clearer understanding into the physical mechanisms responsible for dynamic stall and to capitalize on these unique stall features by using them to improve the turn performance and maneuverability of flight vehicles.

The objective of this summer research program has been to adapt a general purpose laser doppler velocimetry (LDV) two-velocity component system to dynamic stall experiments in the subsonic wind tunnel facility at the USAFA. The preliminary design LDV system, its special constraints, and the characterization of system signal and noise figures are described.

Results presented for the initial operation of the LDV system demonstrate its performance capabilities. The LDV system meets all subsonic wind tunnel constraints, and it makes accurate velocity measurements in the two-dimensional flow field surrounding an airfoil. However, accurate measurements in a wind tunnel environment can be achieved only when optical noise produced by scattered laser light from wind tunnel surfaces is minimized.

ACKNOWLEDGEMENTS

I am grateful to the Air Force Systems Command and the ASEE for support in the summer faculty research program. A special appreciation is due to Auburn University and, in particular, Mr. Fred O'Brien for excellent organization and coordination of the program administration.

In this short space it is not possible to say enough about the superb research environment at the Frank J. Seiler Research Laboratory, U.S. Air Force Academy. My stay at the Academy has been an enriching and enjoyable experience. Special thanks are due to Lt Col Joseph Ford, Capt George Sparks, Capt John Keesee, Ms. Donna Weiss, and Mr. Carl Geddes. In particular, my sincere appreciation goes to Capt Michael Francis for his encouragement, consultation, and valuable assistance.

LIST OF FIGURES

1. INTRODUCTION

The capability to predict the lift, drag, and moment acting on an airfoil is fundamental to the aerodynamicist. Solutions evolved in pursuit of this objective for a host of engineering problems form the basis of the edifice of classical aerodynamics. While considerable confidence exists when tackling steady flows where viscous and potential regions can be treated separately, little quantitative methodology is available for treating unsteady flows where separation and reattachment of the thin viscous layer near the surface occur. In some applications this unsteady separated flow phenomenon arises when an otherwise steady flow environment about a solid device is upset by undesirable unsteady effects due either to self-induced motions of the device itself or to fluctuations or instabilities in the surrounding flow. In other applications, the device is designed to operate in an unsteady manner in order to perform its desired function. A recent review by McCroskey (Ref. 1) examines the current research interest in unsteady stall and other unsteady fluid dynamical effects that occur in a wide range of modern engineering problems.

The Frank J. Seiler Research Laboratory (FJSRL) at the U.S. Air Force Academy is presently conducting a comprehensive experimental research program to study unsteady separated flows and, in particular, the dynamic stall of oscillating airfoils. When dynamic stall occurs, transient forces and moments develop which are fundamentally different from their static counterparts, the most striking differences being large increases in force and moment coefficients above static values, the occurrence of "moment stall" before "lift stall," and the delay of the stall event to angles of attack in excess of the static stall value. The aim of this study is to achieve a clearer understanding into the physical mechanisms responsible for dynamic stall and to capitalize on these unique stall features by using them to improve the turn performance and maneuverability of flight vehicles.

2. BACKGROUND

The FJSRL study is directed toward a detailed examination of the vortex kinetics associated with dynamic stall. Figure 1 depicts a qualitative view of the flow over an airfoil executing a dynamic stall. It has been speculated that the formation, growth, and propagation of a free vortex residing on the airfoil upper surface, together with the accompanying reverse flow region, are central to the dynamic stall problem. However, no sound theoretical models exist. Consequently, detailed measurements of the periodic space/time mean velocity field for an oscillating airfoil exhibiting dynamic stall will provide valuable information about the stall process.

The two current competing techniques used to measure local time-varying velocities are hot-wire anemometry and laser doppler velocimetry (LDV). Both have distinct advantages and limitations. Hot-wire anemometry is a traditionally accepted, highly refined method for unsteady flow studies, and recently it was successfully used by the FJSRL to map the vorticity

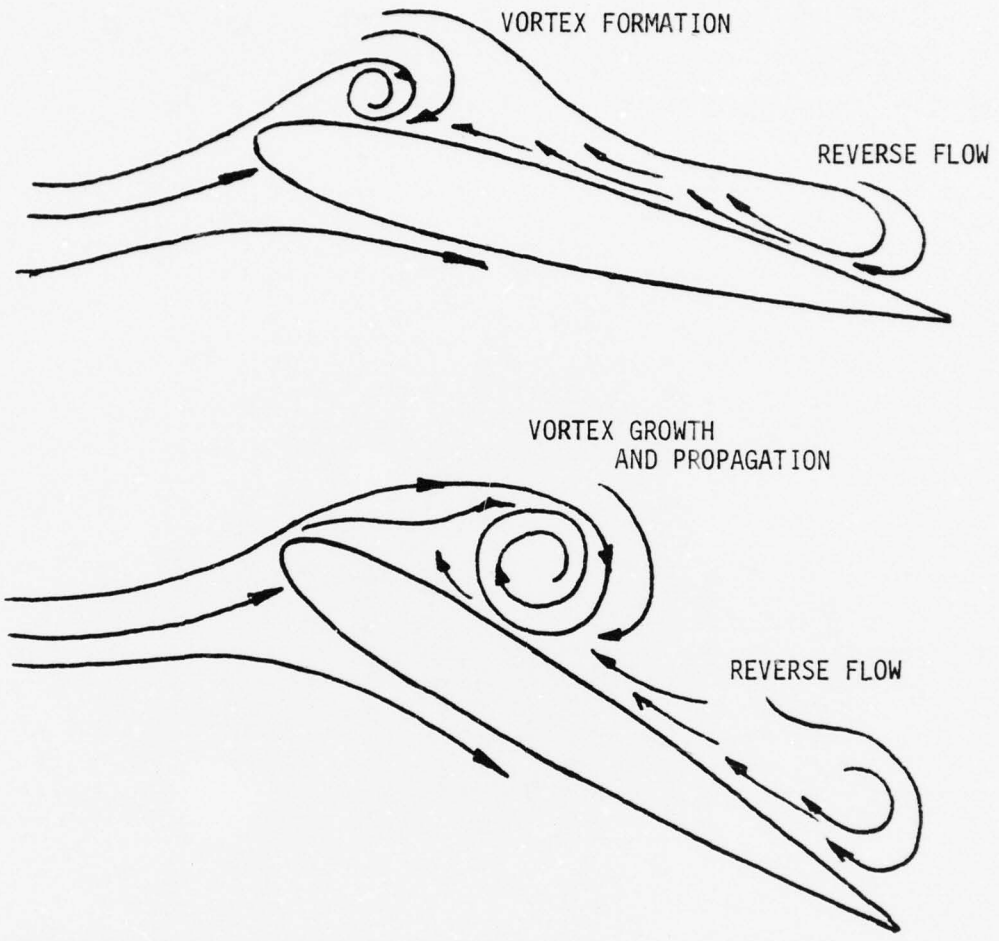

DYNAMIC STALL

--FORMATION AND CONTROL OF A FREE SPANWISE VORTEX

--TRANSIENT FORCES AND MOMENTS FUNDAMENTALLY DIFFERENT (LARGER) FROM STATIC COUNTERPARTS

--BENEFICIAL TO IMPROVING MANEUVERABILITY OF FLIGHT VEHICLES

Figure 1. Unsteady Separated Flows

field in a restricted unsteady separated region behind an oscillating spoiler on an airfoil surface (Ref. 2). However, the technique suffers from two disadvantages which limit its usefulness: (1) a velocity measurement is not absolute, requires careful calibration, and makes long-term drift of experimental conditions a source of error; and (2) a mechanical probe must be inserted into the flow, therefore inevitably disturbing the flow itself, especially in regions of reversal.

LDV has become an increasingly attractive diagnostic tool for the investigation of fluid flows (Ref. 3). It makes an optical measurement of velocity from the Doppler frequency shift of light scattered by particles moving with the fluid and thus is unobtrusive, absolute, and direct. However, the technique is somewhat complicated and expensive. The FJSRL is developing LDV diagnostics to study dynamic stall and related unsteady separated flows, and this report describes the in-progress development of the LDV system.

3. OBJECTIVES

The objective of this research program is to adapt a general purpose LDV two-velocity component system to dynamic stall experiments in the subsonic wind tunnel facility at the U.S. Air Force Academy. Features of this system include (1) specialized high frequency signal processing, (2) an inter-actively controlled two-dimensional LDV translation support structure, and (3) an interface with real-time disc-based minicomputer data acquisition system. This report includes a description of the preliminary LDV system and its special constraints, initial operation of the system and a characterization of both system signal and noise, and the improvement of system signal and noise reduction, which in turn suggest an improved LDV system.

4. LASER DOPPLER VELOCIMETRY (LDV) SYSTEM

4.1 General Considerations

LDV is based on the fundamental concept of a frequency shift in electromagnetic radiation received from an emitting and moving source by a stationary observer. In fluid applications, the source is a small micron-sized particle entrained with the moving fluid which scatters laser light toward a detector. The equation connecting the frequency difference between this scattered light and an unscattered reference laser beam and one velocity component of the particle can be derived from the Doppler effect. Doppler frequency equations, descriptions of various LDV system considerations, and applications can be found in several references and texts (Ref. 4).

Several different optical schemes that use a laser have been developed around this familiar Doppler shift principle. The most suitable arrangement currently available for many wind tunnel experiments is the dual-beam backscatter technique (Ref. 5) shown schematically in Figure 2. It has

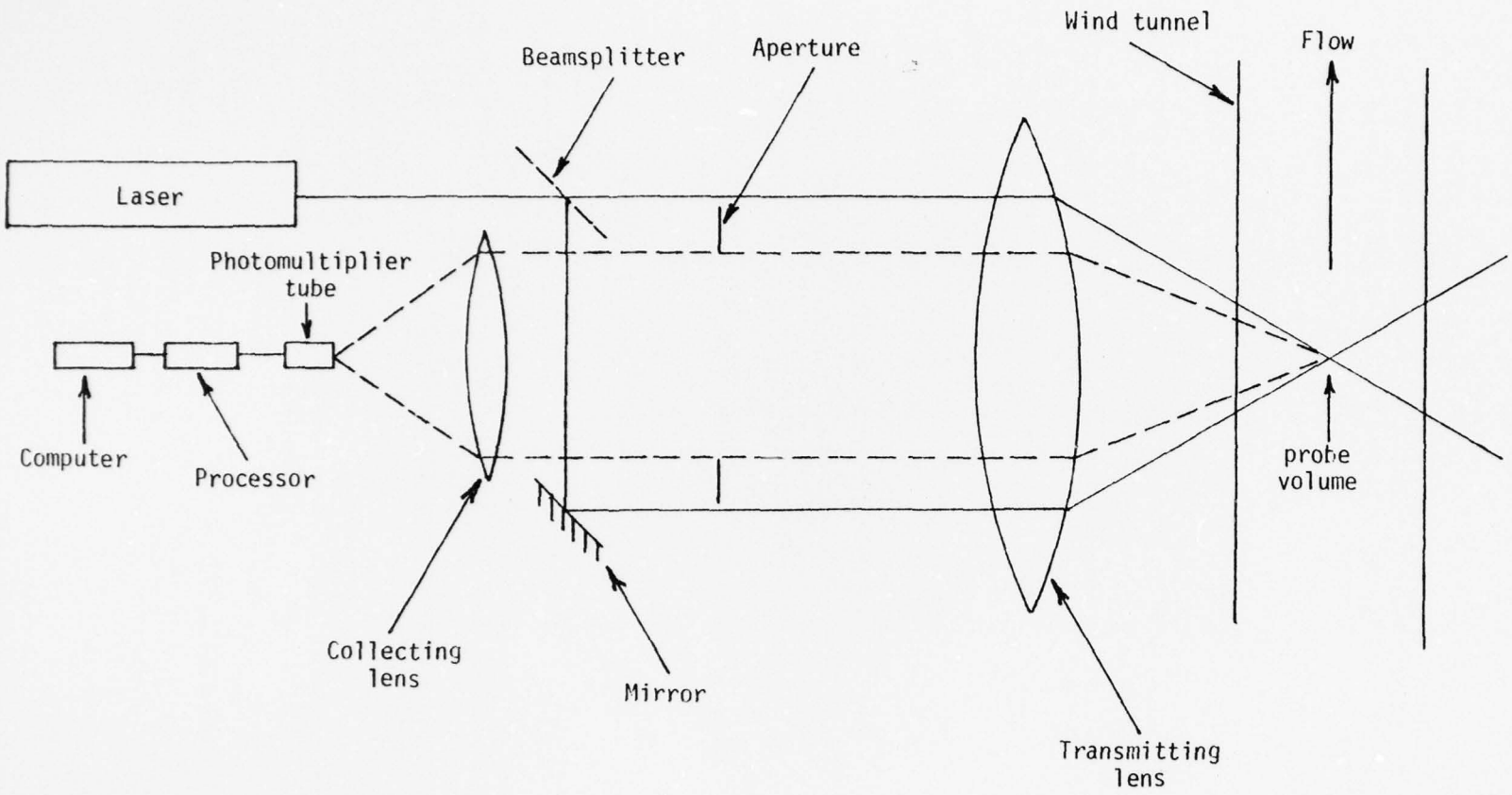

Figure 2. Dual-Beam Backscatter LDV

been adopted for this experimental study and is used here to elucidate the basic ideas of LDV. Monochromatic laser light is divided into two parallel beams of equal power. The beams are focused with a transmitting lens and cross at a point within the flow, called the probe volume. Particles passing through the probe volume scatter light back through the transmitting and collecting lenses and onto a photomultiplier tube which provides an output current proportional to the scattered intensity. This photocurrent is then received by the data processing system. The distinct advantages of this scheme for wind tunnel applications and, in particular, the FJSRL subsonic wind tunnel are discussed in Section 4.2.

The mathematical relationship between the intensity oscillations received by the photomultiplier and the velocity component of a scattering particle can be obtained from Doppler-shift considerations. However, for a dual-beam arrangement, a much simpler and clearer description is obtained from interference fringe considerations. A close-up schematic view of the probe volume is shown in Figure 3. When the two coherent laser beams intersect, their wave fronts interfere constructively and destructively to form a set of parallel plane fringes contained within the ellipsoidal probe volume. The fringes are perpendicular to the plane formed by the two beams and parallel to the bisector between the two beams. From geometry the distance between the fringes δ is

$$\delta = \frac{\lambda}{2 \sin \frac{\theta}{2}}$$

where δ = fringe spacing
λ = laser light wavelength
θ = included angle between the two beams.

When a particle moves through the probe volume and intercepts the fringe pattern, it scatters light with intensity variations that depend on fringe spacing and particle transit time. If the transit time between two adjacent fringes is τ, then the velocity component perpendicular to the fringes is just the distance per time, given as

$$\vec{V} \cdot \vec{n} = \frac{\delta}{\tau} = \left[\frac{\lambda}{2 \sin \frac{\theta}{2}}\right] \frac{1}{\tau}$$

where $\vec{V}$ = particle velocity vector
$\vec{n}$ = unit vector perpendicular to fringes
τ = transit time between two adjacent fringes.

Then the frequency of the scattered intensity oscillations f is $\frac{1}{\tau}$ or

$$f = \frac{2 \sin \frac{\theta}{2} (\vec{V} \cdot \vec{n})}{\lambda}$$

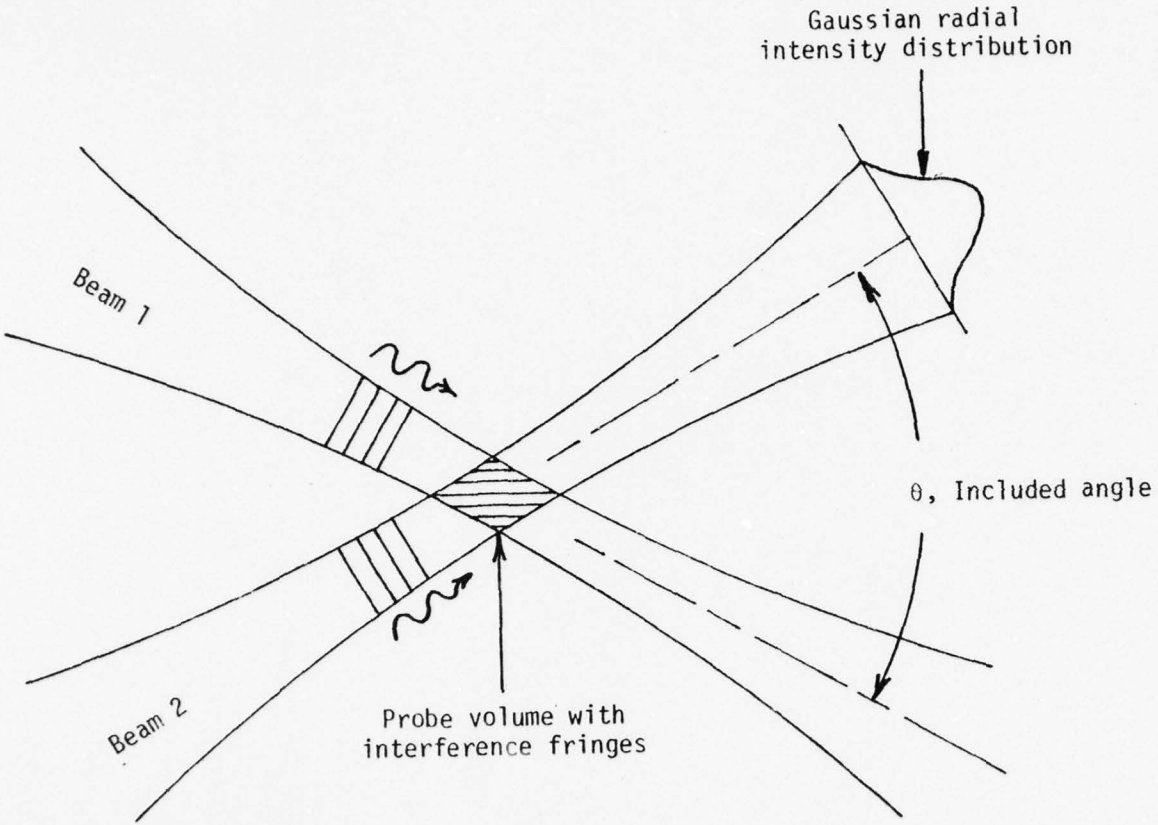

Figure 3. Probe Volume Close Up

which is the same frequency obtained from the Doppler derivation (Ref. 4). This Doppler frequency is in direct proportion to a velocity component.

For two-dimensional studies a second velocity component orthogonal to the first can be measured with a second set of dual-beams which are perpendicular to the first set. If different laser wavelengths are used for the two sets of beams, then two color-coded Doppler signals will represent the two velocity components of a scattering particle, provided all beams cross at the same point.

The dual-beam backscatter system described so far works well for scattering particle velocities that have unambiguous directions. However, since the measured Doppler frequency is proportional to a dot product of velocity, it cannot distinguish direction. That is, two particles with equal speeds but traveling in opposite directions produce identical frequencies. This ambiguity can be removed by frequency shifting one of the two dual beams, with an acousto-optic type Bragg-cell (Ref. 5). By doing so, fringes in the probe volume move in relation to this frequency shift and a particle within the probe volume near zero velocity will register a Doppler frequency equal to the frequency shift imposed by the Bragg-cell. Thus, this imposed incident beam frequency shift provides discrimination between positive and negative velocity components. The basic components of the dual-beam system described here have been incorporated into the FJSRL LDV.

4.2 The FJSRL LDV System

A feasibility study of an LDV system for the USAF Academy subsonic and trisonic wind tunnels was conducted by the FJSRL (Ref. 7). The purpose was to choose an LDV system that could satisfy the special constraints imposed by subsonic and trisonic applications, yet provide accurate, two-dimensional space-time flow velocity capability at minimum cost. The study included a detailed examination of many different trade-offs that led to a preliminary design concept. A summary of the system constraints and the preliminary design, together with some salient trade-offs, are presented here.

System Constraints: The unsteady separated flow research experiments pose a special limitation for the LDV system. All dynamic stall experiments are mounted vertically in the subsonic wind tunnel, and the drive mechanisms for these experiments are positioned below the wind tunnel test section (Figure 4). For two-dimensional studies this arrangement precludes optical entry into the test section through the side windows, the only access being through the top of the wind tunnel test section. The dual-beam backscatter configuration is the only logical LDV optical arrangement which satisfies this constraint, since both the incident and scattered signals pass through the same entry port.

In addition, a dual-beam backscatter system allows the collector optics to be mounted on the same overhead optical support structure as the laser and transmitting optics, thereby requiring only one drive system and eliminating the need for the slave optics detector unit that would be

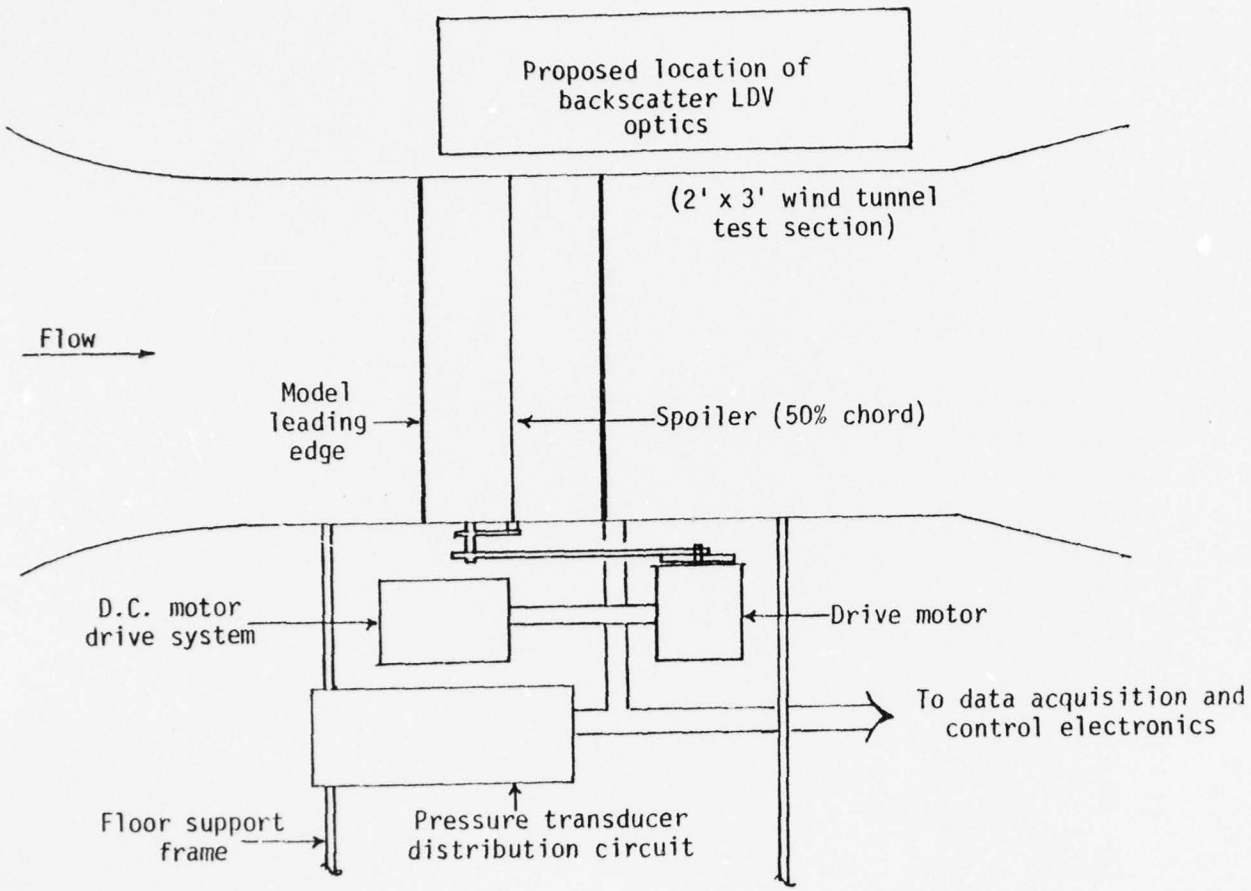

Figure 4. Unsteady Separated Flow - Experimental Schematic

required for a dual-beam forward scatter optical arrangement. The structure designed for this purpose is a dual-plane optical bench truss with three degrees of freedom in translation which allows the backscatter system to scan the probe volume throughout the flow region.

Preliminary Design: The preliminary optical system designed to meet these constraints at minimum cost with existing state-of-the-art LDV technology is shown in Figure 5. A Lexel Model 95-4 argon ion laser produces two powerful (1-watt) visible lines at 5145 Å (green) and 4880 Å (blue) which provide the color-coded beams required for simultaneous, two-dimensional velocity measurements. Two high-power, multi-layer mirrors turn the beam vertically onto an integrated optics assembly (Thermo-Systems, Inc.). This assembly spatially separates the green and blue beams, aligns them, frequency-shifts one green and one blue component, and focuses the four beams to form a probe volume at the midspan position in the test section. The beams enter the test section through an AR-coated, optical quality glass port that reduces specular backscatter. The backscattered light from particles passing through the probe volume is received by a collection optics, photomultiplier system housed in the transmitting optics assembly (Ref. 7, 8).

Signal Processing and Data Acquisition: Two counter-type signal processing units (Thermo-Systems, Inc.) analyze the blue and green photomultiplier signals and produce both analog and digital outputs representing two velocity components (Figure 6). These sophisticated units filter the Doppler signals, measure the time for a particle to cross a specified number of fringes, and convert this time to a velocity. The Thermo-Systems counter uses an operator-selected data validation scheme that allows rejection of spurious signals, thus reducing the data input caused by noise and eliminating velocity bias from particles traversing only a few fringes (Ref. 8). Raw velocity data from the signal processors are supplied to a DEC PDP 11/45 data acquisition system with disc storage and real-time capability. The data acquisition system calculates the mean velocity components at each position as data is collected, and results are printed in real time. In addition, filtered Doppler signals from scattered particles are monitored on 100 MHz storage oscilloscopes. A separate interactive computer control will command electric stepper motors to drive the LDV optical support structure to locate the probe volume at a specified X-Y position in the flow. The data acquisition software and the interactive computer control are presently being designed.

4.3 Preliminary Operation of the FJSRL LDV System - Optics and Signal Processing

This fellowship effort concentrated on the preliminary operation and improved design of the optics and signal processing systems. The following brief chronology outlines these efforts.

Laser and Mirror Requirements: When initially operated, the argon ion laser produced an output beam characterized by a donut mode (TEM_{01}). In addition, the turning mirrors used to direct the laser beam into the

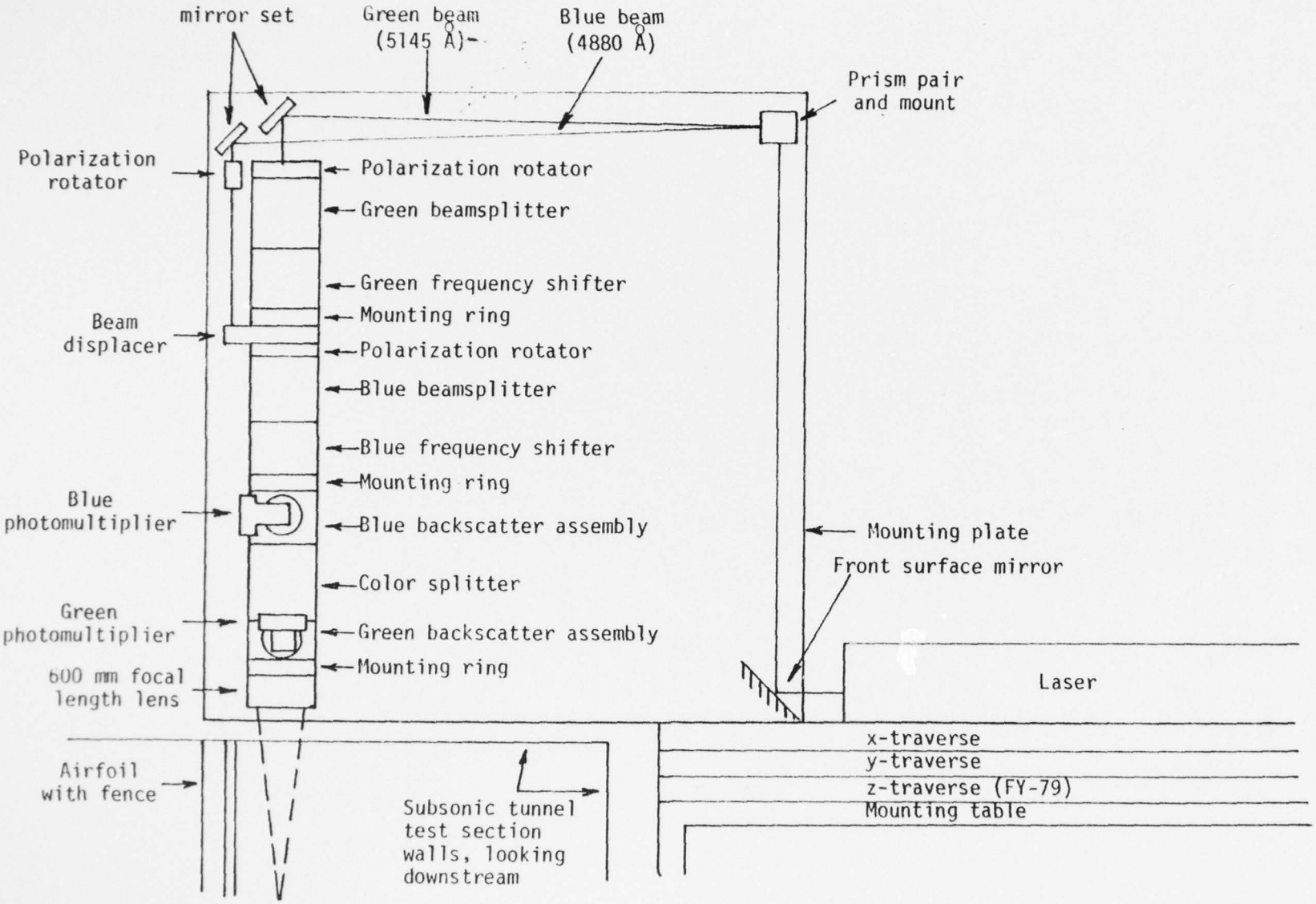

Figure 5. Optical System

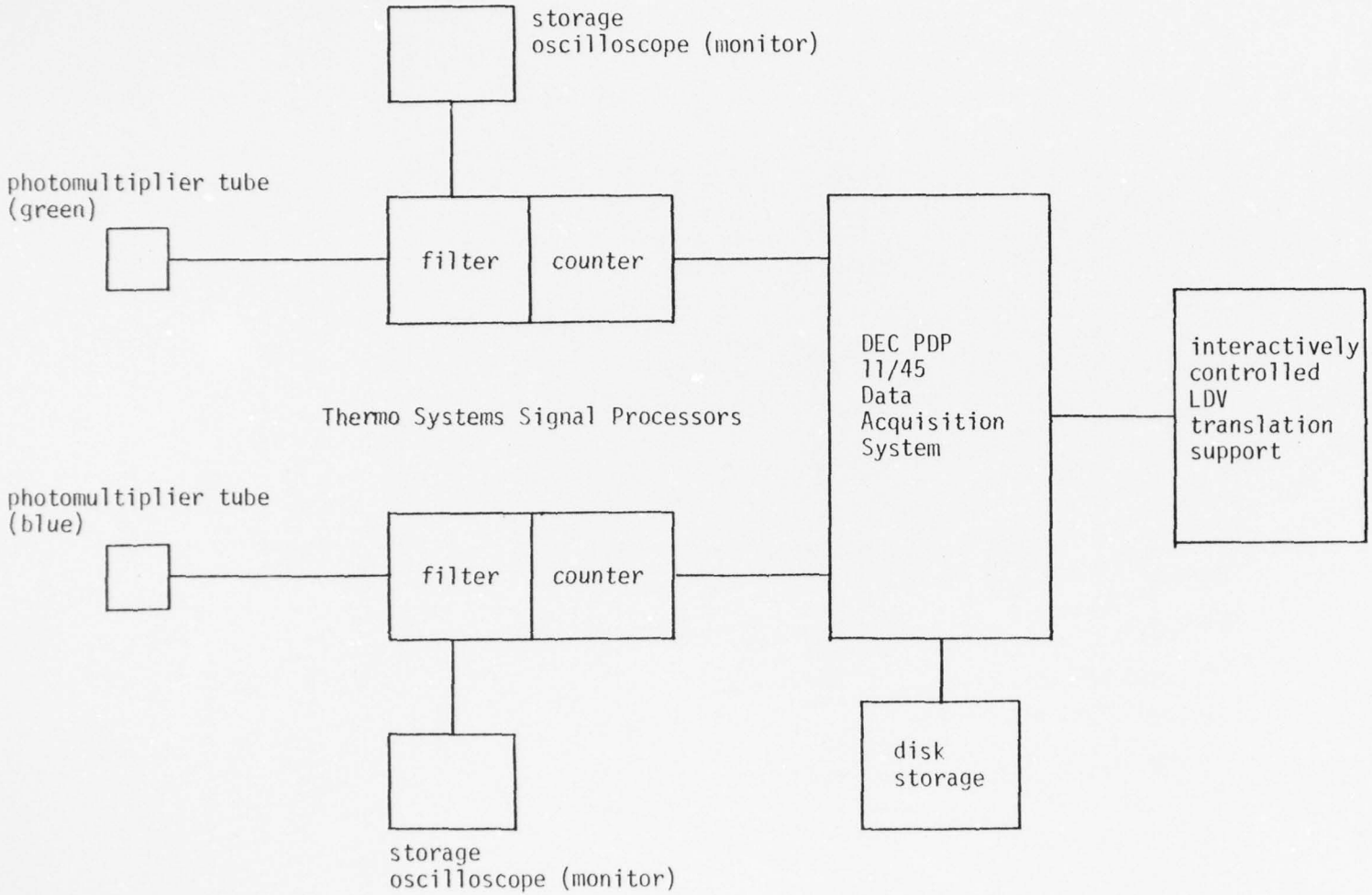

Figure 6. Signal Processing and Data Acquisition

integrated optics assembly were of such poor quality (low power) that they further accentuated the undesirable donut-mode shape. Considerable effort was spent on modifying and tuning the laser to achieve a fundamental mode operation (TEM_{00}). Further, the original mirrors were replaced with high power, argon ion, single-frequency laser mirrors. These modifications provided the high-quality, fundamental mode laser beam required for LDV applications.

Optical System Alignment (green beam): The next step was to carefully align the integrated optics assembly to provide a well-defined probe volume at midspan of the test section. The probe volume was then carefully examined with a microscope objective and revealed a well-defined fringe pattern. When the alignment was completed, a preliminary test-run experiment revealed a large noise and no observable Doppler signals.

Noise Reduction: The following noise sources are commonly found in practice: (1) ambient light, (2) scattered laser light, (3) spurious laser noise, (4) photodetector shot noise, and (5) electronically induced noise. Of these, the single most troublesome noise source encountered in the current experiment was that from scattered laser light--diffuse and specularly reflected laser light from the optical entry port, from the airfoil surface, and from the wind tunnel floor. At this stage of the investigation, it became apparent that improving the signal-to-noise ratio would present the single biggest challenge to successful system operation. Other LDV dual-beam backscatter experiments report a similar difficulty (Ref. 5).

The scattered laser noise sources were systematically eliminated as shown in Figure 7. First, diffuse reflections from the tunnel floor were deflected outside the collection optics solid angle by mounting a mirror flush with the tunnel floor. Next, a beam-picker assembly was positioned to intercept the first-surface reflections from the optical port. Although the port was AR-coated, these reflections still represented a noise source larger than the scattering particle signals. Finally, an isolation cone removed additional stray and diffusely scattered laser light. In the final design, the beam picker/isolation cone assembly could possibly be removed if the transmission lens is moved quite close to the wind tunnel optical access port, thus allowing the first-surface reflections from the port to fall outside the collection optics solid angle. The scheme described here is by no means intended to be a general procedure but only demonstrates the necessity for systematically eliminating laser light reflections in wind tunnel applications.

Preliminary Results: Once optical noise was reduced to tolerable levels, Doppler signals were measured for ambient seeding levels in the wind tunnel. Typical results for two different test section velocities portray large-signal, low-noise Doppler particle bursts (Figure 8). In addition to reducing optical noise, selective electronic filtering of the photomultiplier signals greatly enhanced the signal-to-noise ratio. Data rates for these measurements were typically 200/sec which are consistent with the findings about typical natural seeding levels reported in other wind tunnel facilities (Ref. 5).

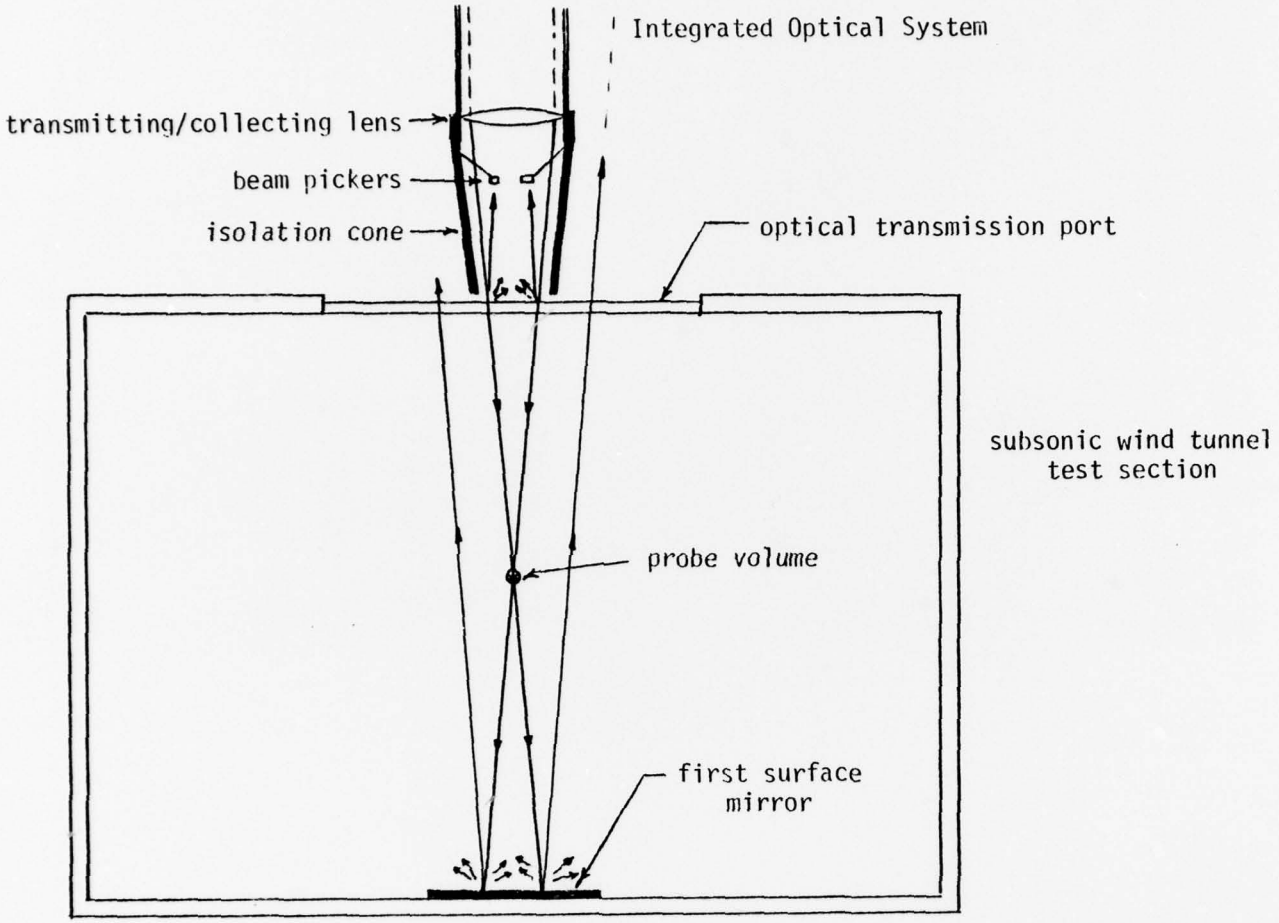

Figure 7. Treatment of Reflected Laser Light Noise

Experimental Conditions

Test Section Velocity (pitot)

61 f/s

LDV Measured Velocity

59 f/s

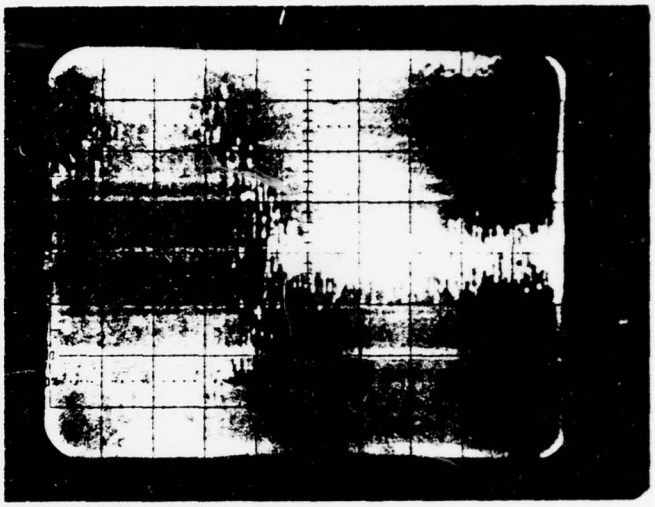

2 μ sec/div

Experimental Conditions

Test Section Velocity (pitot)

120 f/s

LDV Measured Velocity

123 f/s

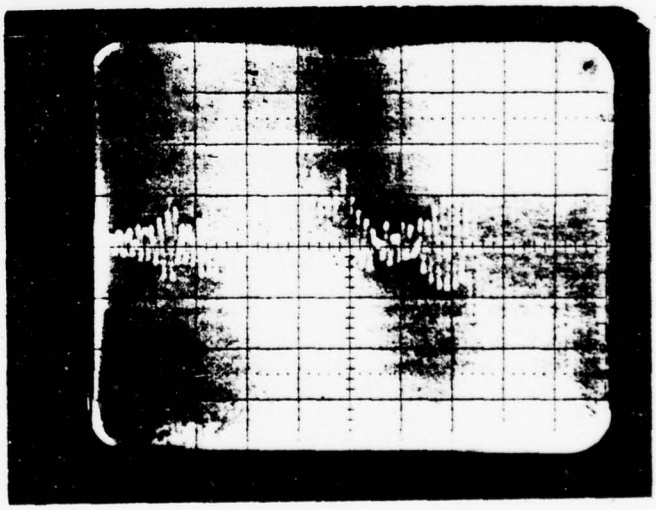

1 μ sec/div

Figure 8. Typical Doppler Signals (green beam)

The LDV counter was used to make velocity measurements of these Doppler signals for a range of test section speeds and comparison with pitot tube measurements is given in Figure 9. A parallel procedure was followed for the blue beam operation with similar results. The completion of these experiments represented the culmination of this summer's faculty fellowship.

5. CONCLUSIONS AND RECOMMENDATIONS

The LDV system designed for application to unsteady separated flow experiments at the FJSRL facility meets all system constraints. Preliminary experiments performed with this system indicate that it is possible to make accurate velocity measurements in the flow field surrounding a two-dimensional airfoil model. However, it was found that accurate measurements in a wind tunnel environment can be achieved only when optical noise produced by scattered laser light from wind tunnel surfaces is reduced to levels below scattering particle signals. Recorded ambient particle seeding levels are large enough to obtain accurate mean velocity measurements for unsteady separated flows at locations outside reversed flow regions. We recognize that the interpretation of LDV signals for unsteady separated flows whose composition is influenced by particle size and seeding, turbulent flow content and global unsteady effects with flow reversal pose special problems. Their solution will require a long range comprehensive effort in the areas of data management, discontinuous signal averaging, and digital correlation techniques, based on signal-to-noise and sampling considerations, and form the first step toward the goal of understanding and modeling unsteady separated flows.

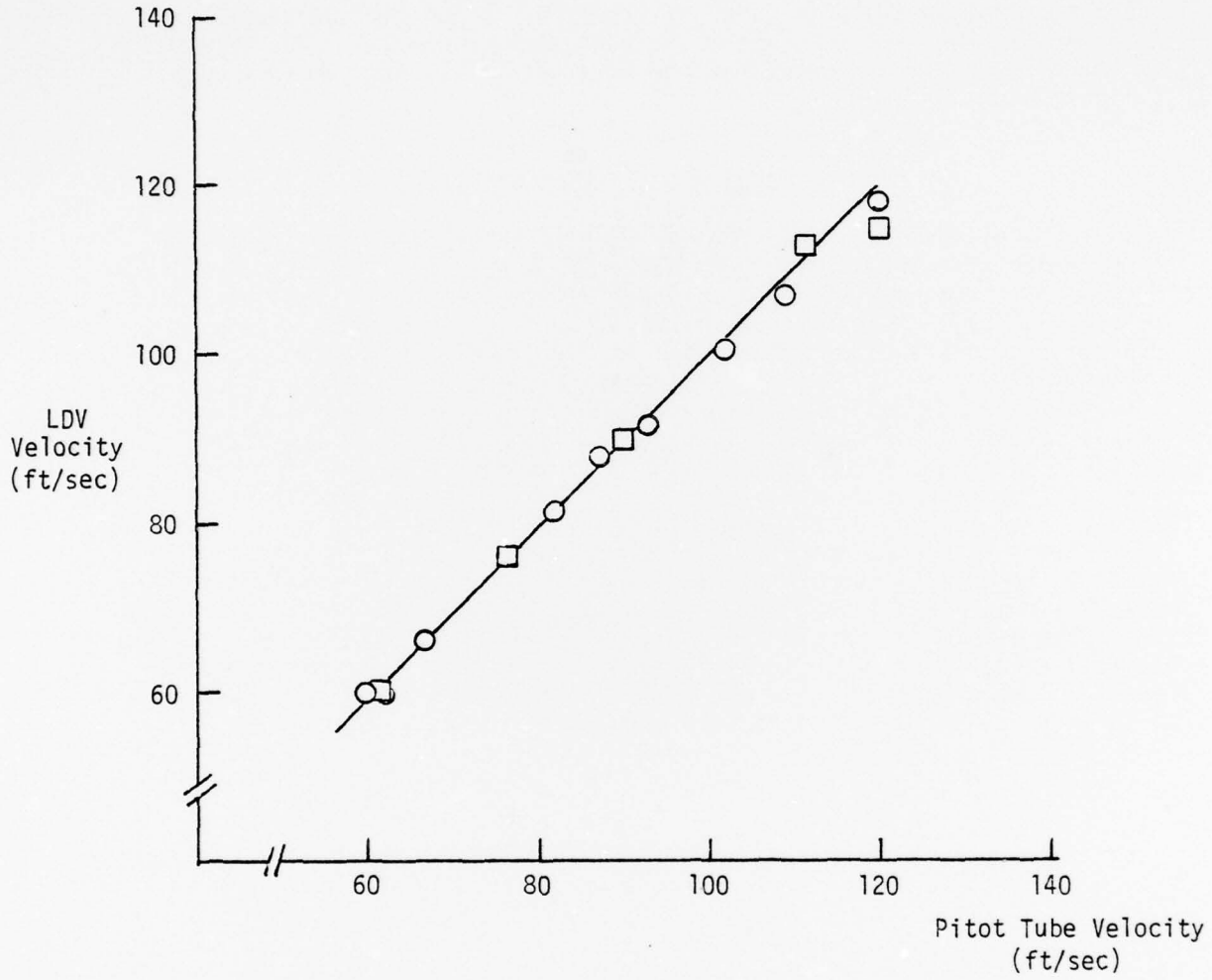

Figure 9. LDV - Pitot Tube Velocity Comparison

REFERENCES

1. McCroskey, W. J., "Some Current Research in Unsteady Fluid Dynamics," Journal of Fluids Engineering, Vol. 99, March 1977, pp. 9-29.

2. Keesee, J. E., Francis, M. S., and Lang, J. D., "A Technique for Vorticity Measurement in Unsteady Flow," AIAA Paper No. 78-801, AIAA 10th Aerodynamic Testing Conference, April 1978.

3. Swinney, Harry L. and Gollub, Jerry P., "The Transition to Turbulence," Physics Today, August 1978, pp. 41-49.

4. Durst, F., Melling, A. and Whitelaw, J. H., Principles and Practice of Laser-Doppler Anemometry, Academic Press, New York, 1976.

5. Cline, V. A. and Lo, C. F., "Application of the Dual-Scatter Laser Velocimeter in Transonic Flow Research," AGARD paper reprinted from Conference Proceedings No. 193 on Applications of Non-Intrusive Instrumentation in Fluid Flow Research, May 1976.

6. Mazuarder, M. K., "Laser Doppler Velocimeter Measurement Without Directional Ambiguity by Using Frequency Shifted Incident Beams," Applied Physics Letters, Vol. 16, No. 11, June 1970, pp. 462-464.

7. Sparks, G. W., Jr. and Francis, M. S., "A Laser Doppler Velocimeter for the USAFA Subsonic and Trisonic Wund Tunnels - A Feasibility Study," Frank J. Seiler Research Laboratory Report SRL-TM-2307-77-1, October 1977.

8. Laser Anemometer Systems, 1977 catalog, Thermo-Systems, Inc., St. Paul, Minnesota.

1978 USAF-ASEE SUMMER FACULTY RESEARCH PROGRAM

sponsored by

THE AIR FORCE OFFICE SCIENTIFIC RESEARCH

conducted by

AUBURN UNIVERSITY AND OHIO STATE UNIVERSITY

PARTICIPANT'S FINAL REPORT

PHYSICAL PROPERTIES OF MOLTEN CHLOROALUMINATE SALT SYSTEMS

Prepared by:	Roger K. Bunting, Ph.D.
Academic Rank:	Associate Professor
Department and University:	Department of Chemistry Illinois State University
Assignment:	
(Air Force Base)	USAF Academy
(Laboratory)	Frank J. Seiler Research Laboratory
(Division)	Directorate of Chemical Sciences
(Branch)	Electrochemistry
USAF Research Colleague:	Lt. Col. Lowell A. King, Ph.D.
Date:	August 15, 1978
Contract No.:	F44620-75-C-0031

PHYSICAL PROPERTIES OF MOLTEN CHLORO-ALUMINATE SALT SYSTEMS

by

Roger K. Bunting

ABSTRACT

A study of the physical properties of sodium/lithium tetrachloro-aluminate salt melts was undertaken to provide data necessary to their application as molten salt electrolytes in primary battery systems. A preliminary phase diagram has been constructed for the $LiAlCl_4/NaAlCl_4$ system. The eutectic mixture melts at 108°C and occurs at the 50 mole percent composition.

Vapor pressures have been determined for $LiCl/AlCl_3$ melts of compositions ranging from LiCl-saturated $AlCl_3$ to 35/65 mole percent $LiCl/AlCl_3$ within the temperature range 170-270°C. Vapor pressures of these systems are roughly twice as great as those of corresponding $NaCl/AlCl_3$ solutions.

The ternary system 20/20/60 mole percent $LiCl/NaCl/AlCl_3$ was also investigated and was found to have vapor pressures essentially identical to those of 40/60 $NaCl/AlCl_3$ in the temperature range studied.

INTRODUCTION

The physical and electrochemical properties of NaCl/$AlCl_3$ salt melts have been extensively investigated in recent years.[1-3] These solutions have been shown to exhibit many of the properties requisite to their application as molten salt electrolytes for primary battery systems, and a thermal battery based upon this electrolyte is currently under development.[4]

Very few data are available on the LiCl/$AlCl_3$ system, however. This research was undertaken to determine physical properties of the LiCl/$AlCl_3$ system and the ternary system LiCl/NaCl/$AlCl_3$ to provide a basis from which to assess their suitability as battery electrolyte components.

PHASE DIAGRAM OF THE LiAlCl$_4$/KAlCl$_4$ SYSTEM

Phase transition phenomena for ten solutions of the LiCl/NaCl/$AlCl_3$ system were investigated by differential scanning calorimetry using a Perkin-Elmer DSC-2. The samples were prepared by combining appropriate weights of LiCl-saturated $AlCl_3$, NaCl-saturated $AlCl_3$ and pure $AlCl_3$. The preparation and purification of these materials have been described elsewhere.[5] The components of each solution were weighed in an inert atmosphere box under argon and contained in a heavy walled glass tube. Gas was then removed on a high vacuum line and the tubes were sealed. The mixtures were melted, thoroughly stirred, then cooled and returned to the dry box where the tubes were opened and the samples ground to a fine powder. A small quantity of each of the homogeneous samples was placed in a stainless steel sample pan and sealed in the dry box prior to DSC analysis.

Compositions of the ten solutions, along with the temperatures of their phase changes, are presented in Table 1.

The DSC analysis curve for sample number 6 (11/40/50 mole percent LiCl/NaCl/$AlCl_3$) is reproduced in Figure 1 as representative of these traces. Melting point of the eutectic was determined as shown, by extending a line drawn on the maximum slope on the approach side of the peak through the interpolated baseline. The temperature for total melting of the sample

Table 1. Phase Transition Temperatures for the System $LiCl/NaCl/AlCl_3$

Sample Number	Component Mole Fractions			Eutectic Temperature, °C	Final Melting, °C
	LiCl	NaCl	$AlCl_3$		
1	0.4	0.1	0.5	105.6 (104)	140.3 (135)
2	0.3	0.2	0.5	107.0 (108)	121.3 (119)
3	0.2	0.3	0.5	106.5 (107)	121.0 (120
4	0.1	0.4	0.5	105.3	144.2
5	0.3	0.1	0.6	81.2	113.3
6	0.2	0.2	0.6	83.7	-----
7	0.1	0.3	0.6	83.6	113.3
8	0.2	0.1	0.7	80.8	105.9
9	0.1	0.2	0.7	84.4	105.9
10	0.1	0.1	0.8	84.1	204.8
		0.5	0.5		152.5 (159)
	0.5		0.5		142.8 (141)

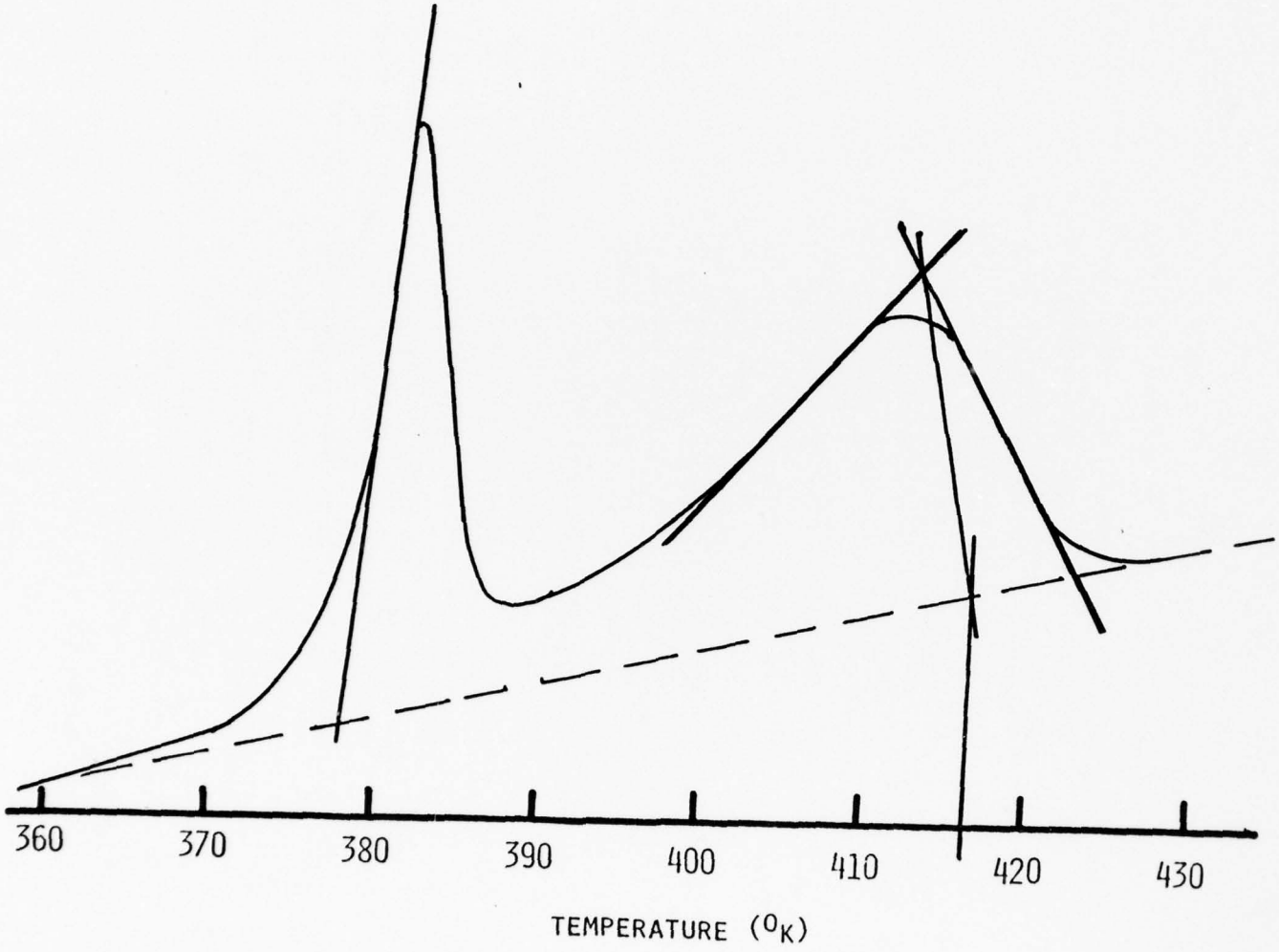

FIGURE 1. DSC ANALYSIS OF SAMPLE 4

was determined by adaptation of a procedure of Vassullo and Hardin.[6] This temperature is taken to be the point on the baseline at the intersection of a perpendicular line passing through the intersection of the steepest slopes on the two sides of the peak.

In addition to the scanning calorimetry method of determining phase transition temperatures, some of the solutions were subjected to conductivity measurements. The conductivity varies linearly with temperature, but displays an abrupt change in slope at the temperature of any phase transition. The samples were sealed under vacuum into a conductivity cell constructed with platinum electrodes. The cell was placed in a controlled temperature bath, and the temperature was gradually raised ($\sim 2°$/hr). Conductivity was determined by measuring resistances, either by use of an impedence bridge circuit or by a circuit described by Olsen et. al.[7] Temperatures of the phase transitions determined by conductivity are included in parentheses in Table 1.

Solutions numbered one through four each contain 50 mole percent $AlCl_3$. These solutions constitute essentially a binary system of $LiAlCl_4$ and $NaAlCl_4$ owing to the strong interaction of chloride ion with $AlCl_3$. A preliminary phase diagram for the binary system has been constructed from these data and is shown in Figure 2.

The composition of the eutectic in this system appears to be very nearly at the 50 mole percent mixture. Further confirmation of this composition was made by measurement of the eutectic fusion enthalpies in the various solutions. A plot of fusion enthalpy for the eutectic portion of the samples against sample composition should yield two straight lines whose intersection at maximum enthalpy will occur at the exact eutectic composition.

The DSC instrument was calibrated against the heat of fusion of tin, taken as 14.45 cal/g. Areas under the eutectic fusion peak for each of the samples 1-4 (cf. Table 1) were converted to enthalpies and recorded in Table 2. Fusion enthalpy of a 50/50 mole percent mix of $LiAlCl_4$ and $NaAlCl_4$ is also included in this table, and the data are plotted in Figure 3.

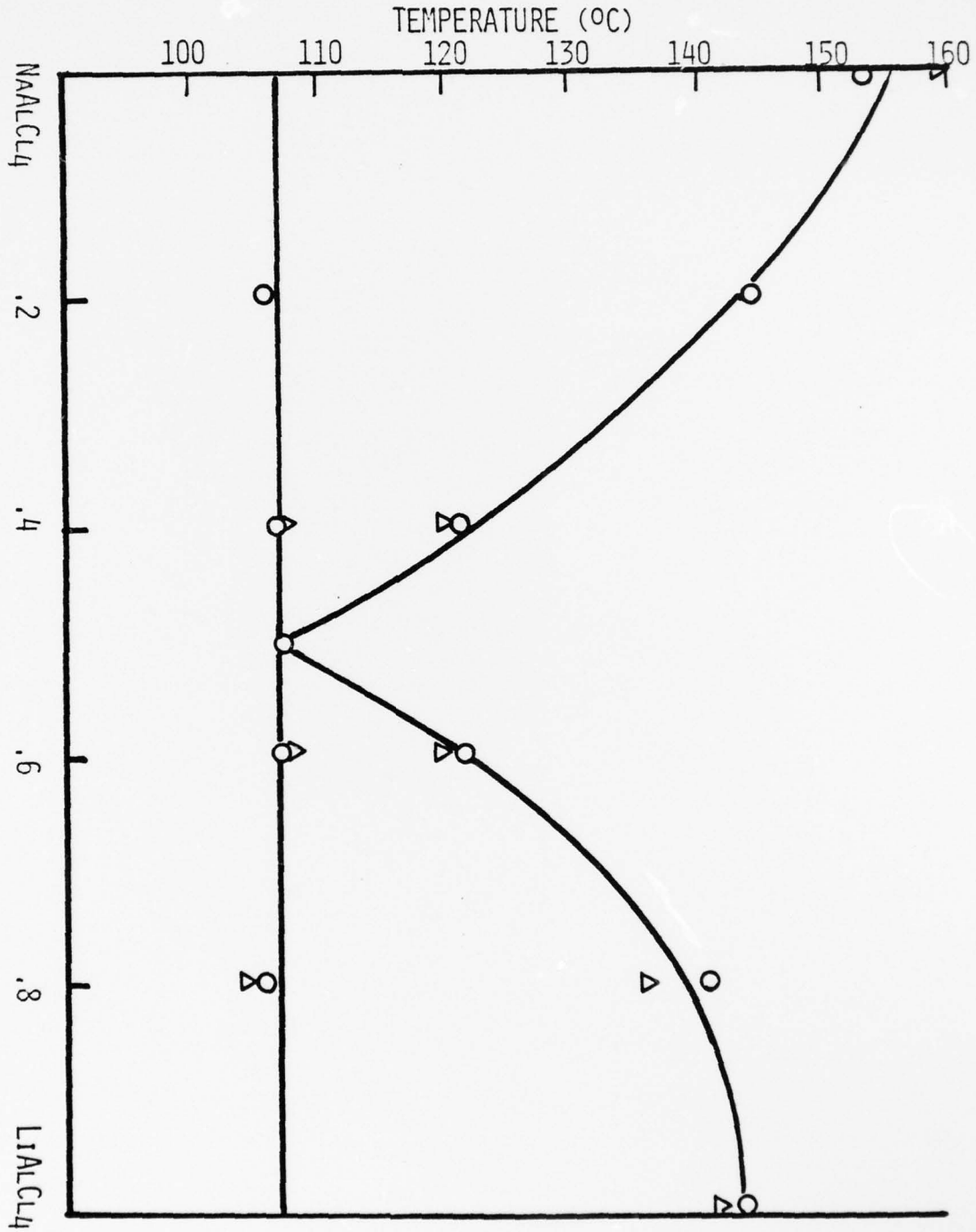

FIGURE 2. PHASE DIAGRAM FOR THE SYSTEM $LiAlCl_4/NaAlCl_4$

Table 2. Eutectic Fusion Enthalpies

Sample No.	Fusion Enthalpy (Cal/g)
1	6.21
2	14.09
3	14.23
4	6.53
50/50 mole % $LiAlCl_4/NaAlCl_4$	17.03

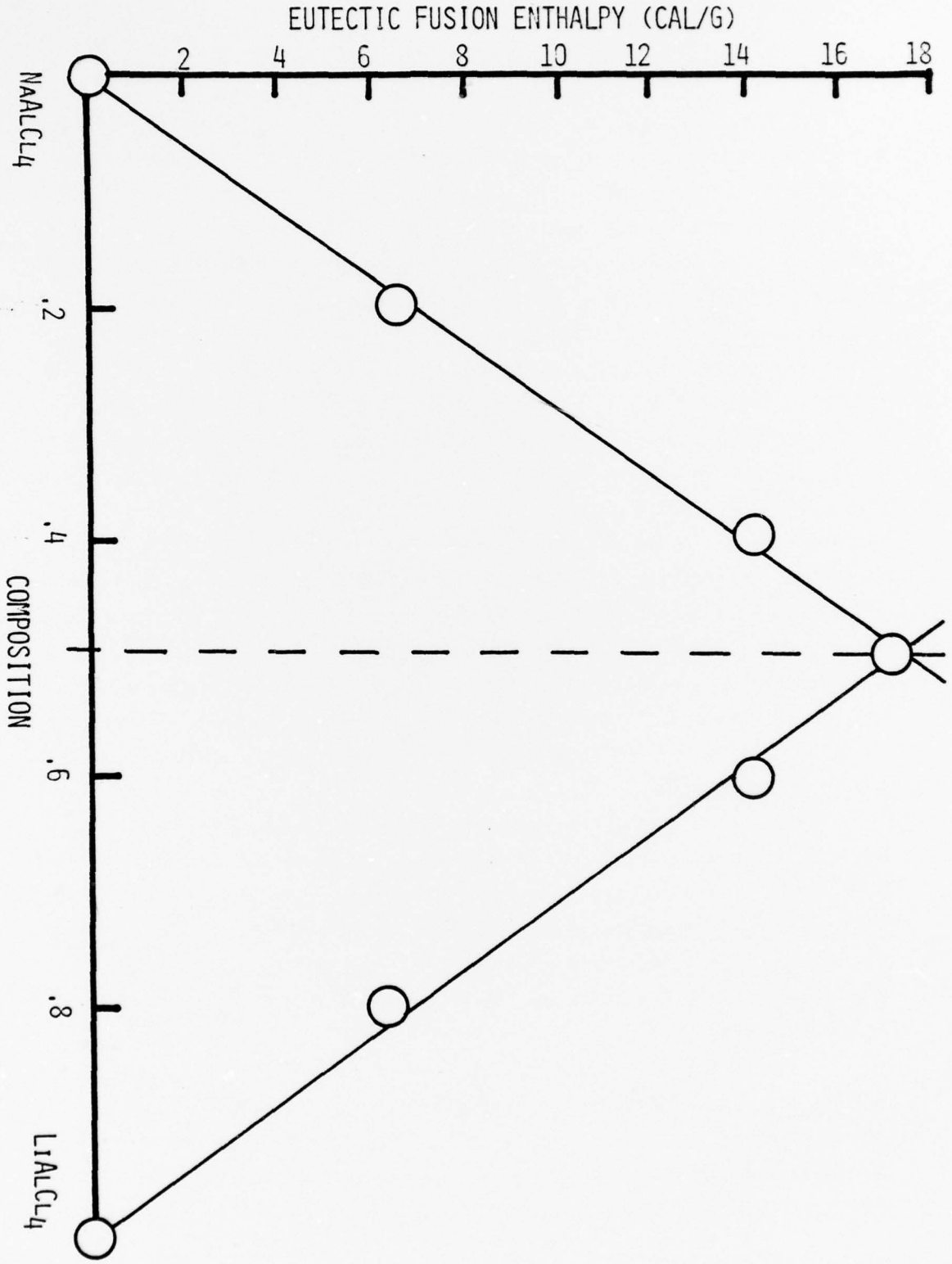

FIGURE 3. DETERMINATION OF EUTECTIC COMPOSITION

VAPOR PRESSURES OF LiCl/NaCl/$AlCl_3$ MELTS

The vapor pressures of [illegible] solutions of the LiCl/NaCl/$AlCl_3$ system were determined within the temperature range [illegible]°C. The best line conforming to the equation $\log P = A/T + B$ was determined by the method of least squares, and the constants A and B evaluated for each solution. Measurements were made by a differential pressure method, with the vapor pressure of these solutions partially counterbalanced by NaCl/$AlCl_3$ solutions of known[2] vapor pressures.

The differential pressure apparatus consists of two isolated sample chambers connected by a mercury manometer, and is shown in Figure 4. Five gram samples of each of the solutions to be measured were prepared in the dry box from appropriate quantities of [illegible]-sublimated $AlCl_3$, NaCl-saturated $AlCl_3$, and pure $AlCl_3$, and were introduced to one arm of the apparatus shown. In the other arm was placed five grams of a NaCl/$AlCl_3$ mixture of composition estimated to roughly balance the pressure. The capping apparatus was attached, and the [illegible] apparatus was removed from the dry box and attached to a high vacuum line. After evacuating to remove all gas pressure, the apparatus was closed to the vacuum system and each arm of the device was heated to melt the samples. The samples were subsequently cooled to room temperature, then again opened to the vacuum system to remove residual pressure.

The presence of residual pressure after melting and resolidifying tetrachloroaluminate melts was reported in the investigation of the NaCl/$AlCl_3$ system. The pressure was shown to be due primarily to hydrogen chloride[3], a probable consequence of small traces of moisture in the apparatus. The melting/solidifying/evacuating sequence was carried out approximately five times on each sample before residual gas pressure was reduced to acceptable limits.

Following the removal of residual gases, the apparatus was sealed by melting the glass tubes under vacuum at the positions indicated by the dashed lines on the diagram of Figure 4. The entire apparatus was then immersed in a controlled temperature bath, and pressures were read by measuring the height of the mercury columns with a cathetometer.

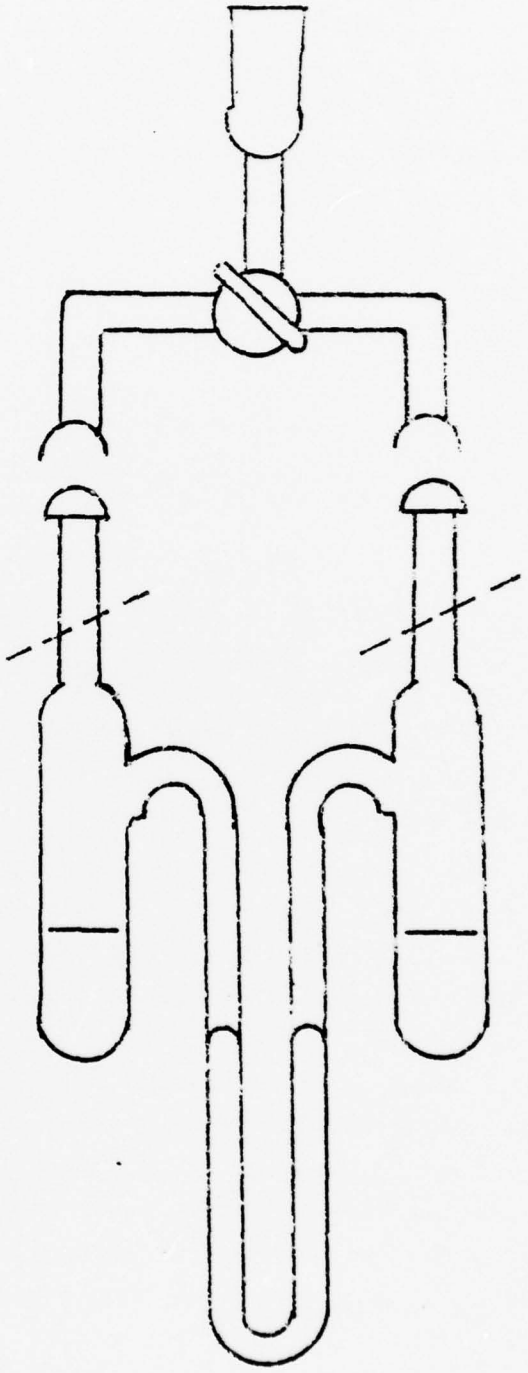

FIGURE 4. APPARATUS FOR DIFFERENTIAL DETERMINATION OF VAPOR PRESSURES

A long glass rod (not shown in the diagram) was sealed onto the apparatus to serve as a means of holding the device in the temperature bath and also as a means of agitating the contents to accelerate temperature and pressure equilibration. The temperatures were controlled to $\pm$ 0.01° as indicated by a platinum resistance thermometer, and samples were agitated at least one half hour at each temperature to insure equilibration.

Measurement of the heights of each of the mercury columns was made to the nearest 0.02 mm, and the vapor pressures of the melts were calculated from the following relationship:

$$P = (H_c - H_s)\frac{D_T}{13.596} + P_c \pm P_r(T/300)$$

where H_c = height of mercury surface in the counterbalance arm (mm)

H_s = height of mercury surface in the sample arm (mm)

D_T = density of mercury at the temperature of measurement

P_c = vapor pressure in counterbalance arm (torr)

P_r = residual pressure at room temperature (torr)

T = absolute temperature

The first term of this equation gives the pressure difference in the two arms of the manometer, corrected to the density of mercury at 0°C. The second term is calculated from published data on the $NaCl/AlCl_3$ system,[3] and the third term corrects for residual gas pressure in the system, and is added if $H_c < H_s$ and subtracted if $H_c > H_s$ when measured at room temperature.

Two approximations have been made in the method. The pressure due to residual gas is assumed to obey the ideal gas law, and no correction has been made for changes in mole fraction of $AlCl_3$ in the melt at different pressures. Errors introduced by the former are considered to be beyond the limits of reproducible measurement at these temperatures and pressures. It is estimated that the differences between the mole fraction changes in the two cells of the apparatus would not exceed 0.2% of the total moles of $AlCl_3$. Maximum pressure differences were approximately 100 torr, and the volumes of the cell compartments above the samples were 14.5 $\pm$ 1.5 ml.

The absence of detectable curvature in the graphical plots of vapor pressure further supports the validity of these approximations.

Data for vapor pressures of the acidic melts of the $LiCl/AlCl_3$ system are presented in Table 3, along with their A and B constants for the equation $\log P = (A/T) + B$. Data for the LiCl-saturated $AlCl_3$ melt and for the ternary mixture 20/20/60 mole percent $LiCl/NaCl/AlCl_3$ are given in Table 4.

Plots of log P vs. 1/T for the acidic melts, including the ternary system, are included in Figure 5. Measurements on each of the solutions have provided a reasonably good straight line, and the lines are very nearly parallel. In comparison with the previously reported $NaCl/AlCl_3$ system, the vapor pressures of $LiCl/AlCl_3$ solutions of corresponding composition at similar temperatures are roughly twice as great. For example, at 238.19°C the 0.65 mole fraction $AlCl_3$ with LiCl has a pressure of 1393 torr, while the corresponding solution in the NaCl system calculates for a pressure of 635 torr at this temperature. Likewise, in the 0.55 $AlCl_3$ melts, at269.42°C the LiCl melt has a pressure of 118 torr while the NaCl melt has only 68 torr.

Vapor pressure data for the LiCl-saturated $AlCl_3$ solution are plotted in Figure 6. These points show considerable scatter, owing to the very small pressures measured. This is a basic melt (i.e., mole fraction of $AlCl_3 < 0.5$) and hence the results need not conform to those found for acidic melts. The least squares line determined for these data is, however closely parallel to the lines for the acidic melts.

DISCUSSION

The vapor pressure line for the ternary mixture 20/20/60 mole percent $LiCl/NaCl/AlCl_3$ falls below the line for 40/60 $LiCl/AlCl_3$, as expected (Figure 5). It does not, however, fall midway between the 40/60 $LiCl/AlCl_3$ line and the 40/60 $NaCl/AlCl_3$ line. Rather, the line for the 40/60 $NaCl/AlCl_3$ melt in this temperature range calculates[3] to be precisely coincident with that of the 20/20/60 $LiCl/NaCl/AlCl_3$ melt.

Vapor pressure data for the 10/30/60 $LiCl/NaCl/AlCl_3$ solution are presently incomplete and are not reported here, but preliminary estimates suggest that the log P vs. 1/T line for this melt will also lie coincident

Table 3. Vapor Pressures of Acidic $LiCl/AlCl_3$ Melts

Fitted to: $\log P = (A/T) + B$

47.5/52.5 mole % $LiCl/AlCl_3$

Temperature, °C	Pressure, torr
169.47	4.75
179.56	5.66
189.33	7.15
199.12	8.76
199.59	8.81
209.50	10.92
219.17	13.28
219.19	13.28
229.18	16.50
239.03	19.94
249.06	24.20
258.95	29.20
268.95	34.89

A = -2100
B = 5.40

45/55 mole % $LiCl/AlCl_3$

Temperature, °C	Pressure, torr
169.43	9.96
179.63	13.61
184.79	15.91
199.12	23.80
211.87	33.11
223.45	44.56
239.26	64.22
249.29	79.69
259.44	98.02
269.42	118.25

A = -2590
B = 6.86

40/60 mole % $LiCl/AlCl_3$

Temperature, °C	Pressure, torr
169.72	67.94
179.66	90.74
189.68	119.10
199.44	153.24
209.73	197.65
219.09	244.46

A = -2462
B = 7.39

35/65 mole % $LiCl/AlCl_3$

Temperature, °C	Pressure, torr
168.95	311.20
179.14	401.07
188.11	497.38
198.90	633.67
208.60	780.47
218.74	960.98
228.76	1169.72
238.19	1392.99

A = -2131
B = 7.31

Table 4. Vapor Pressures for LiCl-Saturated $AlCl_3$ and 20/20/60 Mole Percent LiCl/NaCl/$AlCl_3$

LiCl-Saturated $AlCl_3$		20/20/60 Mole % LiCl/NaCl/$AlCl_3$	
Temperature, °C	Pressure, torr	Temperature, °C	Pressure, torr
169.10	1.78	169.47	30.03
179.57	1.07	179.56	40.61
189.64	4.41	189.33	53.52
189.68	2.59	199.12	70.68
199.00	6.18	199.59	70.71
209.76	5.54	209.50	91.17
209.57	7.38	219.16	115.78
219.10	6.50	219.17	115.78
219.32	9.69	229.18	146.66
229.42	10.34	239.03	183.42
239.27	17.72	249.06	228.12
249.47	14.18	258.95	284.01
259.33	15.88	268.95	353.52
269.49	17.32		
A = -2768		A = -2531	
B = 6.49		B = 7.20	

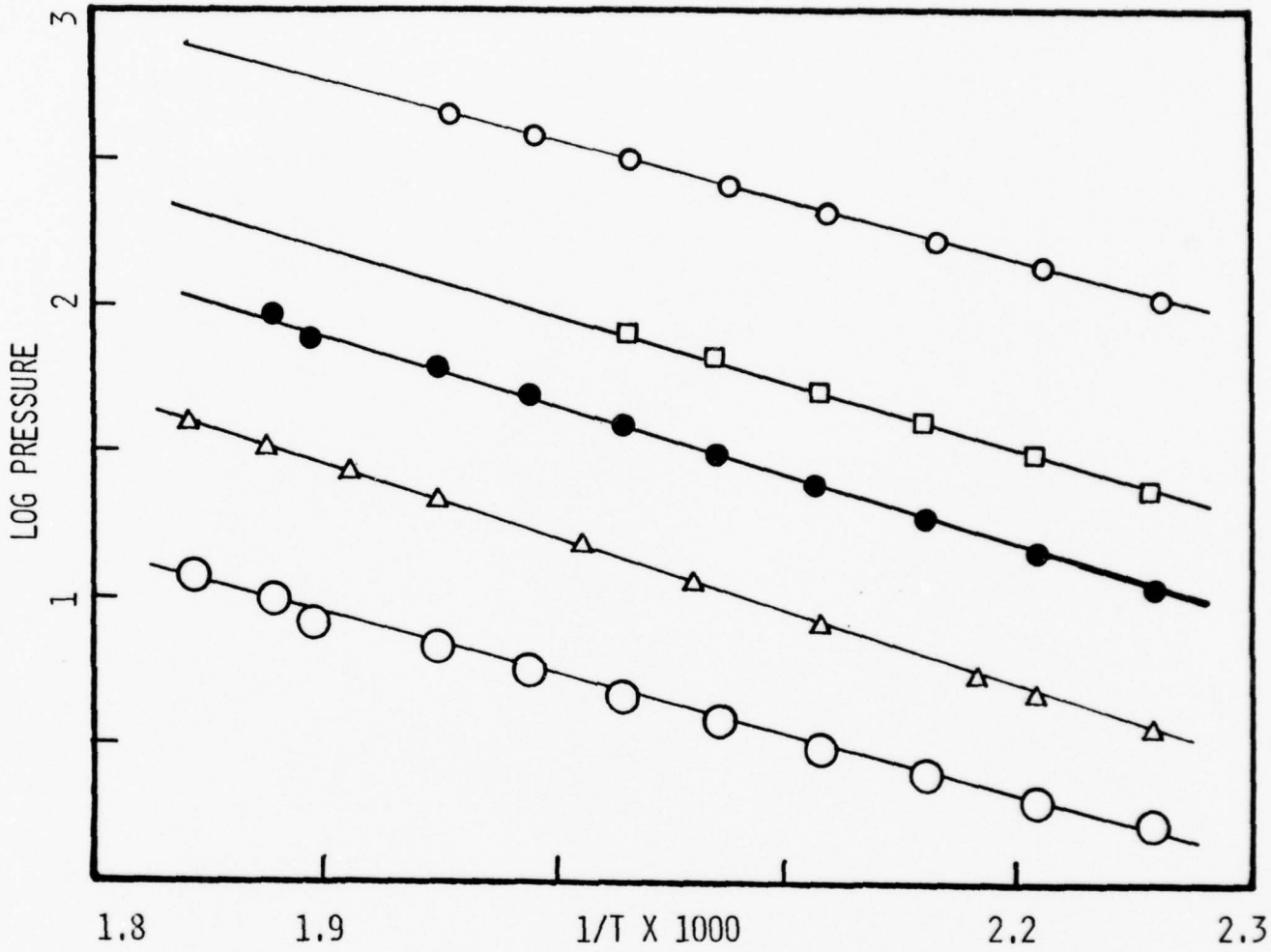

FIGURE 5. VAPOR PRESSURES OF ACIDIC CHLOROALUMINATE SALT MELTS

- ○ 35/65 Mole Percent $LiCl/AlCl_3$
- □ 40/60 Mole Percent $LiCl/AlCl_3$
- ● 20/20/60 Mole Percent $LiCl/NaCl/AlCl_3$
- △ 45/55 Mole Percent $LiCl/AlCl_3$
- ○ 47.5/52.5 Mole Percent $LiCl/AlCl_3$

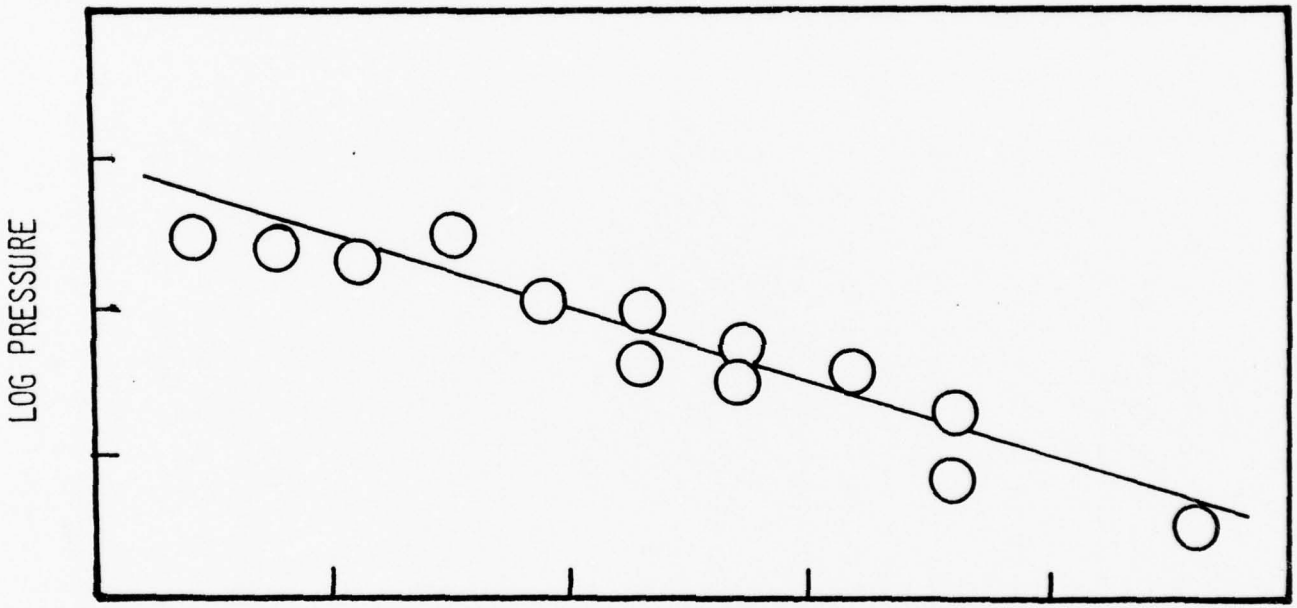

FIGURE 6. VAPOR PRESSURE OF LiCl-SATURATED $AlCl_3$

with that of the 20/20/60 $LiCl/NaCl/AlCl_3$ melt.

The combination of information produced in the vapor pressure study provides a description of $NaCl/AlCl_3$ and $LiCl/AlCl_3$ systems that is not inconsistent with expectation. First of all, the vapor pressures of $LiCl/AlCl_3$ melts would be expected to be greater than those of corresponding $NaCl/AlCl_3$ melts. The small size of the Li^+ cation renders greater covalency between it and its chloride ion than in the case of NaCl. Electron density on the chloride of LiCl is thus reduced, weakening its Lewis basicity. Hence the attachment of this chloride to $AlCl_3$ will be weaker, and the vapor pressure of $AlCl_3$ above these melts will be greater.

The vapor pressures of both $NaCl/AlCl_3$ and $LiCl/AlCl_3$ solutions are, however, quite small in the basic range of composition ($< 50\%$ $AlCl_3$). In the acidic range the magnitude of the vapor pressures is principally a function of the strength of attachment of $AlCl_3$ to $AlCl_4^-$ to give the ion $Al_2Cl_7^-$. Similar reasoning applies here also. Any covalency between the metal ion and $AlCl_4^-$ will lessen the stability of the $Al_2Cl_7^-$ ion, and a greater vapor pressure should result.

The coincidences of the log P *vs.* 1/T lines for the $LiCl/NaCl/AlCl_3$ solutions of compositions 20/20/60 and 0/40/60 (and probably 10/30/60) can be attributed to the fact that in these solutions 40 of the 60 mole percent $AlCl_3$ can attach to chloride, and the remaining 20 can form $Al_2Cl_7^-$ with the *sodium* salt, $NaAlCl_4$. That is, the measured vapor pressure of these solutions is due in essence to the dissociative tendency of the20 mole percent $NaAl_2Cl_7$ present in each. Pressure differences caused by different stabilities of the $LiAlCl_4$ and $NaAlCl_4$ would be imperceptibly small by comparison.

In mixtures containing less than 20 mole percent NaCl, however, some of the $AlCl_3$ (above that bonded as $AlCl_4^-$) could bond only to $LiAlCl_4$, forming theless stable $LiAl_2Cl_7$. Hence vapor pressures of such solutions would be higher, as is found in the case of the 40/60 $LiCl/AlCl_3$. Here the vapor pressure must be contributed essentially by 20 of the 60 mole percent $AlCl_3$ existing as $LiAl_2Cl_7$.

If the preceding interpretation is correct, then a 30/10/60 mole percent $LiCl/NaCl/AlCl_3$ solution whould provide a vapor pressure line lying above

the two (or three) coincident lines described, but below that of the 40/60 $LiCl/AlCl_3$ line. This composition has at the present time not been investigated.

CONCLUSIONS AND RECOMMENDATIONS

The utilization of ternary melts of the $LiCl/NaCl/AlCl_3$ system as battery electrolytes shows considerable promise. $LiCl/AlCl_3$ melts have recently been shown[8] to have somewhat lower electrical conductivities than corresponding melts in the $NaCl/AlCl_3$ system, and it is likely that conductances of the ternary mixtures will also prove to be less than those of $NaCl/AlCl_3$ melts. However, the advantage of a lower melting point in the ternary system may well compensate for a slight loss in conductivity. Conductivities in the ternary system have not been measured, but the melting point of the 25/25/50 mole percent $LiCl/NaCl/AlCl_3$ solution has been shown to be some 40° below that of the NaCl-saturated $AlCl_3$, a distinct advantage for thermal battery application.

The significantly higher vapor pressures of $LiCl/AlCl_3$ melts compared to their NaCl counterparts imply that acid-rich mixtures of these melts will be unsuitable as battery electrolytes. Vapor pressures of the basic melts, however, are low, and evidence suggests that the addition of LiCl to the $NaCl/AlCl_3$ melts will not significantly increase vapor pressures as long as the mole fraction of $AlCl_3$ remains below 0.5.

REFERENCES

1. A. A. Fannin, Jr., L. A. King and D. W. Seegmiller, J. Electrochem. Soc., 19, 801 (1972).

2. A. A. Fannin, Jr., F. C. Kibler, L. A. King and D. W. Seegmiller, J. Chem. Eng. Data, 19, 266 (1974).

3. J. T. Viola, L. A. King, A. A. Fannin, Jr., and D. W. Seegmiller, J. Chem. Eng. Data, 23, 122 (1978).

4. R. A. Marsh, D. M. Ryan and J. C. Nardi, J. Power Sources, in press.

5. R. J. Gale and R. A. Osteryoung, J. Electrochem. Soc., 121, 983 (1974).

6. D. A. Vassullo and J. C. Harden, Analyt. Chem., 34, 132 (1962).

7. E. D. Olsen, R. J. Martin and J. E. Ahnell, J. Chem. Educ., 47, 542 (1970).

8. R. A. Carpio, L. A. King, F. C. Kibler and A. A. Fannin, Jr., J. Electrochem. Soc., in press.

1978 USAF-ASEE SUMMER FACULTY RESEARCH PROGRAM
sponsored by
THE AIR FORCE OFFICE SCIENTIFIC RESEARCH
conducted by
AUBURN UNIVERSITY AND OHIO STATE UNIVERSITY

PARTICIPANT'S FINAL REPORT

TECHNICAL PLANNING FOR THE USAF STANDARD BASE SUPPLY SYSTEM (SBSS); RIMSTOP AND BEYOND

Prepared by:	Marvin S. Seppanen, Ph.D., P.E.
Academic Rank:	Assistant Professor
Department and University:	Department of Industrial Engineering The University of Alabama
Assignment:	
(Air Force Base)	Air Force Academy
(Laboratory)	Frank J. Seiler Research Laboratory
(Division)	Aerospace-Mechanics Sciences
(Branch)	Applied Mathematics
USAF Research Colleagues:	Lt Col J. S. Brush, FJSRL Capt T. D. Baxter, FJSRL Mr. W. B. Faulkner, AFLMC
Date:	August 4, 1978
Contract No.:	F44620-75-C-0031

TECHNICAL PLANNING FOR THE USAF STANDARD BASE SUPPLY SYSTEM (SBSS); RIMSTOP AND BEYOND

by
Marvin S. Seppanen

ABSTRACT

The USAF Standard Base Supply System (SBSS) is an automated inventory accounting system used by all Air Force bases to control their supply functions. The SBSS can be categorized as a multi-item, single-echelon, continuous review inventory system with stochastic, multiple unit demands, backordering and an annual budget constraint. This research was concerned with mathematical inventory control models incorporated in the SBSS. An applied operations research and systems design approach was taken in conduct of this research. This report follows the general progress of the work. The current SBSS was reviewed and modeled using a system flow diagram. A search of the related inventory control theory and practice was made. A data analysis phase included a review of SBSS operating data to estimate demand parameters and to survey the system's operation. The data analysis phase also included a simulation of various models for controlling a single-item inventory with a random demand and lead time process. The final study phase developed a technical study plan for future work required to design a cost/effective SBSS.

The major conclusion of this research is: The SBSS should order more, which in turn leads to fewer orders and less shortage risk. Implementation of this recommendation is difficult due to budget constraints. An ideal starting point would be the class A or high-sales items. A dynamic systems model is suggested to investigate the impact of a major control model change on the SBSS and the wholesale level depots.

A need for future research is indicated in areas of range modeling, erratic demand inventory control, and annual budget constrained inventory policies. While those areas of research would be fruitful, the major task to improve the SBSS is the application of proven theory to the problem at hand.

1. Introduction

The USAF Standard Base Supply System (SBSS) is an automated inventory accounting system used by all Air Force bases to control their supply functions. This research was concerned with mathematical inventory control models incorporated in the SBSS. An applied operations research and systems design approach was taken in conduct of this research. This report follows the general progress of the work. The current SBSS was reviewed and modeled using a system flow diagram. A search of the related inventory control theory and practice was made. A separate literature review paper was prepared and is available from the author. A data analysis phase included a review of SBSS operating data to estimate demand parameters and to survey the system's operation. The data analysis phase also included a simulation of various models for controlling a single-item inventory with a random demand and lead time process. The final study phase developed a technical study plan for future work required to design a cost/effective SBSS.

The motivation for this research was a requirement for the Air Force Logistics Management Center (AFLMC), Gunter AFS, Alabama, to prepare portions of the Air Force General Implementation Plan for DoD Directive 4140.44. That directive is attempting to standardize the retail inventory management and stockage policy of all services. The directive resulted from a joint DoD working group, Retail Inventory Management and Stockage Policy (RIMSTOP) which was charted in 1974 to review each of the services retail level supply systems with a view toward recommending standardized policies.

It is hoped that this document will serve as a technical study plan for future related activities by FJSRL and AFLMC. Validation and implementation of the results of this study will be done primarily by AFLMC.

2. Objective

The objective of this research was to develop a technical study plan which, if successfully implemented, would optimize the cost/effectiveness of the SBSS subject to:

1. the state-of-the-art of inventory control theory
2. the annual stock fund budget constraints
3. the computational capabilities of the current SBSS computer hardware
4. Department of Defense Directive 4140.44, "Supply Management of the Intermediate and Consumer Levels of Inventory," February 28, 1978.

3. The Standard Base Supply System

The SBSS can be categorized as a multi-item, single-echelon, continuous review inventory system with stochastic, multiple unit demands, backordering and an annual budget constraint. The USAF Supply Manual (AFM 67-1, Volume II, Part Two) documents the SBSS in detail. The supply organization of each base uses a UNIVAC 1050-II computer system to maintain records of its base level supply, equipment, POL, munitions and clothing accounts. For the purpose of this study, only consumable supplies are to be considered. Several hundred

computer programs are used in the functioning of the SBSS. Those programs are uniform for all bases although the types of inventories controlled varies widely.

3.1 SBSS Systems Flow Model

Before looking in detail at the mathematical models used by the SBSS to control inventory stockage, a brief overall systems review may be of benefit. Exhibit 1 illustrates the primary flows of information, materiels, orders and money associated with the SBSS using Forrester's (61)* notation. The flows will be individually discussed to review the SBSS purpose and operation.

The reason for the existence of the SBSS is to facilitate the flow of materiels from a multitude of sources to the base user organizations. Thus, first consider the solid or materiels flow lines on Exhibit 1. The SBSS is a retail organization much in the same sense as a local merchant. The SBSS inventory is stocked by the arrival of materiels from number of sources, such as Air Force Depots, GSA and DSA. In turn, items are issued from the SBSS inventory to the final consumer. Many supply items are not stocked at the base, rather are issued directly to the consumer upon receipt.

Orders (the circled flow lines) are the driving force behind the SBSS. Two levels or echelons of orders interact with SBSS. Starting from the left, the consumer's demand action results in the submission of a requisition to the SBSS. Normally the requisition is filled immediately (within a standard operating cycle) or, if the requested materiel is not available, the requsition is logged as a due-out for later filling. On the right side of the systems flow model the SBSS generates orders for filling by its suppliers. These orders are logged as due-ins and are maintained until the arrival of the materiels.

Money (the dollar signed flow lines), the ultimate driving force in our economic system, plays a critical role in the operation of the SBSS. Although somewhat simplified in Exhibit 1, the flow of money goes something like this. Through actions of OMB, Congress, DoD and the Air Force, stock funds are appropriated to a particular Air Force base. Those funds are allocated in turn to the various base organizations for supply requisitioning. Throughout the fiscal year the base organizations use their supply budget to draw supplies from the SBSS. The SBSS in turn purchases materiels from its suppliers using the stock fund and other authorized accounts. The key element in this exchange is not the flow of actual dollars, but the strict fiscal year budget limits placed on each spending authority. At all levels, government fund managers attempt to exactly spend to their budget limit by the close of the fiscal year. The impact of this budget constraint will be developed further in section 6.1.

The final and most frequently used flow in this systems flow model represents information (dashed lines). Only three key information flows are highlighted in this text. First, the item issue process is controlled by the

---

*The number in brackets following an author's name refers to the publication year. See section 8, references.

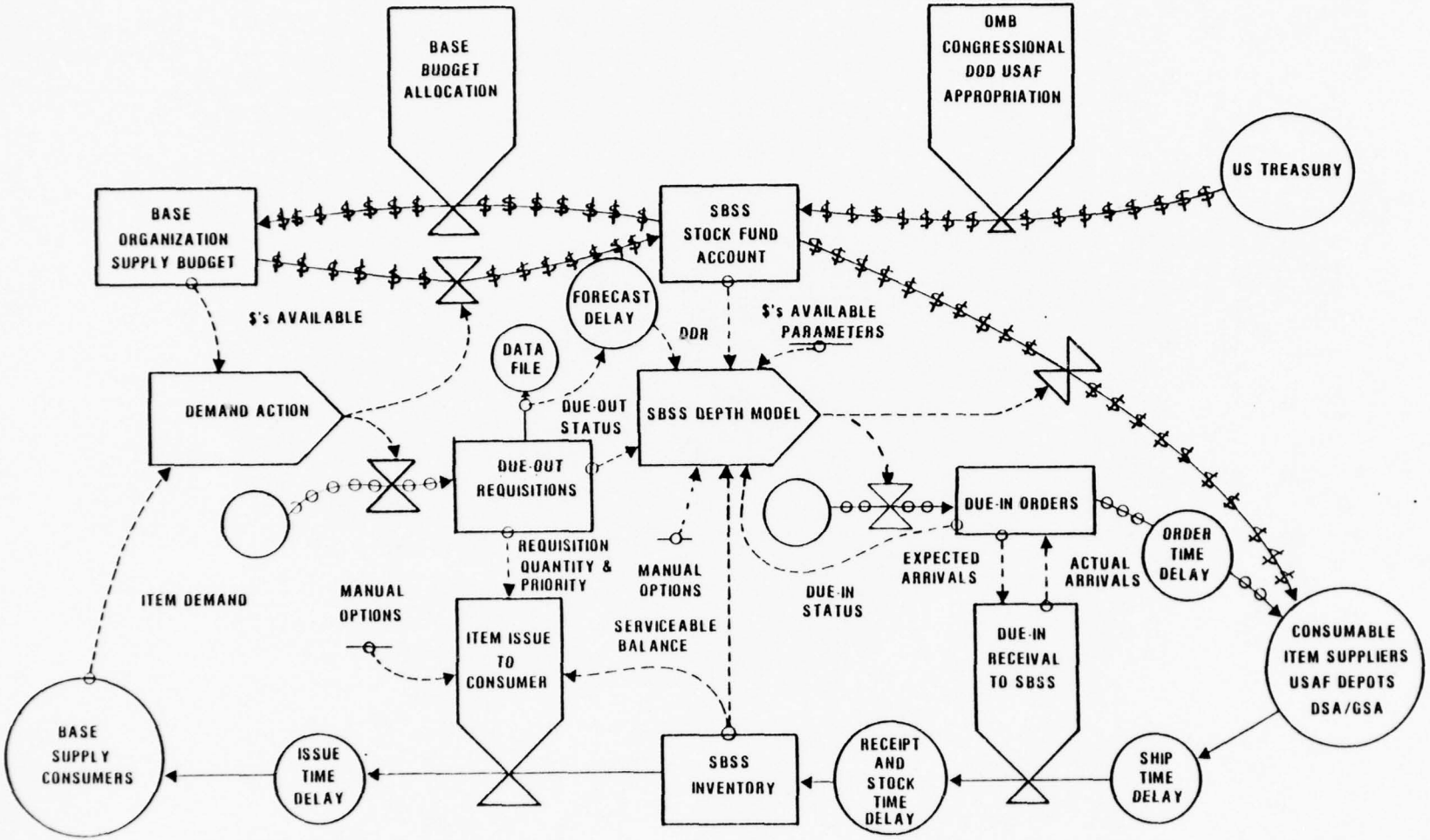

SBSS SYSTEMS FLOW MODEL

EXHIBIT 1

requisition quantity and priority (what is needed and how badly), the serviceable balance (what is available), and manual options to determine if the stock should be issued to the customer. Second, the consumer's demand action is influenced by the availability of funds in the organization's supply budget. This influence grows as the end of the fiscal year end approaches. Third, the depth model is the most intensive information user. Its specific information needs are developed as that model's operation is reviewed in detail.

3.2 SBSS Depth Model

The SBSS depth model is used to determine how much and when to order. DoD inventory planners use the term range model to indicate procedure by which it is determined if an item should be stocked. For the present discussion, these two models can be considered as one, because the SBSS depth model may decide to stock an item at a zero level, hence, not stock it at all.

The SBSS depth model is based on the Economic Order Quantity (EOQ) formula:

$$EOQ = \sqrt{2DA/IP}$$

where D is the annual demand rate,
A is the cost per order ($5.00),
I is the annual inventory carrying rate (50%),
P is the item unit price.

The EOQ formula attempts to minimize the total variable cost (TVC) associated with maintaining the inventory. It should be underscored that the SBSS depth model is EOQ based but only in limited cases is the exact EOQ used.

Here is how the SBSS depth model functions.

1. Forecast the Daily Demand Rate (DDR). The DDR is updated at each demand occurrence using a modified single component exponential smoothing procedure. The SBSS maintains three statistics:

a. current estimate of the DDR
b. the cumulative recurring demand, CRD
c. the date of first demand, DOFD

With each new demand for the quantity, ND, the cumulative recurring demand is updated:

$$CRD = CRD + ND$$

and the new daily demand rate is computed

$$DDR = CRD / Max (180, Current Date - DOFD).$$

At six month intervals the CRD and DOFD are adjusted

$$CRD = DDR \cdot \text{Min}\ (365, \text{Current Date} - DOFD)$$

$$DOFD = \text{Max}\ (DOFD, \text{Current Date} - 365).$$

The net effect of this semiannual adjustment is to convert the forecasting to exponential smoothing with $\alpha = 0.333$. During the six month intervals between adjustments, new demand enter the forecast with an exponential smoothing constant

$$\alpha = N/(365 + N)$$

where N is the number of days since the last adjustment. As N varies from 1 to 182 days, α ranges from 1/366 to 1/3.

2. Variable Stockage Objective (VSO) Lookup. Attachment A-16 of AFM 67-1, Vol. II, Part Two, contains a lookup table for the determination of the VSO. The VSO represents the number of days demand to be considered in the EOQ computation. VOS's of 0, 15, 30, 45, 60, 90, and 365 are determined based on stockage priority code (SPC), number of demands in 365 days and total number of recorded demands, number of days since the first demand, and the daily demand rate. Items with an insufficient number of demands (2 or less if SPC = 1, 3 or less if SPC > 1) are determined by the VSO lookup not to be stocked. The impact of the VSO is examined in section 5.2.

3. Calculate the Requisition Objective (RO). The RO or demand level is the maximum desired inventory position (on-hand inventory, less due-outs, plus due-ins).

$$RO = \text{INT}\ (EOQ_{VOS} + OSTQ + SLQ + 0.999).$$

The economic order quantity is modified by the VSO

$$EOQ_{VOS} = \sqrt{2 \cdot DDR \cdot VOS \cdot A/I \cdot P} = 4.4 \sqrt{DDR \cdot VOS/P}$$

assuming A = $5.00 and I = 50%. The order and ship (lead) time quantity (OSTQ) is given by

$$OSTQ = DDR \cdot OST$$

using a tabulated order and ship time (OST) in days based on the item source and priority.

The safety level quantity (SLQ)

$$SLQ = C \sqrt{3 \cdot OSTQ}$$

where C, the safety factor (number of standard deviations) is set to 1 which implies an 84% service effectiveness assuming normal distribution for the lead time demands and the coefficient 3 has been historically determined as the lead time demand variance/mean ratio.

The reorder point (RP) is given by

$$RP = OSTQ + SLQ.$$

4. Calculate the Total Assets (TA) and the Total Requirements (TR).

$$TA = SA + \text{Due-ins}$$

$$TR = RO + \text{Due-outs}$$

where SB is the serviceable balance or on-hand inventory.

5. Determine if an order is to be placed and the order quantity, Q. An order is placed if

$$TA - \text{Due-outs} \leq RP.$$

The order quantity is

$$Q = INT\ (TR - TA + 0.5).$$

An analysis of the economic impact of the above algorithm is presented in section 5.2.

4. Current Inventory Control Theory and Practice

Since its development in the early 1900's, the economic order quantity (EOQ) formula has perhaps been the most widely used and the most abused formula or technique associated with the field of operations research and/or management science. The sources of abuse arise from the EOQ's underlying assumptions which seldom hold in practice: independent constant, continuous demand rate, instantaneous replenishment, and real order qualities. The impact of violating these assumptions has been widely studied and appear to be most severe when the demand rate is low and sporatic, the exact case experienced with most SBSS items.

Exhibit 2 illustrates the behavior of the ideal (EOQ) inventory over time and a typical SBSS inventory as generated by the single-item inventory simulator presented in section 5.3. The solid lines represent the on-hand inventory; the hashed lines, the inventory position, on-hand plus due-ins. Little similarity exists between the idea/sawtooth pattern and the erratic SBSS inventory.

Gross and Schrady (74) concluded an extensive survey of inventory theory and practice by representing the "levels of effort" in each as intersecting circles on a Venn diagram. They concluded that the area for intersection between inventory theory and practice is quite small and clearly needs expansion. It is upon that need which this research has focused.

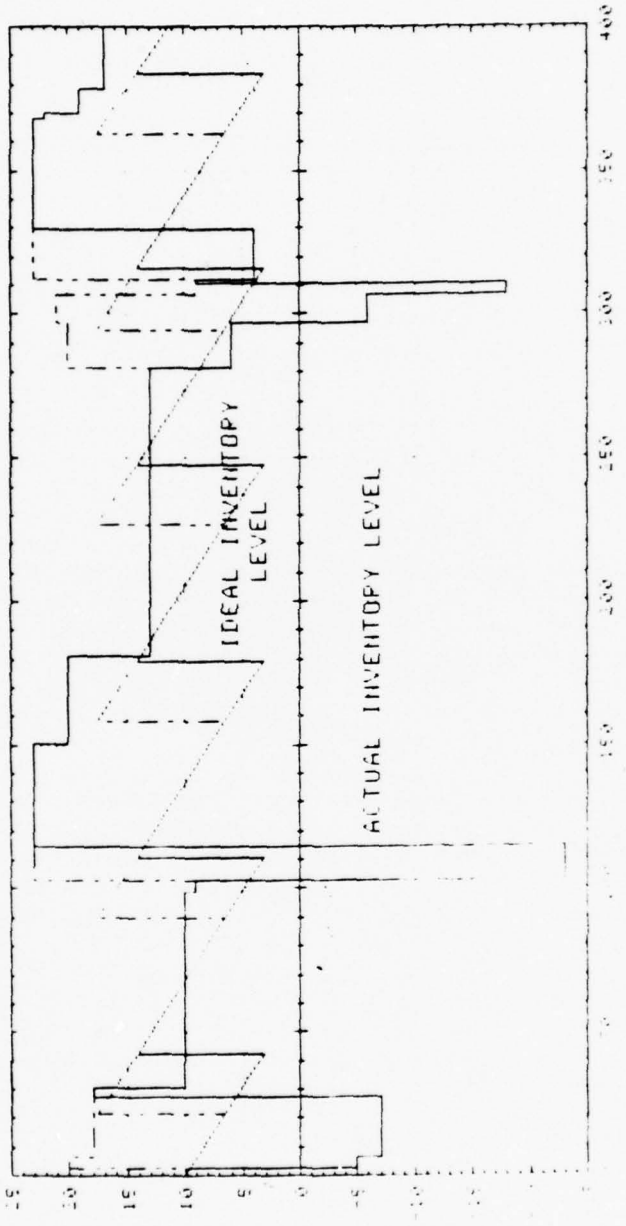

EXHIBIT 2. - INVENTORY PATTERNS

There currently seems to be several general trains of thought related to multi-item inventory control. The division is most marked on the nature of the demands process. The American Production and Inventory Control Society represents the viewpoint of industrial inventory controllers who deal with dependent demand items. Through the use of large scale computer systems, those inventories are managed using deterministic materiels requirement planning (MRP) models. On the other hand, controllers of independent demand inventories have relied on the EOQ formula. In a multi-item environment neither the MRP nor the EOQ systems have been developed to effectively handle constraints, such as budget and storage capacity.

From an inventory theory standpoint, most frequently constraints are handled using the method of Lagrange multipliers. Problems involving constraints, such as the maximum or minimum inventory value, can be solved provided the number of items is relatively small. Such solution techniques for a 20,000-item SBSS inventory would be computationally as well as economically infeasible.

The major stumbling block to the implementation of inventory control theory to large scale systems, such as the SBSS, lies in the handling of backorders or shortages caused by lead time demand variability. The bulk of the current inventory control theory literature is addressed to this problem.

First, there is concern as to how shortage costs should be measured or established. DoD Directive 4140.44 specifies that the measure should relate to the expected essentiality-weighted, time-weighted requisitions short. A host of other shortage measures are used, but all present the same costing problem. For example, how does the cost of being short pencils relate to being short aircraft tires? Certainly, the size and duration of the shortage must be considered along with item essentiality.

Second, how should the inventory model incorporate the stochastic nature of the lead time demand which produces the shortage? The assumptions leading to the EOQ formula do not consider this problem. Hadley and Whitin (63) present a heuristic approximation for the backorder case which can be iteratively solved for lead time demands with computationally suitable density functions. The fact that iteration is required makes this technique infeasible for large-scale inventory systems. Later papers by Das (75), Herron (66), Parker (64), and Presutti and Trepp (70) have developed direct solution methods involving curves fitting techniques to appropriate the tail of the lead time demand distribution. All these papers assume the lead time demand to follow the normal distribution. The important general finding of these researchers is that significantly larger order quantities are required than the EOQ. This extra inventory is ordered to offset possible shortages during future lead times. The larger order quantities reduce the number of orders, hence the exposures to shortages. Kaplan (70) considered lead time demand distributions other than normal and found that the reorder point must increase with the time related backorder cost, while the order quantity may increase, decrease, or remain unchanged depending on the lead time demand distribution. These findings lead to the conclusion that the average inventory must be increased to compensate for lead time demand uncertainties.

This inventory growth requirement leads to considering when an item should be stocked at all. This range model concept (stockage/nonstockage) is

the most neglected in the inventory control theory literature. The SBSS range model is based on the demand frequency. Other factors, such as unit price, *ordering*, *stocking*, *carrying* and backorder costs and demand variability, should be considered when the stockage decision is being made. Croston (74) presents a general cost model for stockage determination. This work is far from a point of direct implementation, thus presenting a necessary area for future research.

Most early inventory texts made mention of an ABC classification of inventory items. When inventory items are ranked by annual dollar sales, the following general results are usually found:

Class A - the top 20% of the items (fast moving) account for at least 80% of the sales,

Class B - the next 30% of the items (moderately moving) account for 15% of the sales, and

Class C - the final 50% of the items (slow moving) account for only 5% of the sales.

In manual inventory control systems, a definite priority was given the higher classification items, while automated systems have tended to treat all items with the same algorithm. It seems apparent that the control applied to a dollar per year sales item should be different than a $10,000 per year item. The SBSS and other automated inventory control system do not make any such item classification distinctions.

The distribution of inventory item sales values have also been found to be of computational importance. Brown (63 and 67) and Herron (75 and 78) have demonstrated a lognormal relationship among item importance ratings and have found that the log standard deviation is a consistent descriptor of the nature of particular inventory types. These properties can be used to make aggregate inventory calculations based on a small, carefully selected sample of inventory items.

A final area of inventory control theory which has received little research emphasis is that of the budget cycle impact. The annual budget cycles of the federal government and most private enterprises directly impact the ordering potential of the inventory controller. In addition, the inventory can serve as an effective inflationary hedge and production smoother. Deaschner (75), Kaplan (77), Lansdowne and Morey (73) and Lewis and Perkins (74) have all reported on the general problem posed by budget constraints but a unified theory has yet to be developed.

5. Analysis

During this research, several concepts were generated which required preliminary validation. Because of the limited time involved, only manual analysis and restricted digital simulation were attempted. The AFLMC had available a set of SBSS data for Peterson AFB covering the period from April 1976 through March 1977. Several aspects of that data were manually analyzed.

5.1 Data Analysis

First, the demand patterns of a few items were studied. Tabulations were made of the requisition frequency (days between requisitions), the demand quantity and the lead time. It was assumed that the requisition frequency would follow the Poisson distribution (exponential inter-requisition intervals), the demand quantity would have a geometric distribution, and the lead times would follow the normal distribution. While sample size, computational and time limitations prevented goodness-of-fit testing of these hypotheses, the data seemed to generally fit. One positive indication of the exponential inter-requisition intervals was a relatively close agreement between the estimates for the mean and the standard deviation. The fit of the geometric distribution to the quantity demanded was also checked using the mean-variance property

$$\text{Mean} = 1/P, \quad \text{Variance} = (1-P)/P^2$$

or

$$\text{Variance} = \text{Mean}\ (\text{Mean} - 1).$$

The lead time demand mean and variance were estimated using the mean and variance estimates calculated from the sample data and the formulas for the lead time demand parameters given by McFadden (72).

$$\mu_{LTD} = \mu_{LT}\mu_{DR} = \mu_{LT}\mu_{RR}\mu_{U/R}$$

$$\sigma^2_{LTD} = \mu_{LT}\sigma^2_{DR} + \sigma^2_{LT}\mu^2_{DR}$$

$$= \mu_{LT}\ (\mu_{RR}\sigma^2_{U/R} + \sigma^2_{RR}\mu^2_{U/R}) + \sigma^2_{LT}\mu^2_{DR}$$

where the subscripts are defined as

LTD - Lead Time Demand
LT - Lead Time
DR - Demand Rate
RR - Requisition Rate
U/R - Units per Prequisition

The estimates of the lead time demand variance/mean ratio varied from 1.10 to 9.79 with an average 3.73 or slightly larger than the currently assumed value of 3.

Second, an analysis was made to determine if the composite sales volume distribution fits the lognormal distribution as suggested by Brown and Herron. Because the data file contained in excess of 8,000 items with demands, the manual tabulation could not include all the inventory items. A sample of 500 items was available. Of that 500, 50 items or 10% had annual sales in excess of $550, the average for all items in the inventory. Those 50 items accounted for 98.98% of the sales. Using Herron (76) approximate method, a log standard

deviation of 2.56 was found, which is centered in the expected range of 2.0 to 3.0 for spare parts inventories. Other computational techniques produced results in a similar range. A fitting of the sales volume order items on normal-normal graph paper did not produce an exact straight line. That may have been due to the limited sample size and the manual computational methods.

Third, the general validity or quality of the SBSS data was surveyed by studying the 50 items with above average sales. It was found that in 6 of 50 cases the total assets greatly exceeded the total requirements (overstocked), while in 29 of 50 cases the reverse was true. In the balance of the cases a rough balance was observed. In one understock case with a requisition objective of 79, a serviceable balance of 1 was recorded without any due-ins or due-outs. In making this analysis, it was observed that the most frequent serviceable balances were zero and one. This was particularly true with items having a large requisition objective (40 or more). The occurrence of such a large number of zero and one serviceable balance levels seems to indicate a circumvention of the SBSS logic. A serviceable balance of one may be used to indicate the presence of stock (regardless of quantity) while a zero indicates a stockout. Such an operating strategy would negate the functioning of the SBSS, but would aid the inventory manager by understating the on-hand inventory value and hence increase the number of annual inventory turnovers.

Another alarming finding in this analysis was the small size of the due-in quantities in relationship to the EOQ. One item with an EOQ of 11 had due-ins of 3, 2, 5, 6 and 4; another item with an EOQ of 36 had due-ins of 10, 108, 2, 5, 217, 6 and 20. Such erratic order quantities seem to indicate the presence of ordering with each requisition. The AFLMC has found by simulation analysis that initially large orders are required to bring the inventories in line with the requisition objectives.

5.2 VSO Analysis

The previous analysis found the order quantities almost always smaller than the EOQ. The reduced order size not only increases the number of orders and the ordering cost, but also increases the exposure to shortages during the lead time intervals. The most apparent reason for the increasing order frequency was the VSO factor in the EOQ formula. VSO factors of 90, 60, ..., effectively reduce the EOQ to $\sqrt{90/365} = 0.50$, $\sqrt{60/365} = 0.41$, ..., of the optimal size. Not only does the VSO factor reduce the order quantity, but the manner in which the VSO determined EOQ is used to calculate the requisition objective can have a negative impact on the order quantity. This is due to the rule which fixes the requisition objective unless it changes by at least the square root of its original value. For example, if RO = 18, then in order to change, the new RO must exceed $18 \pm \sqrt{18} = 18 + 4.24$, or the new RO must be less than 14 or greater than 22. One potential impact of the square root rule is that a decreasing demand rate leads to larger orders, while an increasing demand rate results in smaller orders.

To study the impact of the VSO and the RO square root rule, a standard item example was developed based on a composite of observed item data. Exhibit 3 summarizes the characteristics of the standard item. The top third of Exhibit 4 tabulates the VSO, EOQ, RO, Minimum Order Quantity (MOQ).

	Mean	Variance	Standard Deviation	Coefficient of Variation
Inter-Requisition Period (Days) Exponential	31	961	31	1.00
Requisition Rate (1/Days) Poisson	0.0323	0.0323	0.180	5.57
Units/Requisition (Units) Geometric	5	20.0	4.47	0.894
Daily Demand Rate (Units/Day)	0.161	1.45	1.20	7.74
Order & Ship Time (Days) Normal	21	49	7	0.333
Order & Ship Time Demand (Units)	3.39	31.8	5.64	1.66

Order & Ship Time Demand Variance/Mean Ratio = 9.37

Unit Price, P = $10.00
Ordering Cost, A = $5.00
Holding Cost Rate, I = 50%
Stockage Priority Code, SPC = 4

EXHIBIT 3. - STANDARD ITEM STATISTICS

	STOCKAGE PRIORITY CODE, SPC			
	1	2	3	4
Initial Condition				
VSO (days)	365	365	90	30
EOQ (units)	10.68	10.68	5.30	3.06
Requisition Objective (units)	18	18	12	10
Minimum Order Quantity (units)	12	12	6	4
Expected No. Orders/ Year	4.91	4.91	9.81	14.72
Expected Annual TVC	70.47	70.47	80.00	99.53
Maximum Daily Demand Rate INCREASE				
Daily Demand Rate (units/day)	0.241	0.241	0.231	0.210
VSO	365	365	90	60
EOQ	13.05	13.05	6.34	4.94
Requisition Objective	18 (23)	18 (23)	12 (22)	10 (21)
Minimum Order Quantity	10 (14)	10 (14)	4 (14)	2 (13)
Expected No. Orders/ Year	8.79 (6.28)	8.79 (6.28)	21.06 (6.02)	38.39 (5.91)
Expected Annual TVC	88.44 (85.90)	88.44 (85.90)	134.35 (84.13)	215.13 (80.23)
Maximum Daily Demand Rate DECREASE				
Daily Demand Rate	0.100	0.125	0.100	0.093
VSO	365	365	60	15
EOQ	8.40	9.40	3.40 (8.39)	1.64 (8.09)
Requisition Objective	18 (14)	17 (15)	12 (13)	10 (13)
Minimum Order Quantity	14 (10)	12 (10)	8 (9)	6 (9)
Expected No. Orders/ Year	2.60 (3.65)	3.80 (4.56)	4.55 (4.04)	5.63 (3.76)
Expected Annual TVC	60.55 (55.80)	63.04 (61.84)	55.26 (55.24)	55.25 (53.36)

EXHIBIT 4. - VSO IMPACT ANALYSIS

$$MOQ = INT\ (RO - RP + 0.999).$$

Expected number of orders per year (E(NO))

$$E(NO) = 365 \cdot DDR/MOQ$$

and the Expected Annual Total Variable Cost (TVC)

$$TVC = A \cdot E(NO) + I \cdot P\ (0.5 \cdot MOQ + SLQ)$$

against the four stockage priority codes (SPC). For the standard time example OSTQ = 3.381, SLQ = 3.815 and thus RP = 6.566. Note the VSO is 365 for both the SPC = 1 and 2, 90 for SPC = 3 and 30 for SPC = 4. The corresponding EOQs are reduced about 50% and 71% in the two later priority groups and the TVC increased by 14% and 41%. Note also that the minimum order quantity is equal to EOQ rounded up to the next largest integer in this manner:

$$MOQ = INT\ \Big(INT\ (EOQ + RP + 0.999) - RP + 0.999\Big).$$

The middle third of Exhibit 4 illustrates the impact of the largest possible DDR increase which does not increase the RO, that is the new RO = 22. The DDR can increase from 0.161 by 50, 43, or 30% in the various SPC without exceeding the RO square root limit. Notice the extreme difference between the EOQ and the MOQ caused by the fixing of the RO while the RP increases with DDR. The numbers enclosed in brackets indicate the statistics provided the full EOQ (VSO = 365) were used and the RO was not restricted by the square root rule. In all cases, and in particular the lower SPC cases, the optimal cost is less than that produced by the SBSS algorithm.

The bottom third of Exhibit 4 illustrates the impact of a declining DDR and fixed RO. Again the optimal TVC are consistently less than the SBSS algorithm, but the differences are not as extreme as in the increasing demand case.

A final footnote should be added to this analysis. Because the analysis leading to Exhibit 4 was static, the TVC statistics do not include backorder costs caused by shortages. If a backorder factor were included, its impact would vary directly with the number of orders or inversely with the order quantity. To more accurately model such factors, a single-item inventory simulator was developed.

5.3 Single-Item Inventory Simulator

The AFLMC has available two deterministic simulation programs written in SIMSCRIPT which can be used to evaluate policy changes for the entire SBSS based on actual demands. Neither of these simulators was designed to study in detail the impact of different depth model configurations on the SBSS performance for a single-item inventory. Therefore, a BASIC program was developed to simulate the response of three different inventory models to a common demand pattern for the standard item presented in Exhibit 3.

The single-item inventory simulator was programmed with three different inventory control models.

1. The SBSS algorithm (VSO model)
2. A strict EOQ model, e.g., VSO = 365 (EOQ model)
3. A model based on the results of Presutti and Trepp (70) (Modified EOQ Model). The modified EOQ formula is

$$EOQ = \frac{\sigma}{\sqrt{2}} + \sqrt{\frac{2A \cdot DDR \cdot 365}{I \cdot P} + \left(\frac{\sigma}{\sqrt{2}}\right)^2}$$

where σ is the lead time demand standard deviation. The coefficient $\sqrt{2}$ was developed by fitting the tail of the normal density function with a polynomial. The OSTQ was the same as the VSO model while the SLQ uses the estimated lead time demand standard deviation, SLQ = $C\sigma$.

Because the Presutti and Trepp model requires an estimate of the lead time demand standard deviation, a forecasting procedure had to be incorporated in the simulator. Initially, the simulated lead time demands were tallied by the program and their mean and variance forecasted using exponential smoothing. These forecasted statistics proved to be extremely unreliable and were abandoned as a potential application method. The method finally adopted used McFadden's (72) formula illustrated in section 5.1 with the assumed or input values for the lead time mean and standard deviation and the forecasted daily demand rate mean and standard deviation. The daily demand rate standard deviation was forecasted in a manner parallel to the SBSS daily demand rate forecast.

The simulator exercised each model with the safety factor, C = 0, 1, 2 and 3 which corresponded to support effectivenesses levels of 50, 84, 95 and 99% assuming a normal distribution for the lead time demand. All three models used the same reordering procedure as the current SBSS. The simulator was initialized by simulating 50 demands to fill the various order and materiel pipelines and to establish the forecasting bases. Following this initialization, the counters and tallies were reset to zero and the actual 5000 demand or 427 years' simulation was begun. This simulation length, while excessive compared to real life, seemed to provide stability in the results. However, no statistical confidence limits were computed to determine the appropriate run lengths. This simulation required 72 minutes elapsed time on a PDP 11/45. Considerable computational time reduction could be obtained by converting the program to FORTRAN and using a faster computer system. A variety of statistics were produced by the simulator. Three sets are presented for comparison in Exhibits 5, 6 and 7.

Exhibit 5 illustrates the unit fill rate as a function of the safety factor, C, for each of the three models and the implied service effectiveness, assuming a normal distribution for the lead time demand. As expected, the unit fill rate increases with the safety factor and improves with the model type. Note the poor agreement between the service effectiveness and the simulated unit fill rates. Two reasons may explain this difference. First, the lead time demand does not follow the normal distribution, in fact, the distribution is highly skewed to the right, perhaps gamma or lognormal. This

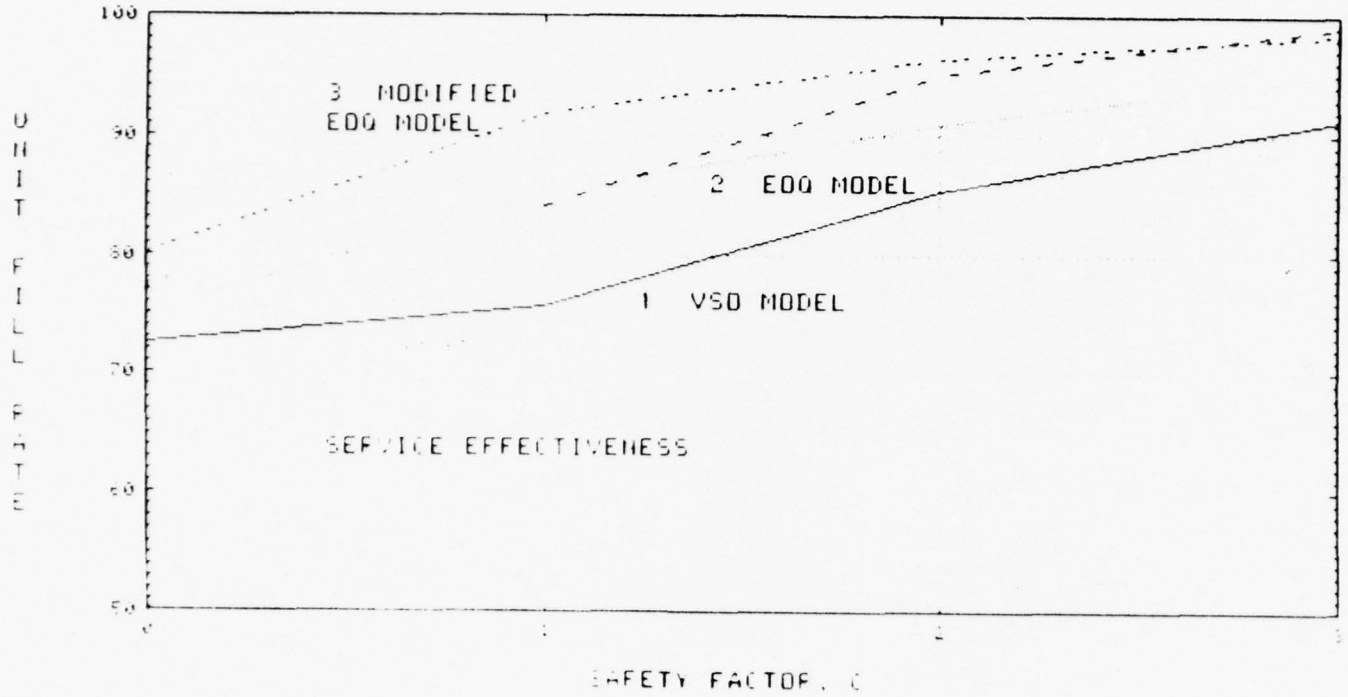

EXHIBIT 5. - SIMULATION ANALYSIS - UNIT FILL RATE

skewness implies that a substantial portion, say 60 to 70%, of the density function lies below the mean, while more than 1% lies above the mean plus three standard deviations. Second, the service effectiveness applies only during the lead time interval. In a well run inventory system, due-in orders should only be outstanding a limited fraction of the time. For example, using the EOQ model with C = 1, due-in orders existed 19% of the time. Thus, the expected storage probability should equal 0.19 (1 - service effectiveness).

Exhibit 6 illustrates the Total Variable Cost (TVC) of maintaining the inventory system as a percent of the sales. TVC includes the ordering and holding cost plus the implied time-weighted backorder cost, λ, as computed by

$$\lambda = (1-\rho)I \cdot P/\rho$$

where ρ = shortage risk = 1 - support effectiveness. Thus,

C	1 - ρ	ρ	λ
0	0.50	0.50	$ 5.00
1	0.84	0.16	$ 26.25
2	0.95	0.05	$ 95.00
3	0.99	0.01	$495.00

The increase in TVC with C is primarily due to the increased backorder cost, in spite of the fact that the actual number of backorders was observed to decrease. It is significant to note the decrease in TVC with the model increase.

Exhibits 5 and 6 demonstrate the advantages of the EOQ model over the VSO model and in turn the modified EOQ over the standard EOQ. Unfortunately, this gain has associated with it larger order quantities which imply larger on-hand inventories. Exhibit 7 illustrates this in terms of the average number of annual inventory turnovers.

Several points should be made concerning the results of the simulation analysis. First, from Exhibit 5 it should be noted that the curves for each model are relatively flat or insensitive to the safety factor. Indeed the model, or more accurately the order quantity, has about the same impact as the safety factor. It appears that this is due to the erratic demand pattern of the standard item and may indeed be true for most SBSS items. Thus, it appears undesirable to consider safety factors other than the current value of 1. Second, note on Exhibit 6 that TVC/sale % of the VSO model with C = 1 is 7.9%, while the modified EOQ model with C = 3 has a cost of only 6.5%. Thus, the TVC cost could actually be reduced while the unit fill rate increased from 75.6 to 98.4% (see Exhibit 5). A clear advantage exists for replacing the current VSO model with either the EOQ or modified EOQ models. The impact of implementing such a change is developed in section 6.

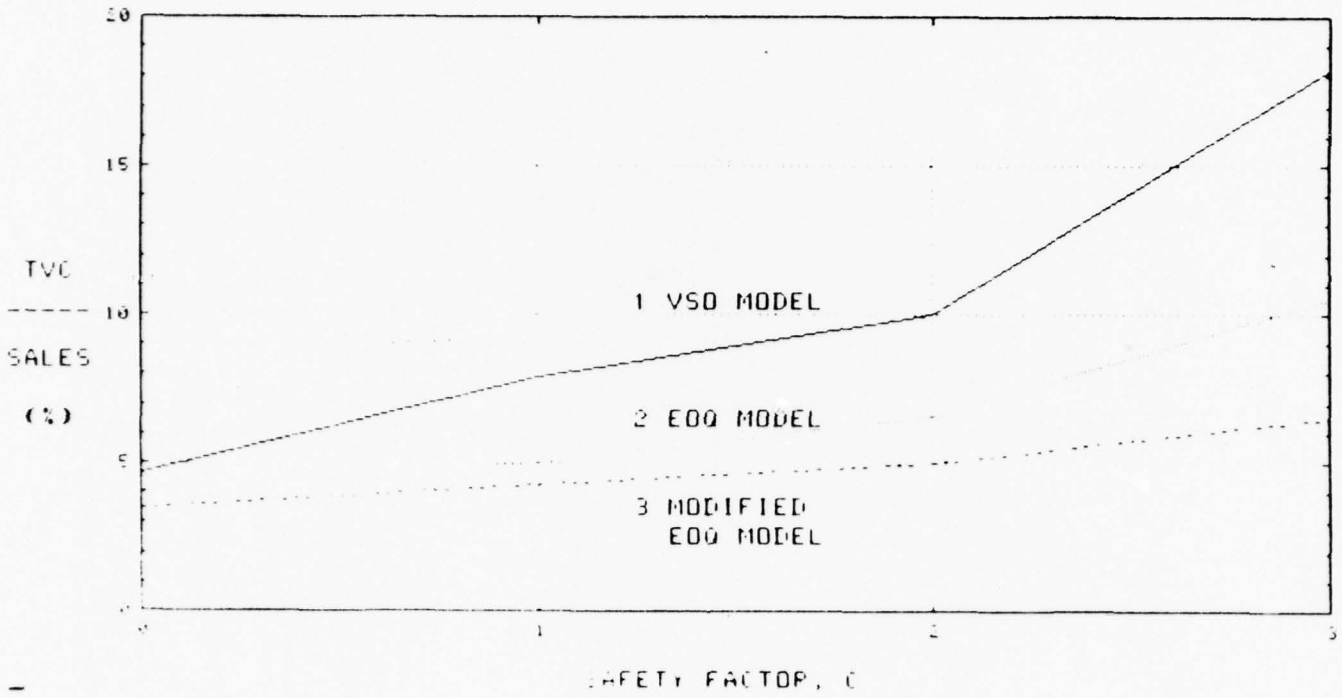

EXHIBIT 6. - SIMULATION ANALYSIS - TVC/SALES x 100%

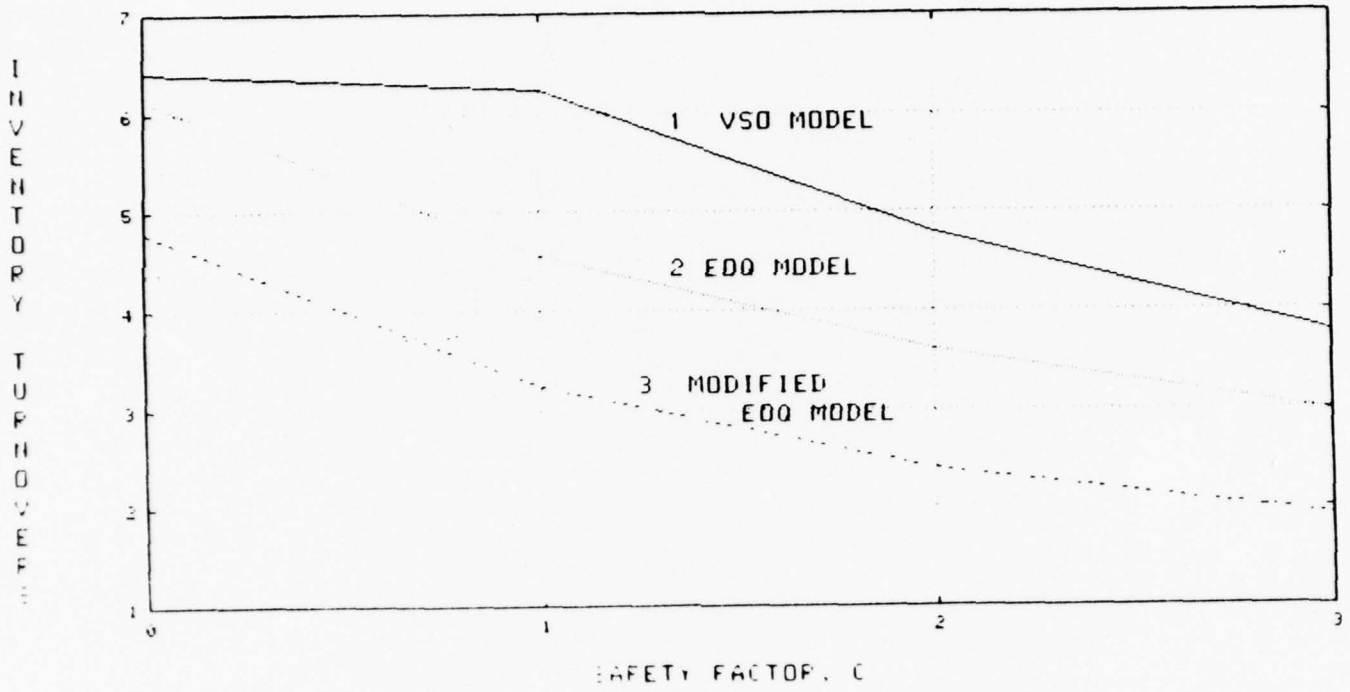

EXHIBIT 7. - SIMULATION ANALYSIS - ANNUAL INVENTORY TURNOVERS

6. SBSS Systems Design

The objective of this research project was to develop a technical plan or systems design structure for future SBSS improvements. Exhibit 8 illustrates a general model for SBSS systems design. This model highlights the objective, constraints, criteria, requirements and alternatives which currently seem appropriate to the SBSS design task. As indicated by the tradeoff loop, any of these elements are subject to change over the course of the design activity. The systems design model can be used to discuss the current state-of-the-art in terms of the indicated requirements and alternatives.

6.1 SBSS Systems Design Requirements

The first requirement, the range model, is currently based on demand frequency and item priority. As such, it is a variance with DoD Directive 4140.44 which desires an economically based range model. A statistical model is suggested as a third alternative. The statistical model would consider the item's demand pattern characteristics, as well as the variable costs and the item's essentiality. For many items the critical point in determining the stockage policy may well be: Can the user wait for the item to be ordered from the depot? Due to the lack of a unified theory for item stockage, the range model represents a critical area for basic research. One avenue to this research is the A-B-C classification of inventory items. Only items in the C or low-usage classification need to be seriously considered for non-stockage. The specific task of designing an SBSS range model is closely associated with the depth model and thus they must be studied as an integrated pair.

The depth model requirement lacks little as far as available theory with exception of modeling for erratic or lumpy demands which unfortunately characterize the SBSS. The single-item simulation analysis reported on in section 5.3 indicated the potential improvements of switching from the VOS model to either the EOQ model or the modified EOQ with backorders. These results should be validated using the currently available SBSS simulators. In addition, information is required concerning the nature of the demand processes and the lead time demand distribution for full implementation of a depth model which considers backorders. A separate study addressing those problems is currently underway at the Air Force Academy. If that study concludes the lead time demand distribution to be other than normal, then a curve fitting analysis must be performed to find the appropriate coefficient for the modified EOQ formula. Also, new service effectiveness parameters must be determined for the appropriate lead time demand distribution. At present and for the foreseeable future, there appears to be no need nor practical means of simultaneously determining the order quantity and the reorder point for all the SBSS items.

Another point of concern related to the SBSS depth model and the simulated alternatives is the way the reorder point and order quantity are applied. At present the reorder point is always rounded down or truncated. This consistently understates the safety level quantity. In addition, it may be desirable to increase the reorder point one-half of the average requisition size to compensate for overshooting due to multi-unit demands. Correcting the reorder point rounding problem would also correct the tendency to over roundup the order quantity. Because many SBSS due-ins are for a few items, an adjusted

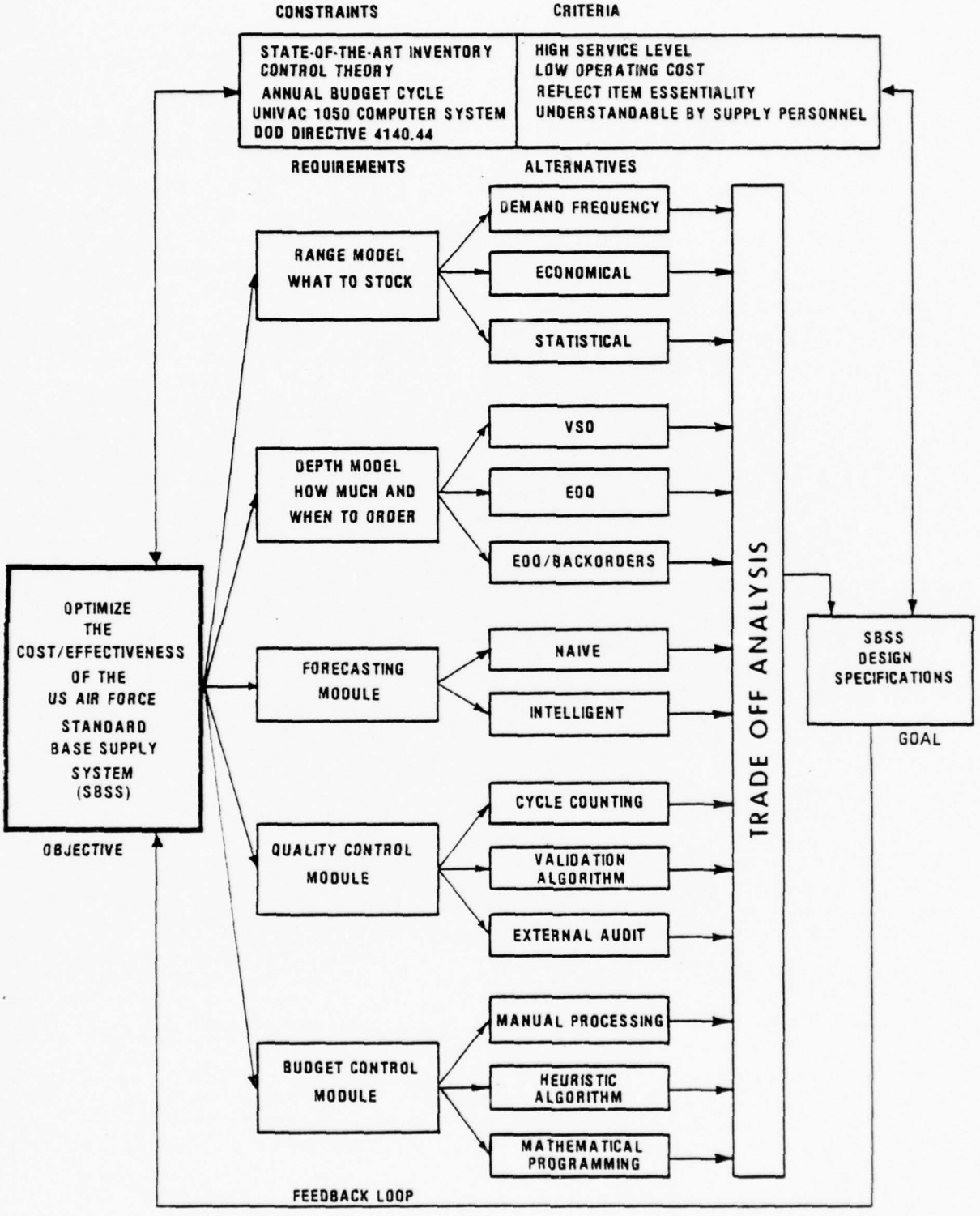

SBSS SYSTEMS DESIGN MODEL

EXHIBIT 8

rounding scheme may be of benefit, see Brown (67), page 49. This rounding correction should be applied to the unit pack algorithm.

The forecasting module is required to predict the future demand rate. The current modified exponential smoothing method appears to be an appropriate "naive" or no external information method for forecasting the mean daily demand rate. A similar method could forecast the daily demand variability. Future depth and range models may also require an enhancement of the requisition rate forecasting method. The single-item simulation analysis has indicated that direct lead time demand forecasting may be of little practical value. Intelligent forecasting techniques which incorporate mission changes and new systems information should be considered whenever possible in the SBSS. Efficient means of merging such information with past demand data for a large number of items deserves further research. Group theory might also be considered as a means of jointly forecasting the demand for similar items.

An SBSS quality control module is an apparent need which was identified during the data analysis phase. Although never validated by field audit, the large portion of zero and one serviceable balances seemed to indicate a misuse in the SBSS logic. A tighter cycle counting scheme may present one solution. Validation algorithms within the SBSS and at the depot level could check the operating characteristics against appropriate standards. External audits of the SBSS may be the most expensive and painful, but may at least be required on a sample basis to determine the validity of the current SBSS. Such an audit may disclose that the present system is sufficiently accurate to require no additional quality control functions.

The budget control module requirement represents the most potential for future inventory control research. No doubt the current VSO model was implemented as a budget control technique, with less inventory being carried for the low demand and priority items. Unfortunately, the major impact of the VSO model seems to be a reduced unit fill rate and an increased total variable cost. A comprehensive budget control module should distribute the funds available for safety level inventories according to item priority. In addition, it should expand or contract the stockage policy to react to remaining funds in the annual budget cycle. Much fundamental research is required to develop this area of inventory theory. The lognormal inventory item importance relationship seems to be of potential benefit in this area of analysis. The listed alternatives simply suggest some potential solution avenues.

6.2 Technical Plan

Much work remains to be done to improve the SBSS to its fullest potential. The work varies from the development of fundamental inventory control theory in the areas of range modeling, lumpy demand depth modeling and budget control techniques to the application of known goodness-of-fit analysis techniques to determine the lead time demand distribution and to validate the lognormal item importance distribution. Exhibit 8, the SBSS systems design model, should serve as general guide for future work. Current priorities should focus on the depth model and the quality control module followed by the range model and finally the budget control module. This ordering roughly corresponds to a decreasing scale of current theoretical knowledge and follows the philosophy of applying first what is known before additional knowledge is sought. This

ordering should not, however, preclude the initiation of basic research efforts in the range model and budget control module areas. Little additional work is foreseen in the forecasting area with exception of the previously noted problem of interfacing demand intelligence with demand data.

6.3 Analytical Needs

As previously mentioned, two SIMSCRIPT simulation models are available to test the operation of the SBSS against a historical demand pattern. In addition, the single-item inventory simulator developed by this effort should be a valuable analysis tool when converted to FORTRAN and when the statistical distributions are validated. This combination of models along with the lognormal item importance relation techniques suggested by Brown and Herron should be sufficient to evaluate the impact of SBSS on a single Air Force base.

It seems quite evident that the major impact of the suggested changes will be to increase the inventory size. In order to accomplish this change, the base stock fund budgets may require a substantial one-time increment. After this initial period, the SBSS should return to its normal annual dollar ordering volume. In addition, the number of orders placed by the SBSS should be substantially reduced with the implementation of the new model. This should result in a decreased staffing at both the SBSS and depot level. Prior to implementing such a major change with significant impacts at both the base and depot level, it is recommended that a dynamic systems model be constructed along the lines of Exhibit 1. Such a model would indicate the staffing and budgeting impact over a several year planning horizon. If properly constructed, the dynamic systems model should be of benefit in justifying the initial budget increases required to bring the base inventories to their optimal levels.

7. Conclusions and Recommendations

Briefly stated, the major conclusion of this research is: The SBSS should order more, which in turn leads to fewer orders and less shortage risk. Implementation of this recommendation is difficult due to ever present budget constraints. An ideal starting point would be the class A or high-sales items.

While some potentially fruitful areas for SBSS related basic research have been indicated, the major task to improve the SBSS is the application of proven theory to the problem at hand. To that end, it is suggested that the Air Force undertake an expanded effort to instruct its logistics personnel in the theory and practice of inventory control. The American Production and Inventory Control Society is actively involved with such an educational program for industrial inventory planners and may be capable of offering assistance to the Air Force.

8. References

Brown, Robert Goodell. "Estimating aggregate inventory standards." Naval Res. Logist. Quart., 10 (1963), pp. 55-71.

Brown, Robert G. Decision Rules for Inventory Management. New York: Holt, Rinehard, and Winston, 1967.

Croston, J. D. "Stock levels for slow-moving items." Opl. Res. Quart., 25 (1974), pp. 123-130.

Daeschner, William Edward, Jr. Models for multi-item inventory systems with constraints. Naval Postgraduate School, AD-A013466, June 1975.

Das, Chandrasekhar. "Some aids for lot-size inventory control under normal lead time demand." AIIE Trans., 8 (1975), pp. 77-79.

Forrester, Jay W. Industrial Dynamics. New York: John Wiley, 1961.

Gross, Donald and David A. Schrady. "A survey of inventory theory and practice." Modern Trends in Logistics Research Proceedings of a Conference Held at the George Washington University, 1974. Cambridge, Massachusetts: MIT Press, 1976, pp. 248-295.

Hadley, G. and T. M. Whitin. Analysis of inventory systems. Englewood Cliff, NJ: Prentice-Hall, Inc., 1963.

Herron, David P. "Use of dimensionless ratios to determine minimum-cost inventory quantities." Naval Res. Logist. Quart., 13 (1966), pp. 167-176.

Herron, David P. "Industrial engineering applications of ABC curves." AIIE Trans., 8 (1975), pp. 210-218.

Herron, David P. "A comparison of techniques for multi-item inventory analysis." Prod. & Inv. Man., 19 (1st Qtr, 1978), pp. 103-115.

Kaplan, Alan J. "The relationship between decision variables and penalty cost parameter in (Q,R) inventory models." Naval Res. Logist. Quart., 19 (1970), pp. 253-258.

Kaplan, Alan J. Retail stockage policy under budget constraqnts. U.S. Army Logistics Management Center, Inventory Research Office. IRO report 241, AD-A041308, June 1977.

Lansdoune, Zachary F. and Richard C. Morey. Multi-item planned procurement and spot buy procedures. Control Analysis Corp., AD-757058, February 1973.

Lewis, Richard Earl and Robert Darol Perkins. An investigation of variable operating and safety level (VOSL) stocking and funding policy. Naval Postgraduate School, AD-776303, March 1974.

Parker, Lawrence L. "Economic reorder quantities and reorder points with uncertain demand." Naval Res. Logist. Quart., 11 (1964), pp. 351-358.

Presutti, Victor J., Jr. and Richard C. Trepp. "More ado about economic order quantities (EOQ)." Naval Res. Logist. Quart., 19 (1970), pp. 243-251.

1978 USAF-ASEE SUMMER FACULTY RESEARCH PROGRAM

sponsored by

THE AIR FORCE OFFICE OF SCIENTIFIC RESEARCH

conducted by

AUBURN UNIVERSITY AND OHIO STATE UNIVERSITY

PARTICIPANT'S FINAL REPORT

ENGINEERING EQUATIONS VERIFICATION STUDY: X-RAY DEPOSITION ANALYSIS

Prepared by:	Philip Feinsilver
Academic Rank:	Assistant Professor
Department and University:	Dept. of Mathematics Southern Illinois University
Assignment:	
(Air Force Base) (Laboratory) (Division) (Branch)	Edwards AFB Edwards AFB Rocket Propulsion Laboratory LKCP
USAF Research Colleagues:	G. Allen Beale
Date:	August 11, 1978
Contract No:	F44620-75-C-0031

ABSTRACT

We are considering calculations for estimating the effects of x-rays on materials that are important for engineering design. Specifically we discuss calculation of surface dosage, dose profiles and front-face mass removal.

For these calculations, present computer codes are over-elaborate while simplified engineering design equations are of questionable accuracy. We present accurate methods that are suitable for programmable electronic hand calculators with magnetic card capability.

We include tables of ranges of percentage errors of results from the design equations and of our approximations from calculated ("exact") values.

FOREWORD

It is a pleasure to thank G. Allen Beale and the LKCP branch of the Edwards AFRPL and, generally, the AFRPL for the opportunity to work with them on this project at their laboratory. They have made our association very pleasant and worthwhile. Special thanks goes to Dennis Coalson, a summer student from U. C. San Diego, for doing the computations, programming, and writing the Appendix.

Warm acknowledgement is due to Larry Quinn of the AFRPL and to J. Fred O'Brien of Auburn University for their guidance and administration of the project.

INTRODUCTION

We are interested in calculating the effects of x-ray radiation on materials. For simplicity, we assume x-rays impinging on the surface of a homogeneous material, the source being an ideal black-body at temperature T'°K. We then would like to calculate:

(1) Surface dosage

(2) Dose profile - how dose varies with distance from surface

(3) Front-face mass removal - due to melting and vaporization

Further effects involve back-face spall, buckling, and debonding of composite materials.

We will discuss in detail (1) - (3). We will present comparison of calculated, "exact", results with those from engineering design equations [4], [3]. Some analytical approximations somewhat less complicated than those extant, e.g. in [5], are given and comparisons presented.

Our main results are (a) that the calculation of (1) and (2) can be readily done "exactly" - i.e. exactly, given a standard theoretical model - on a programmable hand calculator comparable to the, say, TI-59 and (b) that we give relatively simple analytical approximations, suitable for a hand calculator, that are efficient and reliable.

The appendix includes a discussion of the calculator programs and the listings.

PART I. THEORETICAL SETTING. BASIC CALCULATIONS.

X-RAY ABSORPTION OF BLACK-BODY RADIATION

Planck's radiation formula can be expressed as follows:

We assume an ideal black-body at absolute temperature T' radiates photons. Define a "black-body temperature" $T = kT'$ kev, where k is Boltzmann's constant in appropriate units. Planck's relation says that radiation of frequency ν has energy $E = h\nu$ which we take in kev. In terms of the dimensionless variable $u = E/T$ we have the function for black-body radiation intensity

$$B\sigma T^4 E(u) = \sigma T^4 B u^3 (e^u - 1)^{-1}$$

where σ is the Stefan-Boltzmann constant and

$$B^{-1} = \int_0^\infty u^3 (e^u - 1)^{-1} du = \zeta(4)\Gamma(4) = \pi^4/15$$

Thus, since σT^4 is the total flux, $BE(u)$ is the normalized density function of the incident flux as a function of u.

Consider now a material of density ρ gm/cm with absorption coefficient $\mu(E)$. Then the dose, actually dose per fluence, at a depth x cm is [4], [7]:

$$D_T(x) = B \int_0^\infty \mu e^{-\mu\rho x} E(u) du \quad \text{(cal/gm per cal/cm}^2\text{)}$$

The function $\log \mu$ has been empirically determined and analytically expressed as a function of $\log \lambda$, λ being wavelength, e.g. by linear [2] and cubic [3] approximations. We assume in the following that we have exactly, as in [3],

$$\mu = C\lambda^n$$

If we set $\tau = \frac{hc}{1000e} \frac{1}{T} = \frac{12.398}{T}$ (a "temperature wavelength") then

$$\mu = C\tau^n u^{-n}$$

Finally, defining the virtual depth

$$t = \rho x C\tau^n$$

we have

$$D_T(x) = B(\rho x)^{-1} \int_0^\infty tu^{-n}\, E(u)\, e^{-tu^{-n}}\, du$$

$$= B(\rho x)^{-1} \int_0^\infty tu^{b}\, (e^u - 1)^{-1}\, e^{-tu^{-n}}\, du$$

where $b = 3-n$.

Remarks. 1. It is important to remember that C and n and hence t are functions of u - they vary discontinuously across absorption edges.

2. n varies from 2.1 to 2.83; for one edge, n takes values 2.6628 and 2.83.

Our problem is how to calculate this integral as a function of x and T.

SURFACE DOSAGE

At the surface x = 0 we have

$$D_T(0) = B \int_0^\infty C\tau^n\, u^b\, (e^u - 1)^{-1}\, du$$

If there are no absorption edges, this integral is exactly $BC\tau^n$ times $\zeta(1+b)\Gamma(1+b)$, where ζ = Riemann's zeta function and Γ = the standard gamma function.

With edges, we simply integrate over the intervals between successive edges and sum the results over the intervals.

Theoretically there is no problem, since the integrand at zero is like u^{2-n} with $n < 3$ and like e^{-u} at infinity. However, when integrating numerically we would like a function to be, say, C^∞, i.e. having all derivatives continuous, at 0. Specifically, our approach is to use 20-point Gaussian quadrature from 0 to 30; omitting the rest of the integral, beyond 30, leaves a negligible percentage error.

We observe that

$$u^b(e^u - 1)^{-1} = u^{b-1}\, u(e^u - 1)^{-1} = u^{b-1} \sum_0^\infty \frac{B_k\, u^k}{k!}$$

where B_k are the Bernoulli numbers. This series has radius of convergence

2π since the nearest pole is at $2\pi i$. The series alternates. Thus we have the estimate, see [1] page 805, eq. 23.1.15.

$$|R_N| \leq 2.1\ (u/2\pi)^N \qquad N \text{ even} \geq 6,$$

for the remainder of the series after N terms.

We use the series for $0 \leq u \leq 1$ through $N = 6$ for our computations.

Thus,

$$\int_0^1 u^b(e^u - 1)^{-1} = \frac{1}{b} - \frac{1}{2(1+b)} + \frac{1}{12(2+b)} - \frac{1}{720(4+b)} + \frac{1}{30240(6+b)} + \ldots.$$

Then we can integrate for $u \geq 1$ by Gaussian quadrature.

The asymptotic expansion for $I_a(x)$, an incomplete gamma function,

$$I_a(x) = \int_x^\infty u^a e^{-u}\ du = x^a e^{-x}[1+ax^{-1}+a(a-1)x^{-2}+\ldots], \text{ as } x \longrightarrow \infty,$$

is useful for estimating values and errors.

E.g.

$$\int_x^\infty u^a(e^u-1)^{-1} = \int_x^\infty u^a \sum_1^\infty e^{-ku}$$
$$= I_a(x)+2^{-a-1}I_a(2x)+3^{-a-1}I_a(3x)+\ldots$$

And

$$\int_x^\infty u^a(e^u-1)^{-1} \leq (1-e^{-x})^{-1}\ I_a(x) = x^a\ (e^x-1)^{-1}\ [1+\frac{a}{x}+\ldots].$$

E.g. $\int_{30}^\infty u^{17}\ (e^u-1)^{-1} \leq 1.7 \times 10^{-13}$

The Bernoulli approximation and numerical integration is an efficient way to compute $D_T(0)$.

DOSE PROFILES

For $x>0$, the integral for $D_T(x)$ can, theoretically, be directly computed. However, for small t the damping effect of the term $e^{-tu^{-n}}$ near zero is not strong enough to allow accurate numerical computation since $u^b\ (e^u-1)^{-1}$ still diverges at u=0.

To improve convergence we integrate by parts. We have, for an interval I,

$$(B^{-1}\rho x)\, D_T^I(x) = \int_I t\, u^b (e^u-1)^{-1} e^{-tu^{-n}}\, du$$

$$= \int_I u^4 (e^u-1)^{-1}\, d(e^{-tu^{-n}})/n$$

$$= u^4 (e^u-1)^{-1} e^{-tu^{-n}}/n \Big|_I - \int_0^\infty \phi(u)\, e^{-tu^{-n}}\, du/n$$

Where $\phi(u) = (u^4 (e^u-1)^{-1})'$. Here, I is an interval, between successive absorption edges, over which t and n are constant. Since $u^4 (e^u-1)^{-1} \sim u^3$ and analytic at zero, $\phi(u) \sim 3u^2$ at zero so that even without the damping term the integrand is smooth there. To compute $D_T(x)$ we integrate from 0 to 30, integrating numerically for each I and summing the results over all intervals.

FRONT-FACE MASS REMOVAL

The deposition of x-ray energy in a material will cause high heat in turn inducing melting and vaporization. We assume the material is at an ambient temperature T_o ^oC. Let c_p = specific heat in cal/gm^oC, E_m = enthalpy through melt (starting from 0^oK), E_v = enthalpy through vaporization. Then a deposition of

$$H_m = E_m - c_p (T_0 + 273) \quad \text{cal/gm}$$

will cause melting. Similarly a deposition of

$$H_v = E_v - c_p (T_o + 273) \quad \text{cal/gm}$$

will cause vaporization .

We assume an irradiation time of 10^{-8} sec, i.e. essentially instantaneous. Suppose f = cal/cm^2 flux from blackbody radiation at temperature T. Then we expect melting to occur until depth x such that $H_m = fD_T(x)$. Similarly a vaporization layer of thickness x will occur to that depth such that

$$H_v = fD_T(x).$$

Using the dose profiles one can estimate the thickness of melted layers and vaporized layers for various materials and temperatures.

REPRESENTATIVE CASES

We chose four elements Be, Fe, Ni and W as representatives. For each element we calculated $D_T(x)$ for T = .5, 1, 2, 3, 5, 7, 9, 12, 15 and x = 0, 10^{-5}, 10^{-4}, 10^{-3}, 10^{-1}, 10^{0}.

Tables 1-5 give our results to 4 significant figures.

Table 6 gives examples of front-face mass removal.

PART II. ANALYTICAL APPROXIMATION

Small Depth Approximation

We are considering approximation of

$$D_T(x) = B(\rho x)^{-1} \int_0^\infty t u^b (e^u-1)^{-1} e^{-tu^{-n}} du$$

as $t \to 0$. Observe that if $u^{-n} = v$ this would be a Laplace transform, i.e. an integral of the form $H(t) = \int_0^\infty e^{-tu} h(u)du$. We recall the Abelian theorem for Laplace transforms which states that if $h(v) \sim Av^a$ as $v \to \infty$, then $H(t) \sim \int_0^\infty e^{-tu} Av^a du = A\Gamma(1+a)t^{-1-a}$ as $t \to 0$.

We set $g(x) = \int_0^x u^b(e^u-1)^{-1} du$ and note that $g(x) \sim \int_0^x u^{b-1}du = x^b/b$ as $x \to 0$. We now see that

$$G(t) = \int_0^\infty u^b(e^u-1)^{-1} e^{-tu^{-n}} du = \int_0^\infty e^{-tu^{-n}} dg$$

Integrating by parts,

$$\int_0^\infty e^{-tu^{-n}} dg = g(\infty) - \int_0^\infty g(u)\, d(e^{-tu^{-n}})$$

Substitute $u^{-n} = v$ to get

$$= g(\infty) + \int_0^\infty g(v^{-1/n})\, d(e^{-tv})$$

$$= g(\infty) - t\int_0^\infty g(v^{-1/n})\, e^{-tv}\, dv$$

As $v \to \infty$, as we noted above $g \sim v^{-b/n}/b$. We see that as $v \to \infty$, $u \to 0$ so that the lowest energy interval predominates. Thus, regardless of absorption edges we use n,t for the lowest energy interval, i.e. for the longest wavelength.

Using the Abelian theorem we have

$$G(t) \sim g(\infty) - t\,\Gamma(1-\tfrac{b}{n})\, t^{b/n-1}/b, \text{ where } b = 3-n$$

Thus,

$$D_T(x) \sim D_T(o) - B\,\Gamma(2-3/n)\, t^{3/n}\, (\rho x b)^{-1}$$

Since $t = \rho x C\tau^n$ we can express this in the form

$$D_T(x) \sim D_T(o) - K(\rho x)^a\, T^{-3}$$

where $K=BC^{3/n}\Gamma(1-a)b^{-1}\ (12.398)^3$ and $a = \frac{3}{n} - 1$.

Here C and n are those for the lowest energy interval.

Table 7 lists K and a for our representative elements.

LARGE-DEPTH APPROXIMATION

To derive an approximation for large t we use Laplace's asymptotic method. We have

$$\int_0^\infty u^b (e^u-1)^{-1}\ e^{-tu^{-n}}\ du = \int_0^\infty u^b e^u\ (e^u-1)^{-1}\ \exp\ (-u-tu^{-n})\ du$$

For large t the integrand is largest near the minimum of

$u + tu^{-n}$ which is at $v = (nt)^{1/(n+1)}$

Substituting $u = vw$ we have an integral of the form

$$\int_0^\infty g\ (w)\ \exp\ (-vf(w))\ dw$$

with $g = v^{b+1}w^b\ (1-e^{-vw})^{-1}$ and $f = w+n^{-1}w^{-n}$. Since f has its minimum at w=1, Laplace's method says that for large v this integral

$$\sim v^{b+1}(1-e^{-v})^{-1}\ \sqrt{2\pi}\ ((n+1)v)^{-\frac{1}{2}}\ e^{-\beta v}\ ,\ \beta = 1+n^{-1}\ .$$

From the definition of D_T we thus have, for large t, the free approximation

$$D_T\ (x) \sim K_L\ t\ (\rho x)^{-1}\ v^{\alpha} e^{-\beta v}\ (1-e^{-v})^{-1}$$

Where $K_L = B\ \sqrt{2\pi}\ (n+1)^{-\frac{1}{2}}$,$\alpha = 3.5-n, \beta = 1+n^{-1}$, $v = v(n,t)=(nt)^{1/(n+1)}$

This holds only if there is no absorption edge, i.e. v must lie in the interval where the corresponding n and t apply. If v lies past the next absorption edge, then that edge, which we denote by E, is the minimum point and the integral depends mainly on u near E. We can approximate the integrand for u near E and derive the following edge approximations valid for large t.

Define $\Phi(y) = \int_y^\infty \exp(-u^2/2)\,du$. Then set

$$P = E - ntE^{-n}, \quad Q = n(n+1)tE^{-n}, \quad R = E^{4-n} \exp(-E - tE^{-n})$$

Now we define

$$D(E,n,t) = Bt(\rho x)^{-1} RQ^{-1/2} \exp(P^2/2Q)[\Phi(-PQ^{-1/2}) - \Phi((Q-P)Q^{-1/2})]$$
$$d(E,n,t) = Bt(\rho x)^{-1} RQ^{-1/2} \exp(P^2/2Q)\,\Phi(PQ^{-1/2})$$

Remark. The function Φ may be approximated by:

$$\sqrt{\pi/2} - (x - x^3/6) \text{ for } |x| < 1$$
$$x^{-1} e^{-x^2/2} \text{ for } x \geq 1, \quad \sqrt{2\pi} + x^{-1} e^{-x^2/2} \text{ for } x \leq -1.$$

We then have the following method for large t:

1. Consider energy intervals (E, E'), (E', E") between successive absorption edges. NOTE: $E = 12.398/\lambda T$ if λ = wavelength absorption edge.
2. Let n,t correspond to u between E, E' and n', t' correspond to u between E' and E".
3. If $v(n,t) > E'$, then the contribution to the integral from the interval (E, E') is D(E',n,t).
4. If $E < v(n,t) < E'$, then we use the free approximation corresponding to n,t as the contribution from (E, E').
5. If $v(n',t') < E'$, then the contribution from (E', E") is d(E',n',t').
6. Compute for each interval and sum over all intervals for the large t approximation.

This is very quickly computable on a programmable hand calculator.

PART III. ACCURACY OF APPROXIMATION

Dose Profiles

The engineering design equations give, Z = atomic number,

$$D_o = \begin{cases} 3(Z/T)^3 & \text{for } Z \geq 6 \\ 60\,ZT^{-2} & \text{for } Z \geq 12 \end{cases}$$

D_0 corresponds to D_T (10^{-5}) as a depth of 10^{-5} cm is for practical purposes the surface of the material.

Using D_0 as given above, the dose profile is approximated by $D_T(x) = D_0 \exp(-x/\ell)$ where

$$\ell = \begin{cases} .015\,(T/Z)^3\,\rho^{-1}, & Z \leq 6 \\ .0004\,T^{1.5}\,\rho^{-1}, & Z \geq 12 \end{cases}$$

Table 8 gives the ranges of percentage errors using these approximations.

Table 9 gives ranges of percentage errors using the large-and small-depth approximation of Part II.

Optimum Temperature Estimation

Table 10 compares the estimation of T_{op}, the temperature that maximizes dose for a given depth, with the exact results. The engineering design approximation is:

$$T_{op} = \begin{cases} .5Z\,(\rho x)^{1/3} \\ 1.2Z^{.8}\,(\rho x)^{.4} \end{cases}$$

PART IV. CONCLUDING REMARKS

We have shown that it is possible to estimate x-ray dose profiles relatively effectively-accurately and rapidly. The exact values can be computed using a programmable electronic calculator. We have given approximations that are relatively accurate and much faster to compute.

Comparisons with the engineering design equations show that they are often quite inaccurate and generally one is not sure of their reliability. However, we are much obliged to their proponents for the idea that complex codes or long analytical approximations are indeed unnecessary and obfuscating.

The major word of warning is that the analytical analyses [4], [5] and ours depend on accurate determination of the absorption coefficients μ and the associated parameters, particularly n. Given the coefficients μ, then, we have accurate, efficient methods for calculating dose profiles which in turn allows effective determination of x-ray effects, such as front-face mass removal and stress effects.

References

1. Abramowitz, M. and Stegun, I., eds., Handbook of Mathematical Functions, National Bureau Standards, Appl. Math Series #55, 7th printing May 1978

2. Brown, Warren D., X-Ray Attenuation and Absorption Coefficients, Aerospace Group, The Boeing Company #D2-125065-1, Sept 1966.

3. Clark, George L., ed., The Encyclopedia of X-Rays and Gamma Rays, Reinhold Publishing Corp., NY, 1963

4. Langley, R. W., Analytical Relationships for Estimating the Effects of X-Rays on Materials, AFRPL TR-74-52, Edwards AFB CA Sep 1974

5. Analytical Theory of X-Ray Effects, AF Special Weapons Center AF Systems Command, Kirtland AFB NM, Tech Report # AFSWC-TDR-62-92, Oct 1962 (Secret)

6. Capabilities of Nuclear Weapons, P. J. Dolan, ed., Defense Nuclear Agency Effects Manual #1, DNA EM-1, 1 July 1972, esp Chapters 4, 9V. (Secret)

7. Systems Applications Of Nuclear Technology, X-Ray Effects on Air Force Systems, AFSCM 500-7, 28 June 1974 (Secret)

8. System Survivability, AFSC Design Handbook DH 3-4, Revised 1st edition, 15 April 1978 (Secret)

Comments on the Tables

1. Tables 1-5: column label = $\log_{10}x$. Tables 8-10: row label = $\log_{10}x$. In an entry, the letter E signifies that the following number is the exponent of 10 if expressed in scientific notation. 0 is an entry less than 1E-11.

2. Table 2: n=2.83, C=.475 for all u.

3. Table 3: n=2.6628, C=12.54 for u from 0 to 7.1118/T; n=2.83, C=97.61 for greater u.

4. Table 4: n=2.6628, C=15.55 from 0 to 8.3320/T, n=2.83, C=118.10 for greater u.

5. Table 5: n=2.2199, C=18.230 from 0 to 1.8044/T; n=2.261, C=22.10 to 1.8672/T; n=2.11, C=37.445 to 2.2744/T; n=2.1785, C=46.716 to 2.5706/T; n=2.328, C=50.444 to 2.8145/T; n=2.5065, C=60.3 to 10.2017/T; n=2.5825, C=141.25 to 11.5399/T; n=2.6865, C=195.01 to 12.0960/T; n=2.6628, C= 261.49 for greater u.

6. Table 6: value is depth in cm melted or vaporized. f=10 cal/cm^2.

7. Table 7: see text

8. Table 8: entries give extreme values of percentage error with corresponding values of T subscripted. Avg includes errors of all comparable values. * --values not comparable.

9. Table 9: Tungsten intervals were approximated by n=2.22, C=20 for 0 to 1.8672/T; n=2.22, C=45 to 2.8145/T; n=2.5065, C= 60.3 to 10.2017/T; n=2.6, C=150 for greater u.

10. Table 10: values for primed elements are calculated via engineering equations. Others are by using Tables 2-5.

11. * 'd values in Table 9 correspond to very small values that differ in % error greatly, but are of the correct order of magnitude; in contrast to those of Table 8 which were not of comparable magnitude. The small-depth method is good for x= 1E-5 and 1E-4 for t less than .1; otherwise the large-depth approximation is acceptable.

Table 1 Surface Dosages

	Be	Fe	Ni	W
.5	3.874E3	3.174E4	3.936E4	6.679E3
1	5.449E2	5.032E3	6.223E3	1.990E3
2	7.663E1	8.777E2	1.039E3	6.563E2
3	2.433E1	3.564E2	4.038E2	3.523E2
5	5.731E0	1.232E2	1.360E2	1.633E2
7	2.212E0	6.085E1	6.721E1	9.448E1
9	1.086E0	3.536E1	3.926E1	6.069E1
12	4.811E-1	1.863E1	2.086E1	3.527E1
15	2.559E-1	1.118E1	1.259E1	2.260E1

Table 2 Be Dose Profiles

	-5	-4	-3	-1	0
.5	6.240E2	3.035E2	8.859E1	1.395E-1	4.967E-5
1	1.305E2	8.054E1	3.703E1	8.321E-1	8.102E-3
2	2.431E1	1.731E1	1.033E1	1.035E0	6.997E-2
3	8.764E0	6.612E0	4.365E0	7.575E-1	1.050E-1
5	2.359E0	1.881E0	1.361E0	3.810E-1	9.800E-2
7	9.792E-1	8.047E-1	6.096E-1	2.138E-1	7.304E-2
9	5.086E-1	4.235E-1	3.298E-1	1.323E-1	5.335E-2
12	2.382E-1	2.007E-1	1.611E-1	7.342E-2	3.448E-2
15	1.306E-1	1.120E-1	9.170E-2	4.539E-2	2.347E-2

Table 3 Fe Dose Profiles

	-5	-4	-3	-1	0
.5	1.900E3	2.426E2	3.829E0	0	0
1	8.165E2	2.436E2	2.076E1	1.000E-10	0
2	3.077E2	1.720E2	3.301E1	1.316E-5	0
3	1.817E2	1.250E2	3.366E1	8.411E-4	2.900E-9
5	8.413E1	6.641E1	2.513E1	2.201E-2	4.420E-6
7	4.632E1	3.853E1	1.749E1	7.856E-2	1.108E-4
9	2.844E1	2.434E1	1.237E1	1.440E-1	6.522E-4
12	1.568E1	1.377E1	7.779E0	2.167E-1	2.910E-3
15	9.658E0	8.616E0	5.212E0	2.500E-1	6.706E-3

Table 4 Ni Dose Profiles

	-5	-4	-3	-1	0
.5	1.961E3	1.920E2	1.961E0	0	0
1	8.683E2	2.244E2	1.545E1	0	0
2	3.101E2	1.562E2	2.866E1	2.723E-6	0
3	1.802E2	1.171E2	3.044E1	2.785E-4	3.000E-10
5	8.598E1	6.631E1	2.452E1	1.112E-2	1.044E-6
7	4.863E1	3.992E1	1.777E1	4.856E-2	3.792E-5
9	3.042E1	2.581E1	1.289E1	1.004E-1	2.789E-4
12	1.708E1	1.491E1	8.312E0	1.688E-1	1.532E-3
15	1.065E1	9.460E0	5.660E0	2.092E-1	4.032E-3

Table 5 W Dose Profiles

	-5	-4	-3	-1	0
.5	1.281E3	4.835E1	3.502E-3	0	0
1	9.240E2	1.050E2	5.056E-1	0	0
2	4.473E2	1.302E2	3.567E0	0	0
3	2.748E2	1.191E2	6.648E0	3.07E-8	0
5	1.418E2	8.370E1	1.082E1	3.034E-5	0
7	8.543E1	5.706E1	1.150E1	6.323E-4	2.300E-9
9	5.601E1	4.003E1	1.055E1	3.374E-3	1.071E-7
12	3.311E1	2.513E1	8.505E0	1.387E-2	3.397E-6
15	2.142E1	1.688E1	6.693E0	3.057E-2	2.782E-5

Table 6 Front-Face Mass Removal

	H_v	H_m	.5	1	2	3	5	7	9	12	15	T_o
Be	--	412	5E-3	1E-3	0	0	0	0	0	0	0	1100
Be	9422	--	0	0	0	0	0	0	0	0	0	1100
Fe	--	108	5E-4	1E-3	1E-3	1E-3	1E-3	1E-3	1E-3	5E-4	0	1100
Fe	1906	--	1E-4	1E-4	1E-4	1E-4	0	0	0	0	0	1100
W	--	113	5E-5	5E-4	1E-3	1E-3	1E-3	1E-3	1E-3	1E-3	5E-4	1650
W	1289	--	5E-5	5E-5	1E-5	1E-5	0	0	0	0	0	1650

Table 7 Small-Depth Parameters

	K	a	n
Be	814.25	.06007	2.83
Fe	16402.	.1266	2.6628
Ni	20901.	.1266	2.6628
W	26392.	.3514	2.2199

Table 8 % Error--Engineering Design Equations

	Be	Fe	Ni	W
-5	1_2-$131_{.5}$	8_3-$80_{.5}$	$.8_3$-$83_{.5}$	*
-4	7_3-$169_{.5}$	5_3-$90_{.5}$	10_3-$93_{.5}$	*
-3	8_7-135_1	5_{15}-99_2	10_{15}-99_2	*
-1	22_{15}-114_5	*	*	*
0	23_7-104_{12}	*	*	*
Avg	59	34	39	100

Table 9 % Error--Small,Large-Depth Approximations

	Be	Fe	Ni	W
-5	$.05_{15}$-$17_{.5}$	$.2_7$-19_1	$.1_9$-24_2	3_{15}-26_1
-4	$.1_{15}$-17_1	2_2-14_1	1_5-27_3	3_3-42_7
-3	1_{15}-17_2	$.1_1$-17_{15}	3_1-17_{15}	$3_{.5}$-44_2
-1	$5_{.5}$-17_{12}	3_2-10_{15}	3_2-10_{15}	*
0	$3_{.5}$-16_{15}	3_5-6_{15}	3_5-6_{15}	*
Avg	8.5	7	8	19

Table 10 Optimum T

	Be	Be'	Fe	Fe'	Ni	Ni'	W	W'
-5	.5	.05	.5	.4	.5	.4	.5	1.2
-4	.5	.1	1	.9	1	1	2	3
-3	.5	.2	3	2.3	3	2.6	7	7.7
-1	2	1.1	15	5.9	15	16	15	49
0	3	2.5	15	37	15	41	15	123

SURFACE DOSAGE PROGRAM DESCRIPTION

This program is designed to calculate the dosage on the surface of metal for nine blackbody temperatures from one-half to fifteen kev. It is to be used with a corresponding data card for the particular metal of interest.

The dosage integral is calculated between zero and thirty. The total integral is broken up into intervals determined by absorption edges. The first interval from zero to one or to the first absorption edge is calculated using an expansion in Bernoulli numbers. The remaining numbers are calculated by twenty point Gaussian quadrature, the weights and abscissas each having ten significant figures.

All the required information for a given metal will be stored on the same magnetic data card used for the dose profile program. The only operation required to run the program is to read in the program and data for the metal to be studied. No additional keyboard input is needed. The printed output will be the surface dosage for each of the nine blackbody temperatures. Running time is approximately two minutes for each interval.

The operations performed by the Surface Dosage program are as follows:

1. Program begins by initiating all indirect counter registers at their starting locations. (Program location 0-29)

2. All arithmetic calculation of variables for a specific interval are calculated. (30-88)

3. First interval is calculated using an expansion in Bernoulli numbers. (89-162)

4. Remaining intervals are calculated by twenty point Gaussian quadrature. (163-253)

5. Value for each interval is multiplied by 15 C τ^n/π^4. A check is made if all intervals have been calculated. (284-298)

6. The values of all intervals for a single T (blackbody temperature) are summed and printed. A check is then made if the surface dosage has been computed for all T. (299-319)

USER INSTRUCTIONS

SURFACE DOSAGE PROGRAM

STEP	PROCEDURE	ENTER	PRESS	DISPLAY
1	Set partition at 319.79	8	2nd op 17	 319.79
2	Read program into Bank #1		CLR	1
3	Read program into Bank #2		CLR	2
4	Read Gaussian numbers x, w into Bank #4		CLR	4
5	Read in Data in Bank #3		CLR	3
6	Begin Program		RST R/S	

To calculate for new metal, repeat steps 5 and 6.

TITLE Surface Dosage PAGE 1 OF 2

PROGRAMMER Dennis Coalson DATE

TI Programmable **Coding Form**

LOC	CODE	KEY	COMMENTS
	07	7	
	02	2	
	42	STO	
	63	63	
	06	6	
	04	4	
	42	STO	
	77	77	
	00	0	
	42	STO	
1	24	24	
1	03	3	
1	00	0	
1	42	STO	
1	73	73	
1	03	3	
1	01	1	
1	42	STO	
1	74	74	
1	04	4	
2	00	0	
2	42	STO	
2	75	75	
2	05	5	
2	00	0	
2	42	STO	
2	76	76	
2	01	1	
2	42	STO	
2	78	78	
3	76	Lbl	
3	16	A'	
3	00	0	
3	42	STO	
3	20	20	
3	01	1	
3	00	0	
3	42	STO	
3	21	21	
3	73	RC*	
4	74	74	
4	42	STO	
4	25	25	
4	42	STO	
4	26	26	
4	73	RC*	
4	73	73	
4	44	SUM	
4	26	26	
4	94	+/-	
5	44	SUM	
5	25	25	
5	43	RCL	
5	27	27	
5	55	÷	

LOC	CODE	KEY	COMMENTS
5	73	RC*	
5	77	77	
5	95	=	
5	42	STO	
5	62	62	
6	45	Y^x	
6	73	RC*	
6	75	75	
6	65	X	
6	43	RCL	
6	49	49	
6	65	X	
6	43	RCL	
6	61	61	
6	65	X	
7	73	RC*	
7	76	Lbl	
7	95	=	
7	42	STO	
7	28	28	
7	03	3	
7	75	-	
7	73	RC*	
7	75	75	
7	95	=	
8	42	STO	
8	60	60	
8	01	1	
8	32	x⇄t	
8	43	RCL	
8	78	78	
8	22	INV	
8	67	x=t	
8	12	B	
8	73	RC*	
9	74	74	
9	45	Y^x	
9	43	RCL	
9	60	60	
9	65	X	
9	53	(	
9	43	RCL	
9	60	60	
9	35	1/x	
9	75	-	
10	73	RC*	
10	74	74	
10	65	X	
10	02	2	
10	35	1/x	
10	55	÷	
10	53	(	
10	43	RCL	
10	60	60	
10	85	+	

LOC	CODE	KEY	COMMENTS
11	01	1	
11	54	)	
11	85	+	
11	73	RC*	
11	74	74	
11	33	x^2	
11	65	X	
11	01	1	
11	02	2	
11	35	1/x	
12	55	÷	
12	53	(	
12	43	RCL	
12	60	60	
12	85	+	
12	02	2	
12	54	)	
12	75	-	
12	73	RC*	
12	74	74	
13	45	Y^x	
13	04	4	
13	65	X	
13	07	7	
13	02	2	
13	00	0	
13	35	1/x	
13	55	÷	
13	53	(	
13	43	RCL	
14	60	60	
14	85	+	
14	04	4	
14	54	)	
144	85	+	
14	73	RC*	
14	74	74	
14	45	Y^x	
14	06	6	
14	65	X	
15	43	RCL	
15	79	79	
15	35	1/x	
15	55	÷	
15	53	(	
15	43	RCL	
15	60	60	
15	85	+	
15	06	6	
15	95	=	

MERGED CODES

62 [Pgm] [A] 72 [STO] [E'] 83 [GTO] [A']
63 [D'] [E] 73 [RCL] [E'] 84 [B'] [E']
64 [Pgm] [E'] 74 [SUM] [E] 92 [INV] [SBR]

TEXAS INSTRUMENTS INCORPORATED

TITLE Surface Dosage PAGE 2 OF 2

PROGRAMMER Dennis Coalson DATE

TI Programmable **Coding Form**

LOC	CODE	KEY	COMMENTS
16	42	STO	
16	22	22	
16	14	D	
16	76	Lbl	
16	12	B	
16	53	(	
16	73	RC*	
16	20	20	
16	65	X	
16	43	RCL	
17	25	25	
17	85	+	
17	43	RCL	
17	26	26	
17	54	(	
17	55	÷	
17	02	2	
17	95	=	
17	42	STO	
17	29	29	
18	53	(	
18	24	CE	
18	45	Y^x	
18	43	RCL	
18	60	60	
18	65	X	
18	53	(	
18	43	RCL	
18	28	28	
18	94	+/-	
19	55	÷	
19	43	RCL	
19	29	29	
19	45	Y^x	
19	73	RC*	
19	75	75	
19	54	)	
19	22	INV	
19	23	lnx	
19	55	÷	
20	53	(	
20	43	RCL	
20	29	29	
20	22	INV	
20	23	lnx	
20	75	-	
20	01	1	
20	95	=	
20	65	X	
20	43	RCL	
21	25	25	
21	55	÷	
21	02	2	
21	95	=	
21	87	Iff	

LOC	CODE	KEY	COMMENTS
21	01	1	
21	18	C'	
21	42	STO	
21	23	23	
21	73	RC*	
22	20	20	
22	94	+/-	
22	72	ST*	
22	20	20	
22	87	Stf	
22	01	1	
22	12	B	
22	76	Lbl	
22	18	C'	
22	44	SUM	
23	23	23	
23	43	RCL	
23	23	23	
23	65	X	
23	73	RC*	
23	21	21	
23	95	=	
23	44	SUM	
23	22	22	
23	22	INV	
24	86	Stf	
24	01	1	
24	09	9	
24	32	x t	
24	43	RCL	
24	20	20	
24	67	x=t	
24	14	D	
24	01	1	
24	44	SUM	
25	20	20	
25	44	SUM	
25	21	21	
25	12	B	
25	76	Lbl	
25	14	D	
25	43	RCL	
25	22	22	
25	65	X	
25	01	1	
26	05	5	
26	65	X	
26	73	RC*	
26	76	76	
26	65	X	
26	43	RCL	
26	62	62	
26	45	Y^x	
26	73	RC*	
26	75	75	

LOC	CODE	KEY	COMMENTS
27	55	÷	
27	89	π	
27	45	Y^x	
27	04	4	
27	95	=	
27	44	SUM	
27	24	24	
27	00	0	
27	42	STO	
27	22	22	
28	43	RCL	
28	59	59	
28	32	x t	
28	43	RCL	
28	78	78	
28	67	x=t	
28	15	E	
28	01	1	
28	44	SUM	
28	73	73	
29	44	SUM	
29	74	74	
29	44	SUM	
29	75	75	
29	44	SUM	
29	76	76	
29	44	SUM	
29	78	78	
29	16	A'	
29	76	Lbl	
30	15	E	
30	43	RCL	
30	24	24	
30	99	PRT	
30	43	RCL	
30	77	77	
30	32	x≥t	
30	43	RCL	
30	63	63	
30	67	x=t	
31	10	E'	
31	01	1	
31	44	SUM	
31	77	77	
31	61	GTO	
31	00	00	
31	08	8	
31	16	Lbl	
31	10	E'	
31	91	R/S	

MERGED CODES

62 [VA] [→]	72 [STO] [→]	83 [GTO] [→]
63 [LN] [→]	73 [RCL] [→]	84 [↑] [↓]
64 [SIN] [→]	74 [SUM] [→]	92 [INV] [SBR]

TEXAS INSTRUMENTS INCORPORATED

PROGRAM DESCRIPTION

The following Dose Profile program is designed to calculate the dose per fluence at a given depth in cm. for nine blackbody temperatures from one-half to fifteen kev. It is to be used with a corresponding data card for the particular metal of interest.

The dosage integral is calculated between zero and thirty, thirty being a good approximation of infinity for all practical purposes. The integral is broken up into intervals determined by the absorption edges of the metal. Each of the integrals is calculated by twenty point Gaussian quadrature, the weights and absciassas each having ten significant figures.

All the required information for a given metal, such as absorption edges, constants and density, will be stored on a magnetic data card. The only input needed to run the program is the depth of metal at which the dose of radiant energy is to be calculated. The printed output will be the dose per fluence for each of the nine blackbody temperatures at the prescribed depth. The running time is approximately two minutes for each interval.

In summary the operations carried out by the program in the order in which they are performed are as follows:

1. The program begins by initiating all individual counter registers at their starting positions. (Locations 0 - 34)

2. All the arithmetic calculations of variables for a given interval are calculated. (35-84)

3. The calculation of dosage for a specific interval proceeds by -

    a. Calculating the value of the boundary terms. (85-138)

    b. Calculating the value of the integral using twenty point Gaussian quadrature. (139-228)

4. The total value for a particular interval is computed and multiplied by the necessary constants (i.e. $15/\pi^4 \times n$). A check is then made if all intervals have been computed. (257-298)

5. The sum of all the intervals for a given T (blackbody temperature) is printed. A check is then made if total values for all Ts have been calculated.

USER INSTRUCTIONS

DOSE PROFILE PROGRAM

STEP	PROCEDURE	ENTER	PRESS	DISPLAY
1	Set partition at 319.79	8	2nd op 17	 319.79
2	Read program into Bank #1		CLR	1
3	Read program into Bank #2		CLR	2
4	Read Gaussian numbers x_i, w_i into Bank #4		CLR	4
5	Read Data into Bank #3		CLR	3
6	Store x (depth in cm. other than zero) in Register 61	X	STO 61	X
7	Begin Program		RST R/S	

To calculate for second depth, repeat steps 6 and 7 for new depth.

To calculate for new metal, repeat steps 4, 5, and 6.

TITLE Dose Profile PAGE 1 OF 2

PROGRAMMER Dennis Coalson DATE

TI Programmable **Coding Form**

LOC	CODE	KEY	COMMENTS
	07	7	
	02	2	
	42	STO	
	63	63	
	06	6	
	04	4	
	42	STO	
	77	77	
	01	1	
	42	STO	
1	78	78	
1	03	3	
1	01	1	
1	42	STO	
1	74	74	
1	04	4	
1	00	0	
1	42	STO	
1	75	75	
1	05	5	
2	00	0	
2	42	STO	
2	76	76	
2	03	3	
2	00	0	
2	42	STO	
2	73	73	
2	00	0	
2	42	STO	
2	22	22	
3	42	STO	
3	24	24	
3	76	Lbl	
3	16	A'	
3	09	9	
3	32	x≷t	
3	73	RC*	
3	00	0	
3	42	STO	
3	22	22	
4	42	STO	
4	26	26	
4	73	RC*	
4	73	73	
4	44	SUM	
4	26	26	
4	94	+/-	
4	44	SUM	
4	25	25	
4	43	RCL	
5	27	27	
5	55	÷	
5	73	RC*	
5	77	77	
5	95	=	

LOC	CODE	KEY	COMMENTS
5	45	Y^x	
5	73	RC*	
5	75	75	
5	65	X	
5	43	RCL	
6	49	49	
6	65	X	
6	43	RCL	
6	61	61	
6	65	X	
6	73	RC*	
6	76	76	
6	95	=	
6	42	STO	
6	28	28	
7	76	Lbl	
7	12	B	
7	00	0	
7	42	STO	
7	20	20	
7	01	1	
7	00	0	
7	42	STO	
7	21	21	
7	73	RC*	
8	74	74	
8	42	STO	
8	29	29	
8	76	Lbl	
8	17	B'	
8	53	(	
8	43	RCL	
8	29	29	
8	45	Y^x	
8	04	4	
9	55	÷	
9	53	(	
9	43	RCL	
9	29	29	
9	22	INV	
9	23	lnx	
9	75	-	
9	01	1	
9	54	)	
9	65	X	
10	53	(	
10	53	(	
10	43	RCL	
10	29	29	
10	45	Y^x	
10	73	RC*	
10	75	75	
10	54	)	
10	35	1/x	
10	65	X	

LOC	CODE	KEY	COMMENTS
11	43	RCL	
11	28	28	
11	94	+/-	
11	54	)	
11	22	INV	
11	23	lnx	
11	54	)	
11	87	Iff	
11	03	3	
11	13	C	
12	42	STO	
12	23	23	
12	73	RC*	
12	73	73	
12	42	STO	
12	29	29	
12	86	Stf	
12	03	3	
12	17	B'	
12	76	Lbl	
13	13	C	
13	94	+/-	
13	42	STO	
13	23	23	
13	22	INV	
13	86	Stf	
13	03	3	
13	76	Lbl	
13	18	C'	
13	53	(	
14	73	RC*	
14	20	20	
14	65	X	
14	43	RCL	
14	25	25	
14	85	+	
14	43	RCL	
14	26	26	
14	54	)	
14	55	÷	
15	02	2	
15	95	=	
15	42	STO	
15	29	29	
15	53	(	
15	53	(	
15	43	RCL	
15	28	28	
15	94	+/-	
15	55	÷	

MERGED CODES

62 Pgm	72 STO	83 GTO
63 Lbl	73 RCL	84
64 Ind	74 SUM	92 INV SBR

TEXAS INSTRUMENTS INCORPORATED

TITLE Dose Profile PAGE 2 OF 2

PROGRAMMER Dennis Coalson DATE

TI Programmable **Coding Form**

LOC	CODE	KEY	COMMENTS
16	43	RCL	
16	29	29	
16	45	Y^x	
16	73	RC*	
16	75	75	
16	54	)	
16	22	INV	
16	23	lnx	
16	65	X	
16	53	(	
17	04	4	
17	65	X	
17	43	RCL	
17	29	29	
17	45	Y^x	
17	03	3	
17	65	X	
17	53	(	
17	43	RCL	
17	29	29	
18	22	INV	
18	23	lnx	
18	75	-	
18	01	1	
184	54	)	
18	75	-	
18	43	RCL	
18	29	29	
18	45	Y^x	
18	04	4	
19	65	X	
19	43	RCL	
19	29	29	
19	22	INV	
19	23	lnx	
19	54	)	
19	55	÷	
19	53	(	
19	43	RCL	
19	29	29	
20	22	INV	
20	23	lnx	
202	75	-	
20	01	1	
20	54	)	
20	33	x^2	
20	54	)	
20	65	X	
20	43	RCL	
20	25	25	
21	55	÷	
21	02	2	
21	95	=	
21	44	SUM	
21	22	22	

LOC	CODE	KEY	COMMENTS
21	87	Iff	
21	01	1	
21	14	D	
21	73	RC*	
21	20	20	
22	94	+/-	
22	72	ST*	
22	20	20	
22	86	Stf	
22	01	1	
22	18	C'	
22	76	Lbl	
22	14	D	
22	43	RCL	
22	22	22	
23	65	X	
23	73	RC*	
23	21	21	
23	95	=	
23	94	+/-	
23	44	SUM	
23	23	23	
23	00	0	
23	42	STO	
23	22	22	
24	22	INV	
24	86	Stf	
24	01	1	
24	43	RCL	
24	20	20	
24	67	x=t	
24	19	D'	
24	01	1	
24	44	SUM	
24	20	20	
25	44	SUM	
25	21	21	
252	18	C'	
25	76	Lbl	
25	19	D'	
25	43	RCL	
25	23	23	
25	65	X	
25	01	1	
25	05	5	
26	55	÷	
26	53	(	
26	43	RCL	
26	61	61	
26	65	X	
26	43	RCL	
26	49	49	
26	65	X	
26	73	RC*	
26	75	75	

LOC	CODE	KEY	COMMENTS
27	65	X	
27	89	π	
27	45	Y^x	
27	04	4	
27	95	=	
27	44	SUM	
27	24	24	
27	43	RCL	
27	59	59	
27	32	x≠t	
28	43	RCL	
28	78	78	
28	67	x=t	
28	15	E	
28	01	1	
28	44	SUM	
28	73	73	
28	44	SUM	
28	74	74	
28	44	SUM	
29	75	75	
29	44	SUM	
29	76	76	
29	44	SUM	
29	78	78	
29	16	A'	
29	76	Lbl	
29	15	E	
29	43	RCL	
29	24	24	
30	24	CE	
30	99	PRT	
30	43	RCL	
30	77	77	
30	32	x≠t	
30	43	RCL	
30	63	63	
30	67	x=t	
30	10	E'	
30	01	1	
310	44	SUM	
31	77	77	
31	61	GTO	
31	00	0	
31	08	8	
31	76	Lbl	
31	10	E'	
31	91	R/S	

MERGED CODES

62 [INV] [SBR]	72 [STO] [ ]	83 [GTO] [ ]
63 [INV] [GTO]	73 [RCL] [ ]	84 [ ] [ ]
64 [INV] [SUM]	74 [SUM] [ ]	92 [INV] [SBR]

TEXAS INSTRUMENTS INCORPORATED

REGISTERS USED FOR X-RAY DEPOSITION PROGRAMS

BANK #4

REG. #	STORED INFORMATION
00	
↓	Gaussian Abcissas x_i
9	
10	
↓	Gaussian Weights w_i
19	
20	Indirect register for x_i
21	Indirect register for w_i
22	Working Sum
23	Subtotal
24	Total
25	l = b - a
26	s = b + a
27	12.398
28	$t = xC\rho\tau^n$
29	Program used variable

BANK #2

REG. #	STORED INFORMATION
60	B = 3 - n
61	x (depth of metal in cm.)
62	τ = 12.398/T
63	# of T's (blackbody temp)
64	
↓	T's (blackbody temps)
72	
73	Indirect register for a's
74	Indirect register for b's
75	Indirect registers for n's
76	Indirect register for C's
77	Indirect register for T's
78	Counter for # of intervals
79	30240

BANK #3

DATA CARD FOR METAL

REG. #	STORED INFORMATION
30	
↓	Boundary Terms
39	
40	
↓	n's for each interval
48	
49	ρ (density)
50	
↓	C's for each interval
58	
59	Number of intervals

1978 USAF-ASEE SUMMER FACULTY RESEARCH PROGRAM
sponsored by
THE AIR FORCE OFFICE OF SCIENTIFIC RESEARCH
conducted by
AUBURN UNIVERSITY AND OHIO STATE UNIVERSITY

PARTICIPANT'S FINAL REPORT

TARGET MATERIALS FOR LOW ENERGY X-RAY SOURCES

Prepared by:	James C. Lauffenburger, PhD
Academic Rank:	Associate Professor
Department and University	Department of Physics Canisius College Buffalo NY
Assignment: (Air Force Base)	Edwards AFB
(Laboratory)	Rocket Propulsion Lab
(Division)	Propulsion Analysis
(Branch)	Combustion and Plumes
USAF Research Colleague:	David M. Mann, PhD
Date:	August 4, 1978
Contract No:	F44620-75-C-0031

TARGET MATERIALS FOR LOW ENERGY X-RAY SOURCES

J. C. Lauffenburger

ABSTRACT

Quantitative X-ray line source data has been obtained and used to select a suitable target for future X-ray plume analysis. The line source data has been used in a computer study of the proposed plume analysis. Data has also been obtained on the sensitivity of X-ray absorption measurements to elemental density variations.

ACKNOWLEDGEMENT

The author is sincerely grateful to USAF-ASEE for providing this summer research opportunity. THe enthusiasm and excellent administration of this program contributed by Mr. J. Fred O'Brien is greatly appreciated.

I am very grateful for the opportunity to work at the Rocket Propulsion Laboratory. I have been extremely impressed with the abilities of Dr. David Mann, Dr. Jay Eversole and Mr. Thomas Owens. I wish to thank them for all their professional and personal help. I would also like to thank Mr. Allen Kawasaki for much of the computer effort.

LIST OF FIGURES

LIST OF SYMBOLS

μ_i	X-Ray Absorption Coefficient of Element i (cm^2/atom or cm^2/gm)
ρ_i	Concentration of Element i (grams/cm^3 or atoms/cm^3)
L	Absorbing Path Length (cm)
R	Ratio of X-Ray Transmittance Above An Absorption Edge to the Transmittance Below the Absorption Edge
k	Total Absorption Coefficient of All Species Present (cm^{-1})
Δk_{Zr}	Change in Total Absorption Coefficient Across the Zr Absorption Edge
Δk_{Al}	Change in Total Absorption Coefficient Across the Al Absorption Edge
L_{Zr}	Absorbing Path Length for Zr Absorption Measurements
L_{Al}	Absorbing Path Length for Proposed Al Plume Absorption Measurements

1.0 INTRODUCTION

In order to more completely characterize the performance and exhaust plume signature of solid propellant rocket motors, it is necessary to determine the species concentrations, both gaseous and particulate, within the rocket plume. The high concentrations of particulates in a typical metallized propellant plume require that an X-ray spectroscopic technique be used for in situ diagnostics[1]. Two types of measurements are to be made: X-ray absorption and X-ray fluorescence. To accomplish these measurements on typical exhaust species such as Al and Cl, an intense source of X-rays is needed for energies less than 10 keV. Commercially available X-ray sources have generally low fluxes in this energy range. In addition, little information is available on X-ray photon yields as a function of energy.

The purpose of this project was to provide data to allow selection of target materials which will give the greatest sensitivity for the proposed X-ray absorption/fluorescence studies. This involved investigation of both line spectra of possible target materials, and the continuum spectrum of available commercial X-ray tubes.

Figure 1 shows the most significant X-ray absorption cross-sections of the elements present in a solid propellant rocket plume. For maximum absorption by Al or Cl, an X-ray beam which contains high intensities of X-rays at energies slightly higher than the K absorption edges of Al (1.559 keV) and Cl (2.819 keV) is necessary. X-rays are generated by two fundamental processes. Electrons, having kinetic energies of the order of 10^4 eV, impinge upon the surface of a target material. The incident electrons can then interact with the nuclei or the electrons of the target material. When the incident electrons encounter nuclei, the electrons are deflected from their original paths and radiate X-rays of continuously distributed wavelength and

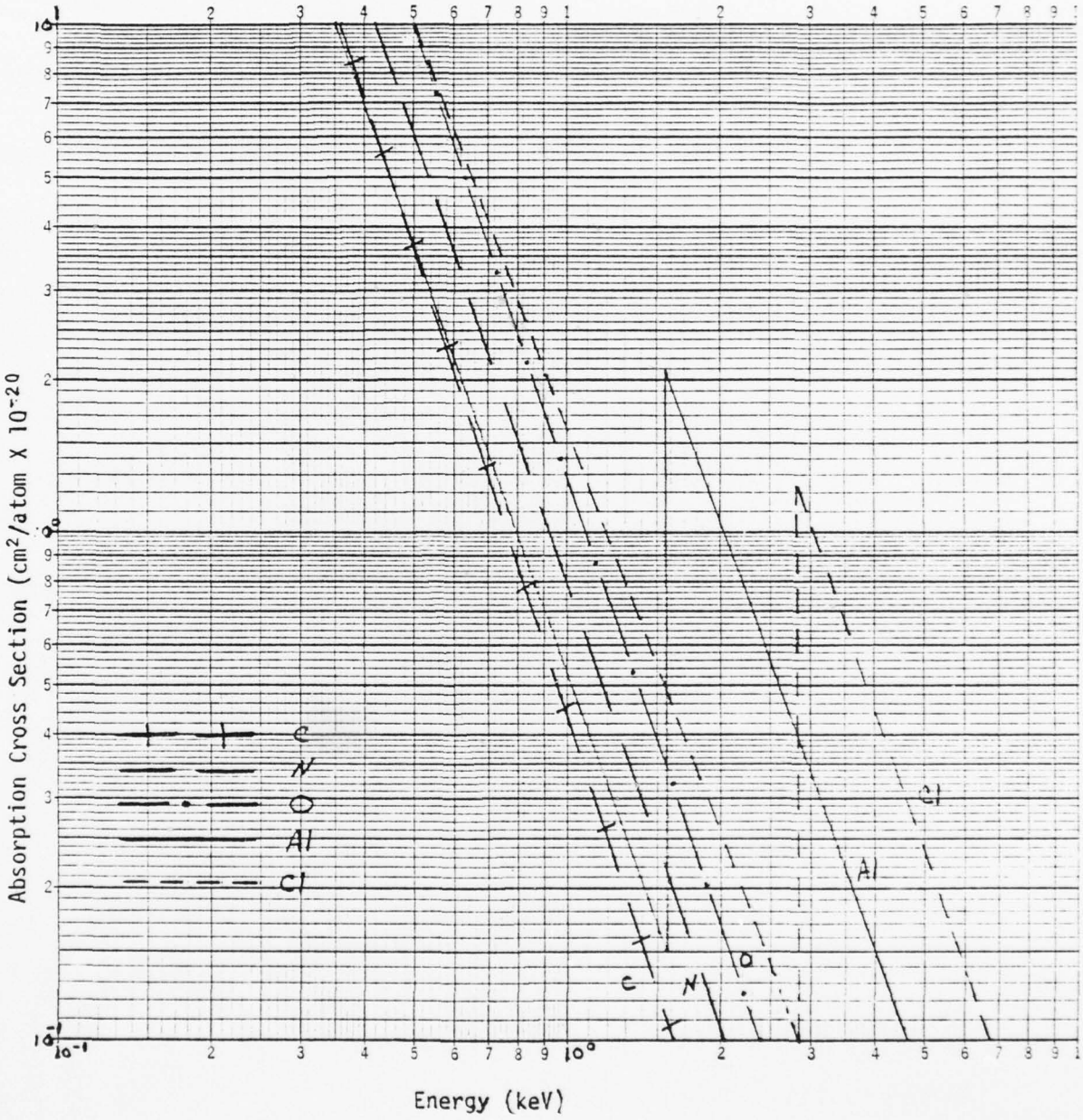

FIGURE 1. Atomic Absorption Cross-Section vs X-Ray Energy for Elements of Interest in Rocket Plumes

energy. These X-rays form the continuum part of a typical X-ray target spectrum and are referred to as Bremsstrahlung radiation. If the incident electrons interact with the inner shell electrons of the target material, the inner shell electrons can be ejected. This has a high probability of occurring when the incident electron energy is greater than the absorption edge energy of the target material. The vacancy in this shell can now be filled by electrons from higher energy levels within the target material. When an electron falls to a lower energy level it radiates an X-ray photon which is characteristic of the shell structure of that element. This last process is the origin of the characteristic X-ray lines of a target spectrum. Figure 2 is an X-ray spectrum of a typical target material. The general shape of the curve is due to the Bremsstrahlung, and the sharp, high intensity regions are the characteristic line spectra.

To obtain the data necessary for an X-ray source to be selected for the plume absorption/fluorescence measurements, a series of experiments on X-ray spectra was conducted. Data on line spectra of candidate materials was obtained using a scanning electron microscope, and continuum spectrum data was obtained using a crystal diffractometer.

2.0 EXPERIMENTAL RESULTS

2.1 LINE SPECTRA

The Si_k emission line (1.74 keV)[2] is appropriate for Al absorption, and the Ag_L emission line (2.98 keV)[2] is appropriate for Cl abosrption. The line intensities of these elements were measured with an X-ray energy spectrometer attached to a scanning electron microscope (SEM). The SEM was used to excite the X-ray spectra of different elements because it provides a small area electron beam with variable energy. This meant that small samples, approximately 5mm X 5mm, could be used and the sample elements could be

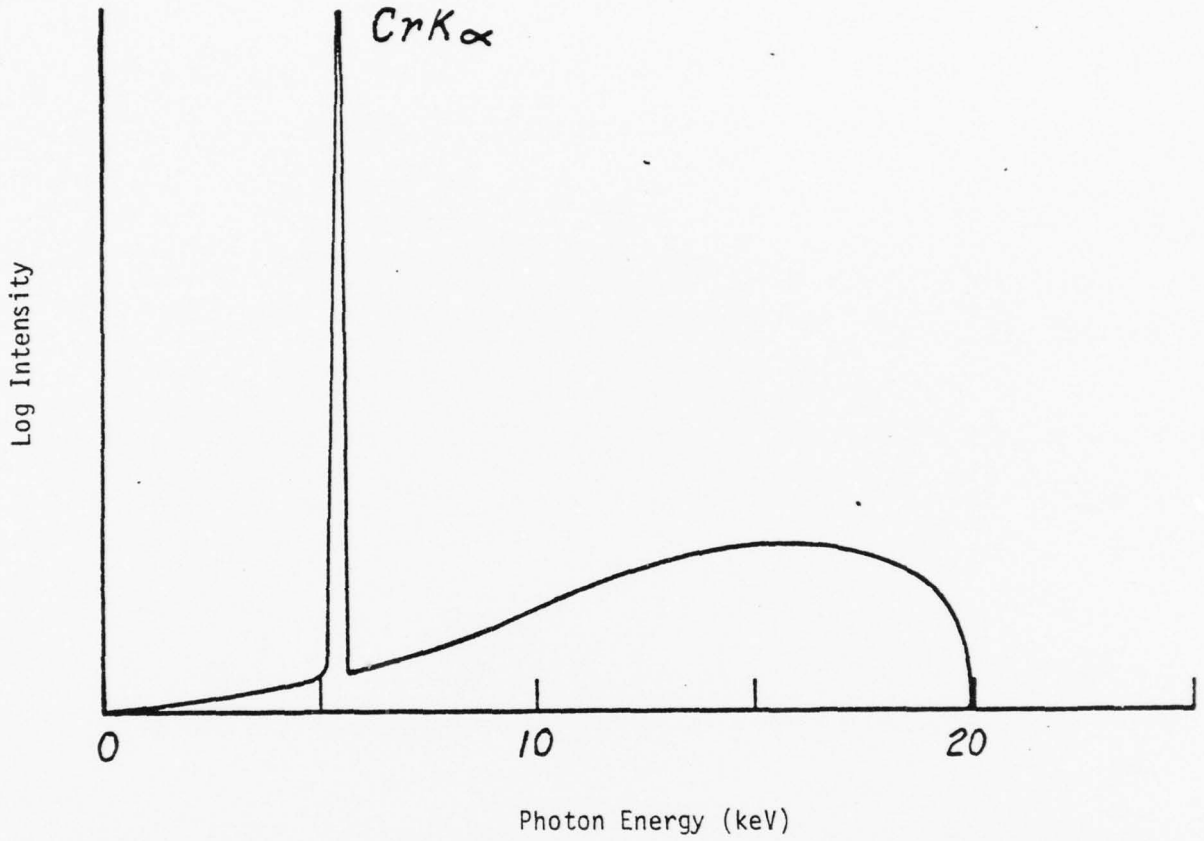

FIGURE 2. Typical X-Ray Emission Spectrum from a Chromium Target with an Accelerating Voltage of 20 kV.

interchanged easily. This provided controlled conditions for all samples investigated. In addition to Si and Ag, the X-ray spectra of other elements were measured to obtain data for another part of the absorption/fluorescence project. The measured line spectra photon counting rates per milliampere of target current per steradian (SCR) are listed in Table 1. The line width is the energy range over which the integrated line count was calculated.

TABLE 1

LINE SPECTRA COUNTING RATES

ELEMENT LINE	SCR ($X10^{11}$ PHOTONS/SEC-mA-STER)	LINE WIDTH (keV)
Si_K	7-12	1.56-1.92
Ag_L	19-26	2.82-3.60
Al_K	10	1.20-1.60
Mo_L	7	2.00-2.60
Cu_K	3	7.80-9.06
Ni_K	3	7.28-8.36
Cr_K	5	5.20-6.04
Rh_L	12	2.56-2.92

Figures 3(a) and (b) are photographs of the energy spectrum analyzer output of the SEM for pure Si and pure Ag targets respectively.

According to McGregor[1], an incident photon intensity of about 10^{11} photons/sec cm^2 in the K_{abs} energy range is necessary for the fluorescence measurements. If the SCR values for Si and Ag of Table 1 are converted to intensities and multiplied by the typical 100mA anode current of a rotating anode X-ray tube, the resulting photon intensities are both greater than 10^{12} photons/sec cm^2. Thus, an X-ray source incorporating Si and Ag as elements in the X-ray target material would have the necessary intensities for the fluorescence measurements.

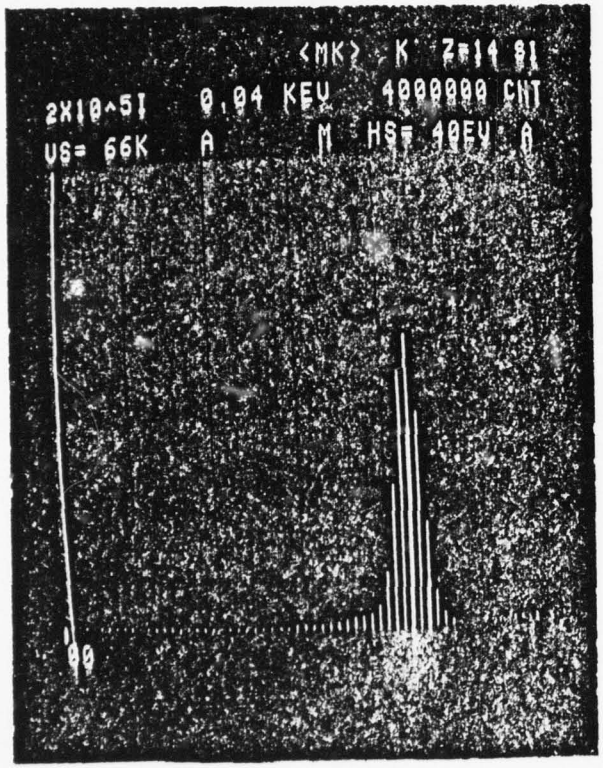

(a)

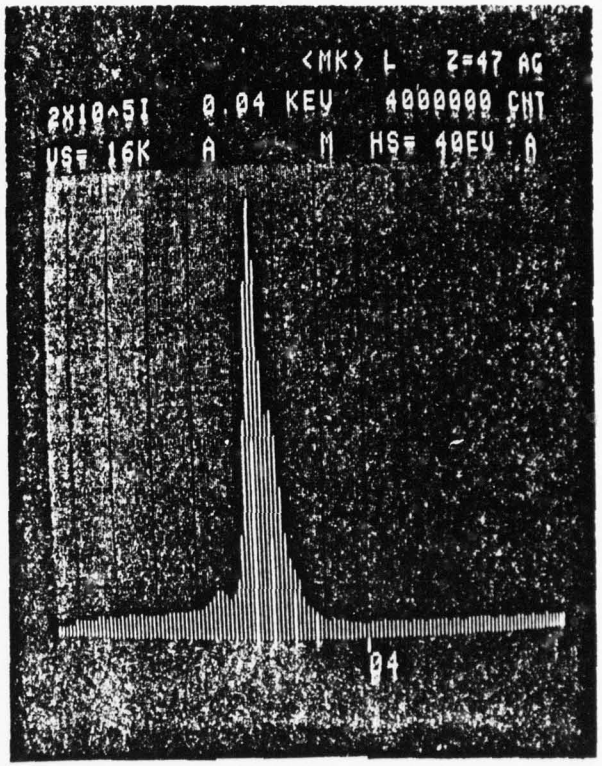

(b)

FIGURE 3. X-Ray Yields vs Energy. a) Silicon Target at 14.5 kV
b) Silver Target of 14.5 kV

In normal use, X-ray tubes are operated at voltages of the order of 40-60 kV. Since the maximum available SEM voltage was 17.5 kV, a series of data for Al, Si, and Ag targets was obtained as a function of SEM voltage. Figure 4 shows this data, and as can be seen, the X-ray line spectra output is a non-linear function of voltage. This implies that even greater photon fluxes could be expected from a target material operated at higher voltages than 17.5 kV. However, the total continuum Bremsstrahlung radiation increases faster than the line radiation flux as the voltage is raised, and at significantly higher voltages ($\geq$25kV) the target will also produce many unwanted, high-energy X-rays. This high energy background radiation will generally degrade the absorption and fluorescence signals. Hence, for a given target, the optimum operating voltage will have to be determined empirically, but most likely will be less than 25 kV. For the purpose of target material selection, data taken at 17.5 kV is considered representative.

Data such as is shown in Figure 3, is being used in a computer model of the plume measurements. Figure 5 is a plot of the X-ray spectrum of a hypothetical target of Al and Si. This spectrum was synthesized from the individual Al and Si spectra measured on the SEM. The computer program uses this composite spectrum as an input X-ray beam and propagates it through an absorbing medium to simulate the absorption measurement through a rocket plume. The program accounts for both scattering and fluorescence, and predicts the attenuated output spectrum. Figure 6 shows the corresponding output spectrum after passing thru a 12 cm length of an absorbing medium of air and Al particles. (For the purpose of this illustration "air" is regarded as a single species and a weighted average of O_2 and N_2 absorption cross-sections is employed.) Two effects take place in the absorption path: a) absorption of both Al_k and Si_k X-rays by the air and Al in the path and b) Al fluorescence after absorption of Si_k radiation. The Si_k radiation is very strongly

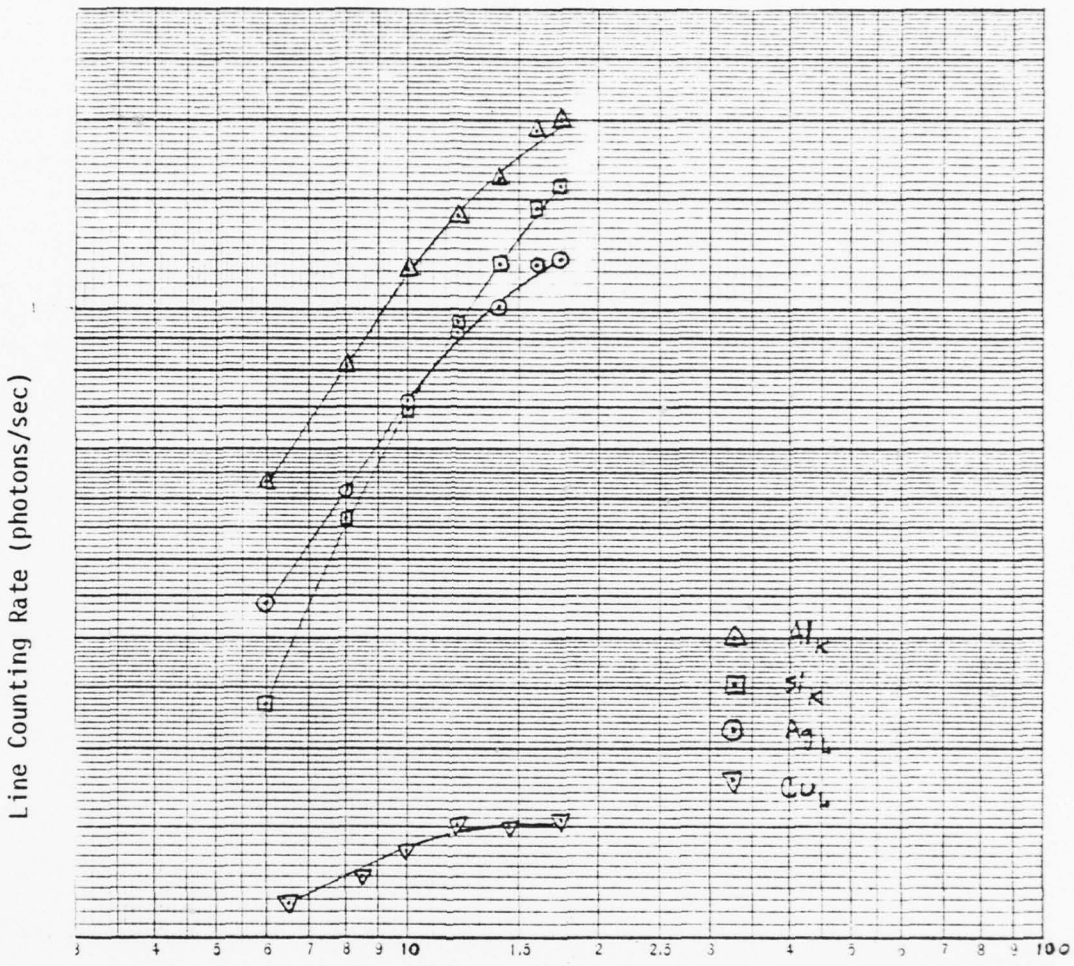

FIGURE 4. X-Ray Yields of Targets vs Scanning Electron Microscope Voltage

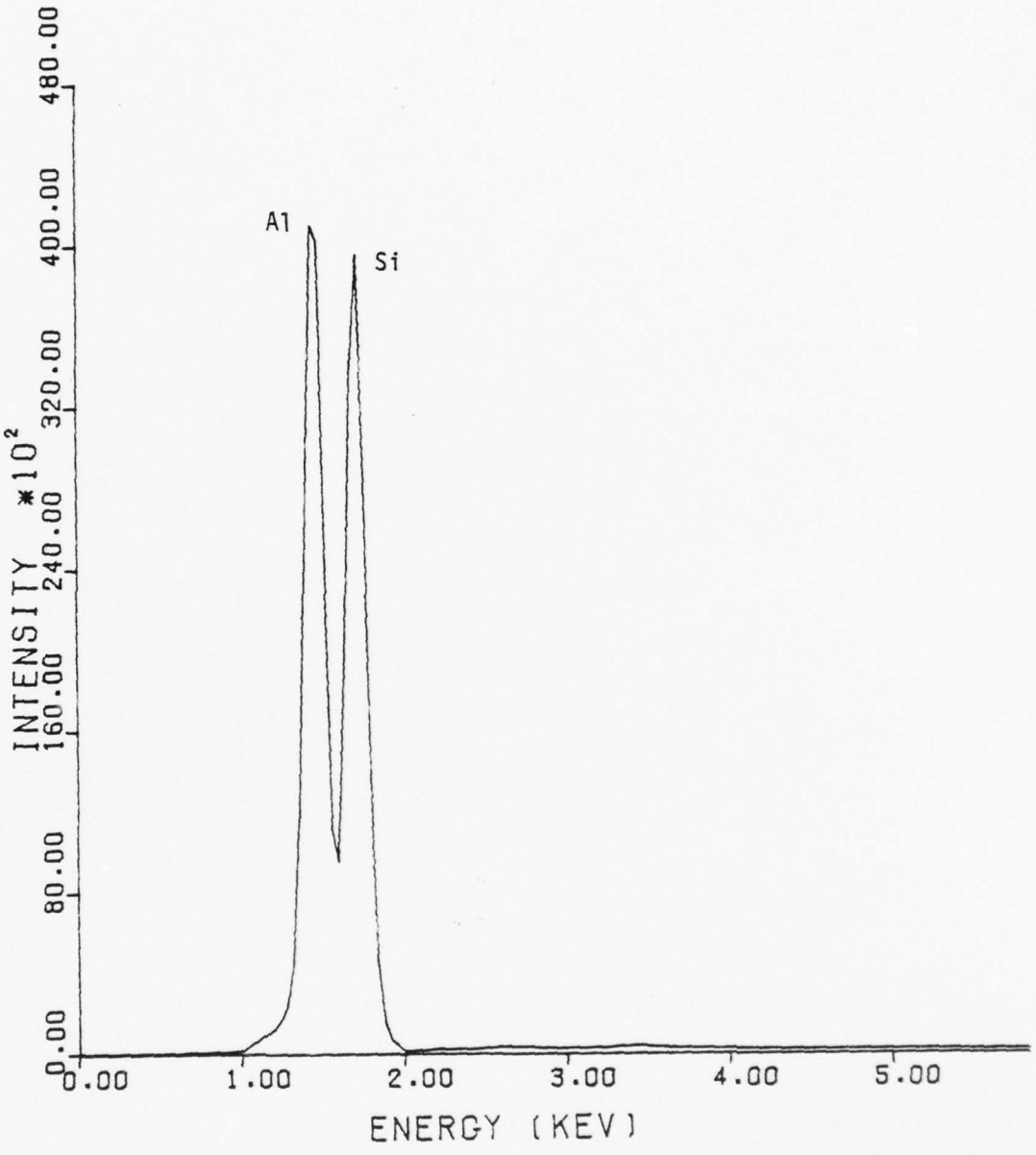

FIGURE 5. X-Ray Spectrum of Candidate Target of Al and Si

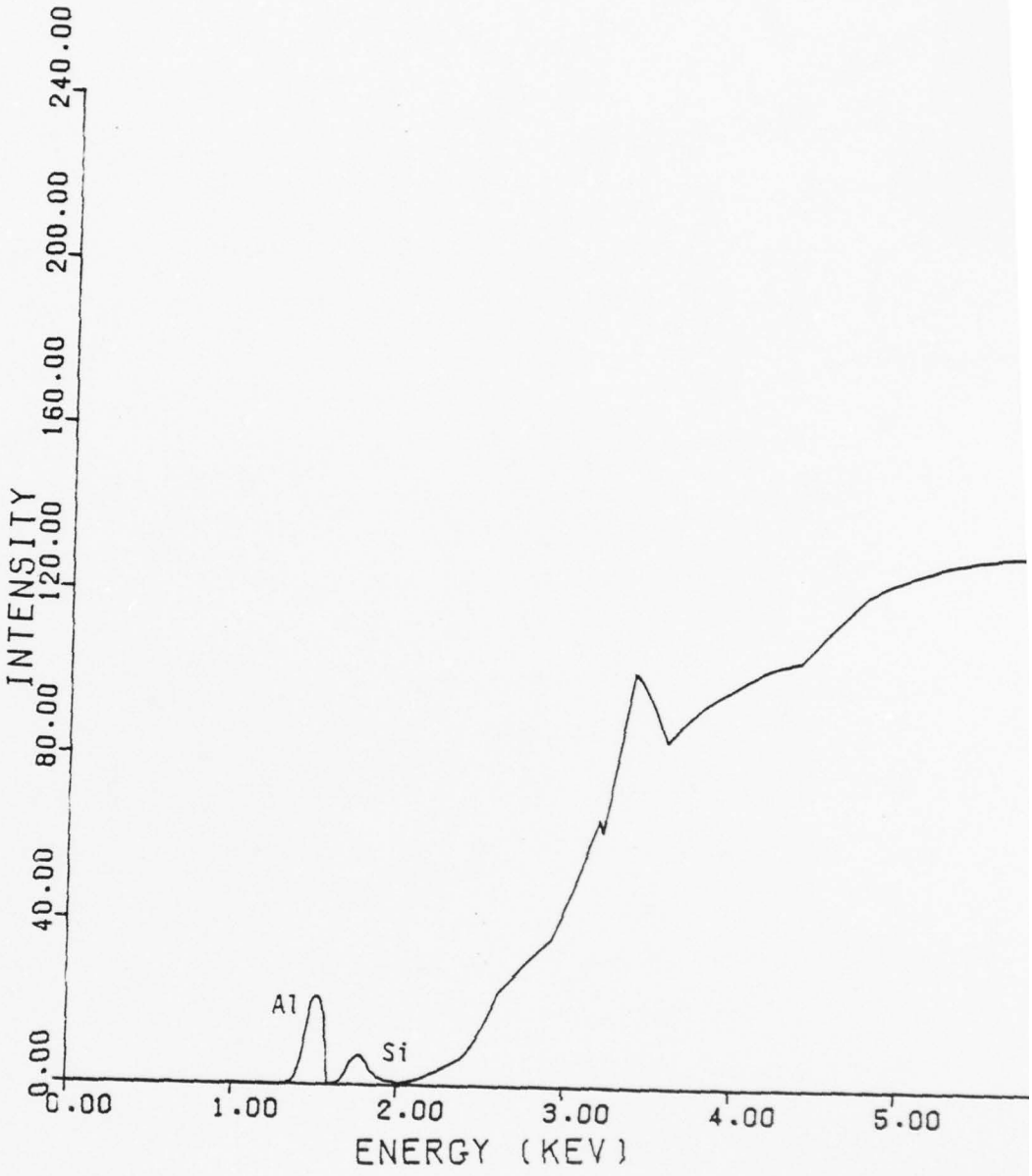

FIGURE 6. X-Ray Output Spectrum from Absorption Program with Al Density of 2 X $10^{18}/cm^3$

absorbed by Al whereas both Si_k and Al_k are absorbed by air. In general, the transmitted intensity of a beam of X-ray of energy E, $I_T(E)$, depends o the incident intensity of the same energy, $I_o(E)$, as [2].

$$I_T(E) = I_o \exp\left(-\left(\sum_i \mu_i \rho_i\right)L\right) \quad (1)$$

Where the index, i, runs over the different absorbing species. If two absorbing species are present, then information about their densities, ρ_i, can be obtained from Eq 1 using the transmitted and incident intensities a two energies.

$$\ln \frac{I_T(Al_k)}{I_o(Al_k)} = -L\left(\mu_{11}\rho_{Al} + \mu_{12}\rho_{air}\right) \quad (2)$$

$$\ln \frac{I_T(Si_k)}{I_o(Si_k)} = -L\left(\mu_{21}\rho_{Al} + \mu_{22}\rho_{air}\right) \quad (3)$$

Eqs. 2 and 3 are a pair of simultaneous equations in the two unknowns ρ_{Al} a ρ_{air}. These can be solved to obtain the individual species densities. Fo the data represented in Figures 5 and 6, the calculated aluminum density i $1.91 \times 10^{18}/cm^3$ and the actual density used by the computer program is $2 \times 10^{18}/cm^3$. If the computer density of aluminum is lowered to $2 \times 10^{17}/$ the output spectrum, using the same input spectrum as Figure 5, is now sho in Figure 7. The aluminum density, calculated from the output spectrum of Figure 7, is now $1.2 \times 10^{17}/cm^3$. Thus, as densities of aluminum of order $10^{17}/cm^3$ are approached, the computer model predicts a 100% measurement error.

In the actual plume experiments, five constituent absorbing species a present and five lines are required to give the incident and transmitted intensities for determining the respective densities. Thus, some target w has five useful energy ranges is necessary. Sensitivity will be best if t

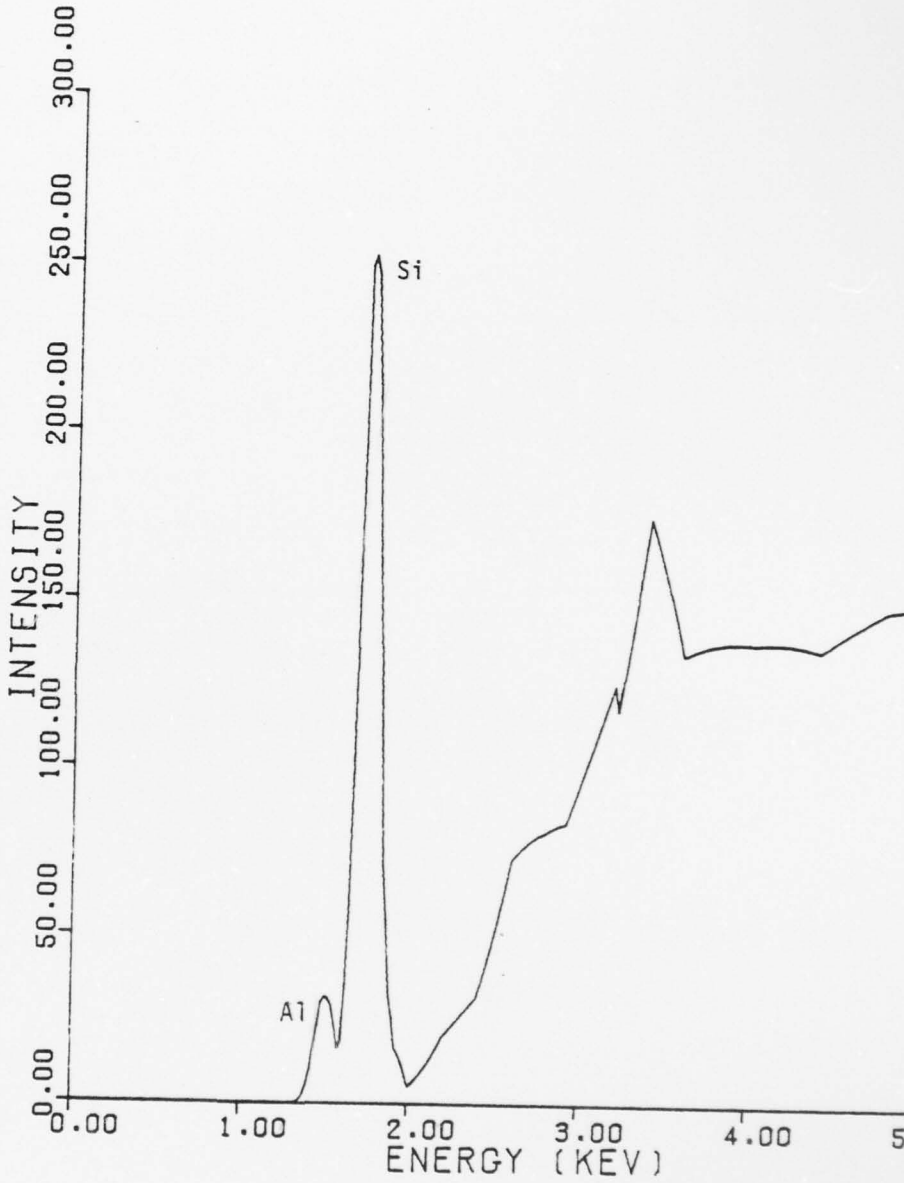

FIGURE 7. X-Ray Output Spectrum from Absorption Program with Al Density of 2 X $10^{17}/cm^3$

lines bracket each of the absorption edges of Al and Cl. For Al detection, the Al_k and Si_k lines can be used effectively. For Cl detection, the Ag_L and Rh_L lines can be used effectively.

The rotating anode lends itself to a multi-element target. This could be most easily accomplished by depositing sections of the pure elements, Al, Si, Rh and Ag on a Cr or Cu commercial anode. A schematic drawing of this type of anode is shown in Figure 8.

2.2 CONTINUUM SOURCE

The alternative possibility is to use a continuum source of X-rays for the plume measurements. In evaluating continuum sources, rather severe limitations were imposed by the available equipment. The SEM was not useful as a continuum source because of its restriction to low voltage. An X-ray crystal diffractometer was the only continuum source available for doing absorption measurements, and it was not ideal since it has a Cu target tube which is considered primarily a line source. However, a significant continuum region was observed between 15 and 25 keV. Observing absorption in Al at 1.6 keV was ruled out because the proportional counter detector system in the diffractometer is only sensitive down to 2-3 keV.

Therefore, an attempt was made to measure absorption in iron (K_{abs} = 5.6 keV). The principle difficulty in this experiment came from the second-order diffraction of the dispersing crystal. The relative intensity of ~13 keV photons to ~5.5 keV photons produced by the X-ray tube was so great that the 2nd-order diffraction of the higher energy radiation completely masked the useful X-rays at 5.5 keV. As a result, no absorption edge in Fe could be observed. Various attempts were made to filter out the higher energy radiation, but even materials which preferentially absorb at short wavelengths still have appreciable absorption at longer wavelengths; at X-ray energies, "bandpass" filters familiar in optics do not exist. A routine method for separating 2nd-order radiation is to use two

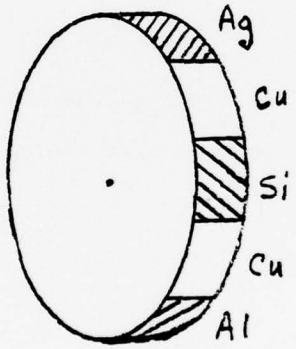

FIGURE 8. Schematic Drawing of Possible Multiple Line Spectrum Anode

crystals in tandem, but here again, the absolute intensity of the low-energy radiation would suffer drastic reduction after two diffractions.

Since the absorption due to Fe could not be observed, it was decided to carry out a measurement on an element whose K absorption edge fell in the main band of the Cu continuum radiation. Zirconium (Zr) has a K absorption edge (18.07 keV) close to the continuum maximum of the copper target source. A series of experiments was run to determine the sensitivity of the transmitted intensity thru a Zr absorber. The concentration of Zr in alcohol was varied to determine the minimum concentration of Zr that was detectable in the presence of the high concentration of oxygen in the alcohol. Figures 9 (a), (b), and (c) show the change in edge absorption as a function of Zr concentration. With an oxygen concentration of 1×10^{22} atoms/cm^3, the minimum detectable Zr concentration is approximately 1×10^{18} atoms/cm^3. The presence of Zr is detected by the ratio of the transmittance above and below the Zr absorption edge. Transmittance (T) is the fraction of incident radiation which is transmitted through an absorbing material. Mathematically,

$$T_A = \frac{I_A}{I_A} \exp(-k_A L) = \exp(-k_A L)$$

Where I is the incident intensity, k is the total absorption coefficient, L is the path length, and the subscript A implies that all values are taken at an energy slightly above the absorption edge. Similarly, for an energy just below the absorption edge,

$$T_B = \exp(-k_B L), \quad \text{and } R = \frac{T_A}{T_B} = \exp((k_B - k_A)L) = \exp(-\Delta k L) \qquad (4)$$

Using the foregoing formulation a comparison can be made between the absorption in Zr and in Al. The quantity $k = \sum_i \mu_i \rho_i$ is the total absorption coefficient and since the concentration of all species is fixed for a given sample,

$$\Delta k = \sum_i (\Delta \mu_i)\rho_i \qquad (5)$$

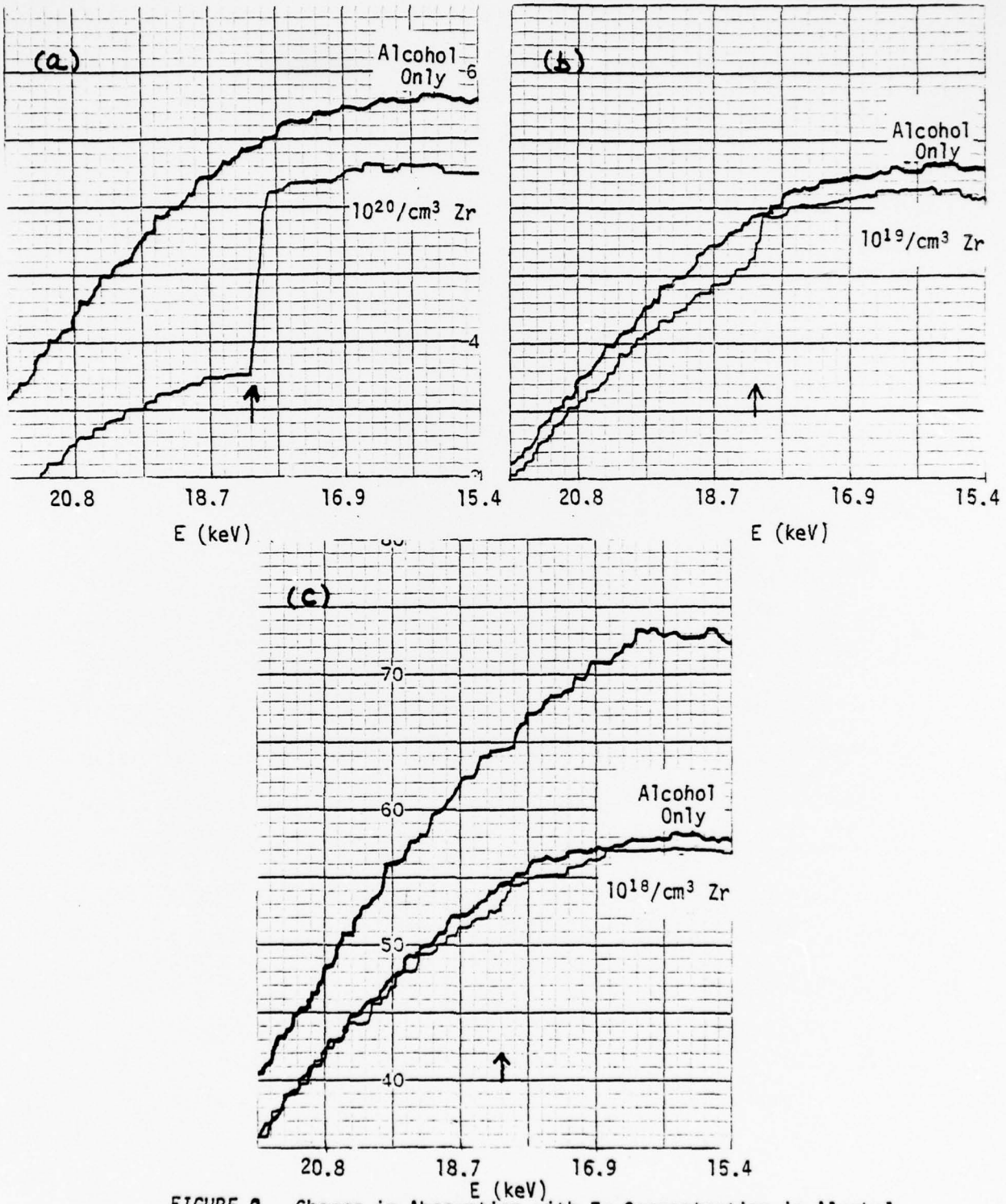

FIGURE 9. Change in Absorption with Zr Concentration in Alcohol. (a) 10^{20} atoms/cc, (b) 10^{19} atoms/cc, (c) 10^{18} atoms/cc. In (c) the upper curve is the unattenuated signal. The arrow indicates the position of the Zr Absorption Edge. [Cu Anode, 35 kV, 20 mA].

where the delta refers to the difference in the absorption coefficients above and below the band edge of the element of interest. If the densities of all species present in a given absorption measurement are comparable in magnitude, only the element being measured will make any significant contribution to Δk. However, as the concentration of the measured species is lowered (other species concentrations remaining constant) the product, $\Delta\mu\rho$, of the measured species, becomes comparable to those of the other species. Therefore, the relative concentration of other absorbing species is more important than the absolute concentration of the measured species.

In Eq. (4), as the product of $\Delta kL \to 0$, we have

$$R \simeq 1 - \Delta kL \tag{6}$$

The basic criterion for detection then becomes:

$$\Delta kL \gtrsim SNR \tag{7}$$

where SNR is the signal to noise ratio for the particular measurement. A discussion of the noise sources and the restrictions placed on optimizing the SNR will be deferred to a later technical report. In this absorption study, Zr in alcohol, the measured SNR was 1% and this was close to the optimal value for the apparatus used. Furthermore, it is reasonable to expect this value to be comparable to or better than that which would be achieved in the plume measurement. Therefore, for comparison of Zr and Al absorption measurements, it is sufficient to set:

$$\Delta k_{Zr} L_{Zr} = \Delta k_{Al} L_{Al}$$

Using the appropriate numbers for Zr in alcohol and Al in the plume[1], it appears that the minimum detectable density of Al would be $\sim 1 \times 10^{17}$ atoms/cm^3 in the plume. Typical aluminized propellants will produce average densities of $\sim 1 \times 10^{18}$ atoms/cm^3, so that a determination of the variation of the Al density in the plume cross-section would be accurate to ~10%. Although the

measurement was made using a continuum source, the foregoing method of analysis is valid for line sources as well.

3.0 CONCLUSIONS

Although the evaluation program for selecting an X-ray source target is not yet completed, most of the necessary data has been obtained. At this point, several specific conclusions can be made and a preliminary recommendation for target construction can be given.

The following conclusions can be drawn from this study:

1. The quantitative X-ray line spectra obtained in this study have all had sufficient intensities, when appropriately scaled, to make the plume fluorescence measurements feasible.

2. The most practical set of elements giving rise to appropriate line spectra include: Al, Si, Ag, and Rh. The low-energy spectra of these elements is depicted schematically in Figure 10.

3. If a line-source target is used, it should be fabricated from a standard Cu or Cr target by plating or evaporating thin films of the elements mentioned above onto separate regions of the target surface. This avoids the difficulties involved with forming alloys, and gives the added option of arranging time sequences of emission of different lines by the geometrical arrangement of the elemental films on the target surface (as in Figure 8).

4. The minimum detectable concentration of Zr dissolved in alcohol was determined using a crystal diffractometer. The critical density of Zr atoms was ~1.0 X $10^{18}/cm^3$, which can be extrapolated to indicate that Al concentrations as low as 1 X 10^{17} atoms/cm^3 could be detected. This is a factor of ~10 times lower than typical Al densities present in rocket plumes.

5. If a continuum source is employed, a relatively large number of photons will be generated at energies greater than the range of interest (>10 keV). These photons have a high potential for creating spurious signals

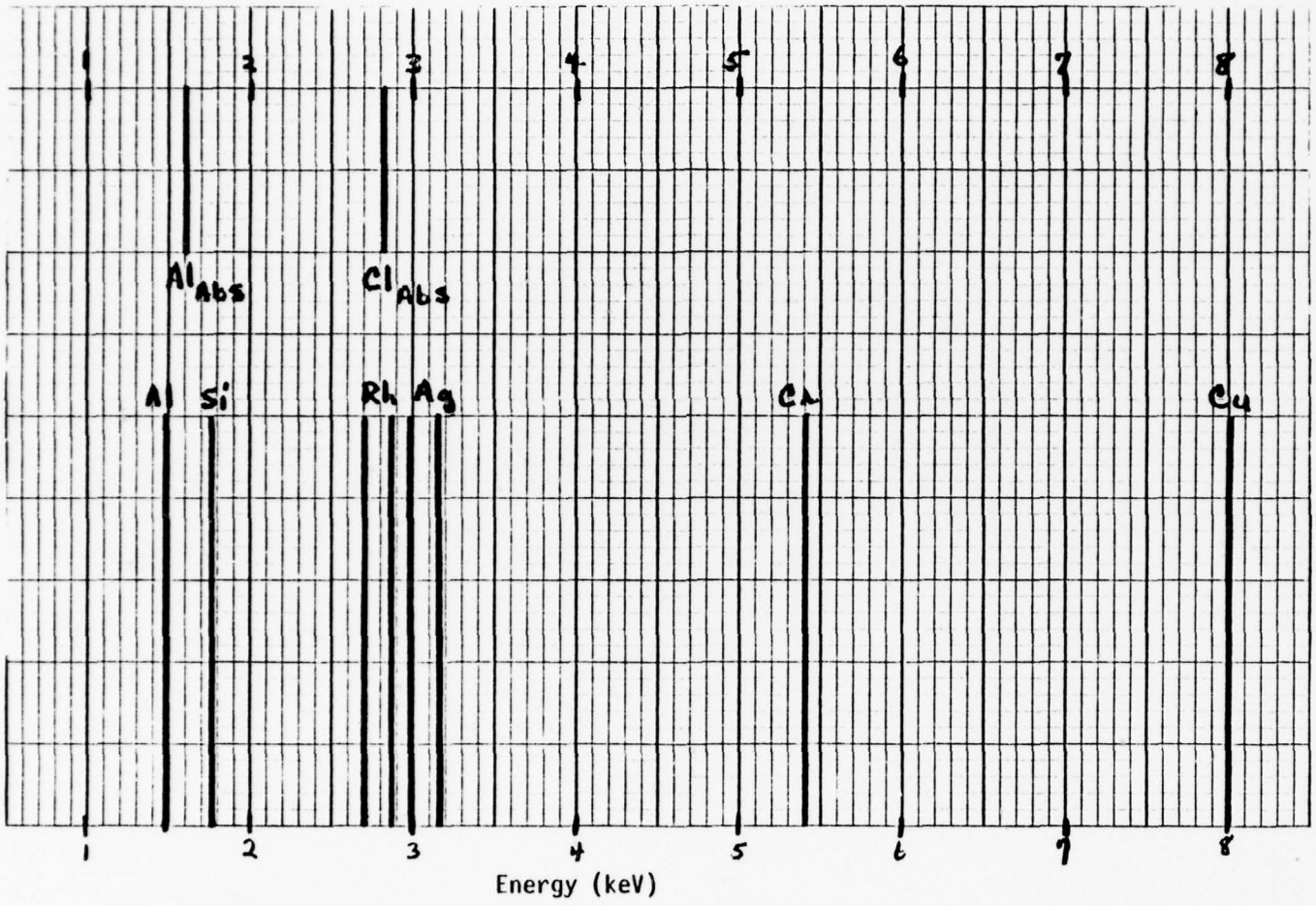

FIGURE 10. Energy Location of Line Spectra and Absorption Edges for Plume Measurements

due to various energy down-conversion mechanisms, and they also contribute to the serious problem of keeping the detector signals below saturation. Therefore, it will be essential to eliminate the high energy portion of the X-ray tube output. The two methods explored so far for accomplishing this are diffraction (crystal) and filtering. Both of these methods have revealed serious drawbacks, which eliminate their consideration. One remaining technique that is currently being explored is specular reflections from thin films.

4.0 RECOMMENDATIONS

In light of the foregoing observations a preliminary recommendation would be to fabricate a line-source target employing Al and Si films to conduct laboratory-scale investigations of Al_2O_3 particles. Once the feasibility of this approach has been verified experimentally for one element (Al) it will be straightforward to extend the source target and proof-of-principle study to the remaining plume constituents.

There are four main points that remain to be addressed before this evaluation is complete:

1. Obtain an accurate estimate of the X-ray continuum intensity in the spectral region of interest (1-8 keV) at high ($\geq$ 25 KV) acceleration potentials.

2. Extend the computer simulation of plume measurements using line spectra input to all elements present in the plume, and to include the fluorescence as well as absorption measurement.

3. Evaluate the technique of using thin metallic films to separate the higher energy part of the spectrum ($\geq$ 10 keV) from the low-energy region of interest.

4. Clear up the ambiguity over the utility of Rh as the line spectrum to be used for Cl absorption. The quoted separation of the L_α and L_β

lines (see Figure 10) is equivalent to the specified resolution of the proposed detector system. If the relative intensity of the Rh_{L_B} line is large, and cannot be resolved from the Rh_{L_α}, Rh will probably not work well in detecting Cl atoms.

REFERENCES

1. McGregor, W. K., "X-Ray Spectroscopy as a Diagnostic Tool in Solid Propellant Combustion Flows," AFRPL/PACP, 1978.

2. Bertin, E. P., Principles and Practice of X-Ray Spectrometric Analysis, Plenum Press, New York, 1975.

1978 USAF-ASEE SUMMER FACULTY RESEARCH PROGRAM

SPONSORED BY

THE AIR FORCE OFFICE OF SCIENTIFIC RESEARCH

Conducted by

AUBURN UNIVERSITY

Participant's Final Report

THE QUANTITATIVE DETERMINATION OF TRACE LEVELS OF TITANIUM IN HYDRAZINE

Prepared by:	Irvin M. Citron, Ph.D.
Academic Rank:	Professor
Department and University:	Chemistry Department Fairleight Dickinson Univ. Rutherford, N.J. Campus

Assignment:	
(Air Force Base)	Edwards AFB
(Laboratory)	Rocket Propulsion Laboratory
(Division)	Liquid Propulsion
(Branch)	Chemistry

USAF Research Colleague:	Mr. Herman Martens
Date:	August 11, 1978
Contract No.	F44620-76-C-0031

THE QUANTITATIVE DETERMINATION OF TRACE LEVELS OF TITANIUM IN HYDRAZINE

by

Irvin M. Citron

ABSTRACT

Hydrazine, during storage in titanium alloy tanks, acquires chemical impurities, metallic impurities quite possibly among them. Titanium would be the most likely metallic impurity in the hydrazine. If present at high enough levels, it might contribute to the deterioration of the hydrazine and thus result in the shortening of the lifetimes of space satellite missions.

This study was initiated to develop a reliable method of determining titanium in hydrazine down to the nanogram per milliliter level (parts per billion). The determination of titanium at such minute levels has not been reported in the literature. Titanium is a refractory metal, easily susceptible to the formation of oxides and carbides and is thus very difficult to analyze with sensitivity and accuracy at dilute levels by such ordinary means as flame atomic absorption. Even the use of a graphite furnace in conjunction with atomic absorption proved impractical because the furnace exhibited serious memory effects in the analysis of successive titanium samples.

The recent development of graphite furnace tubes coated with pyrolytic graphite opened up the possibility that refractory metals such as titanium could be analyzed by atomic absorption with much greater sensitivity and much greater reliability. In this investigation, atomic absorption measurement using the pyrolytic graphite furnace for sample atomization was chosen as the first approach in developing a reliable analytical method for titanium. The choice proved to be a sound one, for the investigation has led to the development of a method of analysis for titanium, following preconcentration (total evaporation) of hydrazine, that is accurate and statistically reliable down to the nanogram per milliliter level.

ACKNOWLEDGEMENTS

The author wishes to express his sincere appreciation to the United States Air Force, to ASEE, and to Auburn University for their sponsorship and support of this summer research. In particular, Mr. J. Fred O'Brien, Jr., Program Director, deserves a special note of gratitude for his excellent administrative efforts to make this summer highly productive and most enjoyable.

The author is indebted to the personnel of the Liquid Propulsion Division Chemistry Branch, of the Rocket Propulsion Laboratory for their pleasant and cooperative attitude during this entire ten week period. In particular, it was a distinct privilege and a most pleasant experience in working with Mr. Herman Martens as research colleague. He provided expert assistance and guidance all along the way and in a most cordial and informal manner. The author also wishes to thank Dr. Claude I. Merrill and Mr. John T. Nakamura for their frequent and helpful suggestions.

A special note of gratitude is due to Dr. Lawrence P. Quinn, Basic Research Program Manager, and to Dr. Richard Weiss, Chief Scientist, for their efficiency and expertise in coordinating the work of the summer faculty research appointees with the research aims and objectives of the Rocket Propulsion Laboratory. Their guidance and leadership met the highest standards of both professional and personal qualities.

LIST OF FIGURES

LIST OF TABLES

NOMENCLATURE

A	absorbance
AA	atomic absorption
APDC	ammonium (I) pyrrolidine dithiocarbamate
Ar	argon
C	concentration (weight/volume)
cc/min	cubic centimeters per minute
DPASV	differential pulse anodic stripping voltammetry
HNO_3	nitric acid
λ	wavelength
μg	micrograms
μl	microliters
mg	milligrams
ml	milliliters
mm Hg	millimeters of mercury (pressure) (Torr)
n	number of samples
N_2H_4	hydrazine
ng	nanograms
ppb	parts per billion = ng/ml
ppm	parts per million = μg/ml=ng/μl
S	standard deviation = $\sqrt{\frac{\Sigma(\bar{x} - x_i)^2}{n - 1}}$
Σ	summation of
Ti	titanium
U	unknown
v	volume
w	weight

INTRODUCTION

The principal aim of this summer research project was to develop a quantitative method to determine titanium (Ti) in hydrazine (N_2H_4) at the nanogram per milliliter (ng/ml) level. Such a method was desirable in order to facilitate the acquisition of reliable data on the Ti content of N_2H_4 after its long-term storage in titanium alloy tanks. No method to analyze Ti at levels as dilute as these were reported in the literature.

Two instrumental techniques which seemed promising in the development of such an analytical method were: (1) atomic absorption with use of a newly developed graphite furnace lined with a coating of pyrolytic graphite to prevent a refractory element such as Ti from forming a carbide or oxide prior to or during atomization (Refs. 1,2); (2) use of a polarographic technique, differential pulse anodic stripping voltammetry (DPASV), which has been used to analyze vanadium, a metal similar in refractory properties to titanium (Ref. 3). Both these techniques were sensitive to Ti down to the parts per million (ppm) level, or μg/ml. With a preconcentration step included in the method, this level of detection could effectively be decreased to the parts per billion (ppb) level, or ng/ml.

Since the atomic absorption method appeared to be the faster and simpler of the two methods cited above, it was decided to pursue this approach first. Fifty pyrolytic-lined graphite tubes were purchased for the graphite furnace. Each graphite tube was rated as having a useful range of from 50 to 200 atomization cycles. The instrumentation used in the development of this analytical method for Ti was a Perkin-Elmer 503 atomic absorption instrument in conjunction with a Perkin-Elmer HGA-2100 graphite furnace and a Beckman 1005 ten-inch linear recorder.

OBJECTIVES

There has been considerable conjecture as to what elements or compounds contribute to the contamination and deterioration of hydrazine as a rocket propellant after long-term storage in titanium alloy tanks. A recent study by C.T. Brown (Ref. 4) utilized an electrochemical test method to determine reaction rates of hydrazine at metallic surfaces and a condensed time scale based on coulometric measurements to yield an accelerated time profile of the metal-N_2H_4 interaction. Data was accumulated on the contribution of various metals (used in tank construction) and other impurities to N_2H_4 decomposition. Some of the data pointed to a large projected contamination of Ti in N_2H_4 after long-term storage (4 to 10 years) while other data pointed to very low levels of Ti in N_2H_4 after the same periods of storage but at higher temperatures. In short, the role of Ti plays, or for that matter, other metals such as aluminum, vanadium, iron, and nickel, in the deterioration of hydrazine was left far from clear. Since titanium was projected in the above study to be the largest of the metal contaminants, it became most desirable to obtain a fast, reliable, and accurate method of analyzing for this metal in hydrazine down to levels of 0.01 ppm (10 ppb) or less, if necessary.

It was to this end that this summer research project was planned. Titanium, being a refractory metal, posed many difficulties which prevented accurate sensitive analyses at low levels by conventional methods. The route chosen by the author and his research colleague has already been outlined in the Introduction. The methodology employed and data accumulated, which point to a very reliable method of analysis of Ti in hydrazine, will be presented in the body of this report.

DEVELOPMENT OF METHOD

The first step in the development of this method was to prepare a series of Ti standards in 0.2% HNO_3 (aqueous solution) and to test these standards in the graphite furnace tube lined with a coating of pyrolytic graphite. The standards ranged in concentration from 0.50 to 5.00 ppm titanium (μg/ml). A plot of this initial data, after averaging and correcting for background readings, yielded a linearity of absorbance with concentration in the range of 0.50 to 2.50 ppm when 20 μl samples were injected into the graphite furnace. When 10 μl samples were injected, linearity was achieved between 1.00 and 5.00 ppm. Both tests indicated that Beer's Law (linearity of absorbance with concentration of absorbing species) was effective between 10 and 50 ng inserted in the graphite furnace for analysis at a wavelength of λ = 365.4nm.

Several other parameters should be noted with respect to the operation of the atomic absorption instrument, graphite furnace and recorder.

Coolant liquid flow rate = 1.5 liters/min.
Ar gas purge rate = 55 cc/min.

Slit width - 0.2 nm
Recorder voltage = 10 mv
Drying temperature and time = 150^{o}C for 20 seconds
Charring temperature and time = 1800^{o}C for 5 seconds
Atomization temperature and time = 2800^{o}C for 7 seconds

The above operational parameters were kept constant through all subsequent experiments.

The results of this first experiment with the pyrolytic graphite-lined furnace tubes were very encouraging because (1) they showed no evidence of a serious memory effect in analyzing consecutive samples of increasing amounts of Ti, (2) they showed a high degree of reproducibility when absorbance readings on the same samples were taken moments later and even several days later, and (3) they showed a linear relationship between absorbance and concentration of Ti over a considerable range of concentration.

Because the investigator had heard reports of a compound called ammonium (I) pyrrolidine dithiocarbamate (APDC) being used as a complexing agent for Ti with subsequent extraction into chloroform prior to Ti analysis, he decided to spend some time in testing the feasibility of using the APDC complexation - organic extraction method as a possible means of concentrating Ti samples into smaller volumes. However, the results of this investigation were entirely negative. No titanium found its way into the organic layer, thus indicating either that a stable complex between Ti and APDC did not form at the pH conditions employed (buffered solutions of pH 4.8) or that the complex was too labile to survive the extraction step. An exhaustive search of the literature revealed no reference to a soluble Ti-APDC complex under acid conditions, but did

reveal that a Ti-APDC precipitate forms at alkaline conditions and that this precipitate has been used for X-ray analysis of titanium (Ref. 5). This precipitate would be of little value to this investigation in the present method of analysis. The soluble Ti-APDC complex, it was later learned from the original source of this information, had been a conjecture based on the fact that APDC complexes other transition elements, iron, copper, nickel, e.g.). It was decided not to pursue this approach any further by testing with other complexing agents at various pH's, for the approach held little promise for an increase in sensitivity for the detection of Ti and would, even if successful, necessitate an extra time-consuming extraction step.

The original line of investigation was continued by spiking several 100 ml samples of reagent hydrazine with standard amounts of Ti ranging from 1.00 μg to 3.00 μg, thus giving the hydrazine samples concentrations of Ti ranging from 10 to 30 ng/ml. Pure hydrazine without a spike of Ti was run through the process as a blank. The N_2H_4 of each sample and blank were completely evaporated by a process of flash evaporation in a preconcentrator. The resulting residues were taken up by 15 ml of 0.2% HNO_3 and evaporated down to a volume of exactly 1.0 ml. Analysis by AA (pyrolytic graphite furnace) showed linearity between absorbance and concentration, but the absorbance readings ranged from only 30% to 50% of the values of the absorbance readings at the same concentrations among the standards. There also seemed to be an increase in the percent recovery of Ti as the concentration increased.

The experiment was repeated with an added step of heating the take-up solution of 0.2% HNO_3 to boiling after preconcentration and changing the total amounts of Ti used to a range of 20 to 60 ng. Other conditions remained the same, except that a fresh series of aqueous standards (in 0.2% HNO_3) were prepared and stored in polyethylene bottles for longer preservation of purity. These standards were run along with the samples during the AA analysis step. This time the results were much more gratifying in that a percent recovery ranging from 35% to 75% was achieved (See Table 1). Again, percent recovery increased with increasing Ti concentration. A plot of sample absorbance versus concentration compared to absorbance of standards versus concentration (See Figure 1) revealed that the decline in absorbance for the samples compared to absorbance of corresponding standards remained remarkably constant at 0.210 throughout the concentration range of 2.00 to 6.00 μg/ml (or 20 to 60 ng Ti examined). The two plots were almost exactly parallel throughout this concentration range. This observation coupled with that of increased percent recovery with increasing concentration pointed toward an apparent finite and constant loss of Ti during the preconcentration step.

Some loss of Ti during the preconcentration step is probably unavoidable because some Ti is swept out under reduced pressure (about 30 mm Hg) during the flash evaporation within the preconcentrator apparatus. Some Ti may also splatter to the sides and neck of the preconcentrator receiving vessel and thus become difficult to recover completely. That this total

loss is constant, however, regardless of initial amounts of Ti (from 20 to 60 ng total Ti examined in the graphite furnace) means that the feasibility of this method for analyzing Ti in N_2H_4 is undiminished. All that need be done is to add an absorbance increment ($\Delta A = 0.210$ in this case) to the absorbance (A) of each sample examined within the 20 to 60 ng Ti range, locate the $A + \Delta A$ on the standard curve, and read off the amount of Ti in the original sample.

It must be emphasized that the value of ΔA is subject to change from one series of analyses to another carried out at a different time under different conditions. The value of ΔA will depend upon how carefully the preconcentration step is carried out. It will also depend on the slope of the standard curve which is subject to change when a pyrolytic graphite tube wears down, when a new one is inserted into the graphite furnace, or when the Ti radiation source loses some of its power. The value of ΔA should be checked by comparison of the absorbance of an aqueous standard with the absorbance of a spiked pure hydrazine sample during each series of analyses carried out within the same time frame. Extrapolation of the standard curve for Ti to the value A = 0.210 (in the above experiment) revealed a constant physical loss of Ti per sample in the preconcentration step of 12.5ng (See Figure 2). This physical loss should remain constant provided that operation of the preconcentrator does not change.

USE OF METHOD ON SAMPLE OF TANK HYDRAZINE

The method developed was used to check the concentration of Ti in a hydrazine sample that had been stored in a titanium alloy tank for about two years. The sample was analyzed (1) "as is", (2) with a standard addition of 1.0 ml of 2.0 ppm Ti per 100 ml N_2H_4, and (3) with a standard addition of 1.0 ml of 4.0 ppm Ti per 100 ml N_2H_4. These three sample solutions were labeled U_1, U_2, and U_3 respectively. The standards were analyzed along with the samples and ΔA was determined to have remained at a value of 0.210. The date and calculations pertaining to this analysis are shown in Table 2 and the graphical derivation of the concentration of the unknowns are shown in Figure 3.

The "as is" analysis, U_1, gave a response that was lower than the optimal lower limit of the standard curve (2.00 ppm or ng/μl), and thus was not amenable to reliable calculation. The two standard addition runs, however, gave comparable results, 7.3 ng/ml and 8.7 ng/ml Ti in the tank hydrazine, respectively. From these results, the amount of Ti in the tank hydrazine was estimated at 8.0 ng/ml or 0.008 ppm.

At this point in the development and testing of the method, the first pyrolytic graphite tube cracked. It had lasted a total of 377 atomization cycles. It had shown remarkably constancy of performance as shown by the reproducibility of standard solution absorbances after a five-day interval (See Figure 4). A new pyrolytic graphite tube was inserted, and after a few days, solutions U_1, U_2, and U_3 were analyzed again along with the standards. From the 12.5 ng loss of Ti during preconcentration a new ΔA of 0.270 was calculated. It was found that a brown precipitate which had formed in the tank-hydrazine Ti solutions had evidently adsorbed some of the Ti in the solutions. The average Ti now calculated was 3.6 ng/ml or ppb. This development points out the importance of performing the AA analysis on tank hydrazine samples soon after the preconcentration and take-up solution steps.

It might be added at this point that, in all, three different pyrolytic graphite tubes were used during this entire summer project. The second tube lasted for a total of 112 atomization cycles. The third tube is still functioning after 105 atomization cycles. The plots of Ti concentration versus absorbance obtained for the same set of aqueous standards using the three different tubes are shown in Figure 5. The data is shown in Table 3. All operational parameters remained exactly the same in utilizing the AA instrument.

PROCEDURAL OUTLINE OF METHOD

1. Prepare a set of standards for Ti in 0.2% HNO_3 (aqueous), ranging in concentration from 2.0 to 6.0 ppm (ng/μl).

2. Take 100 ml of the hydrazine to be analyzed for Ti. Add a standard amount of Ti if it is thought that the concentration of Ti already in the hydrazine is less than 2.0 ppb. Use 100 ml pure N_2H_4 as a blank and 100 ml pure N_2H_4 spiked with a standard addition of Ti as a means of calculating ΔA.

3. Evaporate the 100 ml volumes of hydrazine (with or without the standard additions) to complete dryness in a preconcentrator apparatus. IMPORTANT: This must be a drop-by-drop flash evaporation of hydrazine under reduced pressure and at an elevated temperature. Evaporation of large volumes of N_2H_4 by ordinary means is extremely hazardous!

4. Take up the resulting residue in about 15 ml of 0.2% HNO_3 solution brought to a boil.

5. Evaporate the resulting take-up solution to exactly 1.0 ml volume.

6. Analyze the sample along with the standards by AA using a graphite furnace tube coated with pyrolytic graphite. Suggested parameters for analysis are: λ = 365.4nm, slit width = 0.2nm, recorder voltage = 10 mv, volume of sample used = 10 μl, argon gas purge rate = 55 cc/min., coolant water flow rate = 1.5 liters/min., drying temperature = 150°C for 20 seconds, charring temperature = 1800°C for 5 seconds, atomization temperature = 2800°C for 7 seconds.

7. Plot the standard curve and calculate ΔA by comparing the absorbance of the spiked pure N_2H_4 sample with the absorbance of a corresponding aqueous standard.

8. Add ΔA to the absorbance of the sample to be analyzed and locate $A + \Delta A$ on the standard curve. Read off the concentration of Ti in the sample injected into the furnace.

9. Subtract the standard addition of Ti (if applicable) to get the concentration of Ti in the original sample.

The above procedure may be modified in many ways to suit the specific conditions and needs of the operator.

STATISTICAL EVALUATION OF METHOD

A series of ten samples of pure hydrazine each containing 1.0 ml of 3.00 ppm Ti per 50 ml N_2H_4 were run through the entire procedure of preconcentration, take-up, evaporation and d. c. arc examination of 10 µl by 4A using the pyrolytic graphite planar. Each sample analyzed thus theoretically contained 300 ng Ti in 3.00 ng/µl. Standards were run along with the sample and a new ΔA of 0.4e was calculated for this series. The ΔA was much larger than heretofore, but nevertheless, the ten samples exhibited excellent precision among themselves. The large ΔA can be attributed to a too rapid preconcentration due to the number of samples that had to be done. It was thought that perhaps the smaller volume of N_2H_4 used per sample (50 ml instead of 100 ml) had something to do with the greater loss of Ti during preconcentration, but a subsequent experiment using the same Ti addition to different volumes of N_2H_4 followed by preconcentration and take-up to 1.0 ml final volume showed conclusively that the volume of N_2H_4 preconcentrated has no effect on the results. In this latter experiment two samples containing 30.0 ng Ti yielded a ΔA of 0.385 even though one was preconcentrated from 100 ml and the other from 50 ml. Another two samples, also of 30.0 ng Ti in 100 and 50 ml N_2H_4 respectively, yielded a ΔA of only 0.3.5 (90% recovery of Ti). This proves conclusively that the ΔA factor (mechanical loss of Ti) can be large or small depending on operator efficiency in controlling the drop rate during preconcentration. A very slow drop rate leads to greater percent recovery of Ti and hence a lower ΔA value. See the paragraph on Conclusions and Recommendations for suggestions as to what can be done to standardize efficiency during preconcentration.

Since the data of the standard deviation experiment proved to be consistent and precise, the data were used for a statistical evaluation of the method. The data and results of this experiment are outlined in Table 4. The principal statistical results can be summarized as:

mean $\bar{x}$ = 3.[illegible] ng/µl
standard deviation (s) = 0.[illegible]32 ng/µl
relative standard deviation = 4.4%
range = 0.38 ng/µl
% error = 3.3% (compared to 3.00 ng/µl assumed as true concentration of Ti in solutions examined)

The loss of Ti in the preconcentration step can be regarded as the determinate error in this analysis. This error could be diminished and possibly eliminated through perfection of the technique of preconcentration (as discussed under Conclusions and Recommendations). Under the most favorable circumstances to date, the smallest determinate error E was 4.5 ng Ti lost out of 30.[illegible] ng. Thus the lowest relative determinate error so far has been:

$$\frac{E}{\bar{X}} \times 100 = \frac{4.5\ ng}{30.[illegible]\ ng} \times 100 = 15.0\%$$

Despite the very large determinate error in the standard deviation experiment (E = 25.8 ng; rel. E. = 79.3%), the results were very consistant among themselves, thus indicating the method is statistically valid. The confidence interval of the mean using all the results in the standard deviation experiment (9 degrees of freedom; $t_{0.95} = 2.262$) was:

$$\mu = \bar{x} \pm \frac{ts}{\sqrt{n}} = 3.10 \pm \frac{(2.262)(0.132)}{10} = 3.10 \pm 0.095 \text{ ng}/\mu\text{l}$$
(95% confidence)

If the six central results are used (discarding two results at each extreme), the resulting range is 3.23-3.20 = 0.20 and the mean is 3.08. The statistical constant (6 observations) for using the range in calculating μ is $C_{n(0.95)} = 0.399$. The confidence interval of the mean is then:

$$\mu = \bar{x} \pm CnR = 3.08 \pm (3.99)(0.20) = 3.08 \pm 0.080 \text{ ng}/\mu\text{l}$$
(95% confidence)

If the four highest results are neglected (those furthest from the accepted value of 3.00 ng/μl, the resulting range is 3.04-2.97 = 0.11, the mean is 3.01, and the confidence interval of the mean becomes:

$$\mu = 3.01 \pm (0.399)(0.11) = 3.01 \pm 0.044 \text{ ng}/\mu\text{l}$$
(95% confidence)

Using the results of the experiment on volume effects as a second standard deviation determination, the mean and standard deviation for four determinations were $\bar{x} = 3.00$ and $s_1 = 0.139$. The resulting variance, $s_1^2 = 0.0193$ can be compared to the variance of the initial standard deviation experiment, $s_2^2 = (0.132)^2 = 0.0174$. The ratio of variances is:

$$F = \frac{0.0193}{0.0174} = 1.11 < 3.86$$

which is the statistical value of $F_{0.95}$ for 3 and 9 degrees of freedom respectively. Thus, there is no statistically significant difference at the 95% confidence level in the two variances.

The above results point to a statistically sound and viable method for analyzing Ti in hydrazine.

TEST OF METHOD BY "BLIND EXPERIMENTS"

The method was further evaluated by having the investigator run through the procedure a series of four solutions in which the Ti concentrations were totally unknown to him but known to his research colleague who prepared them. One standard addition of 1.00 ml of 3.00 ng/μl Ti to an equal volume of N_2H_4 (50 ml) was carried through the procedure in order to determine ΔA for this series of "blind experiments". Three drops of glycerol was added to each solution to see if this would diminish the loss of Ti by spattering. Care was taken to preconcentrate each solution as carefully as possible. The glycerol addition did not help to diminish ΔA, for the ΔA value was calculated as 0.267 for those samples preconcentrated on July 24, 25, and 0.309 for those samples preconcentrated on July 26 (See Table 5). Samples 1, 2, and 3 (with the lower ΔA) resulted in 2.28, 2.25, and 2.25 ng/μl Ti respectively being found in solution. Sample 4 (with higher ΔA) resulted in 2.40 ng/μl Ti found. The actual concentration of Ti added to each of the four solutions was 2.00 ng/μl (ppm). Thus the percent error ranged from 12.5% to 20.0% with an average of 14.8%. Considering the high ΔA values that were encountered in this series of trials and the small amounts of Ti under analysis, the relative errors are not unusually high and do not detract from the feasibility of this method. On the contrary, the results emphasize the high degree of precision and reproducibility achieved by the method of analyzing Ti in N_2H_4, and reaffirm the importance of finding a way to preconcentrate hydrazine with minimal losses of dissolved materials.

CONCLUSIONS AND RECOMMENDATIONS

The principal objective of this summer research project has been attained - to develop a reliable quantitative method of determining titanium in hydrazine at the ng/ml level (ppb). The method, utilizing a 100-fold preconcentration of hydrazine followed by uptake with 15.0 ml of 0.2% HNO_3, evaporation to exactly 1.0 ml and analysis of 10 µl injections by atomic absorption analysis at 365.4 nm wavelength (pyrolytic graphite tube), proved to be reliable, reproducible, reasonably rapid, and statistically sound.

The step in the method that is slowest and potentially the most likely to incur error (physical loss of Ti) is the preconcentration step. This step is exceedingly operator-dependent. The flash evaporation must be carefully watched and controlled so that it occurs drop-by-drop at low pressures (15 to 30 mm) and elevated temperature (about 100°C). The author recommends (1) the construction of a preconcentrator with a needle valve that could keep the drop rate at a smaller constant value and with several units connected in series by a manifold to cut down on operator time per sample, or (2) the slow evaporation of the hydrazine under nitrogen at atomspheric pressure. This latter procedure would avert the problems of flash evaporation and would permit many samples to be preconcentrated at once. However, it would present other problems - disposal of the hydrazine vapors or condensate, for example.

The method developed in this study could be adapted to the analysis by AA of other metals found in the construction of the tanks used to hold hydrazine. Examples of such metals are vanadium (Ref. 6), aluminum (Ref. 6), iron (Ref. 7), and nickel (Ref. 8). Such multiple-element analysis from the same solutions would make the method much more efficient and productive from a time-saving standpoint. The author recommends a continuation of this project in order to develop such multiple-element methods. When atomic absorption proves to be non-feasible for a particular metal, the method of differential pulse anodic stripping voltammetry (DPASV) could be investigated (Ref. 9).

References

1. Manning, D.C. and Ediger, R.D., Atomic Absorption Newsletter (1976), 15(2), pp. 42-44.

2. Sturgeon, R.E. and Chakrabartl, C.L., Analytical Chemistry (1977), 49(1), pp. 90-97.

3. Gilbert, D.D., Analytical Chemistry (1965), 37(9), p. 1102.

4. Brown, C.T., Report No. AFRPL-TR-76-21, May 1976, pp. 3-39 and pp. 132-133.

5. Luke, C.L., Analytica Chimica Acta (1969), 41, pp. 237-250.

6. Nickolaev, G.I. and Podgornaya, V.I. (USSR), Zh. Prikl. Spektrok, (1974), 21(4), pp. 593-598 (Russian). CA (1975), Vol. 82, 80068j.

7. Gomiscek, S., Lengar, Z., Cernetic, D., and Hudnik, V., Analytica Chimica Acta (1974), 73(1), pp. 97-106 (English).

8. Pierce, F.D., Gortatowski, M.D., Mecham, H.D., and Fraser, R.S., Analytical Chemistry (1975), 47(7), pp. 1132-1135.

9. Hoff, H.K., and Jacobsen, E., Analytica Chimica Acta (1971), 54, pp. 511-519.

FIGURE 1

ATOMIC ABSORPTION DATA FOR TITANIUM IN AQUEOUS STANDARDS AND AFTER RECOVERY FROM HYDRAZINE (FIRST GRAPHITE TUBE)

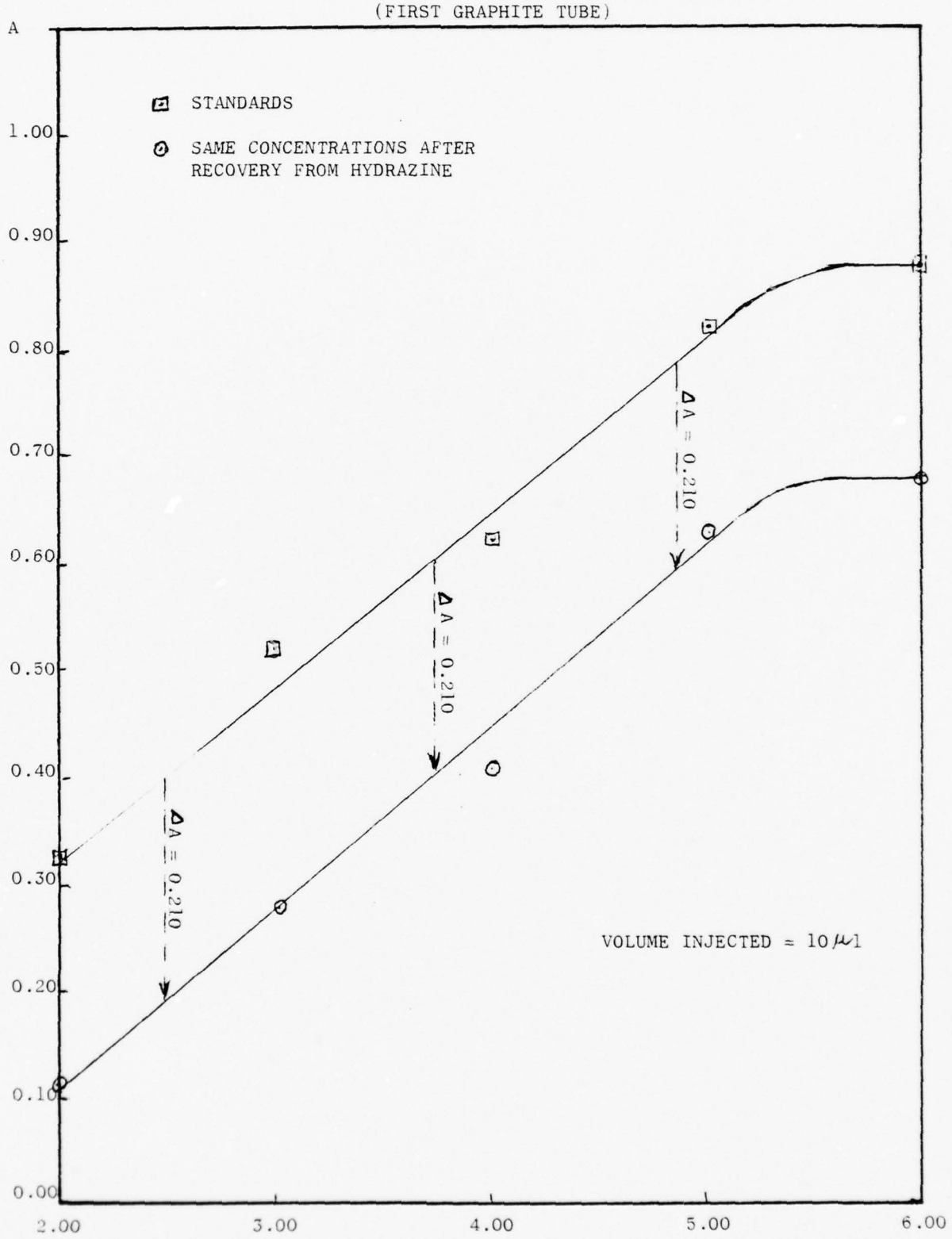

FIGURE 2

EXTRAPOLATION OF STANDARD CURVE (FIRST GRAPHITE TUBE) TO ΔA AND DETERMINATION OF TITANIUM LOSS DURING PRECONCENTRATION

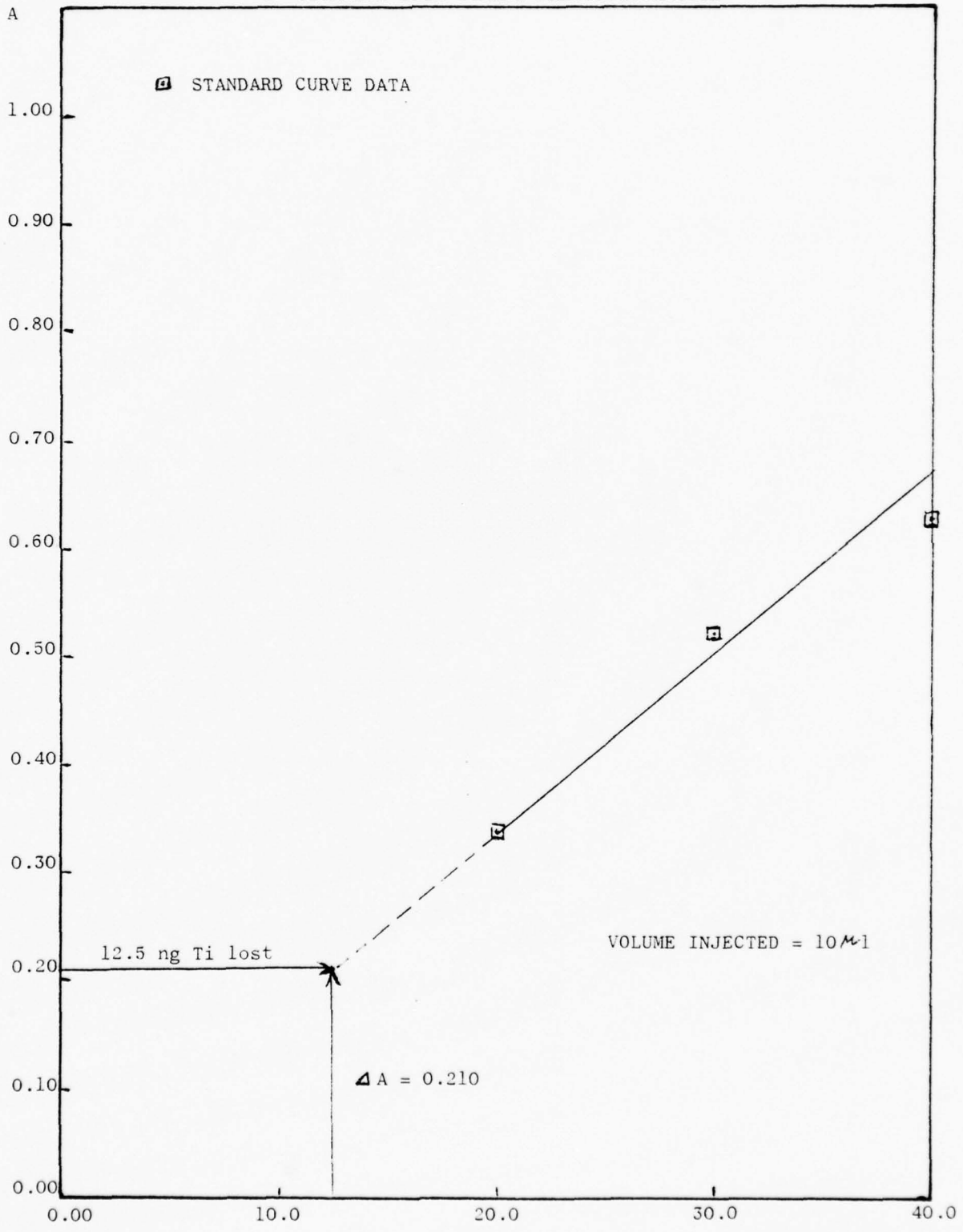

FIGURE 3

APPLICATION OF METHOD TO ANALYSIS OF TITANIUM IN HYDRAZINE STORED FOR TWO YEARS IN TITANIUM ALLOY TANK

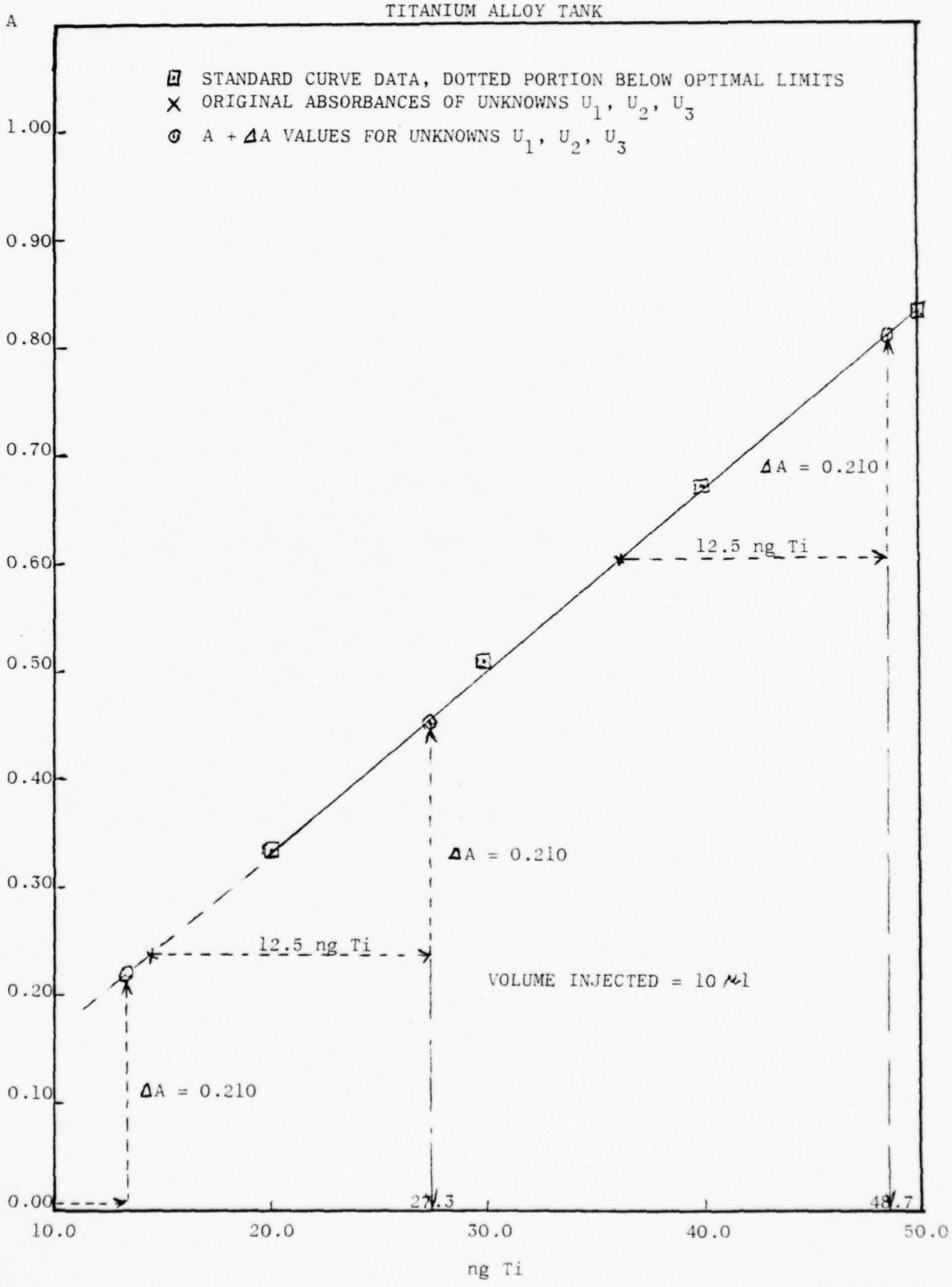

FIGURE 4

REPRODUCIBILITY OF STANDARD ABSORBANCES
AFTER FIVE-DAY INTERVAL (FIRST GRAPHITE TUBE)

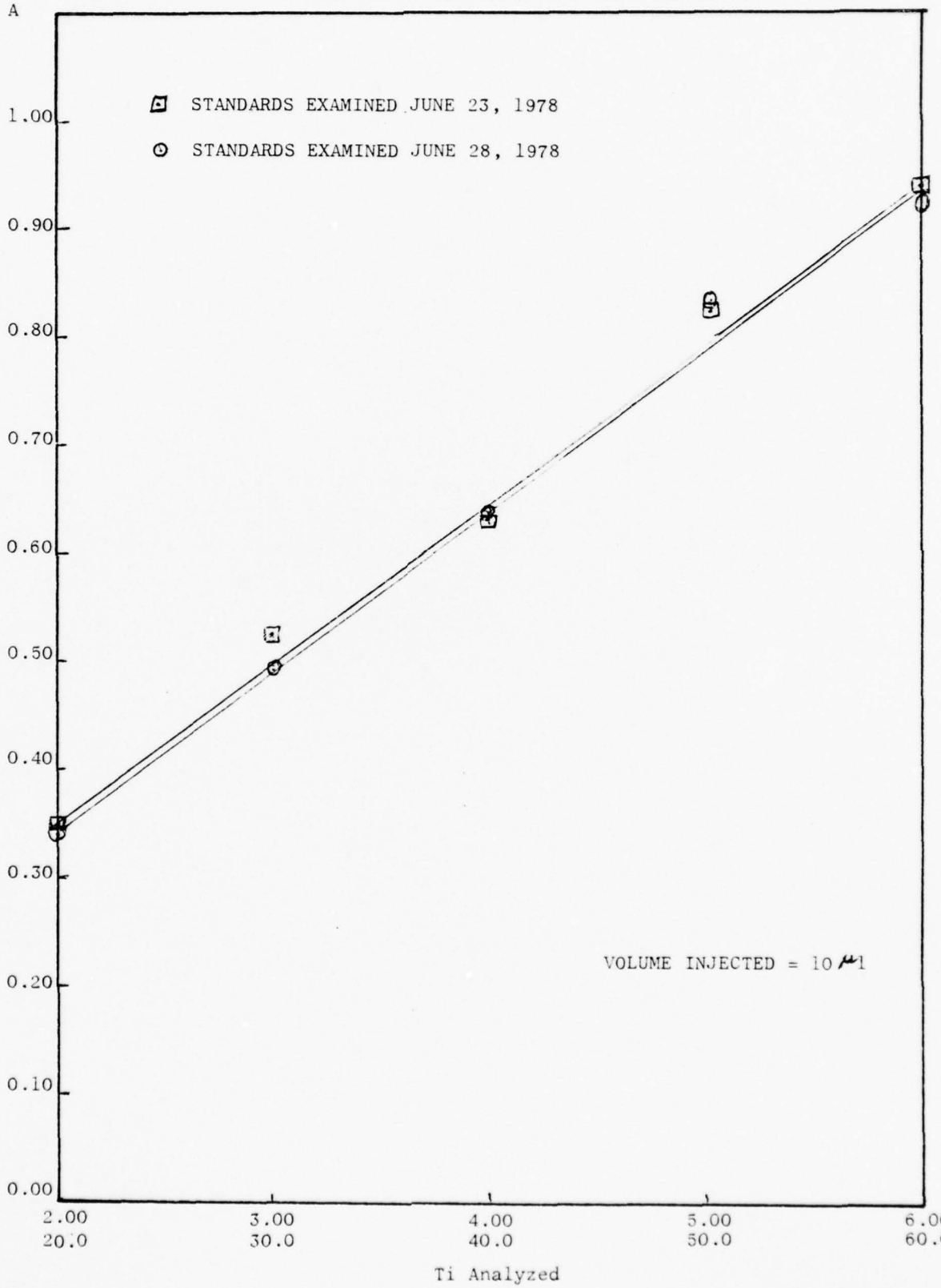

FIGURE 5

PLOTS OF TITANIUM CONCENTRATION VERSUS
ABSORBANCE FOR AQUEOUS STANDARDS OBTAINED
FOR THREE DIFFERENT GRAPHITE TUBES

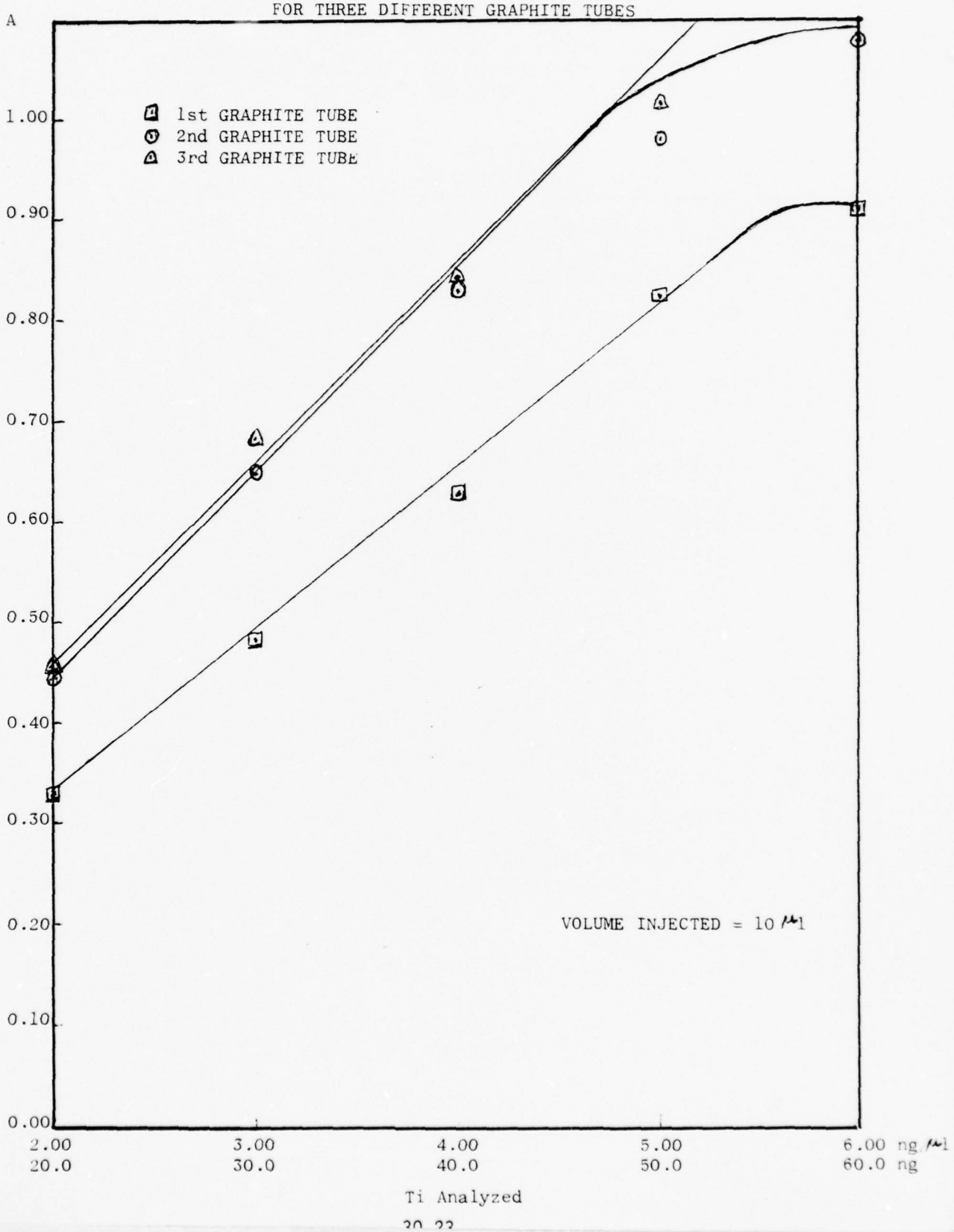

TABLE 1

ATOMIC ABSORPTION DATA FOR TITANIUM IN AQUEOUS STANDARDS AND AFTER RECOVERY FROM HYDRAZINE (FIRST GRAPHITE TUBE)

Standard No.	C_{Ti} ng/μl	ng Ti Examined	A*
1	2.00	20.0	0.332
2	3.00	30.0	0.520
3	4.00	40.0	0.625
4	5.00	50.0	0.820
5	6.00	60.0	0.880

Solution No.	C_{Ti} ng/ l	ng Ti Examined (Theor.)	A*	% Ti Recovered	Δ A
1	2.00	20.0	0.115	34.6	0.217
2	3.00	30.0	0.280	53.8	0.240
3	4.00	40.0	0.410	65.6	0.215
4	5.00	50.0	0.630	76.8	0.190
5	6.00	60.0	0.670	76.1	0.210

Volume injected into graphite furnace = 10 μl

* Absorbance readings corrected for blank and averaged
Blank absorbance reading = 0.040

TABLE 2

DATA AND CALCULATIONS IN THE ANALYSIS OF TITANIUM IN HYDRAZINE STORED FOR TWO YEARS IN TITANIUM ALLOY TANK

Solution Examined	C_{Ti} (ng/μl)	A*	A + ΔA
Blank	0.00	0.00	
Standard No. 1	2.00	0.326	
Standard No. 2	3.00	0.500	
Standard No. 3	4.00	0.660	
Standard No. 4	5.00	0.825	
Solution No. 1 "As Is"	U_1	0.003	0.213
Solution No. 2 Spike: 20 ng Ti	U_2	0.232	0.442
Solution No. 3 Spike: 40 ng Ti	U_3	0.588	0.798 (A = 0.210)

Volume injected into graphite furnace = 10 μl

*Absorbance readings corrected for blank and averaged
Blank absorbance reading = 0.040

CALCULATIONS OF UNKNOWN CONCENTRATIONS

U_1 neglected because A + ΔA = 0.003 + 0.213 < 0.326 corresponding to 2.00 ng/μl

For U_2, A + ΔA = 0.232 + 0.210 = 0.442 corresponding to 2.73 ng/μl on standard curve

U_2 = (2.73 ng/μl x 10 μl) - 20.00 ng = 7.3 ng Ti (per ml N_2H_4)

For U_3, A + ΔA = 0.588 + 0.210 = 0.798 corresponding to 4.87 ng/μl on standard curve

U_3 = (4.87 ng/ l x 10 μl) - 40.00 ng = 8.7 ng Ti (per ml N_2H_4)

Average C_{Ti} in N_2H_4 from tank = $\frac{7.3 + 8.7}{2}$ = 8.0 ng/ml or 0.008 ppm

TABLE 3

DATA FOR TITANIUM CONCENTRATION
VERSUS ABSORBANCE FOR AQUEOUS STANDARDS:
A COMPARISON OF THREE DIFFERENT GRAPHITE TUBES

Standard No.	C_{Ti} ng/μl	Graphite Tube 1 A*	Graphite Tube 2 A*	Graphite Tube 3 A*
1	2.00	0.329	0.450	0.455
2	3.00	0.484	0.650	0.684
3	4.00	0.629	0.830	0.840
4	5.00	0.829	0.980	1.020
5	6.00	0.920	1.080	-----

Volume injected into graphite furnace = 10 μl

*Absorbance readings corrected for blank and averaged
Blank absorbance reading = 0.040

TABLE 4

STATISTICAL EVALUATION OF METHOD

Solution	C_{Ti} ng/μl	A*	A + ΔA	C_{Ti} (Found) ng/μl (x_i)	$\lvert \bar{x} - x_i \rvert$	$\lvert \bar{x} - x \rvert^2$
Standard 1	2.00	0.420				
Standard 2	3.00	0.605				
Standard 3	4.00	0.712				
Standard 4	5.00	0.807				
Standard 5	6.00	----				
Sample 1	3.00	0.183	0.663	3.29	0.19	0.0361
Sample 2	3.00	0.130	0.610	3.03	0.07	0.0049
Sample 3	3.00	0.133	0.613	3.04	0.06	0.0036
Sample 4	3.00	0.188	0.668	3.31	0.21	0.0441
Sample 5	3.00	0.130	0.610	3.03	0.07	0.0049
Sample 6	3.00	0.130	0.610	3.03	0.07	0.0049
Sample 7	3.00	0.149	0.629	3.12	0.02	0.0004
Sample 8	3.00	0.109	0.589	2.93	0.17	0.0289
Sample 9	3.00	0.123	0.603	2.99	0.11	0.0121
Sample 10	3.00	0.170	0.650	3.23	0.13	0.0169
				$\bar{x} = 3.10$		0.1568 $= \Sigma \lvert \bar{x} - x_i \rvert^2$

Volume injected into graphite furnace = 10 μl
*Absorbance readings corrected for blank (0.040) and averaged
ΔA = 0.470 for this series of standards and samples

STATISTICAL RESULTS

Mean ($\bar{x}$) = 3.10 ng/μl

Standard deviation, $s = \sqrt{\frac{\Sigma \lvert \bar{x} - x_i \rvert^2}{n-1}} = \frac{0.1568}{9} = \pm 0.132$

Relative standard deviation = $\frac{0.132}{3.00} \times 100 = 4.4\%$

Concentration found = 3.10 ± 0.132 ng/μl Ti (or 31.0 ng ± 1.32 ng Ti analyzed per sample)

Range = 3.31 - 2.93 = 0.38 ng/μl

% Error (based on accepted value of 3.00 ng/μl = $\frac{3.10 - 3.00}{3.00} \times 100 = 3.3\%$

TABLE 5

RESULTS OF "BLIND EXPERIMENT" ANALYSES USING THE METHOD DEVELOPED

Solution	A*	A + ΔA ✦	ng/μl Ti (Found)	ng/μl Ti (Actual)	% Error
Standard 1	0.380			2.00	
Standard 2	0.540			3.00	
Standard 3	0.660			4.00	
Standard 4	0.765			5.00	
Sample 1	0.150	0.417	2.28	2.00	14.0%
Sample 2	0.147	0.414	2.25	2.00	12.5%
Sample 3	0.147	0.414	2.25	2.00	12.5%
Sample 4	0.125	0.434	2.40	2.00	20.0%
Sample 5 (known)	0.209	0.518		3.00	

*Absorbance values averaged and corrected for blank (0.020)

✦ ΔA for samples 1, 2, and 3 (preconcentrated on July 24, 25) assumed to be $0.518 - (0.209)\ \frac{(0.150)}{0.125} = 0.267$

ΔA for samples 4 and 5 (preconcentrated on July 26) assumed to be $0.518 - 0.209 = 0.309$

1978 USAF-ASEE SUMMER FACULTY RESEARCH PROGRAM

Sponsored by
THE AIR FORCE OFFICE OF SCIENTIFIC RESEARCH
Conducted by
AUBURN UNIVERSITY AND OHIO STATE UNIVERSITY
PARTICIPANT'S FINAL REPORT

EVALUATION OF CURRENT RESEARCH IN FRACTURE AND FAILURE BEHAVIOR OF SOLID PROPELLANT

Prepared by:	Shyhming Chang, Ph.D
Academic Rank:	Associate Professor
Department and University:	School of Engineering California State University-Fresno Fresno, CA 93740
Assignment:	
(Air Force Base)	Edwards Air Force Base
(Laboratory)	Air Force Rocket Propulsion Laboratory
(Division)	Solid Propellant
(Branch)	Physical Behavior
USAF Research Colleague:	Mr. Durwood Thrasher
Date:	August 18, 1978
Contract No.:	F44620-75-C-0031

EVALUATION OF CURRENT RESEARCH IN FRACTURE AND FAILURE BEHAVIOR OF SOLID PROPELLANT

by
Shyhming Chang

ABSTRACT

Two major problems confronting successful firing of solid propellant motors are ballistic failure due to thermal cooldown in storage and rapid pressurization during ignition. Although it has been observed that some motors with pre-existing flaws were fired successfully in a case where the burning rate of propellant exceeds that of crack growth, it is imperative that some realistic failure prediction techniques be developed to cope with these problems. This will include detection of flaw size and site, rational failure criteria in case of motors with subcritical flaws, and prediction of crack initiation and growth.

In this report, emphasis is placed on the survey of fracture mechanics analyses which are pertinent to the prediction of fracture behavior related to solid propellant motors.

First a brief sketch of historical development leading toward current practice is given. Secondly, current research on fracture mechanics is reviewed and summarized. Thirdly, correlations among the theories and experimental data obtained from realistic propellant materials are discussed.

Evaluation and assessment of these theories and experimental results indicate that further improvements are needed in the areas of nonlinear characterization of solid propellant materials, bi-material fracture mechanics, crack propagation under complex stress and strain fields, aging and rehealing characteristics, and numerical techniques related to nonlinear fracture mechanics.

Literature cited in the report is categorized according to "theory", "experimental analysis", "numerical analysis", and "application to solid propellants" to facilitate future investigations in the subject matter of fracture and failure behaviors of solid propellants.

ACKNOWLEDGMENT

The author is indebted to Mr. Durwood Thrasher of AFRPL/Edwards AFB for his constant guidance, assistance, and encouragement during the course of this research program.

Many scientists and engineers at AFRPL have been most helpful in rendering advice and current information pertaining to the program; these are Dr. Richard Weiss, Mr. Thomas Chew, Mr. Arch Johnston, Mr. Ross Stacer, Mr. Robert Biggers, and Capt. Rich Middleton, just to name a few.

The author is also grateful to Mrs. Elsie Gee and Mrs. Jeanne Rhodes for their assistance in preparing the final manuscript.

The author would also like to express his thanks to the fellow faculty research associates, Drs. Irvin Citron, James Laufenberger, Phil Feinsilver and Russel Petersen for their daily stimulating scientific discussions enroute from Lancaster to the AFRPL site.

Finally, but not least, the author is grateful to Prof. J. Fred O'Brien, Jr. of Auburn University and Dr. Larry Quinn of AFRPL for their superb administration of this program.

LIST OF FIGURES

LIST OF TABLES

1. INTRODUCTION

Conventionally, design and life prediction of solid propellant motors were based on discrete failure criteria and cumulative damage criteria [1]. Depending on past experience encountered by various companies, each manufacturer of solid propellant motors adopted its own set of criteria which proved successful in case of unflawed motors; uncertainties being accounted for by the incorporation of factor of safety in its designs. However, with recent developments in viscoelastic fracture mechanics theory, it is now practical to apply fracture mechanics to the prediction of service life of solid propellant motors.

Observations of failure occurrences in the recent past showed that failures in solid propellant motors are largely due to thermal cool-down in storage, rapid pressurization during ignition, or burning in preexisting flaws which acts as a crack driver. For example, some early Minuteman III Stage III development motors had aft-end case-liner failures a few seconds after ignition due to cracks in the material interface or "debonds". This problem recurred in 1970-72 with certain motors having potted voids as well as in defect-free motors at AEDC in an altitude test in 1975.

Therefore, it becomes imperative that service life prediction should include fracture mechanics analysis to insure successful firings of solid propellant motors which will meet all the ballistic tolerances. It was also observed that, despite the presence of flaws, if the propellant burning rate exceeds that of crack growth in the absence of burning within the flaws, then motors are known to fire successfully within the ballistic tolerances.

In view of this, one is confronted with the following problems for the structural prediction of service life of a solid propellant motor.

(a) Determination and detection of critical flaw size and site.

(b) Crack initiation

(c) Crack growth (quasi-static)

(d) Crack propagation (dynamic)

For the detection of spherical voids and planar cracks with a crack angle of 5 degrees or greater, X-ray has been successfully used on structural test vehicles (STV's) and actual motors. More recently, an acoustical holography technique for flaw detection has been developed in Air Force Rocket Propulsion Laboratory contracts with Aerojet and Holosonics, Inc. and is expected to be superior to X-ray in detecting planar flaws.

Depending on the size of flaws, [illegible] are two distinct sets of ana
methods and failure criteria. This [illegible] eneral, governed by the so-
critical flaw size 2 C_{cr} is shown [illegible] .

In the simplest form the criti[illegible]s for impending crack growth
specimen containing a line flaw and [illegible] ension perpendicular t
crack direction is given by the equ[illegible] where k is a constant depend

$$\sigma = k\sqrt{E\gamma/C}$$

the flaw geometry, E is the Young's [illegible], 2 C is the crack size, and
the fracture energy required per unit [illegible]-formed crack surface area.

Current practice for the design and stress analysis of unflawed moto
is to use a discrete failure criterion obtained from a specific experimen
on a simplified specimen which undergoes similar loading conditions (mech
and thermal) to those of a real solid propellant motor. Owing to the tim
temperature dependencies of propellant materials and constantly changing
ing environments as well as complexity of geometry, a rational unified fu
tional type failure criterion in [illegible] stress space has yet to be devel
and verified by experiments for [illegible] 3, 4. On the other hand, a cu
tive damage criterion developed by Fong [illegible] has been widely used for pred
tion of the life of propellants undergoing thermal and mechanical loadings

For the case where flaws exist or where crack formation takes place d
to thermal cool-down or overpressurization at critical sites such as at th
innerbore, bond termination flaws, etc., fracture mechanics analysis must
adopted to assess the criticality of the flaws on subsequent firing of the
motors.

Since Griffith's pioneering work in elastic fracture mechanics in 1924
his theory has been extended to elastic-plastic media 9, viscoelastic media 10,
linearly viscoelastic media 11, and [illegible] to composite materials [illegible]. Many
interesting aspects of developments in theories of fracture mechanics can
be found in Reference [illegible].

The current practice in the study of crack initiation and growth criter
is based on two alternative approaches: namely, energy balance and stress
intensity factor. The former finds its origin in Griffith's work 8, whereas
the latter in Irwin's work 15.

In the "energy" approach, the condition of impending crack growth is
governed by the concept of energy release rate $\partial C'/\partial A$, which is defined as
the rate of strain energy release per unit increment in the surface area of
the crack. When this release rate is equal to or exceeds the critical frac-
ture energy density [illegible] crack growth takes place.

$$-\frac{\partial}{\partial} \quad (2)$$

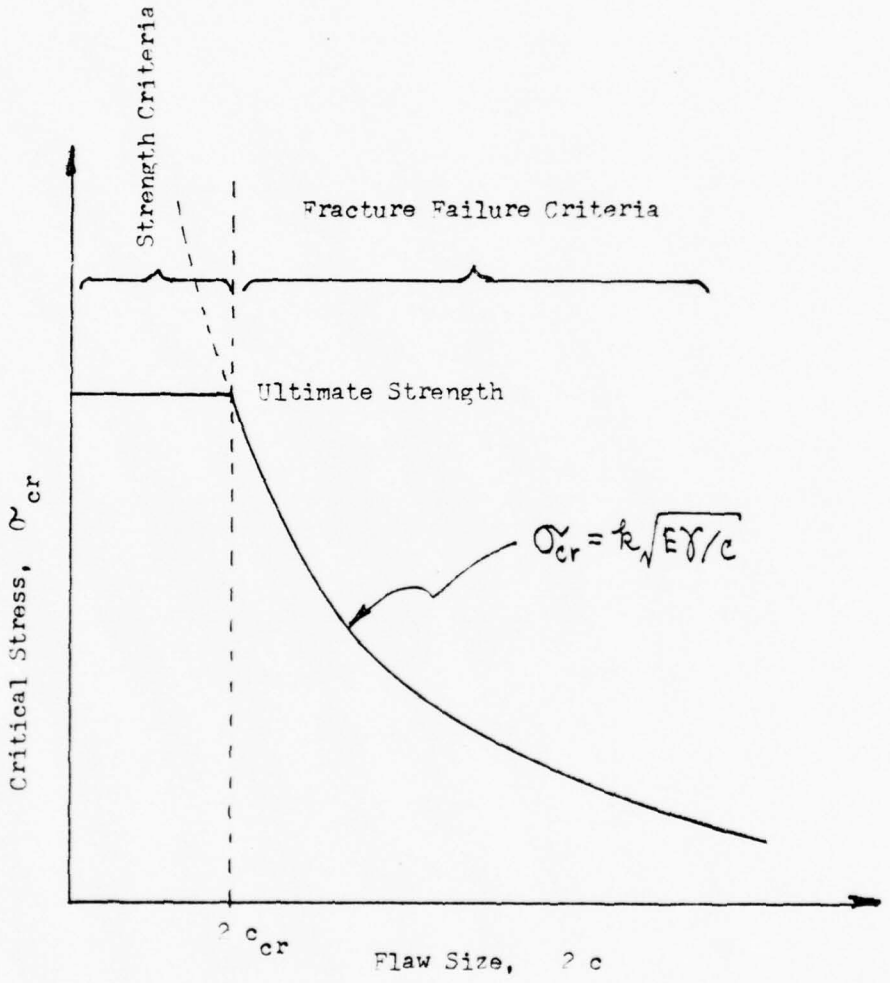

Fig. 1 Strength and Fracture Failure Criteria Regions in a Medium under Uniaxial Tension.

In the "stress intensity factor" (SIF) approach, the crack growth criterion is that if the local state of stress at the crack tip K_I should surpass a certain critical value K_{IC} (characteristic of the geometry, material properties, and applied load) crack growth will initiate.

Owing to complexity in geometry, constitutive nonlinearity, and loading environment encountered by the solid propellant during its life cycle, the prediction of crack behavior is not a trivial matter. The general approach to the solution currently in use is schematically described in Figure 2 to clarify the over-all problems which are encountered in fracture analysis.

In the following sections the primary objective of this report will be stated, current theories and practices concerning prediction of failures due to crack propagation will be reviewed, and those areas needing further improvements will be identified.

2. OBJECTIVES

The objective of this report is primarily concerned with the survey of the current theories and practices related to prediction of failure behavior of solid propellant motors. Based on this survey and the degree of agreement or disagreement between the theory or theories and experimental data as well as real-life failure phenomena, those areas which require further improvement and investigation as well as those research results which can be readily implemented in solid propellant analyses will be identified.

In particular, those theories proposed by Schapery [16-18], Hufferd [19], Lindsey [20], and Swanson [21] will be reviewed and their correlations with experiments examined.

3. SURVEY OF EXISTING THEORIES

In the following subsections, a brief history of the development of fracture mechanics theory is described, then various failure criteria currently in use are summarized. Current theories which show the most promise are then reviewed, and associated numerical and experimental techniques as well as correlations among the theories and existing experimental data are discussed. Finally, various theories are summarized in a table to facilitate future reference.

3.1 Brief Historical Sketch

The origin of fracture mechanics is rightfully traced back to Griffith [8]. Using the surface energy concept and Ingliss' elastic analysis [22], he arrived at an expression for the critical stress σ_{cr} for failure in an infinite

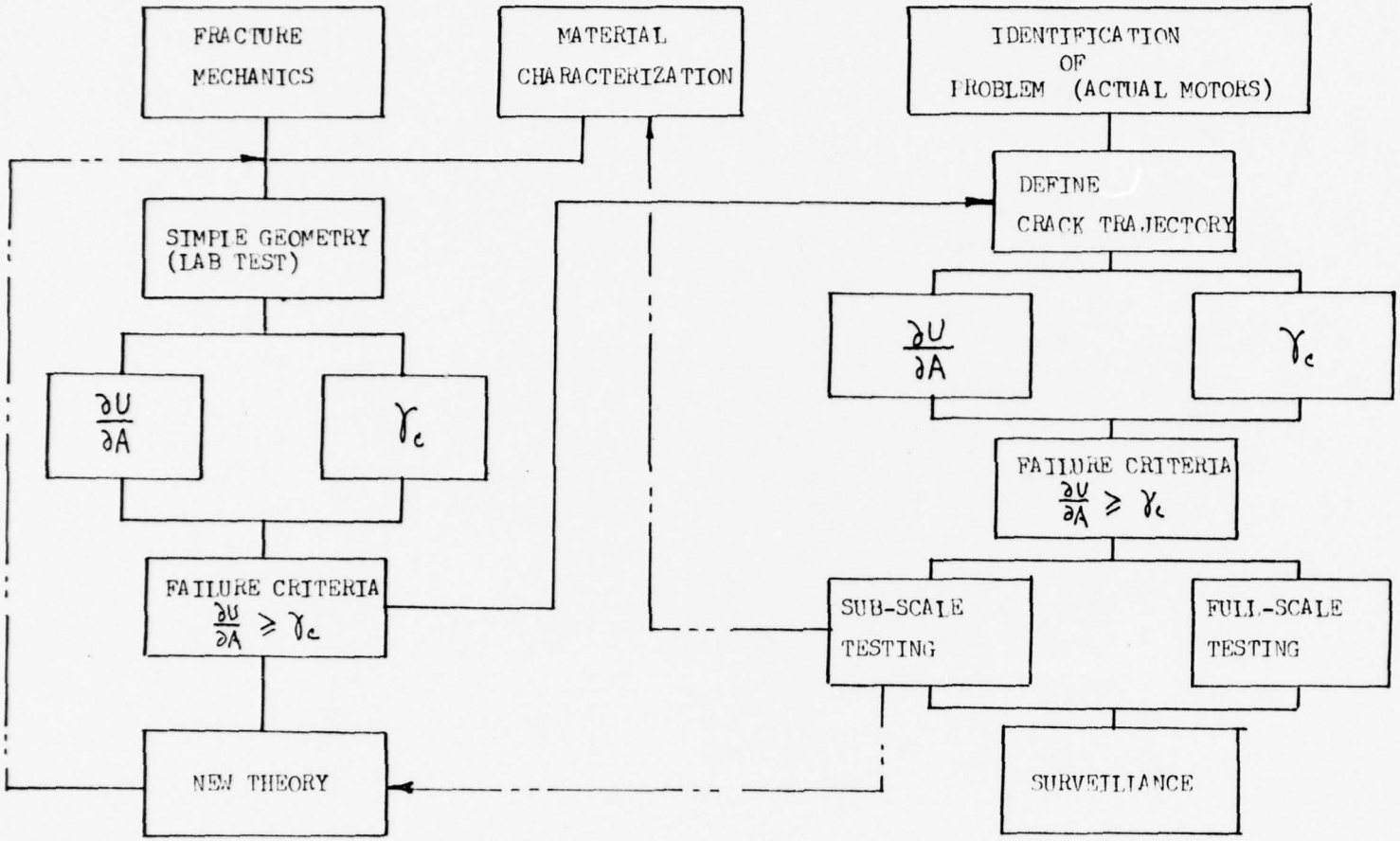

Fig. 2 Schematic Flow Chart for Fracture Analysis.

elastic solid containing a crack of size 2 C as

$$\sigma_{cr} = \sqrt{\frac{2\,ET}{\pi\,(1-\nu^2)C}} \quad \text{(plane strain)} \qquad (3$$

Where E is the Young's modulus, T is the surface energy per unit area, the Poisson's ratio, and C is half the crack size.

In spite of the infinite stress at the crack tip due to overextensio of the elastic theory, the result is surprisingly in agreement with the experiments.

Since no material is capable of sustaining infinite stress, neither t stress and displacement fields which occur at the crack tip nor the finit crack growth rate can be accounted for by Griffith's theory. To remove th difficulty Barenblatt [23] developed a cohesive zone model in the neighborh of the crack tip. On the verge of rupture at the crack tip, the cohesive force increases to resist tearing. As a result a finite crack tip stress achieved.

The alternative approach in the crack problem is the use of stress i sity factor K_I or energy release rate G instead of the fracture energy concept. When the stress intensity factor or the energy release rate G (are dependent on applied load and geometry) reaches a critical value, cra growth takes place. One advantage of this method is perhaps the convenie of evaluating the stress intensity factor by the use of superposition of stress intensity factors for various types of load systems which are avai in tabulated forms [24, 25].

Extension of the Griffith Problem to a linearly viscoelastic problem pioneered by Williams [2]. He used a spherical cavity model and a generaliz of fracture energy balance which is referred to as the thermodynamic powe balance [26]. The critical stress is given in a form similar to Griffith's results:

$$\sigma_{cr} = k\sqrt{(E/2\,C)\,(T_b + T_d + T_v + \cdots)}$$

where k is a geometrical factor, E the modulus, and T_b, T_d, T_v, etc. repr dissipation energy associated with brittle, ductile, and viscoelastic pro respectively.

Further improvements of Williams' theory were made by Knauss and his co-workers [27-30], and were applied to solid propellant of the PBAN type b Layton and Bennett [31]. Reasonable agreement between the theory and exper was observed for constant-strain experiments at various temperatures.

Nuismer [32] has observed some discrepancies between Williams' and Gra theories although both theories were based on similar models. By account

for the mass density change which takes place at the crack tip, he showed that both theories gave equivalent results; he also concluded that the thermodynamic power balance law cannot be used to predict crack growth rate without further modification.

More recently, Schapery [16] extended Barenblatt's cohesive-zone theory [23] to viscoelastic materials. Crack initiation time as well as crack growth time is shown to be related to the stress intensity factor through a relatively simple formula [17]. The most significant aspects of Schapery's theory were probably in removing two shortcomings in the previous theories; namely, the assumption of idealized material at the crack tip zone and the complicated crack growth governing equation which could be solved only by numerical techniques.

Using damage function criteria, Hufferd and his co-workers developed a theory and showed the theory to have a reasonably good agreement with uniaxial and biaxial test data on TP-H1011 propellant.

Based on a linear viscoelastic constitutive law modified by a temperature-strain dependent factor ^{a}F, Lindsey developed a quasiviscoelastic method [34]. The validity of the theory is being tested at Chemical Systems Division of United Technologies on AFRPL Contract F04611-75-C-0027, " Predictive Techniques for Failure Mechanisms in Solid Rocket Motors". Swanson extended Schapery's cohesive-zone theory to the dynamic case [21]. In the absence of dynamic effects, this theory reduces to that of Schapery.

Using Knauss' basic approach [27-29], the stress intensity factor concept, and an extensive finite-element numerical analysis [33, 34], Francis, et al [35] developed a viscoelastic fracture analysis for a two-dimensional realistic rocket geometry using Solithane 113, and found reasonable agreement between the theory and experiment for crack initiation. However, he found that the analytic predictions of crack growth history required a more accurate description of material characterization with temperature dependence than was available.

Swanson used Schapery's theory [16] and approximate analysis [17] in conjunction with existing data on realistic solid propellant materials [19, 35, 36] for a correlation study. The agreement between theory and experimental data was found to be excellent for a wide range of variables (temperature, strain level, strain rate, etc.) provided the fracture energy density was modified to account for history dependence.

Beckwith and Wang [37] also applied Schapery's approximate theory to a constant strain rate experiment on crack initiation and growth rate using biaxial composite-modified double-base (CMDB) propellant specimens to study the effects of strain, temperature, and pressure dependence as well as effects of prestrain damage and rehealing.

Presently, Chemical Systems Division/United Technologies is engaged in an extensive on-going research and development program (AFRPL Contract F04611-75-C-0027) concerned with the failure mechanisms of solid propellants. It is anticipated that the result of this research will bring to light many aspects of failure prediction theories as well as techniques so as to make engineering application of fracture mechanics to the design, analysis, and surveillance of solid propellant motors well standardized routine matters.

3.2 Failure Criteria

In solid propellant motor structural design and integrity verification, it is imperative that a set of criteria be established for analytical assessment and prediction of the physical behavior of motors throughout their service life. Owing to the temperature and time dependence, complex geometry, nonlinear (thermorheologically simple or complex) responses, as well as aging and rehealing processes inherent to some propellant materials, a unified set of criteria such as might exist for a monolithic, isotropic, elastic material is yet to be developed.

From a practical point of view (recognizing factors such as economics, time, and ever-changing materials in development), the current practice is to resort to what may be referred to as discrete failure criteria, in which safety factors based on past experiences are incorporated to account for the uncertainties. In the case of unflawed motors, this approach has proven to be adequate most of the time as demonstrated in the past designs. On the other hand, in the case of motors with flaws, the criticality of flaw size, modes and rate of crack initiation and growth, nonlinear characteristics of material at the crack tip, and aging and/or rehealing characteristics are some of the factors which need to be considered. In general, the crack initiation and growth predictions depend on two failure criteria, namely "critical fracture energy density" and "stress intensity factor".

An overview of the failure criteria is summarized in Figure 3.

In any strength or failure analysis, first the potential modes of failure must be predicted - either analytically, experimentally, or from past experience. Once the modes of failure are known or surmised under various loading conditions experienced by the solid propellant motors, appropriate experiments must be carried out to simulate a realistic loading environment to establish the corresponding failure criteria. The vast amount of effort exerted in the past on research associated with the design of solid propellant motors has more or less standardized procedures for failure prediction [1]. However, new revisions based on more recent findings are definitely in order, particularly in the areas of cumulative damage criteria, probabilistic failure studies, and rate dependent characterization of fracture energy [37].

3.3 Review of Current Fracture Mechanics Theories

As previously mentioned, prediction of crack initiation and growth is governed by two alternative criteria, namely that of "energy" and "stress intensity factor". In their respective fundamental forms, these criteria are described by the following equations.

$$\frac{\partial U}{\partial A} \geq \gamma_c \tag{3.3}$$

$$K_I \geq K_{IC} \tag{3.4}$$

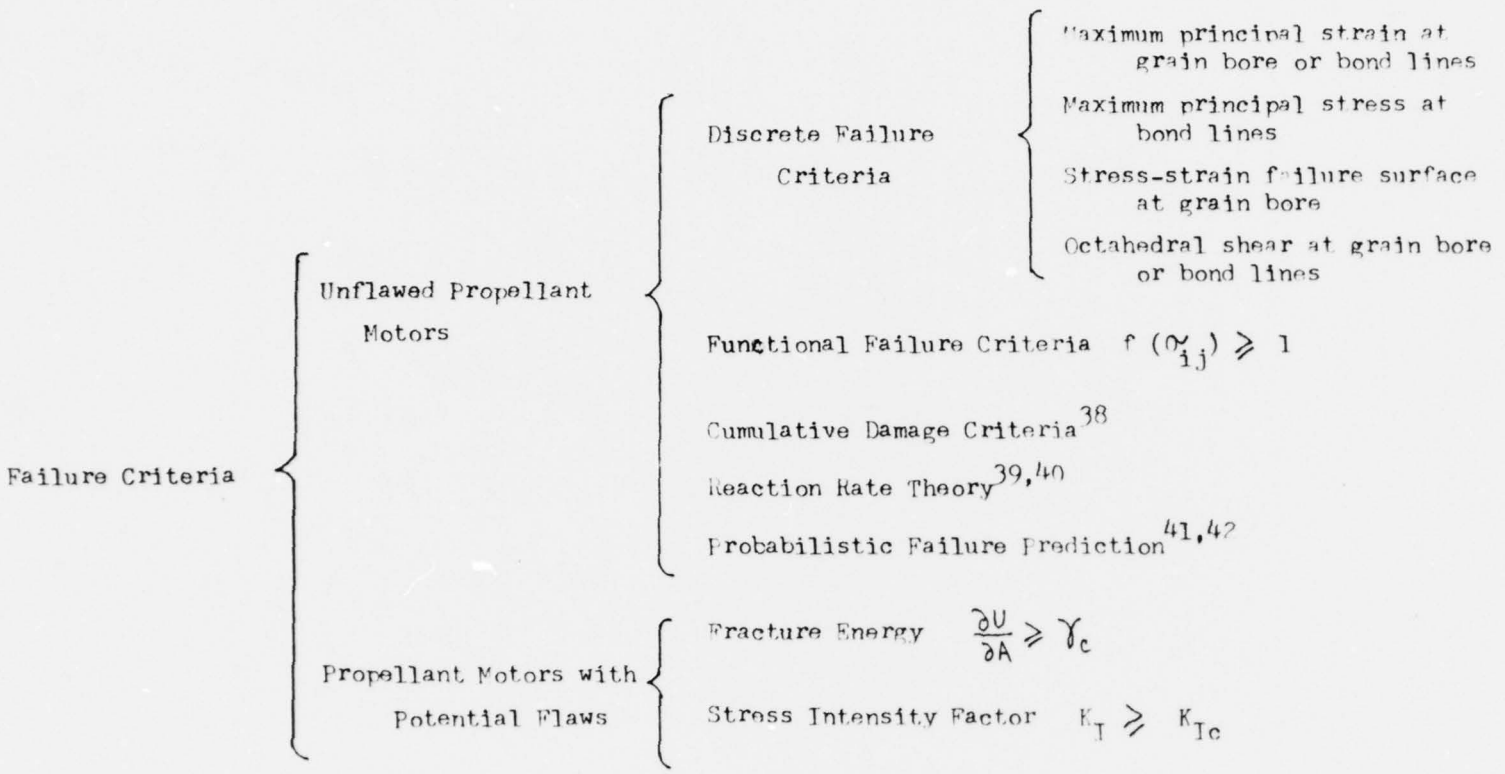

Fig. 3 Overview of Failure Criteria.

In either case, the left hand side of the equation is evaluated by continuum mechanics using various numerical techniques, whereas the right hand side of the equation, which represents the critical value that may be sustained by the material in question, is determined from experiment under various loading conditions (e.g., thermal cool-down, controlled strain rate, relaxation, pressurization, etc.). The true verification of equation (3.3), which requires independent determination of the critical fracture energy solely by physics, is still a task of the future.

On the other hand, with modern developments in numerical analysis utilizing sophisticated computer codes, the left hand side of the equation is readily determined. Owing to the complexity associated with geometries as well as constitutive laws, final solution to all modern engineering problems seems to be at the mercy of available numerical techniques. Perhaps the most versatile and powerful numerical technique available today is the "finite element method".

To meet the demand of ever-increasing sophistication in solid propellant motor analysis, AFRPL has sponsored the development of a family of structural analysis computer programs. The first computer program, developed under a contract to United Technology Center (now CSD) in conjunction with the Texas Institute for Computational Mechanics (University of Texas), is referred to as TEXGAP [45, 46]. The evolution of this computer code in subsequent contracts to other contractors into TEXGAP-2D and TEXGAP-3D (with modifications), together with possible future improvements, is shown in Figure 4. As in any computer code, it must be remembered that the results which one gets are only as good as the data one puts into the computer codes [47].

In the following subsections, some of the theories which have been (or are being) subjected to experimental verification using realistic propellant materials will be outlined and their correlation with the existing experimental data examined.

3.3.1 Schapery's Cohesive-Zone Theory [16-18]

Prior to Schapery's work, the previous theories [27-30] were subjected to two rather restrictive limitations, namely, the fracture zone was modeled by highly idealized material and the prediction of time-dependent crack size was given only numerically (or, if analytically, by severely idealized media). By generalizing Barenblatt's cohesive zone model and introducing an assumption that the second derivative of the logarithm of creep compliance with respect to the logarithm of time is small, he derived a relatively complete theory for the prediction of crack initiation and growth. In his theory, although the material outside the fracture zone is assumed to be linearly viscoelastic, the crack-tip zone material is not restricted to obey any one particular constitutive law. The consequence of his theory is summarized in four equations: namely, stress distribution implicitly in terms of opening-mode stress intensity factor; two displacement field equations in terms of material compliance and stress distribution at and near the crack tip; and a failure criterion equation expressed in terms of stress and displacement fields in the failure zone. To find the solution (crack size as a function of time) to this

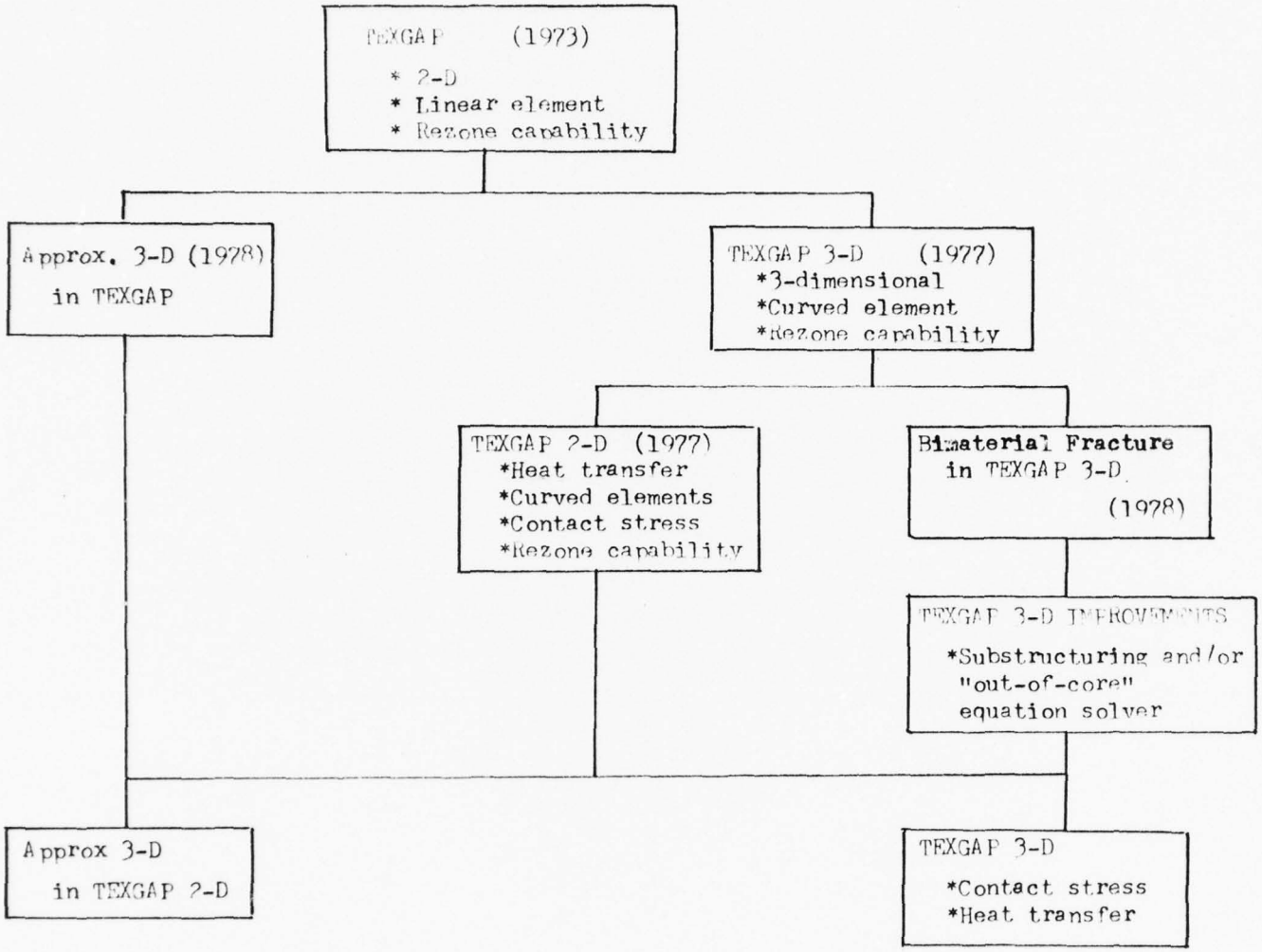

Fig. 4 Evolution and Possible Future Projection of TEXGAP.

set of simultaneous nonlinear integral equations is seemingly an insurmountable task. However, with the introduction of an assumption that the curvature of creep compliance in a log-log space is small (as is the case with most polymeric materials), the four governing equations for the prediction were greatly simplified [17].

Evaluating the work done by the surrounding zone on the failure zone, and equating it to the fracture energy Γ, Schapery arrived at an expression which relates the fracture energy Γ to the material properties and the stress intensity factor

$$\Gamma = Cv(\tilde{t}_{\alpha})\ K_I^2/8 \qquad (3.5)$$

where Cv(t) is related to the uniaxial plane strain creep compliance D(t), for a constant value of Poisson's ratio ν, by the relation

$$Cv(t) = 4(1-\nu^2)D(t)\ , \qquad (3.6)$$

K_I is the opening mode stress intensity factor, and $\tilde{t}_{\alpha}$ is approximately equal to one third the time required for the crack tip to travel the failure zone width α at the rate of $\dot{a}$, i.e.

$$\tilde{t}_{\alpha} \doteq \alpha/(3\dot{a}) \qquad (3.7)$$

Finally with a power law approximation

$$C_v = C_1 t^n \qquad (3.8)$$

and the help of equations (3.6) and (3.7), the crack propagation speed $\dot{a}$ is explicitly given as

$$\dot{a} = \tfrac{1}{2}\pi (C_1/8\Gamma)^{1/n} \lambda_n^{1/n} \quad (K_I / \sigma_m I_1)^2 \qquad (3.9)$$

where σ_m is the maximum stress in the failure zone and I_1 is related to the stress distribution f in the failure zone.

$$I_1 = \int_0^1 f(\alpha n)/\sqrt{n}\ dn \qquad (3.10)$$

In the special case for which Γ is proportional to velocity and $\sigma_m I_1$ is constant, expression (3.9) reduces to

$$\dot{a} = AK_I^q \qquad (q = 2\ (1 - 1/n)) \qquad (3.11)$$

where A is a constant represented by the coefficient of the K_I^2 term in equation (3.9).

For the case where stress intensity factor is a nondecreasing function of time and the failure stress distribution is a constant, the crack initiation law is given by

$$\Gamma = \frac{1}{8} K_I^2 (t_i) C_v^{(2)} (t_i) \tag{3.12}$$

where $C_v^{(2)}$ is referred to as secant compliance, defined by

$$C_v^{(2)} = C_v^{(2)} (t) = \left[K_I^2(t)\right]^{-1} \int_o^t C_v(t-\tau) \left[\frac{dK_I^2(\tau)}{d\tau}\right] d\tau \tag{3.13}$$

In essence, the result of Schapery's theory is given by equation (3.9) for the crack growth rate and equation (3.12) for the calculation of initiation time.

Agreement was remarkably good between this theory and experimental data previously obtained by Knauss for predicting the time to failure of a centrally cracked solithane 50/50 specimen under load [28], and reasonably good for predicting the crack velocity in a long strip under moderate strain.

Swanson [48] has carried out a detailed correlation study of Schapery's approximate analysis above with the existing data on PBAN propellant [19, 36, 49, 50]. Unlike the solithane specimens of previous comparisons, he noticed that the fracture energy for highly-filled propellant can no longer be assumed constant but is possibly related to crack propagation rate $\dot{a}$. As for the prediction of initiation time [50], a strong time dependence of fracture energy was observed. He concluded that at least for the class of propellant data used for comparison, the form of time dependence of fracture energy may be related to loading history and requires further investigation.

Beckwith and Wang [37] carried out a series of experiments on CMDB (Composite Modified Double Base) propellant. They found significant effects of strain level on the crack propagation speed, although for a constant strain level test the power-law form of equation (3.11) was retained. This led them to consider a crack propagation law of the form

$$\dot{a} = A(\varepsilon_o) K_I^q \tag{3.14}$$

where the strain level (ε_o) dependence may enter coefficient A through creep compliance or the nonlinear characterization of the failure zone. However, the exact functional relation between A and ε_o requires further investigation. Based on crack growth data on HTPB obtained at United Technologies, Chemical Systems Division, Schapery observed a power-law equation of the form [50],

$$\dot{a} = \frac{1}{a_T}\left[\frac{K_I}{f}\right]^q \tag{3.15}$$

where f is a factor dependent on the strain level by the equation

$$\log f = \log K_I - \frac{1}{q} \log \dot{a} - \frac{1}{q} \log a_T \qquad (3.16)$$

Due to the lack of data points, determination of the exponent q requires further experimental work.

Beckwith and Wang also discussed the effects of temperature and pressure on the crack growth rate. They found that the general temperature-time shift principle is satisfied, whereas a pressure enhancement of approximately 25 to 30 percent on the stress intensity factor was observed. The latter finding on pressure enhancement is consistent with the previous observation of Layton and Bennett [31].

To sum up, Schapery's power-law equation seems to be in extremely good agreement for unfilled polymeric materials. However, due to a relatively large value assumed by the exponent q, experimental determination of accurate crack initiation time could be quite difficult. As for solid propellant, due to the relatively close packing of the solid filler, the local strain is quite nonlinear although the global strain may be small. There is an urgent need for a nonlinear viscoelastic fracture analysis, both analytical and experimental, based on the foundation already laid for the linear analysis.

3.3.2 Swanson's Dynamic Crack Propagation Theory [21]

Using the elastic-viscoelastic correspondence principle, Swanson examined dynamic, opening-mode, constant velocity crack propagation in a general linear viscoelastic material. Both the singular line crack and cohesive zone models were examined. Since the singular line model leads to a solution which is physically unrealistic, only the result for the cohesive zone model which was developed by Schapery will be highlighted here. Application of the correspondence principle to Craggs' elastic solution [51] leads to a relation between the fracture energy and the opening mode stress intensity factor as well as dynamic factor A_1 and creep function J of the material.

$$\Gamma = \frac{K_I^2}{4} \frac{C}{\alpha}^{3/2} \int_0^t A_1 (t-\tau) \frac{\partial}{\partial \tau} \int_0^\tau J(\tau - \xi) \sqrt{\xi} \, d\xi \, d\tau \qquad (3.17)$$

where C is the crack velocity and α is the failure zone width. With the creep function J approximated by the power law

$$J = J_1 t^n \qquad (3.18)$$

the governing equation (3.17) for crack propagation simplifies to

$$\Gamma = \frac{(1-\nu) B_1 J_1 \alpha^n}{4} \frac{K_I^2}{C^n} \left\{ 1 - B_2 \alpha^{n/2} \sqrt{\rho J_1} \, C^{(1 - n/2)} \right\} \qquad (3.19)$$

where B_1 and B_2 are related to the exponent n and the Gamma function of n in (3.18).[1] By setting mass density ρ to zero, Schapery's quasi-static result is readily obtained. The limiting value is readily shown to be

$$C_{max} = 1/\left[B_2 \alpha^{n/2} \sqrt{\rho J_1}\right]^{2/(2-n)} \qquad (3.20)$$

Figure 5 shows a typical comparison between the quasistatic and dynamic prediction of crack velocity.

For the same value of stress intensity factor, the crack velocity is smaller for dynamic case due to the inertia effect. This is in agreement with general observation, however further experimental work is needed to substantiate the quantitative results of this theory.

Since the elastic-viscoelastic correspondence principle is applicable as shown in references 17 and 32, extension of this theory to a more complex stress state should not present undue difficulty.

3.3.3 Hufferd's Damage Function Theory [19]

Based on a nonlinear viscoelastic constitutive law with permanent memory and the thermodynamic power balance of Williams [2], Hufferd and his co-workers derived a nonlinear integro-differential equation for the determination of crack length as a function of time.

For a simple geometry, material behavior, and constant uniaxial strain rate stretching of a large thin sheet containing a crack with size 2a, this equation may be solved explicitly for the normalized crack size λ as a function of time:

$$\lambda(t) = \frac{a(t)}{a(0)} \doteq P \cosh Pt \qquad (3.21)$$

where P is the fracture dissipation power defined by $P = \sqrt{B/2\gamma}$ and B is defined by an integral involving the fracture energy density γ, geometry, loading history, and relaxation modulus of the material.

For a more complex geometry, the locus of the crack extension must be postulated by the use of some criterion. Instead of the usual maximum stress criterion, the damage function criterion which is appropriate to material with permanent memory was used in the analysis.

The solution is then obtained in a form analogous to equation (3.21):

$$\lambda = F\left[\sqrt{d} - \sqrt{d_c}\right] \doteq \cosh C\left[\sqrt{d} - \sqrt{d_c}\right] \qquad (3.22)$$

where d is the experimentally confirmed damage function expressed in terms of the first and second stress invariants θ_1 and θ_2 as a function of loading history,

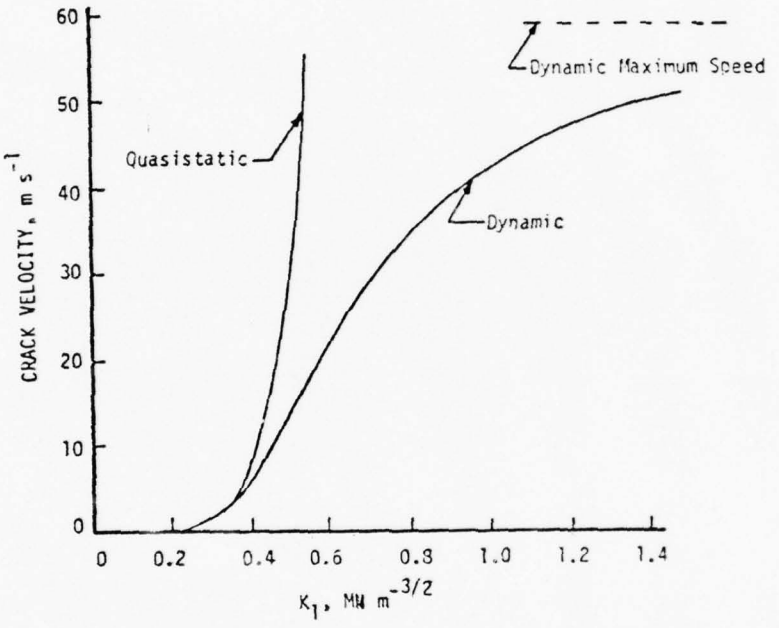

Fig. 5 Comparison of Quasistatic and Dynamic Cohesive Zone Viscoelastic Fracture Theories
(Fig. 2 of Reference 21)

$$d(t) = \max_{0 \le s < \infty} \left[\theta_1^2 (t-s) - 3\theta_2 (t-s) \right] \qquad (3.23)$$

and d_c is the critical damage measure.

Time dependence enters in equation (3.22) implicitly through d and d_c in which flaw geometry and loading conditions are incorporated.

Extensive uniaxial and biaxial tests were carried out for TP-H1011 and ANB-3066 propellants, and they indicated reasonable agreement for crack size extensions up to about twice the original size. Strictly speaking, equation (3.21) was derived with the assumption that the normalized crack size λ is nearly equal to 1. Application of this theory to a more realistic propellant environment was investigated under the AFRPL/CSD/UT Failure Mechanisms Program; predictions were made for UTP 18,803A motor failure tests. It was determined that more research is needed before the theory will be ready for engineering application.

3.3.4 Lindsey's Quasiviscoelastic Method [20]

It is well known that in the case of simultaneous straining and thermal cool-down, analysis based on linear thermorheologically simple constitutive law often underpredicts the stress. Since a nonlinear viscoelastic constitutive law capable of handling multitudes of thermal as well as mechanical load histories is yet to be developed, similitude tests are sometimes utilized for nonlinear characterization. Simple uniaxial or biaxial test specimens are subjected to a load history (thermal and/or mechanical) similar to that encountered by the solid propellant under analysis. The constitutive law for the uniaxial case then takes a familiar hereditary form except for the temperature strain correction factor $a_F(t, \varepsilon)$.

$$\sigma = \int_0^t a_F(T, \varepsilon) E \left[(t - \tau)/a_T \right] \dot{\varepsilon} \, d\tau \qquad (3.24)$$

Based on this constitutive model and appropriate numerical analysis referred to as the quasiviscoelastic method (See Section 5. Reference 1 for detail.), Lindsey proposed to establish fracture criteria in terms of K_I for the cylindrical bore crack and $K_I - K_{II}$ failure envelope for the end crack.

The method of analysis consists of the division of time into small intervals during which the crack is assumed to be stationary, and the application of quasielastic analysis during each time interval. This method is currently under experimental verification at Chemical Systems Division/United Technologies.

3.5 Summary

A brief history of the development of viscoelastic fracture mechanics, an overview of the necessary considerations for failure prediction, and some pertinent theories for predicting crack initiation and growth are presented in the above sections.

Current theories associated with linear viscoelastic fracture analysis have been demonstrated to be adequate in predicting the fracture behavior of linearly viscoelastic material. However, in some experimental correlation studies made, the fracture energy of propellant was found to be highly dependent on strain rate as well as on past loading history. The exact nature or form of this time dependence is not well known and further studies are needed for better characterization of the constitutive law taking into account the phenomena of debonding, aging, rehealing, etc. Rational mechanics[53] does provide foundations for the nonlinear characterization of viscoelastic materials [54]. However, a useful, realistic characterization is needed for solid propellant. Recently, Quinlan [55] proposed a constitutive model with debonding particularization of his general theory to solid propellant material and experimental verification is an objective of current and planned work under AFRPL sponsorship.

The extension of the existing fracture theory (which has proven appropriate for predicting opening-mode fracture) to a more complex geometry is currently in progress under the AFRPL "Failure Mechanisms" program at Chemical Systems Division/United Technologies on scaled-down cylindrical bore specimens under thermal cool-down and pressurization. A successful outcome from this program should be useful in setting up standards for future investigations.

Some of the theories surveyed and experimental applications of these theories to solid propellant materials are summarized in Tables 1 and 2.

4. CONCLUSIONS AND RECOMMENDATIONS

The fracture energy density Γ, regarded to be relatively constant for Solithane 113, was observed to be highly dependent on time when the theory was applied to solid propellant materials. Since Schapery's theory does allow Γ to be time dependent, investigations of the exact form of this time dependence for a variety of propellant materials and loading conditions may be useful.

Of all the theories reviewed, Schapery's cohesive-zone model seems to be the most sound from the analytical point of view as well as its capability in predicting crack growth for a wide range of parameters. Possible extensions of Schapery's theory include [56]:

(i) Fracture analysis for a complex geometry giving rise to a complex stress field,

(ii) Nonlinear fracture mechanics adopting the J-integral as the failure criterion,

(iii) Nonhomogeneous media fracture analysis,

(iv) Bimaterial fracture mechanics.

TABLE 1. SUMMARY OF VISCOELASTIC FRACTURE MECHANICS THEORIES

Author	Year	Constitutive Law	Crack Tip Model	Method of Analysis	Prediction of Crack	
					Initiation	Growth
Williams[2]	1965	Linear Viscoelastic	Spherical Void	Elastic-Viscoelastic Correspondence Principle	Yes	No
Knauss[28]	1970	Linear Viscoelastic	Linear Viscoelastic Solution	Numerical	Yes	Yes
Nuismer[32]	1974	Linear Viscoelastic	Griffith Crack	Correspondence Principle	Yes	No
Schapery[16]	1975	Linear Viscoelastic	Cohesive Zone	Correspondence Principle	Yes	Yes
Hufferd[19]	1975	Nonlinear Viscoelastic	Far field stress - displacement	Damage Function Criteria	Yes	Yes
Lindsey[20]	1976	Linear Viscoelastic	Stress Intensity Factor	Quasiviscoelastic Method	Yes	Yes
Swanson[21]	1977	Linear Viscoelastic	Cohesive Zone	Correspondence Principle	No	Yes

TABLE 2. SUMMARY OF SOME APPLICATIONS OF VISCOELASTIC FRACTURE THEORIES TO SOLID PROPELLANT MATERIALS

Author	Year	References	Materials	Experiment	Results
Layton & Bennett[31]	1970	2	PBAN	Biaxial Constant strain rate	$\frac{\partial U}{\partial A}$ vs a; γ vs t } a vs t
Francis, Carlton & Lindsey[49]	1974	28	PBAN Solithane 113	2-D Cylinder Pressurization	a vs t
Hufferd[19]	1975	19	TP-H1011 ANB-3066	Uniaxial/Biaxial Constant stress Constant strain rate	a vs t a vs σ
Swanson[48]	1976	17, 19, 49 50, 51	PBAN		K_I vs a a vs σ
Beckwith[37]* & Wang	1978	17	CMDB	Constant strain rate	Effects of Strain, temp, pressure, and prestrain damage

* Francis and Carlton also reported similar results in the AFRPL/CSD(UT) Failure Mechanism Program (1976).

Although some experimental data exist on bimaterial (adhesive) fracture, it has not quite achieved the sophistication of cohesive fracture analysis [57].

Aging of the solid propellant can be detrimental for propellants with long storage time, possibly under a hostile environment. Some data are available from an AFRPL-sponsored program in which the ten-year mechanical characteristics of TP-H1011 and ANB-3066 were accurately predicted from one-year accelerated aging tests [58]. However, aging characteristics may vary depending on the constituents of the propellant, and thus a general conclusion obtained from one type of propellant may not necessarily apply to others [59].

There is evidence indicating that the assumptions of linear thermorheologically simple behavior are not justified for some propellants [54, 60]. This will lead to a need for more sophisticated numerical techniques. The finite element method enjoys perhaps the most popularity; however, with the more sophisticated material characterization, it can become very costly. Searching for an alternative method [61], if it proves to be less expensive and just as effective, would be a worthwhile effort.

Basically, solid propellant material is a particulate composite material with relatively stiff particles embedded more or less uniformly in the softer matrix material. Almost universally, the energy criterion is adopted for fracture analysis in the case of macroscopic flaws. The criterion expressed in equation (1.1) requires calculation of the strain energy release rate by the use of continuum mechanics, and the independent measurement of fracture energy density by the use of physics; however, independent estimation of the latter term solely from physics is yet to be accomplished [11]. On the other hand, a seemingly unflawed propellant may contain microscopic flaws which form nuclei for subsequent macroscopic flaws. Wu proposed a characteristic volume concept for composite materials and application of a functional failure criterion to such a volume containing a microscopic flaw [11]. Such an approach or an extension of such would be desirable in establishing a more unified failure criterion for solid propellants.

Based on observations made by Lindsey [20] and Knauss [62], the actual profile of the crack tip in propellants tends to be blunt rather than sharp. This indicates that conventional fracture mechanics based on stress intensity factor could possibly be replaced by strain failure criteria near the crack tip. This, of course, is quite speculative*, but further investigation might substantiate this concept.

In view of the above discussions and survey of the current research on failure and particularly on fracture behavior of solid propellant, the following recommendations are made:

For Immediate Future Implementation or Development:

1. Standardization of viscoelastic fracture mechanics analysis and incorporation in the JANNAF Solid Propellant Structural Integrity Handbook.

* In fact Bills[63] contends that such rounded crack tips occur only in a laboratory test specimen and never in actual motors.

2. In-depth correlation studies of all available experimental data.

3. Correlation studies of similtude tests on nonlinear behavior.

4. Experimental verification of existing theories as applied to complex stress fields.

5. Nonlinear characterization of solid propellant behavior (debonding, aging, rehealing, etc.).

6. Nonlinear fracture mechanics.

7. Extension of existing theories to bimaterial (adhesive) fracture analysis.

8. Experimental verification of dynamic fracture theory.

9. Investigation of the feasibility of simple strain failure criteria at the crack tip.

10. Reexamination of the validity of the use of fracture failure criteria obtained from lab test specimens in the prediction of fracture behavior of actual solid propellant motors.

For Future Investigation:

1. Functional failure criteria based on a critical volume concept.

2. Development of economical numerical analysis techniques.

3. Independent evaluation of the time-dependent fracture energy density.

4. Adoption of the J-integral as a failure criterion in anisotropic nonhomogeneous material.

REFERENCES

Letters (A), (B), (C), (D) appearing at the end of each reference refer to the following categories:

(A) Basic Theory
(B) Experimental
(C) Numerical Analysis
(D) Solid Propellant Applications

1. JANNAF Solid Propellant Structural Integrity Handbook, CPIA Publication 230, September 1972. (D)

2. Williams, M. L., "Initiation and Growth of Viscoelastic Fracture", Int. J. Fracture Mech., Vol I, Dec. 1964, pp. 292-310. (A)

3. Smith, T. L., "Ultimate Tensile Properties of Elastomers. I. Characterization by a Time and Temperature Independent Failure Envelope", J. Pol. Sci., Vol I, 1963, pp. 3597-3615. (A) (B)

4. Nelson, J. M., and Kruse, R. B., "Evaluation of Failure Criteria for HTPB Propellants", JANNAF/SMBWG, CPIA Pub. 264, May 1975, pp. 233-250. (D)

5. Bills, K. W., Jr., "Solid Propellant Cumulative Damage Program", Final Report, AFRPL-TR-68-131, Oct. 1968. (D)

6. Mellette, R. V., "Modification of Aerojet Cumulative Damage Criterion to Utilize Nonlinear Stress Allowable", JANNAF/SMBWG 14th Meeting, CPIA Pub. 283, Vol I, Apr. 1977, pp. 23-40. (B) (D)

7. Martin, D. L., Jr., "The Application of Smokeless Propellant Motors", JANNAF/SMBWG 14th Meeting, CPIA Pub. 283, Vol II, Apr. 1977, pp. 105-120. (D)

8. Griffith, A. A., "The Theory of Rupture", Proc. 1st. Int. Cong. App. Mech, Delft, 1924, pp. 55-63. (A)

9. Irwin, G. R., Fracture Dynamics, Fracture of Metals, American Society of Metals, Cleveland, 1948, pp. 147-166. (A)

10. Rivlin, R. S., "Rupture of Rubber, Part I. Characteristic Energy of Tearing", J. Polymer, Sci., Vol X, No. 3, 1953, p. 291. (B)

11. Wu, E. M., "Strength and Fracture of Composites", Chapter 5. Composite Materials, Vol V, Fracture and Fatigue, L. J. Broutman, Ed., Academic Press, 1974, pp. 191-247. (A)

12. Advances in Applied Mechanics, Vol. VII, H. L. Dryden and T. von Karman, Eds., Academic Press, 1962. (A)

13. FRACTURE, Vol. II and VII, H. Liebowitz, Ed., Academic Press, 1968. (A)

14. Advances in Research on the Strength and Fracture of Materials, D. M. R. Taplin, Ed, Vols. I, IIIA, IIIB, Pergamon, 1977. (A)

15. Irwin, G. R., "Fracture", Encyclopedia of Physics, Springer, Vol. VI, 1958, pp. 551-590. (A) (B)

16. Schapery, R. A., "A Theory of Crack Initiation and Growth in Viscoelastic Media, I. Theoretical Development", Int. J. Fracture, Vol XI, 1975, pp. 141-159. (A)

17. Schapery, R. A., "A Theory of Crack Initiation and Growth in Viscoelastic Media,II. Theoretical Development", Int. J. Fracture, Vol. XI, 1975, pp. 369-387. (A) (C)

18. Schapery, R. A., "A Theory of Crack Initiation and Growth in Viscoelastic Media, III. Analysis of Continuous Growth", Int. J. Fracture, Vol. XI, 1975, pp. 549-562. (A)

19. Hufferd, W. L. Laheru, K. L., and Jacobs, H. R., "On the Fracture of Viscoelastic Materials", JANNAF/SMBWG 1975, CPIA Pub. 264, pp. 339-350. (A)

20. Lindsey, G. H., "Quasiviscoelastic Methods", Interim Report, Chemical Systems Division/United Technologies, Proj. 2540, Contract No. F04611-75-C-0027, AFRPL. (A)

21. Swanson, S. R., "Dynamic Viscoelastic Crack Propagation", JANNAF/SMBWG 14th Meeting, CPIA Pub. 283, 1977, pp. 141-150. (A)

22. Ingliss, C. E., "Stresses in a Plate Due to the Presence of Cracks and Sharp Corners", Trans. Inst. Nav. Arch., Vol. 55, 1913, pp. 219-230. (A)

23. Barenblatt, G. I., "The Mathematical Theory of Equilibrium Cracks in Brittle Fracture", Advances in Applied Mechanics, Vol. VII, H. L. Dryden and T. von Karman, Eds., Academic Press, 1962, pp. 56-129. (A)

24. Paris, P. E., and Sih, G. C., "Stress Analysis of Cracks", ASTM Special Techniqal Publication No. 381, 1964. (A)

25. Parmerter, R. Reid, "Stress Intensity Factors for Three-Dimensional Problems", AFRPL-TR-76-30, 1976. (A)

26. Williams, M. L., "Fracture of Viscoelastic Materials", Fracture of Solids, Interscience Publishers, 1963, pp. 157-188. (A)

27. Knauss, W. G., "Stable and Unstable Crack Growth in Viscoelastic Media", Trans. Soc. Rheology, Vol. XIII, 1969, pp. 291-313. (A)

28. Knauss, W. G., "Delayed Failure-The Griffith Problem for Linearly Viscoelastic Materials", Int. J. Fracture Mech., Vol. VI, 1970, pp. 7-20. (A)

29. Knauss, W. G., and Dietmann, H., "Crack Propagation Under Variable Load Histories in Linearly Viscoelastic Solids", Int. J. Engr. Sci., Vol VIII, 1970, pp. 643-656. (A)

30. Mueller, H. K., and Knauss, W. G., "Crack Propagation in a Linearly Viscoelastic Strip", J. App. Mech, Vol. 38, 1971, pp. 483-488. (A)

31. Layton, L. H., and Bennett, S. J., "A Fracture Mechanics Approach to Surveillance", JANNAF/SMBWG 8th Meeting, CPIA Pub. 193, Vol. I, 1970, pp. 209-226. (D)

32. Nuismer, R. J., "On the Governing Equation for Quasi-Static Crack Growth in Linearly Viscoelastic Materials", J. App. Mech, Vol. 41, 1974, pp. 631-634. (A)

33. Graham, G. A. C., "Two Extending Crack Problems in Linear Viscoelasticity Theory", Quarterly of Applied Mathematics, Vol. 27, No. 4, 1970, pp. 497-507. (A)

34. Kobayashi, A. S., Maiden, D. E., Simon, B. J., and Isida, S., "Application of Finite Element Analysis to Two-Dimensional Problems in Fracture Mechanics", ASME Paper No. 69-WA/PVP-12, 1969. (C)

35. Bennett, S. J., "The Use of Energy Balance in Rocket Motor Grain Integrity Studies", JANNAF/SMBWG 8th Meeting, CPIA Pub. 193, Vol. I, 1970, pp. 393-403. (D)

36. Jacobs, H. R., Hufferd, W. L., and Williams, M. L., "Further Studies of the Critical Nature of Cracks in Solid Propellant Grains", AFRPL-TR-75-14, 1975. (A) (B) (C) (D)

37. Beckwith, S. W., and Wang, D. T., "Crack Propagation in Double-Base Propellants", AIAA Paper No. 78-170, AIAA 16th Aerospace Science Meeting, Huntsville, AL, Jan 16-18, 1978. (D)

38. Bills, K. W., "Applications of Cumulative Damage in the Preparation of Parametric Grain Design Curves and Prediction of Grain Failures in Pressurization", Aerojet Solid Propulsion Company Report 134-26F, August, 1970. (D)

39. Graham, P. H., Robinson, C. N., and Henderson, C. B., "Analysis of Dilatational Failure of Heterogeneous Materials by Reaction Rate Theory", Int. J. Fracture Mech., Vol. V, 1969, pp. 57-62.(A)

40. Henderson, C. B., Graham, P. H., and Robinson, C. N., "A Comparison of Reaction Rate Models for Fracture of Solids", Int. J. Fracture Mech., Vol. VI, 1970, pp. 33-40. (A)

41. Heller, R. A., and Kamat, M. P., "Probabilistic Life Prediction for Motors Subjected to Random Thermal Loads", JANNAF/SMBWG 14th Meeting, CPIA Pub. 283, Vol. II, 1977, pp. 61-76. (A) (D)

42. Cost, T. L., and Dagen, J. D., "Probabilistic Service Life Prediction of Solid Rocket Motors Subjected to Thermal Loading Using Computer Simulation", JANNAF/SMBWG 14th Meeting, CPIA Pub. 283, Vol. II, 1977, pp. 77-90. (A) (C) (D)

43. Zienkiewicz, O. C., and Cheung, Y. K., The Finite Element Method in Structural and Continuum Mechanics, McGraw-Hill, 1967. (C)

44. Oden, J. T., Finite Elements of Nonlinear Continua, McGraw-Hill, 1972. (C)

45. Francis, E. C., et. al., "Case Liner Bond Analysis", AFRPL-TR-74-23. (C) (D)

46. Becker, E. B., and Dunham, R. S., "TEXGAP-3D, A User Oriented Three-Dimensional Static Linear Elastic Stress Analysis Program", User's Manual, The Texas Institute for Computational Mechanics, The University of Texas, March 1977. (C) (D)

47. Shuey, H. M., "The Third Thoughts on Structural Integrity", JANNAF/SMBWG 14th Meeting, CPIA Pub. 283, Vol II, 1977, pp. 1-6 (D)

48. Swanson, S. R., "Application of Schapery's Theory of Viscoelastic Fracture to Solid Propellant", J. Spacecraft, Vol. XII, No. 9, 1976, pp. 528-533. (D)

49. Francis, E. C., Carlton, C. H., and Lindsey, G. H., "Viscoelastic Fracture of Solid Propellants in Pressurization Loading Conditions", J. Spacecraft and Rockets, Vol. XI, 1974, pp. 691-696. (D)

50. Bennett, S. J., "The Use of Energy Balance in Rocket Motor Grain Integrity Studies", JANNAF/SMBWG 8th Meeting, CPIA Pub. 193, Vol. I, 1970, pp. 393-403. (D)

51. Craggs, J. W., "On the Propagation of a Crack in an Elastic Brittle Material", J. Mech. Phys. Solids, Vol. VII, No. 1, 1960, pp. 66-75. (A)

52. Francis, E. C., CSD/UT, and Hufferd, W. L., University of Utah, Personal Communications. (D)

53. Lockett, F. J., and Stafford, R. O., "On Special Constitutive Relations in Non-Linear Viscoelasticity", Int. J. Eng. Sci., Vol. VII, 1969, pp. 917-930. (A)

54. Farris, R. J., et. al., "Development of a Solid Rocket Propellant Nonlinear Viscoelastic Constitutive Theory", AFRPL-TR-75-20, 1975. (D)

55. Quinlan, M. H., "Materials with Variable Bonding", Archive for Rational Mechanics and Analysis, Vol. 67, No. 2, 1978, pp. 165-181. (A)

56. Schapery, R. A., University of Texas, Personal Communications.

57. Francis, E. C., and Jacobs, H. R., "Fracture Considerations for Surveillance Programs", J. Spacecraft, Vol. XIII, No. 8, 1976, pp. 451-455. (D)

58. Layton, L. H., "Chemical Aging Studies on ANB-3066 and TP-H1011 Propellants", AFRPL-TR-74-16, 1974. (D)

59. Biggers, R., and Stacer, R., AFRPL, Personal Communications. (D)

60. Bills, K. W., Jr., and Bischel, K. H., "Time Temperature Superposition Does Not Hold for Solid Propellant Stress Relaxation", JANNAF/SMBWG 14th Meeting, CPIA Pub. 283, Vol I, pp. 69-85. (D)

61. Quinlan, P., University College, Cork, Ireland, Personal Communications. (A)

62. Knauss, W. G., California Inst. Tech., Personal Communications. (A)

63. Bills, K. W., Jr., and Blatz, P. J., "Nonlinear Fracture Mechanics-New Theories of Solid Propellant Response and Fracture Behaviors", Naval Weapons Center, NWC TP 5684, Feb. 1975, p. 66. (B) (D)

1978 USAF-ASEE SUMMER FACULTY RESEARCH PROGRAM
sponsored by
THE AIR FORCE OFFICE OF SCIENTIFIC RESEARCH
conducted by
AUBURN UNIVERSITY AND OHIO STATE UNIVERSITY

PARTICIPANT'S FINAL REPORT

AN INVESTIGATION OF CRITICAL EROSION ANALYSIS DEFICIENCIES.

Prepared by:	Russell E. Petersen Ph D
Academic Rank:	Professor
Department and University:	Department of Aerospace & Mechanical Engineering University of Arizona
Assignment:	
(Air Force Base) (Laboratory) (Division) (Branch)	Edwards AFB Rocket Propulsion Laboratory Solid Rocket Division (MK) Ballistic Missile & Space Propulsion Branch (MKB)
USAF Research Colleague:	Robert L. Acree, Capt, USAF
Date:	August 4, 1978
Contract No.:	F 44620-75-C-0031

AN INVESTIGATION OF CRITICAL EROSION ANALYSIS DEFICIENCIES

by

R. E. Petersen

ABSTRACT

The solid rocket motor nozzles to be used in future generations of ballistic missiles will be subjected to extremely harsh corrosive environments. The resulting erosion, particularly in the throat regions, will produce variations in performance quantities such as Isp and thrust. Although degradation in performance is certainly not desirable, if the amount of nozzle erosion could be predicted reliably, various measures such as propellant tailoring and grain design could be taken to minimize overall losses in performance and objectives.

In this report the several phenomena that are involved (or conceivably could be involved) in nozzle erosion are discussed and comments are made on their relative importance.

Certain examples from the pertinent literature are reviewed, including both reports and documents from rocket industry contractors and journal articles appearing in the open literature.

The predictive theories of nozzle erosion presented in the literature are discussed and assessments are made of their merits and deficiencies.

ACKNOWLEDGMENTS

The author is sincerely grateful to the following organizations for support of this summer research: AFOSR, Air Force Systems Command (AFSC), ASEE and Auburn University.

The organizational ability and cooperativeness of the program director, Mr. J. Fred O'Brien Jr., and of the AFRPL contact person, Dr. Lawrence P. Quinn, are much appreciated.

Discussions with professional experts such as Mr. Robert Geisler and Mr. Lester Tepe, of AFRPL, have contributed much to an understanding of the physical aspects of the problem.

The dedicated efforts of Mrs. Brenda Crain in the typing and of Mr. Gene Stout in the photo-reduction are gratefully acknowledged.

Finally, it is a pleasure to express a deep appreciation of the very great contributions of my Air Force Research Colleague, Capt Robert L. Acree, USAF, to all aspects of the project.

INTRODUCTION

The demands for ever-improved capabilities for new generations of ballistic missiles impose severely corrosive environments for solid rocket motor nozzles. Apart from circumstances which lead to actual failure of the nozzle as a whole, erosion at the throat can affect the performance of a rocket motor. While this in itself is not desirable, if the erosion were reproducible and predictable within acceptable limits*, various measures such as propellant tailoring and grain design could be taken to minimize overall losses in performance and objectives.

The expense and time required for forming advanced carbon/carbon materials, constructing sophisticated nozzle designs, and conducting full scale hot firing tests (as were performed in the USAF Missile-X First Stage ADP [1,2]) make it extremely desirable that reliable predictive theories of erosion be developed. A "theory" on theoretical treatment which could utilize information obtained from relatively cheap and simple experiments would be a significant improvement over the present situation.

The large number of variables associated with the extremely complex phenomenon known as rocket nozzle erosion and the lack of adequate knowledge as to their relative importance has hindered the development of a rigorous mathematical theory capable of performing such prediction. These circumstances thus dictate that there must, of necessity, be a certain amount of empiricism involved in any erosion mechanism theories.

The objectives of this work were to assess deficiencies in current erosion prediction theories and to recommend means of resolving and/or eliminating these deficiencies. It is the purpose of this report to first, categorize the various aspects of nozzle erosion and to rate them as to their significance; second, to present a review of representative literature pertinent to the problem; third, to consider and summarize prediction theories existing in both the open literature and in various contractor documents; and, finally, to make an assessment of the deficiencies of these theories.

---

*One can argue that if, for testing under presumably identical circumstances, the erosion were not sufficiently "reproducible", then there would be no hope in making it "predictable"; on the other hand, one could equally as well reason that, if the various phenomena were well enough understood, the erosion results would be as expected, and there would be no question as to reproducibility. This presumes sufficient "quality control" in both the nozzle manufacture and in the testing methods.

THE VARIOUS ASPECTS OF EROSION

Erosion in solid rocket motors is a far more serious problem to nozzle designers than erosion in liquid rocket engines. Solid propellant motors are subjected to more corrosive chemical environments and usually operate at higher pressures and temperatures. Solid propellants are typically loaded with 15 to 30% (by weight) of finely ground aluminum. This results in the appearance of molten droplets of unburned aluminum and of aluminum oxide, Al_2O_3, both of which contribute to the erosion of material from the walls of the nozzle.

In common usage, the term erosion is usually taken to mean the wearing away of a surface by the physical process of particle impact, or scouring, as in sandblasting or the geological process of forming the Grand Canyon, but in rocketry the term has come to mean the process of mass removal from a surface by any means whatsoever, be it purely mechanical (particle impact, spalling), thermophysical (sublimation, melting), or chemical (surface reactions with diffusion of reactants towards and products away from the surface), or any combination of the above. Furthermore, several nozzle materials (phenolics most notably) undergo thermal expansion, delamination and interlayer decomposition resulting in swelling of thematerial and an apparent negative surface recession (although mass has been removed from the surface). These various aspects of erosion are outlined in Figure 1.

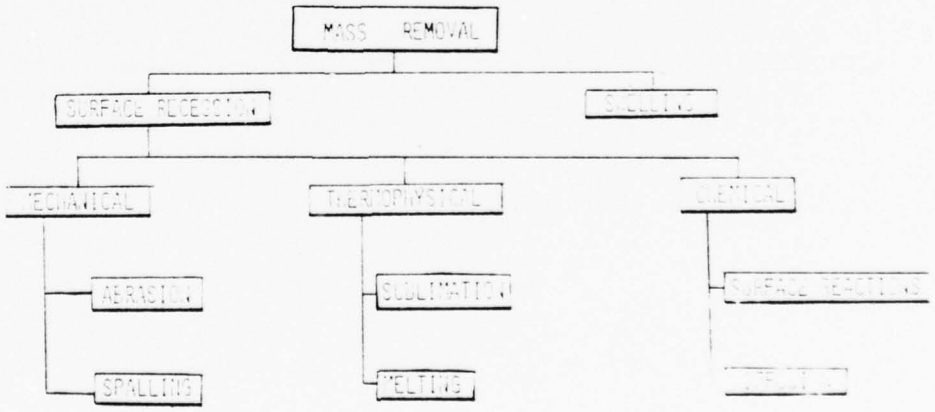

Figure 1. The Various Aspects of Nozzle Surface Recession

Several general observations were made before examining the literature in detail concerning the relative importance of these various facets of erosion:

1) There seems to be little doubt that chemical erosion (for which the term corrosion seems apt) always plays a role in the surface recession of rocket nozzle materials.

2) According to conventional wisdom, the purely mechanical effect of wearing away of surface material (as in sand blasting) appears to be of only slight importance. This may or may not be the case. Zeamer's comment, "...the kinetic energy of particles is relatively small compared to the thermal energy..."[3] seems to be the referenced justification[4] for deeming that direct mechanical erosion is unimportant. In passing, one wonders if this is a case where, if a statement is repeated often enough, with enough conviction, it eventually becomes accepted as the gospel truth.

3) The impact of liquid metal or metallic oxide droplets on carbon surfaces transfers heat to the surfaces which can cause melting in the case of carbon phenolics and could tend to promote sublimation of graphites and, in any case, act as a secondary contributor to chemical corrosion. The likelihood of direct impact on nozzle surfaces depends upon the geometry of the nozzle under consideration. For the entrance regions of submerged nozzles, especially those portions exposed to slots in the propellant grain, the likelihood is quite high, whereas in throat regions, the likelihood is much smaller. The diverging exit sections, where the surface is contoured for higher motor thrust, are especially vulnerable to particle impact.

4) The thermophysical effects of melting and sublimation have not been considered as significant erosion mechanisms. It seems ironic that the temperature range where these can start to become significant (3000 to 3300°K) is attained at least in some cases at the surface of the throat and entrance regions.

Each of the above aspects of erosion is discussed in more detail in the literature review which follows.

LITERATURE REVIEW

This consisted of a detailed examination and perusal of literature on solid rocket motor nozzle materials, design, fabrication, testing, and performance prediction. This literature fell into two general categories: engineering analyses and testing reports resulting from government and industry programs, and journal articles appearing in the open literature.

The engineering reports and documents contained much detailed information regarding all aspects of the hardware development problem, including manufacturing techniques for carbon/carbon billets, submerged nozzle construction and assembly details, testing methods, erosion calculation procedures, etc. Review of this material tended to impart a feel for the magnitude and scope of the manufacturing and testing problems as seen at the working level.

The journal articles were more tightly written and restricted in scope, and were primarily concerned with predictive theories of erosion. This material presented physical models of the erosion process(es) which, with good physical insight, outlined simplified techniques which predicted general performance trends.

Appearing below are brief comments on the more important documents and articles, together with encapsulated summaries of pertiment observations.

(1) Post Test Analysis of the P-1 Firing (ref 4)

This report documents posttest analysis results of the P-1 nozzle firing and contains results of a detailed chamber flow analysis concerning particle impingement on the P-1 nozzle in a vectored position. Certain "cold flow" data were obtained from experimentaly observed flowfields with similiar geometries.

The observation to be made concerning the flow (fig. 2) is that the flow is highly complex and that "...modeling of the flowfield in the vicinity of the P-1 nozzle entrance is difficult because of the 3-dimensionality and highly viscous nature of the flow."[4] Three aspects of the flowfield that cannot be treated with available chamber flow computer codes are:

(a) the region of separated flow (usually recirculating) existing between the grain and submerged nozzle;

(b) the swirl flow around the outside of the nozzle when in a vectored position, and

(c) the non-uniform velocity field of the flow approaching the nozzle.

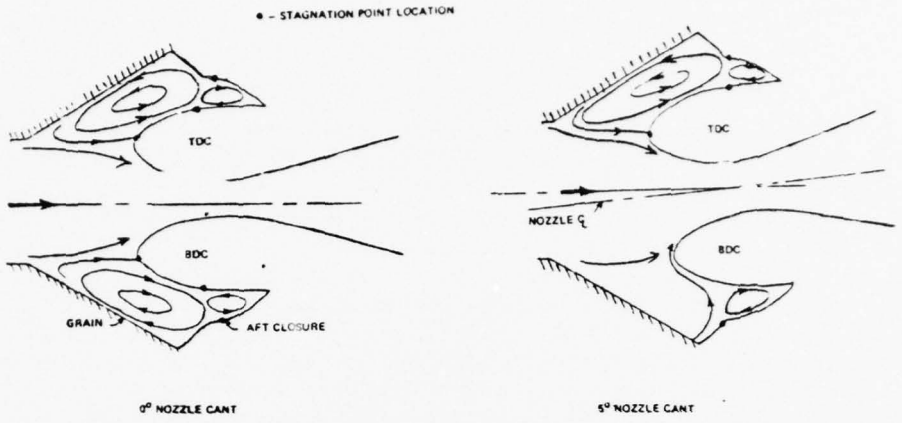

Figure 2. Vortex flow in a submerged region.

(2) Post Test Analysis of the P-2 Firing (ref 2)

This report discussed predictions and results from the P-2 nozzle test. Shown below in figure 3 is a flow chart for a thermochemical heating and erosion analysis of rocket nozzle components. The complexity of the analysis, the types of computer codes, and the information flow between the codes are typical of the calculations procedures used by the rocket industry.

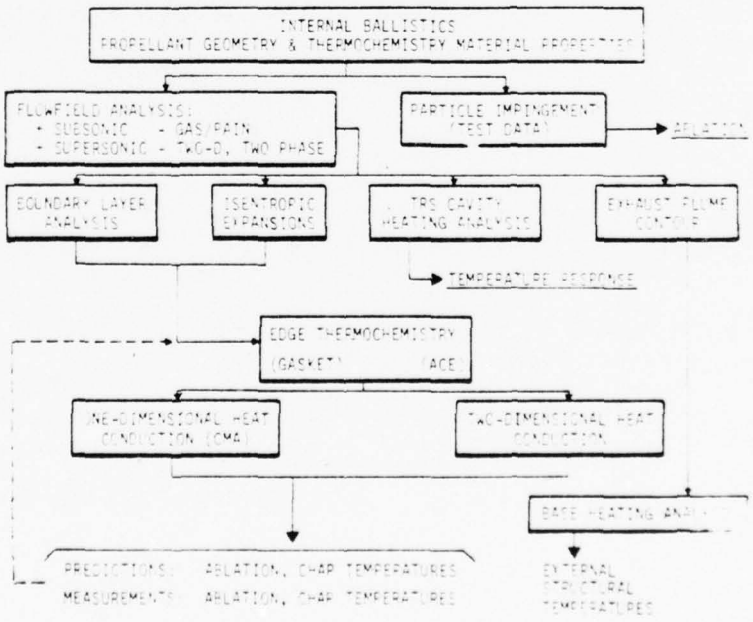

Figure [illegible] CCD Nozzle Thermochemical Ablation Analysis

In spite of the sophistication and complexity of these programs, liberal "correction factors" or multipliers must be applied to make the predictions agree with test data. For instance, in the P-2 test report "for the ITE (integral throat entrance) region, this correlation involves a simple multiplier to the non-dimensional char rates (B_c) that are output from program GASKET (graphite kinetic ablation)." The quantity B_c (or sometimes B' or B') is defined by

$$B_c = \frac{\dot{m}_w}{\rho_e u_e C_M}$$ where

$\dot{m}_w$ is the mass removal flux, ρ_e and u_e are the density and velocity at the boundary layer edge, and Cm is the Stanton number for mass transfer. "A fixed heat transfer coefficient multiplier of 0.75 times the result of the boundary layer program is used with the additional multiplier times the B_c values. Figure 4 shows this multiplier plotted as a function of area ratio as correlated from the Navy LVM-1 contract and the current C/CAN contract (F04611-76-0081). Above the line used for the data from these contracts is a dashed line which is the correlation of the P-2 ablation data. The reason for this shift is not understood. In fact, the reason for an axial variation of "ablation kinetics" is not completely understood. It is more than likely a function of surface roughness, angle of the surface "sites" that can react with the gas, and other factors. Until a more sophisticated model is developed, CSD will use this semi-empirical method of correlation and prediction. In general, it has worked well, and as more data are obtained, the accuracy of this method will improve."

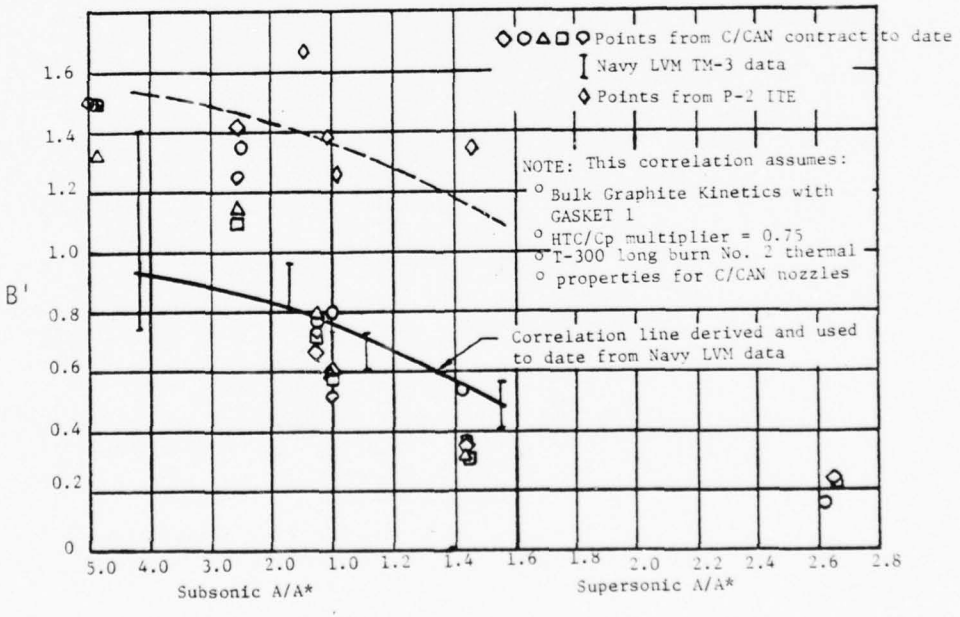

FIGURE 4 ANALYSIS FLOW CHAR RATE MULTIPLIER AS A FUNCTION OF AREA RATIO FOR P-2 ITE

(4) Hercules Report TR-70-98-Sep 70. This contains detail on an interesting flow field analysis which is applicable to solid rocket motors in the region from the head end of the grain port to the nozzle throat. The treatment was for axi-symmetric (or 2-D), subsonic (but compressible), isentropic, irrotational, frozen flow. The governing equations were cast into finite difference form and 1178 modes were used. The flow was assumed to be "steady", but quasi-steady would be more descriptive because part of the boundary is the receding surface of the burning propellant. This difficulty was coped with by applying burn rate data for the propellant used to determine the burning propellant surface at various portions of the total burn time and repeating the analysis for each partial burn time. Shown below are streamlines (the numbers are proportional to the amount of flow between the centerline and the line in question) for a Minuteman motor at 2 seconds.

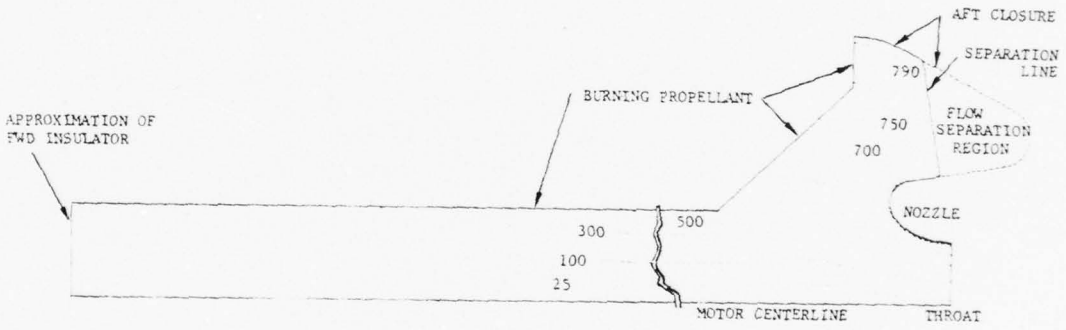

Fig. 5. Streamlines for Axi-symmetric "steady" Inviscid Frozen Flow.

Note that the boundary of the eddy flow region (flow separation region) was taken to be a straight line drawn from the point of separation, as calculated from a boundary layer analysis, to the stagnation point on the submerged nozzle.

(5) Aerotherm Report 75-143 - Oct 75. AFRPL Graphite Performance Prediction Program. Vol. I. Recommendations for a Standardized (Industry-wide) Analytic Procedure for MX Nozzle Throat Recession Calculations. Aerotherm performed a sensitivity study to determine the most critical variables used in predicting material response. "For the throat, the hetergenous surface kineticd constants and the heat transfer coefficient were the most important."

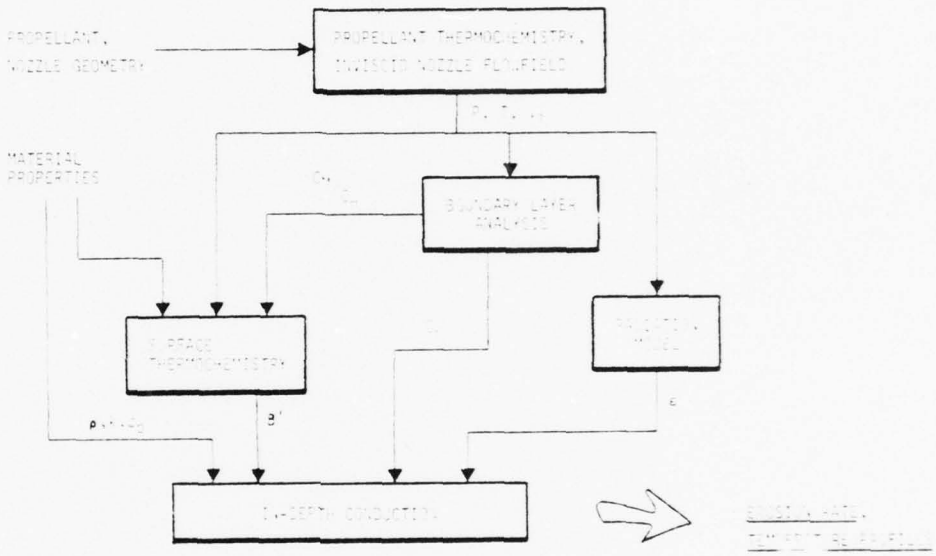

Fig 6. Baseline method - combination of 1D or 2D potential flow solution in subsonic region and M.O.C. (2D) in supersonic region. Can handle chemical reactions. Chemical equilibriums.

(6) ARC (Atlantic Research) Report - Aug 78. CNO (carbon nozzle opportunities). Much detail on nozzle materials and fabrications and discussions of nozzle tests and failures. P. 95 "These results show that propellant with the lower aluminum content is more corrosive than the higher aluminum content propellant". (At least for short burn times). This tends to support the idea that chemical erosion dominates (the aluminum tends to consume the oxygen). "The time factor effect is probably two-fold. First, the stagnation point recession at the cowl overwarp/inlet interface becomes very severe at long burn times and the resulting turbulence becomes quite dominant. Second, is the effective, or time-averaged area-ratio reduction in the axial curvature of the I.T.E., since the convective heat transfer rate increases as the local area ratio decreases. In addition, the heat transfer rate is enhanced by surface roughness, which also tends to become more severe with time." ...Much detail on visual observations of nozzles after motor firings.

(7) Thermophysical properties of graphite are shown in figures 7 and 8. Figure 7 shows a proposed phase diagram for graphite due to Whittaker*, illustrating results of recent research which has shown the existence of a number of polymorphic "carbyne" forms of graphite at high temperatures. Figure 8, taken from the Industrial Graphite Engineering Handbook** shows the vapor pressure of graphite over the temperature range of interest to rocket applications (the theoretical chamber temperature for a ballistic missile propellant of current interest*** is 3760°K).

When carbon changes from the solid to vapor phase (sublimation), at least five species of carbon vapor can exist: C, C_2, C_3, C_4 and C_5. Sublimation does not seem to have been considered in current prediction models, which may be a critical omission considering the chamber temperatures of current propellants. Below surface temperatures of 2500°K sublimation effects can be dismissed totally, whereas at surface temperatures above 3500°K, there is little doubt that sublimation is of overwhelming importance.

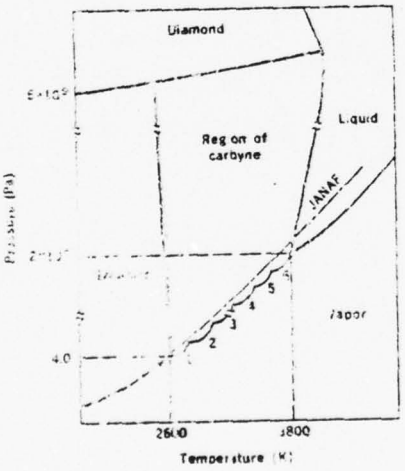

Figure 7. A proposed phase diagram for Graphite.

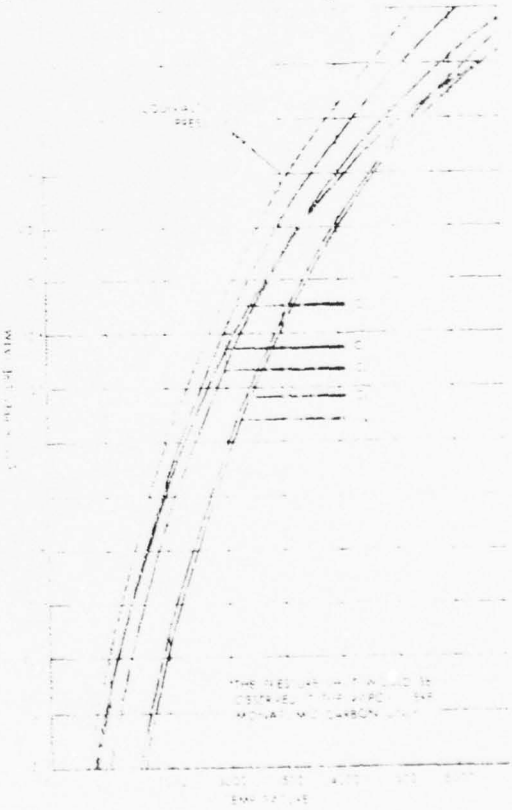

Figure 8. Vapor pressure of Graphite.

---

* A. Whittaker, "Carbon: A New View of Its High-Temperature Behavior", Science, Vol. 200, 19 May 1978.

** "The Industrial Graphite Engineering Handbook", Carbon Products Division of Union Carbide Corporation, 1969.

*** 90% Solids, 21% Aluminum, hydroxyterminated-polybutadiene binder

(8) Semi-quantitative Prediction of Graphite Nozzle Insert Erosion - L. J. Delaney, et al., AIAA Journal, Aug 64. This paper exhibits good physical insight. Considers chemical kinetics and diffusive mass transport. "The limiting factor in determining the permissible amount of throat erosion is unlikely to be degradation of Isp, P_c, thrust or mass ratio. More probably, the limit on erosion will be dictated by the practical problem of fabricating inserts which will provide acceptable reproducible erosivities." Delaney concluded that only three surface reactions need be considered:

$$C(s) + CO_2\,(g) \rightarrow 2CO(g) \quad , (1)$$

$$C(s) + H_2O\,(g) \rightarrow CO(g) + H_2(g) \quad , (2) \text{ water-gas reaction}$$

$$C(s) + H_2\,(g) \rightarrow C_2H_2\,(g) \quad , (3)$$

Reactions (1), (2) involve 2 moles of gas produced for 1 reacting, thus $N_j = 2\,N_i$, (4).

For diffusion of i towards and j away from surface, the molal flux at distance z through the b.l. is:

$$N_{iz} = -c\,\mathcal{D}_{ij}\,\frac{dx_i}{dz} + x_i\,(N_{iz} + N_{jz}) \quad , (5).$$

Integrating (5) subject to b.c. yields a transcendental equation

$$N_{iz} = k_{ia}\,\ln\left[(1 + x_{ia})/\left(1 + \frac{N_{iz}}{cK}\right)\right] \quad , (6).$$

(6) was used in erosion calculations at each time increment for $i = CO_2$ and $i = H_2O$.

The contribution of reaction (3) to the erosion mechanism will show little effect below 2500°K, and above 2500°K one may assume equilibrium at the surface for all three carbon reactions.

$$N_{C_2H_2} = k_{C_2H_2}\,x_{C_2H_2} \quad , (7) \text{ and}$$

$$x_{C_2H_2} = \frac{-(k_{H_2O}\,\bar{x}_{H_2O}/k_{C_2H_2}) + \bar{x}_{H_2}}{1/K_3 + (k_{C_2H_2}/k_{H_2})} \quad , (8).$$

where overbars on the X_i denote freestream values, otherwise surface values.

The total rate of carbon loss

$$N_C = N_{CO_2} + N_{H_2O} - 2\,N_{C_2H_2} \quad , (9).$$

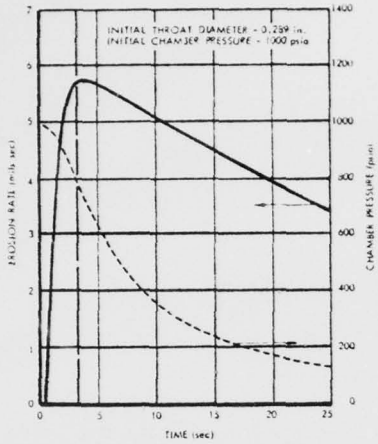

Fig. 9. Calculated erosion rates and chamber pressures for NASA test with Arcite 368.

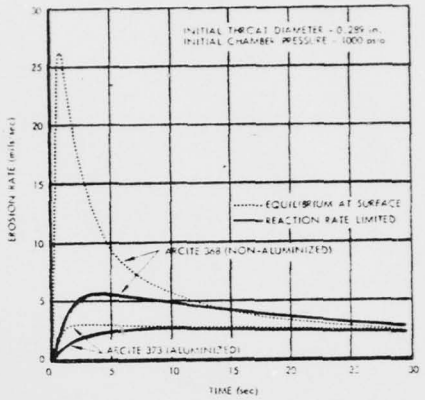

Fig 10. Calculated erosion rates assuming infinite reaction rate at surface.

Figure 9 shows the initial rapid increase in the predicted erosion rate which is soon arrested by the drop in chamber pressure, even though the surface temperature continues to rise. The authors point to this as showing the considerable importance of pressure in the erosion phenomenon, although they do not make clear just how the pressure enters into the theoretical predictions.

Figure 10 shows that calculations based on chemical equilibrium at the surface give a very high peak in the instantaneous erosion rate which results in an average erosion rate which is much higher than the measured value. This serves to indicate that there is indeed a kinetic limitation on graphite erosion.

(9) Mechanical Contributions to Graphite Erosion (ref 11)

In this report Gowariker presents a semi-empirical analysis of mechanical and chemical contributions to the erosion rates of graphite throats in solid rocket motor nozzles. The author assumes that the total erosion rate can be expressed as $\dot{r} = \dot{r}_c + \dot{r}_m$, where the chemical contribution $\dot{r}_c$ depends on the composition of combustion gases, the flame temperature, the Reynolds and Schmidt numbers of the flow, the density of the graphite throat, and the geometry of the nozzle; the mechanical contribution $\dot{r}_m$ is a function of the characteristic velocity of the gases and the porosity of the throat.

The treatment of the chemical contributions is virtually the same as that of Delaney[10] with the exceptions that Gowariker uses a slightly more sophisticated expression for the mass transfer coefficient and (although he lists the same set of reactions as did Delaney) he considers the contribution of the acetylene reaction to be negligible. He thus arrives at the expression

$$\dot{r}_c = (N_{CO_2} + N_{H_2O}) / \sigma$$

where σ is the density of the graphite.

The mechanical contribution is alleged to be a function of the porosity of the surface material at the throat. It is claimed (without any explaination or justification) that there is a linear relationship between $\dot{r}_m$ and the grouping $\tau_w/\rho c^*$, where τ_w is the wall shear stress, ρ is the average density of the gases, and c^* is their characteristic velocity. The wall shear stress is expressed in terms of the friction factor, f, and hence the expression $\dot{r}_m = \alpha_1 \cdot c^* f$, where α_1 is a constant of proportionality. The percentage porosity P of the graphite surface is taken as a measure of structural resistance to flow as follows:

$$f = \alpha_2 \cdot (\log P)^2$$

where α_2 is another constant. Substituting this expression for the friction factor we obtain

$$\dot{r}_m = \alpha_3 \, c^* \, (\log P)$$

where α_3 is a final constant to be determined using experimental erosion rate data. The above expression is presented entirely without physical justification, although an allusion is made to an old NACA Technical Memo of von Karman's.

The final expression for a given propellant and chamber operating conditions, by combining the corrosion expression with the mechanical erosion expression above is

$$\dot{r} = A/\sigma + B(\log P)^2$$

where A and B depend on gas composition, temperature, pressure, velocity, etc., but are independent of σ and P. The percentage porosity, P, is defined as

$$P = \frac{\text{volume of open pores}}{\text{volume of external pores}} \times 100$$

The author, in a rather ingenious and involved method, measured P for 19 different grades of graphite materials and found P to range from 3.5% to 13.8%, while σ ranged from 106.1 to 116.7 lb/ft^3 (the density bore no simple relation to the porosity). The expression for $\dot{r}$ appeared to correlate reasonably well with experimental data for propellant "A", although there was considerable scatter. Nowhere in the paper is the composition of propellant "A" identified, although it is mentioned that ultimately four physical propellants were tested: one with low flame temperature, two with high flame temperatures (aluminized and non-aluminized) and the last oxygen-balanced. Burn times ranged from 13 to 30 seconds.

There is much to criticize in the paper, particularly with the lack of physical justification for the key steps in the development of the expression for $\dot{r}$, but the correlation of experimental data with the derived result suggests that perhaps surface porosity may indeed be a significant parameter (apart from graphite density) although why it should appear functionaly as the square of the log is not at all clear.

(10) Correlation of Graphite Nozzle Throat Erosion (ref 12)

In this report Mayberry, et al., presented an impressive correlation of erosion data obtained from 43 solid rocket motor firings. The correlation included nozzle and propellant properties as well as chemical reactions at the surface. The principal chemical reactions considered were:

$$C + H_2O \rightleftarrows CO + H_2$$

$$C + CO_2 \rightleftarrows 2CO$$

$$C + \tfrac{1}{2}O_2 \rightleftarrows CO$$

$$C + OH \rightleftarrows CO + \tfrac{1}{2}H_2$$

$$C + O \rightleftarrows CO$$

The acetylene reaction has been notably omitted.

Using the above set of reactions and thermochemical analysis computer programs to calculate gas composition and thermal properties the following correlation was obtained:

$$\left(\frac{ER \cdot D_t}{\mathcal{D}_{co,m}}\right) = 0.0188 \left(\frac{D_t V \rho_{gp}}{\mu}\right)^{.8} \left(\frac{\rho_m}{\rho_{g,p}}\right)^{-1.4} \left(\frac{t\, \mathcal{D}_{co,m}}{D_t^2}\right)^{0.09} \left(\frac{\mu\, c_p}{k}\right)^{-0.60} X$$

$$\left(\frac{\mu}{\rho_g \mathcal{D}_{co,m}}\right)^{0.98} \left(\frac{X}{D_t}\right)^{-0.47} \beta^{0.11} \varepsilon^{0.98}$$

which is of the form $Sh = \Psi \left[Re, \left(\frac{\rho_m}{\rho_{gp}}\right), Fo, Pr, Sc, \left(\frac{X}{D_t}\right), \beta, \varepsilon \right]$.

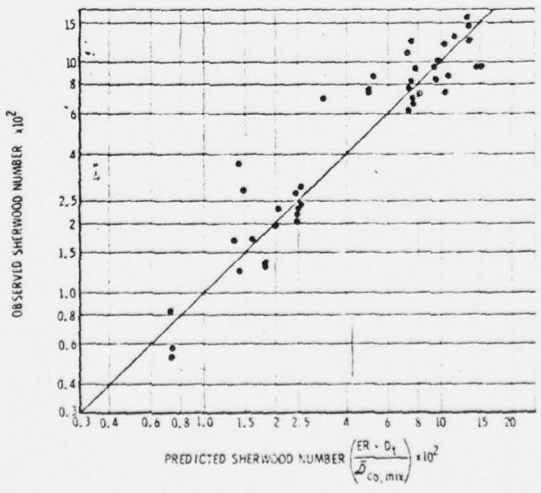

Figure 11. Nozzle throat erosion Correlation.

The nomenclature used in this correlation is as follows:

ER = burn-time average radial erosion rate

V = average velocity of gas-particle flow at the nozzle throat

D_t = initial throat diameter

t = burn time

x = subsonic entry length (distance from stagnation point to throat)

ϵ = total alumina cloud emissivity

μ, c_p, k = viscosity, specific heat, thermal conductivity

T = temp. of gas at nozzle throat

β = blowing parameter, dimensionless

ρ_g = gas density

ρ_{gp} = density of gas-particle mixture

ρ_m = graphite throat material density

$\bar{\mathcal{D}}_{CO,mix}$ = mean binary diffusion coefficient of carbon monoxide

X = mole fraction

MW_{gp} = molecular weight of gas particle mixture

MW_{meo} = molecular weight of metal oxide (Al_2O_3)

Sh = Sherwood number ($ER \cdot Dt / \bar{\mathcal{D}}_{CO,mix}$)

Re, Pr = Reynolds and Prandtl numbers

Sc = Schmidt number ($\mu / \rho_g \bar{\mathcal{D}}_{CO,mix}$)

Fo = Fourier number for mass, ($t \bar{\mathcal{D}}_{CO,mix} / D_t^2$)

The blowing parameter β is defined as

$$\beta = \frac{MW_{carbon}}{MW_{gp}(1 - X_{meo}) - X_{meo} MW_{meo}} (X_{H_2O} + X_{CO_2} + 2X_{O2} + X_O + X_{OH})$$

It is not clear why this is called the blowing parameter nor why this grouping should affect erosion, although the authors allege that a larger β results in a greater erosion rate. The correlation obtained, however, shows that β appears raised only to the 0.11 power.

The correlation is impressive in that it incorporated data from 43 motor firings with an erosion rate range of 18-fold (.425 to 7.9 mil/sec), a throat diameter range of 8-fold (.056 - .46 feet), a burn-time range of 26-fold (2.8 - 73 sec.), an operating pressure reange of 3.5-fold (280-900 psig), and a graphite-density range of 1.3 fold (107.9 - 139.8 lb_m/ft^3).

The authors point out that the impingement, deposition, and subsequent melt-off of high melting oxides and propellant agglomerates have not been considered.

(11) BATES Motor Erosion Data Correlations - R.L. Geisler presentation at JANNAF Nozzle Sub-Committee Meeting, Jul 78.

This is perhaps the most recent correlation of erosion data. Since 1963, there have been 1600 firings at AFRPL's BATES motor facility.

Geisler presented data for six different propellant formulations with three tests per formulation in a 75 lb charge, 2 inch throat motor (A) and six tests per formulation in a 15 lb charge, 1 inch throat motor (B). All 54 tests were conducted at a design chamber pressure of 68 atm (1000 psia) and an initial nozzle area ratio of 9.5. All formulations were 90% solids loaded (i.e., 10% HTPB binder by weight), but they varied in aluminum content from formulation 1 (15% Al by weight) to formulation 6 (30% Al). In every case the throat inserts were of HLM 85 graphite having a bulk specific gravity of approximately 1.83.

The principal drawback for the correlations is the limited burn time, the maximum being less than 4 seconds. Erosion rates were obtained by dividing the difference of total erosion from motor A (75 lb_m) and motor B (15 lb_m) by their difference in total burn times. Figure 12 implies that there is an initial period with no erosion, of the order of 1.3 seconds. That there is an initial "dead" period is not doubted, since it takes time for the nozzle throat surface to reach a significant temperature, but that it can be measured by a straight line through two points extrapolated to zero erosion is open to question. Figure 13 gives an indication of the variation of throat surface temperature with time into the burn. Figure 12, showing erosion rates for all six formulations, indicates that the greater the % Al, the lower the erosion rate. Figure 14 shows the variation of the mole percentage in the free stream at the throat for the species H_2, OH, H_2O, and CO_2 (the numbers being obtained from a thermochemical equilibrium program) versus erosion rate. The implication is that H_2O and OH are the principal contributors to the chemical erosion. Figure 15 gives the equilibrium thermochemical mole percentage of OH for each formulation, plotted versus erosion rate.

The implication of all this is that the presence of increasing amounts of aluminum, although increasing the chamber temperature somewhat, tends to consume more of the available oxygen from the propellant, thus leaving less available for the formation of H_2O and OH radical.

Geisler concludes that chemical attack (H_2O and OH) is the only significant mechanism for throat erosion (the recession rate is inversely proportional to H_2 concentration in the throat free stream), and that carbon/carbon and bulk graphite appear to have equivalent recession rates at equivalent densities. His contention that the BATES motor is a good (relatively) low cost screening tool must be modified by the limitation in total burn times.

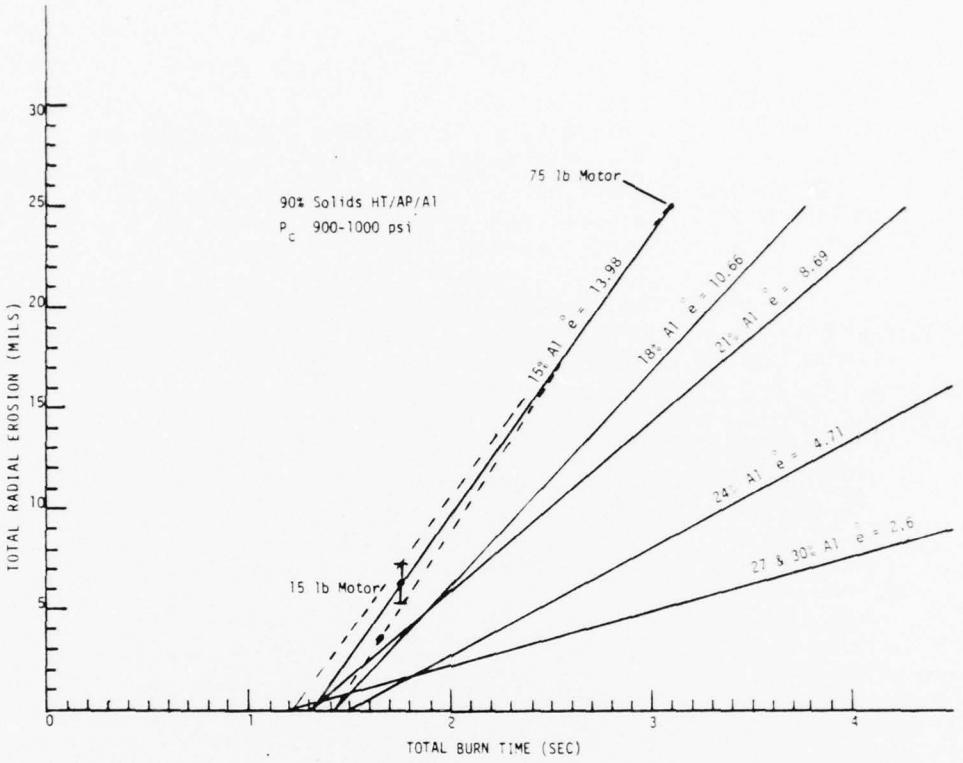

FIGURE 12 EROSION VS TIME

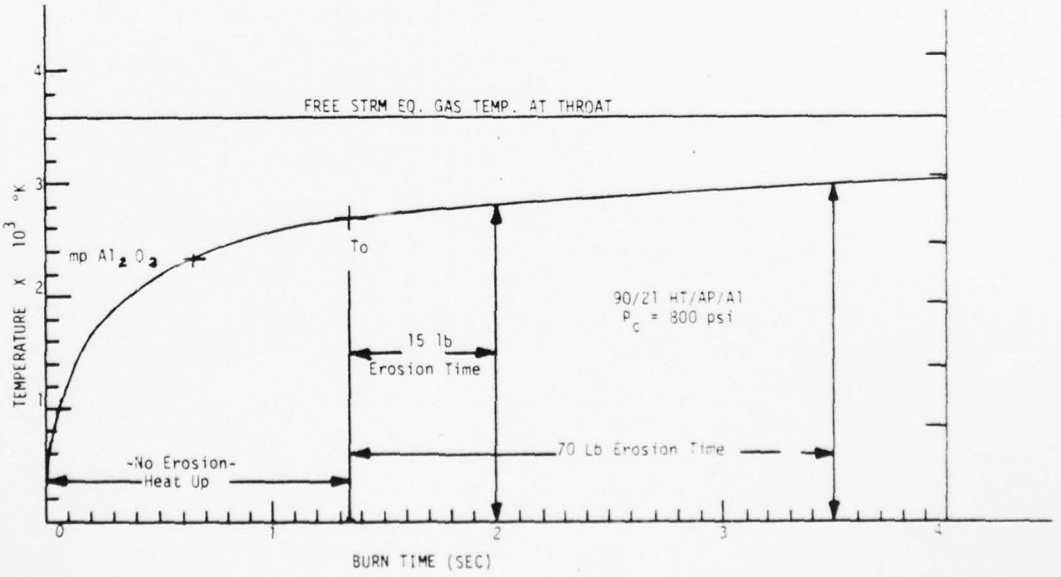

FIGURE 13 BATES MOTOR NOZZLE TEMP.

EROSION PREDICTIONS

With the exception of the purely correlative treatments, all of the papers and reports reviewed in the previous section have several features in common - equilibrium thermochemical programs which calculate compositions, temperatures, pressures, transport properties, etc. and heat transfer programs. The latter are necessary not only for determination of surface temperatures which would obviously enter in melting calculations (and sublimation, if it were considered), but also for heat transfer coefficients (Nusselt and Stanton numbers). Chemical corrosion calculations require not only a selection of pertinent chemical reactions along with the appropriate rate constant data, but also mass transfer coefficients which, together with diffusion coefficients, enter in the calculations which account for the diffusion transport of reactants to and products from the chemically reacting surface. By the analogy between mass and heat transfer, the following is obtained:

$$\rho_e u_e C_M = \rho_e u_e C_H \left(Pr/Sc \right)^{2/3} \qquad (1),$$

where C_m and C_H are Stanton numbers for mass and heat transfer, Pr and Sc are the Prandtl and Schmidt numbers. Having obtained C_m, along with the Reynolds and Schmidt numbers, the Sherwood number (Nusselt number for mass transfer) can be calculated*. From this, the throat diameter and the binary diffusion coefficient for a given species, i, one can calculate the mass transfer coefficient for that species, β_i.

It will be recalled from the previous section that the contractor documents also had various types of flow field analyses. While these are interesting in themselves and are of direct importance in particle impingement studies, they are of auxiliary importance (especially the inviscid core flow) to the heat transfer analysis necessary for throat erosion predictions. The "cold flow" studies mentioned in item (2) of the literature review were useful in helping to gain a "feel" for the nature of the eddying separated flow between the grain and the submerged nozzle and the swirl flow around the outside of a vectored nozzle.

DIFFUSION-CONTROLLED VS. KINETICS-CONTROLLED

The following equation, due to Frank-Kamenetskii[13], illustrates the meaning of the above term:

$$J_i = \frac{C_{ie}}{1/\beta_i + 1/k_i} \qquad (2),$$

where J_i = molar flux, C_{ie} = reactant concentration at the boundary layer edge, β_i = mass transfer coefficient (for diffusion), and k_i = kinetic rate coeff. ("rate constant"), all for species i. When $k_i \gg \beta_i$, the process is said to be "diffusion controlled". Equation (2) is derived assuming the reaction to be first order:

$$J_i = \beta_i (C_{ie} - C_i') \text{, (Supplied by diffusion)} = k_i C_i' \text{ consumed by reaction).}$$

Solving for the surface concentration, C_i' , $C_i' = \frac{B_i C_{ie}}{(K_i + B_i)}$

from which equation (2) results. It can be seen that at low temperatures, the rate constants will be low and hence the erosion process is kinetics-controlled.

ASSESSMENT OF DEFICIENCIES

In assessing the deficiencies in journal articles dealing with erosion prediction, it is fairly easy to pick out flaws: this step in the argument is presented without physical justification, that assumption appears to be unreasonable, the theory is supported by meager experimental results, etc. The journal paper is, so to speak, "standing alone and exposed".

It is a delicate and difficult task, however, to assess deficiencies in the extensive and elaborate network of computer programs which comprise the erosion predictions of rocket industry contractors. On reading the documentation, it is obvious that a great deal of time and skillful effort has been expended by teams of qualified professionals. Nevertheless, that the predictions leave much to be desired is evident by recalling, for example, statements from item (3) of the Literature Review section (CSD's report on the P-2 test): "... a fixed heat reansfer coefficient multiplier of 0.75 times the result of the boundary layer program is used..."; again".. Above the line used for the data from these contracts is a dashed line which is the correlation of the P-2 ablation data. The reason for this shift is not understood..."

In using the above example, there was no intention to single out CSD. In the recent attempts of Aerotherm (GASKET 2 Final Report AFRPL-TR-76-70) to obtain kinetics type rate constant data for C/C graphite materials, it was found that the so-called "rate constants" varied with the particular material being tested. The resulting information, while no doubt useful, can hardly be considered to have the type of generality desired in a prediction analysis.

If one attempts to define the "deficiency" of a prediction theory in terms of the departure of the "prediction" from "measured", the prediction of Delaney, et al for Arcite 368 (a non-aluminized propellant) gave, for certain conditions, an erosion rate of 4 mils/sec. This is a departure of 17.6% which would appear to be a very good prediction, but it must be noted that there was only one experimental data point!

In the correlation of Mayberry, et al.,[12] the observed Sherwood number (a measure of erosion rate) is plotted vs. the predicted Sherwood number on a log-log basis (Figure 11), a method which allows the greatest percentage departure to be seen by inspection. This turned out to be obs.Sh. = 3.6 for pred. Sh. = 1.4, giving a departure of 61%. "Most" of the large scatter points, however, were within 40% and the average deviation of data was 21% for an increase of 30.4-fold of observed Sherwood number.

CONCLUSIONS AND RECOMMENDATIONS

The objectives of this work have been to assess the deficiencies in current erosion prediction methods and to suggest appropriate measures for their elimination. In the previous sections, the author has attempted to identify the strengths and weaknessess of various predictive methods, both empirical and analytical. The following comments summarize findings of this work and outline recommendations for future research on nozzle erosion.

The single most significant deficiency is the disparity between rocket nozzle materials of current interest and the materials modeled in the predictive theories. Carbon/carbon materials are still undergoing development with regard to manufacturing and fabrication and are considerable more complex than their graphite predecessors. However, existing predictive theories are based on isotropic surface models anf thus do not treat the details of weave and fiber orientation of these newer materials.

Delaney and Gowariker were among the first to model nozzle erosion theoretically. Their models contained good physical insight into the problem and indicated general erosion trends. However, Delaney's simplified model[10] made predictions (such as the decline of instantaneous erosion rate with time) which contradict experimentally observed results.[9] And Gowariker's inclusion of material porosity in erosion calculations[11] was left largely unjustified. Thus the theoretical analyses are less than satisfactory for predicting nozzle erosion.

The motor correlations of Mayberry, et al.[12] and of Geisler both appear to have merit for predicting erosion. Such correlations bring together the results and experience gained through many rocket motor firings, and although empirically based, they indicate the important physical parameters which influence erosion. And for a problem as admittedly complex as the prediction of nozzle erosion, a certain amount of empiricism must be conceded. The limitations of such correlations are that they were developed for graphite materials only, and in the case of Geisler's correlation, the data were obtained from short burn times only (typically less than four seconds).

The computer erosion calculation procedures in use by the rocket industry seem to be the most appropriate technique for predicting material performance trends (and should be accurate to the degree that the erosion models are physically based). But these also seem inadequate for predicting accurate nozzle erosion rates. These methods suffer from the material dependence of their models. Upon reflection, one can suggest that the actual usefulness of these calculation precedures is in providing the indepth temperature response of the structure (for use in design studies), not for prediction of actual erosion.

In summary, several methods are available for predicting material performance trends. However, the accurate estimation of nozzle erosion rates is generally unsatisfactory and depends heavily on engineering judgement.

The most important recommendation-resulting from this work is the suggestion to catalogue the results of all rocket motor tests involving carbon/carbon materials. This would be the first step towards incorporating carbon/carbon data into nozzle erosion rate correlations and would also provide phenomenological data from which better predictive theories may be developed.

It is also recommended that the inclusion of sublimation into the prediction models be reexamined. Inclusion of sublimation effects may be justified due to the increased flame temperature of recent propellants.

It would also be a desirable research objective to quantify the effects of mechanical erosion. One can suggest a series of cold flow tests involving air-entrained Al_2O_3 particles and subscale nozzles simulating representative space and ballistic motor chamber geometries. If such tests included flow visualization movies, one could also learn more concerning the complex nature of the submerged flow regions.

It would also be desirable to have a non-interfering technique for measuring instantaneous erosion rate. It has been noted that the variation of erosion rate with time is not linear, due to the increased degradation of the nozzle surface with time. Instantaneous erosion rate data would permit better correlation of existing data obtained from different duration burn times and would allow more accurate prediction of long duration motor firings.

Finally, it is suggested that erosion prediction theoretical results be presented in the manner of the correlation of Mayberry, et al.[12], which plots predicted Sherwood number vs. observed Sherwood number on a log-log basis. A glance at the resulting plot would give a quick visual assessment of the magnitude and scope of deficiencies. Consistent departures from the anticipated values within a specific range of parameters would then be assessed on a equal basis.

REFERENCES

1. "Baseline Design Test Report, Preprototype Static Test No. 1, MX Lower Stage Movable Nozzle System Advanced Development Program", Contract No. F04701-74-C-0215, Report No. A101-001 CSD, 15 February 1977.

2. "Baseline Design Test Report, Preprototype Static Test No. 2, MX Lower Stage Movable Nozzle System Advanced Development Program", Contract No. F04701-74-C-0215, Report No. A101-003 CSD, 18 November 1977.

3. Zeamer, R.J., "Survey Paper on Erosion Produced by High-Speed Two-Phase Flow in Solid Propellant Rocket Motors", Reactions Between Gases and Solids, AGARD Conference Proceedings No. 52, February 1970.

4. "Baseline Design Test Report, Preprototype Static Test No. 1, MX Lower Stage Movable Nozzle System Advanced Development Program", Contract No. F04701-74-C-0215, Report No. A101-001 CSD, Addendum 1, 30 June 1977.

5. Ellis, R.A., "Propellant Grain with Nozzle Assembly (C/CAN Program)", AFRPL-TR-78-11, Interim Report for Period 30 September 1976 to 20 January 1978.

6. Heaton, H.S. and Daines, W.L., "Flowfield Analysis of Rocket Motors", AFRPL-TR-70-98, September 1970.

7. Murphy, A.J., et al., "AFRPL Graphite Performance Prediction Program, Interim Report, Vol. I - Recommendations for a Standardized Analytic Procedure for MX Nozzle Throat Recession Calculations", AFRPL-TR-75-59, October 1975.

8. Tomlinson, P.A., and Bird, J.O., "Carbon Nozzle Opportunities", AFRPL-TR-78-46, August 1978.

9. Chemistry and Physics of Carbon, Col. 4, P.L. Walker, Jr., Editor, Marcel Decker, Inc., N.Y., 1968.

10. Delaney, L.J., et al., "A Semiquantitative Prediction of the Erosion of Graphite Nozzle Inserts", AIAA Journal 2, August 1964.

11. Gowariker, V.R., "Mechanical and Chemical Contributions to the Erosion Rates of Graphite Throats in Rocket Motor Nozzles", Journal of Spacecraft and Rockets 3, October 1966.

12. Mayberry, J.L. et al., "Correlation of Graphite Nozzle Throat Erosion in Solid-Rocket Motors", AIAA Journal 6, November 1968.

13. Diffusion and Heat Exchange in Chemical Kinetics, D.A. Frank-Kamenetskii, Princeton University Press, Princeton, N.J., 1955.

1978 USAF-ASEE SUMMER FACULTY RESEARCH PROGRAM
sponsored by the
AIR FORCE OFFICE OF SCIENTIFIC RESEARCH
and conducted by
AUBURN UNIVERSITY AND OHIO STATE UNIVERSITY

PARTICIPANT'S FINAL REPORT

ADAPTIVE/PREDICTIVE DATA COMPRESSION FOR ELECTROCARDIAGRAMS

Prepared by:	Michael Hankamer, Ph.D.
Academic Rank:	Assistant Professor
Department and University:	Electrical Engineering Texas A&I University Kingsville, Texas 78363
Assigned to:	Brooks AFB School of Aerospace Medicine Clinical Sciences Division Aeromedical Cybernetics Branch
USAF Research Colleague:	M. E. Womble, Ph.D.
Date:	August 18, 1978
Contract Number:	F44620-75-C-0031

ADAPTIVE/PREDICTIVE DATA COMPRESSION

FOR ELECTROCARDIAGRAMS

by

Michael Hankamer

ABSTRACT

The power of the computer has made digital transmission of electrocardiagrams increasingly popular; however, for efficient transmission the digitized ECG data must be preprocessed (compressed) into fewer bits per second in order to use available transmission channels.

In this study, an adaptive predictor mechanism is considered for combination with differential pulse-code modulation (DPCM) to effect the data compression: rather than the samples themselves, only the differences from the predicted values are transmitted. Since the range of values of the differences is expected to be much smaller than the range of values of the samples, data compression is achieved.

The predictor is a linear, minimum mean-square error (LMMSE) predictor derived on the assumption that the digitized ECG signal is a periodically stationary random sequence. A software program is being written to implement the predictor for testing with actual ECG data. The program will be used to study (and optimize) the predictor performance. Data collected are to be used to help specify further source coding to achieve additional data compression. Some source coding techniques are considered briefly.

ACKNOWLEDGMENT

The author is grateful to the Air Force Systems Command and the American Society for Engineering Education for providing the support for this summer research. Mr. J. Fred O'Brien of Auburn University has been an exceptional administrator for this project.

The Aeromedical Cybernetics Branch of the Clinical Sciences Division of the School of Aerospace Medicine has been a particularly pleasant experience. Dr. M. E. Womble and Ms. Linda Campbell have been most helpful during my stay.

FIGURES

INTRODUCTION

Digital transmission of electrocardiagrams (ECG's) has become increasingly popular, for three reasons. First, digital transmission has much greater noise immunity for a fixed signal-to-noise ratio. Moreover, the decreasing cost of microprocessors and other digital logic has provided the ability to do significant signal processing and control cheaply. Thus the ECG can be sampled, digitized, and pre-processed into an efficient transmission format economically. Finally, the cost of mass storage is becoming economical: the received ECG may be electronically stored in discrete form in lieu of being restored to analog form for later analysis, processing, etc.

Preprocessing into an efficient transmission format is the current "sticky wicket" in digital electrocardiagraphy. American Heart Association (AHA) standards call for 500 samples/second per lead at a precision of 9 bits/sample: for a 3-lead vectorcardiagram (VCG) a data rate of 13.5 Kbps is called for. But an unconditioned (dial-up) voice-grade telephone modem has a typical data rate capability of 2400 bps, so it follows that for real-time transmission, the VCG/ECG must be preprocessed: compressed into a fewer number of bits/second.

Compression algorithms fall into two catagories: time and frequency. Both are well covered in the literature. For example, some representative time compression algorithms can be found in Dower and Stewart [1], Cox, et.al. [2], and Weaver [3]; representative frequency compression algorithms are described in Young and Huggins [4], Ahmed, et.al. [5], and Womble, et.al. [6]. For both catagories, compression ratios of about 10:1 have been reported. The frequency representation has received somewhat more emphasis in light of its traditional attachment to the pattern recognition problem. Time representations have received somewhat less emphasis in light of their attachment to the transmission problem--appropriate algorithms have not been economical.

Womble, et.al. [6] used the optimum least mean-square (LMS) frequency representation in an algorithm to achieve a 12:1 laboratory compression ratio. This report considers the complementary solution: an optimum LMS time representation in a compression algorithm. The theory and possible extensions of such a representation are contained in the body of this report. Preliminary data on the adaptive predictor to be derived herein will be included (if available) as Appendix C.

PREDICTION ALGORITHMS

We model the sampled ECG data as a periodically stationary random sequence; that is, one for which

$$E\{s(n)\} = E\{s(n+kN)\} \tag{1}$$

$$R_s(n,m) \triangleq E\{s(n)s(m)\} = E\{s(n+kN)s(m+lN)\} \triangleq R_s(n+kN,m+lN) \tag{2}$$

for some positive integer N and any integers k, l, and n. It must be noted that the actual ECG data sequence is not periodically stationary; however, with proper 'massaging' (baseline removal, gain control, blocking, and centering about a fiducial point, etc.) it can be made close enough. Noble, et.al., used these techniques in preparing ECG data for frequency compression, for this report we assume such steps have already been taken.

Given the periodically stationary random sequence $s(n)$ we wish to consider the problem of predicting the nth member $s(n)$ given the M preceeding members $s(n-1), s(n-2), \ldots, s(n-M)$. We restrict ourselves to linear, minimum mean-square-error (LMMSE) predictors of the form

$$\hat{s}(n) = a_1 s(n-1) + a_2 s(n-2) + \cdots + a_M s(n-M) = A^T \underline{s} \tag{3}$$

where $\hat{s}(n)$ is the prediction, and $A^T = \{a_1, a_2, \ldots, a_M\}$ and $\underline{s}^T = \{s(n-1), s(n-2), \ldots, s(n-M)\}$ are Mx1 row vectors. The mean-square prediction error, $e^2(n) = [\hat{s}(n)-s(n)]^2$, can be written in matrix form as

$$e^2(n) = [A^T \underline{s} - s(n)]^T [A^T \underline{s} - s(n)]$$

which becomes

$$e^2(n) = A^T \underline{s}\underline{s}^T A - 2A^T \underline{s} s(n) + s^2(n) \tag{4}$$

Taking the expected value of the mean-square error (MSE)--remember that $\underline{s}$ and $s(n)$ are random:

$$\epsilon(n) = \mathcal{E}\{e^2(n)\} = A^T \mathcal{E}\{\underline{s}\underline{s}^T\} A - 2A^T \mathcal{E}\{\underline{s}s(n)\} + \mathcal{E}\{s^2(n)\} \tag{5}$$

The matrix $\underline{s}\underline{s}^T$ is MxM; its ijth element is $s(n-i)s(n-j)$. Taking the expectation over all elements yields the MxM symmetric correlation matrix Λ_s. The column vector $\underline{s}s(n)$ has the ith element $s(n-i)s(n)$; taking the expectation over all elements yields the correlation vector Γ. Thus

$$\epsilon(n) = A^T \Lambda_s A - 2A^T \Gamma + \mathcal{E}\{s^2(n)\} \tag{6}$$

The elements of the column vector A have not yet been chosen--we will use them to minimize the MSE $\epsilon(n)$. To effect the minimization, take the derivative of $\epsilon(n)$ with respect to A and set it equal to zero.

$$\frac{\partial \epsilon(n)}{\partial A} = \Lambda_s A + A^T \Lambda_s - 2\Gamma = 0 \tag{7}$$

Noting that $\Lambda_s A = A^T \Lambda_s$ by symmetry, we can solve for A to get

$$A_{opt} = \Lambda_s^{-1} \Gamma \tag{8}$$

from which it follows that the minimum mean-square error is given by

$$\epsilon(n)_{min} = \mathcal{E}\{s^2(n)\} - \Gamma^T \Lambda_s^{-1} \Gamma \tag{9}$$

for each n. Note that the minimum mean-square error $\epsilon(n)$ depends on n;

the predictor is adaptive. This results from the random sequence $\underline{s}$ being at most periodically stationary: wide-sense stationarity would be required to make the minimum mean-square error independent of n.

Suppose M=N; e.g., one full period is used in forming the estimate of the next sample. Since the random sequence is periodically stationary, it can be shown that the matrix Λ_s is circulatory: $\Lambda(n+1)$ differs from $\Lambda_s(n)$ by just a row and column shift. For this case the column vector Γ is identically the last column of Λ_s and it follows that the optimal predictor A_{opt} $(=\Lambda_s^{-1}\Gamma)$ is exactly the vector $\{0,0,\ldots,1\}^T$. The optimum prediction is just the sample value from one period earlier. Carried to its logical conclusion, we have proved that the optimal LMMSE prediction of a heartbeat is the prior beat.

The answer is intuitively obvious, and not particularly helpful, since by implication, the first beat must be sent in full--compression can occur only on succeeding beats. Let us briefly consider another formulation. Let $\underline{s}$ be the heart signal and $\underline{x} = \underline{s}+\underline{v}$ be the measured heart signal (corrupted by the noise term $\underline{v}$). Using the same linear predictor as before,

$$\hat{s}(n) = A^T\underline{x} = A^T\underline{s} + A^T\underline{v}$$

The squared error $e^2(n) = [\hat{s}(n)-s(n)]^2$ can be written in matrix form as

$$e^2(n) = [A^T\underline{s} + A^T\underline{v} - s(n)][A^T\underline{s} + A^T\underline{v} - s(n)]^T$$

Expanding, taking expected values, and minimizing as before yields the optimum predictor coefficients

$$A_{opt} = [\Lambda_s + \Lambda_v]^{-1}\Gamma$$

where we have assumed that $s(n)$ and $v(n)$ are uncorrelated and $v(n)$ has zero mean. A_{opt} is no longer the trivial predictor as before; the reason being that Λ_v is not circulatory (by the implicit assumption that the noise is not periodic). This result is of impressive simplicity--it is not practical. The reasons are simple. First, both Λ_s and Λ_v are required; finding them would require assumptions on one or the other (or both) or would require experimental determination. Second, the result cannot be extended to the full-period vector formulation: the extension requires periodicity.

It is to be noted that this particular approach is very close to the Kalman formulation of the control problem. In it, the signal $s(n)$ is assumed to be an autoregressive source driven by a random generator $v(n)$.

$$s(n+1) = \Phi^T\underline{s} + v(n)$$

---

*A simple proof is given in Appendix A.

The measurement $x(n) = s(n) + w(n)$, where $w(n)$ is measurement noise. The Kalman formulation then desires a linear estimator $\hat{s}(n) = A^T\underline{x}$ such that the mean-square error is minimized. The autoregressive assumption is probably reasonable, and the Kalman formulation has the advantage that the estimator is recursive. But it is very restrictive in terms of noise models; i.e., the same objections as the preceeding formulation.

The approach to be adopted is to modify the first predictor by truncating it to $M<N$ terms. In so doing, neither Λ_s nor Γ is circulatory and hence the predictor is no longer trivial. Moreover, it is adaptive; using the most recent information available about the specific waveform it is attempting to predict. The algorithm is explained in Appendix B.

FUTURE DIRECTIONS

This portion of this report is being written without benefit of clergy--that is, the software adaptive predictor is not yet running. Without data to determine the quality of the predictor, it is extremely difficult to make any meaningful statements about what should follow. We expect the predictor to be quite accurate; e.g., the difference $\hat{s}(n)-s(n)$ should be small for most measurements. Recall that the predictor length M is variable and (from Appendix B) that the predictor complexity depends roughly on M^2. Thus two important questions yet to be answered are: How will the accuracy (i.e., mean-square prediction error) vary with M? Is there an optimum predictor length? Answers require the predictor difference statistics--experiment.

Yet another point to consider is that no matter how good the predictor, it must occasionally fail--for example, due to noise in the measurement--and as was pointed out in an earlier report [7], any differential method of data transmission is limited by the magnitude of the worst difference. For example, if the worst difference requires 3 bits to transmit, then <u>every</u> difference must be encoded into 3 bits in lieu of additional processing and the compression is fixed at N:3. The average number of bits required to transmit a difference can be reduced by source coding, but to effectively source code requires the predictor difference statistics; again, experiment. Source coding procedures are general, however, and so we turn to techniques.

The classical method is Huffman coding(see [8], sec. 3.4), a variable-length procedure that assigns unlikely messages (i.e., big differences) very long codewords in order to save very short codewords for the likely messages (i.e., small differences). The <u>average</u> codeword length is always less than that required to send the messages directly. The Huffman code normally requires a large codebook (memory) but Weaver [3] proposed a procedure later formalized by Hankamer [9] to reduce the codebook dramatically with only a small increase in average word length. Thus the modified Huffman procedure is quite attractive if the differences are such that only a very small minority differ significantly from zero.

(a) LMS predictor (b) tree encoder

Figure 1. Tree Encoding

A more recent approach to the source coding problem is called tree encoding. It is an extension of predictive DPCM employing some of the results of error control coding and rate-distortion theory. The procedure is complex, but the idea is rather simple. Ordinary predictive DPCM makes a LMS prediction of the next sample based on some statistical knowledge of the source and transmits the difference--irregardless of its size. A tree encoder takes a look at the difference and, if necessary, modifies its prediction. Since each set of previous estimates can have multiple predictions extending from it, the prediction sequence has the branchlike structure of a tree (see Figure 1), hence the name tree encoding. The data to be transmitted is the path through the tree, and the "best" path is chosen by the encoder according to some pre-selected distortion measure. An excellent reference for this approach is Anderson and Bodie [10]. In particular, their Figure 3 (see Figure 2, next page) block diagrams an encoder--note that the quantized error is returned to the predictor. Their Figure 8 (also Figure 2, next page) indicates the complexity of the general encoder.

Huffman coding offers the possibility of exact reproduction of the transmitted sequence, but at a cost (in bits transmitted per sample) dependent on the probability structure of the differences. Tree encoding, on the other hand, offers the ultimate in compression (one bit transmitted per sample), but at the cost of only being able to reproduce the sequence to within the distortion measure. Which of the two methods is more appropriate is an open question at this time.

One last point to consider: the ultimate reduction possible using this predictive DPCM is 1 bit/sample. Assuming a sample precision of 9 bits/sample, the ultimate compression ratio is only 9:1. Womble, et.al. have already exceeded 12:1 in the laboratory using a frequency algorithm. In order to further compress the data, one must somehow begin to delete samples. One method was implied in the pre-transmission "massaging"--in blocking each heartbeat to a centered N-sample segment

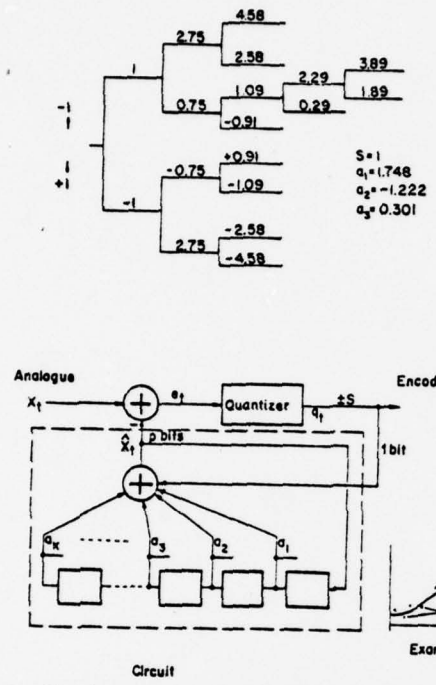

Fig. 3. Circuit, code tree, and example for DPCM. Recursive realization of McDonald model.

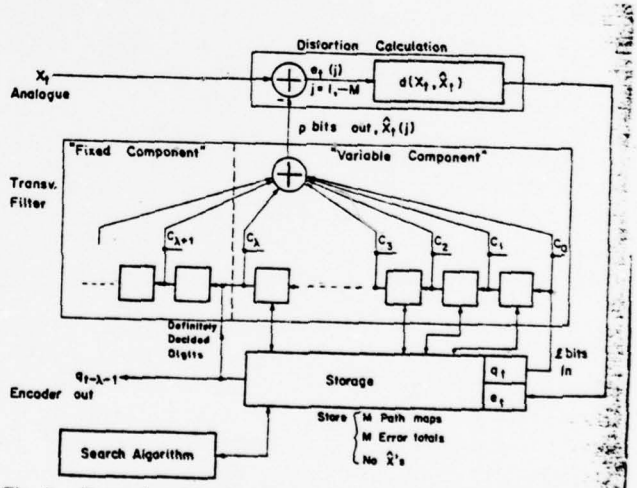

Fig. 8. General multipath encoder using transversal code generator.

Figure 2. Tree encoders. Some block diagrams.

for transmission, some samples (usually between beats) are deleted. If the predictor proves to be good, then another method suggests itself--interpolation. That is, transmit only every second (or third, or fewer) samples; interpolate the remaining points using a MMSE interpolator. The interpolator would have basically the same form as the predictor (hence approximately the same MSE) and be readily extendible into a non-adaptive, full-period vector form.

REFERENCES

[1] Dower, G.E., and D. Stewart, "An ECG compression code," J. Electrocardial., VI, No. 2 (1973) 175-176.

[2] Cox, J.R., et.al., "AZTEC, a preprocessing program for real-time ECG rhythm analysis," IEEE Trans. Bio-Med. Eng., BME-15 (Apr 68) 128-129.

[3] Weaver, C.S., Digital ECG Data Compression (Working Paper), SRI International, 333 Ravenswood Ave., Menlo Park, CA 94025 (20 July 1977).

[4] Young, T.Y., and W.H. Huggins, "On the representation of electrocardiagrams," IEEE Trans. Bio-Med. Eng., BME-10 (Jul 63) 86-95.

[5] Ahmed, N., et.al., "Electrocardiagraphic data compression via orthogonal transforms," IEEE Trans. Bio-Med. Eng., BME-22 (Nov 75) 484-492.

[6] Womble, M.E., et.al., "Data compression for storing and transmitting ECG/VCG's," Proc. IEEE, Vol. 65, No. 5 (1977) 702-706.

[7] Hankamer, M., "Electrocardiagram data compression: discussion and recommendations," unpublished report for the Aeromedical Cybernetics Branch, Clinical Sciences Division, School of Aerospace Medicine, Brooks AFB, TX (28 Jul 1978).

[8] Gallager, R.G., Information Theory and Reliable Communication, John Wiley, 1968.

[9] Hankamer, M., "An almost optimum Huffman procedure with reduced memory requirement," unpublished memorandum, 1 Aug 78.

[10] Anderson, J.B., and J.B. Bodie, "Tree encoding of speech," IEEE Trans. Inform. Thy., IT-21, No. 4 (Jul 75) 379-387.

APPENDIX A

Let us assume that M=N=3; a full period estimate of the next sample s(n+1) of the periodic random sequence $\underline{s}$ is being derived. The correlation matrix Λ_s is given by

$$\Lambda_s = \begin{bmatrix} R(n,n) & R(n,n-1) & R(n,n-2) \\ R(n-1,n) & R(n-1,n-1) & R(n-1,n-2) \\ R(n-2,n) & R(n-2,n-1) & R(n-2,n-2) \end{bmatrix}$$

and the correlation vector Γ is given by

$$\Gamma = \begin{bmatrix} R(n+1,n) \\ R(n+1,n-1) \\ R(n+1,n-2) \end{bmatrix} = \begin{bmatrix} R(n+1-3,n) \\ R(n+1-3,n-1) \\ R(n+1-3,n-2) \end{bmatrix} = \begin{bmatrix} R(n-2,n) \\ R(n-2,n-1) \\ R(n-2,n-2) \end{bmatrix}$$

where we have used the periodicity of $R(\cdot,\cdot)$. We note that Γ is in fact the last column of Λ_s since R(n,m) = R(m,n).

THEOREM: The optimum estimator coefficient vector $A_{opt}=\Lambda_s^{-1}\Gamma=\{0,0,\ldots,1\}^T$ for any sample.

Proof: From above, we know that $\Lambda_s A_{opt}=\Gamma$. We may find the i^{th} entry of the vector A by Carson's Rule.

$$a_i = \frac{|\Lambda_s(i)|}{|\Lambda_s|}$$

where $|\cdot|$ indicates the determinant and $\Lambda_s(i)$ is the matrix Λ_s with the i^{th} column replaced by Γ. If $i\neq N$, then $\Lambda_s(i)$ has two identical columns, from which it follows that its determinant is zero and hence $a_i=0$. If i=N, then we are replacing the last column by itself, from which $|\Lambda_s(N)| = |\Lambda_s|$ and hence $a_N=1$.

QED

APPENDIX B

We assume that the ECG data has been properly "massaged" and has been transformed into N-sample data blocks prior to entering the predictor. If so, then the prediction algorithm has the functional block diagram given in Figure B-1. Two comments about the program are in order.

First, the correlation functions used in the matrix Λ and vector Γ are statistical averages taken over an ensemble of random sequences, so we must provide an "ensemble" for the program to work with. This is done by providing the program with an ensemble of two: H1 and H2. H1 is initially random and H2 contains a population average heart signal. Ensemble averages for the various correlations are computed on the basis of this "ensemble" with H1 having probability p and H2 having probability (1-p). As samples enter the program, H1 and H2 are continuously updated in such a fashion that H2 always contains the prior period and H1 contains the average of the preceeding periods. The probability p is left free to weight the ensemble in any desirable fashion.

Second, the difficult part of the program is the inversion of the MxM matrix Λ. Currently it is being done by standard subroutine algorithms, but since Λ is symmetric and partially circulatory, it seems likely that a simpler special-purpose algorithm could be designed to reduce the complexity.

Matrix manipulation is typically one of the most time-consuming operations a computer is called upon to perform; running time is approximately proportional to M^2. We note that there are actually two matrix manipulations in this program: the matrix inversion and the correlation updating. Since each operation must be performed for each new sample, it is imperative that M not be allowed to grow too large.

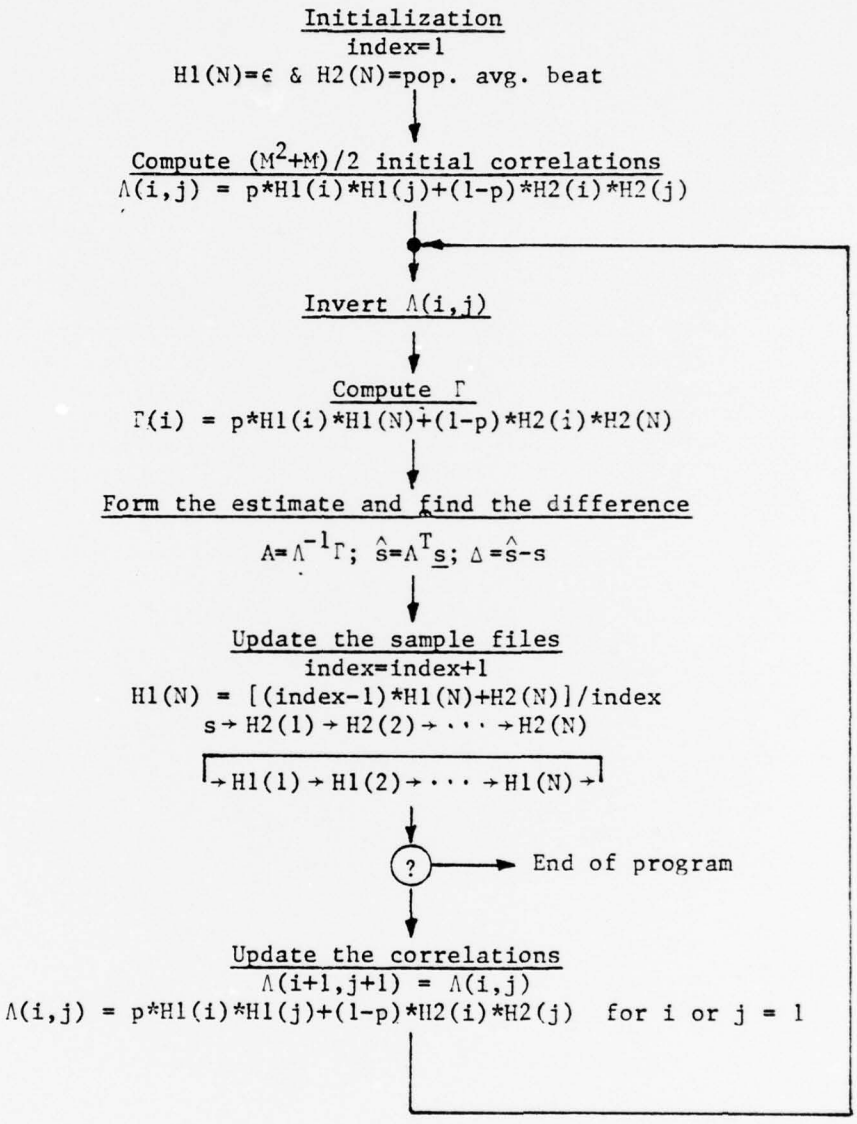

NOTE: most recent data is assumed to be stored at beginning (first term) of arrays.

Figure B-1. Adaptive-predictor program (flow chart)

APPENDIX C

(No data available as of August 18, 1978)

1978 USAF-ASEE SUMMER FACULTY RESEARCH PROGRAM

sponsored by

THE AIR FORCE OFFICE OF SCIENTIFIC RESEARCH

conducted by

AUBURN UNIVERSITY AND OHIO STATE UNIVERSITY

PARTICIPANT'S FINAL REPORT

IN VITRO STUDY OF MICROWAVE EFFECTS ON CALCIUM EFFLUX IN RAT BRAIN TISSUE

Prepared by:	Wesley W. Shelton, Jr., Ph.D.
Academic Rank:	Assistant Professor
Department and University:	Department of Electrical Engineering Florida Institute of Technology
Assignment:	
(Air Force Base)	USAF School of Aerospace Medicine, Brooks AFB, Texas 78235
(Laboratory)	Biochemistry
(Division)	Radiation Sciences Division
(Branch)	Radiation Physics Branch
USAF Research Colleague:	James H. Merritt
Date:	25 August 1978
Contract No.:	F44620-75-C-0031

IN VITRO STUDY OF MICROWAVE EFFECTS ON CALCIUM EFFLUX IN RAT BRAIN TISSUE

by

Wesley W. Shelton, Jr.

ABSTRACT

Considerable experimental evidence has accrued identifying adverse central nervous system response to radiofrequency and microwave radiation, the appearance and severity of change being a function of such variables as power density, frequency, exposure duration, and facilitating factors (e.g., drugs, stress). A yet uncertain and highly contested question is that of a threshold (or threshold values for the variables) characterization of radiofrequency/microwave irradiation at which a threat to human well-being becomes manifest.

This study investigated the prospect of microwave-induced alteration of $^{45}Ca^{++}$ efflux in brain tissue at low values of pulse repetition frequencies (PRF) and power densities under in vitro experimental conditions. Rat cerebral tissues were incubated for 30 min with $^{45}Ca^{++}$ and then transferred to fresh solution (efflux medium) for a 20 min exposure to pulsed microwave irradiation according to one of several PRF-power density exposure schemes: 16 Hz at 0.5, 1.0, 2.0, and 15.0 mW/cm^2, and 32 Hz at 1.0 and 2.0 mW/cm^2. Measurements of radioactivity in the efflux medium and in the tissue sample were used to calculate an efflux value for each sample. Control samples were placed in the irradiation chamber with the power off to accomplish "sham" conditions.

Preliminary statistical treatment of the data indicates that no significant differences exist between irradiation and control efflux values.

I. INTRODUCTION

A. Background

A considerable amount of experimental evidence has accrued establishing adverse physiological responses to radiofrequency and microwave radiation. With regard to the central nervous system, the evidence is drawn from multi-faceted studies describing electrophysiological, neurochemical, morphological, and behavioral modifications induced by these radiations, the appearance and severity of change being functions of such variables as power density, frequency, and facilitating factors (e.g., drugs, stress, etc.).

Still controversial, however, is the ultimate question regarding bioeffects of electromagnetic radiations: are there critical, or threshold, values of these variables for which the onset of adverse bioeffects appears, and what are they? Massive experimentation in the Soviet Union and East European countries has led them to conclude that a basic safety criterion is that exposure levels should remain below 10 $\mu W/cm^2$. Less than adequate reporting procedures by the latter researchers left Western researchers in uncertainty regarding the conclusions drawn from those works. Spurred by the recognition of a need for safety standards in the face of ever-increasing use of electromagnetic radiations, Western research soon led to a power density of around 10 mW/cm^2 as the basic exposure safety standard. This three orders of magnitude variance from the Soviet standard is still a contested point, and currently much research is still being invested in the examination of these standards.

B. Brief Literature Survey

Bawin, Kaczmarek and Adey (1) reported a range of frequencies, 6-20 Hz, whose sinusoidal modulation (80-90% modulation depth) of a 147-MHz carrier could produce significant increases in $^{45}Ca^{++}$ efflux at low power densities (around 1 mW/cm^2) in neonatal (2-7 days in age) chick forebrains. The latter experimental subject was selected for its reportedly high sensitivity to small perturbations in extracellular Ca^{++} concentrations. The maximal response occurred at 16 Hz, where $^{45}Ca^{++}$ efflux was found to be 18.5% above controls. Frequencies outside this range, as well as the unmodulated carrier itself, were ineffective in producing any efflux changes.

A subsequent report by Bawin and Adey (2) considered the actions of only the slow modulation frequencies on $^{45}Ca^{++}$ efflux, motivated by the apparent absence of effects on efflux in brain tissue irradiated with unmodulated carrier in an earlier experiment (1). Samples of cat cortical tissue were included in this experiment along with chick brains. Here, it was concluded that direct application of 6-16 Hz sinusoidal fields

could produce a decrease in $^{45}Ca^{++}$ efflux in chick and cat brain tissue. However, this effect was observed only when signals in the "window" of neuroactive frequencies possessed amplitude values within another "window" ranging from 56 to 100 V/m. The reduction in efflux was found to be as much as 15% below that of controls.

The findings reported in the two original papers (1, 2) have been reasserted in later reports (3, 4).

C. Experimental Rationale

The experimentation described in this report was designed to investigate the prospects of microwave alteration of $^{45}Ca^{++}$ efflux under conditions more compatible with those of immediate interest to the Air Force. Thus, the insult selected is pulsed microwave emission of low power density as observed in the far-field region. The selection of Sprague Dawley rats introduces a mammalian brain less sensitive to small perturbations of extracellular divalent ion concentrations than chick brain while at the same time permitting ease in tissue access. Several combinations of modulation frequencies (or pulse repetition frequencies, PRF) and power densities were constructed from representative values within and external to the respective "windows" specified above. The correspondence between the amplitude (electric field intensity, E) and incident power density (PD) as seen in the far-field region was taken as

$$E\left(\frac{\text{Volts}}{\text{m}}\right) = \sqrt{PD\left(\frac{\text{mW}}{\text{cm}^2}\right) \times 3770} \qquad (5).$$

$^{45}Ca^{++}$ efflux findings from rats exposed to this variety of irradiation schemes were compared to those of control rats which underwent "sham" irradiation.

II. METHODS AND MATERIALS

A. Animals and Sample Preparation

Male albino Sprague Dawley rats, 140-200 g, were used exclusively in these experiments and were allowed Purina Chow and water ad libitum. The animals were sacrificed by means of cervical dislocation and the cerebral hemispheres rapidly removed. Frontal lobe samples were obtained with a #10 surgical blade by three cuts: a midsagittal cut, a horizontal cut originating at the frontal poles and extending to about midpoint along the longitudinal axis, and a coronal cut approximately 5 mm posterior to the frontal poles. Thus, two samples were obtained per animal. The samples were then weighed and placed in beakers partially immersed in ice prior to incubation while additional samples were obtained. Three pairs of forebrain samples were processed together in a group as either experimentals or controls. Each day consisted of a morning and an afternoon

experimentation session. In each session an experimental group was first processed, followed by a control group which subsequently occupied the same chamber apparatus to accomplish "sham" irradiation. Four groups (one set) of experimentals and four groups of controls comprised the sample population for each experiment. The basic procedures used in these experiments are expressed by the flow chart in Figure 1. Additional details are provided in the individual experiment descriptions given below and in Table 1.

B. Incubation Medium

The incubation medium used in these experiments was that described by Cooke and Robinson (6): 124 mM NaCl, 26 mM $NaHCO_3$, 5 mM KCl, 12 mM KH_2PO_4, 1.3 mM $MgSO_4$, 0.75 mM $CaCl_2$, 10 mM glucose.

C. $^{45}Ca^{++}$ Solution

10 μCi/cc of incubation medium (obtained from ICN Pharmaceuticals, Inc.) (half-life 164 days).

D. Anechoic Chamber

An L-band horn transmitter was positioned vertically above a plexiglass water bath which was centered beneath at the horn center-point. The irradiation was performed in the center of the 10 ft X 10 ft test center of an Emerson and Cumming 10 ft X 10 ft X 24 ft tapered Eccosorb anechoic chamber. The samples were contained in glass beakers and arranged in two parallel rows of 3 beakers each by a floating styrofoam holder, the array dimensions being restricted to values much smaller than those of the mouth of the horn. The samples were maintained in the far-field region, and the $\hat{k}$-vector was normal to the array surface. Heating effects were considered negligible as a result of measurements made in media-filled beakers under exposure conditions. Incident power densities at the sample-array plane wave were obtained using a Narda Electromagnetic Radiation Monitor (Model 8316b) and Isotropic Probe (Model 8231). A gentle back-and-forth, lateral motion (approx. one cycle per second) was imparted to the array by a long plexiglass rod (1/2" dia.) attached to the floating styrofoam holder in the water bath and adapted to the shaft of a Research Specialties shaking water bath maintained approximately 1 yd away from the immediate irradiation area. Water was maintained at 30°C by a Neslab heating unit outside the chamber and routed to and from the plexiglass reservoir in the chamber by tubing. Lateral displacements of the styrofoam holder were limited such as to keep the samples at all times underneath the horn mouth.

E. Experiments I-V

These experiments were designed to provide data regarding $^{45}Ca^{++}$ efflux after 20 minutes of irradiation at one of six selected regimens.

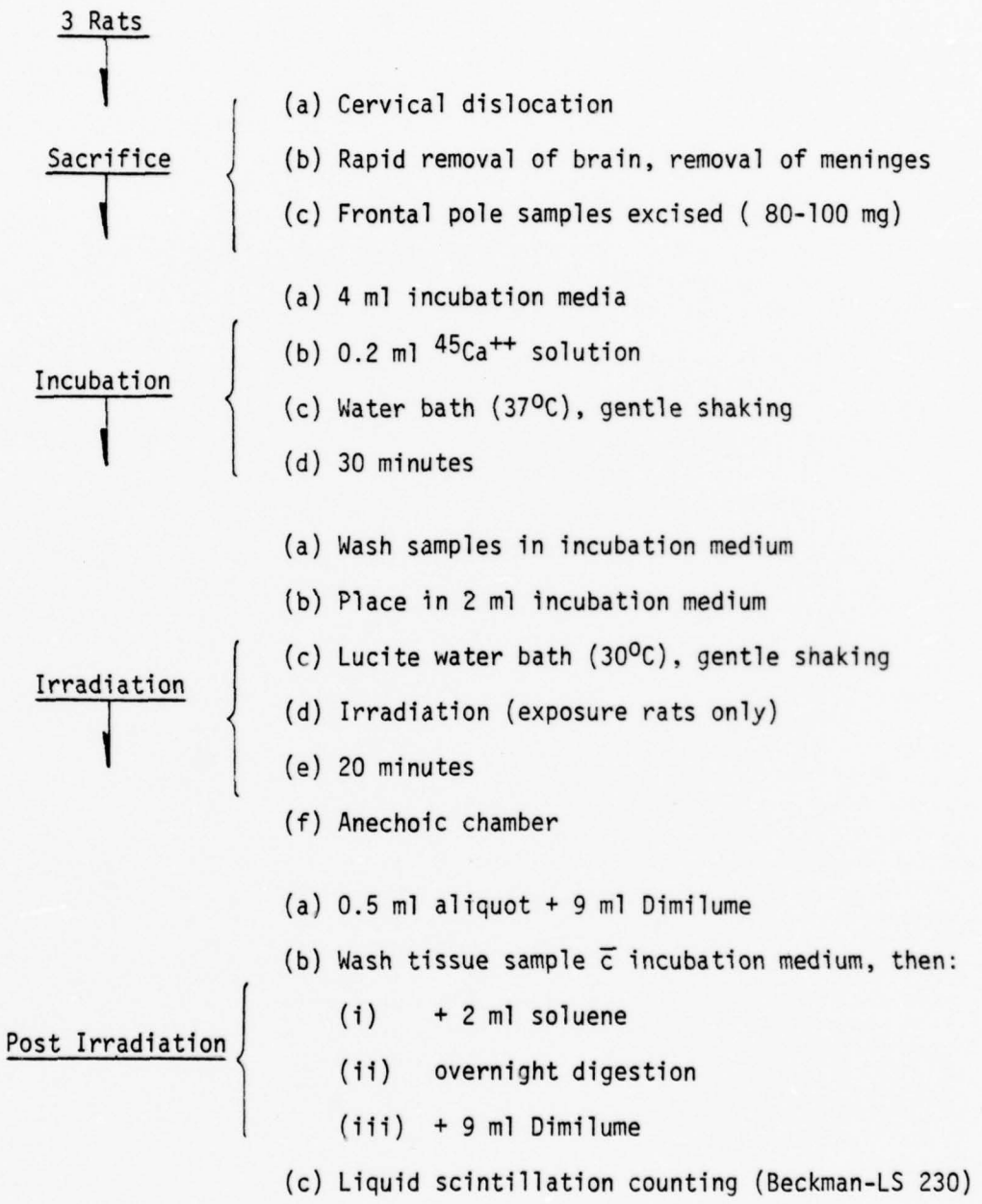

Figure 1. Flow Chart for Basic Experimental Procedures

Each regimen is characterized by a pulse repetition frequency (PRF) and incident power density chosen on the basis of the "window" values described by Bawin, Kaczmarek and Adey and Bawin and Adey (1, 2). The protocol is graphically presented in Table 1. An asterisk accompanying a power density or PRF specification indicates that value to be within the "window" for that parameter.

Exp.#	Pwr Density (mW/cm^2)	Carrier Freq (GHz)	P.W. (msec)	PRF (Hz)	Duty Factor	# Samples Exposure	# Samples Control
I	1.0*	1	20	16*	0.32	24	24
II	2.0	1	20	16*	0.32	24	24
III	0.5*	1	20	16*	0.32	24	24
IV	1.0*	1	10	32	0.32	24	24
V	2.0	1	10	32	0.32	24	24
VI	15.0	1	20	16*	0.32	24	24
VII,VIII	1.0	1	20	16*	0.32	24	24

Table 1. Exposure Parameters

F. Experiment VI

This experiment involved irradiating tissue at an incident power density exceeding the upper limits of the current U.S. standard in an attempt to elicit changes in $^{45}Ca^{++}$ efflux. See Table 1 for exposure details.

G. Experiment VII

This experiment was basically the same as Experiment I except that the irradiation was interrupted for approximately 1 minute after 4 and 8 minutes of accrued irradiation. During the interruption, 0.5 ml aliquots were obtained from each sample and 0.5 ml of fresh incubation medium added in replacement. The experiment was terminated after 12 minutes of irradiation, and the post-irradiation treatment described in Figure 1 was employed. The data acquired in this experimentation were used to determine any changes in the kinetics of $^{45}Ca^{++}$ that might be induced by microwave irradiation. The exposure parameters are given in Table 1.

H. Experiment VIII

This experiment was a repetition of Experiment I except for changes in tissue handling techniques. Two basic modifications were employed: three washes from wash bottle at approximately 3-4 ml per wash (instead of the usual single washing); and more attention to removal of pia from brain surface (also adding another factor of having a lengthier time interval between extraction of sample to delivery to incubation medium). See Table 1 for irradiation scheme.

III. RESULTS

The term "efflux value" in this study was taken to mean specifically

$$\text{efflux value} = \frac{\text{CPM (medium)}}{\text{CPM (tissue)} + \text{CPM (medium)}}$$

where CPM (medium) is the total counts-per-minute (CPM) in the efflux medium as determined from measurements made on the aliquots and CPM (tissue) is the total CPM measured in the tissue at the end of an experiment. The denominator, then, represents the total CPM in the tissue at the outset of an experiment. A slight modification in the use of this expression was necessary in Experiment VII, the kinetics study. In the latter study, the net loss of $^{45}Ca^{++}$ during each interval between samplings (0-4 min., 4-8 min., and 8-12 min. of radiation or control treatment) and successive efflux values were derived by taking the ratio of each of those values to total tissue $^{45}Ca^{++}$ content determined to be present at the outset of the experiment.

All results were subjected to only the basic statistical analysis because of time limitations, and further such analysis will be performed shortly, though confidence in the basic findings here is expressed. Nonetheless, the treatments applied permitted preliminary evaluations of any differences between exposed and control efflux values. Extreme values were also scrutinized and discarded where statistical protocol allowed.

A summary of all results of this study is presented in Table 2.

Experiments I-III. The results of the first three experiments are graphically displayed in Figure 2. No statistically significant difference could be found between radiation and control efflux values in any of the experiments, as indicated by the modest t-values in Table 2. The PRF used in all three cases was within the "window" for this variable, and the 0.5 and 1.0 mW/cm^2 values were within the power density "window."

Experiments IV and V. Figure 3 is a graphical presentation of the results observed in the 32 Hz PRF study. Again, no significant differences could be found between control and radiated groups.

Expt.	Pwr Dens. mW/cm^2	Efflux Value (m±S.D.)		Student's t-test
		Exposed (n)	Control (n)	t
I	1.0	36.8±5.6 (24)	39.5±4.2 (23)	1.9
II	2.0	34.4±6.1 (24)	32.3±6.9 (24)	-1.1
III	0.5	36.7±4.5 (24)	36.6±4.1 (24)	-0.1
IV	1.0	40.3±5.0 (24)	39.1±4.6 (24)	0.9
V	2.0	39.0±5.0 (22)	39.4±4.0 (24)	0.3
VI	15.0	39.4±6.8 (24)	38.4±4.0 (24)	-0.6
VII	1.0			
	(4 min)	18.8±3.7 (24)	18.7±3.1 (24)	-0.1
	(8 min)	9.0±2.3 (24)	9.1±2.5 (24)	-0.1
	(12 min)	6.8±1.8 (24)	7.3±1.7 (24)	1.0
VIII	1.0	45.5±6.8 (24)	48.5±8.7 (24)	1.3

Table 2. Summary of efflux values. Efflux values are expressed as mean percentages (m) and standard deviations (S.D.), and the number of samples (n) used in calculating each value is given in parentheses.

Experiment VI. The results of this experiment failed to reveal any significant changes from normal efflux behavior despite the high level (15 mW/cm^2) of power density used.

Experiment VII. Initial experimentation indicated that the vast portion of efflux occurred by the time 12 minutes of accrued irradiation had elapsed. Thus, sampling at regular 4-minute intervals between the start of irradiation and 12 minutes of total irradiation was considered to be appropriate for observing any efflux differences that might be induced by irradiation during the most active phase of the efflux phenomenon. The 20-minute point is essentially covered by Experiment I.

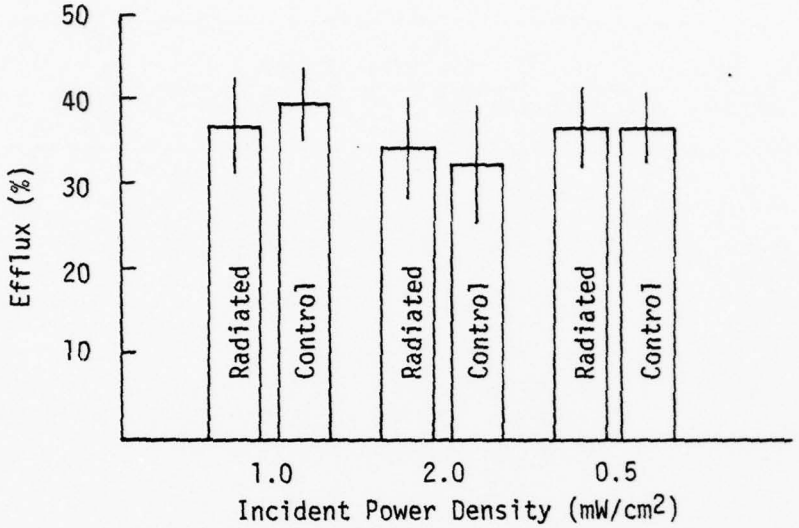

Figure 2. Experiments I, II, III: Efflux values plotted versus various incident power densities at a PRF of 16 Hz. Standard deviations are indicated by vertical lines atop the bars.

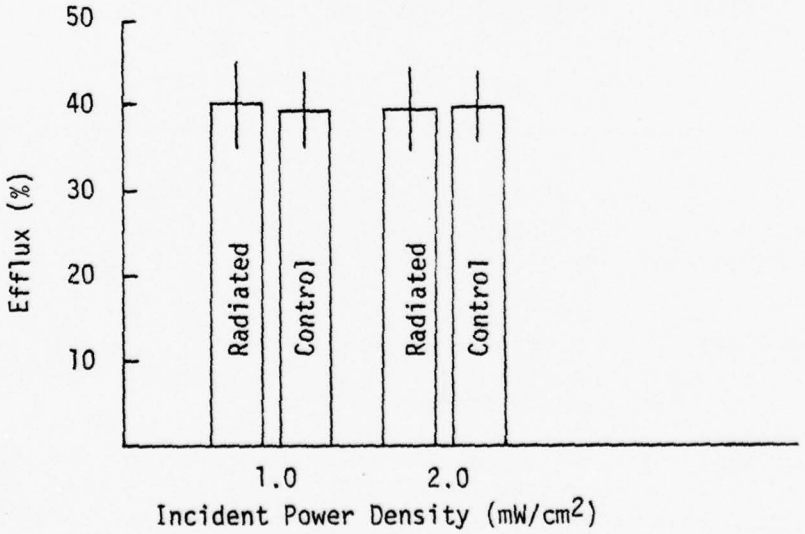

Figure 3. Experiments IV, V: Efflux values plotted versus various incident power densities at a PRF of 32 Hz. Standard deviations are indicated by vertical lines atop the bars.

The sampling technique used for Experiment VII was developed to allow completion of investigation into the biological end-points just described within the time frame provided: the more valid alternative would have been to process an entire control and exposure set of animals for each sampling time. The technique of successively taking aliquots of the efflux media and replacing with fresh $^{45}Ca^{++}$-free medium in preparation for the next sample complicates the kinetics interpretation of the results since the external $^{45}Ca^{++}$ concentration is altered (reduced) twice during the experiment. But the results here are conclusive regarding a valid index of change in efflux. A graphical presentation of the findings are presented in Figure 4. The points plotted are the respective set (24 animals) averages taken on three "efflux figures" derived for each sample in a given set by successive incrementation of the net efflux values described above. The values plotted are given in Table 3.

	Efflux Figure (m±S.D.)		
	t=4 min	t=8 min	t=12 min
Radiated	18.8±3.7	27.8±3.5	34.6±4.1
Control	18.7±3.1	28.1±4.1	35.3±4.0

Table 3. Efflux figures used to construct the graph in Figure 4. The times given indicate accrued irradiation time.

Experiment VIII. Although no significant efflux value differences are evident in this "special handling" experiment, the substantially higher means indicate that the $^{45}Ca^{++}$ efflux was enhanced by the processing changes employed in this experiment as pointed out by comparison with Experiment I.

IV. CONCLUSIONS AND RECOMMENDATIONS

The results of all experimentation performed in this in vivo study failed to reveal any significant alteration of the $^{45}Ca^{++}$ efflux behavior in brain tissue irradiated by low-PRF pulsed microwaves presented in the far-field region at low power densities or at a power density slightly in excess of current U.S. standards. As stated earlier, further in-depth statistical analysis must yet be applied to the data, and this task is expected to be completed within a few weeks of the date of this report.

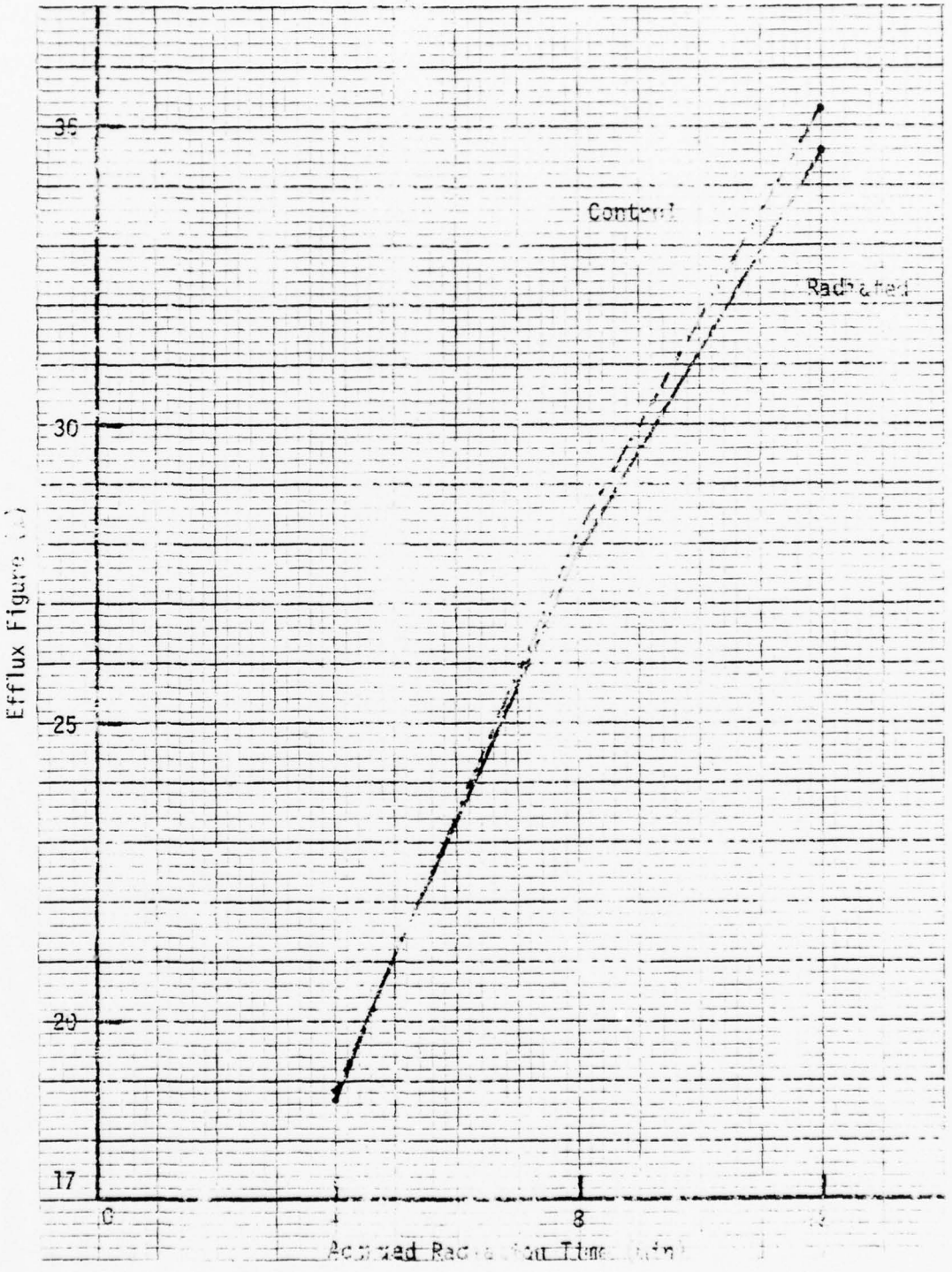

Figure 4. Plot of efflux figures for Experiment VII. See text and Table 3.

Reports by others (1, 2, 3, 4) of definite changes materializing in RFR-treated (in vivo) brain tissue appears to be a reproducible finding as demonstrated by the original researchers themselves as well as by others employing similar methodology (personal communication). Although the present study was motivated in part by those reports, a direct comparison between those results and the results presented herein is not practical in view, principally, of the dissimilar parameter selections used in the basic experimental procedures. The most prominent differences are the use, by others, of VLF sinusoidal modulation of a 147 MHz carrier for experimental insult and chick and cat brain tissues for efflux analysis. Furthermore, differences are apparent in what is meant by the term "efflux," which in the case of others is based on normalization of measured CPMs to sample weights. More insight into laboratory procedures, instrumentation, and experimental protocol might contribute to an explanation of why no transport perturbation was evoked in this experiment: for instance, tissue handling technique is known to be a critical factor in the experimental procedure. The weight of evidence, though, would seem to dictate assessment that whereas efflux anomalies indeed appear under the experimental conditions set forth by others (1, 2), they simply fail to develop within the experimental framework utilized in the present work.

Certainly further work needs to be pursued within the totally in vivo regime described in the preceding paragraphs. A more comprehensive range of carrier frequencies and modulation schemes as well as a more exhaustive analysis of tissue-handling considerations (e.g., superficial lacerations, uniformity of sample geometries, distribution of absorbed $^{45}Ca^{++}$ in samples during "loading" -- perhaps an autoradiography study in this regard) would be essential elements to be incorporated into additional experimentation to describe efflux behavior in other important regions of the RFR/microwave range.

But in vivo experimentation is clearly not the most optimal approach to the study of mammalian brain pathology. The damage inevitably incurred by the superficial aspect of the tissue during resection as well as the isolation of the sample from the intricate and delicate homeostatic cerebral environment, to name a few disadvantages, pose serious obstacles to the projection of in vivo into the real-life situation.

A plausible first step toward improvement in experimental design would be the introduction of live animals for at least the 'loading' phase of the experiment. Here, the $^{45}Ca^{++}$ would be administered intracisternally by hypodermic needle prior to irradiation. Brain tissue "loading" would then proceed in vivo. For a short-term study, however, the removal of the brain sample after the treatment period would follow the same procedures employed in the in vitro study. In such a study, several different carrier frequencies with appropriate PRF and power density characteristics simulating specific communications or radar (e.g., PAVE PAWS, MLS) scenarios could be selected for experimental irradiation.

Ultimately, completely in vivo studies (with their attendant complexities) are desired. As with the previous experimentation suggestion, dosimetry considerations become more acute because of the bone, skin, and other tissues interspersed between incident radiation and the brain itself. However, this poses no insurmountable obstacle and techniques are available for deriving valid estimations of energy distribution under such circumstances. Such experimentation would have as an initial goal the identification of appropriate biological end-points and the evaluation of techniques to be used in measuring changes in the end-points.

V. REFERENCES

1. Bawin, S. M., Kaczmarek, L. K., and Adey, W. R. "Effects of Modulated VHF Fields on the Central Nervous System," Ann. N.Y. Acad. Sci. 247: 75-81 (1975).

2. Bawin, S. M., and Adey, W. R. "Sensitivity of Calcium Binding in Cerebral Tissue to Weak Environmental Electric Fields Oscillating at Low Frequency," Proc. Natl. Acad. Sci. 73:1999-2003 (1976).

3. Bawin, S. M., and Adey, W. R. "Calcium Binding in Cerebral Tissue," Proc. Symposium on Biological Effects and Measurement of Radio Frequency/Microwaves, February 1977 (Ed. D. G. Hazzard).

4. Bawin, S. M., and Adey, W. R. "Interaction Between Nervous Tissue and Weak Environmental Electric Fields," USNC/URSI Annual Meeting, October 1975 (Eds. C. C. Johnson and M. L. Shore).

5. Radiofrequency Radiation Health Hazards Control (AFR 161-42), November 1975.

6. Cooke, W. J., and Robinson, J. D. "Factors Influencing Calcium Movements in Rat Brain Slices," Amer. J. Physiol. 221:218-225 (1971).

1978 USAF-ASEE SUMMER FACULTY RESEARCH PROGRAM

sponsored by

THE AIR FORCE OFFICE OF SCIENTIFIC RESEARCH

conducted by

AUBURN UNIVERSITY & OHIO STATE UNIVERSITY

Participant's Final Report

Effect of Microwave Exposure on Certain Neuroendocrine Parameters in Various Regions of the Rat Brain

Prepared By:	Rex D. Stith, Ph.D.
Academic Rank:	Associate Professor
Department and University:	Department of Physiology Health Sciences Center University of Oklahoma
Assignment:	USAF School of Aerospace Medicine
(Air Force Base)	Brooks AFB TX 78235
(Laboratory)	Neurochemistry
(Division)	Radiation Sciences
(Branch)	Radiation Physics
USAF Research Colleague:	David N. Erwin, Ph.D.
Date:	August 15, 1978
Contract No.:	F44620-75-C-0031

EFFECT OF MICROWAVE EXPOSURE ON CERTAIN NEUROENDOCRINE PARAMETERS IN VARIOUS REGIONS OF THE RAT BRAIN

by

Rex D. Stith

ABSTRACT

The central nervous system, especially its neuroendocrine component, is suspected of being one of the physiological systems most sensitive to microwave exposure. However, there are many problems to be solved in order that we might gain a better understanding of this interaction. The possible roles of specific frequency effects, thermal effects, thresholds for power density, stress effects, and pulsed-wave (PW) versus continuous-wave (CW) effects are all problems requiring better understanding.

Rats were exposed to 1.2-GHz CW microwave radiation at power densities of 0, 5, and 15 mW/cm^2. Upon sacrifice, brains were dissected into 6 major regions. In addition, blood samples were obtained. All tissue samples were frozen in liquid N_2 and stored at $-30^{o}C$. A total of 80 rats were utilized.

Tissues are being kept until service laboratories are able to provide requested assays. Therefore, no data have been obtained. However, the assays will be performed, and much information will be forthcoming. Parameters to be measured are norepinephrine and dopamine, cyclic adenosine monophosphate, and tyrosine hydroxylase.

I. INTRODUCTION

On the basis of recorded disturbances of brain bioelectrics phenomena, behavioral studies, morphologic data, and biochemical assays of neurotransmitters, brain enzymes, and hormones, there remains little doubt that microwave irradiation can affect normal brain functioning. The severity and reversibility of such alterations depend in large part on the radiation intensity, frequency, and duration of exposure. Present U.S. exposure standards are based on the concept that most deleterious effects of microwave radiation occur above an intensity of 10 mW/cm^2. In principle, exposures at power densities below 10 mW/cm^2 do not lead to body rectal temperature increases exceeding the compensatory capabilities of mammalian thermoregulatory mechanisms; within the range of 5-10 mW/cm^2 insignificant temperature increases are observed. No measurable temperature increases occur in normal conditions during exposures at power densities below 5 mW/cm^2; 1 mW/cm^2 may be considered the "athermal" exposure level, even at higher ambient temperature and air humidity. Most U.S. scientists have supported the view that above 10 mW/cm^2, alterations in the physiology of most tissues studied are the result of an increased thermal load, either local or whole body.

However, many studies reported by scientists in Eastern European countries, and an increasing number in Western countries including the U.S., purport to demonstrate alterations within the central nervous system upon exposure to power densities below 10 mW/cm^2 and even in the $\mu W/cm^2$

range. At certain power densities and in the case of a certain relationship between the wavelength and the geometry of the head, focal lesions caused by local temperature increases may occur. Furthermore, very little is known about possible electromagnetic effects on biological systems exposed to "athermal" densities. In certain brain regions, microwave absorption and temperature effects may be 4 to 6 times higher than the mean temperature increase. It is regrettable that no systematic, controlled investigations on a well-known chain of biochemical events in microwave-irradiated animals are to be found in the literature.

Besides the question of thermal versus nonthermal effects, experiments should be designed which will investigate differences in PW and CW irradiation, the role of the animal's stress response in central nervous system alterations, and the time course of onset, duration, and reversibility of the effects of microwave exposure. In addition, care must be taken in extrapolating results to conditions and effects in man. We have chosen to expose rats to a microwave frequency that will allow certain extrapolations to man to be made, based upon specific absorption rate and to one that is environmentally pertinent. Microwaves of 7.2 GHz are employed in television, citizen band radios, microwave ovens, and military and meteorological radars.

It is widely agreed that exposure to nonthermogenic intensities of microwaves may result in subtle, discreet changes in the neuroendocrine status of an affected animal. By measuring several parameters within a well-known biochemical schema, we hope to assess the physiological (neuroendocrine) effects of microwave exposure.

II. OBJECTIVE/BASIS

The overall objective of this project is to learn the techniques and theory of radiofrequency radiation (RFR) research by conducting experiments on the bioeffects of RFR on rodents under specified and controlled conditions. The project involves investigating the effects of nonthermogenic (5 mW/cm^2) and thermogenic (15 mW/cm^2) exposures at 1.2-GHz RFR on certain neuroendocrine parameters of the rat.

This project is based on the hypothesis that acute whole body exposure of rats to 1.2-GHz CW microwave radiation will result in quantifiable alterations in the neuroendocrine status of the brain.

III. BODY OF REPORT

A. Materials and Methods

Sprague-Dawley rats, 150-225 g, were used throughout the study. They were maintained in a vivarium on water and commercial chow *ad libitum*.

All exposures were made in an anechoic chamber in which temperature and humidity were controlled. Each rat was restrained in a clear plastic box and positioned in front of the horn so that the long axis of the body was parallel to the electric field. Radiation was produced by a Cober Model 1831 microwave generator and transmitted to an American Electronics Laboratory Model H5001 horn by a flexible cable. Power density measurements were made with a National Bureau of Standards EDM-1B probe.

Radiation was delivered as a continuous wave at 1.2 GHz with

power densities of 5 and 15 mW/cm^2.

Rats utilized in the first series of experiments served as controls. In experiment IA, 10 rats were individually restrained in a clear plastic box outside of the chamber for 10 minutes (pre-exposure period), their rectal temperatures recorded, and then sacrificed. In experiment IB, 10 rats were taken from their cages and immediately sacrificed. Experiment IC involved placing rats in a restraining box for the pre-exposure period as before and then placing them in the exposure chamber for 30 minutes (exposure period) with no radiation emitted. They were sacrificed at the end of the exposure period. The next group (ID) was restrained and subjected to pre-exposure and exposure periods in addition to a 10-minute postexposure period. This group was sacrificed after the 10-minute postexposure period.

Experiment II involved a similar protocol except that rats were exposed to a power density of 5 mW/cm^2. A group of 10 rats was sacrificed after the exposure period, and a group of 10 was sacrificed after the post-exposure period.

Experiment III was conducted like experiment II except that rats were exposed to a power density of 15 mW/cm^2.

At the indicated times, rats were sacrificed by guillotine or by exposure of the head to a power of 6 kW for 300 msec. Tissues from those guillotined were assayed for tyrosine hydroxylase. Tissues from those sacrificed by high-power microwave exposure were assayed for norepinephrine, dopamine, and cyclic AMP. Blood samples were also collected and assayed for growth hormone and thyroid-stimulating hormone.

Brains were dissected into cortex, cerebellum, midbrain, hippocampus, hypothalamus, and brain stem. All tissues were stored at -30°C until assay.

B. Results

The results are not yet compiled. Assays of materials are still taking place.

cAMP is being assayed by the Wilford Hall USAF Medical Center lab.

Norepinephrine and dopamine are being assayed in the laboratory of Mr. Jim Merritt, Radiation Sciences Division, USAF School of Aerospace Medicine, Brooks AFB.

Blood hormones are being assayed by the Internal Medicine Division, USAF School of Aerospace Medicine, Brooks AFB.

Our laboratory is in the process of assaying for tyrosine hydroxylase.

Upon completion of all assays, data will be expressed as mg per mg protein. Means and standard errors will be calculated and statistically analyzed.

The data will be incorporated into a technical report and/or a journal publication as their significance merits.

1978 USAF-ASEE SUMMER FACULTY RESEARCH PROGRAM

sponsored by

THE AIR FORCE OFFICE OF SCIENTIFIC RESEARCH

conducted by

AUBURN UNIVERSITY AND OHIO STATE UNIVERSITY

PARTICIPANTS FINAL REPORT

APPLIED BEHAVIOR ANALYSIS IN FLYING TRAINING RESEARCH

Prepared by: Academic Rank: Department and University:	Jon S. Bailey, Ph.D. Associate Professor Department of Psychology Florida State University
Assignment: (Air Force Base) (Laboratory) (Division) (Branch)	 Williams AFB Human Resources Laboratory Flying Training Research
USAF Research Colleague:	Ronald G. Hughes
Date:	August 18, 1978
Contract No.:	F44620-75-C-0031

APPLIED BEHAVORIAL ANALYSIS IN FLYING TRAINING RESEARCH

by

Jon S. Bailey

ABSTRACT

Research developments in learning theory over the past fifty years have led to principles of behavior which have been shown in innumerable applied settings to be valuable in analyzing and modifying human behavior. When applied to flying training using simulators, these principles suggest that a significant contribution could be made in improving the way in which Instructor Pilots teach new students via more effective use of simulator functions. In addition, flying skills could probably be acquired more readily if tasks were presented in a more systematic manner taking the principles of learning into account.

When the simulator is conceptualized as merely an inferior copy of an aircraft, its potential as a teaching device (perhaps superior to the actual plane, in this regard) is likely to be overlooked. Thus, a behaviorial analysis of optimal conditions of learning would make a major contribution to both the design and use of current and future flight simulators.

In this paper an attempt is made to elucidate the basic principles of behavior and to relate them to the task of improving flying training. A pilot study demonstrating how the segmenting and backward chaining of a dive bombing task can lead to improved learning is presented as a possible model for this type of research.

ACKNOWLEDGEMENTS

The author is grateful to the Air Force Systems Command for support of this summer research. Fred O'Brien's skilled administration of the project and his willingness to solve problems of all kinds made the ten week tour enjoyable and worry free.

The author is indebted to the staff of the Research Branch of the Flying Training Division of the Human Resources Laboratory at Williams for providing a cordial environment in which to work. Particular thanks go to Lt Bill Jones, Capt Ed Chun, Capt Rick Perry, Capt Steve Marinella, Maj Jay Paulson, and Mr Tom Farnan for their excellent technical support. In addition, Dr Liz Martin provided valuable counsel and advise during the early stages of my project. To Capt George Buckland I am most appreciative for his willingness to dialogue on research issues large and small; his sage wit helped to boost morale on more than one occasion.

Finally, I would like to thank Col Dirk Prather for his encouragement of my notions about improving flying training and to Dr Wayne Waag for his excellent administrative support. Mr Jim Smith deserves thanks for setting the tone for the research branch which resulted in such complete cooperation from all members of the Human Resources Laboratory.

Perhaps most of all, I am indebted to Dr Ron Hughes, my research colleague, who led me through the maze, was a sounding board for ideas, and broadened and deepened by understanding of simulation research. Without his assistance little of merit or substance would have come from my summer tour.

LIST OF FIGURES

INTRODUCTION

Psychology has emerged in the last few decades as science of human behavior with not only a well founded theoretical base (Skinner, 1953, 1969) but also a reliable technology (Ayllon & Azrin, 1968; Bandura, 1969; Risley, 1970) capable of making significant contributions to the culture. This technology of behavior change appears well suited to applied problems such as flying training since it is predicated on an analysis of behavior which considers learning to be a significant factor. A cohesive theory or model of learning in flying training and a technology capable of improving the acquisition of flying skills would appear to be a natural outcome as sophisticated behavioral techniques are applied to an important applied problem. When the acquisition of flying skills occurs largely at 15,000 ft the process may be difficult to observe and therefore analyze; but, the advent of flight simulators where not only can conditions of learning be observed but also manipulated directly, now permits experimental research on the learning process to take place. This merging of behavioral psychology and problems of flying training represents an exciting new area of applied research which should reap benefits in both areas.

Applied Behavior Analysis

One fairly recent spinoff of fifty years of research in learning theory has been a field of psychology in which basic principles of behavior derived from the laboratory are applied to problems of human behavior (Baer, Wolf & Risley, 1968; Kazdin, 1978). Termed Applied Behavior Analysis, this field has made significant contributions to rehabilitation, mental retardation, clinical psychology, delinquency, community psychology, and a variety of related human services specialities (Kazdin, 1975). The contributions have been made possible by advances in conceptual and methodological spheres and have allowed for the emergence of a technology of behavior change (often referred to as behavior modification) which promotes improvements in human learning through an analysis of the contingencies surrounding a person's actions (Skinner, 1953; 1968; 1969). Deficits in behavior are often found to be due to inadequate antecedents to prompt behavior, lack of reinforcement for behavior which does occur or for a variety of interrelated reasons traceable to an enviornment incapable of supporting the desired behavior (Bailey, in press; Martin & Pear, 1978). While the most obvious examples of the contribution of applied behavior analysis may be seen in clinically related fields, advances in the analysis of the educational process have also been made (Keller, 1968; Miller & Weaver, 1976; Skinner, 1968;). Here, the approach has brought the principles of behavior to bear on the problems of understanding what is necessary to establish and maintain new repertoires. (This approach has much in common with concurrent developments in instructional technology but appears to have evolved independently.) With the precedent set for the applicability of behavior analysis to so many varied educational areas (ranging from pre-schools to elementary classrooms to college instruction) the extension to an analysis of flying training seems predictable.

Basic Principles of Behavior

The basic principles of behavior presented here represent the results of years of basic and applied research. (The interested reader is referred to the Journal of the Experimental Analysis of Behavior and the Journal of Applied Behavior Analysis for primary sources of this research.) As mentioned earlier, most of the applied work has been carried out in health or education related areas (e.g. Bostow & Bailey, 1969; Iwata, Bailey, Brown, Foshee & Alpern, 1976; Johnson & Bailey, 1974) and little direct work in military training is available for citation. For purposes of exposition, an attempt will be made to relate each of the basic principles to the topic of flying training.

I. Reinforcement

Perhaps the most widely recognized principle in the behavioral framework is that of reinforcement. This principle stresses the importance of the consequences of behavior, in particular positive consequences which follow (i.e. are contingent upon) a certain action or response and which strengthen or make the behavior more likely. In flying training such consequences are already well institutionalized and may be seen in the form of grades on exams, verbal feedback from an Instructor Pilot (IP) on flying proficiency or, ultimately, promotion for superior performance. The purpose of a good O.E.R. is to strengthen the behavior leading up to it. (The function of a negative evaluation as a punisher will be described in the next section.) There is little doubt that learning of almost any kind can be improved through the increased use of reinforcement for desirable behavior.

Two clear cases in flying training appear relevant here. Since so much of the instruction of the undergraduate pilot is carried out in a one-to-one setting with the IP, the opportunity for increased reinforcement for correct behavior in the form of social approval is obvious. Informal observations of IP - student interactions reveal a dearth of positive feedback. Most of the interactions are either instructional or negative in nature. While the research has not been carried out with this subject population (Broden, Bruce, Mitchell, Carter & Hall, 1970; Copeland, Brown & Hall, 1974; Hall, Lund & Jackson, 1968) the implications seem obvious: Increased uses of approval statements of a positive (e.g. "Hey, that's great", "Very nice maneuver", "Nicely executed") are bound to not only improve learning but also morale. Since most IPs appear disinclined naturally to be a wellspring of positive feedback, training to improve this form of communication with students may need to be added to Pilot Instructor Training.

A second example of the use of reinforcement can be seen in the way that simulators are used in teaching. An experienced pilot can readily tell from his instruments and his view from the cockpit when he has completed a maneuver successfully, much like an experienced pianist can tell when a piece has been played well. For the novice, such automatic feedback is absent and for rapid learning to take place it needs to be supplemented in the early stages of learning. The addition of counters, tones, or other stimuli which could be used to confirm correct performance could easily be added to the simulated cockpit. With the development of automated performance measurement (Waag, Eddowes, Fuller & Fuller, 1975) the feasibility of having the computer continuously monitor and score a student's flying skill seems apparent.

II. Punishment

Any time a consequence is designed to follow a given bit of behavior such that the strength or probability of the behavior occurring in the future is reduced, the process is referred to as punishment. Since there may well be numerous side effects (Azrin & Holz, 1966) of using punishment (e.g. anxiety and fear may increase, student may associate learning of the task with aversiveness, student may learn to avoid the source of the punisher) the use of this procedure is not commonly recommended in educational settings (Skinner, 1968). However, in flying training, the student may need to be made very aware of the natural punisher for poor attention to the details of flying, viz, crashing. Thus, most simulators are designed to provide this feedback to students. To be most effective they could probably be designed to give negative feedback early enough to allow the student to correct his error. A "freeze" function currently exists on the simulators used in Instrument Flight Simulators. In one sense, this function resembles the use of "Time-out from positive reinforcement" (usually referred to simply as T.O.) in the clinical literature (Bostow & Bailey, 1969). If flying the simulator is a reinforcing activity, then being in T.O. for a short time upon erring in a flying task may well be an effective punisher that could be used more widely. (Note: This author could find no published reports on the effects of the freeze function in flying training, thus this analysis should be considered tentative until such applied research has been carried out.)

In advanced instruction, such as in air-to-air or air-to-ground combat, it may be worthwhile to add feedback of a more realistic, but no doubt aversive nature. Failure to "check six" could be programmed to result in a malfunction that would simulate the plane's being hit with enemy fire, for example.

III. Shaping and Chaining

Most good instructors know that to keep their students interested, challenged, and involved in the task at hand they need to continually raise the criterion for a good performance. In behavior theory this is known as "shaping" (Kazdin, 1975) and as with the latter two principles, examples for useage with IPs and in adaptive simulators may be easily seen. Expecting an undergraduate pilot to complete an instrument approach correctly on the first try may well be setting the standard too high. In reinforcing approximations to the final performance, the good IP will no doubt have his student reach the final criterion more quickly. As the student progresses, the criterion can be raised so that only better and better performance rate an approval.

Simulators could be computer programmed so as to present tasks to students so they would gradually take on more and more of the functions. In taking off, for example, the student might initially only have to control the throttle, on successive takeoffs he would be required to manipulate the stick to control the attitude. Later, the student would also be required to adjust the trim of the elevators, retract the flaps, and so on. When a perfect takeoff could be executed the student would be required to cope with gradually more difficult crosswinds and various emergency conditions. Programming a simulator to require increasingly more behavior does not seem at all infeasible and would probably greatly reduce the time required to master many skills.

Many behaviors in flying consist of sequences of responses, where early responses must occur in a certain order (e.g. the overhead pattern) so that the final outcome (i.e. a safe landing) can be achieved. Analyzed behaviorally, we can see that only the last member of a chain is actually reinforced. This means that early members of the chain will usually not be learned very readily and their slow acquisition may well retard the development of the rest of the chain of behavior. The most direct solution, which is readily arranged in a simulator, is to have the task designed so that only the last member of the chain must be carried out to achieve the reinforcer. As shown in Figure 1 with the 30° dive bomb task, a pilot can first be positioned so as to fly the final. When this is mastered, the roll-in is added and so on until the whole task is completed.

Figure 1 about here

IV. Prompting and Fading

In the initial stages of learning, new behaviors are weak and may not readily occur when they should. At these times it may be advisable to add stimuli to help initiate a response -- such events are called prompts (e.g. Van Houten & Sullivan, 1975). As a general rule, once a behavior begins to occur regularly when the prompt is given, the prompt will be faded. This use of extra stimuli to cue behavior and then gradually withdrawing it so that the behavior can stand alone under naturally occurring environmental stimuli seems readily applicable to flying training. In the overhead pattern the student must know when to put the speed brakes down, when to extend the landing gear and when to lower the flaps. A simulator could easily be adapted to cue these responses at the proper time and when they were occurring appropriately the cues could be faded. Similar useage of prompting and fading of cues could be combined with shaping (as in training the takeoff) to provide a powerful combination of behavioral techniques to guarantee the rapid acquisition of complex tasks.

V. Discrimination and Stimulus Control

It is most desirable for pilots to constantly respond to their environment so that they can make the necessary adjustments to keep their plane safely aloft. When a pilot responds appropriately to changes in the environment he is said to be under stimulus control and this form of responding is clearly a goal of flying training. The student pilot must learn to discriminate the various wind conditions he will confront and develop appropriate responses to them, for example, stimulus control is gained as the student has repeated exposure to instances of the stimuli involved and these are readily programmed in a simulator. Learning to cope with an engine failure is safely acheived in a simulator and clearly the more instances the student has in which to detect this malfunction the more readily he will be able to respond in an emergency. Students also need to detect changes in wind direction and visibility and to take the necessary action. Both conditions can be programmed in a simulator and very fine discriminations in both could be taught using systematic stimulus presentation techniques.

Stimulus control is also important in advanced training when a pilot must spot a target quickly and respond appropriately. Repeatedly confronting the pilot with a variety of targets and gradually requiring shorter and shorter reaction times could improve the acquisition of complex maneuvers such as the pop-up which is employed in air-to-ground combat. Arranging for simulations of enemy aircraft to occasionally appear while pilots are flying formation should also aide in the development of good visual discrimination.

VI. Generalization

Once a behavior has been strengthened in one environment there is a likelihood that it will occur in similar environments; the more similar the environment the more likely the behavior is to occur. It is, of course, this form of stimulus generalization that has motivated engineers to make the simulator as much like the plane as possible. It is important to note that in human factors work, when the goal of stimulus generalization is sought, effects of increased similarity between the simulator and the aircraft must be measured by looking at changes in behavior and the costs of increased fidelity must be weighed against the benefits. Adding motion, for example, to a simulator with a wraparound visual field may not actually enhance performance in the target aircraft (Martin & Waag, 1978) and furthermore the sophisticated hydraulic systems necessary for motion are extremely costly. Research to discover how much visual field may be required to allow a simulator to be used in certain maneuvers, such as carrier landings, (Perry, 1978) also demonstrates the importance of stimulus generalization in flying training.

When a response is strengthened and this then increases the probability of similar responses occurring, response generalization has been said to have taken place. Learning a certain sequence of behaviors verbally (e.g. takeoff procedures) should lead to them actually being performed at a later time. Practicing visual-motor tracking tasks could well improve ones ability to make the fine adjustments in the stick necessary to maintain proper attitude. Indeed, rehearsing a certain maneuver to ones self (Prather, 1978) may well improve performance of critical flying skills.

Flying Training and Simulators

Learning to fly an aircraft is unique in that inadequate preparation for the task can lead to more than a failing grade. It is perhaps the literal life or death nature of the consequences that has led, and rightly so, to conservative strategies for training. Rather than risk less than perfect transfer of training, the aircraft itself has been preferred over the use of modern day simulators for teaching flying skills. However, economic contingencies and fuel shortages have become translated into a guideline from the Office of Management and Budget to reduce flying hours by 25% by 1981 (Committee on the Armed Services, 1976). Presumably the only reasonable way to meet this goal and still maintain high standards of safety is by employing simulators wherever possible in the training process. Simulators have come a long way since the pioneering work of Ed Link on his "Pilot maker" in 1929. The development of the full-mission simulator capable, potentially, of almost exactly duplicating every feature of an operational aircraft has been recent indeed (Hagin & Smith, 1974). While engineering technology and computer

science have made great strides in providing for fidelity of visual (Nass, Seats, & Albery, 1975), motion (Kron, 1975), and handling characteristics (Kron, 1975), few advances in exploring the use of a modern day simulator as an ideal teaching device have been made (Caro, 1977a). In the hands of an experienced pilot there is a natural tendency to use a simulator much like the aircraft would be used, thus overlooking the fact that the aircraft itself is certainly a less than perfect setting for maximizing the acquisition of skills required to fly a plane. Safety requires the IP to put proper maneuvering above analyzing the instructional process and the stress involved in correcting student errors may result in less than optimal forms of feedback. Since the cockpit is operational and the instruments require constant monitoring to maintain proper attitude, the student may be easily overloaded with information in the early stages on instruction and be unable to process it systematically as would be desirable. No opportunity to practice a particular part of a maneuver in the aircraft is feasible even though it would perhaps be most desirable from a learning point of view.

The Design of Simulators

Historically, engineers and pilots have been principally responsible for the design of simulators and it should come as no surprise that fidelity to imitating the aircraft has been the primary goal of the development effort (Caro, 1977b). Any notion that psychological fidelity is the real goal has been ignored and the proposition that simulators should be designed primarily as training devices is virtually unheard of in simulator design circles (Caro, 1977b).

Current advanced simulators are equipped with certain training "features" that are presumed to facilitate the acquisition of flying skills (Isley & Miller, 1976). In some cases the features are simple hardware applications (programmed malfunctions, hard copy printout), in others these features merely mimic what an instructor might do (automatic briefing, checkride and demonstration). Only a few of the features would appear to approach the potential of a sophisticated training simulator (performance oriented guided practice, performance record/playback and adaptive training) and in no case have the features been adequately evaluated (Isley & Miller, 1976). Even their limited usage is based upon an unvalidated model of behavior change. This practice of designing simulator "training" features on the model of the instructor has, no doubt, severely retarded the development of a model of flying training. An alternative model would emphasize the skills to be acquired and suggest more effective ways of training based upon a task analysis. From this model should flow implications for true training features and procedures and research to evaluate them prior to their incorporation in the training syllabus or installation in future training simulators.

The lack of appreciation for the role of the simulator as a teaching device is understandable in light of the relatively recent emergence of a behaviorally-based technology of teaching and the fact that psychologists specializing in the learning process have not been involved in the design phase of simulator development. This oversight, upon investigation, is directly traceable to the conspicuous absence of any substantial body of knowledge demonstrating how the principles of learning can be used to improve

simulator deployment. How the significant body of relevant research in applied behavior analysis could have escaped the attention of those involved in simulator research is difficult to explain. The need for correction of this glaring deficit is greater than can be met in one paper but a start needs to be made.

Behavioral/Task Analysis of Flying Training: A New Model for Simulator Design

Any task which can be readily observed can be analyzed behaviorally. Flying a sophisticated jet aircraft, although admittedly a difficult task, is not different in principle from carrying out any other complex sequence of behaviors. Viewed in the abstract, it may be seen as a set of rapid, continuous, fine-motor responses to a multiplicity of visual and proprioceptive cues from both inside and outside the aircraft. What makes the task unusual is that decisions and responses must be made so rapidly and flawlessly since either a delayed response or an incorrect judgment could be fatal. It is this latter element, no doubt, that puts such stress on the pilot and which probably makes acquisition of the motor skills in the aircraft itself so labile.

A behavorial analysis of flying, then, would begin with a micro analysis of the tasks to be acquired (Meyer, Laveson, Weissman & Eddowes, 1974) and would then proceed to determine how each task could be simplified for purpose of instruction. This general approach is already used in so-called "part task" trainers, such as the T-4, where students learn to respond to the instrument panel before they spend any time in the actual aircraft. The Air Force has also recognized the contribution of cognitive pre-training in facilitating the acquisition of flying skills (Smith, Waters & Edwards, 1975) which is clearly a method of simplifying a task by presenting certain of the materials in a different format and in a different point in time from the rest of the task. With simplification of the task as the goal for any behavioral analysis one may begin to ask how can a task be broken down?

Component Analysis

One way of analyzing a complex task is to look at the components which make up the whole task and to determine how they can be taught more efficiently (Meyer, et al, 1974). Landing a plane, for example, requires that the student be able to fly straight-and-level, do steep turns, fly a gradual descent, all the while keeping the airspeed properly adjusted, correcting for crosswinds and so on. (In the operational aircraft these behaviors must be performed concurrently, whereas in the simulator they could theoretically be presented as separate tasks and then later be required as more and more complex concurrent operants.)

Chain or sequence analysis

Another way of analyzing a flying task is to view it as a chain of behavior. In this conceptualization the pilot must execute a sequence of behaviors in a certain order (the overhead pattern is also an excellent example of this). With long chains, acquisition of the task is frequently difficult because the early members or components of the chain are so far removed from the reinforcer. Such chains of behavior can be simplified, and

therefore presumably taught more efficiently, if they are presented in a backward sequence. (A pilot experiment illustrating this approach appears at the end of this report.)

Dimenson of difficulty analysis

Still another way to analyze a difficult task is to determine the dimensions which are responsible for making it difficult. Some skills may be hard to acquire because they require too rapid motor responses (time dimension). In such cases a capability for performing a task (e.g. strafing or formation flying) initially in slow motion might allow the student to master the motor skills first and then be required to perform the task at faster and faster speeds until normal operational velocities are reached. (It should be clear that a simulator is the only feasible device for such training to take place and that such a use of the simulator represents a potentially important feature which is independent the fidelity of its motion or visual system.)

Size becomes an important dimension when one considers tasks such as bombing or strafing where a larger or more salient target is easier to hit initially. Thus, the simulated visual scene could be programmed to have large targets readily discernable from the background. These targets would be used early in a bombing training task and as the student gained proficiency, the targets could be automatically made smaller and more difficult to spot. Presumably a similar strategy could be used in simplifying any task that requires a motor response to some small segment of the visual environment (e.g. aerial delivery of cargo or in-flight refueling).

Augmented Feedback

Still another way to simplify a task for purposes of instruction is to determine if judgmental aides might be developed to improve performance. Such aides can be used to enhance a feature of the environment, such as height and distance from the runway, as with VASI that permits a more rapid acquisition of landing. A similar device for carrier landings (the so-called "meatball") and another aide for improving bombing (Hughes, Paulsen, Brooks, & Jones, in press) illustrate the notion of providing additional cues to pilots to improve performance.

Summary of Behavioral/Task Analysis Model

This brief introduction to the behavioral/task analysis model should serve as a clear contrast to the current deployment of simulators. Designing a simulator around a model of an instructor pilot who feels most comfortable teaching in an actual plane is destined to be replaced with a model based upon an analysis of the tasks to be taught. A sophisticated behavioral/task analysis employing research which shows how tasks can be broken into components, the components ordered sequentially, and the dimensions of difficulty adjusted so that acquisition of a skill proceeds smoothly and quickly seems in keeping with the current state-of-the-art in computer generated visual systems and other recent engineering developments.

Application of the Model: A Preview.

To illustrate the application of the model, a hypothetical case will be given. Learning to land an aircraft is clearly one of the most difficult tasks for a new pilot to master (Eddowes & King, 1975) and provides an excellent example of how the model might be employed.

The overhead pattern is a ready example of a chain of behaviors consisting of the initial approach, downwind leg, final turn, and final approach (ATCM 51-4). Our model would suggest that training on the last segment would be most fruitful. First, we would proceed to determine what the behavioral components of the final are and would use cognitive pretraining where feasible to prepare the student for each component. The student must be able to adjust the speed brakes, control pitch attitude and adjust the throttles, for example, in the round out phase of the final approach. The simulator would be programmed to require that the student take responsiblity for each of these concurrent behaviors in some specific order. Similarly, the components of the touchdown and the landing roll would be presented to the student in a graduated manner. When all of the components had been acquired the simulator would be positioned "on final" and the student required to complete this portion of the overhead pattern to criterion. (The training to this point would be highly individualized in terms of time to criterion, although all students would go through training in the same order.) This approach of teaching the last part of the overhead pattern first, not only allows the student to experience the immediate reinforcement (a safe landing) but also provides overlearning of that part of the task which is most difficult. When the final can be executed to criterion, the final turn would be added to the chain. Here again, the components of this segment would be presented, via preprogrammed exercises in the simulator until the student could execute all of them successfully (trimming, slowing air speed, correcting for wind conditions, etc). At this point the student would be positioned so that he was just at the beginning of the final turn and would then fly the rest of the pattern. To facilitate the acquisition of these two components, the simulator would be adjusted so that they could be flown initially in slow motion. With each successful execution, the simulator would program faster speeds until normal operational speeds were reached. In addition, an extra wide runway could be provided on the first few tries and it would gradually be made narrower and narrower on each pass until the normal width was reached. Next, the downwind leg would be added, and so on, working backward, training components and adjusting the dimensions of difficulty at each stage.

This approach to teaching a task to a new student could be programmed into an advanced simulator without any additional hardware being required and although the process may sound lengthly it would actually take less time than is normally required to learn a task. Furthermore, the backward chain allows a student to gain immediate positive feedback for a correct performance which should cause rapid acquisition of the skill.

CONCLUSIONS AND RECOMMENDATIONS

The purpose of the above discussion has been to lay out the basic framework of the behavior analysis approach and to suggest ways that the principles of behavior might be applied to flying training. Since there is little debate that flying is an acquired skill one may immediately begin to ask what principles of behavior relate most directly to the acquisition of the repertoire. Clearly there is a great deal of research to be done inasmuch as the foundation has yet to be laid. Very basic questions such as, "What teaching techniques can IPs use to improve learning?", have yet to be asked. In addition we need to know how best to use the functions currenty found on most modern simulators. How should the "freeze" be used? Should it be used as a time-out or should the student be allowed to initiate the freeze mode to allow him to momentarily reduce information overload? When should replay be employed and does it really enhance learning? How might individualized instruction techniques be used to accelerate learning? In the larger realm of simulator design the simpliest questions have not yet been tackled. What are the effects of automated adaptive instructon on the acquisition of flying skills? How may the components of each task be analyzed and then what is the best sequence to teach them in? How might immediate automatic feedback from the computer be used to enhance learning and increase motivation? What visual aides could be developed that would facilitate the acquisition of complex flying repertoires? How are these prompts best faded from the environment? How might the special characteristics of the simulator, which allows one to fly in slow motion, enlarge parts of the visual scene and give control of many operations to the computer, be used to speed up flying training while reducing errors and improving generalization to the aircraft? The prospect of entering this new era of simulator research is exciting and the payoff to both the field of psychology as well as the Air Force should be great indeed.

In order to concretely illustrate the research method being proposed, a brief description of a pilot study carried out by the author during the 10-week summer assignment is presented below.

Behavior Analysis Research in Flying Training:

An Illustrative Case

THE EFFECTS OF BACKWARD CHAINING ON THE ACQUISITION OF DIVE BOMBING.

Most complex behaviors may be best described as sequences or chains of behavior (Kazdin, 1975). The implication of analyzing a task to be performed in this way is that those responses furtherest removed from the reinforcement will not be strengthened maximally and may slow the acquisition of the behavior. This concept is not new (Skinner, 1938) and suggestions for teaching chains of behavior are readily apparent in behavioral texts (Ferster, Culbertson & Boren, 1975; Kazdin, 1975; Martin & Pear, 1978). Basically one arranges the task so that the last member of the chain occurs first; it is followed by reinforcement and then the next-to-last response is added and so on. While the procedure seems clear enough and the implications for solving applied problems are not difficult to envisage there has been surprisingly little applied work on chaining. That which has been done to date (Hollander & Horner, 1975; Martin, England & England, 1971) has not been well controlled so that actually comparing chaining with a whole task method is not yet possible.

It is important to note that perhaps the only well controlled study with humans (Weiss, 1978) showed that forward chaining of a button pushing task was actually superior to backward chaining. In this study, however, the task was an artificial chain of behavior and the forward chaining might have also been conceptualized as a shaping procedure. Thus, backward chaining vs. whole task learning with an actual applied behavior has yet to be demonstrated in the research literature.

In flying training, many of the tasks to be acquired may be conceptualized as chains of behavior (e.g. circling the runway and landing -- referred to as the overhead pattern). Importantly, if failure to perform the overhead pattern is cited as a significant factor in undergraduate pilots being "washed out" (Eddowes & King, 1975) thus, being able to teach the task more effectively may result in a direct savings to the Air Force. Advanced pilots are confronted with a topographically similar task when they learn air-to-ground combat and must learn to perform the 30^{o} dive bomb task. The similarity to the overhead pattern and ready access to advanced pilots as well as an existing computer program for the dive bombing task, all made carrying out a study on chaining with this task feasible. The purpose of the pilot study was to evaluate the feasibility of comparing a whole task with a backward chaining method of teaching the 30^{o} dive bomb task.

METHOD

Subjects

Four volunteer Instructor Pilots (IPs) from Williams Air Force Base were recruited as subjects. All had approximately equivalent flying hours in the same two jet aircraft (T-37, T-38) and none had any previous experience with the dive bomb task.

Setting

The study was conducted on the Advanced Simulator for Pilot Training (Hagin & Smith, 1974) located at the Human Resources Laboratory at Williams A.F.B. The simulator has a wraparound visual capability via seven 36-inch cathod ray tubes onto which can be projected computer generated images of various scenes (Gum, Albery & Basinger, 1975; Rust, 1975). For this study the motion platform was not in operation and the g-seat was inflated but not otherwise operational. Configuration of the visual scene for the study included a conventional gunnery range visual data base similar to that used by Gray and Fuller (1977) and Hughes, Paulson, Brooks, and Jones (in press) as well as a depressible bombing sight (A-37 Optical Sight Unit). The aerodynamic mathematical models driving the simulator were those of the T-37 aircraft (commonly used for undergraduate pilot training).

Procedure

Subjects read a programmed text on the 30^{0} dive bomb task prior to coming to the laboratory. Upon arrival they were given an informal test and a form to record their total flying hours. They were then briefed on the task by the senior IP, taken to the simulator and shown how to operate the device. With the IP seated beside them in the cockpit, they viewed a demonstration of the task which had been prerecorded by an expert pilot. The subjects were then positioned on the downwind leg of the pattern and allowed to fly five passes at the target; they were given no feedback other than the sight of a small circle on the ground that could be seen once they dropped the bomb.

The dive bomb task was divided into four segments for purposes of instruction: final, roll-in, base-leg, and downwind. Following the five baseline trials the subject was positioned on the final portion of the task and then would fly the remaining part of the maneuver. Location of the bombs could be seen at the console on a cathode ray screen and a digital readout of the plane's heading, airspeed, altitude, g-lead and dive angle as well as the distance of the bomb from the target appeared there. The IP would give the subject feedback and hints on how to improve his performance and another trial would be initiated. This procedure continued until a subject could drop two successive bombs within 140 ft. of the target. When he did, he was then placed one segment further back in the chain and the process began again until the whole task, beginning at the downwind leg could be completed to the criterion of two successive hits within 140 ft. At this point the subjects were again given five trials without feedback and the experiment ended.

RESULTS

The primary dependent variable was the circular error score (i.e. distance of simulated bomb impact point from the target) and the data for each subject may be analyzed separately.

Subject #1 was run before the decision was made to have a pretest score for each pilot. Therefore, the data for this subject, shown in Figure 2, omits this information. The data show that the pilot met the criterion in three trials for the final segment of the task. When the roll-in was added, little difficulty was experienced and only two trials were needed to meet criterion. For this subject the most trials were required when the base leg was added to the task. Here, it took the pilot nine trials to meet the criterion and a gradual downtrend in the circular error can be seen over time. No clear trend can be seen when the downwind segment was added. On the post test, the subject's average circular error was 139 ft., one foot less than the criterion score.

Figure 2 about here

The data for subject #3 are shown in Figure 3. The pretest for this pilot averaged 308 ft. A clear down trend for the scores may be seen in the final and the base leg (the roll-in was omitted by error at the console). The subject had little difficulty when the downwind segment was added. While his post test average of 163 ft. exceeded the criterion it still represented an improvement of 145 ft. over the pretest scores.

Figure 3 about here

Subject #4's data are shown in Figure 4. As can be seen his pretest averaged 250 ft. from the target. As each segment was added errors increased and then, within ten trials or less, criterion would be met. As with the previous two subjects, the addition of the downwind segment produced the least disruption of behavior. As with subject #1, this pilot averaged less than the criterion on the five post-test trials (X = 138 ft.).

Figure 4 about here

The data for the last subject is shown in Figure 5. Here the pretest for subject #5 can be seen as 546 ft. His data resembles that of the others in showing clear down trends as each segment is added. For this pilot the base leg addition proved to be of no problem while the downwind addition required six trials to meet criterion. This subject had the greatest improvement from pre to post-test (316 ft.) but his post-test scores (X = 230 ft.) did not meet the criterion.

Figure 5 about here

DISCUSSION

The results of this study indicate a clear, systematic reduction in circular error with the use of backward chaining method of introducing the task. Conclusions regarding the superiority of the method must await a comparison with the standard forward, unsegmented manner of training the task. It is planned to run additional subjects on the dive bomb task to provide this information.

The backward chaining method has several advantages over traditional training of such tasks. With the task broken into segments, less information must be processed on any given trial, presumably allowing learning to occur more efficiently. In addition, by starting with the last element the subject can come into contact with the reinforcer for successful execution of the task and this should build confidence in the subject without the need for any other form of support.

The application of behavior principles to problems of flying training would appear to represent an approach worthy of further research. Tasks such as the one used in the present study allow for easy quantification of the dependent variable and it parallels other significant maneuvers that must be mastered by pilots. Furthermore, the ability to vary other dimensions of the task (speed of the aircraft simulator, size of the target, etc) should allow precise comparisons of various methods of teaching such tasks. It is hoped that this pilot study will perhaps pave the way towards a heightened research effort in the application of behavior principles to problems of flying training.

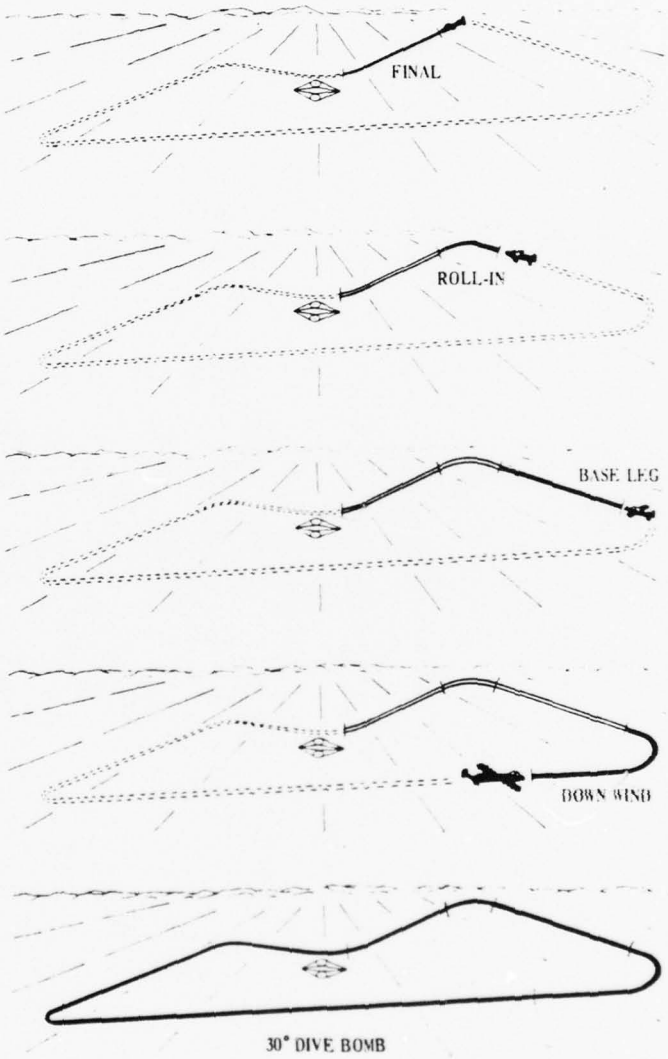

Figure 1. Illustration of segmented backward chaining of 30° dive bomb task

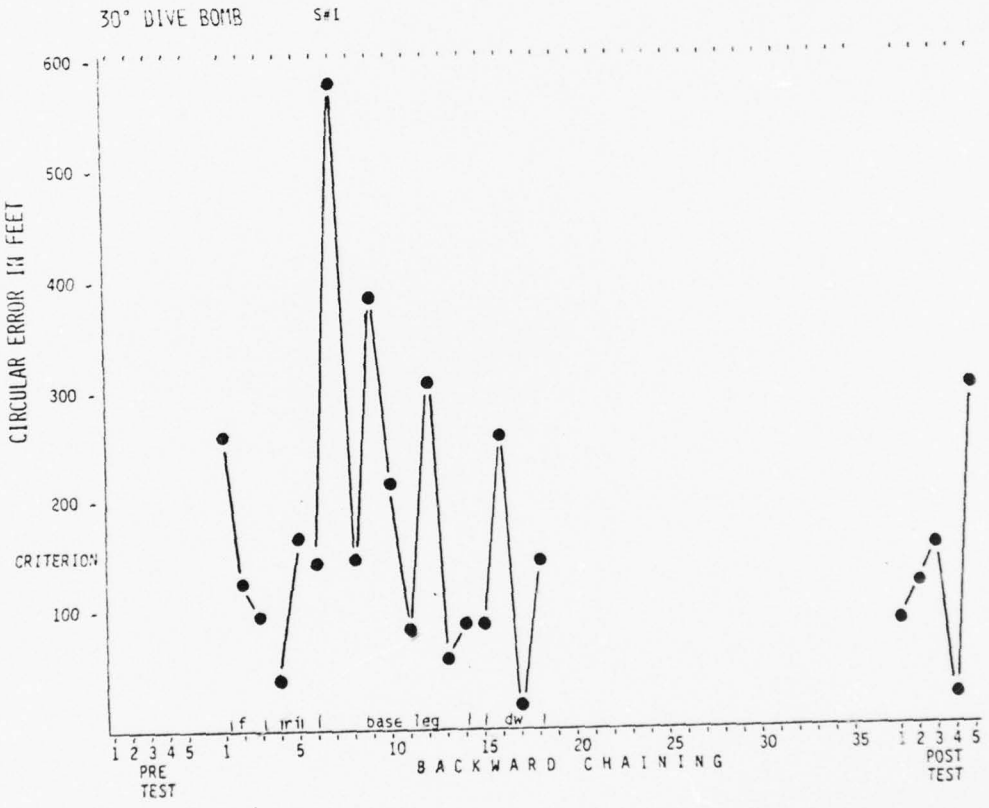

Figure 2. Circular error for 30° dive bomb task for subject #1 showing scores for the pretest, backward chaining trials and post test.

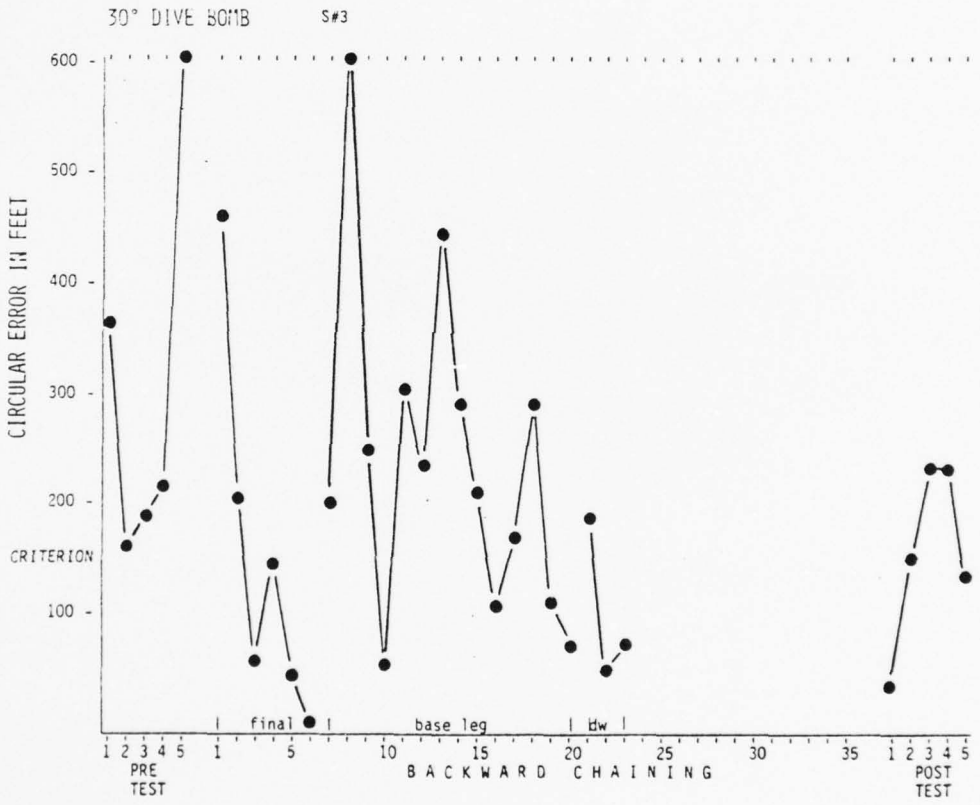

Figure 3. Circular error for 30° dive bomb task for subject #3 showing scores for the pretest, backward chaining trials and post test.

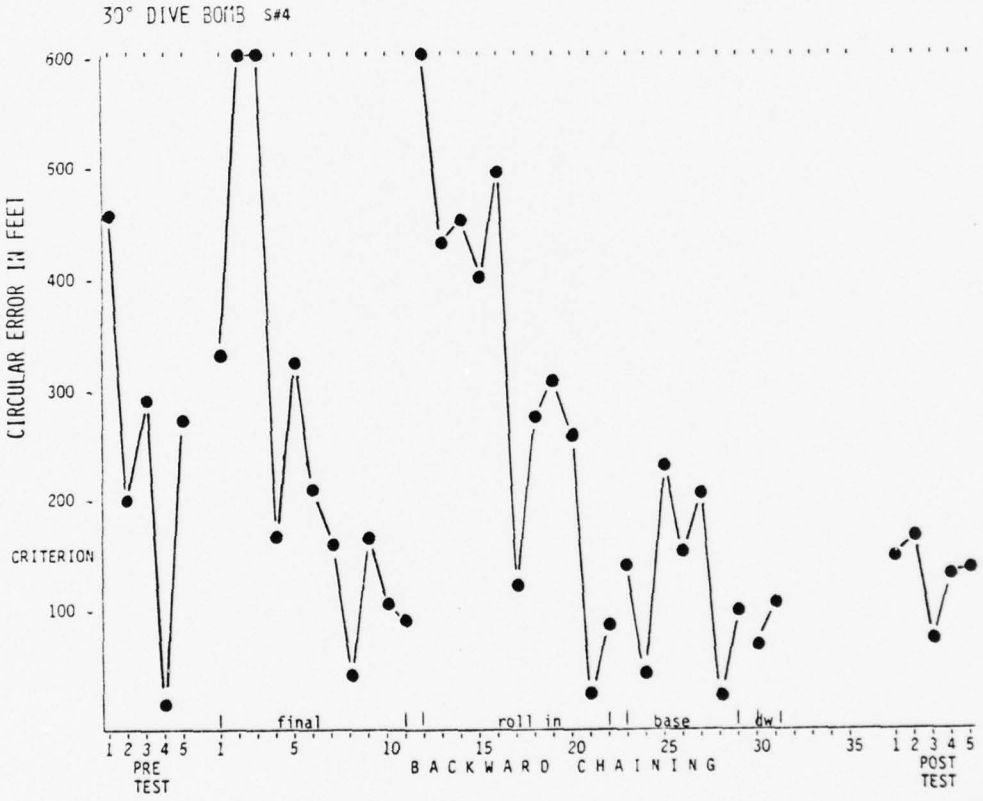

Figure 4. Circular error for 30° dive bomb task for subject #4 showing scores for the pretest, backward chaining trials and post test.

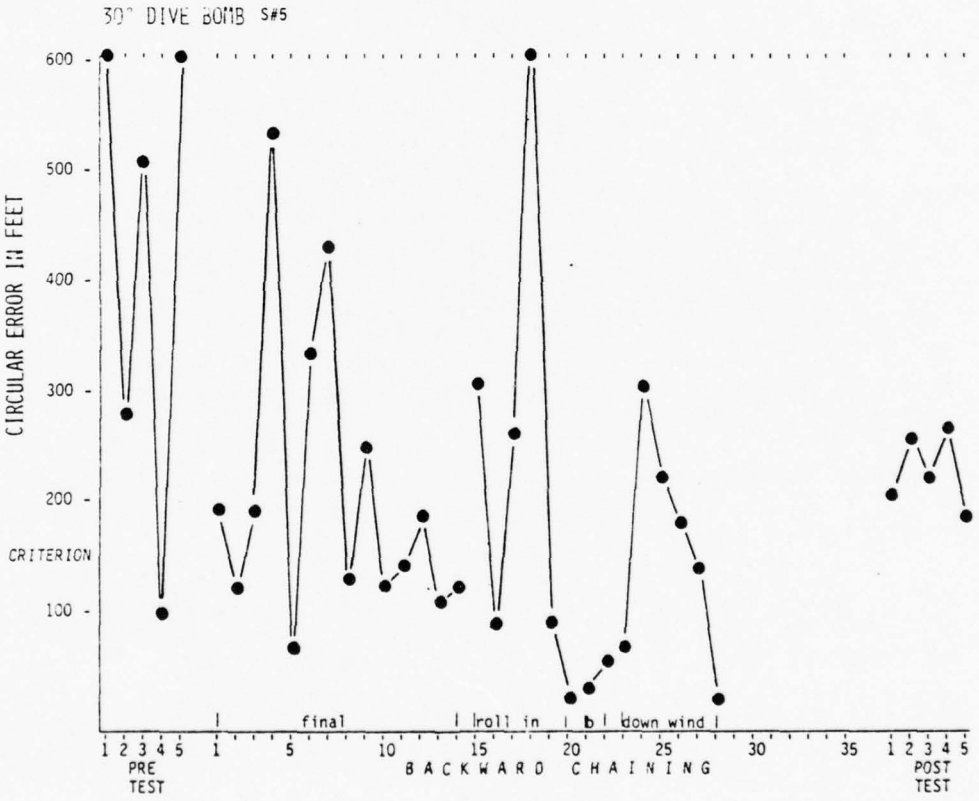

Figure 5. Circular error for 30° dive bomb task for subject #5 showing scores for the pretest, backward chaining trials and post test.

REFERENCES

Ayllon, T. & Azrin, N. H. The token economy: A motivational system for therapy and rehabilitation. New York: Appleton-Century-Crofts, 1968.

Azrin, N. H. & Holz, W. C. Punishment. In W. K. Honig (Ed.) Operant behavior: Areas of research and application. New York: Appleton-Century-Crofts, 1966, pp. 380-447.

Baer, D. M., Risley, T. R., Wolf, M. M. Some current dimensions of applied behavior analysis. J. of Applied Behavior Analysis, 1968, 1, 91-97.

Bailey, J. S. A handbook of research methods in applied behavior analysis. Plenum Pub. Co., in press.

Bandura, A. Principles of behavior modification. New York: Holt, Rinehart & Winston, 1969.

Bostow, D. E. & Bailey, J. S. Modification of severe disruptive and aggressive behavior using brief timeout and reinforcement procedures. J. of Applied Behavior Analysis, 1969, 2, 31-38.

Broden, M., Bruce, C., Mitchell, M. A., Carter, V. & Hall, R. V. Effects of teacher attention on attending behavior of two boys at adjacent desks. J. of Applied Behavior Analysis, 1970, 3, 199-204.

Caro, P. W. (a) Some factors influencing Air Force simulator training effectiveness. AFOSR-TR-77-971, March 1977 (a).

Caro, P.W. (b) Some current problems in simulator design, testing, and use. AFOSR-TR-77-990, March 1977 (b).

Committee on Armed Services, U. S. Senate, 94th Congress, 2d session, May 13, 1976. "Flight Simulators". Hearing before the subcommittee on research and development.

Copeland, R. E., Brown, R. E., and Hall, R. V. The effects of principal-implemented techniques on the behavior of pupils. J. of Applied Behavior Analysis, 1974, 7, 77-86.

Eddowes, E. E. and King, N. W. Self-perceived problems of student pilots eliminated from undergraduate pilot training. AFHRL-TR-75-8, Williams AFB AZ: Flying Training Division, Air Force Human Resources Laboratory July 1975.

Eibeck, A. C., and Beardsley, H. W. Advanced simulation in undergraduate pilot training: Computer image generation. AFHRL-TR-75-59 V, Williams AFB AZ: Flying Training Division, Air Force Human Resources Laboratory October 1975

Gray, T. H. and Fuller, R. R. Effects of simulator training and platform motion on air-to-surface weapons delivery training. AFHRL-TR-77-29, Williams AFB, AZ: Flying Training Division, Air Force Human Resources Laboratory, July 1977.

Gum, D. C., Albery, W. R., and Basinger, J. D. Advanced simulation in undergraduate pilot training: An overview. AFHRL-TR-75-59 (I), Wright Patterson AFB, Ohio: Advanced Systems Division, Air Force Human Resources Laboratory, December 1975.

Hagin, W. V. and Smith J. F. Advanced simulation in undergraduate pilot training (ASUPT) facility utilization plan. AFHRL-TR-74-43. AD-786 411, Williams AFB, AZ: Flying Training Division, Air Force Human Resources Laboratory, June 1974.

Hall, R. V., Lund, D., and Jackson, D. Effects of teacher attention on study behavior. J. of Applied Behavior Analysis, 1968, 1, 1-12.

Hollander, M., and Horner, V. Using environmental assessment and operant procedures to build integrated behaviors in schizophrenics. J. of Behavior Therapy and Experimental Psychiatry, 1975, 6, p. 289-94.

Hughes, R. Enabling features versus instructional features in flying training simulation. AFHRL-TR-in press, Williams AFB, AZ: Flying Training Division, Air Force Human Resources Laboratory.

Hughes, R. G., Paulsen, J. G., Brooks, R. B., and Jones, W. E. Visual cue manipulation in air-to-surface weapons delivery task. AFHRL-TR-in press, Williams AFB, AZ: Flying Training Division, Air Force Human Resources Laboratory.

Isley, R. N. and Miller, E. J. The role of automated training in future army simulators. Hum RRO FR-ED-76-27. Oct. 76, Pensacola, Florida

Iwata, B. A., Bailey, J. S., Brown, K. M., Foshee, T. J. and Alpern, M. A performance-based lottery to improve residential care and training by institutional staff. J. of Applied Behavior Analysis, 1976, 9, 417-432.

Johnson, M. and Bailey, J. S., Cross-age tutoring: Fifth graders as arithmetic tutors for kindergarten children. J. of Applied Behavior Analysis, 1974, 7, 223-232.

Kazdin, A. E. Behavior modification in applied settings. Homewood, Ill.: The Dorsey Press, 1975.

Kazdin, A. E. History of behavior modification. Baltimore: University Park Press, 1978.

Keller, F. S. "Goodbye teacher..." J. of Applied Behavior Analysis, 1968, 1 79-90.

Kron, G. J. Advanced simulation in undergraduate pilot training: motion system development. AFHRL-TR-75-59 (II), Williams AFB, AZ: Flying Training Division, Air Force Human Resources Laboratory, October 1975.

Kron, G. J. Advanced simulation in undergraduate pilot training: G-seat development. AFHRL-TR-75-59 (III), Williams AFB, AZ: Flying Training Division, Air Force Human Resources Laboratory, October 1975.

Martin, E. L. and Waag, W. L. The contributions of platform motion to simulator training effectiveness: Study I - Basic Contact. AFHRL-TR-78-15, Williams AFB, AZ: Flying Training Division, Air Force Human Resources Laboratory, January 1978.

Martin, G. L., England, G., and England K. The use of backward chaining to teach bed-making to severely retarded girls: A demonstration. Psychological Aspects of Disability, 1971, 18, 35-40.

Martin, G. L., Kehoe,B., Bird, E., Jensen,V., and Darbyshire. Operant conditioning in dressing behavior of severely retarded girls. Mental Retardation, 1971, 9 (3), 27-31.

Martin, G. and Pear, J. Behavior Modification: What it is and how to do it Prentice-Hall, Inc: Englewood Cliffs, N. J., 1978.

Meyer, R. P., Laveson, J. I., Weissman, N. S., and Eddowes, E. E. Behavioral taxomony of undergraduate pilot training tasks and skills: Executive summary. AFHRL-TR-77-29, Williams, AFB, AZ: Flying Training Division, Air Force Human Resources Laboratory, Dec. 1974.

Miller, L. K. and Weaver, F. H. A behavioral technology for producing concept formation in university students. J. of Applied Behavior Analysis, 1976, 9, 289-300.

Nass, L., Seats, P., and Albery, W. Advanced simulation in undergraduate pilot training: Visual display development. AFHRL-TR-75-59 VI, Williams, AFB, AZ: Flying Training Division, Air Force Human Resources Laboratory, October 1975

Perry, R. A. Personal communication, 1978.

Prather, D. Personal communication, 1978.

Risley, T. R. Behavior modification: An experimental-therapeutic endeavor. In L. A. Hammerlynck, P. O. Davidson, and L. E. Acker (Eds.) Behavior modification and ideal mental health services. Calgary, Canada: University of Calgary Press, 1970, pp. 103-127.

Skinner, B. F. Contingencies of reinforcement: A theoretical analysis. New York: Appleton-Century-Crofts, 1969.

Skinner, B. F. The behavior of organisms. New York: Appleton-Century-Crofts, 1938.

Skinner, B. F. Science and Human Behavior. New York: Free Press, 1953.

Skinner, B. F. The technology of teaching. New York: Appleton-Century-Crofts, 1968.

Smith, B. A, Waters, B. K., and Edwards, B. J. Cognitive pretraining of the T-37 overhead traffic pattern. AFHRL-TR-75-72, Williams AFB, AZ: Flying Training Division, Air Force Human Resources Laboratory, December 1975.

Van Houten, R. and Sullivan, K. Effects of an audio cueing system on the rate of teacher praise. J. of Applied Behavior Analysis, 1975, 8, 197-202.

Waag, W. L., Eddowes, E. E., Fuller, J. H., and Fuller, R. R. ASUPT Automated objective performance measurement system. AFHRL-TR-75-3, Williams AFB, AZ: Flying Training Division, Air Force Human Resources Laboratory, March 1975

Weiss, K. M. A comparison of forward and backward preocedures for the acquisition of response chains in humans. J. of Experimental Analysis of Behavior, 1978, 29, 255-259.

1978 USAF-ASEE SUMMER FACULTY RESEARCH PROGRAM

sponsored by

THE AIR FORCE OFFICE SCIENTIFIC RESEARCH

conducted by

AUBURN UNIVERSITY AND OHIO STATE UNIVERSITY

PARTICIPANT'S FINAL REPORT

A PROPOSED MODEL SYSTEM:PRODUCTION PLANNING AND CONTROL FOR A RESEARCH AND DEVELOPMENT FUNCTION

Prepared by:	Owen W. Miller, D. Sc.
Academic Rank:	Professor
Department and University:	Department of Industrial Engineering University of Missouri - Columbia

Assignment:	
(Air Force Base)	Luke/Williams
(Laboratory)	Human Resources Laboratory
(Division)	Flight Training
(Branch)	Tactical Research
USAF Research Colleague:	Robert B. Bunker
Date:	August 11, 1978
Contract No.:	F44620-75-C-0031

A PROPOSED MODEL SYSTEM: PRODUCTION PLANNING AND CONTROL FOR A RESEARCH AND DEVELOPMENT FUNCTION

by

OWEN W. MILLER

ABSTRACT

There is an increasing interest in improving productivity and accountability by managers of research and development functions.

Published efforts to date have indicated that there is an increasing tendency to apply techniques proposed in management-by-objectives techniques to achieve accountability and to utilize performance measurement procedures in an attempt to improve productivity in the research and development environment. This paper proposes that both of these techniques will be effectively applied in research if a model is adopted which is patterned along the lines of the production planning, scheduling, and control model used so successfully in the industrial production environment.

This model is based on the premise that management-by-objectives is accomplished by involving the scientist with the administrator and will lead to the strengthening of the R&D organization.

A description of the system and a methodology for implementing the proposed model is included.

ACKNOWLEDGEMENT

The author wishes to thank the Air Force Systems Command, ASEE, Auburn University and Mr. Fred O'Brien for the opportunity to become exposed to and participate in the fascinating field of flying training simulators. The potential for their expanded use in improving efficiency of learning seems unbounded.

The author wishes to thank those FTO Branch personnel who were patient with him in the conduct of his summer program. He wishes in particular to thank Mr. Robert Bunker, Branch Chief and Janice A. Reed for their assistance. Thanks also to Betty Richardson and Maureen Huyett for their splendid help.

INTRODUCTION

The rapid expansion of the use of simulators for training pilots has been largely due to several factors; the introduction of effective visual cues, the development of more sophisticated fighter aircraft which, in turn, increases the complexity of the flying tasks, the exponentially increasing costs of flying training in these advanced aircraft, the cost of fuel and the ever-increasing effectiveness of the transfer of learning from the aircraft simulator to the aircraft (Ref 1).

The Air Force Human Resources Laboratory (AFHRL) has established an impressive research and development organization whose Flying Training Division (AFHRL/FT) at Williams AFB is charged with the responsibility to "....conduct research to generate information which can be used to improve Air Force flying training" (Ref 2). Implicit in this charge is the management goal of improving the flying skills of student pilots through the effective use of aircraft simulators.

The management of the AFHRL/FTO Branch at Luke AFB has been presented with the problem of trying to meet the escalating demands for simulator training research with restrictions placed on the availability of needed resources. For example, the Tactical Research Branch located at Luke Air Force Base (FTO), Arizona, is charged with increasing the productivity of its flying training research activities but must do so with the presently available resources; namely, research psychologists, systems engineers, instructor pilots, and aircraft simulators. In addition, this Branch is unique in that it must share its air-to-air combat simulator (SAAC) with the Tactical Air Command who trains pilots in an air combat maneuvering role. This is a challenge to increase the productivity of the Branch. An additional complicating factor is that there are system imposed deadlines for the completion of specific research tasks. The Branch manager and the respective research project managers (i.e., research psychologists) are often hampered by having insufficient information to permit them to make very accurate estimates of resource requirements needed and the availability of such resources on a scheduled time scale (Ref 3). It is suspected by the author that this is the classic problem concerning the difficulty of measuring and improving productivity in the research and development environment, both for government and private organizations.

The idea of improving productivity in the research and development environment has been addressed by many authors, with diverse and sometimes dramatically opposing viewpoints. For example, the concept of introducing performance standards, which forms the fundamental basis for industrial productivity improvements, was felt to have an "adverse effect on the scientific mission in the Research and Development Laboratories" (of the Air Force) by the U. S. Civil Service Commission (Ref 3), who, in 1966, proposed that a critical review be made of the policies and practices in the Air Force Research and Development Establishment. Another author stated

that "...complete autonomy from management and their influence and pressures on the other hand, is also undesirable. This influence from managers and other scientists does tend to increase productivity" (Ref 4). The introduction of management-by-objectives into the research laboratory to increase productivity of engineers and scientists, has been used with a great deal of success. For example, Martino (Ref 5) reported an increased output with reduced manpower, having more than doubled the number of projects completed while reducing the professional work staff of a medium sized engineering organization by approximately 25% over a 3 year period.

Badowy (Ref 6) reported in his study on the application of MBO as a technique for improving productivity in R&D laboratories that, "...individual and organizational effectiveness are contingent on several factors; 1) that employees know what is expected, 2) are given an opportunity to participate and be involved in their work, and 3) get feedback on how they are doing in their work."

The thesis presented in this paper is that the techniques of production planning, scheduling and control are effective MBO techniques and, if used diligently, will increase productivity in research and development laboratories.

OBJECTIVES

Management-by-objectives is based on the premise that the supervisor and employees share in the establishment of organizational and staff goals, and also share in the accountability for achieving those goals. Innovation is a major contributor to increases in productivity and the successful implementation of MBO encourages both supervisors and employees to utilize their innovative talents in the process of achieving the organization's goals (Ref 7). Mc Gregor (Ref 8) attributes MBO success to the fact that this management technique brings together the needs of both the individual and the organization and thus contributes to the building of an effective R&D organization.

The objective of this study is to present a proposed methodology for effectively applying MBO in a research and development function. The MBO procedure proposed is through the application of techniques used in operating a production planning, scheduling and control system.

The expected productivity increases to be gained through the successful implementation of this procedure are many because it successfully integrates the scientist into the process. It would provide:

1. A means for determining the current and future demands for research resources and assessing the degree of research resource availability to meet those demands.

2. A means of establishing and periodically revising the "research master schedule" of present and future research activities.

3. A means for determining the R&D organization's ability to accept and carryout proposed new research tasks.

4. A means for determining whether to continue one or more research projects.

5. A means for developing standard data estimates for specific research subtasks.

6. A means for determining ahead of incident occurrence, where the research project "critical path" will be affected by "slippage" of scheduled completion dates of research subtasks.

7. A means for eliciting the ideas of all R&D personnel for alternative methods of performing research subtasks.

8. A means for realistically scheduling the professional development activities of personnel for scheduling professional seminars, short courses and professional conferences on their respective load charts.

9. A means for determining whether to assign new work as "in-house" or to a subcontractor.

10. A guide for determining critical research task priorities and for re-prioritizing research efforts.

11. A means for emphasizing and achieving accountability of research personnel.

12. A means for applying an objective performance measurement for R&D professional personnel.

THE MODEL

A production planning, scheduling and control system as applied to the industrial setting may be defined as "getting the right material, to the right place and at the right time" (Ref 9). One might supplement this definition by the phrase "with the objective to produce a product of acceptable quality, and at a cost which will permit the producer to make a fair profit for his efforts".

The research and development laboratory has a much more difficult assignment than does the industrial manufacturer because the end product is

not always so tangible or clearly defined. For example, the end product for the industrialist is usually specified in terms of a blueprint which contains a bill of materials, end product and component drawings, each of which has specified dimensions and tolerances.

The end product for the R&D laboratory is rarely so specifically defined, yet the degree to which the research organization is able to specifically describe the goal of their research in a large measure determines how effective or "productive" they will be. However, even though the researcher must deal with the more complex and somewhat vaguely defined end product, the traditional functions of production planning and control can be effectively utilized by him to increase his productivity.

The functions of industrial planning (determining what is to be made, how, where, etc.), scheduling (when it is to be made), dispatching (assigning the work to be performed at the respective work stations) and follow-up (periodically monitoring the actual performance and comparing it with the scheduled plan) have their parallel in the R&D setting. These corresponding functions are, research planning (determining the research question(s) to be answered, or hypothesis to be tested, determining the experimental procedure for testing the posed hypothesis), scheduling (determining when each of the components or subtasks or elements of the research design are to be performed), dispatching (the assigning of subtasks to researchers and their professional colleagues) and follow-up (periodically monitoring the actual performance).

In order for the system to function properly each of the production control functions must be incorporated into a viable management information system that will achieve the objectives listed above. Karger and Murdick proposed guidelines for designing a management information system for an engineering and research organization (Ref 10). This paper follows their proposed guidelines but goes into depth in the design of the research program schedules, the work subtask breakdowns, the estimates of resource requirements, sequential relationships and estimates of time required for each subtask, the estimate of the critical path and task completion dates and a procedure for updating the program schedules.

It is to be emphasized that the active involvement of the researcher in the research planning, scheduling, dispatching and follow-up is the heart of this proposed model, and that this active involvement encourages innovation and accountability and provides the incentive that leads to productivity increases in the R&D process.

METHODOLOGY

1. Identification of the research question(s) to be answered.

2. Initial breakdown of research project into subtask components and elements.

3. Initial estimates of resource requirements needed to carryout the research task (eg. - professional skills required, equipment, etc.).

4. Estimates of the most likely times required to perform subtasks.

5. Determination of the sequential relationships among subtasks.

6. Determination of the "critical path" and earliest completion date for the research project.

7. Recording of resource demands on resource loading charts.

8. Comparisons of the initial schedule of subtasks with availability of required resources.

9. Resolution of any apparent schedule conflicts or inconsistencies.

An example:

1. Identification of the research questions to be answered.

An ongoing research project entitled "Trainer Evaluation - Bogey Spotter" is concerned with the general goal of improving the capability of fighter pilots to spot an adversary while in flight. The hypothesis to be tested is, "Is the specific proposed trainer device and its training syllabus an effective means of improving a fighter pilot's ability to spot an adversary?"

2. Initial breakdown of the research project into subtask components.

Figure 1 is a list of the project manager's first estimate of an "optimum" breakdown of the total job into subtask components.

Figure 2 represents AFHRL Form 22 which the project manager is required to fill out for every "in-house" research project proposed to be undertaken. This is required by Air Force Regulation 80-4 (Ref 11).

Note the difference in the amount of detailed breakdown on the two forms. The intent of Form 22 is that it is to serve as a management information and control tool, but because of the minimal information presented it falls short of that goal (Ref 12). Note also that the time scale of this form is in months, which is too broad a time period for effective scheduling and control since many research projects require less than 1 year to complete.

INITIAL IDENTIFICATION OF PROPOSED WORK UNIT SUBTASKS

Work Unit Nr: 1123-12-04
Title: Bogey Spotter-Trainer Evaluation
Work Unit Manager: J.R.
Date: 7/17/78

Sub-task No.	Brief Description	Req. Res.	Est. Hrs.	Notes
1	Select Team	Mgr.	4	Simul. or Seq. activity
2	"	Se	4	
3	"	I.P.	4	
4	Write Research Agreement	Mgr.	8	
5	To Williams AFB - Approval	--	40	
6	To Luke Commander - Approval	--	24	
7	To TAC - Approval	--	40	
8	Literature Search	Mgr.	80	Simu. or Seq.
9	Develop Research Design	Mgr.	60	
10	"	IP	16	Simu. or Seq.
11	"	R.P.	20	
12	"	Se	8	
13	Programming	Je	16	
14	Obtain Data - Train Students/Sim.	Mgr.	30	
15	"	Stud.	30	Simul.
16	"	I.P.	30	
*17	Obtain Data - Students/A/C	Mgr.	10	*Class starts flying on 1 Sept. 78
*18	"	A/C	120	
*19	"	Stud.	80	
*20	"	IP	80	Simul.
21	Initial Analysis of Data	Mgr.	40	
22	Statistical Data Reduction	Je	8	
23	Analysis of Stat. Results	Mgr.	24	Simul.
24	"	Pr	24	
25	Draft Tr.	Mgr.	240	Simul.
26	"	Rp	24	

FIGURE 1. ILLUSTRATION OF INITIAL IDENTIFICATION OF PROPOSED WORK UNIT SUBTASKS

PROGRAM SCHEDULE | WU NR. 1123-10-04 | AS OF DATE 7/17/78 | MANHOURS PROJECTED _____ ACTUAL _____

WORK UNIT MANAGER: JR

LINE	MILESTONES	COMPLETION DATES QU	COMPLETION DATES YR
1	Phase I Research Design		
2	Experimental Group Training		
3	Aircraft Data Collection		
4	Data Analysis		
5	Draft TR		
6			
7			
8			
9			
10			
11			
12			
13			
14			
15			
16			
17			
18			
19			
20			
21			
22			
23			
4	TITLE: Bogey Spotter - Trainer Evaluation		

FY 19 78 | CY 19 78 | FY 19 | CY 19 | FY 19 | CY 19 | COMPLETION DATES

J F M A M J J A S O N D J F M A M J J A S O N D J F M A M J J A S O N D J F M A M J J A S O N D

HOURS IN 100'S: % 110 100 75 50 25

Δ SCHEDULED | ▲ COMPLETED | ◇ RESCHEDULED | ◆ COMPLETED RESCHEDULED | ⊘ NEGATED | REVISED PROJECTION □

FIGURE 2. EXAMPLE OF AFTRL FORM 22.

AFTRL FORM 22

3. Initial estimate of resources needed.

Figure 1 also has a list of the types of resources needed and the estimated number of hours for each of these critical resources. For example, column 3 lists the personnel skills assumed needed - the project manager, (usually a research psychologist), a systems engineer (computer systems analyst, programmer), and an instructor pilot. The Flying Training Division states as a policy that "a research team routinely consists of a research psychologist, a systems engineer and a research instructor pilot, who together develop, accomplish and report the results of flying training research studies (Ref 13). It is important to recognize the specific research needed, how much and when in order to avoid the dilemma of finding that the needed personnel are unavailable due to other assignments or TDY when needed in this research task. This will be addressed again in steps 7 and 8.

4. Estimate the most likely times to complete each of the required subtasks.

This is perhaps the most difficult part of the planning procedure, but also, one of the most important aspects. It is imperative that viable estimates of the time required for resources be available, for without these estimates, the organization may quickly find itself in chaos. For example, promised deadlines will not be met, over or under utilization of critical resources will occur, and the credibility of the organization to perform its function quickly follows.

Many researchers may abhor the idea of being asked to establish times for completion of research tasks simply because many of those tasks have a degree of uncertainty of successful completion. However, by breaking a major research effort into subtasks, many of which are somewhat repetitive and routine in nature, it will be found that only a few subtasks have a great deal of uncertainty about the time required for completion. For example, in the bogey spotter trainer evaluation, the most uncertain time estimates expected would be for task 9, "develop research design", and task 21, "initial analysis of data".

After this system has been in existence for some time, say approximately one year, one of the many benefits to be expected is that the researchers will find that they will become better estimators for task time, and thus, the planning and scheduling system will be even more effective. This will contribute to increased productivity since the manager will be able to determine where time is available to undertake additional research tasks, and to encourage researchers to increase their professional skills by additional reading, attending professional society meetings, visiting other organizations performing similar research, etc. All of this is based upon an effective utilization of existing resources which, in turn, is based upon an effective procedure for breaking research tasks into subtasks and estimating accurate times for performing those tasks. This will accomplish both accountability

on the part of the researchers and will permit productivity increases in their efforts.

5. Determine sequential relationships among subtasks.

Figure 3 lists the sequential relationships which exist among the subtask. This step is a necessary one as it describes the parallel or simultaneous and sequential relationships which exist in carrying out the research project. The analyst or planner lists each subtask and determines which subtask precedes the one considered. For example, in Figure 3, the Bogey Spotter Trainer Evaluation, subtasks 1, 2 and 3 may be performed simultaneously, but subtask 4 is preceded by the completion of tasks 1, 2 and 3 before it can start. With this information, and with the time estimates, it is possible to develop a PERT chart (Ref 14) which graphically pictures the scheduled task relationships and permits the calculation of the "critical path".

6. Determine the "critical path" and earliest completion date.

Figure 4 is a modified Gantt chart which depicts the information provided in Figures 1 and 3. Note that this chart graphically portrays each of the subtasks on a time scale and also indicates the precedence relationships by means of vertical dash lines.

The critical path is depicted by double lines. Note, that except for subtask 17, the critical path is represented by the project manager's activities. Since the chart is plotted to scale, it is easy to determine that approximately 72 days will be required to complete the overall research project, assuming that the subtask estimated times are reasonably accurate.

A critical date is 18 September 1978, the scheduled date for which the student pilots have been scheduled to fly their training missions in the aircraft, the date scale then indicates that the latest starting date for this project is 16 August 1978. Any later starting date will prevent the task from being completed on 28 November 1978 unless some subtask adjustments are made. An examination of Figure 4 will illustrate where these adjustments might be made in the event it is not possible to start this study by 16 August.

7. Record resource demands on resource loading charts.

Figure 5 is a resource load chart schedule for the project manager, who, in this example, is a research psychologist. It is a simple matter to transfer the information from the Gantt chart for the Bogey Spotter Trainer Evaluation, Figure 4, to a resource load chart, Figure 5. It is proposed that such a load chart be made for each critical resource and kept up to date. This will prevent the project manager from inadvertantly scheduling a subtask

INITIAL IDENTIFICATION OF PROPOSED WORK UNIT SUBTASKS
SEQUENTIAL RELATIONSHIPS OF SUBTASKS - WORKSHEET

Title: Bogey Spotter-Trainer Evaluation
Date: 7/17/78

Subtask No.	Brief Description	Preceded by	Notes
1	Select Team	--	Simul.
2	"	--	
3	"	--	
4	Write Research Agreement	1,2,3	
5	To Williams AFB -- Approval	4	
6	To Lake Comdr. -- Approval	5	
7	To TAC Comdr. -- Approval	6	
8	Literature Search	1,2,3	
9	Develop Research Design	8	Simul. or Seq.
10	"	8	
11	"	8	
12	"	8	
13	Programming	9,10,11,12	
14	Obtain Data -- Train Students/Sim	9,10,11,12.13	Simul.
15	"	9,10,11,12,13	
16	"	9,10,11,12,13	
17	Obtain Data -- Students in A/C	15	Simul.
18	"	15	
19	"	15	
20	"	15	
21	Initial Analysis of Data	19	
22	Statistical Data Reduction	21	
23	Analysis of Statistical Results	22	Simul.
24	"	22	
25	Draft TR	24,0	Simul.
26	"	24	

FIGURE 3. ILLUSTRATION OF IDENTIFICATION OF SEQUENTIAL RELATIONSHIPS AMONG SUBTASKS

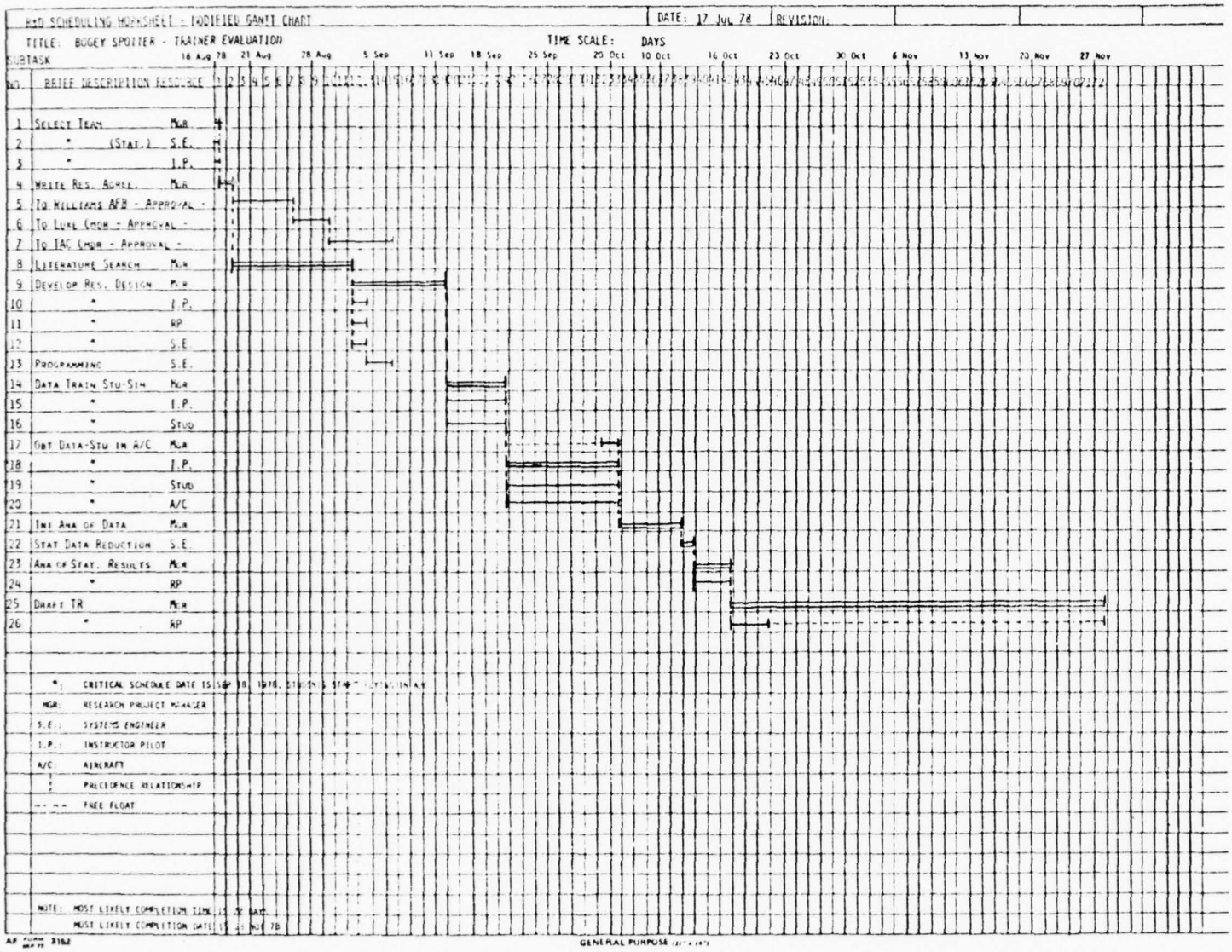

FIGURE 4. ILLUSTRATION OF R & D MASTER SCHEDULE FOR TRAINER EVALUATION-BOGEY SPOTTER PROJECT

when the critical resource has already been scheduled for another activity.

8. Compare this initial master schedule of subtasks with the availability of required resources.

The first pass at developing the master schedule is with the assumption that all needed resources are available, eg, the systems engineer, the instructor pilot and the project manager have time available to perform these tasks at the scheduled times. It is also necessary to review the load schedule for the Simulator for Air-to-Air Combat (SAAC) to determine its availability where the project requires its use. This project does not require the SAAC simulator. Figure 5 is an example of a resource load chart. Note that a separate load chart must be maintained for each critical resource. On Figure 5, the only overlap for the project manager is subtask 8 on the Bogey Spotter with subtask 22 on the Turkey Shoot Project, Figure 6.

An alternate method for determining whether resource capacity is available is indicated in Figure 7. A transparency overlay is made for the Bogey Spotter and superimposed over the Gantt chart for the Turkey Shoot. This quickly identifies the conflict with these two subtasks for the project manager. These overlays can be used for the Gantt charts indicating the activities for the Instructor Pilots, research psychologists and systems engineers.

9. Resolve apparent schedule conflicts.

It is suggested that the project manager now review the modified Gantt charts to resolve the anticipated schedule conflicts. For example, the conflict between subtask 4 Bogey Spotter and subtask 20, Turkey Shoot, the following alternatives might be considered.

Bogey Spotter - subtask #4 - Write research agreement

a. Select team and write research agreement prior to August 16.

or

b. Request another research psychologist to assist writing task #3

or

c. Delay writing the research agreement until subtask #20, Turkey Shoot is completed, then request a priority on Williams and/or Luke and/or TAC approval to reduce the time to complete the approval subtasks.

Turkey Shoot - subtask #20 - Analysis of statistical results

a. Seek help of an additional research psychologist to reduce the statistical analysis to one and one-half days instead of the originally scheduled 3 days.

or

RESOURCE LOAD CHART — Page 1 of 2
Research Psychologist J.R. Title: Project Mgr.

Original Planning Date: 7/17/78
Revision Date:
Initial Estimated Completion Date: 28 Nov 78 Revised Completion Date:
Work Unit Assignment: 1123-12-04 Title: Trainer Evaluation-Bogey Spotter

Sub-task No.	Est. Hrs. Most Likely	Start Date	Critical Path comp. Date	Comments	Status	Action
1	4	16 Aug	16 Aug			
2	8	16 Aug	17 Aug			
8	80	17 Aug	31 Aug	Conflict with Subtask 22 TS.		
9	60	31 Aug	12 Sept			
14	30	12 Sept	18 Sept*	*Critical Date Stud. Start L/C 8 Days Open		
17	10	*29 Sept	2 Oct			
21	40	2 Oct	10 Oct			
23	24	12 Oct	16 Oct			
25	240	16 Oct	27 Nov			

Project total resource required hours through 27 Nov 78 -- 496 Hrs.
Resource total hours available through . . . . 27 Nov 78 -- 576 Hrs.
Note: See Page 2 of 2

FIGURE 5. ILLUSTRATION OF A RESOURCE LOAD CHART

Resource Load Chart — Page 2 of 2

Research Psychologist J.R. Title: Project Mgr.

Original Planning Date: 15 May 78
Revision Date:
Initial Estimated Completion Date: 29 Sept 78 Revised Completion Date:
Work Unit Assignment 1123-12-04 Title: Turkey Shoot -- SAIC

Sub-task No.	Est. Hrs. Most Likely	Start Date	Critical Path com. Date	Comments	Status	Action
1	4	7 June 78	7 June			
4	80	7 June	21 June			
5	60	21 June	30 June	2 Days open		
10	8	7 July	19 July			
15	40	7 July	14 July			
17	120	14 July	7 Aug			
18	16	7 Aug	9 Aug	3 Days open		
20	24	15 Aug	17 Aug			
22	240	17 Aug	29 Sept	Conflict with task 8 B.S.		
Project total resource required hours through 29 Sept 78 -- 592 Hrs. Resource total hours available through . . . 29 Sept 78 -- 640 Hrs.						
Profess. Devel. A. Prof. Soc. Mg. B. Short Course C. Other		9 Nov 78	13 Nov 78	Conflict - See #25 Bogey Spotter		
Other A. TMR B. Prog. Report C. MASIS + JOCAS		1/3mos. - 16 hrs. Bi-monthly - 4 hrs. 1/6 mos.-8 hrs.				

FIGURE 5. (CONT'D) ILLUSTRATION OF A RESOURCE LOAD CHART

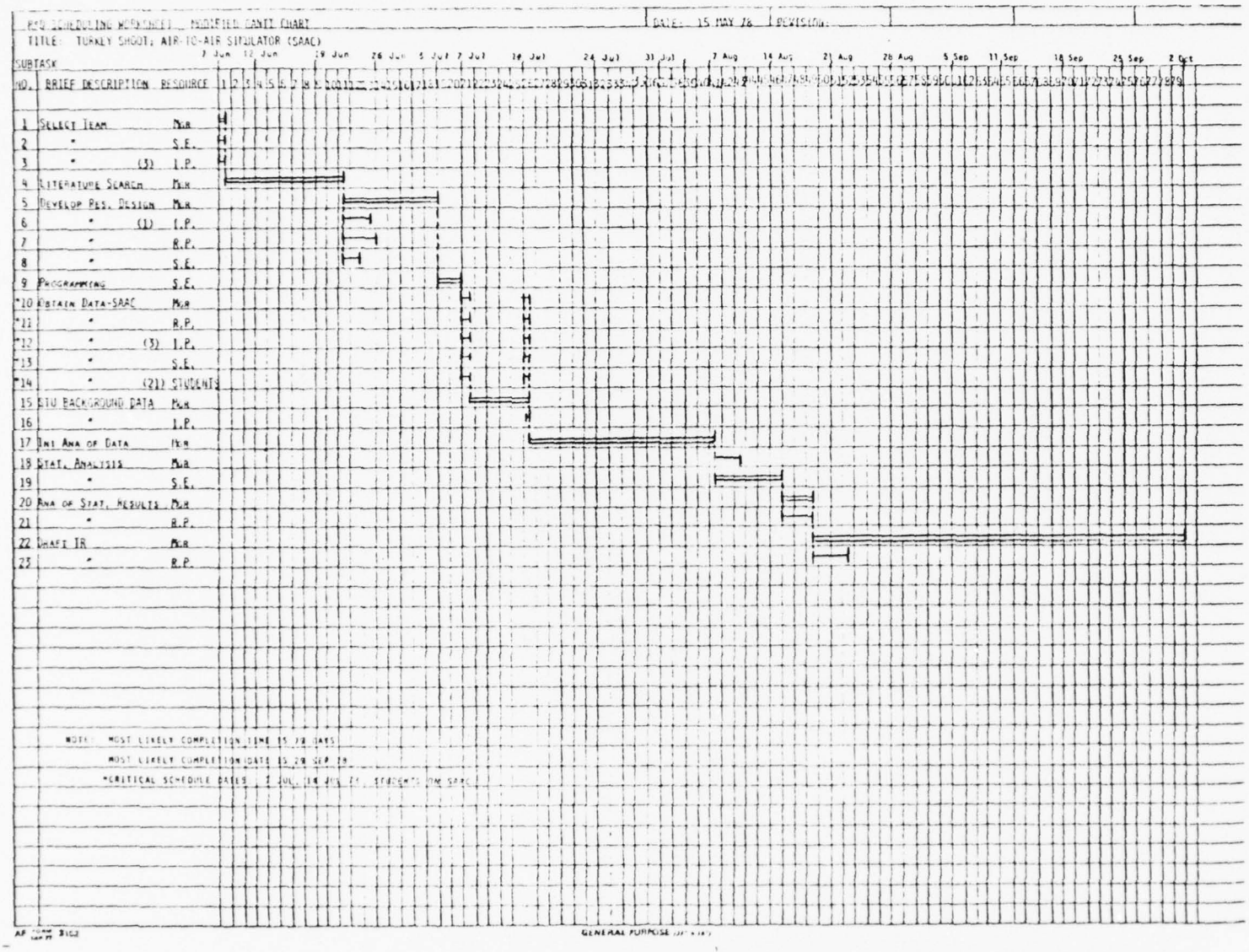

FIGURE 6. ILLUSTRATION OF R & D MASTER SCHEDULE FOR TURKEY SHOOT (SAAC) PROJECT

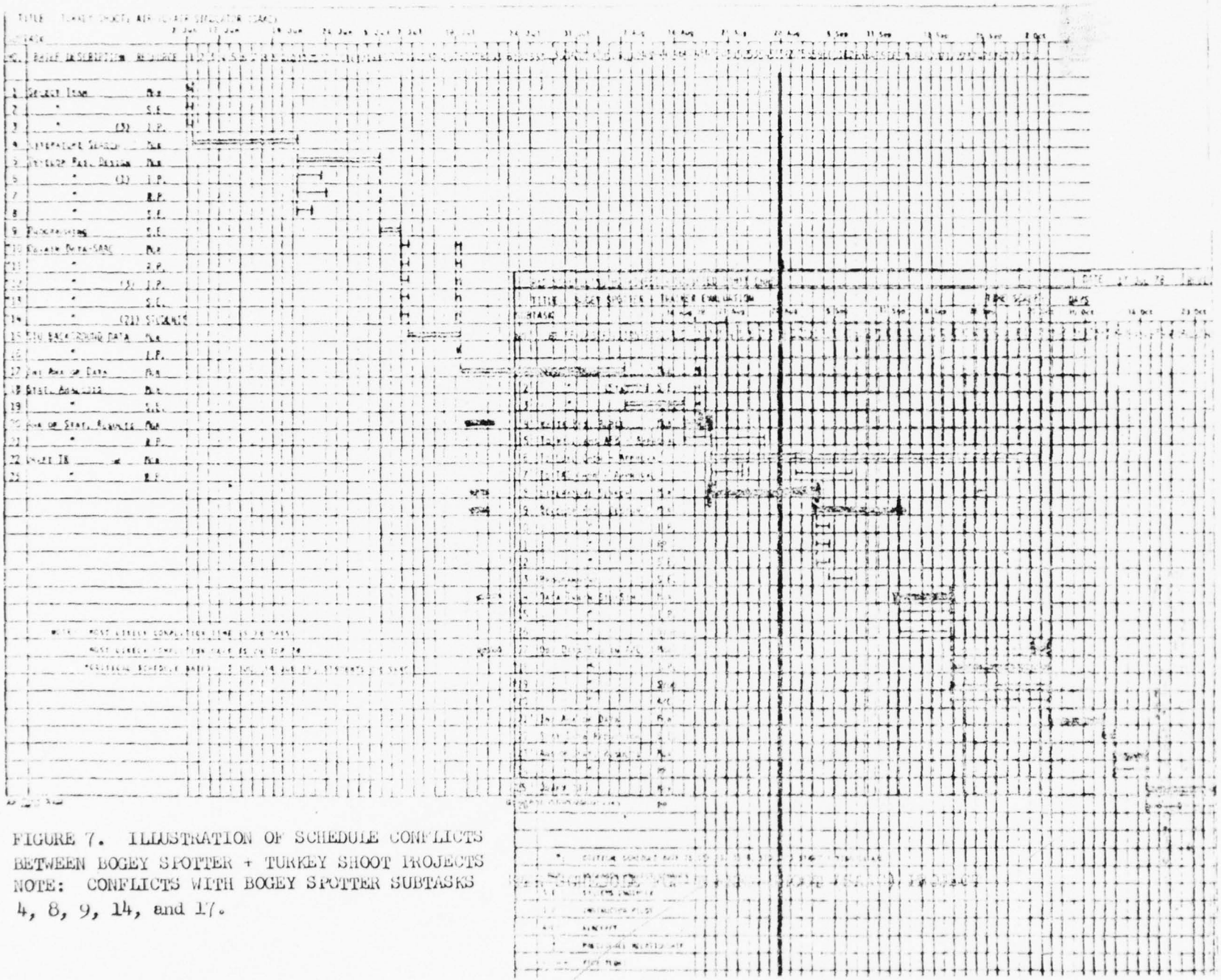

FIGURE 7. ILLUSTRATION OF SCHEDULE CONFLICTS BETWEEN BOGEY SPOTTER + TURKEY SHOOT PROJECTS NOTE: CONFLICTS WITH BOGEY SPOTTER SUBTASKS 4, 8, 9, 14, and 17.

b. Delay the start of the technical report, and seek additional help in writing the statistical report to reduce the expected writing time by one and one-half days.

The advantages of the time estimates and plotting the modified Gantt chart is that it immediately identifies areas of conflict and causes the analyst to think of alternative means for meeting the scheduled completion time, far before the crisis in the form of scheduled conflict appears.

EVALUATION OF PROPOSED SYSTEM

Any proposed system should be evaluated by at least two criteria, economic feasibility and potential acceptance.

Economic feasibility:

The economic cost of operating this program is the incremental cost of the additional manhours required for the project managers to break their research projects into detailed subtasks. Since the project managers (primarily the research psychologists) already must break their research tasks into basic subtasks, the increased costs in operating this system is presented as estimated incremental costs of additional manhours required over the present system. See Figure 8 for a detailed economic evaluation of the proposed system.

The FTO organization is presently comprised of 5 research psychologists, 3 systems engineers and 2 managerial personnel. The economic evaluation indicates that there is a potential savings of 3120 manhours total/year to be gained over the present productivity, assuming that the present mode of operation does not significantly change. Note that this 3120 manhours per year is a savings based on an estimated 20 projects/year being completed as compared with approximately 10 projects per year now being completed. This figure is a savings over and above an estimated required need for 2 additional systems engineers to take care of the additional workload imposed by doubling the number of research tasks.

Intangibles

This system requires that the Branch Manager and deputy managers review projects with the research project managers monthly instead of 4 times per year as presently done. This procedure will enable both the Branch Manager and the project managers to anticipate proposed schedule conflicts and problems long before they actually occur, and this lead time will permit effective planning by them to develop and evaluate alternative causes of action rather than operate in a "crisis" mode which seldom leads to "Optimum" solutions to problems.

ECONOMIC EVALUATION OF PROPOSED SYSTEM

A. Incremental Costs Over Present System

1. Additional professional Manhours to break research projects into detailed subtasks:

   16 Hours/Research Project x 20 projects/year: = 320 Manhours

2. Periodic management review of ongoing projects:
   (presently use quarterly reviews -- proposed are monthly reviews)
   (estimates include seminars).

   8 additional reviews/year x 20 projects/year x 8 manhours/project
   (4 hrs./supvr. + 4 hrs./each project manager) = 1280 Manhours

3. Additional manhours of clerical activity to update and revise status of ongoing projects

   20 projects/yr x 8 hrs./project x 8 additional reviews/year=
   1280 manhours

4. Increased Support Services:
   2 Systems engineers x 2000 hrs/year 4000 Manhours
   Total Additional Manhours Required/yr 6880 Manhours

B. Estimated Incremental Benefits

1. Increased accountability by each project manager.

2. Increased productivity of organization
   Estimated present 10 projects/year revised to 20 projects/year - net increase = 10 projects/year.

   (a 100% increase in productivity) Present production:
   Say: 5 people x 2 projects/yr/person = $\frac{10{,}000 \text{ hrs/yr}}{10 \text{ project/yr}}$ = 1,000 hrs/proj/person

C. Net Savings in Manhours

10,000 hrs/yr saved
6,880 hrs/yr adtl req.
3,120 manhours/year

See page 2 of 2

FIGURE 8. ECONOMIC EVALUATION OF PROPOSED SYSTEM

D. Intangibles

1. Improved morale of personnel through participative management (MBO).

2. Opportunity to improve professional capability of professional personnel.

3. Opportunity for professional to assist in setting the branch research goals.

4. Opportunity for professional personnel to be evaluated on an objective rating procedure which is based on specific performance on research subtasks.

FIGURE 8. (CONT'D) ECONOMIC EVALUATION OF PROPOSED SYSTEM

Although researchers often consider themselves as independent professionals, it is believed that they would welcome the accountability imposed upon them by this system (Ref 3).

Additionally, the management of the R&D function cannot afford to permit too lax a control over its research resources since time, equipment and funds are a scarce resource. The manager who exercises effective control over them often has the greatest opportunity of increasing the productivity of his organization and increases the opportunity for professional advancement for his professional personnel.

SYSTEM IMPLEMENTATION

Any new or revised system will have a degree of resistance towards acceptance (Ref 15).

In order to minimize this potential resistance, the persons involved must be thoroughly indoctrinated with the proposed system and how it will function. It is especially important that the organization personnel be invited to give their input as to the potential problems to be encountered and how they might be minimized.

It is especially important to emphasize the advantages to everyone in the organization - increased opportunities for increasing professional skills, the increased opportunity for attendance at professional society meetings, attendance at short courses, ability to complete more research projects, etc.

MAINTENANCE, REVISION OF SYSTEM

The system requires that the project manager and Branch and/or Section Managers review the progress of each ongoing research project approximately once/month. It is suggested that many of the ongoing projects be periodically presented as a seminar to the branch professionals in order to make them aware of successes, and problems faced by the researchers in the conduct of their projects. It is also strongly suggested that inputs be invited from other branch professionals concerning existing or anticipated problems. It is especially beneficial to researchers to obtain opinions from their colleagues pertaining to alternative ways of successfully carrying out their subtasks. Even though most researchers do presently contact their colleagues informally, a seminar presentation with invited comments will add an additional dimension to the input of ideas for the solution of problems. This technique has been used successfully in other organizations.

In the conduct of the problem, the modified Gantt chart, Figures 4 and 6, and the resource load charts, Figure 5, must be updated at least once per month. Air Force Regulation 80-25 (Ref 12) requires that estimates of time and cost for in-house research projects not deviate by more than 10%,

or it requires a detailed explanation of the researcher. This is a rather stringent and certainly unrealistic constraint to be placed on the estimation and performance of research activities. It is not uncommon in the industrial setting for production performances to vary by 25 per cent or more from the established standard data times for the performance of repetitive activities. However, breaking tasks into finely detailed subtasks will permit the development of standard data for the estimation of subtask resource time requirements that will progressively become more accurate.

CONCLUSIONS AND RECOMMENDATIONS

There is a decided need for increasing accountability and productivity of the research function. Industry has long effectively used MBO and the concepts of effective production planning and control to achieve both accountability and productivity improvement of the industrial organization. The concepts of effective productive planning and control require detailed planning of the steps required to reach the desired output (the completed research task) and an effective means for periodically monitoring the research production system to determine where potential problems may be expected to occur. Advance planning and continuous monitoring permit the development and evaluation of alternatives which will allow the completion of the required research program with less disruption and hasty decision making that would be done without such a systematic program.

It is recommended that this model be reviewed by the FTO Branch and steps be taken to initiate the planning and control procedures as soon as possible.

REFERENCES

1. Caro, P. W., "Aircraft Simulator and Pilot Training", Human Factors, Vol 15, No. 6, 1973, pp 502-509

2. Flying Training Research Plan, 1978-1982, Flying Training Division, Williams Air Force Base, Arizona 85224, 1 March 1978, p 1

3. Management of Human Resources in the Air Force Research and Development Establishment, U. S. Civil Service Commission, 1966, pp 1-2

4. Pelz, D. C., "Freedom in Research", International Science and Technology, Feb 1964, pp 54-66

5. Martino, J. P., "Managing Engineers by Objectives", IEEE Transactions in Engineering Management, Vol. EM-23, No. 4, November 1966, pp 168-174

6. Badowy, M. K., "Applying Management by Objectives to R&D Labs.", Research Management, Vol 19, No. 6, November 1976, pp 35-40

7. Walters, J. E., Research Management: Principles and Practices, Sparton Books, Washington, D. C. 1965

8. Mc Gregor, D., The Human Side of Enterprise, Mc Graw-Hill, Inc. 1960

9. Voris, Wm., Production Planning and Control, Irwin Pub. Co., 1964

10. Karger, Delinar W. and Murdick, Robert G., "Management Information System for Engineering and Research", IEEE Transactions in Engineering Management, Vol EM-24, No. 2, May 1977, pp 72-75

11. AFHRL-Regulation 80-4; "R&D Laboratory Work Unit Planning, Prioritization and Approval Procedures."

12. AFHRL Regulation 80-25, "R&D Technology Management Reviews"

13. Flying Training Research Plan, 1978-1982, Flying Training Division, Williams Air Force Base, Arizona 85224, 1 March 1978, p 7

14. Moder, J. J. and Phillips, C. R., Project Management with CPM and PERT, Reinhold Pub. Co., 1964

15. Nadler, G., Work Design, Irwin Pub. Co., 1964

SUPPLEMENT

The original planned program effort was to carry out two projects: one concerning the development of a model for determining workload requirements and the second was to be a mini-study to determine the feasibility of developing and implementing an automated instruction program for a SAAC basic flying maneuver.

Considerable effort was expended in outlining the methodology for carrying out the second project. Based on the work done on the proposed automation of a basic flying maneuver, it is recommended that efforts be continued since the CAI offers a fertile field for increasing efficiency both for simulator training and the transfer of learning to aircraft.

An opportunity arose in the ninth week of the program to implement the first stage of the proposed model production planning and control model for the F-16 project (ASPT F-16 Phase I and II Research) at Williams AFB. A brief summary is presented on this project.

During the week of July 31, 1978 the Engineering Branch at Williams AFB was assigned the task of configuring a simulator of the F-16 aircraft. This was assigned top priority.

The production planning and control master scheduling model was implemented by the planners who had the responsibility for proposing a master plan complete with clearly identified subtasks, estimated times to complete each task, the identification of sequential relationships existing among the subtasks, the determination of a critical path and an estimate of the specific resources required to carry out this top priority project.

Attached Figure 9 is a modified Gantt chart which is the planner's first estimate for the scheduling of this project. It was felt by many of the engineering personnel that the use of this technique permitted them to program the required activities in considerably less time than the conventional procedures would have required. In addition, it was believed that this permitted a more effective scheduling of the subtasks than could have been obtained using the customary techniques to develop a master schedule for a major undertaking.

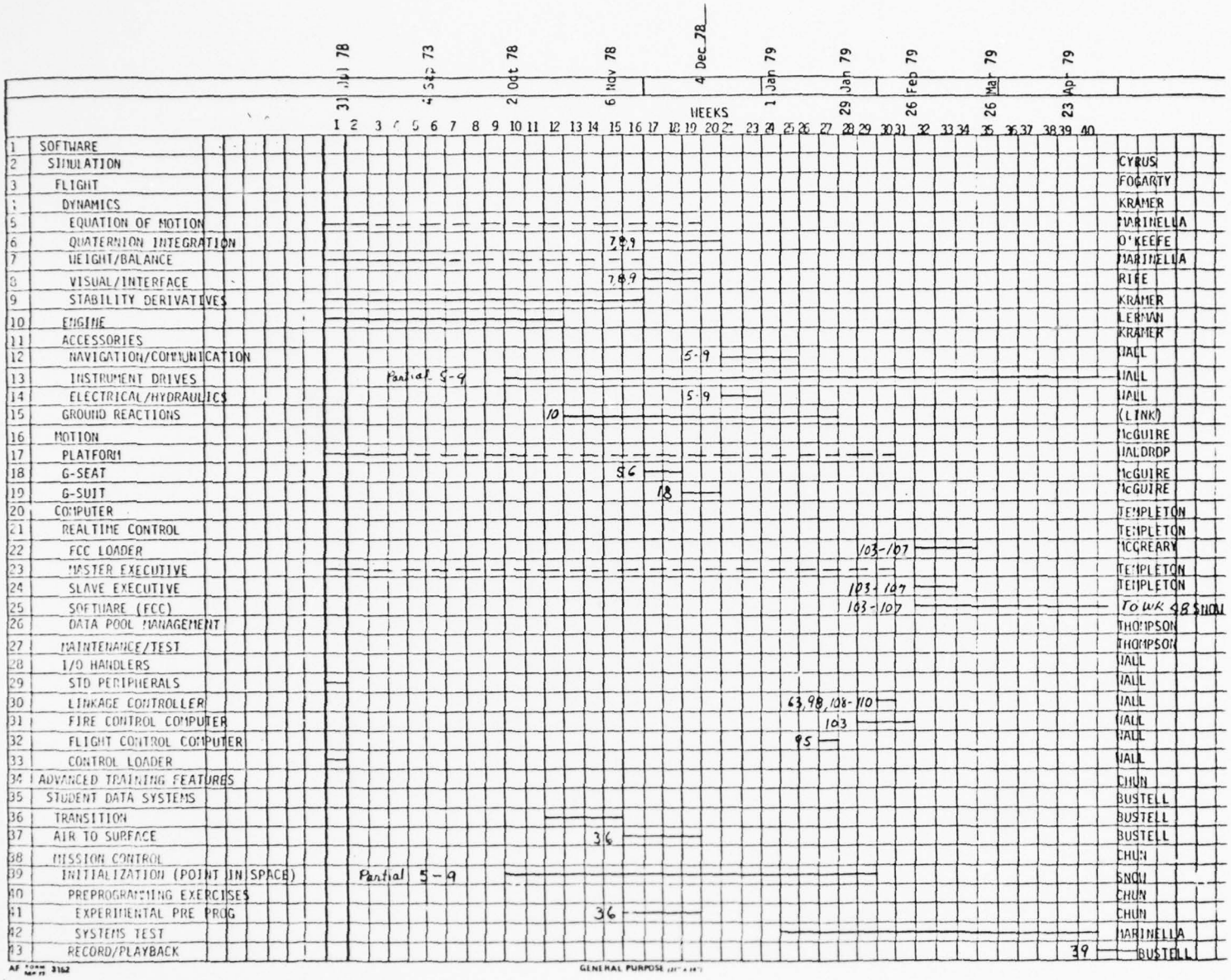

3 Aug 78

FIGURE 9. INITIAL MASTER SCHEDULE I-Ic PHASE I

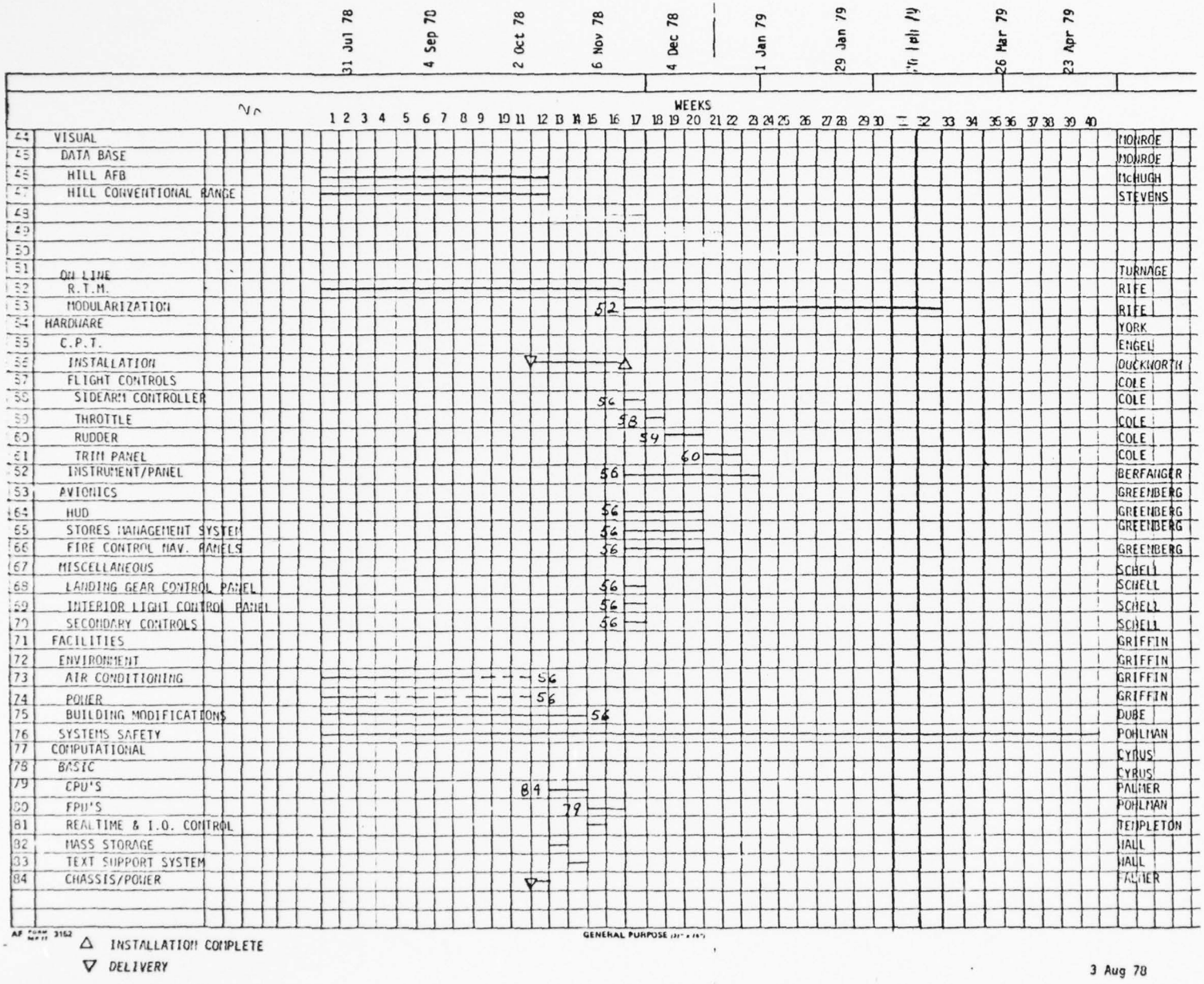

FIGURE 9. (CONT'D) INITIAL MASTER SCHEDULE F-16 PHASE I

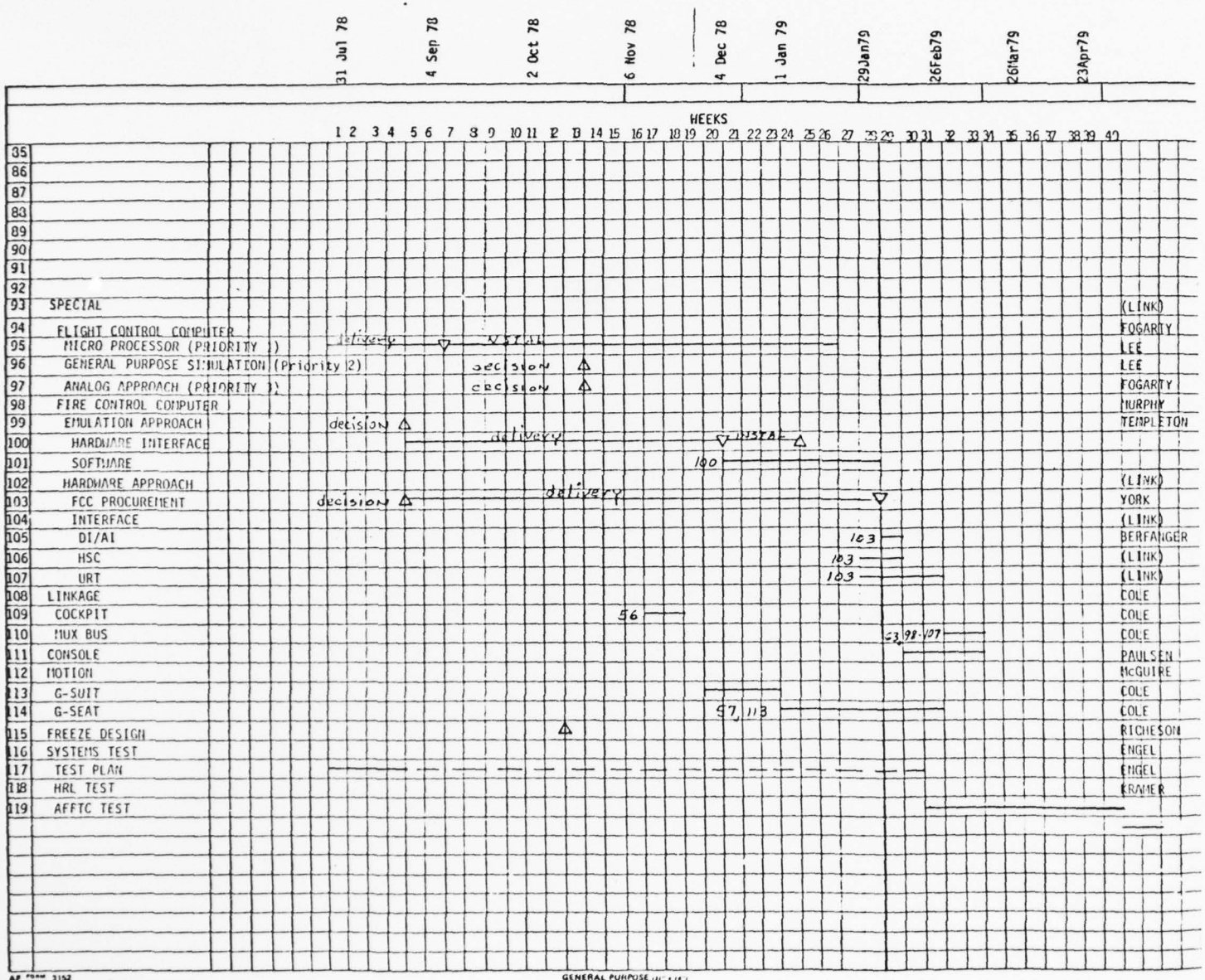

FIGURE 9. (CONT'D) INITIAL MASTER SCHEDULE F-16 PHASE I

1978 USAF-ASEE SUMMER FACULTY RESEARCH PROGRAM

sponsored by

THE AIR FORCE OFFICE OF SCIENTIFIC RESEARCH

conducted by

AUBURN UNIVERSITY AND OHIO STATE UNIVERSITY

PARTICIPANT'S FINAL REPORT

USING FOURIER COEFFICIENTS AS A PROPOSED INDICATOR OF ACM PILOT TRACKING SKILLS (TERMINAL PHASE) FOR THE SIMULATOR FOR AIR-TO-AIR COMBAT (SAAC)

Prepared by:	Dean E. Nold
Academic Rank:	Professor
Department and University:	Department of Electrical Engineering Technology Purdue University - Fort Wayne Campass
Assignment:	
(Air Force Base)	Luke AFB
(Laboratory)	Human Resources Laboratory
(Division)	Flight Training
(Branch)	Tactical Research
USAF Research Colleague:	Robert B. Bunker
Date:	August 11, 1978
Contract No.:	F44620-75-C-0031

USING FOURIER COEFFICIENTS AS A PROPOSED INDICATOR OF ACM PILOT TRACKING SKILLS (TERMINAL PHASE) FOR THE SIMULATOR FOR AIR-TO-AIR COMBAT (SAAC).

by

DEAN E. NOLD

ABSTRACT

SAAC (Simulator for Air-to-Air Combat) is a simulator designed to teach fighter pilots air-to-air combat maneuvers while simulating the performance of F-4E fighters.

Preliminary investigations suggest that it is possible to discriminate between SAAC pilots of different experience levels by analyzing the Fourier Series coefficients of aircraft control movements. A pilot smoothness index (PSI) is proposed based upon the Fourier Series coefficients. In the proposed system, the Fourier coefficients would be calculated for the time window that consists of the endgame phase of target tracking and during the trigger squeeze period. During this interval, additional information, such as MIL ERROR, rudder control pressure, etc., would be recorded and studied.

ACKNOWLEDGEMENT

The author is grateful to the Air Force System Command - Office of Scientific Research for support of this summer research project.

The author is indebted to Mr. J. Fred O'Brien, Jr., the Program Director of the 1978 USAF-ASEE Summer Faculty Research Program, Lt Col Branby, 57TTW/OLAA for his many helpful suggestions, Mr. Robert Bunker for his support, and to Mr. Randy Saxton for his data processing services.

Introduction

From a control systems point of view, a pilot is usually thought of as a continuous feedback control system as shown below in Figure 1.

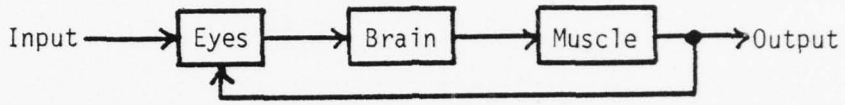

Figure 1. - Simulation of a Pilot During Tracking

However, in trying to evaluate pilot performance, the pilot has all of the characteristics of a sampled-data control system. In other words, actions taken by a pilot occur at discrete instants of time. The pilot determines the error, applies corrective measures and then waits for the next error to appear. As a pilot gains experience, he anticipates his next control input, makes smaller control movements, and begins to simulate (or approach) a continuous control system. His objective is to minimize his errors with small control movements.

Research Objective

The objective of this investigation was to determine whether one could mathematically detect any changes in the frequency spectrum curves, (i.e., the relationship between different frequency components that exist in non-sinusoidal movements) of the aircraft control movements between pilots of different levels of flying experience. It is hoped that this technique will aid in the evaluation of pilot performance during SAAC air-to-air combat maneuvers.

SAAC (Simulator for Air-to-Air Combat) is a two-aircraft simulator designed primarily to teach combat fighter pilots air-to-air combat maneuvers while simulating the performance of F-4E fighters.

The SAAC System

Analog voltages corresponding to aileron and elevator control movements, and the D to A converter are both sampled by the SAAC computer at a rate of 20 Hz. However, the software program needed to drive a six-channel strip recorder is sampled at a rate of 10 Hz as shown in Figure 2.

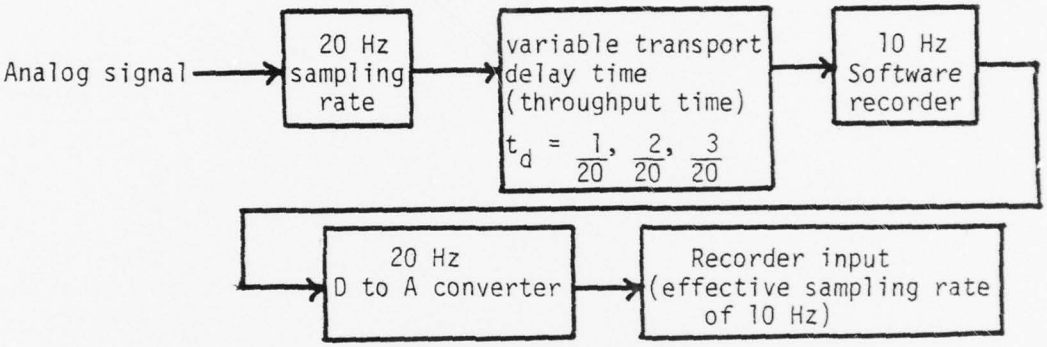

Figure 2. - Functional Block Diagram of the SAAC System

The effective overall sampling rate is 10 Hz since the 10 and 20 Hz signals are synchronized. This implies that the frequency spectrum curves should be valid up to A5 Hz bandwidths. It was assumed for this experiment that the variable transport delay time (throughput time) i.e., 1/20, 2/20, 3/20 seconds, is negligible. However, this variable delay time which can cause output distortion and jitter will be avoided in the proposed system as discussed in the conclusions and recommendations section of this report. Further, the effective bandwidth of the proposed system is increased to 10 Hz thus increasing the accuracy of the results.

Numerical Method for Determining Fourier Coefficients

Assuming that the aircraft control movements are periodic, i.e., f(x) =

$f(x + 2\pi)$, one can easily determine the Fourier coefficients by the following technique:

$$f(x) = A_o + \sum_{n=1}^{\infty} (a_n \text{ Cos } nx + b_n \text{ Sin } nx)$$

$$A_o = \frac{1}{q} \left[f(x_1) + \ldots\ldots + f(x_q) \text{ Cos}(nx_q) \right]$$

$$a_n = \frac{2}{q} \left[f(x_1) \text{ Cos}(nx_1) + \ldots + f(x_q) \text{ Cos}(nx_q) \right]$$

$$b_n = \frac{2}{q} \left[f(x_1) \text{ Sin}(nx_1) + \ldots + f(x_q) \text{ Sin}(nx_q) \right]$$

Combining terms of the same frequency, the Fourier series can be written in the form of:

$$f(t) = A_o + C_n \text{ Sin}(nx + \gamma)$$

$$\text{where: } C_n = \sqrt{a_n^2 + b_n^2}$$

Since one is interested in the frequency characteristics of the aircraft control movements, the A_o term of the Fourier series can be neglected. The A_o term of the Fourier series is also called the "dc" (direct current) term since this value reflects the average of the function evaluated for the period T.

Feasibility Study

Two different fighter pilots were selected to fly a barrel roll in the SAAC. The objective of this phase of the experiment was to determine if one could mathematically detect any changes in the frequency spectrum of aircraft control movements of pilots at different skill levels.

Pilot number 1. An exceptionally well qualified fighter pilot flew a barrel roll trying to simulate three different pilot skill levels.

Skill Level 1: Experienced Fighter pilot

Skill Level 2: Intermediate Fighter pilot

Skill Level 3: Low-time Fighter pilot

Pilot number 2. A medium-time fighter pilot flew a barrel roll trying to simulate an experienced fighter pilot.

Skill Level 1A: Experienced Fighter Pilot

For the skill levels listed above, the Fourier coefficients were calculated for pitch and roll. The instant the aircraft became inverted in the barrel roll, data was taken from the strip recorder at 0.1 second intervals (10 Hz) for a period of two seconds. The frequency spectrum curves shown in Figures 3 and 4 indicate a shift toward lower frequencies as the skill level of the pilot increases.

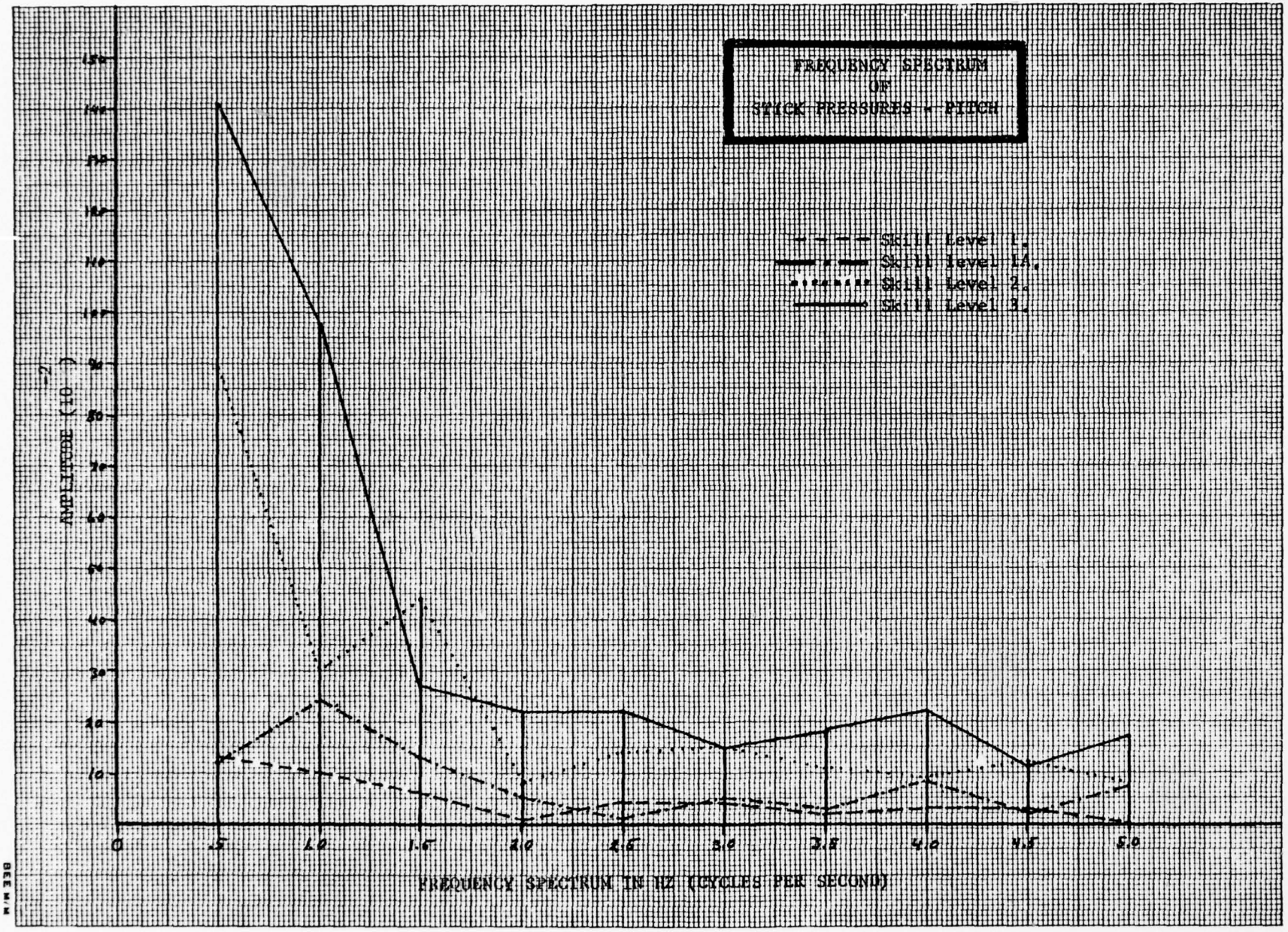
FREQUENCY SPECTRUM
OF
STICK PRESSURES v. PITCH
Skill Level 1.
Skill level 1A.
Skill Level 2.
Skill Level 3.
AMPLITUDE (dB)
0
.5
1.0
1.5
2.0
2.5
3.0
3.5
4.0
4.5
5.0
FREQUENCY SPECTRUM IN HZ (CYCLES PER SECOND)

Figure 3

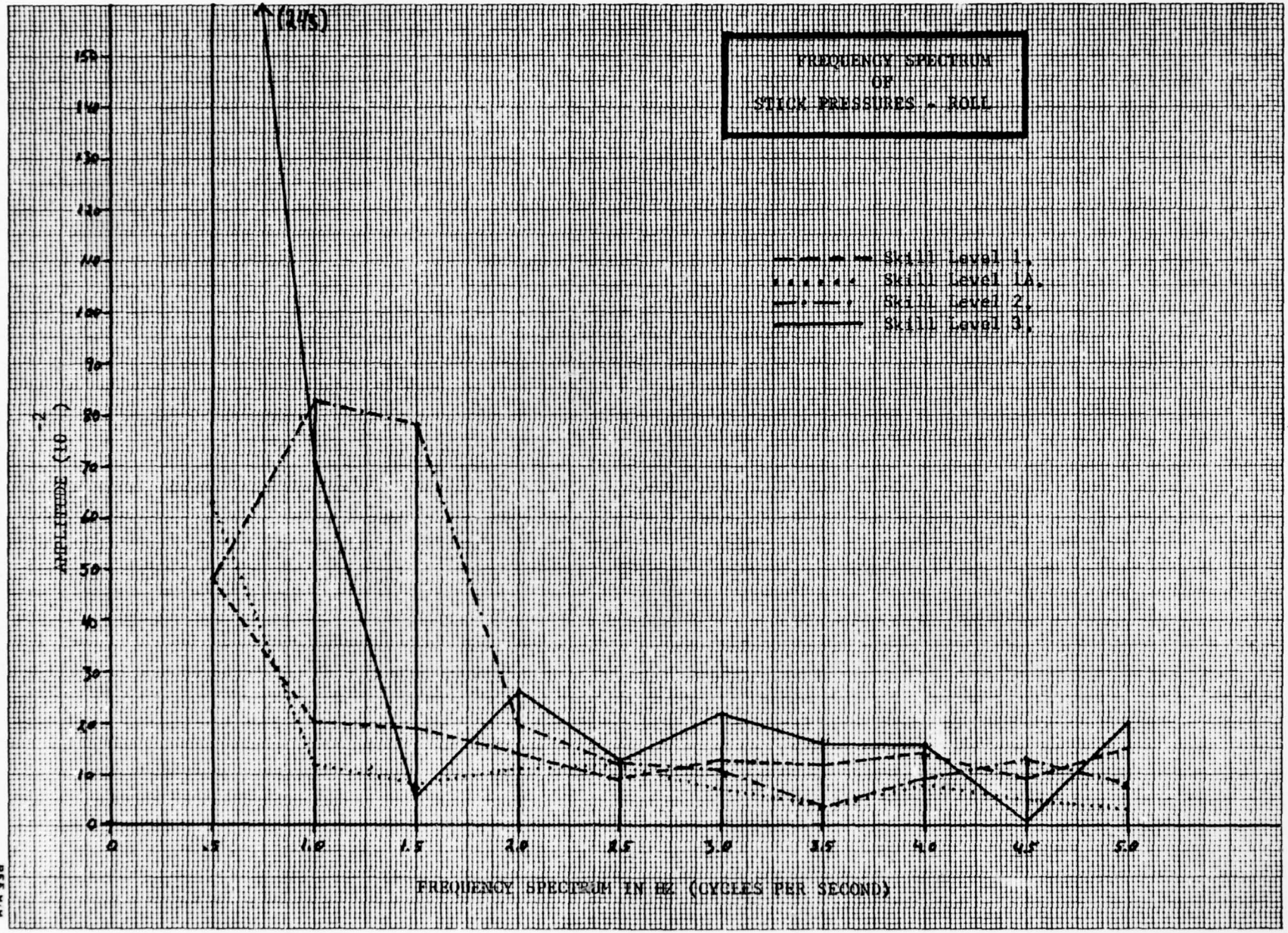
FREQUENCY SPECTRUM
OF
STICK PRESSURES - ROLL
Skill Level 1.
Skill Level 1A.
Skill Level 2.
Skill Level 3.
AMPLITUDE (10 -2)
0
10
20
30
40
50
60
70
80
90
100
110
120
130
140
150
.5
1.0
1.5
2.0
2.5
3.0
3.5
4.0
4.5
5.0
FREQUENCY SPECTRUM IN HZ (CYCLES PER SECOND)

Figure 4

A Technique in Determining the Changes in the Frequency Spectrum Curves

From Figures 3 and 4, it would appear that there is correlation between the shape (slope) of the frequency spectrum curve (of control movements) with the skill level of the pilot. Frequency spectrum curve slope changes can easily be determined by comparing the output signals from two bandpass filters as shown in Figure 5 below.

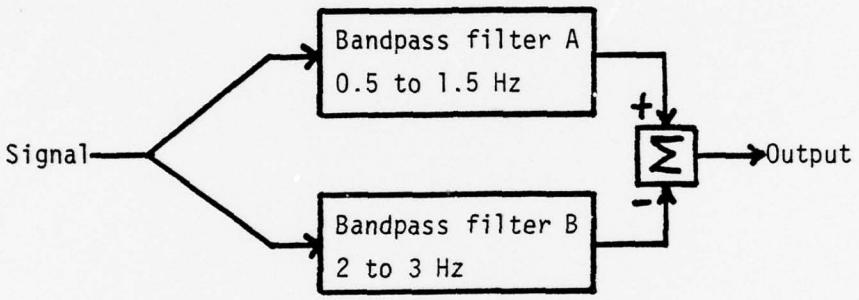

Figure 5. - Signal Processing Technique

Suppose we define pilot smoothness index (PSI) as:

$$PSI \approx \text{(area under frequency spectrum curve between 0.5 to 1.5 Hz)} - \text{(area under frequency spectrum curve between 2.0 to 3.0 Hz)}$$

For our particular example we would simply add and subtract the appropriate values of the Fourier coefficients.

$$PSI \approx \sum_{n=1}^{n=3} C_n - \sum_{n=4}^{n=6} C_n$$

The results of this experiment are given in Table 1.

Table 1

Rating of Smoothness by Using the PSI

PITCH

PILOT SKILL LEVEL	PSI
1	.200
1A	.380
2	1.27
3	2.06

ROLL

PILOT SKILL LEVEL	PSI
1	.500
1A	.541
2	1.668
3	2.613

Low-Pass Filter Technique (Another Method)

Mc Dowell's investigation (Ref. 1) was brought to the attention of this author in the final stages of this report. The results of his research indicate that the frequency domain based measures of a pilot's control movements discriminate between different pilot experience levels. Further, such changes in the pilot's behavior are reflected by a shift in his control input power spectra toward lower frequencies.

Both the low-pass filter and the Fourier coefficient method, while indicating similar results, suggest that little useful information exists above 2 Hz.

Control stick movement signals used in the low-pass filter technique are sampled at a 15 Hz rate. The control signals, as shown in Figure 6, are then fed into five different low-pass butterworth filters (n = 2 or two-pole) having approximate cut-off frequencies of 1/8, 1/4, 1/2, 1 and 2 Hz. The cumulative power output from each filter is then calculated by dividing the power from each filter output by the total signal power.

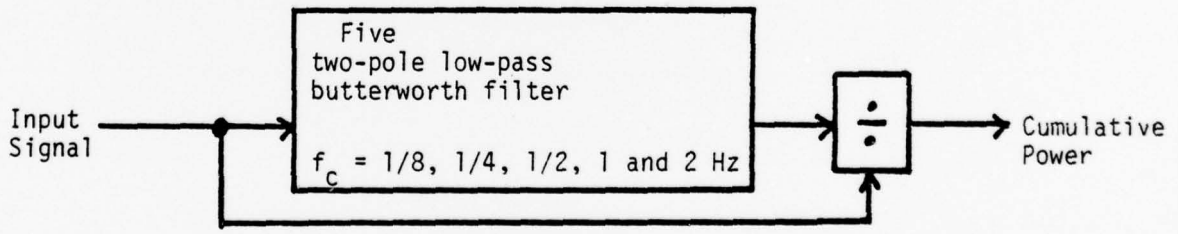

Figure 6. Low-Pass Filter Technique

Figure 7 indicates the cumulative power that exists below five different cut-off frequencies as a function of different skill level pilots flying a vertical S maneuver.

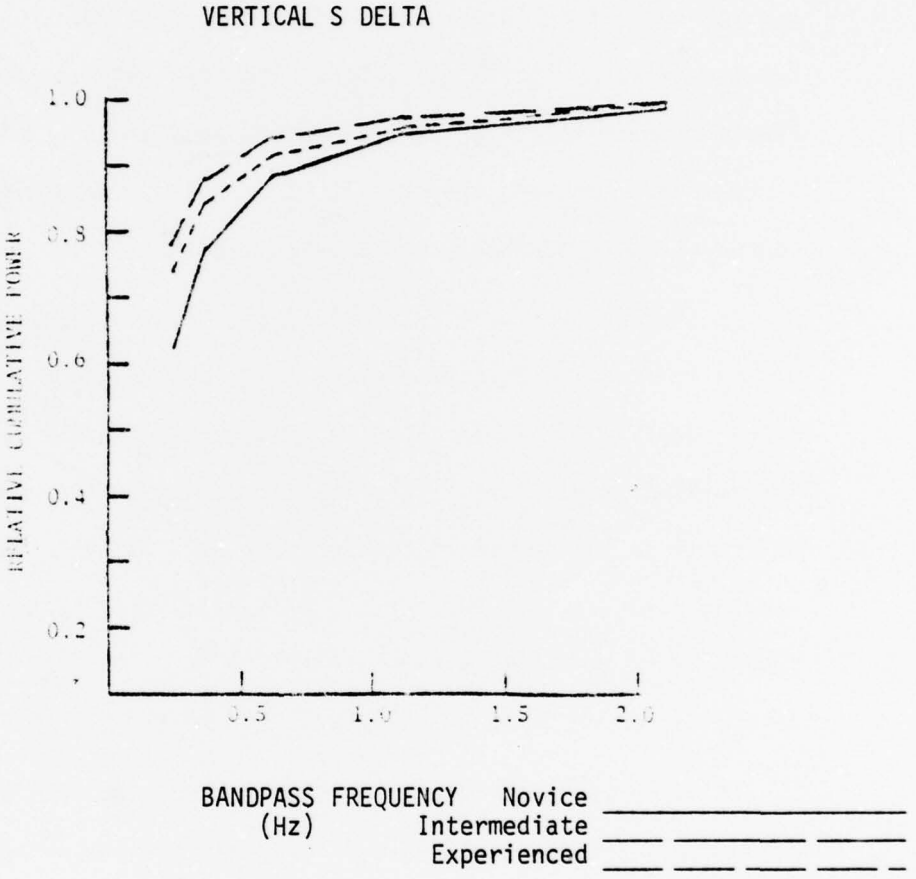

Figure 7. - Aileron Filter Outputs

It appears that the cumulative power obtained by using the low-pass filter method includes the A_o (dc) term of the Fourier Series. Thus control stick movement information could be "masked" since the A_o term can be much larger than the frequency coefficient terms of the Fourier Series, i.e., C_n.

CONCLUSIONS AND RECOMMENDATIONS

1. In the system being proposed, it is assumed that fighter pilot smoothness is most descriptive of his best tracking ability during the endgame phase (the latter phase of target tracking) and during the trigger squeeze period. For example, Beare and Kahn (Ref. 2) demonstrated that tracking error increases as the average rate of stick movement in a human compensatory tracking system. In other words, one would expect correlation between pilot smoothness and target MIL ERROR.

2. Preliminary analysis (Ref. 4) of the SAAC system suggests that frequency spectrum shifts (of control stick movements) due to different pilot skill levels fall within the steady-state closed-loop bandwidth of the pilot-in-the-SAAC-loop. Thus, high frequency control stick movements would be reflected to the output of the SAAC system. (Smith's data (Ref. 5) regarding the pilot-in-the-loop for a T-33 type aircraft yields a steady-state closed-loop bandwidth of approximately 1 Hz. The SAAC system bandwidth; however, appears to be slightly over 1.5 Hz for both pitch and roll).

3. It is recommended that SAAC software programs incorporate the manual Fourier coefficients technique. The determination of the Fourier coefficients, pilot smoothness, etc. would be for the "time window" of two seconds before first trigger squeeze and during the trigger squeeze interval.

4. It is recommended that SAAC software programs be developed in order to statistically evaluate the target MIL ERROR signal for the time window defined above.

5. It is recommended that the rudder control (deflection) signal be monitored in order to insure that SAAC pilots are using correct flying techniques while in the time window.

6. Using the time window concept, it would appear that the Fourier coefficient technique is well suited for this application.

7. Since computations are not done in real-time, problems associated with computational delays (i.e., variable transport delay time or throughput time) can easily be avoided by feeding the SAAC control movement signals into a circulating buffer located within the SAAC computer.

8. Since control signals are sampled and stored in the SAAC memory at a rate of 20 Hz, the frequency spectrum bandwidth is increased to 10 Hz.

ADDENDUM

This section of the report contains the results of using the Fourier coefficient technique when applied to a (SAAC) class of five fighter pilots. The pilots were evaluated on the first and last days of their SAAC simulator training. For this investigation, each pilot flew two consecutive standard target tracking maneuvers. During the entire maneuvers, the following signals were recorded and later analyzed.

1) Pitch Control Pressure
2) Roll Control Pressure
3) Rudder Control Pressure
4) Trigger Switch Status
5) Target Mil Error

From the two tracking maneuvers, two "trigger squeeze windows" were then selected by the following procedures:

1) The "Kill" time window was determined by the pilot's first computer kill.
2) The "No-Kill" time window was then determined by selecting the mid "No-Kill" trigger squeeze in the other tracking maneuver.

With the aid of a computer, 60 separate frequency spectrum curves were plotted for pitch, roll, and rudder. The following conclusions can be made after reviewing this data.

1) The bandpass frequencies of 0.4 to 2 Hz, and 2 to 3.6 Hz appear to be satisfactory in detecting shifts in the frequency spectrum curves.

2) As shown in Table A-1, the average PSI is always lower for a kill track vs a no-kill track. Further, the PSI appears to improve with training.

3) As shown in Table A-3, the high frequency content contained in control movements appears to be lower for a kill vs a no-kill track. Further, the high frequency control movements appears to decrease with training. Table A-5 shows the statistical analysis of the tracking error for each maneuver. Table A-6 indicates the number of target hits and rounds fired.

If this investigation is to be continued, it is recommended that the variable time window be made fixed. This would result in better accuracy and shorter computer programs. In order for one to determine the fixed time, the following data is provided:

Analysis of Trigger Squeeze Times

Minimum Time	0.1 seconds
Maximum Time	3.6 seconds
Mean Time	0.87 seconds
Standard Deviation	0.67 seconds
Sample Size	123

[illegible]	Plain Day [illegible] Driving		Rain [illegible] Driving	
	Downhill Track	Hill Ascent	No-Kill Theory	Hill Track
1	1.56	[illegible]	[illegible]	[illegible]
2	[illegible]	[illegible]	[illegible]	[illegible]
[illegible]	[illegible]	[illegible]	[illegible]	[illegible]
[illegible]	[illegible]	[illegible]	[illegible]	.39
[illegible]	[illegible]	[illegible]	[illegible]	[illegible]
Average	[illegible]	[illegible]	[illegible]	[illegible]

Where: SDI Overall = $\sqrt{[illegible]}$

[illegible]

[illegible]

Pilot		First Dry or Instrument		Last Dry or Instrument	
		No-Yaw Trim	Yaw Trim	No-Yaw Trim	Yaw Trim
1	Pitch	0.22	-.72	-.1	0.34
	Roll	-.5	-.46	0.1	-.1
	Rudder	7.20	5.35	7.46	7.2
2	Pitch	0.49	-.47	-.75	-.75
	Roll	1.5	0.51	-.47	0.6
	Rudder	-.31	0	-.21	-.73
3	Pitch	-.53	0.14	-.75	-.47
	Roll	0.52	-.16	-.1	-.44
	Rudder	1.12	1.47	.46	-.31
4	Pitch	0.58	0	-.72	-.63
	Roll	0.17	1.47	-.45	0.11
	Rudder	5.34	5.35	7.46	7.21
5	Pitch	-.18	1.24	1.03	-.03
	Roll	-.39	0.00	2.52	0.47
	Rudder	10.74	7.47	7.08	8.03

T-Plan A-2

OVERALL - HIGH FREQUENCY CONTENT OF CONTROL PRESSURES
BANDPASS FILTER B OUTPUT
(2.0 to 3.6 Hz)

Pilot	First Day of Training		Last Day of Training	
	No-Kill Track	Kill Track	No-Kill Track	Kill Track
1	7.98	5.40	2.16	3.19
2	5.58	1.63	1.91	2.83
3	5.38	5.03	3.57	2.99
4	5.44	4.00	3.76	6.27
5	6.34	4.21	6.98	4.52
Average	6.14	4.05	3.68	3.96

Where: $\text{OVERALL} = \sqrt{(\text{PITCH})^2 + (\text{ROLL})^2 + (\text{RUDDER})^2}$

TABLE A-3

INDIVIDUAL-HIGH FREQUENCY CONTENT OF CONTROL PRESSURES
BANDPASS FILTER B OUTPUT
(2.0 to 3.0 Hz)

Pilot		First Day of Training		Last Day of Training		Average
		No-Kill Track	Kill Track	No-Kill Track	Kill Track	
1	Pitch	6.91	2.01	1.29	1.34	2.89
	Roll	1.04	1.82	0.84	0.55	1.06
	Rudder	3.86	4.67	1.45	2.81	3.21
2	Pitch	2.45	1.35	0.09	1.56	1.59
	Roll	4.98	0.75	1.47	0.24	0.36
	Rudder	0.54	0.53	0.71	0.73	0.63
3	Pitch	1.55	4.20	1.57	0.91	2.06
	Roll	5.11	2.65	2.95	1.36	3.02
	Rudder	0.66	0.80	1.26	2.50	1.31
4	Pitch	3.03	3.10	1.13	3.96	2.56
	Roll	1.99	2.27	2.47	2.46	2.30
	Rudder	4.64	1.13	2.60	4.20	3.14
5	Pitch	1.48	2.66	2.36	0.78	1.63
	Roll	2.84	0.93	2.74	2.09	2.15
	Rudder	5.47	3.11	5.07	3.99	4.42

TABLE A-4

TRACKING ERROR
(MEAN TRACKING ERROR/STANDARD DEVIATION)

Pilot	First Day of Training		Last Day of Training	
	No-Kill Track	Kill Track	No-Kill Track	Kill Track
1	15.4/7.4	6.4/5.2	11.7/6.5	20.6/23.6
2	59.4/35.5	26.1/11.7	27.9/7.7	43.5/26.5*
3	38.3/22.2	41.2/16.7	40.2/31.2	12.9/6.7*
4	36.8/20.9	22.8/13.2*	34.3/20.5	56.5/38.7
5	17.4/14.0	14.3/6.4	22.6/7.1	16.0/12.2

* Pilot did not obtain a computer "kill" in both tracking maneuvers. The lowest miss error tracking interval was then selected.

TABLE A-5

NUMBER OF HITS
(Number of Hits/Rounds Fired)

Pilot	First Day of Training		Last Day of Training	
	No-Kill Track	Kill Track	No-Kill Track	Kill Track
1	0/160	6.5/225	0/135	1.9/80
2	0/39	12.2/186	0/130	0/255*
3	0/40	12.0/95	0/50	2.4/115*
4	0/45	0/50*	0/120	3/6/205
5	0/40	12.4/285	0/50	5.0/90

* Pilot did not obtain a computer "Kill" in both tracking maneuvers. The lowest miss error tracking interval was then selected.

TABLE A-I

REFERENCES

1. McDowell, E. D., The Development and Evaluation of Objective Frequency Domain Based Pilot Performance, AFOSR-77-3294. Williams AFB, Arizona: Flying Training Division, Air Force Human Resources Laboratory, 1978.

2. Beare, A. C. and Kahn, A., Describing Functions for Compensatory Tracking of Sine Waves Plus Noise, Proc. 3rd Annual NASA-University Conf. on Manual Control, NASA SP-144.

3. Newell, F. D., Inflight and Ground Simulation Measurements of Pilot Transfer Characteristics in the Compensatory Roll Tracking Task, Proc. 3rd Annual NASA-University Conf. on Manual Control, NASA SP-144.

4. Personal communications with R. B. Bunker, dated July 18, 1978.

5. Smith, H. J., Human Describing Functions Measured in Flight and on Simulators, Proc. 2nd Annual NASA-University Conf. on Manual Control, NASA SP-128.

1978 USAF - ASEE SUMMER FACULTY RESEARCH PROGRAM

SPONSORED BY

THE AIR FORCE OFFICE OF SCIENTIFIC RESEARCH

CONDUCTED BY

AUBURN UNIVERSITY

FINAL REPORT

NEUTRON PRODUCTION FROM COLLECTIVE ION ACCELERATION AND PLASMA HEATING EXPERIMENTATION USING A 6Mev 150 KILOAMPERE FIELD EMISSION GENERATOR

PREPARED BY:	ALBERT J. FRASCA PH.D.
ACADEMIC RANK:	ASSOCIATE PROF. PHYSICS
UNIVERSITY:	WITTENBERG UNIVERSITY SPRINGFIELD, OHIO
ASSIGNMENT:	
(AIR FORCE BASE)	KIRTLAND AFB
(LABORATORY)	AIR FORCE WEAPONS LABORATORY
(DIVISION)	EXPERIMENTAL PHYSICS (DYP)
(BRANCH)	TRANSIENT RADIATION EFFECTS
USAF RESEARCH COLLEAGUE:	CAPT ROBERT F. HOEBERLING
DATE:	AUGUST 12, 1978
CONTRACT NO:	F44620-75-C-0031

ABSTRACT

Neutron Production from Collective Ion Acceleration and Plasma Heating Experimentation Using a 6MeV 150 Kiloampere Field Emission Generator.

By

Albert J. Frasca Ph.D.
Wittenberg University
Springfield, Ohio

The production of neutrons from two different accelerator configurations were analysed for neutron yield and energy distribution. The accelerator used in the experimentation was a Pulserad 1590 which is a six MeV pulsed electron beam device with a current capability of approximately 150 kiloamperes.

The collective ion acceleration configuration produced protons and deuterons with energies in excess of 30 MeV and the resulting collisions in carbon produced a highly forward directed neutron flux of comparable energy. The plasma heating configuration produced about 10^{9} neutrons which is about 10^{-3} times that produced by the collective ion configuration. As anticipated, the neutron spectrum from the plasma heating experimentation did not yield the high energy neutron spectrum observed in the collective ion geometry. However, it is now thought that many of the neutrons produced were from low efficiency collective ion effects and not from the deuterium gas within the target chamber.

The methods for detection and analysis consisted of several independent techniques: (a) thermal activation (b) fast neutron activation and (c) time-of-flight. The time-of-flight systems were used to observe the neutron energy spectrum at 150° and 90° to the incident beam. Silver activation counters were used to determine the total neutron yield after correction for scattered neutrons. The gold activation was utilized to obtain angular correlations of neutrons produced above 23Mev using the Au^{197} (n,4n)Au^{194} reaction.

INTRODUCTION

The use of field emission electron generators for collective ion acceleration and electron beam heating experimentation has increased rapidly during the last few years. Collective ion acceleration has the capability of accelerating positive particles to many times the electron beam's kinetic energy. Interest in this technique has risen as a means for obtaining very high energy positive ions without having to develop high energy accelerators. The studies on electron beam heating of plasmas have been of interest as a means of heating gases such as deuterium to temperatures high enough to cause fusion. Both techniques were studied this summer by members of the Air Force at Kirtland AFB using the Pulserad 1590.

One of the interesting results from collective ion acceleration or electron beam heating is the generation of neutrons by (P,n), (γ,n) and (d,n) reactions. The primary emphasis of this report is the study of the resulting neutron yields from the two different experimental configurations.

The machine used for all the neutron experimentation was the Pulserad 1590 which delivers a six megavolt 150 kiloampere electron beam pulse of less than 100 nanoseconds duration. The reproduceability of the machine was not very good and was significantly changed by alterations in the anode-cathode distance, beam foil thickness, beam foil material, misallignment of the cathode, location of carbon calorimeter block, and impedance variations during the beam discharge.

The two basic configurations utilized for experimentation are given below. The figure on the left is the plasma heating configuration and the figure on the right is the collective ion acceleration configuration.

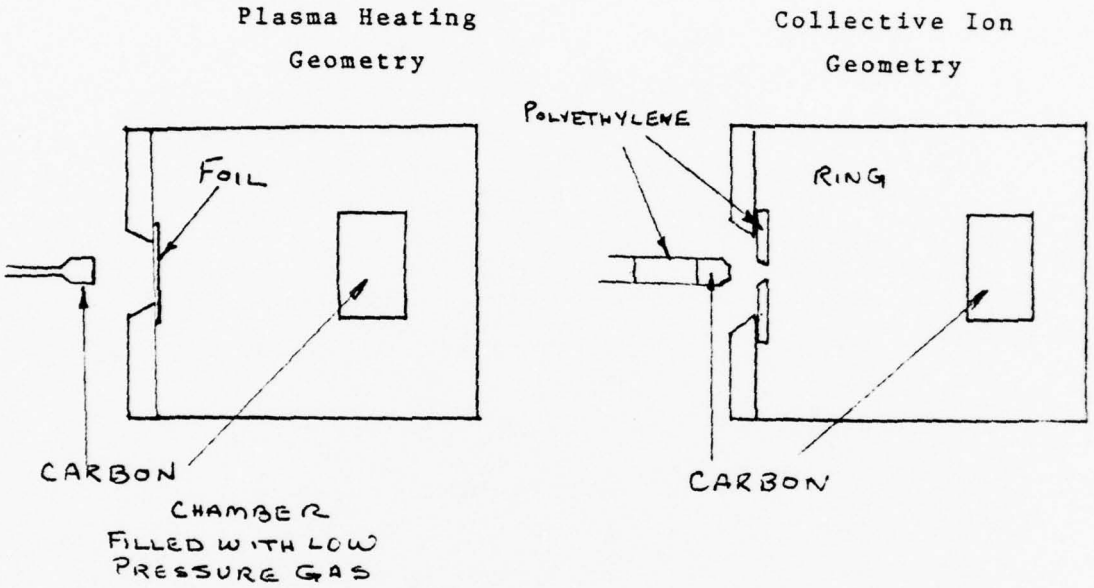

During the discharge of the machine, a large X-ray yield is observed due to the high energy electrons colliding with the sides of the target chamber. Thus a large Bremsstrahlung radiation peak is detected by the time-of-flight detectors. This pulse, which is an accumulation of X-rays from the discharge, acts as the trigger pulse for the time-of-flight detectors. Because of an impedance mismatch, the machine oscillates and discharges several times and these discharges can be identified by periodic Bremsstrahlung bursts following the initial discharge. Depending on which configuration is utilized, as many as three

X-ray bursts are detected approximately 200 nanoseconds apart. The second and third bursts can be eliminated from detection by the t-o-f detectors by using about one-fourth inch of lead as a shield. The initial discharge is easily detected even with this amount of lead since the initial burst of X-rays has some very high energy components where the second and third bursts are much weaker in voltage and therefore generate "softer" X-rays.

The neutral gas configuration gave rise to stronger multiple bursts than the collective ion acceleration configuration. The reason for the difference apparently rests with the impedance match or mismatch of the Brumlein^{column} and the target configurations.

NEUTRON PRODUCTION

Neutron production occurs with both experimental configurations. However, the collective ion acceleration configuration produces approximately 10^3 more neutrons than the plasma heating configuration. The possible mechanisms for neutron production are discussed below:

a) Photoneutron Mechanism. In this case γ-rays or X-rays interact with nuclei and cause neutron ejection. In order to have this reaction occur requires photons with energies around 8 or 9 Mev. However, in the lighter elements like deuterium only 2.226Mev is required. Thus with the large Bremsstrahlung radiation with a maximum photon energy of 6Mev it is possible to observe photo-disintegration of the deuteron in the plasma heating configuration. The reaction is given below:

$$_1H^2 + \gamma \rightarrow n + {}_1H^1 - 2.226\text{Mev}.$$

The resulting neutron and proton share the remaining energy. That is:

Energy of incident photon - 2.226Mev = Sum of neutron and proton kinetic energy.

In this reaction neutrons should not be observed with an energy of over 4Mev since the maximum electron energy is 6Mev. Therefore these neutrons will only contribute to the high energy neutron spectrum.

Even though the Bremsstrahlung yield is large, the low cross-section (1.5 millibarns) for photoneutron production along with the low deuterium pressure (1.2 torr) makes the probability of occurrence of this reaction quite small. This is confirmed by experiments with and without deuterium gas in the target chamber.

b) Fusion Mechanism. Heated deuterium nuclei that collide inside the gas filled chamber give rise to neutrons. The deuterium nuclei (Deuterons) collide with other deuterium nuclei and undergo the following nuclear transformation:

$$_1H^2 + {}_1H^2 \rightarrow n + H_e{}^3 + 3.24\text{Mev}.$$

The two particles produced in the interaction are the neutron and a "light" helium nucleus. They share 3.24Mev of kinetic energy and since the neutron is the lighter of the two particles it gets most of the energy. About 2.54 Mev is acquired by the neutron and 800 Kev by the helium-3 nucleus. The neutron production should be isotropic and monoenergetic because it has a positive Q value (Q = 3.24 Mev) and because of the random motion of the heated deuterium nuclei (1×10^6 $\dot{K} \simeq 100$ Kev). Thus. if fusion is occurring in the gas cell, a symmetrically generated and monoenergetic neutron source should be detected.

c) Collective Acceleration of Deuterons. Collective acceleration of deuterons inside the gas chamber can also cause neutron production by having a high energy deuteron collide with a stationary deuteron. The equation that governs, the interaction is given above, but in this case the neutron spectrum will not be symmetric. It will have an asymmetric energy and abundance distribution. Both of the distributions should be strongly peaked in the forward direction.

A careful analysis of the neutron distribution should reveal the extent of fusion versus collision neutrons in beam heating experimentation. Our studies, due to detection inabilities and machine irregularities, do not show any correlation with the type of gas, its pressure, or the resulting neutron flux. If the above reaction is contributing to the neutron flux produced the yield must be quite low (less than 10^7 neutrons).

d) Deuteron - Carbon Mechanism. The collective acceleration of deuterium with a resulting collision with the carbon calorimeter block at the back of the chamber or a collision with the metal walls of the chamber can also give rise to neutrons. The reactions that can occur are:

$$_1H^2 + C^{12} \rightarrow n + N^{13} \qquad Q = -.281 \text{ Mev}$$

$$_1H^2 + C^{13} \rightarrow n + N^{14} \qquad Q = +5.32 \text{ Mev}$$

$$_1H^2 + Fe^{54} \rightarrow n + Co^{55} \qquad Q = +2.8 \text{ Mev}$$

$$_1H^2 + Fe^{56} \rightarrow {}_1n + Co^{57} \qquad Q = 4.06 \text{ Mev}$$

$$_1H^2 + Fe^{56} \rightarrow 2n + Co^{56} \qquad Q = -7.6 \text{ Mev}$$

$$_1H^2 + AL^{27} \rightarrow n + Si^{28} \qquad Q = +9.35 \text{ Mev}$$

The C^{12} (d,n) N^{13} reaction has a low negative Q value thus it is a primary source of neutrons. The total cross section for this reaction is approximately 120 millibarns at 3 Mev and is reasonably constant over a wide energy interval. All collectively accelerated deuterium nuclei colliding in the carbon block could undergo this reaction. The contribution of the C^{13} (d,n) N^{14} reaction is only 5% of the C^{13} (d,n) N^{14} reaction at 3 Mev, thus the yield should not be a significant contributor to the resulting neutron flux.

Reactions of the deuterium with the iron or aluminum in the chamber walls offer other sources of neutrons. Collectively accelerated deuterons colliding with the walls generate neutrons by the reactions given above. These reactions give rise to some long half-life daughter nuclei which can be detected. Extensive experiments with the residual radioactivity have not been carried out but the chambers are radioactive with intensities of several mr/hour after several weeks. This activity is a combination of activated iron, carbon and other materials in the stainless or aluminum walls. (Both aluminum and stainless steel vessels were used). The half-life values from some of the produced daughter isotopes are listed below:

Isotopes	Half-Life	Isotopes	Half-Life
$_7N^{12}$	.011 Sec	Co^{55}	8 hours
$_7N^{13}$	9.96 Min	Co^{56}	77.3 days
Co^{54}	.194 Sec	Co^{57}	270 days
		Si^{28}	Stable

e) Window Ionization Mechanism. During the plasma heating experimentation, two different windows were used to isolate the (gas) chamber from the vacuum system. The metal foils used were various thicknesses of titanium (1 mil, 3 mil, 12 mil). Tests with kapton sheets in place of the metal foils were attempted. However the severe flexing of the sheets and the resulting electric field variation required the use of the more rigid metal foils.

Each firing of the machine would destroy the kapton window and thus generate a number of additional reaction which produce neutrons. For example, the kapton sheet would vaporize and the ionization from it would give rise to a number of protons which could be collectively accelerated and cause a number of (p,n) reactions in the carbon calorimeter block or in the walls of the chamber. When titanium foils were used, it wasn't clear if the titanium foils ionize prior to discharge due to the pre-pulse voltage or if pin holes in the foils give rise to prepulse ionization and ultimately, collective acceleration.

Experimentation reveals that a large number of neutrons ($\sim 10^9$) are produced using kapton sheet and no gap between the calorimeter block and the kapton. Also, tests with the titanium foils and no gap reveal the same results but with fewer neutrons produced (factor of five lower). The tabulation at the end of the report along with the interpretation summarize the beam plasma results.

COLLECTIVE ION CONFIGURATION

In our collective ion acceleration work, the beam orifice was made of polyethylene with a natural abundance of deuterium. The resulting plasma generated around the orifice was composed of hydrogen ions, carbon ions, and some deuterium ions. Upon discharge, the resulting collective acceleration produced (p,xn) and (d,xn) reactions. The (p,xn) reactions will be discussed in this section for reactions with carbon and stainless steel. (Aluminum chambers were not used).

The collective acceleration of protons with resulting collisions with the carbon calorimeter block or the walls of the stainless steel vacuum chamber gave rise to the following reactions.

$$_1H^1 + {}_6C^{12} \rightarrow n + {}_7N^{12} \qquad Q = -18.4 \text{ Mev}$$

$$_1H^1 + {}_6C^{13} \rightarrow n + {}_7N^{13} \qquad Q = 3.0 \text{ Mev}$$

$$_1H^1 + Fe^{54} \rightarrow n + Co^{54} \qquad Q = -9.6 \text{ Mev}$$

$$_1H^1 + Fe^{56} \rightarrow 2n + Co^{55} \qquad Q = -15 \text{ Mev}$$

$$_1H^1 + Fe^{56} \rightarrow n + Co^{56} \qquad Q = -5.38 \text{ Mev}$$

The neutron spectrum resulting from collective ion experimentation shows a very high energy neutron yield at 150° to the beam direction. This can only result by fast proton and deuteron collisions with carbon and the chamber walls. The neutron energies appear to exceed 30 Mev in the back angle of 150° which would correspond to neutrons of over 40 Mev in the

forward direction. The proton needed to generate these neutrons would have energies of over 40 Mev. A careful study of the t-o-f neutron monitors shows an intense neutron spectrum in the 14-40 region with the intensity of neutrons between 14 and 4 Mev to be small and very few below 4 Mev. The following figure gives a typical neutron t-o-f spectrum with a carbon calorimeter block to stop the protons. When a deuterized polyethylene block was used rather than carbon, a strong neutron enhancement results in the 2 to 3 Mev region.

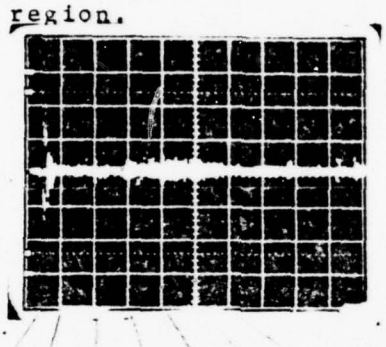

Vertical Scale-20mv /cm

Horizontal scale - 200 ns/cm

100 30 15 7 5 3

X-ray from discharge

mev mev mev mev mev mev

Neutron Energy

DATA: Carbon block calorimeter in chamber
Polyethylene ring geometry
June 20, 1978 Third Shot
Flight path 100 ft at 150°

Until a careful study is carried out with various chambers and targets, it will be very difficult to analyse the origin of all the neutrons. However, if the calorimeter block is moved close to the polyethylene ring, it can be assumed that most of the collectively accelerated ions will collide with it and it is the major source of neutrons. Studies have been done to demonstrate the collimation of the ion beam. Until such time as the ion beam profile is obtained, the number of ions hitting the walls and

causing (p,xn) and (d,n) reactions cannot be approximated. Toward the end of the report are a number of oscilliscope photographs of the t-o-f spectrum along with the associated time to energy conversion.

NEUTRON DETECTION

Neutron detection was accomplished using several detectors. The fast neutrons were detected directly with a time-of-flight (t-o-f) system using a NE102 plastic scintillator optically coupled to a 56 AVP photomultiplier tube. The system is capable of resolving nanosecond events and was used to measure the neutron arrival time following a discharge of the PR1590. The flight paths used were: 160 feet at 150° to the beam direction and 100 feet at approximately 90° to the beam direction. The detector at 160 feet and 150° was used to determine the arrival time the energy of the neutron was obtained. The following equation was used to convert from travel time to neutron energy.

$$t = \frac{72.3d}{E}$$

t = Neutron travel time in nanosecond
d = Neutron flight path in meters
E = Neutron energy in Mev.

The time of travel is obtained by measuring the duration between the initial X-ray burst on the oscilloscope and the neutron pulse on the same oscilloscope trace. To this time interval must be added the travel time for the X-rays. By using a long flight path and 150°, the neutron arrival after the initial X-ray burst was sufficiently later to allow visual differentiation. Since neutrons manufactured in the back angles are traveling slower than their counterparts in the forward direction, it is quite advantageous to use back angle measurements and then by kinematics calculate the neutron energies in the forward direction.

The neutron t-o-f detector at 90^{o} to the beam has a rather clear view of the neutron flux without significant attenuation of the low energy component. Thus the time spectrum can be converted to a true energy spectrum. Knowing the number of neutrons made in a particular energy region is thus obtained and can be utilized to calibrate the thermal neutron counter (silver) used in the test cell. The fact that high energy neutrons can be immediately analysed, allows for a rapid feed-back as to efficiency of the collective ion effect and its yield. With this information, optimization changes can be made and results quickly obtained. A drawing of the experimental configuration is given for clarification.

NEUTRON MONITORING SYSTEM

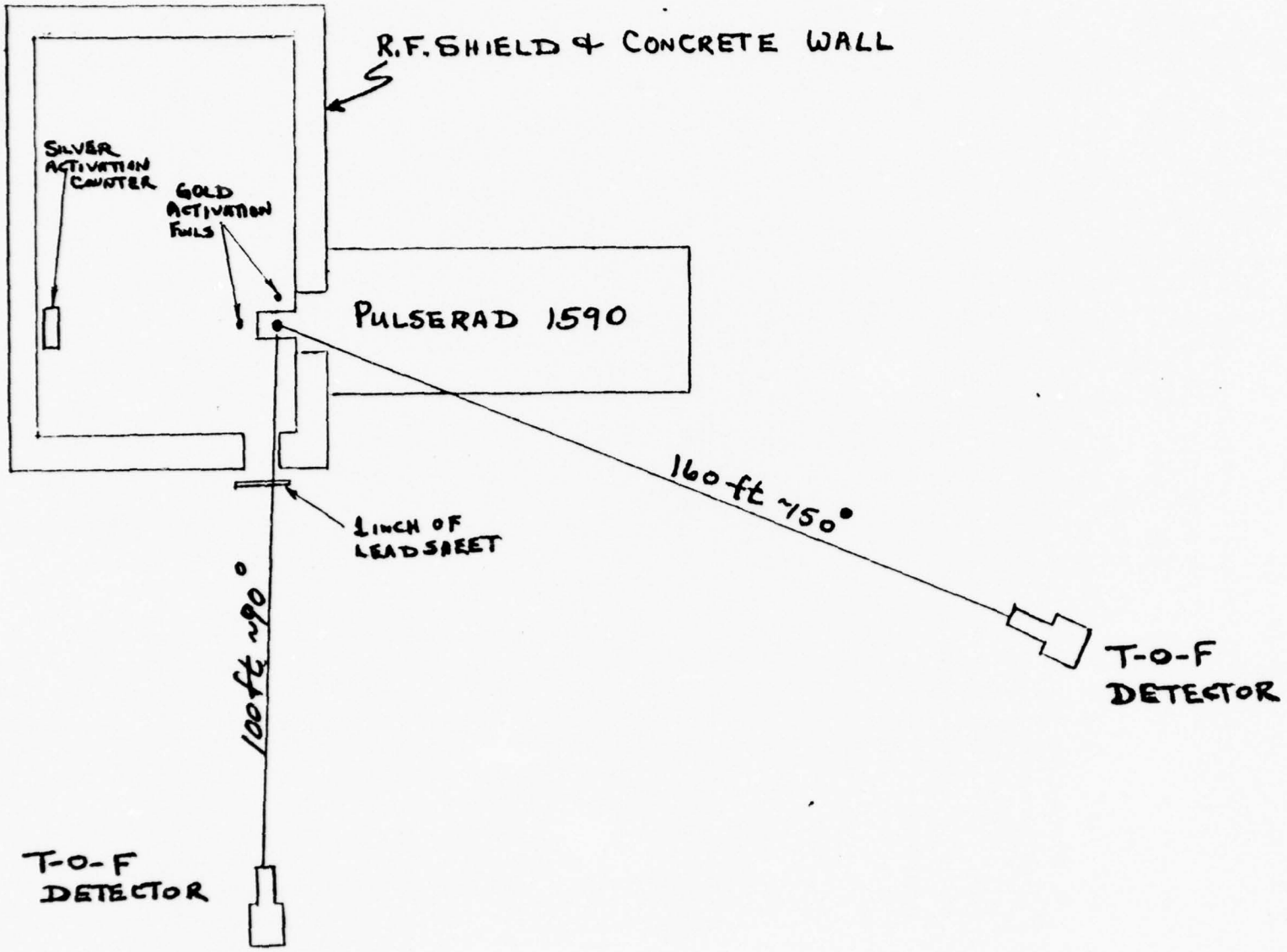

The silver activation system was built by Los Alamos Scientific Laboratory in the 1960's and it utilizies thin walled geiger tubes wrapped with silver foil and housed in a 12"x12"x6" block of polyethylene. The polyethylene is responsible for slowing down fast neutrons. When thermalized, the silver captures them. The resulting beta decay of the silver is then detected by the geiger tubes. The devices had been calibrated when manufactured using several neutron sources available at the time. When we calibrated them using a standard pulse neutron source, the calibration was confirmed. However, when these detectors are used in a closed and concrete walled room (test cell) allowances have to be made for thermal neutrons and epithermal neutrons inside the room that are not part of the direct flux but components of the scattered flux. To add a further complication, this scattered flux is not isotropic due to the large hole in the shielding for the machine installation. Experimental testing confirmed that the thermal neutrons detected by the counter were primarily neutrons thermalized outside the detector but later captured by the silver as they traveled through the detector. It was found that these detected "background" thermal neutrons were as high as seven times the number directly detected by the counter. This result was obtained when the detector was against the concrete wall of the test cell opposite the target chamber. To eliminate this problem the counter was clad with cadmium sheet of thickness .030 inches. This eliminated thermal neutrons from the outside. However, the epithermal neutrons could still enter, slow down and be detected. This counting contribution had to be determined by inverse square counting rates. It was found that if the neutron detector (silver counter) was mounted against the target end of the machine that only a few epithermal neutron were

counted (∿15%). However, the epithermal contribution was about 85% when the detector was placed against the wall on the opposite side of the test cell. Graphs showing the epithermal enhancement of the count rate are given in the back of the report. The above information is quite valuable in knowing how to interpret the silver activation result. Also, it is quite important to know the energy of the neutrons generated by the machine. The Los Alamos equations for calculating neutron yields from a discharge machine and using the silver activation counters are given below:

$$\frac{\text{14 Mev Neutron}}{\text{Neutrons Produced}} = 60(5.0 + d)^2(N)$$

$$\frac{\text{2.5 Mev Neutron}}{\text{Neutrons Produced}} = 30(5.3 + d)^2(N)$$

d = Distance in inches from neutrons source to face of polyethylene block

N = Number of counts detected during the first minute after activation.

As can be seen, the neutron yield calculation is quite sensitive to neutron energy. The t-o-f system gave the neutron energy spectrum which was used with the silver activation counter to ultimately arrive at a total neutron production per discharge of the PR1590. A typical result from the silver activation counter is given on the next page.

The silver activation monitors were to be operated with four geiger tubes in each polyethylene block. The beta particle from the silver decay would penetrate the thin walled tube and thus a pulse was registered by the counter. In order to keep the count rate to manageable levels and save as many tubes as

AUGUST 1, 1978
SHOT #2
DETECTOR 39 INCHES AWAY
3 MIL TITANIUM FOIL
VACUUM & CARBON IN CHAMBER

SILVER ACTIVATION MEASUREMENT FOR PLASMA HEATING GEOMETRY.

FIRST 1 MINUTE COUNT = 69806/2 TUBES

NEUTRON YIELD

AVE. NEUT. ENERGY ~ 2.5 MeV (ISOTROPIC)
DISTANCE FROM SOURCE $d = 39$ INCHES
EPITHERMAL CORRECTION $\epsilon = .20$

$$N = 30(5.3+d)^2 \left(\frac{\text{1 MINUTE COUNT}}{\text{TUBE}}\right)(4 \text{ TUBES})(1-\epsilon)$$

$$N = 6.6 \times 10^9 \text{ NEUTRONS}$$

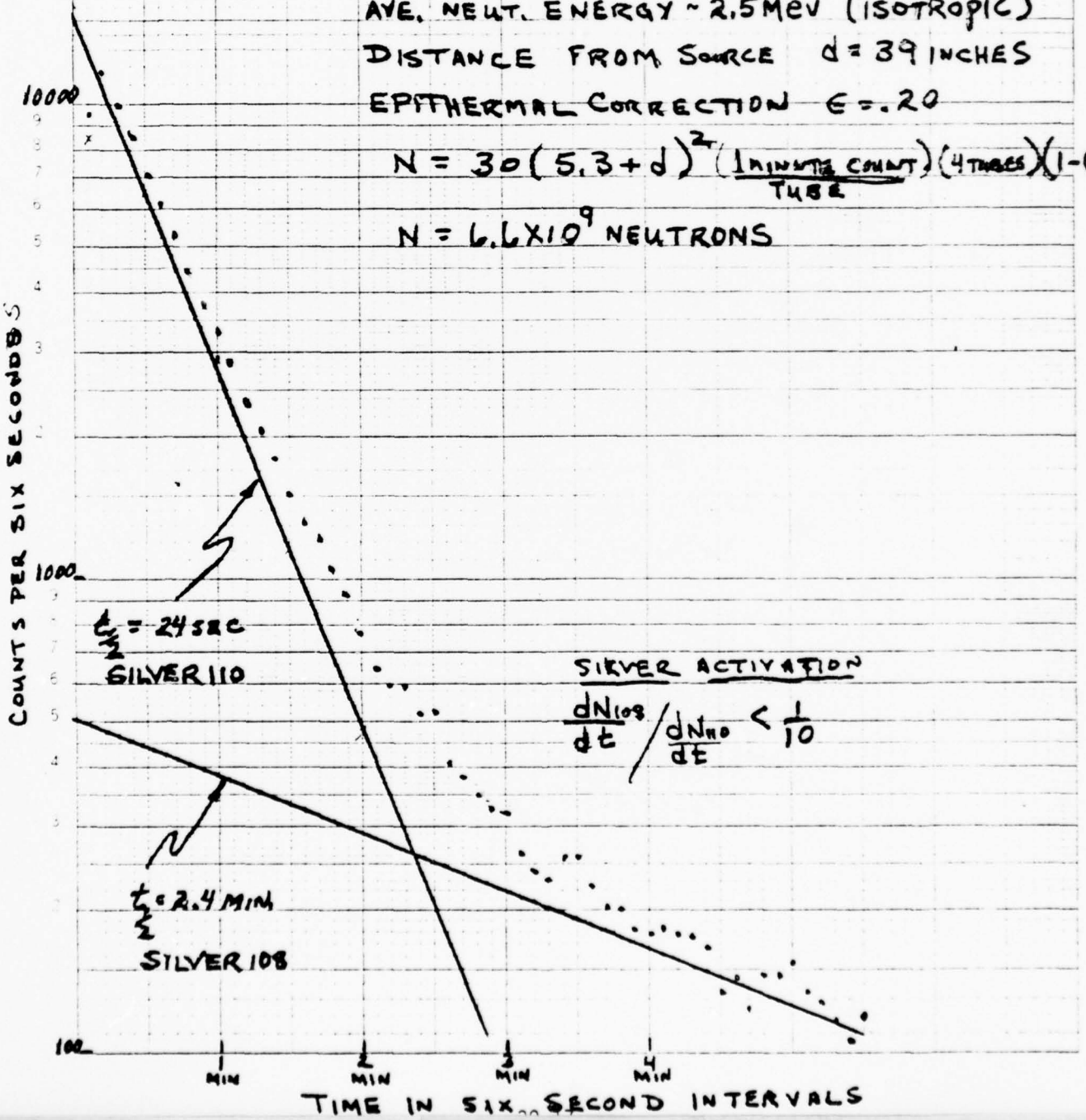

possible, only two tubes (rather than four) were used in each polyethylene block. Thus the calibration that we obtained had to be corrected for the number of tubes utilized. To actually perform a calibration of neutron yield from the decay curve given above the following information has to be determined:

a) Integrated count rate for 1 minute
b) Epithermal background correction factor (B)
c) Neutron spectrum information
d) Number of tubes used in the detector
e) Distance of monitor from target and walls and the forward to backward neutron ratio.

In our experiments two tubes were used. The total integrated count for the first minute was obtained by adding the number of counts obtained in the first 10 intervals of six seconds each and then multiplying by two. The epithermal background is obtained by knowing the location of the detector in the room and using the chart in the back of this report. The time-of-flight system gives the number of neutrons within any energy range by using the time to energy conversion in the back of this report. Thus, the equation for neutron yield becomes:

$$\text{Neutrons Produced} = \begin{bmatrix} 120 \\ \text{to} \\ 30 \end{bmatrix} (5.0 \times d)^2 (4) \begin{bmatrix} \text{counts per tube} \\ \text{for first minute} \end{bmatrix} \begin{bmatrix} \text{front to} \\ \text{back} \\ \text{correction} \end{bmatrix} (1 - e)$$

In order to use the above equation to calculate the neutron yield in the previous graph, several approximations have to be made. Assume the neutrons made in this experiment are between 2.5 and 14 Mev. This would necessitate using a neutron correction factor of about 45 rather than 30 or 60. The distance from the source to the detector is 30 inches. Knowing this and referring to the epithermal graph, the correction

factor (ε) can be obtained. The factor of 4 in the equation is to correct for the use of four tubes in the original calibration. Normally this result will have to be corrected for direction since it is thought that the yield in the forward direction could be as high as 10 times that in the back angles. Thus, the above result would be a maximum value for neutron production. The higher the energy of the neutrons the more forward the trajectory. For beam plasma heating the trajector should be more isotropic than with the collective ion acceleration geometry.

The gold activation (n,4n) reaction was used to measure fast neutron isotropy. The gold foils which have a threshold of 23 Mev were placed around the target at various angles to confirm the forward to backward high energy neutron yield when using the collective ion acceleration geometry. Monitoring the activation of the gold foils using a GeLi detector was used to confirm the (n,4n) reaction The foil intensity variations served as a measure of the neutron anisotropy. The following figure gives the nuclear decay associated with the gold activation.

ACTIVATION ANALYSIS FOR

NEUTRON ENERGY DISCRIMINATION

REACTION: $Au^{197}(n, 3n)Au^{195*}$ — THRESHOLD ENERGY 14.8 MeV

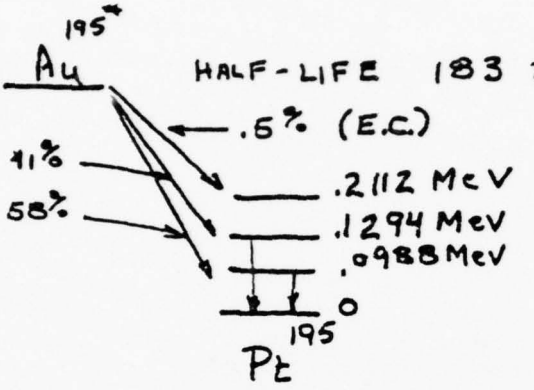

γ-RAYS FROM Pt^{195}

.097 MeV	10%
.129 MeV	1%

REACTION: $Au^{197}(n, 4n)Au^{194*}$ — THRESHOLD ENERGY 23.2 MeV

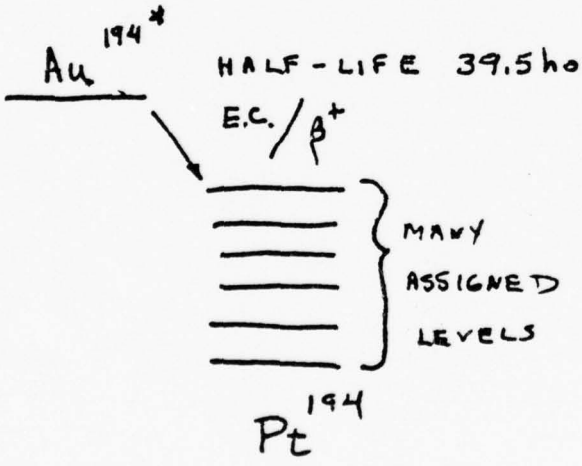

γ-RAYS FROM Pt^{194}

.294 MeV	12%
.328 MeV	68%
1.469 MeV	8%
1.596 MeV	3%
1.887 MeV	4%
2.044 MeV	4%

NEUTRON PRODUCTION

RESULTS

Neutron production statistics in the plasma heating configuration generate many more questions than they answer. A careful study of the plasma heating silver activation data chart at the end of the report will substantiate the above statement. As can be seen, the neutron production does not appear to be dependent on the chamber material, gas in the chamber or the pressure on the chamber, however, there may be a correction with the type of window used in the chamber. That is kapton or titanium. The kapton seemed to generate the largest neutron yields but sufficient data was not collected to confirm this hypothesis.

It is thought that an interaction between the cathode and the window during the prepulse and ultimate discharge is the primary neutron source. It is believed that a simple collective acceleration or simple acceleration of ions in the A-K gap that later collide with the cathode and its plated titanium surface generate the neutrons by (p,n) reactions:

$$Ti^{51}(p,n)V^{51} \qquad Q = +1.68 \text{ Mev}$$

Since V^{51} is stable it is difficult to determine the extent of this contribution. However, it has been found that most often the neutron yield is the largest when the energy deposited in the calorimeter block (carbon) is the smallest and when the chamber gas is not significantly excited.

The fact that large neutron yields result when kapton is used is probably due to the collective acceleration of the ions on the kapton during the initial discharge or during the two secondary discharges.

The time-of-flight results for the plasma heating experiments substantiate neutron productions in the 10^8 to 10^9 region. The spectrum that results also indicates that the energies are in the 1 to 5 Mev region.

Unfortunately the collective ion acceleration work was not completed when this report was written. However, the test results substantiated the manufacture of high energy neutrons above 30 Mev. The following figures illustrate some of the preliminary results.

PLASMA HEATING CONFIGURATION

Time - Of - Flight

Neutron Data

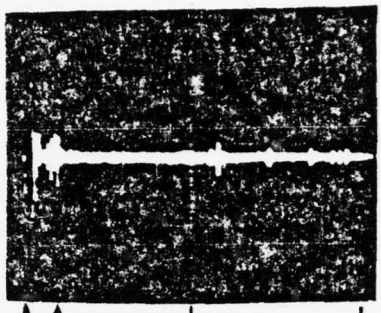

Vertical Scale - 50mv/cm
Horizintal scale - 500ns/cm

Data: Vacuum in chamber, titanium foil
June 27, 1978 shot #2
Flight path 160ft at 150°

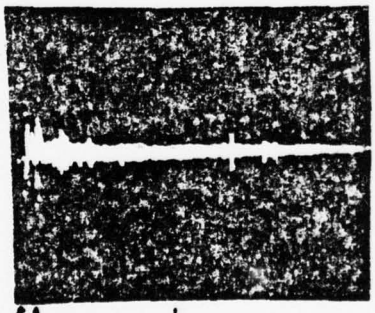

Vertical scale - 50mv/cm
Horizontal scale - 500 ms /cm

Data: .4 Torr deuterium in chamber, titanium foil.
June 28, 1978 shot #1
Flight path 160 ft at 150°

Calculation of Neutron Energy vs. Lab Angle of Scatter

$$Q = E_n\left[1 + \frac{M_N}{M_2}\right] - E_i\left[1 - \frac{M_i'}{M_2}\right] - \frac{2\sqrt{M_i E_i M_N E_N}}{M_2}\cos\theta$$

E_i, M_i' = Energy and mass of incident particle

E_n, M_n = Energy and mass of neutron

E_2, M_2 = Energy and mass of residual nucleus

θ = angle neutron makes with beam direction.

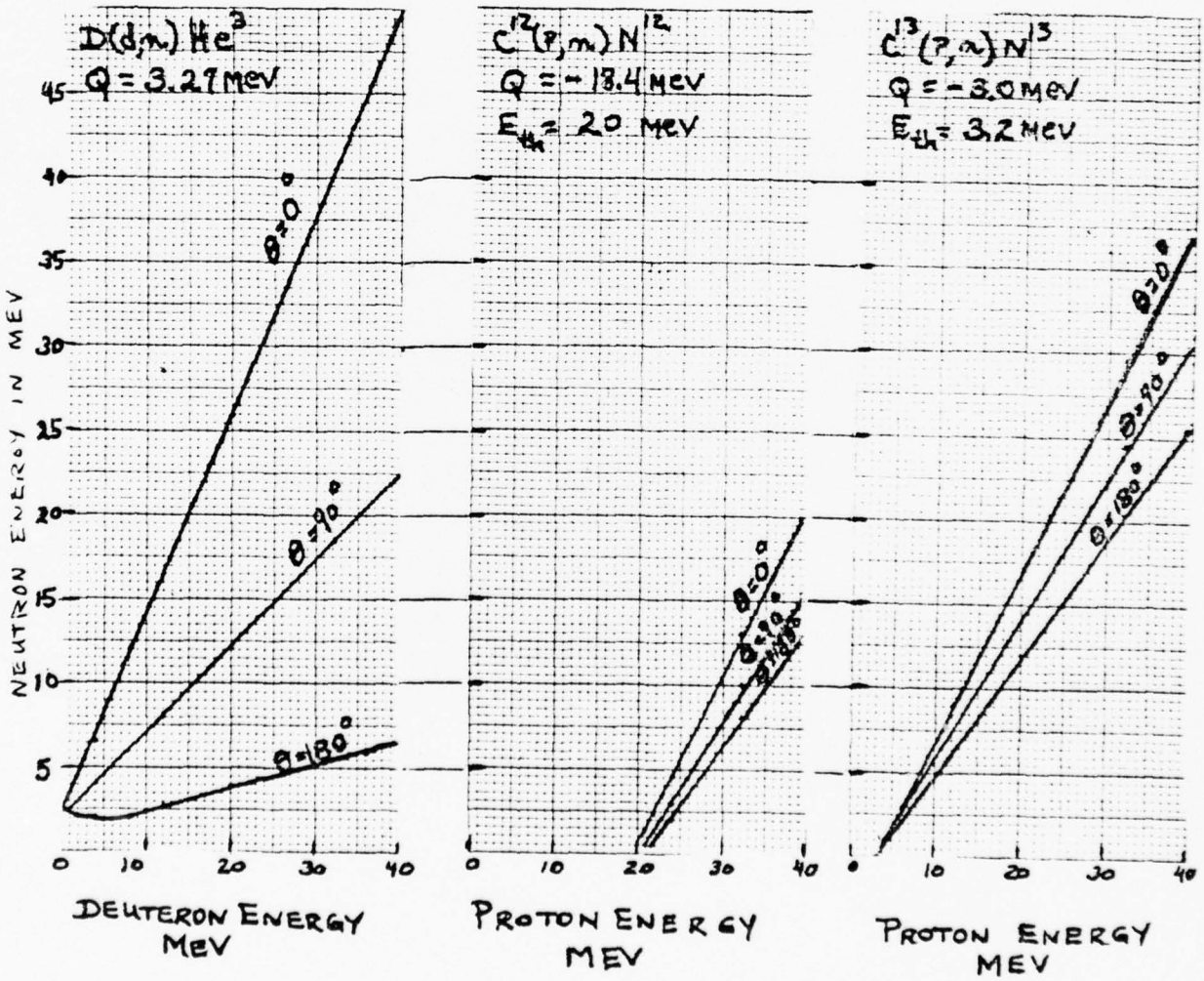

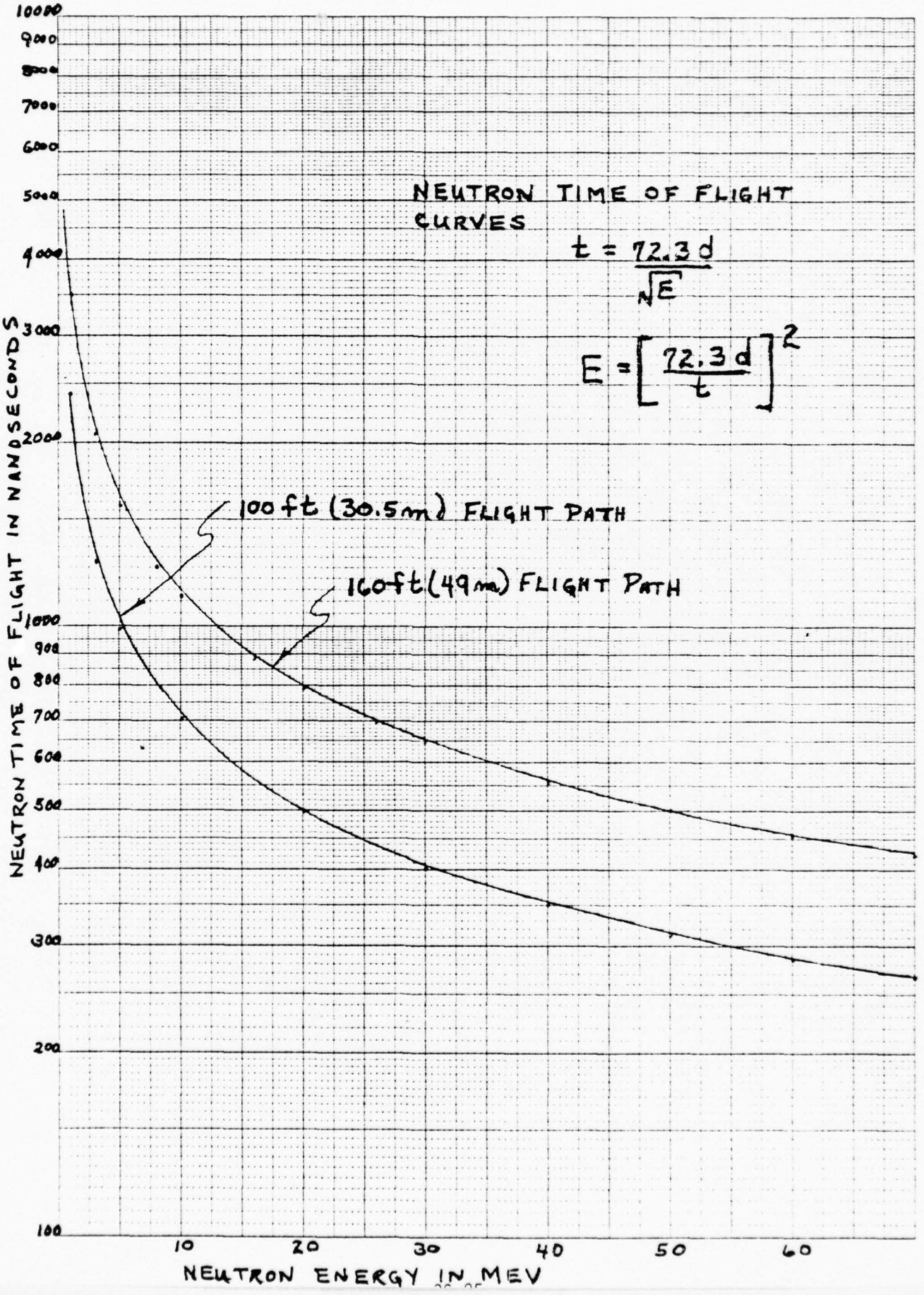
NEUTRON TIME OF FLIGHT CURVES
$t = \frac{72.3\,d}{\sqrt{E}}$
$E = \left[\frac{72.3\,d}{t}\right]^2$
100 ft (30.5 m) FLIGHT PATH
160 ft (49 m) FLIGHT PATH
NEUTRON TIME OF FLIGHT IN NANOSECONDS
NEUTRON ENERGY IN MEV
10000
9000
8000
7000
6000
5000
4000
3000
2000
1000
900
800
700
600
500
400
300
200
100
10
20
30
40
50
60

46 5130

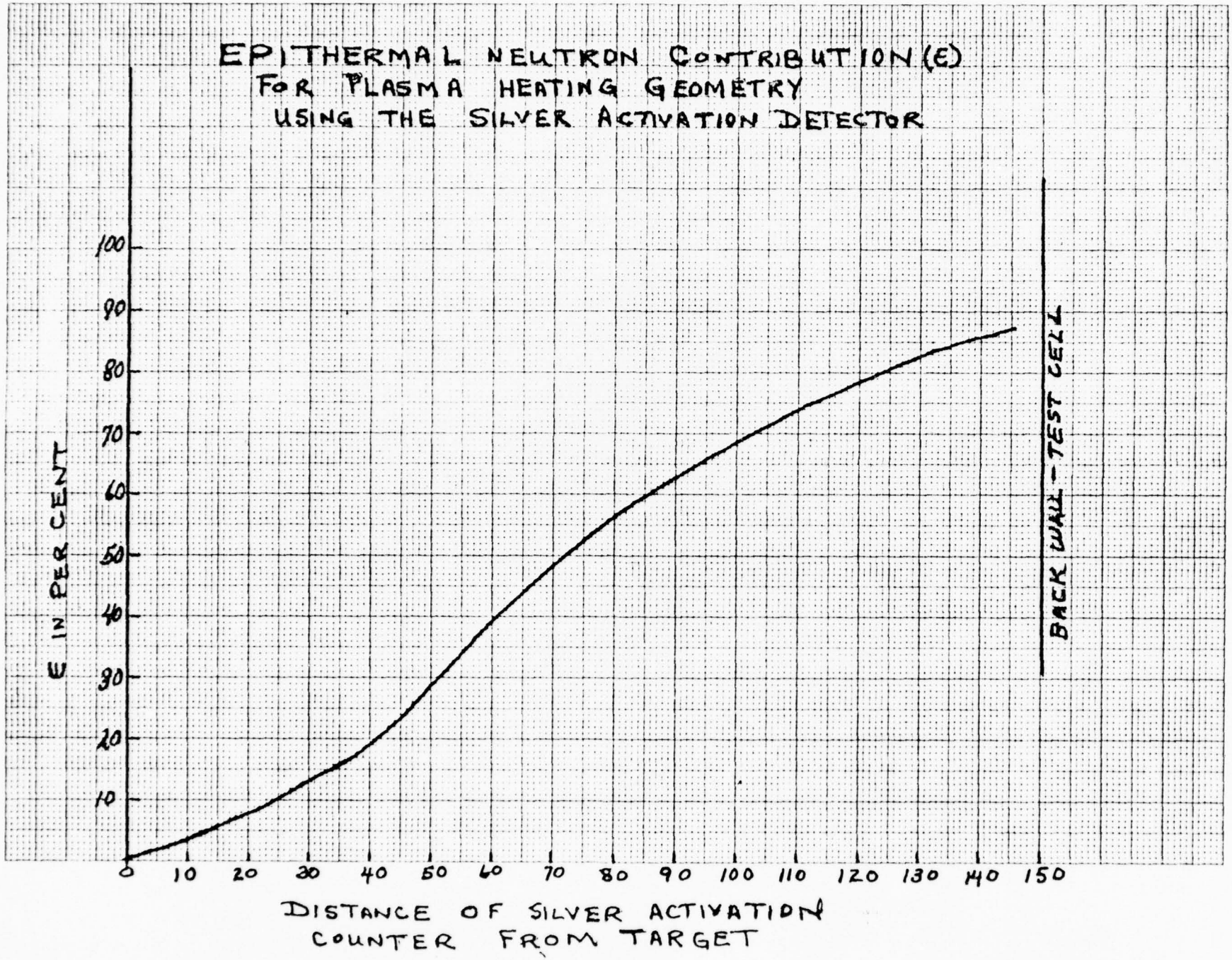
EPITHERMAL NEUTRON CONTRIBUTION (E)
FOR PLASMA HEATING GEOMETRY
USING THE SILVER ACTIVATION DETECTOR
E IN PER CENT
100
90
80
70
60
50
40
30
20
10
0
10
20
30
40
50
60
70
80
90
100
110
120
130
140
150
BACK WALL - TEST CELL
DISTANCE OF SILVER ACTIVATION
COUNTER FROM TARGET

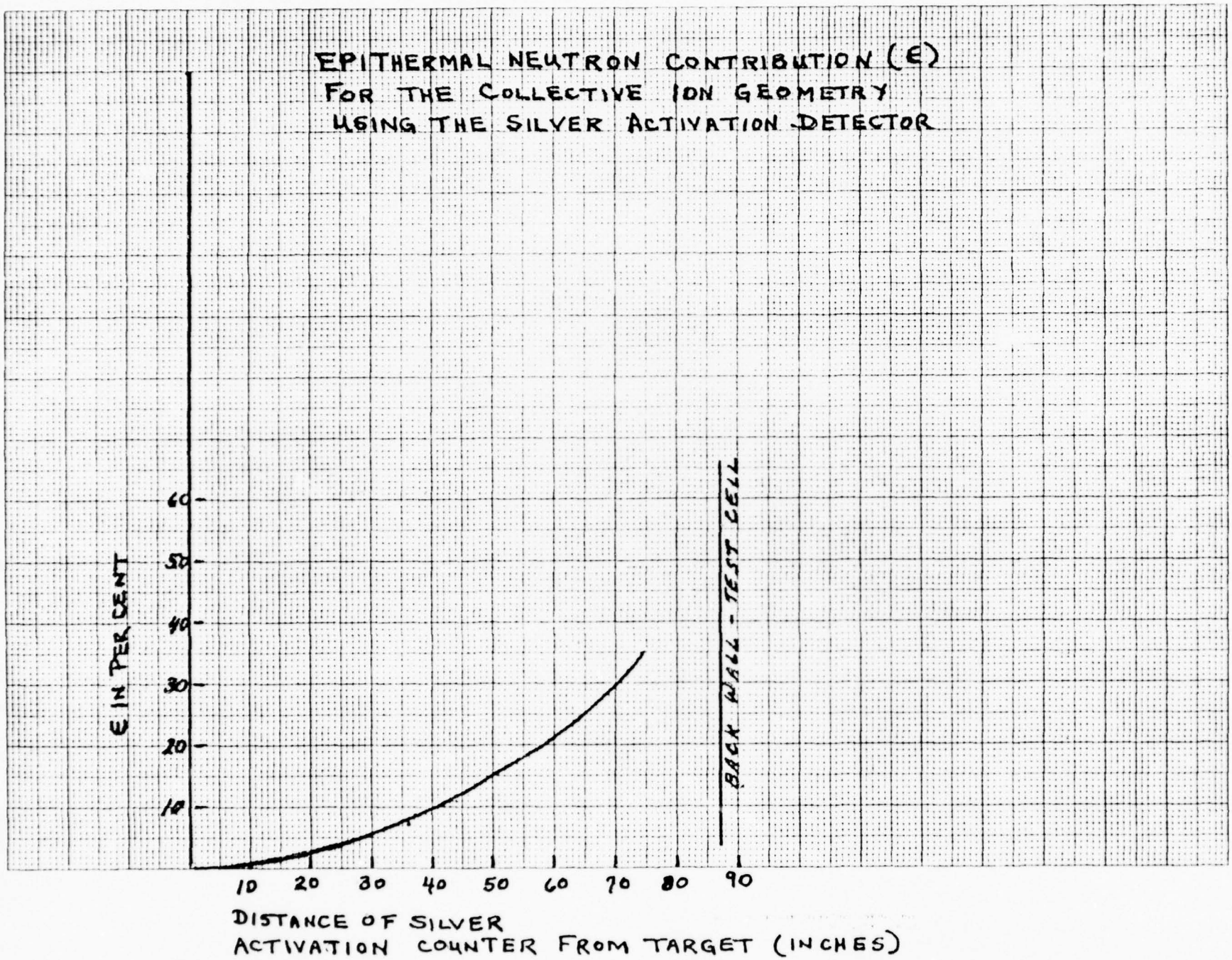
EPITHERMAL NEUTRON CONTRIBUTION (ε)
FOR THE COLLECTIVE ION GEOMETRY
USING THE SILVER ACTIVATION DETECTOR
ε IN PER CENT
60
50
40
30
20
10
BACK WALL - TEST CELL
10
20
30
40
50
60
70
80
90
DISTANCE OF SILVER
ACTIVATION COUNTER FROM TARGET (INCHES)

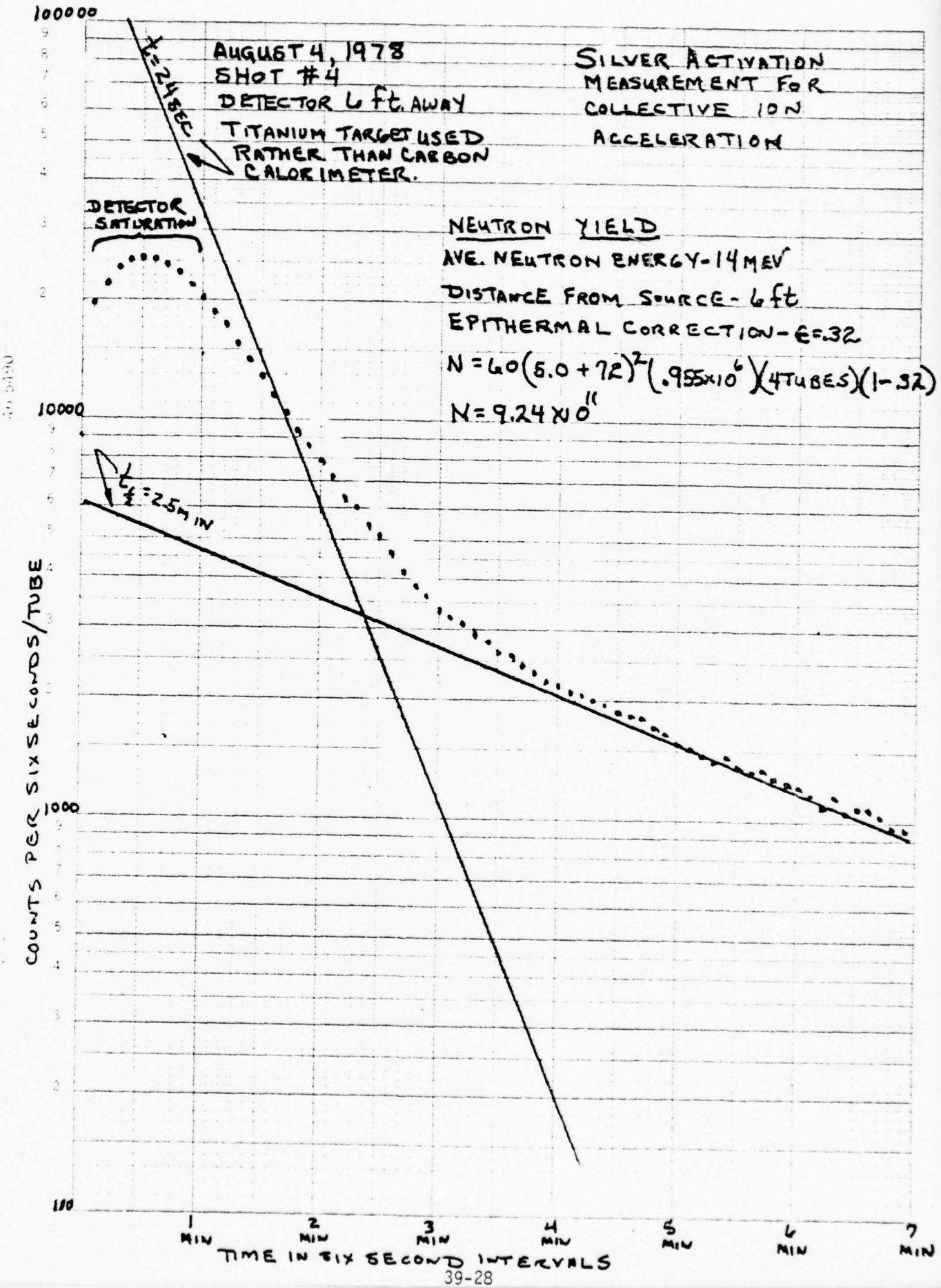
AUGUST 4, 1978
SHOT #4
DETECTOR 6 ft. AWAY
TITANIUM TARGET USED RATHER THAN CARBON CALORIMETER.
SILVER ACTIVATION MEASUREMENT FOR COLLECTIVE ION ACCELERATION
NEUTRON YIELD
AVE. NEUTRON ENERGY-14 MEV
DISTANCE FROM SOURCE-6 ft
EPITHERMAL CORRECTION-ε=.32
N = 60(5.0 + 72)²(.955×10⁶)(4 TUBES)(1-.32)
N = 9.24 X 10¹¹
t½ = 24 SEC
t½ = 2.5 MIN
DETECTOR SATURATION
COUNTS PER SIX SECONDS/TUBE
100000
10000
1000
100
1 MIN
2 MIN
3 MIN
4 MIN
5 MIN
6 MIN
7 MIN
TIME IN SIX SECOND INTERVALS

PLASMA HEATING

SILVER ACTIVATION DATA

DAY & SHOT	GAS & PRESSURE (TORR)	FOIL	SILVER DETECTOR DISTANCE (INCHES)	CARBON BLOCK USED	CHAMBER MATERIAL	FIRST MINUTE COUNTS	NEUTRON YIELD
7-14	DEUT 1.2	KAPTON	21	YES	S.S.	77000	2.6×10^9
7-17#1	DEUT 1.2	KAPTON	21	YES	S.S.	199600	6.7×10^9
7-17#2	DEUT 1.2	Ti 12MIL	21	YES	S.S.	42400	1.4×10^9
7-17#3	DEUT 1.2	Ti 3MIL	21	YES	S.S.	21500	$.73 \times 10^9$
7-17#4	DEUT 1.2	Ti 1MIL	21	YES	S.S.	41300	1.4×10^9
7-18#1	DEUT 1.2	Ti 1MIL	-	-	S.S.	1600	SHORT
7-19#1	DEUT 1.2	Ti 3MIL	47	NO-POLY	AL	42000	5.2×10^9
7-19#2	DEUT 1.2	Ti 3MIL	47	NO-AL	AL	24000	3.0×10^9
7-19#3	DEUT 1.2	Ti 3MIL	94	NO-AL	AL	19900	4.1×10^9
7-19#4	DEUT 1.2	Ti 3MIL	12	NO-AL	AL	204200	8.5×10^9
7-20	DEUT 1.2	Ti 3MIL	47	NO-AL	AL	4900	$.60 \times 10^9$
7-20	DEUT 1.2	Ti 3MIL	47	NO-AL	AL	61800	7.5×10^9
7-21#1	DEUT 1.2	Ti 3MIL	47	NO-AL	AL	35300	4.3×10^9
7-24#1	DEUT 1.2	Ti 3MIL	47	YES	AL	13850	1.7×10^9
7-24#2	DEUT 1.2	Ti 3MIL	47	YES	AL	42500	5.2×10^9
7-24#3	DEUT 1.2	Ti 3MIL	47	YES	AL	65500	8.1×10^9
7-24#4	AIR 1.0	Ti 3MIL	47	YES	AL	42850	5.3×10^9
7-25#1	AIR 1.0	Ti 3MIL	47	YES	AL	102610	13.0×10^9
7-25#2	AIR 1.0	Ti 3MIL	47	YES	AL	125300	15.0×10^9
7-27#1	AIR 1.0	Ti 3MIL	78	YES	AL	30400	5.7×10^9
7-27#2	AIR 10.0	Ti 3MIL	78	YES	AL	20000	3.7×10^9
7-27#3	AIR 10.0	Ti 3MIL	78	YES	AL	5100	$.96 \times 10^9$
7-27#4	AIR 10.0	Ti 3MIL	78	YES	AL	23300	4.4×10^9
7-27#5	AIR 10.0	Ti 3MIL	78	YES	AL	9380	1.7×10^9
7-27#6	AIR 10.0	Ti 3MIL	112	YES	AL	28600	6.1×10^9
7-28#1	AIR 10.0	Ti 3MIL	39	YES	AL	23960	2.2×10^9
7-28#2	AIR 10.0	Ti 3MIL	47	YES	AL	26150	3.2×10^9
7-28#3	AIR 10.0	Ti 3MIL	47	YES	AL	42600	5.2×10^9
7-28#4	AIR 10.0	Ti 3MIL	29	YES	AL	24350	1.5×10^9
9-31#1	AIR 10.0	Ti 3MIL	47	YES	AL	45300	5.6×10^9
7-31#2	AIR 10.0	Ti 3MIL	47	YES	AL	13260	1.6×10^9
8-1#1	DEUT 11.0	Ti 3MIL	47	YES	AL	12630	1.6×10^9
8-8#2	VACUUM	Ti 3MIL	39	YES	AL	69800	6.6×10^9
8-1#3	AIR 10.0	Ti 3MIL	112	YES	AL	12650	2.7×10^9

COLLECTIVE ION GEOMETRY

SILVER ACTIVATION DATA

DAY & SHOT	A-K GAP (INCHES)	TARGET	SILVER DETECTOR DISTANCE (INCHES)	CHAMBER MATERIAL	FIRST MINUTE COUNTS	NEUTRON YIELD
8-4 #1	2.0	Ti	72	S.S.	$.74 \times 10^{6}$	$.71 \times 10^{12}$
8-4 #2	2.0	Ti	72	S.S.	$.76 \times 10^{6}$	$.73 \times 10^{12}$
8-4 #3	2.0	Ti	72	S.S.	—	—
8-4 #4	2.0	Ti	72	SS.	$.96 \times 10^{6}$	$.92 \times 10^{12}$
8-4 #5	2.0	Ti	72	S S.	1.96×10^{6}	1.89×10^{12}
8-4 #6	2.0	Ti	72	S.S.	1.33×10^{6}	1.29×10^{12}
8-4 #7	1.0	Ti	72	S S.	$.44 \times 10^{6}$	$.44 \times 10^{12}$
8-4 #8	1.0	Ti	72	S.S.	$.67 \times 10^{6}$	$.65 \times 10^{12}$
8-4 #9	1.0	Ti	72	S.S.	$.92 \times 10^{6}$	$.89 \times 10^{12}$
8-4 #10	1.0	Ti	72	S S.	1.73×10^{6}	1.67×10^{12}
8-5 #1	1.0	Ti	72	S.S.	$.68 \times 10^{6}$	$.66 \times 10^{12}$
8-5 #2	1.0	Ti	72	S.S.	0	0
8-7 #1	1.75	Ti	72	S S.	1.00×10^{6}	$.96 \times 10^{12}$
8-7 #2	1.75	Ti	72	S.S.	—	—
8-7 #3	1.75	Ti	72	S.S.	$.58 \times 10^{6}$	$.56 \times 10^{12}$
8-7 #4	1.75	Ti	72	S.S.	—	—
8-7 #5	1.75	Ti	72	S.S.	$.75 \times 10^{6}$	$.72 \times 10^{12}$
8-7 #6	2.0	Ti	72	S.S.	$.63 \times 10^{6}$	$.61 \times 10^{12}$
8-7 #7	2.0	Ti	72	S.S.	$.46 \times 10^{6}$	$.44 \times 10^{12}$
8-7 #8	2.0	Ti	72	S.S.	$.25 \times 10^{6}$	$.24 \times 10^{12}$
8-7 #9	2.0	Ti	72	S S.	$.35 \times 10^{6}$	$.34 \times 10^{12}$
8-7 #10	2.0	Ti	72	S.S.	1.06×10^{6}	1.02×10^{12}

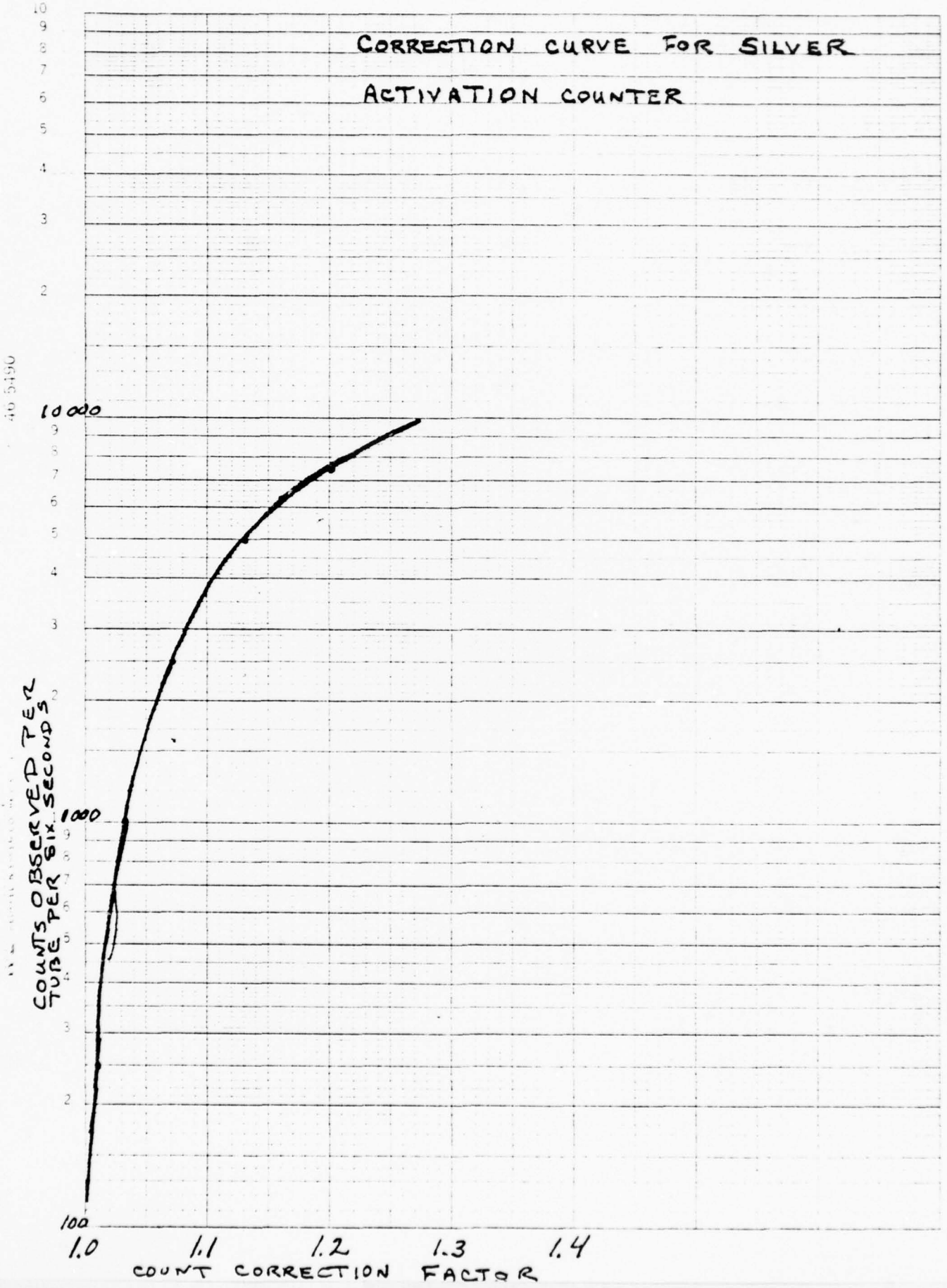
CORRECTION CURVE FOR SILVER
ACTIVATION COUNTER
COUNTS OBSERVED PER TUBE PER SIX SECONDS
10000
1000
100
1.0
1.1
1.2
1.3
1.4
COUNT CORRECTION FACTOR

1978 USAF-ASEE SUMMER FACULTY RESEARCH PROGRAM

Sponsored By

THE AIR FORCE OFFICE OF SCIENTIFIC RESEARCH

Conducted By

AUBURN UNIVERSITY AND OHIO STATE UNIVERSITY

PARTICIPANT'S FINAL REPORT

LASER-INDUCED FLUORESCENCE STUDIES OF SnO and PbF

Prepared by:	Robert B. Green
Academic Rank:	Assistant Professor
Department and University:	Department of Chemistry West Virginia University
Assignment:	
(Air Force Base)	Kirtland Air Force Base
(Laboratory)	Air Force Weapons Laboratory
(Division)	Advanced Laser Technology Division
(Branch)	Chemical Laser Branch
USAF Research Colleague:	Captain Steven J. Davis, PhD
Date:	August 11, 1978
Contract No.:	F44620-75-C-0031

LASER-INDUCED FLUORESCENCE STUDIES OF Sn and PbF

Robert B. Green

ABSTRACT

Certain diatomic intermediate species such as SnO and PbF are primary candidates for chemically-pumped electronic transition lasers. Reliable lifetimes for SnO and PbF are important in the calculation of optical gain for potential laser systems. Laser-induced fluorescence was used in this study to directly obtain this information.

In this experiment a heated oven ($Sn + SnO_2 \rightleftarrows 2SnO$) and a flame ($Sn + N_2O \rightarrow SnO^* + N_2$) were used to produce ground state SnO for laser pumping. Neither approach was successful presumably because of the low probability of the transition of interest and it was concluded that an indirect approach must be devised. Gain/loss measurements were also made for SnO using extra-cavity and intra-cavity laser techniques. No gain or loss was measured but these experiments indicated that particulate light scattering may be a problem in low gain systems.

The radiative lifetime of PbF was measured directly in a flame with laser-induced, time-resolved fluorescence. It was concluded that the vibrational levels of PbF were thermalized before they fluoresced. The average lifetime of the $A^2\Sigma$ state was calculated to be 3.6 μs ± 0.4 μs. A Stern-Volmer plot at several pressures showed that total product quenching was negligible.

ACKNOWLEDGEMENTS

The author is indebted to the staff of the Chemical Laser Branch of the Advanced Laser Technology Division of the Air Force Weapons Laboratory for providing a pleasant and helpful work environment. In particular, I am grateful to Capt Steven J. Davis, Major Ronald R. Bousek, Lt Greg R. Bradburn, and Dr. David J. Benard for providing equipment, facilities, and technical assistance. I also appreciate the data analyzation done by Virginia Bertrand. It has been a pleasure to work with Leonard Hanko who was essential to the completion of these studies.

Appreciation is due to ASEE and Auburn University and especially Mr. J. Fred O'Brien for administration of this project.

INTRODUCTION AND OBJECTIVES

The objective of this research was to obtain fundamental lifetime data for SnO and PbF. These molecules are candidates for electronic transition chemical lasers. Laser-induced fluorescence is the most direct method for obtaining the information necessary for evaluation of these candidates.

Since 1965, all of the chemical lasers which have been reported are based on rotational-vibrational transitions within a single electronic state with one exception. Recently, the first example of continuous wave (cw) laser action on a transition between two distinct electronic states pumped only by a chemical reaction was demonstrated at the Air Force Weapons Lab (1).

Electronic transition lasers, as opposed to vibrational transition chemical lasers, are of interest for several reasons. In addition to being the result of higher energy transitions, shorter wavelengths permit tighter focusing of the laser beam with smaller optics. The transmission characteristics of electronic transition chemical lasers are also desirable.

SnO is a particularly interesting chemical laser candidate because it can be produced in an electronically-excited state by the reaction of Sn with N_2O with measured photon yields as high as 50% (2). PbF, the species resulting from the chemiluminescent reaction of Pb with F_2 (3), is another metal fluoride which should be considered as an electronic transition chemical laser candidate.

Reliable lifetimes for SnO and PbF are important in the calculation of optical gain for potential laser systems. Oscillator strengths can be determined from lifetimes and compared to theoretically calculated values. Thus, measured lifetimes also may serve as sensitive tests of theoretical wave functions.

EXPERIMENTAL

The experimental approach was to prepare ground state molecules in the gas phase and pump them to the desired state by laser excitation. Then the subsequent fluorescence decay could be measured photometrically.

A. SnO

There were several possibilities for preparing gas phase SnO in sufficient quantity to permit a lifetime measurement.

Initially SnO was prepared by the equilibrium reaction:

$$Sn + SnO_2 \rightleftarrows 2\ SnO$$

A powdered mixture of Sn and SnO_2 was placed in a quartz cell to which 10 torr of argon was added (See Figure 1). The reaction chamber which was contained within a furnace was then heated to approximately 1000°C to produce SnO vapor. The 2.54 cm diameter, 100 cm long quartz chamber was equipped with Brewster windows at either end to permit passage of the pumping laser beam. A 22 cm, 90° sidearm at approximately the middle of cell was used to view laser-excited fluorescence. The cell which was sealed during the reaction was evacuated with a vacuum pump and the pressure was monitored with a thermocouple gauge.

Two different optical excitation sources were used for this experiment: a Molectron Spectroscan 10 nitrogen laser-pumped dye laser and a Coherent Radiation CR-8 argon ion laser. The nitrogen laser-pumped dye laser was pulsed at 100 Hz, and the typical energy/pulse was 20 μJ. The linewidth of the dye laser was typically 0.5 nm (FWHM) and the pulse duration was approximately 8 ns. The laser was equipped with a motorized grating for continuous wavelength scanning, thus laser excitation spectra could be obtained. The prism-tuned argon ion cw laser was operated at discrete frequencies. In both cases, the laser beam was focused in the viewing region of the reaction cell.

The laser-induced fluorescence was monitored with a photomultiplier (PM) mounted normal to the laser beam. Various filters were used in conjunction with the PM tube to reduce scattered light and blackbody radiation from the furnace.

The PM output was preamplified and fed to an oscilloscope and a PAR Model 164/162 boxcar averager for pulsed laser experiments. The output of the boxcar which was the average of many shots was displayed on a strip chart recorder. In a few instances a lock-in amplifier was used to process the PM signal in the pulsed experiments since the SnO lifetime was on the order of the laser duty cycle. In most cases, the PAR 121 lock-in amplifier was used for the cw laser experiments. The argon ion laser beam was mechanically chopped at 700 Hz. The signal from the PM was preamplified, displayed on an oscilloscope, and synchronously detected with the lock-in amplifier.

In the pulsed laser experiment, the wavelength region of an absorption to a specific vibrational level was scanned with the nitrogen laser-pumped dye laser and then the fluorescence decay waveform was scanned by the boxcar signal averager while exciting the transition of interest. In the cw experiment, the argon ion laser was tuned on and off the appropriate laser emission lines while the oscilloscope and lock-in amplifier were monitored.

The experiments which were conducted using the pulsed laser and the cw laser are summarized in the schematic diagram below.

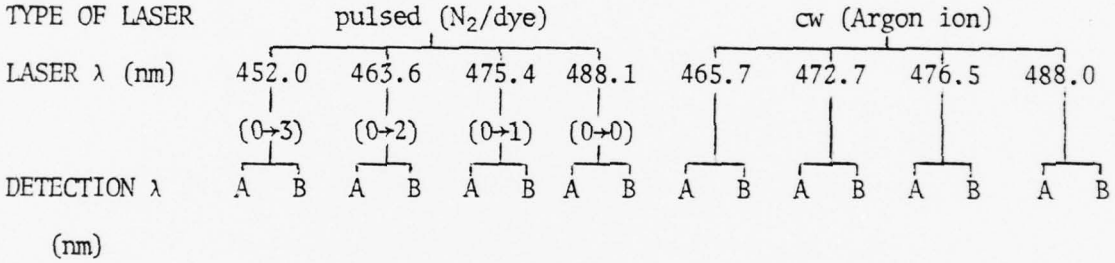

A = 529.3 nm, B = 640.0 nm

The $a^3\Sigma$ state of SnO is the first level above the ground state and is a candidate for a chemical laser. The laser wavelengths indicated above in the schematic diagram for the pulsed experiment coincide with the most probable electronic transitions to vibrational states in the $a^3\Sigma$ manifold as predicted by Franck-Condon considerations. Since the cw laser was not continuously tunable, the indicated wavelengths correspond to emission lines characteristic of the argon ion laser which are within the absorption bandwidth of SnO($a^3\Sigma$). Franck-Condon factors (4) and the chemiluminescence spectrum for SnO indicate that emission at 530.0 nm ($v' = 0 \rightarrow v'' = 2$) and 636.5 nm ($v' = 0 \rightarrow v'' = 6$) should be the most

intense. The detection wavelength indicated above (A or B) is the peak of the filter bandpass (approximately 10 nm wide). In a few cases, a long-pass cutoff filter (> 560.0 nm) was used but blackbody radiation made this approach unsuccessful.

No fluorescence was seen from SnO using the heated cell although furnace temperatures as high as 1200°C were attained in some cases.

A second approach to generating sufficient SnO for lifetime measurements was a chemiluminescent reaction:

$$Sn + N_2O \rightarrow SnO^* + N_2$$

Ground state SnO resulting from chemiluminescence should be available for optical pumping.

The reaction chamber consisted of a four-inch diameter, stainless steel cross with one-inch diameter sidearms mounted at the intersection of the cross and perpendicular to it (See Figure 2). Brewster windows were attached to the one-inch sidearms with Ultratorr fittings for passage of the laser beam. The four ends of the cross were capped with a plate with an outlet for a vacuum pump, a top window, a side window, and a burner. The burner plate had two electrodes for heating, and a jacket for water cooling. A tungsten basket was suspended between the electrodes and an alumina crucible containing the Sn metal was placed in the basket. A ceramic cylinder was placed around the electrodes and crucible and was packed with insulation. A tantalum foil cover with an opening for the crucible mouth isolated the heating section from the rest of the reaction chamber. Nitrous oxide and the carrier gas (argon or helium) were brought into the reaction chamber through concentric tubes. During operation, the Sn metal was heated to produce atomic Sn

while the carrier gas was flowed into the crucible. N_2O was added to produce the chemiluminescent flame. A one-half inch diameter tantalum foil cone was placed on top of the crucible and condensed the flame. The flame could be brought to various positions in the viewing area by adjusting the gas flows. 0.5 torr of N_2O and 3.5 torr of Ar produced an intense blue flame fringed in green, at the top of the burner cone. An emission spectrum of the flame over the region of interest is shown in Figure 3. The assignments for $a \rightarrow X$ transitions from $v' = 0$ were taken from Reference 5.

An additional pumping source was used for flame experiments to provide higher peak powers: a Phase-R Model 1100 flashlamp-pumped dye laser. It produced approximately 50 mJ pulses of 0.5 μsec (FWHM) duration with Coumarin 460 and LD 490 dyes. The laser was prism tuned, producing a polarized beam with a 0.5 nm spectral width.

An experimental plan similar to that outlined previously was followed except that the flame was the source of SnO (See Figure 4). The flashlamp-pumped dye laser was operated at 463.6 nm and 478.4 nm. In all cases, the lasers were focused at the center of the cross opposite the window and the position of the laser beam with respect to the flame was varied.

No fluorescence was observed from SnO in experiments using the nitrogen laser-pumped dye laser, argon ion laser, or the flashlamp-pumped dye laser.

The SnO experiments were then moved to Building 617 which has facilities for fluorine use. The experimental apparatus was generally similar to that described previously with a few exceptions (See Figure 4). The burner was schematically similar to the one illustrated in

Figure 2. A resistively-heated tungsten crucible was used to atomize the Sn. The carrier gas entered the reaction chamber around the outside of the crucible through a ring and carried atomized Sn up through a throat where oxidant was injected through a concentric ring. Mixing occurred at the ring and the SnO flame was produced. This burner permitted sustained operation at the high temperatures necessary for atomizing refractory Sn.

The Molectron Spectroscan 10 nitrogen laser-pumped dye laser was the excitation source and a SnF flame was used to optimize the experimental system. Laser-induced fluorescence experiments for SnO were repeated using this apparatus. Sn + O_2 flames were studied in addition to Sn + N_2O flames. No laser-induced fluorescence was observed from SnO in the flame.

It was apparent that the radiative lifetime of SnO could not be readily measured by laser-induced fluorescence. Emission spectroscopy of the SnO flame showed that several a→X transitions existed which might exhibit gain in a chemical laser system. The flame work was extended to the measurement of gain or loss on the SnO $a^3\Sigma$ states.

The gain/loss experiment was performed using two approaches. In the first case, the SnO flame was placed in a resonant cavity formed by two confocal (>99%R) mirrors (See Figure 5). The mirrors were aligned with the Spectroscan 10 nitrogen laser-pumped dye laser beam. The laser emission leaving the resonant cavity was detected by a photodiode. The signal was amplified (when necessary) and fed to a boxcar signal averager and oscilloscope. When the confocal mirrors were exactly parallel and

the laser wavelength was scanned, gain or loss at SnO transitions should appear as an enhanced signal within the power curve of the dye. No gain or loss was detected in this experiment over the wavelength region 400 to 600 nm.

In a variation of this experiment, an argon ion laser-pumped dye laser was used as the source. The dye laser was mechanically chopped and the emission leaving the resonant cavity which contained the burner was detected with a photomultiplier and processed with a lock-in amplifier. The signal was displayed on a strip chart recorder. The dye laser wavelength was scanned across the 606.4 nm SnO transition to determine if gain could be detected. No gain was detected but wavelength-independent scattering was noted. This scattering diminished the transmitted laser light by approximately a factor of two. The scattering was eliminated only when the helium carrier gas or the heat to the crucible was turned off. This scattering was apparently due to particulates formed from the reactants and/or products of the Sn and N_2O reaction.

In the second case, the SnO burner was placed within the active cavity of a flashlamp-pumped dye laser (Phase-R 1100) which was operated in a broadband mode (See Figure 6). The appropriate dye was concentration-tuned to approximately center the dye emission band over the SnO transition wavelength of interest. The output of the dye laser was dispersed through a 0.3 m monochromator and detected with a photodiode array and a multichannel analyzer. The dye emission spectrum was displayed on an oscilloscope. Gains or losses within the dye power curve should be indicated by positive or negative spikes.

SnO transitions at 530.0 nm and 606.4 nm were probed for gain and the 475.4 nm transition was investigated for absorption. The Sn atom transition at 658.8 nm was also studied. On several laser shots, apparent gain was seen at nominally 606.4 nm but could not be further substantiated. The multi-channel analyzer was also operated in the signal accumulation mode to minimize shot-to-shot variations and compared to the dye emission curve without the flame. Gain or loss could not be verified for the transitions investigated.

B. PbF

PbF can be produced by the following reaction under conditions similar to the environment in a chemical laser:

$$Pb + F_2 \rightarrow PbF^* + F$$

This reaction gives a blue flame fringed in red when helium is used as the carrier gas. Figure 7 is a flame spectrum showing $A^2\Sigma \rightarrow X^2\Pi$ transitions of PbF.

In order to determine if a radiative lifetime could be measured by laser-induced fluorescence, an excitation spectrum was run. The apparatus at Building 617 was used with nitrogen pumped-dye laser excitation (See Figure 4). Optimum pressures of fluorine and helium along with crucible temperature were determined by maximizing the PbF $A^2\Sigma \rightarrow X^2\Pi$ laser-induced fluorescence (spectrally unresolved). The laser beam was focused into the cell to obtain maximum signal and the photomultiplier position was also optimized.

The PM output was preamplified and fed to an oscilloscope and a boxcar signal averager. The boxcar averager was set and held beyond the laser scatter peak to insure that the signal contained only fluorescence. The output of the boxcar which was the average of many shots was displayed on a stripchart recorder. The time base of the boxcar/recorder system was calibrated by recording a sine wave from a function generator whose frequency was measured on a frequency counter. An excitation spectrum of the PbF flame ($A^2\Sigma \rightarrow X^2\Pi$) is shown in Figure 8.

The lifetimes of several vibrational levels of the $A^2\Sigma$ state of PbF were measured by following the fluorescence decay after laser excitation. The PM voltage was reduced until a further reduction produced no change in the measured lifetime. The excitation spectrum indicated that PbF absorbed strongly at 429.2 nm, ($v' = 2 \leftarrow v'' = 0$), 436,5 nm, ($v' = 1 \leftarrow v'' = 0$) and 444.1 nm ($v' = 1 \leftarrow v'' = 0$). Time-resolved signals were obtained by setting the dye laser to one of these wavelengths and scanning the boxcar aperture over the fluorescence decay curve. Each run took approximately 15 minutes to permit the necessary signal averaging. The results of these measurements are shown in the Table. Since the fluorescence signals were several microseconds long, the eight nanosecond laser pulse caused no convolution. Semilog plots of fluorescence intensity versus time were made from decay curve data. A typical plot is shown in Figure 9.

Lifetime measurements while exciting at 436.5 nm were repeated using a Biomation Model 6500 Waveform Recorder and a Hewlett-Packard Memory/Display signal averager for signal processing. The Biomation

unit recorded the decay waveform in 25 μs and stored it in a single memory. The rapid data accumulation time of the Biomation essentially eliminated any perturbation of the lifetime measurement due to dye performance degradation or change in flame conditions that might occur during longer run times. The waveform was then signal averaged in the Hewlett-Packard unit and read out on an XY recorder. Signal averaging permitted the use of higher pre-amplication and the attainment of better signal-to-noise ratios. The results of these measurements are shown in the Table.

In additional experiments, the quenching effects of all species in the chamber were studied as a function of pressure. The pressure was varied by choking the flow with a valve on the downstream side of the reaction chamber and the lifetime of PbF ($A^2\Sigma$) was measured as outlined before. A Stern-Volmer plot of the data is shown in Figure 10. The slope of the line is the quenching rate coefficient, k, where $1/\tau = kp + 1/\tau_o$ and τ is the measured lifetime, τ_o the lifetime without foreign gases, and p the foreign gas pressure.

CONCLUSIONS AND RECOMMENDATIONS

It is clear that the lifetime of SnO ($a^3\Sigma$) cannot be measured readily by laser-induced fluorescence. This is not surprising since gas-phase lifetimes have been estimated to be 300 μs from matrix isolation studies (6). The low probability of the forbidden $a^3\Sigma$ transitions coupled with low ground state populations make this a difficult measurement. Indirect methods may be a surer approach to the lifetime measurement of SnO ($a^3\Sigma$). Gain/loss experiments for SnO should be further considered. Stable, long path length flames on burners capable of maintaining temperatures

(> 1500°K) necessary for the production of SnO in the $a^3\Sigma$ state along with signal averaging should give more definitive data. The gain experiments did indicate that particulate light scattering may be a problem in low-gain laser systems.

The average lifetime of PbF($A^2\Sigma$) calculated from studies using the boxcar signal averager was 3.7 $\pm$ 0.6 μs. All semilog plots were linear for greater than one lifetime indicating that the fluorescence decay was a single exponential. Although there is limited data for comparison, the relatively close agreement of lifetimes from several vibrational levels suggest that the vibrational levels are thermalized before they fluoresce. However, since no attempt was made to spectrally resolve the fluorescence, it is not certain where the fluorescence originated.

The data taken with the Biomation Waveform Recorder agree well with the results taken with the boxcar signal averager. This is reassuring since the PbF fluorescence signal will diminish over an extended period of time due to degradation of the laser dye.

The Stern-Volmer plot of the $1/\tau$ versus the pressure in the reaction chamber shows that the total product quenching was negligible at the pressures which were studied.

More extensive measurements of the quenching in the PbF system should be made. Resolution of the laser-induced fluorescence would also provide useful information although the emission may be too weak. The development of a better way to generate atomic Pb for the burner would provide longer term signals and eliminate some of the difficulties encountered in this study.

REFERENCES

1. W. E. McDermott, N. R. Pchelkin, D. J. Benard and R. R. Bousek, Applied Phys. Lett., 32, 469 (1978).

2. G. A. Capelle and C. Linton, J. Chem. Phys., 65, 5361 (1977).

3. C. R. Dickson and R. N. Zare, to be published in Optics Pura-Y-Aplicada.

4. J. R. Lillis, Laser Digest, AFWL-TR-76-131, 271 (1976).

5. M. J. Linevsky and R. A. Carabetta, Chemical Laser Systems, GE Report No. 75SOS4271, General Electric Company, Philadelphia, PA, 1975.

6. B. Meyer, J. J. Smith and K. Spitzer, J. Chem. Phys., 53, 3616 (1970).

TABLE

PbF ($A^2\Sigma \rightarrow X^2\Pi$) Lifetimes

Laser Excitation Wavelength	Number of runs	Calculated Lifetimes (Average)
429.2 nm (2,0)	2	3.5 μs
436.5 nm (1,0)	16	3.7 μs ± 0.4 μs
	5	3.7 μs ± 0.4 μs*
444.1 nm (0,0)	2	3.6 μs
Average of all runs	3.6 μs ± 0.4 μs	

* These lifetime measurements were made with the Biomation/HP Signal Averager. The remaining measurements were obtained using the PAR 162/164 boxcar signal averager. Each run was the average of many laser shots depending on the sampling mode.

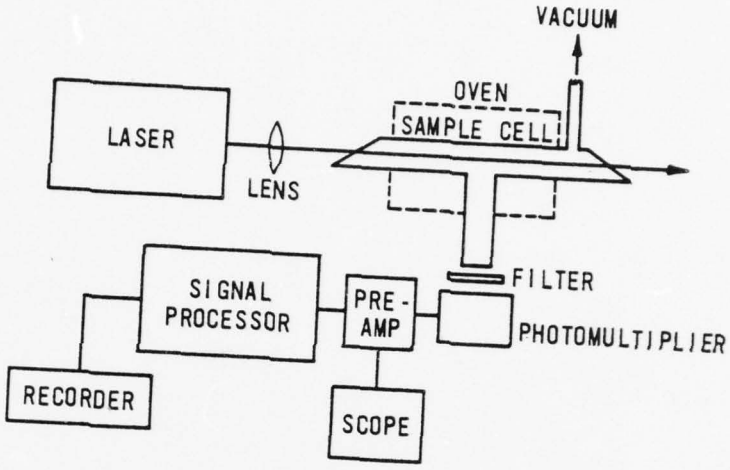

Figure 1. Schematic diagram of apparatus with oven.

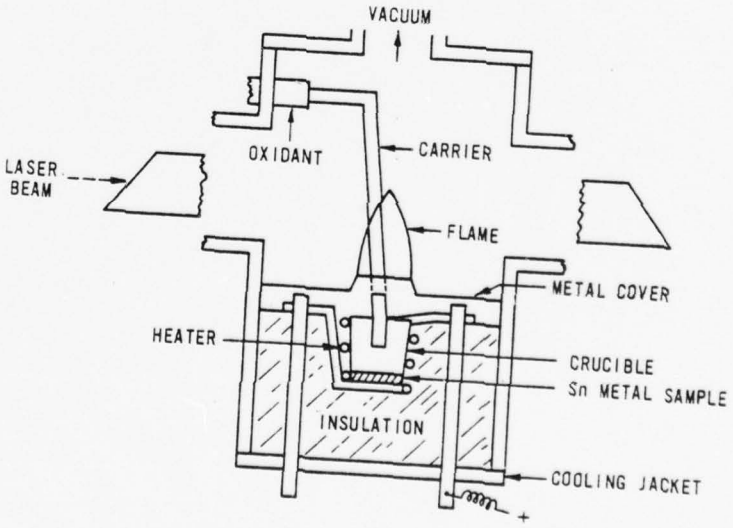

Figure 2. Schematic diagram of metal oxide burner.

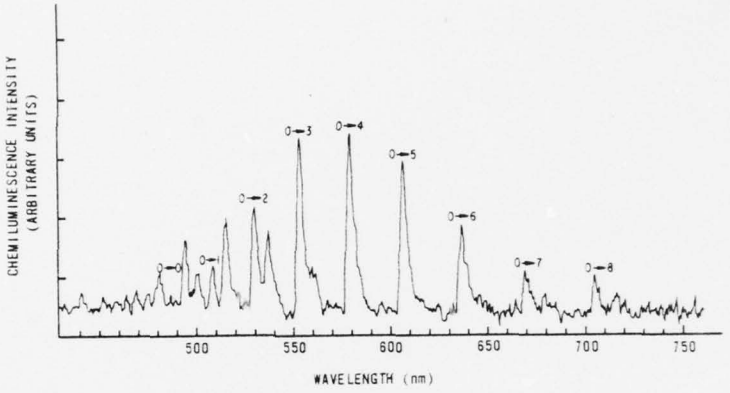

Figure 3. Chemiluminescence spectrum of SnO (uncorrected for photomultiplier response).

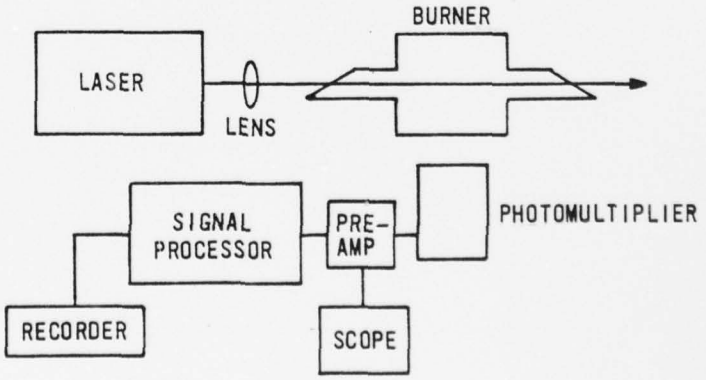

Figure 4. Schematic diagram of apparatus with metal oxide burner.

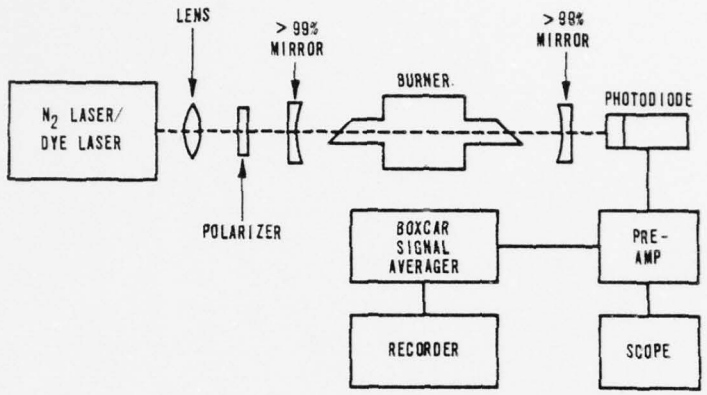

Figure 5. Schematic diagram of apparatus for extra-cavity gain/loss experiment.

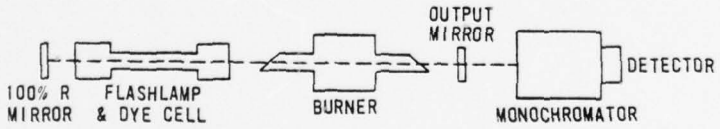

Figure 6. Schematic diagram of apparatus for intra-cavity gain/loss experiment.

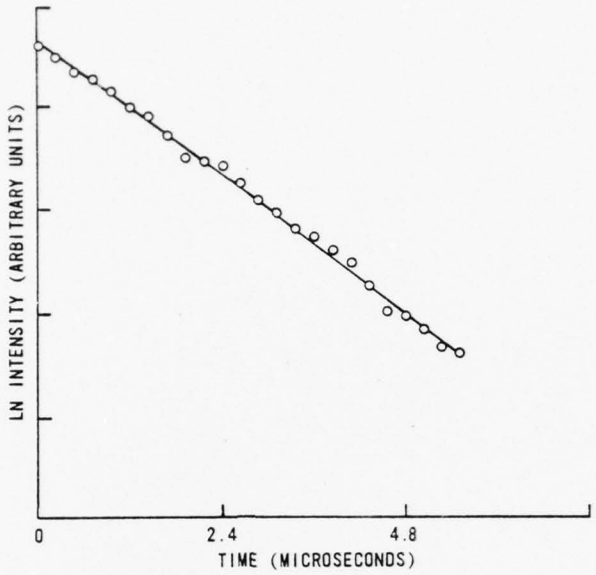

Figure 9. Typical semilog plot of fluorescence intensity versus time.

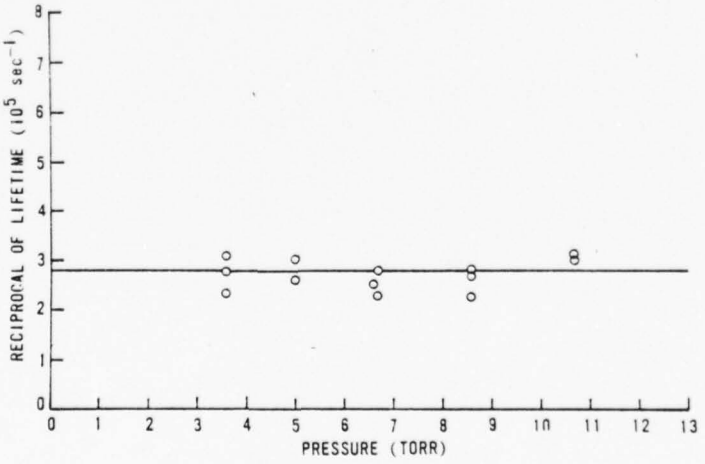

Figure 10. Stern-Volmer plot for the v' = 1 level of the $A^2\Sigma$ state of PbF. The lifetime for this run was determined to be 3.6 μs.

1978 USAF-ASEE SUMMER FACULTY RESEARCH PROGRAM
sponsored by
THE AIR FORCE OFFICE SCIENTIFIC RESEARCH
conducted by
AUBURN UNIVERSITY AND OHIO STATE UNIVERSITY

PARTICIPANT'S FINAL REPORT

ADAPTIVE IDENTIFICATION AND CONTROL OF A GIMBALED LASER POINTING AND TRACKING SYSTEM

Prepared by:	Robert L. Gutmann, PhD
Academic Rank:	Assistant Professor
Department and University:	Department of Electrical and Computer Engineering University of Massachusetts At Amherst

Assignment:

(Air Force Base)	Kirtland Air Force Base
(Laboratory)	Weapons Laboratory
(Division)	Laser Development
(Branch)	Beam Control Systems, LRO
USAF Research Colleague:	Robert L. Van Allen, Capt, PhD
Date:	August 15, 1978
Contract No:	F44620-75-C-0031

ADAPTIVE IDENTIFICATION AND CONTROL OF A GIMBALED LASER POINTING AND TRACKING SYSTEM

BY

ROBERT L. GUTMANN

The increasing use of lasers and precision infrared and television sensors has motivated the development of highly accurate pointing and tracking systems. One obstacle faced in obtaining increased accuracy in gimbaled pointing and tracking systems is due to the fact that the parameters in the mathematical model that describes the pointer and tracker are not precisely known. Furthermore, the model parameters tend to drift with time as components age and the loading on bearings change. Two methods of overcoming this obstacle are presented in this report. In the adaptive control approach, the controller is built with variable feedback gains. These feedback gains are adjusted by the control algorithm to account for unknown gimbal parameters and nonlinearities such as friction and a cubic spring term. In the adaptive identification approach the gimbal parameters are identified from recorded input-output test data. The philosophy presented here is to use the identifier algorithm to gather data so that a simplified adaptive controller may be designed. The adaptive controller has the advantage that it responds to the parameter drifts mentioned above, whereas the identifier is not "in the loop" and cannot so respond.

The adaptive controllers and identifiers presented here are Lyapunov-based model-reference types. Sample computer simulations are also presented to demonstrate the algorithms.

LIST OF FIGURES

NOMENCLATURE

EI	Inner-outer gimbal angle
$\dot{EI}$	Inner-outer gimbal angle rate
WØ	Outer gimbal rate feedback to inner gimbal
W1	Acceleration torque disturbances
V1	Hydraulic pressure loop input command
U	Control signal generated by the adaptive controller
F1	Torque to the static plus Coloumb friction
C1	Cubic spring term
EM1, EM2	Model state variables
E1, E2	Error terms
K1 thru K6	Adaptive gains
AN1, AN2, BM1, BM2, CM1, CM2,	Adaptive model parameters

ACKNOWLEDGMENT

The author is sincerely grateful for the opportunity and support provided by the Air Force Systems Command. The efforts of Mr. Fred O'Brien, Auburn University and LtCol "Bud" Hoeft are especially appreciated in administering this Summer's program. The technical guidance and assistance offered by Captain Robert Van Allen, Dr. Paul Merritt and Dr. Lynn Ebbesen have made this summer extremely rewarding and enjoyable.

1. INTRODUCTION.

Today, with the widespread use of lasers and precision infrared and television sensors, the development of highly accurate pointing and tracking systems is becoming essential. Without these accurate pointing and tracking systems, the benefits of the very narrow laser beam and the high resolution capability of modern sensors diminish rapidly. Furthermre, in an airborne environment, these systems must be able to isolate the laser or sensor from vibration type disturbances. For this reason these devices are usually mounted on gimbals along with disturbance sensing devices. Outputs from the sensors are fed back to the gimbal actuators through control loops in order to isolate the inner gimbal platform from disturbances. For the system chosen for consideration here, four gimbals are utilized, two inner gimbals and two outer gimbals (one inner and one outer gimbal for azimuth and one pair for elevation).

In order for the control loops to properly isolate the gimbals, it is crucial that the gimbals and the associated actuator mechanism operate in a perfectly known and predictable fashion. As is the case in most physical systems, a precise mathematical model is not generally available. Furthermore the parameters associated with the mathematical model tend to vary over time as components in the electronic and hydraulic systems shift with age and as the loading on mechanical joints and bearings changes as a function of aircraft speed and wind velocity. In general, it is difficult to design fixed control loops that provide adequate precision in pointing and tracking and in gimbal isolation for a wide range of values of the parameters in the mathematical models. Additionally, for improved accuracy, it is often desirable to remove gimbal and actuator nonlinearities such as friction and nonlinear spring terms so that the controller deals with a system which is essentially linear.

It is for these reasons that some of the control loops that isolate the gimbals from external motion are designed in a flexible fashion so that they may adapt to the actual gimbal assembly and actuators. The remainder of the control loop then "sees" a linear system with known

mathematical model parameters. That is, an inner adaptive control loop adjusts its feedback gain terms so that the adaptive controller along with the gimbal assembly and associated actuators respond as if they were a linear system with known parameters (even though the gimbal and actuators contain nonlinearities and unknown parameters). The outside control loop may then be fixed and designed to control a known linear system.

One other option for the system designer is to measure or identify the unknown gimbal assembly and actuator parameters prior to designing a fixed controller. Although this is an acceptable design procedure in some instances, it may be risky in others. This is due to the potential variation of parameter values with age as indicated above. The advantages of the identification method of design center around the fact that the design may be accomplished "off-line" on a computer operating on data previously recorded.

In the remainder of this report we describe a particulary successful method that may be used both for adaptive control and identification. Furthermore, this method is applied to a gimbal elevation channel in designing an adpative controller to remove the effects of unknown parameters and nonlinearities. In addition an identification algorithm is developed that may be used to identify gimbal parameters and nonlinearities.

2. OBJECTIVES

The objectives of this project were to provide Lyapunov-based algorithms for the adaptive control and identification of an inner gimbal assembly and the associated hydraulic actuator. Simulations were provided in order to demonstrate the applicability and usefulness of the algorithms. Aircraft equipment problems and scheduling difficulties related to on-board testing have made the collection of data and actual hardware testing impractical to accomplish during the summer time frame. Such activities are, however, planned for the future.

The following algorithms are provided for adaptive control purposes:

a. Single input, four adaptive gains.

b. Two input, four adaptive gains.

c. Three input, six adaptive gains.

Simulation results are provided for the adaptive controllers. In addition, an adaptive identification algorithm is provided for parameter identification purposes. Simulations of this algorithm are also provided.

3. THE PLANT

We are concerned here with the design of adaptive control and identification algorithms for one channel of the inner gimbal assembly of a four gimbal pointing and tracking system. Figure 3.1 depicts a system block diagram of the portion of the system under consideration: the elevation hydraulic pressure loop and inner gimbal assembly. This block diagram is derived from information contained in (6). The block diagram consists of the inner gimbal hydraulic pressure loop and the inner gimbal assembly. It is felt that the effects of unknown parameters and friction are most serious in the inner gimbal structure. It should also be noted that the azimuth inner gimbal assembly is functionally equivalent so that the algorithms developed for the elevation channel are expected to operate equally well in the azimuth channel.

Ideally, only the inner gimbal structure would be included in the system to be investigated, however it is necessary to inject signals into the system for control purposes, and the nearest access point to the gimbal is the pressure loop electronic input. Signals generated by the adaptive controller will be added to the channel at this point. The effects of the pressure loop must therefore be accounted for in the design of a controller (refer to Section 4.2 for a discussion of this aspect).

The friction model used represents static plus coloumb friction. Figures 3.2 and 3.3 depict these models. Coloumb friction force is assumed to be at a constant level and opposed to motion, provided that the gimbal is in motion. If the gimbal is not in motion, static friction is assumed to be equal to, and opposed to applied torque, up to the maximum static friction level, known as the breakaway point. The maximum static friction level is assumed to be somewhat higher than the Coloumb friction level, however both friction levels are assumed to be unknown. The nonlinear spring term is assumed to be a cubic function of spring displacement.

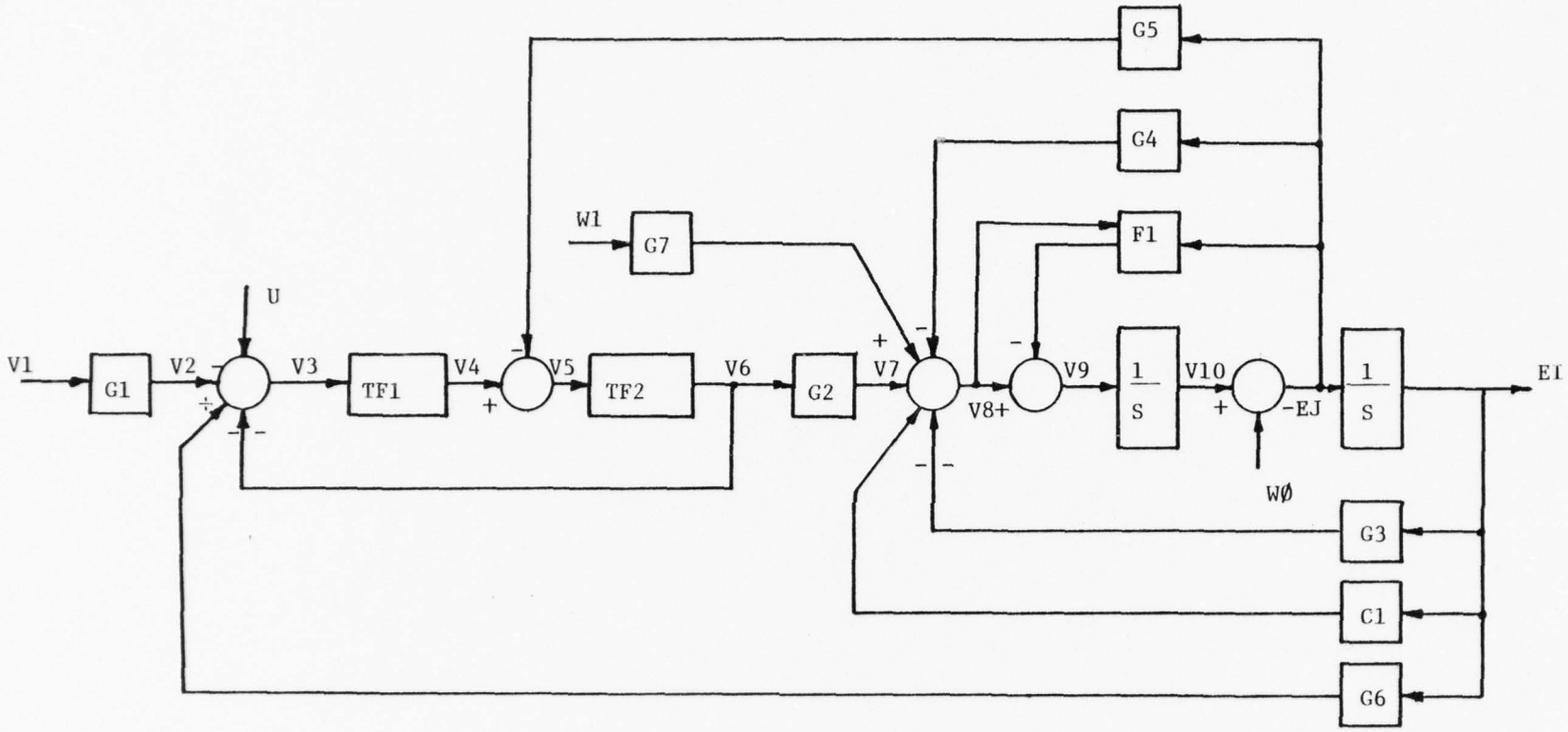

G1 = 178.57
G2 = 0.0056
G3 = 353.64
G4 = 62.59
G5 = 3.5
G6 = 56835.77

K11 = 0.0024
Z1 = 5.414×10^{-4}
P1 = 5.88×10^{-3}
K22 = 3333.3
P2 = 0.00379

$$TF1 = \frac{K11\ (S \cdot Z1 + 1)}{(S \cdot P1 + 1)}$$

$$TF2 = \frac{K22}{(S \cdot P2 + 1)}$$

F1 = F1C + F1S
C1 - CS - EI^3

Figure 3.1 The Elevation Pressure Loop and Inner Gimbal Assembly

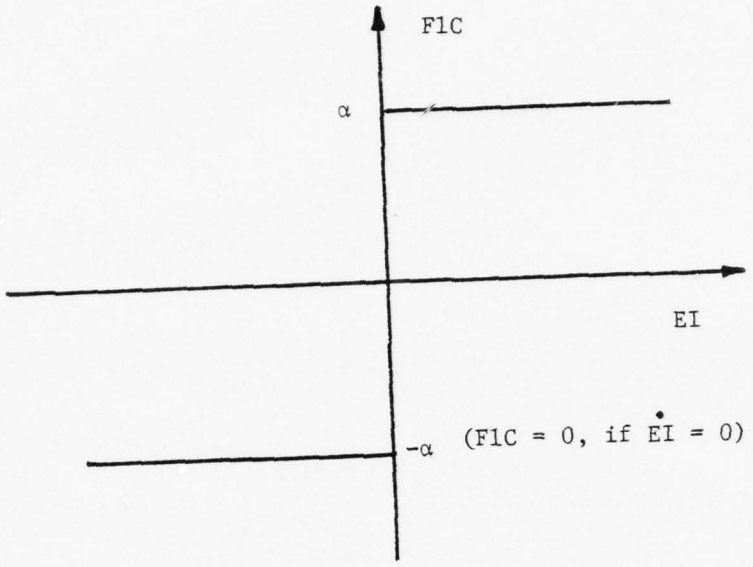

Figure 3.2 Coloumb Friction Model

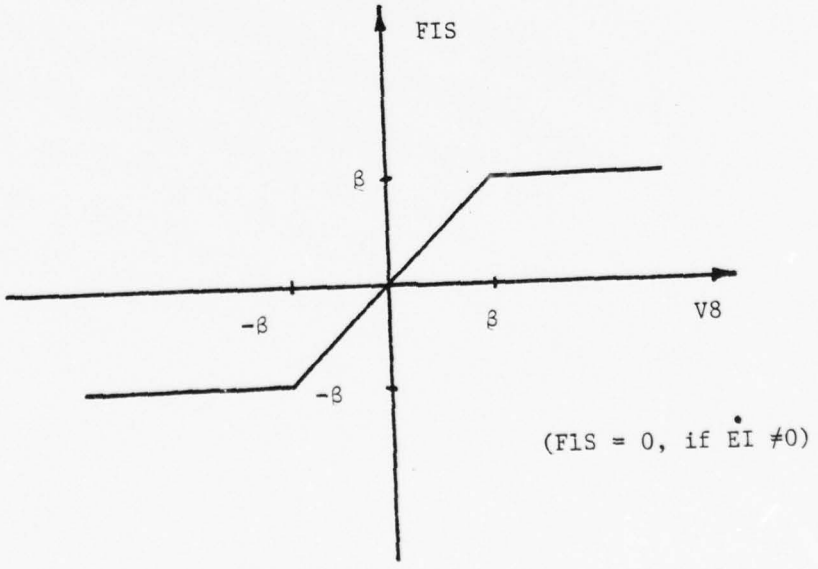

Figure 3.3 Static Friction Model

The parameter as well as its sign are assumed to be unknown in practice.

The values of all parameters used in simulating the plant were obtained from (6). However many of these parameters are assumed to be unknown in practice. The simulation used is discussed in Appendix I.

4. ADAPTIVE CONTROL

4.1 General.

The technique described here is known as Lyapunov-based model reference adpative control. Several excellent references exist on this subject. For instance, refer to (8), (9), (10), or (12). Several other methods of designing adaptive controllers exist, however, Lyapunov-based designs have a distinct advantage in that they guarantee overall system stability.

A block diagram of a functional model reference adaptive control system is shown in Figure 4.1. With respect to this figure, the "plant" is the system to be controlled. It is assumed that not all of the plant parameters are known. A "model" of the same order (number of state variables) as the plant is chosen by the system designer. The input to the model is the same as the reference input to the system. An adaptive controller is chosen so that the difference between the plant output (plant state variables) and the model output (state variables) goes to zero. The net closed loop system, then has the same input-output properties as the model. That is, the plant now behaves like the model. In the usual case, the model contains only linear elements. Hence when the error signal becomes small, the nonlinearities such as friction and cubic spring terms are effectively removed.

The difference between the model and plant outputs is known as the error signal. The concept of the control scheme is to drive the error signal to zero. Differential equations for the behavior of the error signal may be written (refer to Section 4.3). The stability properties of these differential equations may be determined by the system designer. That is, it is possible to design a controller such that the system of differential equations describing the error signals is asymptotically stable (i.e., the error signal asymptotically approaches zero). Lyapunov's direct method is utilized to show the asymptotic stability of this system. Refer to (5) or (12).

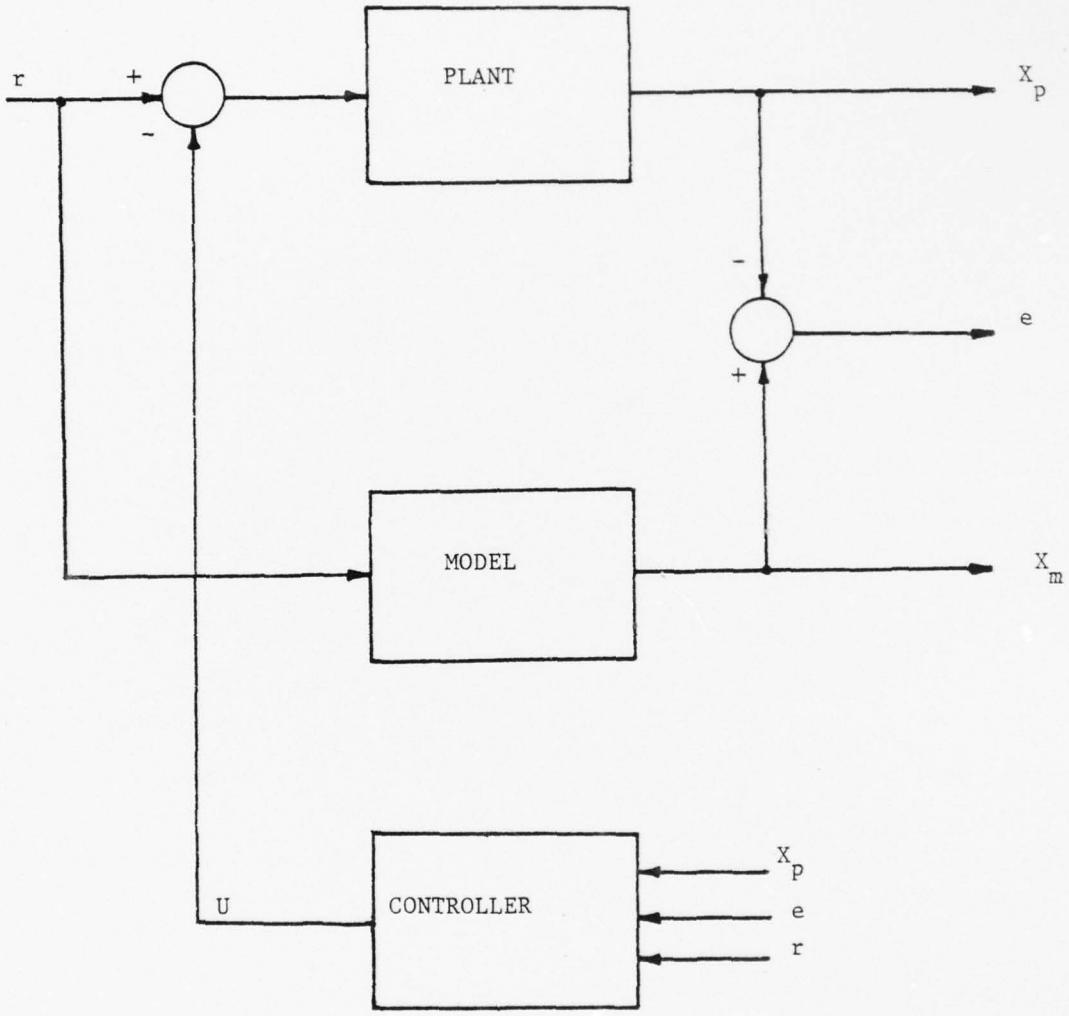

r = reference input
X_p = plant output
X_m = model output
e = error signal
U = control signal

Figure 4.1 Model Reference Adaptive Control System

These techniques have been applied to an electrically activated NASA telescope as described in (2) and (3). The effects of friction and unknown parameters were successfully reduced in this application. Similar effects are produced in a simple d.c. electric motor and reported in (7), (11), (13), and (14). A preliminary feasibility study for applying adaptive control techniques to a gimbaled pointing and tracking system was conducted by this author and a colleague and are reported in (4).

4.2 The Model.

As stated in Section 4.1, the model is chosen by the system designer and constitutes the desired overall system behavior after the adaptive controller gains have converged. The choice of model parameters is the prerogative of the system designer. In this instance, parameters were chosen so that the zero frequency gain and cut off frequency of the model are roughly equivalent to what is assumed for the gimbal without any modification to the present system. Furthermore, friction and nonlinear terms are not present in the model. Therefore driving the error between plant and model to zero is equivalent to removing the effects of friction and the nonlinear terms (as well as the effects of unknown gimbal parameters).

As stated in (4), one of the primary concerns in designing the adaptive controller and the associated model is the effect of the hydraulic pressure loop dynamics and the electronic compensation network. The effects of the hydraulic pressure loop were studied in (4). It was determined that this loop had negligible effect on the performance of the adaptive controller. For this reason the hydraulic pressure loop appears in the model as a constant gain term. The effects of the electronic compensation are somewhat more difficult to predict. This is due mainly to the fact that the exact point in the electronic compensation at which a control signal may be injected has not yet been firmly established. At one injection point the control signal would pass through electronic networks with poles at 101, 1000, and 174 Hz. These could be handled in the same fashion as the hydraulic pressure loop: treated as a constant gain. At the other possible injection point, the control signal would pass through a network consisting of poles at 0.159, 5.57, 12.3 and 407 Hz. (as well as the three poles above). In this case, it would be necessary to compensate the control signal for the

poles at 0.159, 5.57 and 12.3 Hz with a pole-zero cancellation network. Such a network is not anticipated to cause any difficulties, however the precise effects have not been simulated. Such a simulation is highly recommended if the second injection point is used. The plant shown in Figure 3.1 as well as the simulations conducted for this report treat the electronic networks as constant gains.

4.3 The Adaptive Controller.

As stated earlier, the function of the adaptive controller is to force the error between the model and plant to zero. It accomplishes this by generating a feedback control signal consisting of various plant signals, each multiplied by a gain. The gain terms are time-varying; they do however, converge to a steady-state value in a correctly mechanized controller. As shown in Section 4.4, for the system under consideration, about 20-30 sec. are required for the gains to converge. This is expected to pose no problems in the operational system (since the controller could be allowed to converge in an idle period prior to operating the system as a pointer-tracker). As the gains converge to their steady-state values, the error signal is converging to zero.

The adaptive controllers presented here are derived in a fashion similar to those presented in (4) and (13). With respect to Figures 3.1 and 4.1, we construct a control signal, U, of the form

$$U = K1 \cdot EI + K2 \cdot \dot{EI} + K3 \cdot V1 + K4 \cdot W1 + K5 \cdot F2 + K6 \cdot CS1 \qquad (4.1)$$

Where

$$F2 = \begin{cases} \text{sign}(\dot{EI}) & \text{if } \dot{EI} \neq 0 \\ \text{sign}(EM2) & \text{if } \dot{EI} = 0 \end{cases}$$

EM will be defined below

$CS1 = EI^3$

The signal U is assumed, for this discussion, to be injected at the electronic input point of the hydraulic pressure loop, as indicated in Figure 3.1. Refer to Section 4.2 for a discussion of the necessary changes if the control signal is injected into the electronic compensation prior to the pressure loop. In Equation (4.1), the gains K1 through K6 are time-varying and are termed the "adaptive gains." The adaptive control algorithm adjusts the values of K1 through K6 continuously. The terms K1•EI, K2•$\dot{EI}$, and K3•V1 adapt for the unknown parameters G5, G4, G3 and the pressure loop gain shown in Figure 3.1. The term K4•W1 adapts for the unknown parameter G7 of Figure 3.1. Finally, the terms K5•F2 and K6•CS1 adapt for friction and a nonlinear spring respectively.

The model is second order and is described by

$$\begin{pmatrix} \dot{EM1} \\ \dot{EM2} \end{pmatrix} = \begin{pmatrix} 0 & 1 \\ -AM1 & -AM2 \end{pmatrix} \cdot \begin{pmatrix} EM1 \\ EM2 \end{pmatrix}$$

$$+ \begin{pmatrix} 0 & -1 & 0 \\ BM1 & 0 & BM2 \end{pmatrix} \cdot \begin{pmatrix} VI \\ W0 \\ W1 \end{pmatrix}$$

where

EM1, EM2 are the two model state variables
V1, W0, W1 are input signals from Figure 3.1
AM1, AM2, BM1, BM2 are model parameters.

The model parameters determine the response of the model to the various system inputs. These are chosen by the controller designer.

An error signal is defined by

$$E \triangleq \begin{pmatrix} E1 \\ E2 \end{pmatrix} \triangleq \begin{pmatrix} EM1 \\ EM2 \end{pmatrix} - \begin{pmatrix} EI \\ \dot{EI} \end{pmatrix}$$

When E is driven to zero by injecting the control signal U into the plant, it can be seen that the plant will be responding as if it were described by the model differential equations. That is, we will have

$$\begin{pmatrix} EI \\ \dot{EI} \end{pmatrix} = \begin{pmatrix} EM1 \\ EM2 \end{pmatrix}$$

provided we drive the error signal, E, to zero.

We use the following algorithm to determine the gains K1 through K5. It may be shown (refer to (4) or (12))that this selection of gains will drive the error signal to zero. Define

$$H1 = P12 \cdot E1 + P22 \cdot E2$$

where

P12, P22 are positive constants.

Then pick

$$\dot{K1} = - GAM1 \cdot H1 \cdot EI$$
$$\dot{K2} = - GAM2 \cdot H1 \cdot \dot{EI}$$
$$\dot{K3} = - GAM3 \cdot H1 \cdot V1$$
$$\dot{K4} = - GAM4 \cdot H1 \cdot W1$$
$$\dot{K5} = - GAM5 \cdot H1 \cdot F2$$
$$\dot{K6} = - GAM6 \cdot H1 \cdot CS1$$

where GAM1 through GAM6 are positive constants.

The initial conditions for K1 through K6 are chosen to be the designers best apriori guess of the quantities (AM1-G3),(AM2-G4), (BM1 - pressure loop gain), (BM2 -G7), (Coloumb friction level), and (C5) respectively.

The controller presented here is the most general type considered. It may be that all six adaptive gains are not required, or that in some simple test configurations, the input signals WØ and W1 may not be present. For these reasons two simplified controllers are also presented. These are derived from the general controller simply by deleting gain terms. All three controllers are summarized in Appendix B.

4.4 Adaptive Control Simulation Results

In this section we present some of the key simulation results. Parameter values are chosen at their nominal values as found in (6). These parameter values are assumed, however, to not be precisely known in practice, so that the true plant parameter values are not available to the controller.

Friction values (static and coloumb) are chosen on the basis of experimental data provided in (1).

The following figures are plots of the output signals, EI, and the error signal El = EMl - EI, for two configurations of the adaptive control algorithms. Not all possible configurations of the algorithm are shown, since at this stage, the simulations merely confirm the operability of the algorithms using the simulated plant in Figure 3.1. Actual performance predictions must await the gathering of more test data and the evaluation of that data using the parameter identification algorithm presented in Section 5. Plans for gathering this data have been established at this time.

Table 4.1 summarizes the simulation results presented in Figures 4.2 - 4.5.

Table 4.1 - Simulation Summary

Figure Number	Inputs	Gains
4.2	Vl = 0.1 sin(1.2566t) WØ = 0 Wl = 0	None
4.3	Vl = 0.1 sin(1.2566t) WØ = 0 Wl - 0	Kl, K2, K3, K4
4.4	Wl - 0.1 sin(1.2566t) WØ = 0.5 cos(1.2566t) Wl = 0	None
4.5	Vl = 0.1 sin(1.2566t) WØ = 0.5 cos(1.2566t) Wl - 0	Kl, K2, K3 K4

These plots verify the effectiveness of the algorithms under the condition indicated in Table 4.1

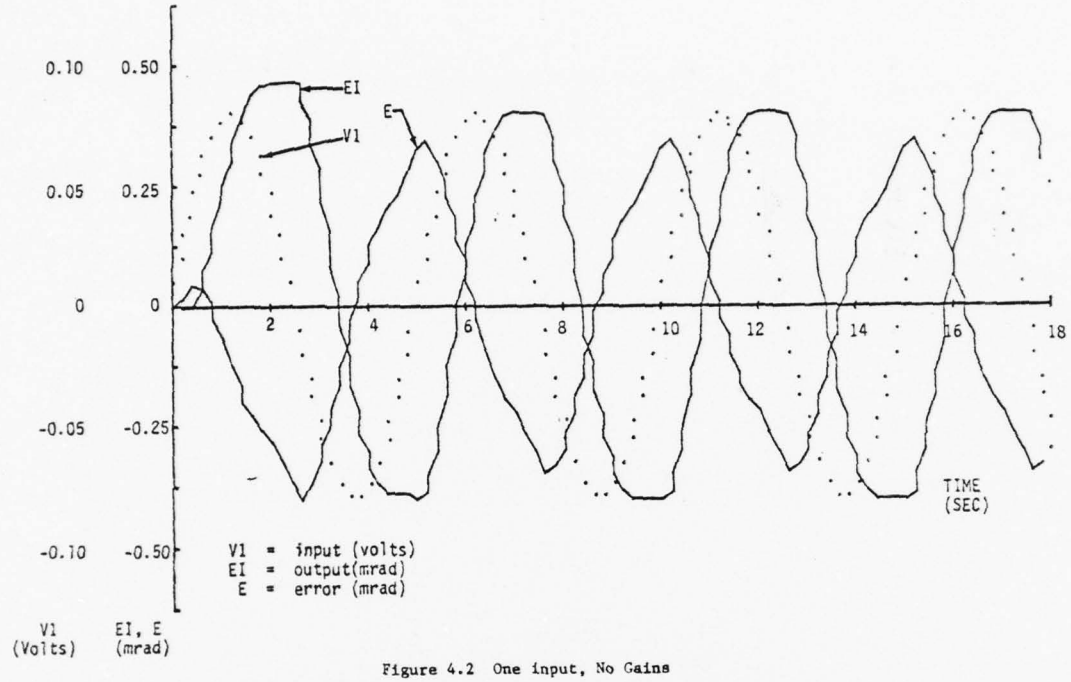

Figure 4.2 One input, No Gains

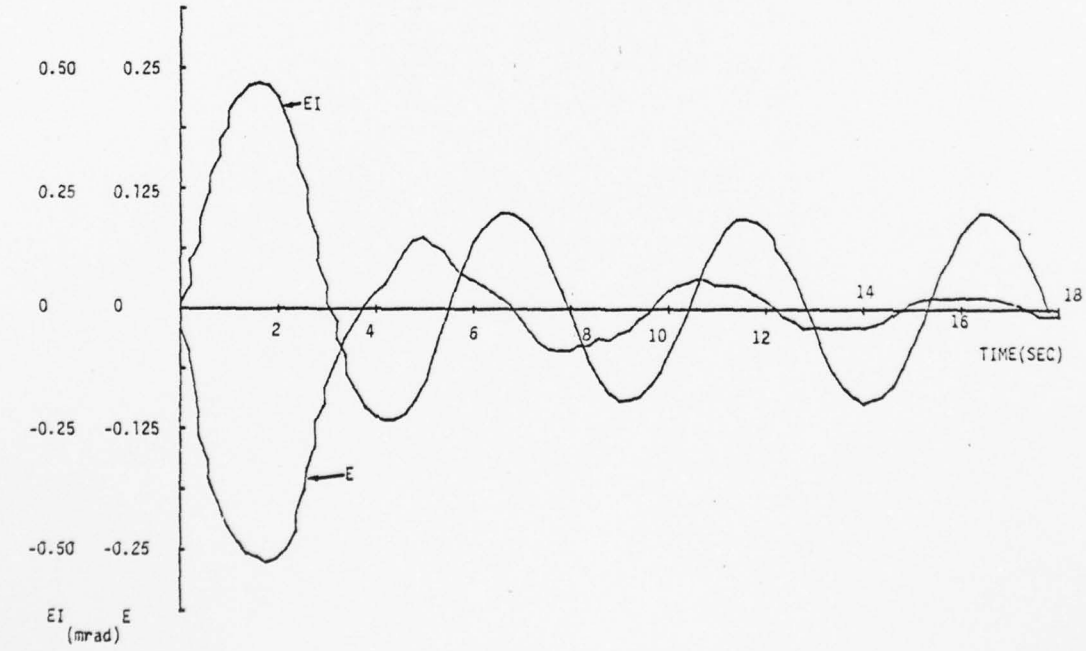

Figure 4.3 One input, Four Gains

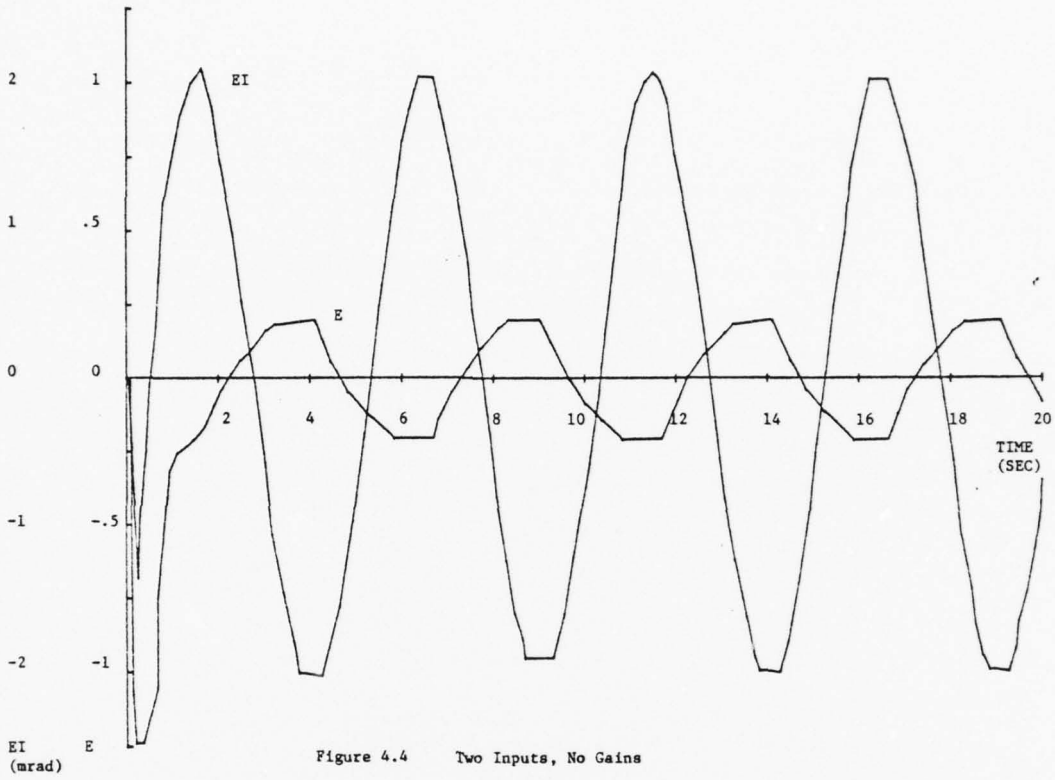

Figure 4.4 Two Inputs, No Gains

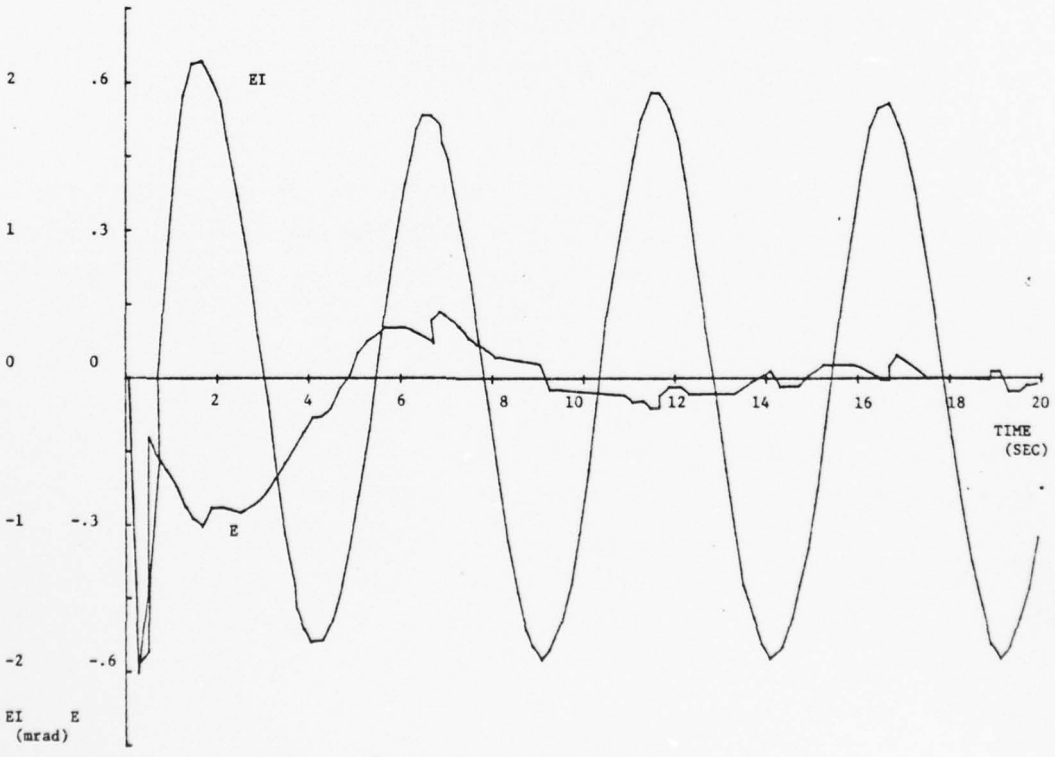

Figure 4.5 Two Inputs, Four Gains

5. ADAPTIVE IDENTIFICATION

5.1 Introduction

It is possible to operate the adaptive control system described in Section 4 in an identification mode. This section describes an identification algorithm that may be used on system signals recorded during testing. Such a technique may be used to identify

(i) friction levels;

(ii) nonlinear spring terms

(iii) linear spring terms;

(iv) damping terms; and

(v) miscellaneous gain terms

associated with the inner gimbal assembly and pressure loops. The necessary recorded signals are

(i) pressure loop electronic commands;

(ii) pressure loop output pressure;

(iii) inner-outer gimbal angle;

(iv) inner-outer gimbal angle rate (if available) and

(v) outer gimbal rate gyro output.

The following section describes the adaptive identification technique. In the next section the identification equations are presented. Simulation results are presented in the following section. The algorithm is summarized in Appendix C.

5.2 Adaptive Identification

Lyapunov-based designs of model-reference adaptive identification schemes are similar to the Lyapunov-based model-reference adaptive controllers described in Section 4. The primary differences are that

(i) no control signal, U, is generated for identification; and

(ii) the parameters in the model equations are adjustable.

Excellent references for adaptive identification are (8) and (12). This section describes the technique as applied to the inner gimbal assembly of Figure 3.1.

Figure 5.1 depicts a block diagram of the identification technique. In this figure the plant contains unknown parameters (to be identified) and the model contains adjustable parameters. Both the model and the plant receive the same inputs ("r" in Figure 5.1). The adaptive identification algorithm adjusts the model parameters until the error signal ("e" in Figure 5.1) goes to zero. At this point the model parameters are assumed to be equal to the (unknown) plant parameters. It can be shown that this will be the case if the input signal, r, is periodic and contains a sufficient number of frequencies. Additional details of this aspect are given in Section 5.3

With respect to the plant given in Figure 3.1, we assume that the parameters G2, G3, G4 and G7 and the parameters associated with F1S, F1C and C1 are unknown.

Since we are measuring the pressure input to the gimbal loops directly, we need not be concerned with the dynamics of the pressure loop as in the adaptive control case. This is due to the fact that no control signals are injected into the plant for identification purposes. Identification data is recorded as the system is operating with normal input signals.

The model used for identification is, in all practical respects, structured identically to the plant except that the parameters in the model are adjustable. The model gains are adjusted by the adaptive identification algorithm which is presented in the following section and summarized in Appendix C. During identification, we are assured by our choice of identification algorithms that the model parameters will asymptotically approach the same values as the corresponding plant parameters.

5.3 Identification Algorithm

In this section we present the equations that constitute the Lyapunov-based model-reference adaptive controller for the inner gimbal assembly shown in Figure 3.1. The algorithm, as derived, is summarized in Appendix C. As in the case of the adaptive controller, however, the final algorithm to be used on actual data will depend on several factors, including noise levels of the various signals, the characteristics of the system input signals and the severity of the system nonlinearities.

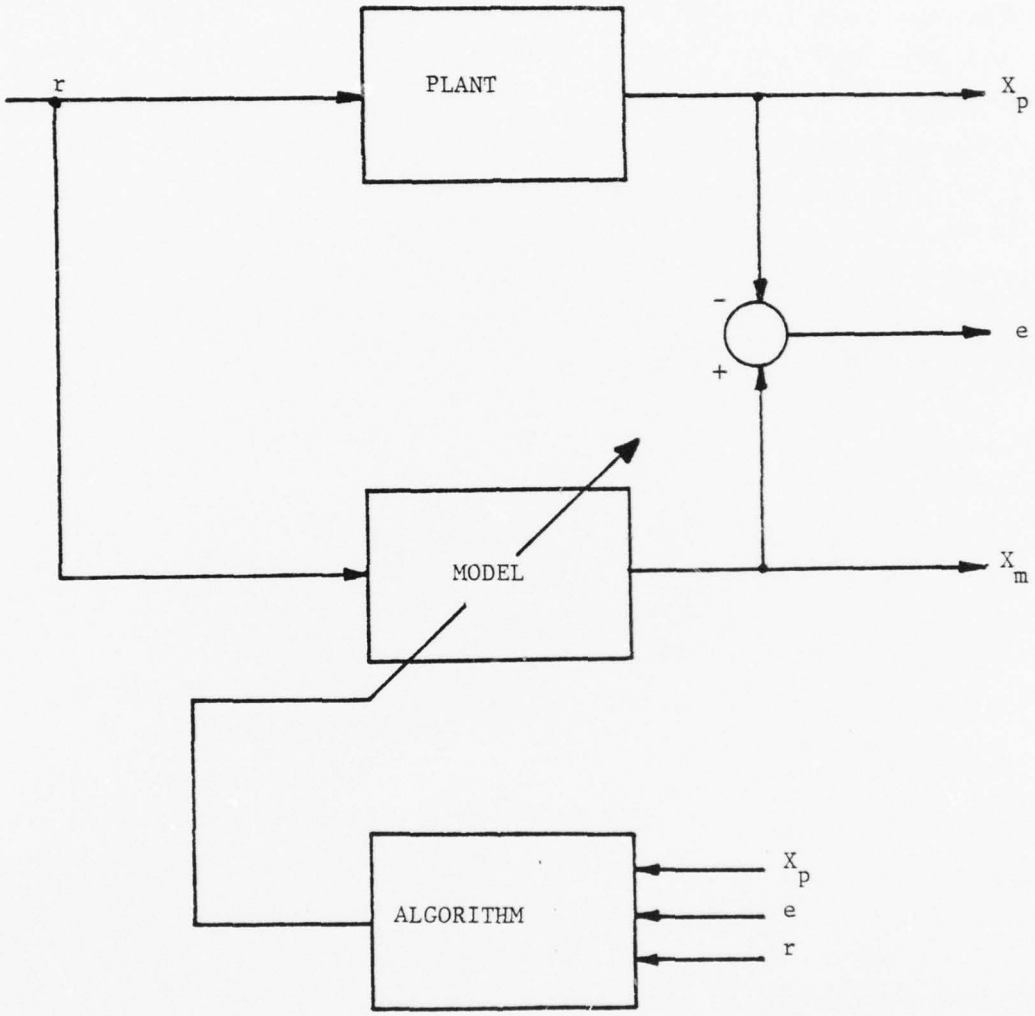

r = reference input

X_p = plant output

X_m = model output

e = error signal

Figure 5.1 Model Reference Adaptive Identification System

The model differential equation used for identification is somewhat more complex than the model used for control. This is primarily due to the fact that system nonlinearities appear in the identification model and not in the control model. The identification model is given by

$$\begin{pmatrix} \dot{EM1} \\ \dot{EM2} \end{pmatrix} = \left[\begin{pmatrix} 0 & 1 \\ -AN1 & -AN2 \end{pmatrix} - \begin{pmatrix} 0 & 1 \\ -AM1 & -AM2 \end{pmatrix} \right] \cdot \begin{pmatrix} EI \\ \dot{EI} \end{pmatrix}$$

$$+ \begin{pmatrix} 0 & 1 \\ -AM1 & -AM2 \end{pmatrix} \cdot \begin{pmatrix} EM1 \\ EM2 \end{pmatrix} + BM \begin{pmatrix} V6 \\ WO \\ W1 \end{pmatrix}$$

$$- CM \begin{pmatrix} F2 \\ C1S \end{pmatrix}$$

where

EM1, EM2 are the model state variables;
AN1, AN2 are adjustable gains;
BM, CM are adjustable matrices, defined below;
EI, $\dot{EI}$, V6, WO, and W1 are system signals as depicted in Figure 3.1
F2, C1S are defined below

The matrices BM and CM are of the form

$$BM = \begin{pmatrix} 0 & -1 & 0 \\ BM1 & 0 & BM2 \end{pmatrix}$$

$$CM = \begin{pmatrix} 0 & 0 \\ CM1 & CM2 \end{pmatrix}$$

The functions F2 and C1S are given as before by

$$F2 = \begin{cases} \text{Sign } (\dot{EI}) & \text{if } \dot{EI} \neq 0 \\ \text{Sign } (EM2) & \text{if } \dot{EI} = 0 \end{cases}$$

and

$$C1S = EI^3$$

As in Section 4.3, we define the error signal E as

$$E \triangleq \begin{pmatrix} E1 \\ E2 \end{pmatrix} \triangleq \begin{pmatrix} EM1 \\ EM2 \end{pmatrix} - \begin{pmatrix} EI \\ \dot{EI} \end{pmatrix}$$

Defining H1 as before,

$$H = P12 \cdot E1 + P22 \cdot E2$$

it can be shown that if we pick

$$\dot{AN1} = - GAM1 \cdot H1 \cdot EI$$
$$\dot{AN2} = - GAM2 \cdot H1 \cdot EI$$
$$\dot{BM1} = - GAM3 \cdot H1 \cdot V6$$
$$\dot{CM1} = - GAM5 \cdot H1 \cdot F2$$
$$\dot{CM2} = - GAM6 \cdot H1 \cdot CS1$$

then we are assured that the error term, E, will tend asymptotically to zero (initial conditions for AN1, AN2, BM1, BM2, CM1 and CM2 are chosen to be the designers best a-priori guess of the quantities G3, G4, G2, G7, Coloumb friction level, and C5, respectively). The intent is to drive the adjustable model parameters to the value of the unknown plant parameters and not necessarily to drive E to zero in the identification scheme. It may be shown that if the signals V1, W0, and W1 are periodic and linearly independent over the interval (0,00) then the adjustable parameters AN1, AN2, BM1, BM2, CM1, and CM2 will converge to G3, G4, G2, G7, Coloumb friction level and C5 respectively (refer to (12)).

The algorithm is summarized in Appendix C.

5.4 Simulation Results

In this section we present a typical parameter identification result. Figures 5.2, 5.3 and 5.4 depict the time histories of

D1 $\triangleq$ AN1 -G3

D2 $\triangleq$ AN2 -G4

D3 $\triangleq$ BM1 - pressure loop gain

(note that we are using BM1 to identify the entire pressure loop gain and not just G2 in this simulation - the pressure loop gain is assumed to be

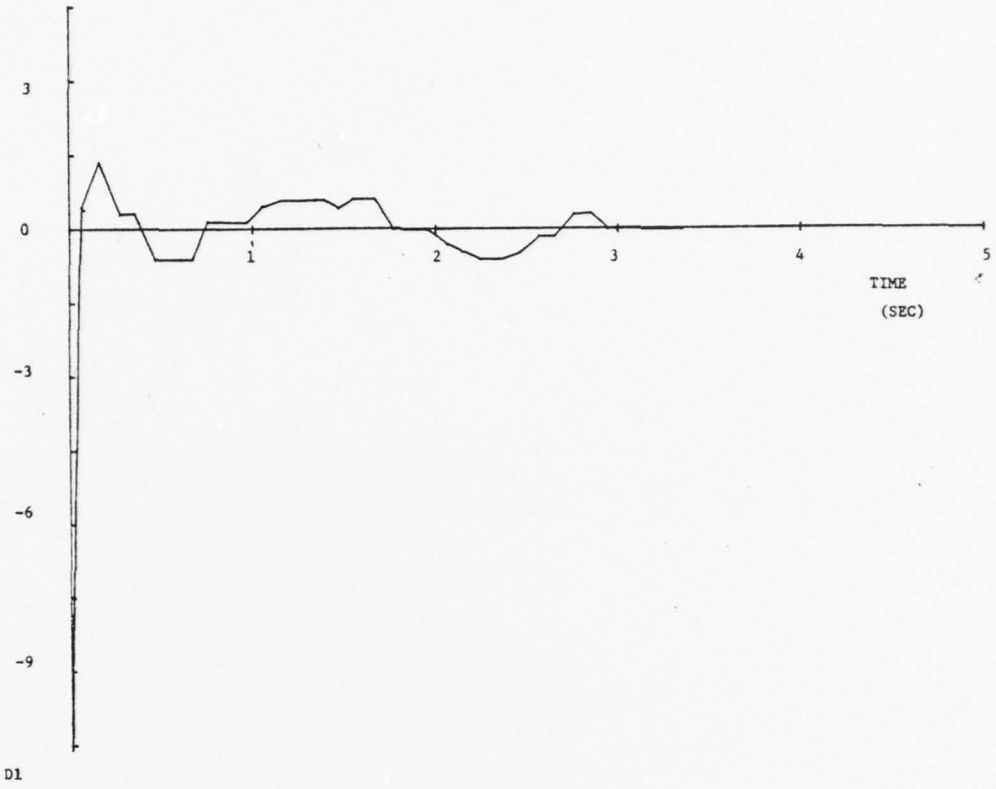

Figure 5.2 Error in G3 Estimate

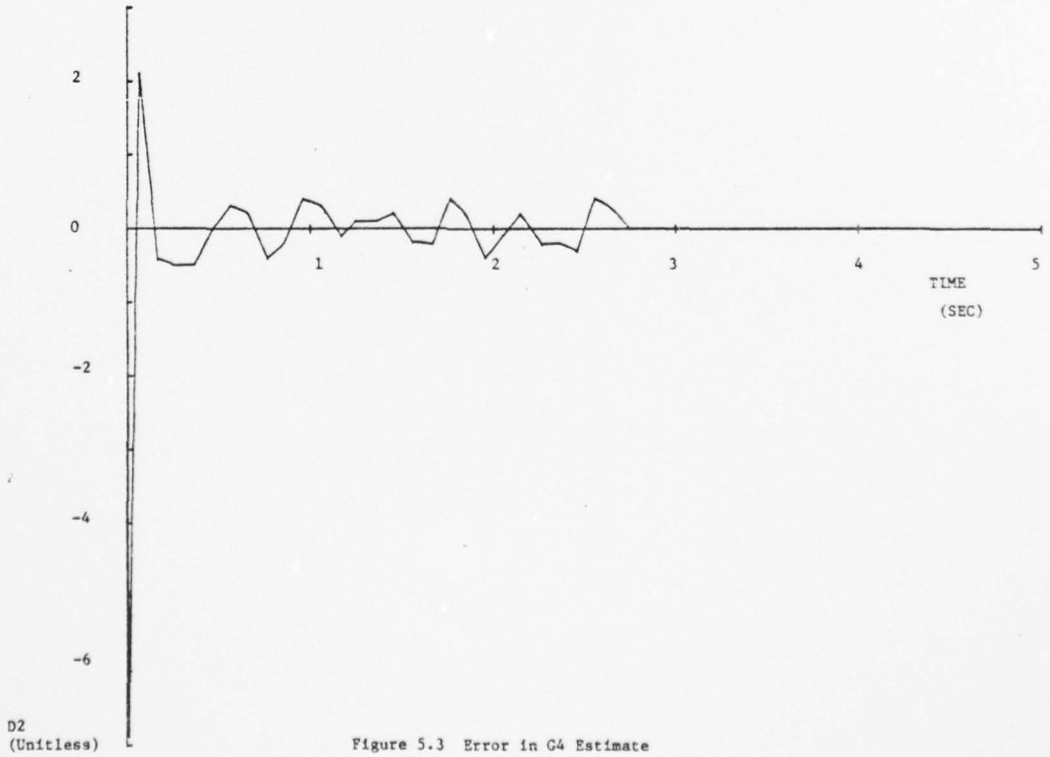

Figure 5.3 Error in G4 Estimate

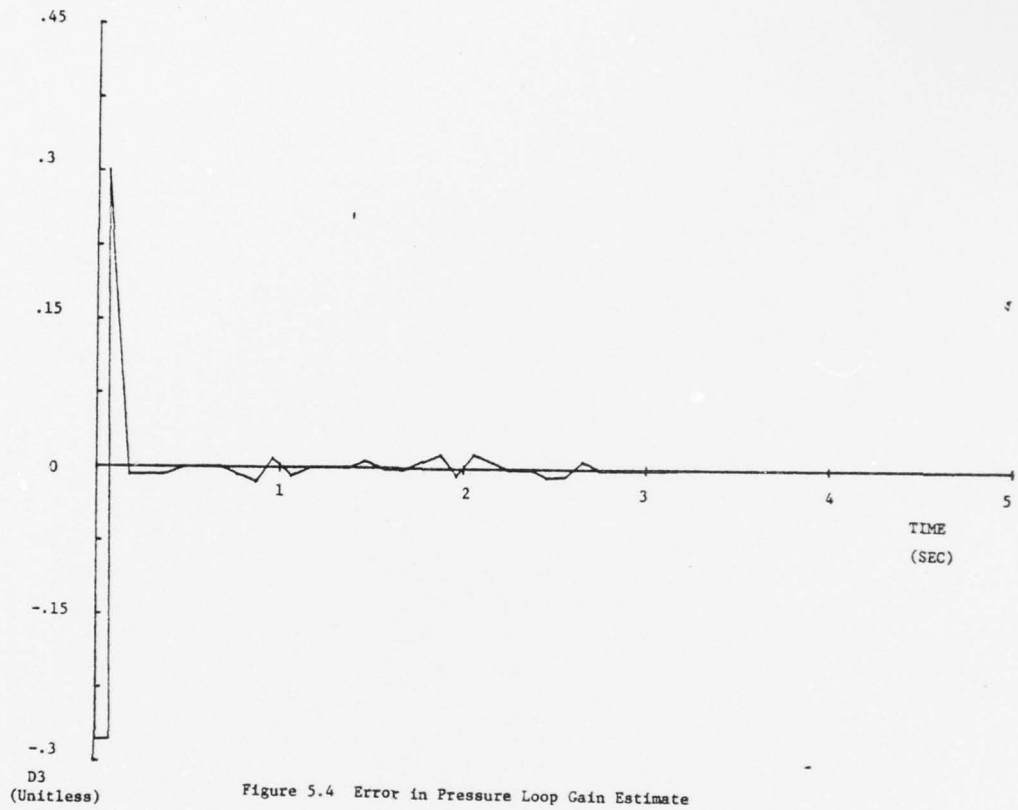

Figure 5.4 Error in Pressure Loop Gain Estimate

unity for simulation purposes). In these figures we are using the algorithm of Appendix C to identify the parameters G3, G4 and the pressure loop gain. System inputs are given by

$$V1 = 0.1 \sin(1.1255t) + 0.3 \cos(18.81t)$$

$$W\emptyset = 0.$$

$$W1 = 0.$$

Since the terms D1, D2 and D3 represent identification errors, it may be concluded that the algorithm identified these three parameters in less than five seconds.

REFERENCES

1. Crothers, K. D. and Thune, R. L. "Final Peformance Data After Cycle IIB of the APT Servos," Report No. 734420.1/033, 19 August 1976.

2. Gilbart, J. W., Monopoli, R. V., and Winston, G. C. Combination Open Loop, Closed Loop, and Adaptive Compensation: Its Application to an Optical Tracking System, Proc. 1972 Int. Conf. Cybernetics and Society, Washington, D. C., October 1972.

3. Gilbart, J. W. and Winston, G. C. Adaptive Compensation for an Optical Telescope, Automatica, April 1974.

4. Gutmann, R. L. and Monopoli, R. V., "Adaptive Control of a Laser Tracking System: A Feasibility Study," Applied Technology Associates Memo No. ATA-R-5. Albuquerque, NM, July 1978.

5. Hahn, W. Stability of Motion, Springer-Verlag, New York, 1967.

6. Hughes Aircraft Co. "Operation and Maintenance Handbook Airborne Pointing and Tracking System Volume I," Report No. P73-1, HAC Ref No. C-5945.

7. Kessler, F. M., Jr. "Design of Adaptive Control for Systems with Measurement Noise," M. Sc. Thesis, University of Massachusetts, Amherst, May 77.

8. Landau, I. D. A Survey of Model Reference Adaptive Techniques, Theory and Applications, Automatica, July 1974.

9. Monopoli, R. V. Model Reference Adaptive Control with an Augmented Error Signal, IEEE Trans. Auto. Control, Vol. AC-19, 1974.

10. On Model Reference Adaptive Control Systems, Proc. 1977 Allerton Conf on Circuit and System Theory, October 1977.

11. Monopoli, R. V. and Kessler, F. M., Jr. Measurement Noise in Model Reference Adaptive Systems, Proc. 1977 Joint Auto. Control Conf., San Francisco, CA

12. Narendra, K. S. and Kudva, P. Stable Adaptive Schemes for System Identification and Control--Parts I and II, IEEE Trans. on Syst., Man. and Cybernetics, Vol. SMC-4, No. 6, November 1974.

13. Reed, R. M. "Digital Implementation of a Lyapunov Designed Model Reference Adaptive Controller," M.S. Thesis, University of Massachusetts, Amherst, 1977.

14. Sciabarrasi, J. E. and Monopoli, R. V. A Real Time, Lyapunov Designed, Adaptive Controller, NASA Grant NGL-22-010-018 Report No. 75-2, 1975.

APPENDIX A

SIMMULATION PROGRAM

The simulation results presented in this report were obtained using an integration routine known as MIMIC. A sample adaptive identification program is presented below. This program was used to generate the plots shown in Section 4. Only slight modifications were made to generate the plots of Section 5.

```
MIMIC (VERS 3.4 01/25/75 MOD 01)    07/05/76  13.07.57.

 ***MIMIC SOURCE-LANGUAGE PROGRAM***
$LIST
$TERMINAL IV
$ABSERR
$PLOT PRINTER
                    CON(G1,G2,G3,G4,G5,G6)
                    CON(R11,Z1,P1,R22,P2)
                    CON(W1,G7,G8,CPL,SPL)
                    CON(DBL,A1,A2,E1,P12,P22)
                    CON(GAM11,GAM12,GAM21,GAM22,GAM31)
                    CON(GAM32,GAM41,GAM42)
                    CON(GAM51,GAM52,N1,N2)
                    PAR(FACT)
          DTMIN     = .0004
          V0        = 0.05*COS(1.2566*T)
          V0        = 0.1*COS(1.256*T)
          V1        = INT(V0,0.)
          V2        = G1*V1
          V3        = V2+G6*E1-V6+G7*P2-G*G1
          V4        = (R11*Z1/P1)*V3+R11*(1.-Z1/P1)*PTR(V3,P1)
          V5        = V4-G5*E1D
          V6        = R22*PTR(V5,P2)
          V7        = G2*V6
          V8        = V7-G4*E1D-G3*E1
          DBND      = PSW(ABS(E1D)-DBL,TRUE,TRUE,FALSE)
          SPLZ      = PSW(ABS(V8)-SPL,TRUE,TRUE,FALSE)
          STAT      = AND(DBND,SPLZ)
          COUL      = NOT(STAT)
 COUL     P1        = PSW(E1D,-CPL,0.,CPL)
 STAT     P1        = V8
          NBND      = NOT(DBND)
 NBND     P2        = PSW(E1D,-CPL,0.,CPL)
 DBND     P2        = PSW(E1D,-CPL,0.,CPL)
 NBND     P3        = 0.
 DBND     P3        = PSW(E1D,-CPL,0.,CPL)
          E1DD      = V8-G6*P1
          V9        = INT(E1DD,0.)
          E1D       = V9-V0
          P1        = INT(E1D,0.)
          EMDD      = -A1*E1D-A2*E1+V1*P1
          X9        = INT(EMDD,0.)
```

```
      EMU    = X9-X0
      EM     = INT(EMU,0.)
      E      = EM-E1
      EU     = EMU-E1U
      E1     = P12*E+P22*EU
      U1     = E1*E1U*FACT
      U2     = E1*E1*FACT
      U3     = E1*V1*FACT
      U4     = E1*F2*FACT
      U5     = E1*F3*FACT
      PP1    = GAM11*U1
      IP1    = INT(GAM12*U1,45.)
      PP2    = GAM21*U2
      IP2    = INT(GAM22*U2,290.)
      PP3    = GAM31*U3
      IP3    = INT(GAM32*U3,1.)
      PP4    = GAM41*U4
      IP4    = INT(GAM42*U4,1.5)
      PP5    = GAM51*U5
      IP5    = INT(GAM52*U5,0.)
      K1     = -(PP1+IP1)
      K2     = -(PP2+IP2)
      K3     = -(PP3+IP3)
      K4     = -(PP4+IP4)
      K5     = -(PP5+IP5)
      U      = K1*E1U+K2*E1+K3*V1+K4*F2+K5*F3
      P1     = INT(E*E,0.)
             PIN(1,.99)
             UUI(1,V1,V7,V8,E1U,E1)
             UUI( ,EM,E,EU,P1,EMU)
             UUI( ,K1,K2,K3,K4,X0)
             UUI( ,P1,P2,P3,V9,X9)
             UUI( , )
             PLU(1,E1,E,FACT)
             TIP(FLOW GAINS TAU INPUTS)
             TTX(TIME IN SECONDS)
             PLU(1,E,EU)
             PLU(1,K1,PP1,IP1)
             PLU(1,K2,PP2,IP2)
             PLU(1,K3,PP3,IP3)
             PLU(1,K4,PP4,IP4)
             END
```

APPENDIX B

ADAPTIVE CONTROL ALGORITHMS

The following equations summarize the six gain, three input adaptive controller derived in Section 4. The other (simpler) adaptive controllers are obtained by deleting gain terms from the controller presented here. If WØ is not an input to the gimbal system (outer gimbal planned) then WØ should also be removed from the $\dot{EM1}$ equation, below.

MODEL:

$$\dot{EM1} = EM2 - W\emptyset$$

$$\dot{EM2} = -36 \cdot EM1 - 12 \cdot EM2 + 1 \cdot V1$$

ERRORS:

$$E1 = EM1 - FI$$

$$E2 = EM2 - \dot{FI}$$

GAINS:

$$H1 = 5.6 \times 10^{7}\ E1 + 1.72 \times 10^{8}\ E2$$

$$\dot{K1} = -0.5 \cdot H1 \cdot EI$$

$$\dot{K2} = -0.5 \cdot H1 \cdot F\dot{I}$$

$$\dot{K3} = -1.6 \times 10^{-4} \cdot H1 \cdot V1$$

$$\dot{K4} = -4.5 \times 10^{-4} \cdot H1 \cdot W1$$

$$\dot{K5} = -5. \times 10^{-4} \cdot H1 \cdot F2$$

$$\dot{K6} = -5. \times 10^{-4} \cdot H1 \cdot CS1$$

Where

$$F2 = \begin{cases} 0.2\ \text{sign}\ (EI) & \text{if } EI \neq 0 \\ 0.4\ \text{sign}\ (EM2) & \text{if } EI = 0 \end{cases}$$

$$CS1 = EI^{3}$$

INITIAL CONDITIONS:

$K1_o$ best guess of -(G3 - 36.)

$K2_o$ best guess of - (G4 - 12.)

$K3_o$ best guess of - (pressure loop gain - 1)

$K4_o$ best guess of - (G7)

$K5_o$ best guess of - (Coloumb friction level)

$K6_o$ best guess of -(CS)

CONTROLLER:

$$U = (K1 \cdot EI + K2 \cdot \dot{EI} + K3 \cdot V1 + K4 \cdot W1 + K5 \cdot F2 + K6 \cdot (CS1) \cdot 178.57$$

The numerical values of the model parameters and various gains are subject to adjustment as test data is obtained.

APPENDIX C
IDENTIFICATION ALGORITHM

The following summarizes the six parameter identification algorithm derived in Section 5.

MODEL:

$$\dot{EM1} = EM2 - W\emptyset$$

$$\dot{EM2} = -(AN1-36)\cdot EI-(AN2-12)\cdot \dot{EI} -36\cdot EM1-12\cdot EM2 + BM1\cdot V1 +BM2\cdot W1 - CM1\cdot F2 - CM2\cdot CS1$$

where

$$F2 = \begin{cases} 0.2 \cdot \text{sign}(\dot{EI}) & \text{if } \dot{EI} \neq 0 \\ 0.4 \cdot \text{sign}(EM2) & \text{if } \dot{EI} = 0 \end{cases}$$

$$CS1 = EI^3$$

ERRORS:

$$E1 = EM1 - EI$$

$$E2 = EM2 - \dot{EI}$$

PARAMETERS:

$$J1 = 5.6 \times 10^7 \cdot E1 + 1.72 \times 10^8 \cdot E2$$

$$\dot{AN1} = -J1\cdot EI\cdot 333.33$$

$$\dot{AN2} = -J1\cdot \dot{EI}\cdot 163.333$$

$$\dot{BM1} = J1\cdot V1\cdot 0.225$$

$$\dot{BM2} = J1\cdot W1\cdot 0.225$$

$$\dot{CM1} = -J1\cdot F2 \cdot 5 \times 10^{-4}$$

$$\dot{CM2} = -J1\cdot CS2 \cdot 5 \times 10^{-4}$$

INITIAL VALUES:

$AN1_o$ best guess of G3

$AN2_o$ best guess of G4

$AN3_o$ best guess of G2

$AN4_o$ best guess of G7

$AN5_o$ best guess of Coloumb friction level

$AN6_o$ best guess of CS

1978 USAF-ASEE SUMMER FACULTY RESEARCH PROGRAM
Sponsored by
THE AIR FORCE OFFICE OF SCIENTIFIC RESEARCH
Conducted by
AUBURN UNIVERSITY AND OHIO STATE UNIVERSITY

PARTICIPANT'S FINAL REPORT

NONLINEAR ADAPTIVE OPTICS

Prepared by:	Donald C. Haueisen, Ph. D.
Academic Rank:	Assistant Professor
Department and University:	Department of Physics and Engineering Pacific Lutheran University
Assignment:	Kirtland AFB Air Force Weapons Laboratory Advanced Laser Technology Advanced Laser Optics
USAF Research Colleague:	David A. Depatie, Ph. D.
Date:	August 11, 1978
Contract No.:	F44620-75-C-0031

NONLINEAR ADAPTIVE OPTICS

by
Donald C. Haueisen

ABSTRACT

The generation of a phase conjugate wave at 10μ through the third order nonlinear interaction of degenerate, four wave mixing has been investigated experimentally. Conjugate waves have been observed in germanium and, for the first time, in molecular gases.

Using a TEA CO_2 laser, a conversion efficiency of 3% has been observed in germanium. The nonlinear susceptibility has been calculated to be 2×10^{-9} esu.

Conjugate wave generation in NH_3 has been measured as a function of pressure for several of the CO_2 laser lines. In CCl_2F_2, a resonant effect in the nonlinear susceptibility has been observed by varying the laser frequency in the region of a sharp molecular absorption edge. And in NF_3, 0.1% conjugate wave conversion efficiency has been obtained. The value of the nonlinear susceptibility for the molecular gas measurements was on the order of 10^{-10} esu.

These experiments demonstrate the feasibility of measureable conjugate wave generation in molecular gases at 10μ and indicate directions for future experimental and theoretical study.

ACKNOWLEDGEMENT

It is a pleasure to acknowledge the help and support of the ALO staff throughout the course of this study, and particularly that of Dave Depatie who was especially responsible for making this a productive and very enjoyable experience.

Thanks are also due to AFOSR and ASEE for sponsoring this program under the capable administration of Mr. J. Fred O'Brien and Auburn University.

I. INTRODUCTION

Propagation of an optical beam through an inhomogeneous medium, such as the atmosphere, results in distortion of the optical wavefronts and degredation of the beam quality. This wavefront distortion can lead to severe limitations on the extent over which an originally collimated optical beam, such as a laser beam, can be propagated, and of the ability to focus that beam onto some target.

One means of compensation for laser beam distortion due to propagation through an inhomogenous medium is that known as nonlinear adaptive optics.[1] This scheme makes use of a phase conjugate wave generated through a nonlinear interaction in an appropriate material. The phase conjugate wave is a time-reversed replica of a given wave, and will therefore "undo" all distortion encountered by that given wave. The process which makes use of this phase conjugate property to compensate for distortion is outlined in Figure 1. In (A), an originally well defined probe beam is propagated backward through the inhomogeneous medium. For this now distorted probe beam, a phase conjugate or time-reversed wave is generated, which in (B) propagates through the medium in the forward direction and emerges as a, once again, well defined beam. To deliver appreciable power in the forward direction, amplification of the phase conjugate wave can be done without necessarily limiting the distortion compensation. This amplification may even take place in the nonlinear interaction itself under appropriate conditions.

The nonlinear interaction most readily used to generate a conjugate wave, and that with which the present study is concerned, is degenerate, four

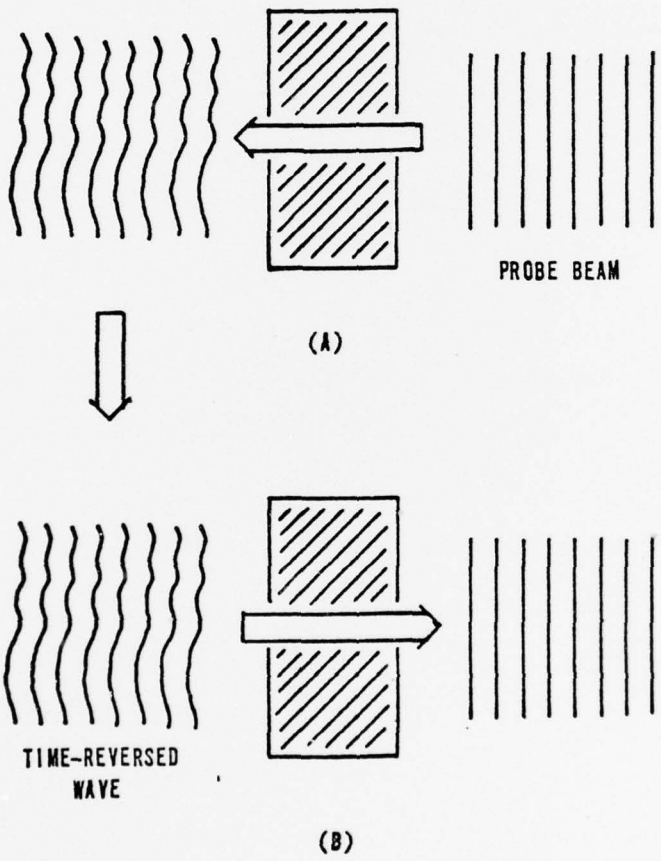

Figure 1. Wavefront distortion due to propagation through an inhomogeneous medium can be compensated by (A) allowing a probe beam to propagate backward through the distorting medium and then (B) generating a time-reversed replica of the distorted probe which propagates in the forward direction.

wave mixing,[2,3] a process derived from the third order electric susceptibility. To obtain a conjugate wave, the mixing is done with two strong counter-propagating pump beams, which themselves are phase conjugate waves, and a weak input object wave, all of which are of the same frequency and overlapping in the nonlinear material. An output image wave, the phase conjugate of the object wave, is then produced in the nonlinear mixing. The geometry of the process is depicted in Figure 4 where waves are shown spatially separated only for clarity.

This third order nonlinear interaction removes photons from the pump beams and adds them to the object and image waves. Because the mixing is degenerate with all frequencies equal, and assuming an isotropic medium, the total momentum of two photons taken from the pump beams, one photon from each, is equal to the total momentum added to the object and image waves, again one photon to each, being exactly zero in both cases. Hence, photon momentum is conserved and the process is phase-matched for all angles of object and image waves relative to the pumping direction. An equivalent statement is made by simply noting that for a degenerate process in an isotropic medium, all phase velocities are equal. This inherent phase-matched property of degenerate, four wave mixing, can be a considerable advantage over certain other nonlinear processes, particularly three wave mixing.

A number of degenerate, four wave mixing experiments have been reported. These include mixing in CS_2 with a frequency doubled, pulsed Nd:YAG laser at 5320Å,[4] and with a pulsed ruby laser at 6943Å,[5,6] as well as a CW experiment in sodium vapor using a dye laser around 5900Å.[7]

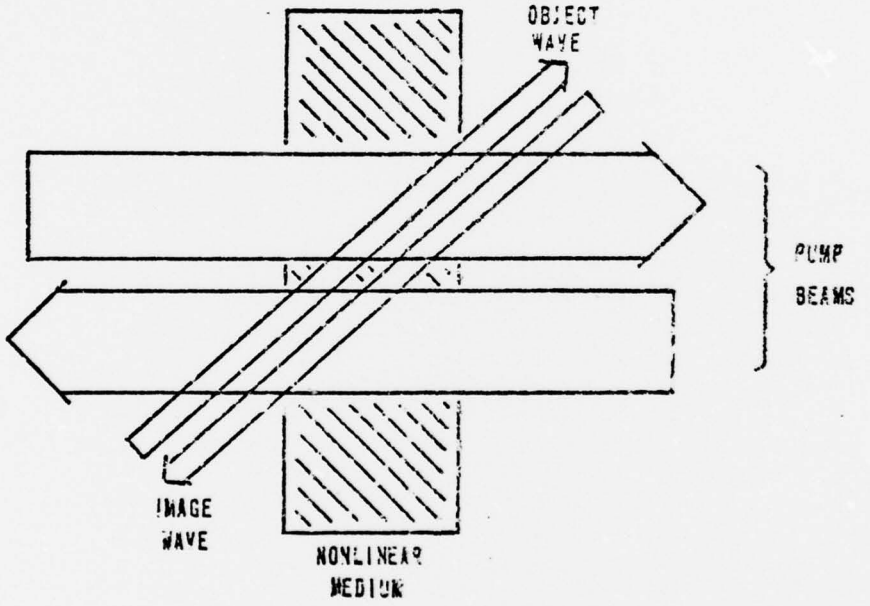

Figure 2. Conjugate wave generation through degenerate four wave mixing is done with two strong counter-propagating pump beams and an input object wave, all of the same frequency and overlapping in the nonlinear medium. The image wave, phase conjugate to the object wave, is generated by the four wave mixing process.

Other conjugate wave generation experiments have been done, using three wave mixing in a lithium formate crystal,[8] with stimulated Brillouin scattering,[9-11] and stimulated Raman scattering.[12]

II. THEORETICAL OUTLINE

The phase conjugate wave has the property that its complex amplitude is everywhere the complex conjugate of the given wave. With this given wave described by a scalar electric field

$$E(\bar{r},t) = E(\bar{r})e^{-i\omega t} + E^{*}(\bar{r})e^{i\omega t} \tag{1}$$

the conjugate wave, according to the above, is given by

$$E_{conj}(\bar{r},t) = E^{*}(\bar{r})e^{-i\omega t} + E(\bar{r})e^{i\omega t} \tag{2}$$

and it is clear that $E_{conj}(\bar{r},t)$ is just $E(\bar{r},-t)$, making explicit the time-reversed nature of the conjugate wave.

The four wave mixing interaction is described by the third order electric susceptibility, $\chi^{(3)}$, a third rank tensor, defined by the relation

$$\bar{P}^{(NL)} = \chi^{(3)}\bar{E}_1\bar{E}_2\bar{E}_3 \tag{3}$$

where $\bar{P}^{(NL)}$ is the nonlinear polarization resulting from the mixing of the three applied electric fields $\bar{E}_{1,2,3}$. For conjugate wave generation through degenerate mixing, $\bar{E}_{1,2}$ are taken as the counter-propagating pump waves, having the form

$$E_p e^{i(\pm kx-\omega t)} + E_p e^{i(\mp kx-\omega t)} \tag{4}$$

where E_p can be taken as a real quantity. $\bar{E}_3$ is the object wave, assumed to have the form of (1), namely

$$E_o(\bar{r})e^{-i\omega t} + E_o^*(\bar{r})e^{i\omega t} \tag{5}$$

Using (4) and (5) in (3) results in terms in $\bar{P}^{(NL)}$ at frequencies $\pm\omega$ and $\pm 3\omega$. The component at ω , corresponding to degenerate mixing is given by

$$P_i^{(NL)}(\omega) = \chi_{ijkl}^{(3)}(\omega = \omega+\omega-\omega)\, E_{p,j}e^{i(kx-\omega t)}E_{p,k}e^{i(-kx-\omega t)}E_{o,l}^*(\bar{r})e^{i\omega t}$$

$$= \chi_{ijkl}^{(3)}(\omega=\omega+\omega-\omega)E_{p,j}E_{p,k}E_{o,l}^*(\bar{r})e^{-i\omega t} \tag{6}$$

where the subscripts refer to polarization directions. Note that $P^{(NL)}(\omega)$ carries the phase information of the object wave, but as the conjugate wave given in (2).

Now using Maxwell's wave equation with the nonlinear source term of (6)

$$\nabla^2 E - \frac{n^2}{c^2}\frac{\partial^2 E}{\partial t^2} = \frac{4\pi}{c^2}\frac{\partial^2 P^{(NL)}}{\partial t^2} \tag{7}$$

the wave equation reduces to

$$\nabla^2 E(\bar{r}) + \frac{n^2\omega^2}{c^2}E(\bar{r}) = -\frac{4\pi\omega^2}{c^2}\chi^{(3)}(\omega)\, E_p^2 E_o^*(\bar{r}) \tag{8}$$

This equation can be solved for each plane wave component of $E(\bar{r})$ and $E_o^*(\bar{r})$. If the change in amplitude of each component of $E(\bar{r})$ is small on the scale of a wavelength, if the pump waves are not depleted so that E_p can be taken to be constant, and if the generated wave $E(\bar{r})$ is small

compared to $E_o(\bar{r})$, an approximate solution to (8) is given by

$$E(\bar{r}) = i \frac{2\pi\omega}{cn} \chi^{(3)}(\omega) E_p^2 L E_o^*(\bar{r}) \tag{9}$$

where L is the dimension of the pumped region perpendicular to the direction of propagation of the object wave, $E_o(\bar{r})$. A further assumption has been made that all plane wave components of $E_o^*(\bar{r})$ interact with the pumped region over the same distance L. Also (9) only applies to the generated wave in the region beyond the nonlinear interaction.

In (9) it can be seen that the nonlinearly generated wave $E(\bar{r})$ bears the phase conjugate relationship to the object wave with an amplitude that depends on the pump intensity, the object wave intensity and the interaction length as well as the nonlinear susceptibility. Phase-matching has been used in obtaining (9) in the assumption that the plane wave components of $E(\bar{r})$ and $E_o^*(\bar{r})$ have wave vectors of equal magnitude.

In terms of intensities, (9) becomes

$$I = \left(\frac{4\pi}{cn}\right)^4 \omega^2 \left|\chi^{(3)}(\omega)\right|^2 L^2 I_p^2 I_o \tag{10}$$

where intensity is related to electric field by $I = (cn/8\pi) E^2$.

The nonlinear susceptibility $\chi^{(3)}(\omega = \omega+\omega-\omega)$ derived quantum mechanically with perturbation theory contains terms of the form[13]

$$N\hbar^{-3} \sum_{ijk} \frac{\mu_{gk}\,\mu_{kj}\,\mu_{ji}\,\mu_{ig}}{(\omega_{kg}-\omega-i\,\Gamma_{kg}/2)\,(\omega_{jg}-2\omega-i\Gamma_{jg}/2)\,(\omega_{ig}-\omega-i\Gamma_{ig}/2)} \tag{11}$$

where N is the density of atoms or molecules, i, j, k, run over the energy eigenstates of the system, g is the ground state, $\hbar\omega_{ig}$ is the

energy of the $i^{\underline{th}}$ level above the ground state, and Γ_{ig} is the linewidth of the $i \rightarrow g$ transition. In most gaseous systems, the sum over ijk is dominated by a relatively small number of terms for which the denominator is small. In the case that ω is equal or nearly equal to an allowed transition frequency from the ground state (one photon resonant), or when 2ω approaches an allowed transition (two photon resonant), $\chi^{(3)}$ becomes resonantly enhanced.

In the case of a molecular system with one molecular vibration frequency nearly matched to the applied frequency, both one photon resonance and two photon resonance will occur due to the nearly equal spacing of vibrational energy levels. In such a case, all three factors in the denominator of (11) become small and very substantial enhancement of $\chi^{(3)}$ is possible. Although exact resonance is restricted by resonant absorption, enhancement by a factor of at least 10^5 can be expected with much larger factors theoretically possible. In practice, these large enhancement factors probably mean that phase conjugation in molecular systems will only be observed under near resonant conditions.

III GERMANIUM EXPERIMENTS

To become familiar with equipment, experimental procedures and problems, preliminary experiments involved degenerate, four wave mixing at 10.6μ in germanium. One such experiment has been done very recently at Los Alamos Scientific Laboratory.[14] This experiment has been successfully repeated at AFWL and the experimental set-up used at AFWL is shown in Figure 3. A Lumonics Model 103 TEA CO_2 laser provided the source of

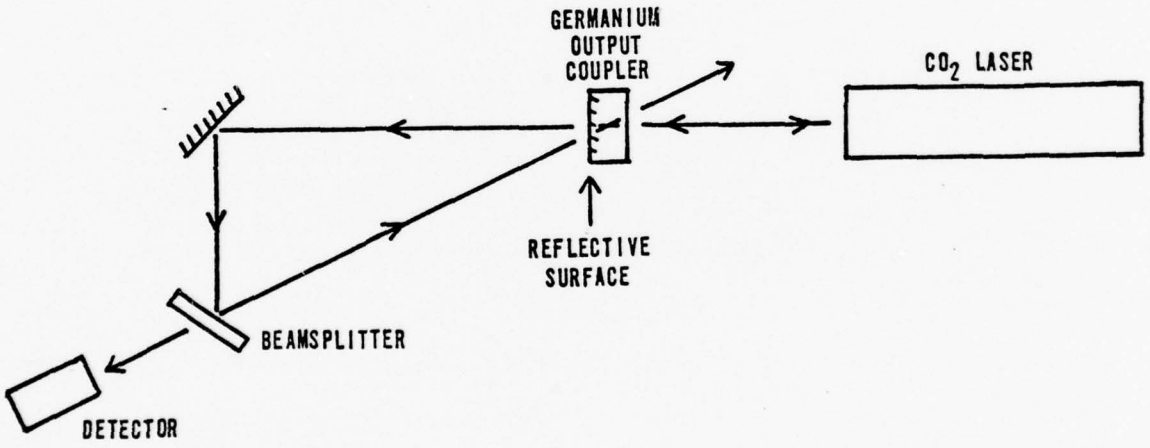

Figure 3. Geometry used to observe conjugate wave generation at 10.6μ in germanium with the inverted output coupler of a TEA CO_2 laser.

radiation at 10.6μ. The laser was operated without nitrogen to eliminate the long tail in the output pulse and delivered up to 0.5j, depending on the output coupler, in a 200 ns pulse with a beam size of about 7mm. In this first experiment, an 8.5%T germanium output coupler was mounted external to the laser plasma tube, and in an inverted configuration with the 1 cm germanium substrate inside the cavity. The internal laser oscillation then provided the counter-propagating pump beams for the germanium. The output of the laser was then directed back through the germanium with a beamsplitter. The conjugate image wave was detected behind this same beamsplitter with a Molectron P4-70 pyroelectric detector, the output of which was read directly from an oscilloscope trace. Shot to shot variation in the mode structure of the CO_2 laser led to substantial variation in the observed output. Signal levels reported are a visual average of the largest signals observed and carry an uncertainty of probably 25%. In this first germanium experiment, with a laser output of 500 kW, the image wave was observed to be about 3% of the object wave.

A similar experiment was done with a separate piece of AR coated germanium inside the laser cavity. A 35%T output coupler was used, giving a laser output of 600 kW with the 3.15cm germanium slab inserted into the cavity. The object wave intensity in this case was about 1.1 kW. Using (10), the third order susceptibility was determined to be about 2×10^{-9} esu. This is in very reasonable agreement with previous similar measurements.[15]

One interesting demonstration was done using conjugate wave generation in germanium. In this experiment, the object wave was diverged with a lens before reflecting from the beam splitter and entering the germanium. The beam characteristics of the emerging image wave were then investigated, and the beam was found to refocus, coming to a minimum width with maximum intensity at a location consistent with the focal length of the lens used to diverge the image wave. This expeirment gives direct confirmation and a very clear demonstration of the time-reversed nature of the nonlinearly generated phase conjugate wave.

In one other expeirment with the 3.15cm intracivity AR coated germanium, the input object wave was omitted and a low loss optical cavity constructed with its axis intersecting the pumped region of the germanium, as shown is Figure 4. In this configuration, with sufficient parametric gain in the pumped region of the germanium, oscillation within the second cavity can be established. Oscillation is initiated by surface as well as spontaneous parametric scattering and is maintained by amplification through the four wave mixing process. Transmission through one of the cavity reflectors provides oscillator output and means of detection. In this experiment, there was evidence of oscillation although it was not entirely conclusive. With a laser cavity power of 4MW, a well collimated output was observed which depended very critically on alignment of the oscillator cavity mirrors, but which, however, lacked a clearly defined threshold. Calculations indicated that parametric oscillation should have been possible, but losses in the oscillator cav-

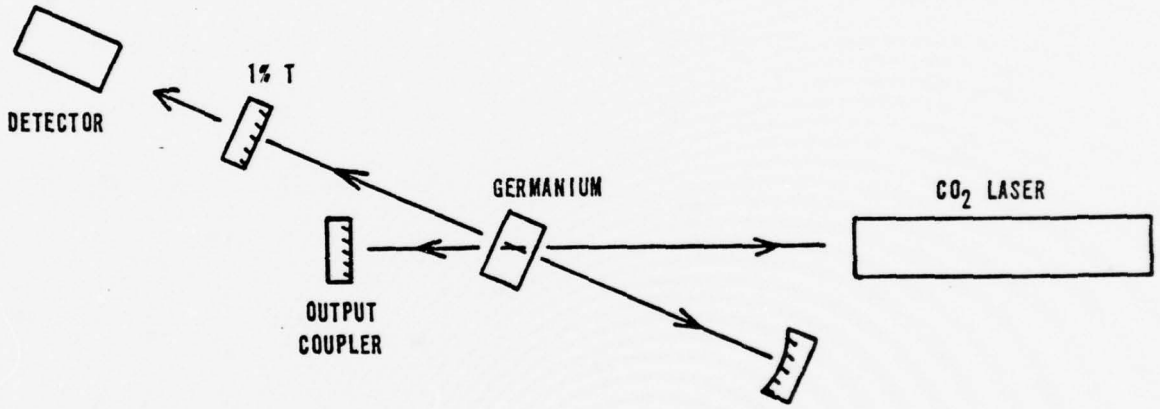

Figure 4. Schematic for a degenerate, parametric oscillator at 10.6μ using four wave mixing in germanium.

ity due to absorption in the germanium and degradation of the germanium AR coating, which were not taken into account, may have been substantial and prevented oscillation. Laser output was considerably reduced with insertion of the germanium into the laser cavity, indicating absorptive loss, and surface damage to the germanium was evident after several shots even at moderate power levels.

Conjugate wave generation was attempted with two other materials. A signal comparable to that observed with germanium was seen using a 5cm long AR coated GaAs single crystal. But in a 6.4mm sample of ZnSe, no conjugate wave generation was observable.

IV MOLECULAR GAS EXPERIMENTS

Conjugate wave generation experiments were carried out in a number of molecular gases with absorption bands in the vicinity of the CO_2 laser frequencies. The proximity of vibrational transitions and molecular absorption to the laser frequency leads to enhancement of the nonlinear susceptibility through the resonant denominators of (11).

The experimental set-up used for these experiments is shown in Figure 5. A 35cm gas cell with AR coated ZnSe windows was placed intracavity in the CO_2 laser, which was again operated without nitrogen. A 50%T output coupler was used to keep intracavity intensities low and prevent damage to the ZnSe AR coatings. With the cell filled with air, or evacuated, the laser output was typically 2 MW. With a beamsplitter and mirror arrangement, one half of this output was directed back through the cell, making an angle of about 3^0 with the intracavity beam direction. Because of the relatively small angle, the detector was placed at a distance of about 1m from the beamsplitter with two intervening apertures to reduce the strong background signal resulting from looking with the detector nearly down the CO_2 plasma tube. This background signal was reduced to a level equivalent to an image wave intensity equal to about 10^{-5} of that of the object wave. No thorough attempt was made to optimize the positions of the apertures and detector so that the measured signals give lower limits to the conjugate wave conversion efficiency rather than absolute values.

Measurements were made in several gases, both as a function of

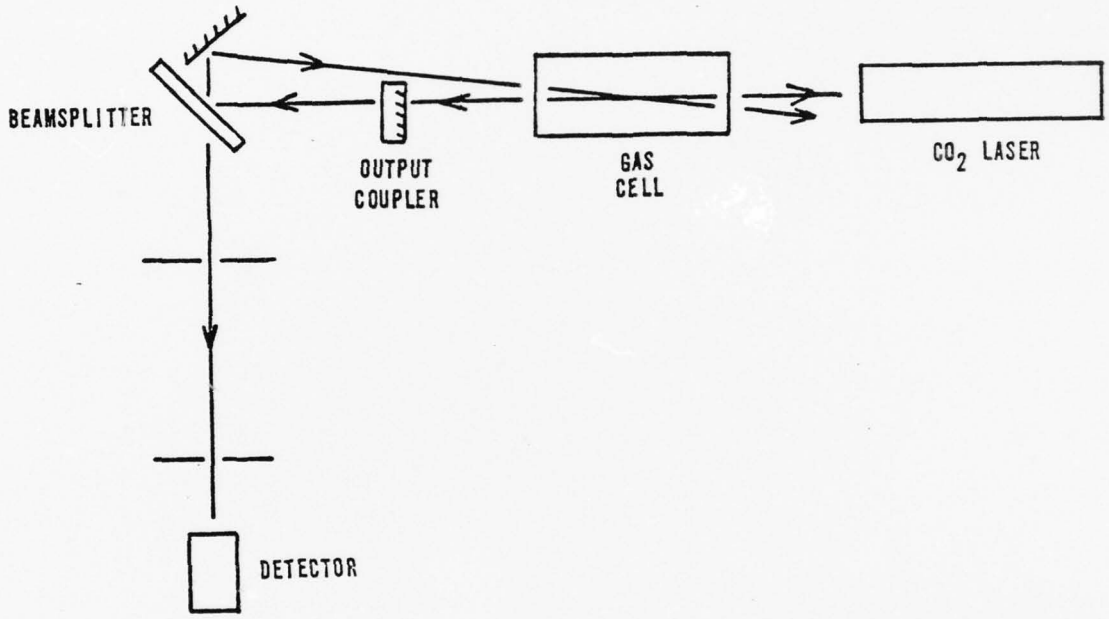

Figure 5. Experimental set-up used to observe conjugate wave generation in molecular gases.

gas pressure at fixed frequency and as a function of laser frequency. For the variable frequency measurements, the CO_2 laser cavity total reflector, radius of curvature of 400cm, was replaced by an AR coated ZnSe lens with a focal length of 508cm and a diffraction grating. The grating allowed line tuning of th CO_2 output over substantial portions of both the 10.4μ and 9.4μ bands with megawatt output.

Ammonia

The ν_2 vibration of NH_3 forms a broad absorption band from about 700 cm^{-1} to 1100 cm^{-1} with rotational structure resolved at low pressure in each of the P, Q and R branches.[16] The untuned CO_2 laser output at 944cm^{-1} on the P-20 line of the 10.4μ band falls in about the center of this NH_3 absorption band, between the two components of the inversion doubled Q branch. Figure 6 is a plot of the conjugate wave signal as a function of NH_3 pressure for the untuned CO_2 laser output. The signal level recorded is again an average of the larger signals observed, a wide variation being caused by poor consistency in beam characteristics. Laser output power as a function of NH_3 pressure is also shown in Figure 6. It is believed that the laser oscillated on the P-20 line throughout this measurement although that was not directly confirmed.

From Figure 6, it is seen that as NH_3 pressure was increased, the conjugate wave signal at first increased and then fell off at higher pressure. The initial rapid increase can be attributed to the dependence of the nonlinear susceptibility on density, shown in (11), and the quadratic dependence of the conjugate wave signal on susceptibility in (10). However, pressure broadening of the am-

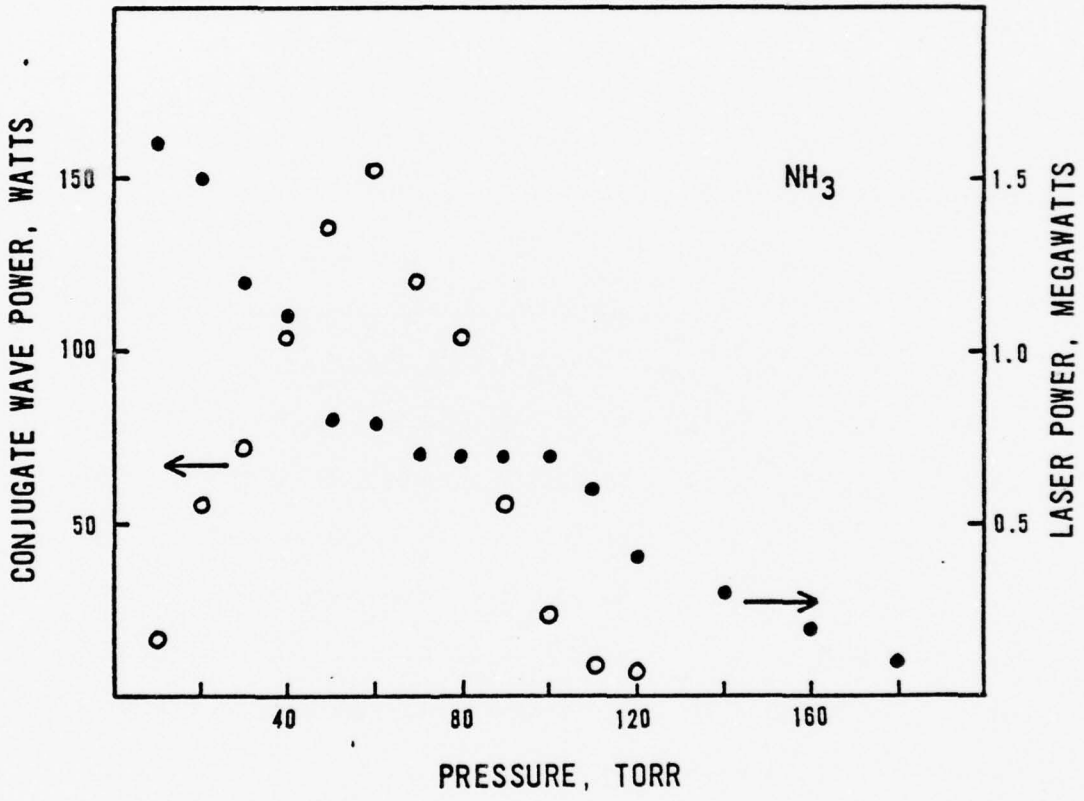

Figure 6. Conjugate wave power and laser output power at 10.6μ in NH_3 as a function of gas pressure.

monia absorption lines eventually limits conjugate wave generation in several possible ways. Direct absorption of the conjugate wave will increase with line width as the line begins to overlap the laser frequency. Line broadening can also lead to absorption of, and saturation by, the pump beams and the object wave. This effect is indicated by the decreasing laser output with increasing NH_3 pressure seen in Figure 6. Finally, the nonlinear susceptibility in (11) decreases with linewidth if the frequency is within about a linewidth of the resonant frequency. It is probable that all of these linewidth effects contributed to some degree to the observed behavior.

At the peak in the conjugate wave signal at 60 torr, the intensity was measured to be about 150W. For an input object wave of 400 kW, half the laser output at 60 torr, this is a conversion efficiency of .04%. Using an interaction length of 10cm, the nonlinear susceptibility at $.944cm^{-1}$ in NH_3 at 60 torr is found, from (10), to be about $2x10^{-11}$ esu. This number should be taken as a lower limit due to the lack of optimal conditions in these experiments.

With the laser in the line tunable configuration, the pressure dependence of the conjugate wave signal was investigated for several other CO_2 laser lines. Table 1 gives the maximum observed signal for several CO_2 lines, along with the laser output and NH_3 pressure at maximum signal. It is known that several of the CO_2 lines[17] are in near coincidence with vibration-rotation lines in the ν_2 absorption band of NH_3.[18] These lines, several of which are given in Table 1, are on the order of 1000 MHZ from NH_3 absorption lines, and using an

CO_2 LINE	WAVENUMBER	CONJUGATE POWER	PRESSURE	LASER POWER
10.4μ band				
P-12	951.2 cm^{-1}	400 W	18 torr	3 MW
P-14	949.8	240	25	2.5
P-26	938.7	300	35	1.5
P-28	936.8	280	40	1.2
P-32	933.0	400	3.5	1.5
R-8	967.7	40	1.5	1.8
R-10	969.1	320	25	1.5
R-12	970.5	180	50	1.2
9.4μ band				
P-20	1046.9	50	40	1.5

Table 1. Maximum conjugate wave signal as a function of NH_3 pressure for selected CO_2 lines, and the pressure and laser power at maximum signal.

average pressure broadening of 25 MHZ/torr,[19] pressures in the range of 40 torr will broaden lines sufficiently to overlap the laser lines. The pressures listed are generally consistent with this broadening, although there is no obvious explanation for the very low values for the P-32 and R-8 lines. The situation is actually quite complicated and a detailed explanation of the data in Table 1 is not possible at present. A theory of conjugate wave generation with absorption[20] must be used where the nonlinear susceptibility arises from a distribution of vibration-rotation lines with separate resonant frequencies, oscillator strengths and linewidths. Further, with differing signs of the various contributions to the nonlinear susceptibility, interference effects may become important.

Freon 12

A somewhat simpler situation than for ammonia is encountered with CCl_2F_2, Freon 12. This molecule has a broad, mostly unresolved absorption band centered at about $900cm^{-1}$ with a relatively sharp absorption edge at $940cm^{-1}$.[21] Using the laser in the line tunable configuration, the conjugate wave signal was measured, for several gas pressures, as a function of frequency as the frequency approached this absorption edge. For this purpose, several of the P branch CO_2 lines in the 10.4μ band were used. A high resolution absorption spectrum of Freon 12 around $940cm^{-1}$ is shown in Figure 7(A) and the conjugate wave signal as a function of wave number for pressures form 1 to 8 torr is plotted in Figure 7(B). The most striking observation to be made from these data is the resonant effect in the nonlinear susceptibility. At each pressure, the conjugate wave signal increases significantly as the absorption edge is approached. Laser power was maintained

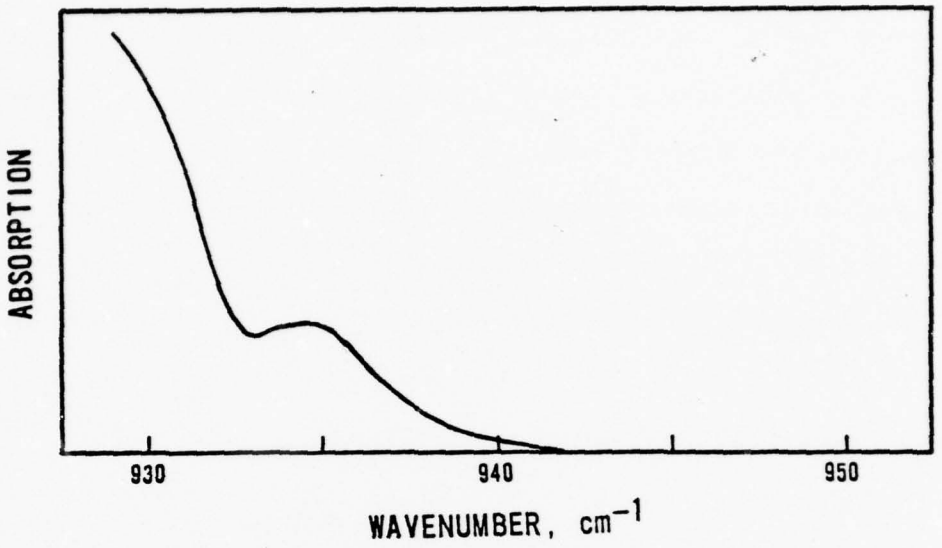

(A)

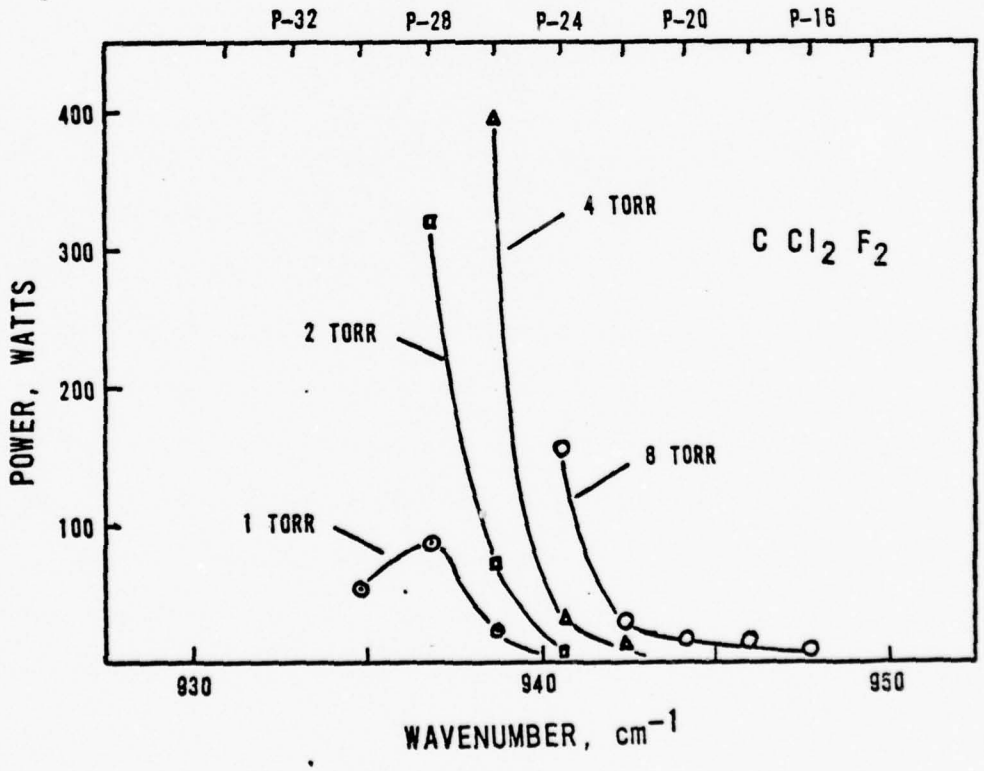

(B)

Figure 7. (A) High resolution absorption edge of Freon 12 around 940 cm^{-1}. (B) Frequency dependence of the conjugate wave power in Freon 12 at pressures of 1, 2, 4 and 8 torr.

constant to the extent possible, although for the lowest wave number measurement at each pressure, the power did decrease. However, this was still the wave number at which maximum or near maximum signal was observed. Laser oscillation was entirely quenched for the next CO_2 line of lower wave number beyond the last data point shown at each pressure.

The maximum signal observed in Freon 12 was 400W for the P-26 line at 4 torr. The laser output power for this measurement was 2MW with 1MW for the input object wave.

Nitrogen Trifluoride

The situation in NF_3 is similar to that in Freon 12. The ν_3 absorption band of NF_3[22] is centered at about 900cm^{-1}and is mostly unresolved. At low pressure the band extends to 940cm^{-1} on the high wave number end, close to the P-20 CO_2 laser line. Conjugate wave measurements were made in NF_3 as a function of pressure with the laser untuned and operating on the P-20 line. Figure 8 shows the results. A large signal was observed in the range from 60 to 65 torr. The laser output at this pressure was 700kW, yielding an efficiency of 0.1%. Using (10), this gives a value for the nonlinear susceptibility of 5×10^{-10} esu. This result can be shown to be in reasonable agreement with a simple classical calculation of the nonlinear susceptibility of NF_3.[23]

Other Gases

Several other molecular gases were briefly investigated. These were done with the laser untuned and oscillating on the P-20 line at 10.6μ.

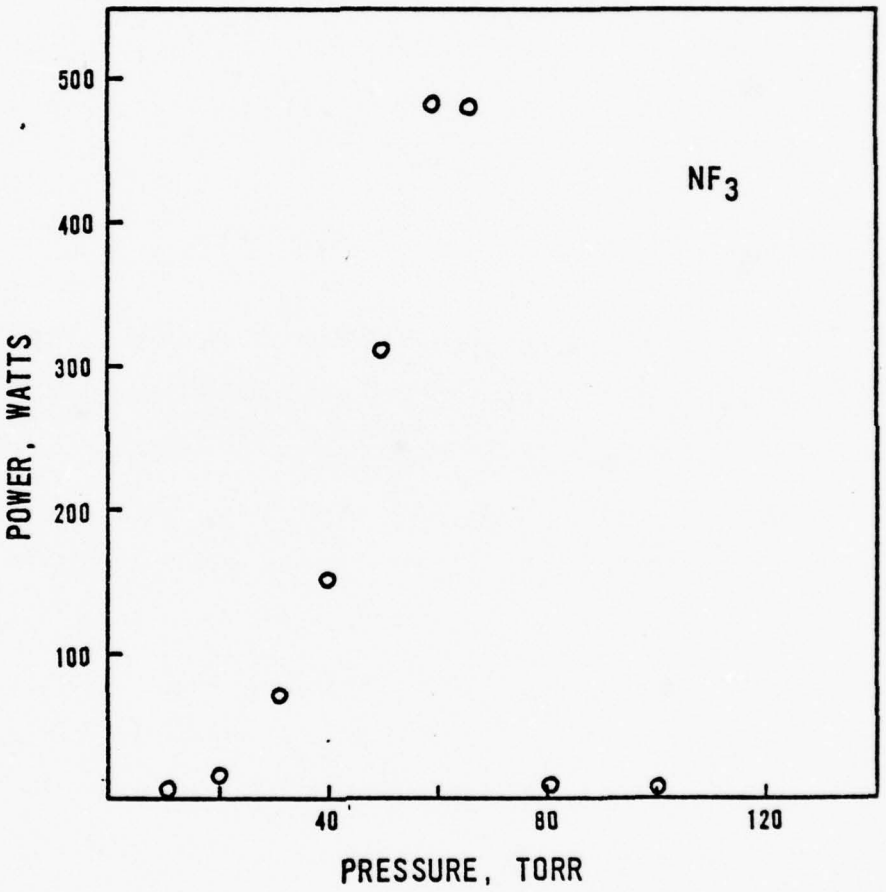

Figure 8. Conjugate wave generation in NF_3 as a function of pressure.

In SF_6, where there is a very complex line structure coincident with the CO_2 laser output, a small effect was observed. The conjugate wave signal peaked at about 3 torr. Although higher SF_6 pressures did not eliminate laser oscillation, this small low pressure effect would probably be expected on the basis of the coincidence of the laser and absorption lines and the resulting absorption and saturation effects. Similar to SF_6, a small effect was seen in BCl_3. Maximum signal in this case was observed for pressures less than 1 torr.

In Freon 21, a moderate effect peaked toward high pressure and was still increasing at 200 torr, the limit of the apparatus. The absorption bands in Freon 21 in the vicinity of the laser output[21] are distant by about $100 cm^{-1}$ in both directions. In this case, the lack of a strong resonant effect does not prevent an observable conjugate wave signal. An alternate explanation may be in impurities in the gas sample. A purity of 99% for Freon 21 is claimed by one principle producer.

Freon 116 showed a very small conjugate wave signal at high pressure. But in carbon dioxide and in methyl fluoride no effect was observed. In both CO_2 and CH_3F strong absorption is well removed from the laser frequency, precluding a resonant effect in the nonlinear susceptibility and a measureable conjugate wave signal.

In conclusion, it should be emphasized that all of the foregoing results are very preliminary and are most useful in indicating directions for further study. It has been shown that conjugate wave generation is observable in molecular gases in the infrared. This has been accomplished at megawatt power levels where an infrared

absorption is in the vicinity of the laser line, resonantly enhancing the nonlinear susceptibility. Calculated values of the nonlinear susceptibilities in these experiments are on the order of 10^{-10} to 10^{-12} esu. The resonant effect has been clearly demonstrated by observing the conjugate wave signal while line tuning the laser output near a strong molecular absorption band. So while this report presents data in a new area of infrared nonlinear optics, that of conjugate wave generation in molecular gases, detailed analysis awaits further experimental and theoretical work.

REFERENCES

1. A. Yariv, Opt. Commun. 21, 49 (1977).

2. P. W. Hellwarth, J. Opt. Soc. Am. 67, 1 (1977).

3. A. Yariv and D. M. Pepper, Opt. Lett. 1, 16 (1977).

4. D. M. Bloom and G. C. Bjorklund, Appl. Phys. Lett. 31, 592 (1977).

5. S. M. Jensen and R. W. Hellwarth, Appl. Phys. Lett. 32, 166 (1978).

6. D. M. Pepper, D. Fekete and A. Yariv, Appl. Phys. Lett. 33, 41 (1978).

7. D. M. Bloom, P. F. Liao and N. P. Economou, Opt. Lett. 2, 58 (1978).

8. P. V. Avizonis, F. A. Hopf, W. D. Bomberger, S. F. Jacobs, A. Tomita and K. H. Womack, Appl. Phys. Lett. 31, 435 (1977).

9. B. Y. Zel'dovich, V. I. Popovichev, V. V. Ragul'skii and F. S. Faisullov, JETP Lett. 15, 109 (1972).

10. O. Y. Nosach, V. I. Popovichev, V. V. Ragul'skii and F. S. Faisullov, JETP Lett. 16, 435 (1972).

11. V. Wang and C. R. Guiliano, Opt. Lett. 2, 4 (1978).

12. B. Y. Zel'dovich, N. A. Mel'nikov, N. F. Pilipetskii and V. V. Ragul'skii, JETP Lett. 25, 36 (1977).

13. N. Bloembergen, Nonlinear Optics (W. A. Benjamin, New York 1965).

14. E. E. Bergmann, I. J. Bigio, B. J. Feldman R. A. Fisher, Opt. Lett. Scheduled to appear Sept. 1978.

15. J. J. Wynne and G. D. Boyd, Appl. Phys. Lett. 12, 191 (1968).

16. J. S. Garing, H. H. Nielsen and K. Narahari Rao, J. Mol. Spectrosc. 3, 496 (1959).

17. F. R. Petersen, D. G. McDonald, J. D. Cupp and B. L. Danielson in Laser Spectroscopy, R. G. Brewer and A. Mooradian, ed. (Plenum Press, New York 1974) pp. 555-569.

18. J. J. Hillman, T. Kostiuk, D. Buhl, J. L. Faris, J. C. Novaco and M. J. Mumma, Opt, Lett. 1, 81 (1977).

19. E. D. Hinkley, K. W. Nill and F. A. Blum, in Laser Spectroscopy of Atoms and Molecules, H. Walther, ed. (Springer-Verlag, New York 1976). pp. 125-196.

20. R. L. Abrams and R. C. Lind, Opt. Lett. 2, 94 (1978).

21. J. G. Calvert, W. H. Chan, E. Niple, R. J. Nordstrom, J. H. Shaw, W. R. Skinner and W. M. Uselman, PF Report 4221-A1, EPA Grant No. P803868-1, April 1976.

22. E. L. Pace and L. Pierce, J. Chem. Phys. 23, 1248 (1955).

23. A. Elci, D. Rogovin, D. Depatie and D. Haueisen, to be published.

USAF-ASEE SUMMER FACULTY RESEARCH PROGRAM

sponsored by

THE AIR FORCE OFFICE SCIENTIFIC RESEARCH

conducted by

AUBURN UNIVERSITY AND OHIO STATE UNIVERSITY

PARTICIPANT'S FINAL REPORT

INELASTIC DYNAMIC RESPONSE OF REINFORCED CONCRETE

Prepared by:	James W. Jeter, Jr.,PhD.
Academic Rank:	Associate Professor
Department and University	Department of Mechanical Engineering Virginia Military Institute
Assignment	
(Air Force Base)	Kirtland Air Force Base
(Laboratory)	Air Force Weapons Laboratory
(Division)	Civil Engineering Research Div
(Branch)	Technology & Applications Br
USAF Research Colleague:	Donald M. Cole
Date:	August 11, 1978
Contract No.:	F44620-75-C-0031

INELASTIC DYNAMIC RESPONSE OF REINFORCED CONCRETE

BY

DR. JAMES W. JETER, JR.

ABSTRACT

Economical considerations in the design of protective structures require that the design process include the considerable strength which remains in the construction material even after permanent deformation has occurred. Reinforced concrete is the predominant material in protective structures. Although a variety of theories have been developed to describe post yield behavior of reinforced concrete, to date, there has been quite limited successful application of these theories to blast and shock analysis.

For this study, two promising concrete material models, the endochronic model and the elastic-plastic strain hardening-fracture model, were considered as possible avenues to an accurate model of the behavior of dynamically loaded reinforced concrete structures. Existing finite element codes for the material models, which had been developed primarily for the study of compression loaded structures, were used with available nonlinear dynamic structural analysis programs to study a dynamically loaded beam which had been previously investigated experimentally. For both models the reinforcing steel was modelled separately from the concrete, rather than having the structural properties of the steel and concrete "smeared."

Since both material codes had been previously used primarily for compressive loadings, errors were expected when the possibility of tensile cracking was added to the material behavior, and several were found. Although several corrections and alterations have been added to the codes, currently neither of them is capable of simulating the experimental beam behavior. Additional study and possible modifications are needed before either of these approaches can be declared a comprehensive model of non-linear concrete behavior.

ACKNOWLEDGEMENT

This work was sponsored by the Air Force Scientific Research Office and ASEE. The author is grateful for their support of this summar research. A deep appreciation is also due to Mr. J. Fred O'Brien, Jr. of Auburn University and Dr. A. Gunther, Chief Scientist of AFWL, Kirtland Air Force Base, for their excellent administration of this project. Their work has made this summer enjoyable as well as productive.

The association with the Structural Dynamics Section of the Civil Engineering Research Division of the Weapons Laboratory has been a gratifying experience both professionally and personally. In particular, thanks are due to Mr. Don Cole for his timely suggestions and guidance during the course of the summer, and to Mr. Rod Galloway for various discussions related to this project. The author is grateful to Mr. Telford Knox for his assistance in computer-related problems and to Mrs. Gin Kinifick, who typed this paper.

LIST OF FIGURES

NOMENCLATURE

A_u	material constant used in the elastic-plastic-strain hardening-fracture model; different for tension-compression and for compression-compression stress state.
f'_c	ultimate uniaxial compressive stress of concrete test cylinder
f_t	uniaxial tensile cracking stress
I_i	first invarient of the strain tensor
J_2	second invarient of the stress tensor
P	beam load, kips
r, z	coordinate axes
$\ddot{d}$	matrix containing the accelerations of all node points for the SAMSON
F^{ext}	matrix containing external forces acting on the node points for the SAMSON code
F^{int}	matrix containing internal forces acting on the node points for the SAMSON code
M	lumped mass matrix for all mode points for the SAMSON code
ε	uniaxial strain
ε_f	equivalent plastic fracture strain
ε_p	equivalent plastic strain
ε_u	equivalent plastic ultimate strain
K	material constant used in the elastic-plastic hardening-fracture model; different for tension-compression and compression-compression stress states
σ	uniaxial stress
$\sigma_{1,2,3}$	principal stresses

τ	effective stress
τ_o	effective stress at which nonlinear behavior first occurs
τ_u	ultimate effective stress

INTRODUCTION

Due to the growing costs associated with protective construction, a conservative elastic design approach is undesirable, since it would result in an overdesigned and overexpensive structure. Instead, the design philosophy must take advantage of the considerable strength which remains in the construction material even after permanent deformation has occurred. The major material currently used in protective construction is reinforced concrete. Although a variety of theories have been developed to describe post yield behavior of reinforced concrete, to date there has been quite limited successful application of these theories to blast and shock analysis.

OBJECTIVE

The objective of this research effort is to review existing analytical methods for analysis of the inelastic behavior of reinforced concrete subjected to blast and/or shock loading and to evaluate the models using existing experimental data. The evaluation approach primarily involves incorporating promising material models into existing dynamic finite element programs which are then used to model the experimental conditions.

CONCRETE MATERIAL PROPERITES

Typical stress-strain curves for plain concrete subjected to uniaxial tension and uniaxial compression are shown in Figure 1. In tension, concrete behaves as a linear elastic-fracture material, exhibiting no significant permanent strain before it fails by the formation of a crack. The behavior of the material in compression, however, is somewhat more involved. The initial linear elastic region eventually develops into a non-linear region. This behavior is the result of the formation of microcracks with the material, causing permanent deformation and a loss in stiffness similar to the strain hardening seen in metals. Continued growth and intersection of these cracks decreases the stiffness of the concrete until a slope of zero is eventually reached. This point is defined as the ultimate compressive strength of the concrete (f'_c). If the load corresponding to this stress were maintained, the concrete would lose stiffness and crush. However, if the concrete specimen is loaded by incrementing strain rather than stress, resistance to deformation would still be available and crushing would not immediately occur. This portion of the curve depicts the strain softening phenomenon of concrete. Under these conditions, failure does not occur until the ultimate strain (ε_u) is reached. A similar situation would exist if the heavily loaded portion of a structural member were able to transfer part of its loading to an adjacent part of the structure. Since this type of load redistribution is extremely important in inelastic behavior of materials, a realistic model of strain softening is essential when the strain corresponding

to the ultimate stress is exceeded. If the concrete is subjected to a triaxial or biaxial loading rather than the uniaxial loading considered here, the material behavior will be affected, primarily through a strengthening or weakening in the compressive state due to the compression or tension stresses on orthogonal planes.

CONCRETE MODELS

Existing analytical models for the inelastic behavior of plain concrete as applied to static problems were reviewed recently by PMB Systems Engineering, Inc. (ref. 1). Based on comparisons made in that study, it was decided to center attention on two specific models: the linear elastic-plastic strain hardening-fracture model developed by Chen and Chen (ref. 2), and the endochronic model developed by Bazant and Bhat (3).

The linear elastic-plastic strain hardening-fracture model appears to be the best to date of a series of models which deal with the inelastic behavior of concrete using the plasticity approach developed primarily for use with metals. The method postulates an initial discontinuous surface in three-dimensional stress space which represents the end of the elastic region, loading surfaces which are used to relate incremental stress and strain once inelastic behavior begins, and a failure surface which represents the outmost extreme of the loading surface. All three types of surface are defined by equations of the same form:

$$\tau^2 = \left(\frac{K^2}{3} J_2 - \frac{K^2}{36} I_1 \pm \frac{1}{12} I_1^2 + \frac{1}{3} + A_u I_1\right) \qquad (1)$$

where

$\tau = \tau_o$, a specified value, when the equation represents the initial discontinuous surface.

$\tau = \tau_u$, a specified value, when the equation represents the failure surface, corresponding to ultimate stress.

τ = effective stress at all other times - it corresponds to the new discontinuous surface if the material is being loaded into the plastic region.

K, A_u are material constants which are different for the tension compressive stress state and the compression-compression stress state.

J_2 = the second invarient of the stress tensor

I_1 = the first invarient of the strain tensor

The initial discontinuous surface and the failure surface are depicted in Figure (2a); the more easily visualized two-dimensional case is shown in Figure (2b). When the state of stress lies within the initial discontinuous surface, the material is assumed to be linear elastic; if the state of stress is between the two surfaces, plastic behavior exists and the loading surface defines a new discontinuous surface which replaces the initial discontinuous surface. Unloading from the current discontinuous surface is done on the assumption of linear elastic behavior, but loading from the surface involves plastic behavior and is defined by stress-strain increment relations developed directly from the loading surface. When unloading and loading, additional plastic deformation does not occur until the current loading surface is reached. Note that in the pure tension region of Figure (2b), there is virtually no difference between the initial discontinuous surface and the failure surface, so the brittle characteristics of concrete in pure tension is reflected in the model.

The endochronic model is a more recent development for modeling nonlinear material behavior. In this model, the inelastic strain accumulation is characterized by a scaler parameter called intrinsic time. The intrinsic time parameter can be defined in such a fashion that phenomena such as strain hardening, strain softening, cyclic loading, etc. can be correctly predicted. The intrinsic time parameter defined in reference (5) is sufficiently general that the more common inelastic concrete characteristics are represented. Although this definition involves a plethora of material parameters which normally would be determined through an optimization process, a study of a variety of experimental data in reference (3) indicated that only the uniaxial ultimate compressive stress must generally be adjusted from one material to another.

It is important to note that both of these modes were developed to reflect the predominantly compressive characteristics of concrete since most designs would avoid the low tensile strength characteristics of the material. Dynamically loaded structures, however, are often subjected to stress reversals, so that the tensile behavior of the concrete could become significant. Thus, the success of either of these approaches in analyzing a dynamically loaded structure is dependent on how well tension is modeled.

FINITE ELEMENT FORMULATION

The discussion to this point has centered on the problem of duplicating the inelastic behavior of plain concrete. In order to model reinforced concrete, the interaction between the concrete and the reinforcing steel must be developed. The two different approaches commonly used to mesh the steel and concrete in finite element programs are shown in Figure (3). The composite element model "smears" the

steel through the corresponding concrete elements, producing concrete elements of high strength at the location of the steel. The discrete elements approach defines new elements to represent the steel reinforcement. Although perhaps less efficient for many applications, the latter method provides the most convenience and flexibility for a study of this type and was chosen for that reason.

ENDOCHRONIC MODEL

The finite element formulation for the endochronic model has been developed previously at the Air Force Weapons Laboratory for use with the SAMSON nonlinear dynamic finite element structural analysis program (4). This program allows for a two-dimensional analysis and allows for structure-media interaction subject to the limitations of the model of the inelastic behavior of the structural material. The endochronic model formulation was developed and used primarily for uniaxial compressive stress states, although tensile considerations were built in. Some of the complications which must be included if tension is allowed are as follows: cracking in one direction without cracking in the orthogonal direction; cracking perpendicular to the out of plane direction; closing of a crack so that compressive stresses are permitted; effect of tensile cracking on the strain associated with the strain invariants, which, in turn, is used in calculating intrinsic time; possibility that cracking will produce an unrestrained mode which will undergo excessive displacement; requirement of a bookkeeping process to set stresses to zero when cracking occurs. The two-dimensional nature of the SAMSON analysis simplifies accounting for most aspects of the cracking phenomenon. The three possible cases which must be considered are: a free surface in the out of plane direction; one free surface in the plane of stress and two free surfaces in the plane of stress. The first case corresponds to no cracks (conventional plane stress theory) or a crack normal to the out of plane direction. In either situation, the out of plane stress is zero and the out of plane strain is dependent on the in plane strain. The second case corresponds to a single crack normal to one of the in-plane directions or one such crack combined with a crack normal to the out of plane direction. The third case involves either cracks normal to both of the in-plane directions or these cracks combined with a crack normal to the out of plane direction. In either situation, the element has lost all ability to resist strain. The accounting process which corresponds to these cases appears to be simple, but is actually more involved. For instance, it is obvious that if a crack forms perpendicular to a given direction, the stress in that direction reduces to zero, but the effect on strain is also significant, since the strain invarient is used to determine the intrinsic time parameter. The total strain must be reduced and should not be related directly to the motion of the adjacent nodes. If permanent deformation is ignored prior to tensile cracking, the only strain present in the direction normal to

a crack will be any strain due to deformation in the other in-plane direction (assuming no crack has formed in that direction).

The effect of cracking on the restraint of adjacent node points is another complication which is difficult to deal with. The acceleration of a node point in the SAMSON formulation is defined by the equation:

$$\ddot{d} = [M]^{-1} \left(F^{ext} - F^{int} \right) \qquad (2)$$

where

$\ddot{d}$ is a matrix containing the accelerations of all node points;

M is a global lumped mass matrix for all node points;

F^{ext} is a matrix containing external forces acting on the node points; and

F^{int} is a matrix containing internal forces acting on the points.

Equation (2) implies that, for the most common case where no external forces are applied to a node point, instantaneous cracking of an element would cause an imbalance of internal forces, beginning a complicated interaction process which would culminate in the production of an unrestrained motion. It is not clear how this possibility can be accounted for unless node points are restrained in some fashion after cracking, possibly by including vertical steel reinforcement. Presently, no accounting is being made.

ELASTIC-PLASTIC-STRAIN HARDENING MODEL

The finite element formulation for the elastic-plastic-strain hardening-fracture material has been developed previously by PMB Associates for use with the ANSR structural analysis computer code(5). The ANSR code is oriented towards the analysis of structures subjected to earthquake loads and is therefore compatible with the type of problem being studied in this effort. A significant difference between the ANSR code and the SAMSON code is the lack of two-dimensional elements and formulations in the ANSR code. Thus, the elastic-plastic-strain hardening-fracture material must be considered using the more complicated, three-dimensional concept shown in Figure (2a) rather than the more easily visualized two-dimensional version shown in Figure (2b). The nature of the material model requires that a different approach to non-linear behavior be used depending on whether the material is subjected to a tension-tension, tension-compression, or compression-compression stress state. An immediate

problem involves defining which of these states is considered to exist when the material is actually subjected to a three-dimensional stress condition. A hypothesis used to define the stress state is included in the ANSR code.

Tests to determine the stress state and the corresponding constitutive relations are based on the concepts of an effective stress and equivalent plastic strain. The effective stress is found using a function of the same form as the functions defining the initial discontinuous surface and the failure surface,

$$\tau^2 = \frac{K^2}{3} J_2 - \frac{K^2}{36} I_1^2 \pm \frac{1}{12} I_1^2 + \frac{1}{3} A_u I_1$$

where

τ = effective stress

K, A_u = material constants (different for tension-compression and compression-compression stress states)

J_2 = second invarients of the strain tensor

I_1 = first invarients of the stress tensor, and

the sign of the third term depends on the stress state. The equivalent plastic strain is found by adding incremental values based on the equation

$$d\varepsilon^{\rho} = (d\varepsilon^{\rho}_{ij} d\varepsilon^{\rho}_{ij})^{1/2}$$

The complicated three-dimensional stress situation is treated as a one-dimensional stress situation for analyzing the non-linear behavior by using a plot of effective stress vs equivalent plastic strain developed from experimental data. The plots corresponding to the three possible stress states, tension-tension, tension-compression, and compression-compression are shown in Figure (4). It is seen that the alternatives for the tension-tension stress state are linear elastic behavior or cracking. The alternatives for the tension-compression stress state are linear elastic, elastic-strain hardening, and crushing. The alternatives for the compression-compression stress state are the same as for the tensile-compressive state except strain softening may occur before crushing. Note that cracking/crushing is defined in terms of the effective stress or equivalent plastic strain, so no directional

characteristics can be associated with this behavior. Once crushing or cracking occurs, the element is considered to be completely failed. Also, the possibility of a compressive reloading after tensile cracking has been ignored. For these reasons, there is no need to assess the impact of cracking on the loading function.

The logic in the elastic-plastic strain hardening-fracture material model subroutine can be summarized approximately as follows:

a. Given the strain increment and assuming linear elastic constitutive relations, determine a trial stress increment, then a trial stress value.

b. Use the trial stress-value and the stress state-check discussed earlier to determine the stress state.

c. If the material has not already crushed or cracked, determine whether the current nonlinear surface has been violated; if not, the linear elastic computations are correct and the calculations for this strain step are complete, except for updating the bookkeeping. If the current nonlinear surface has been reached or exceeded, the elastic portion of the stress and the strain are computed, then the plastic portion is computed, using the appropriate section of the equivalent stress-equivalent plastic strain curve to determine the applicable incremental stress-strain relations.

d. If a multi-segmented piecewise-linear stress-strain curve is used, checks must be made to insure that the laws appropriate to the particular segment are used, and checks for crushing must also be made. Once the appropriate plastic strain increments are found, the bookkeeping can be updated.

EXPERIMENTAL TEST CASE

A dynamically loaded beam investigated experimentally by Feldman, Kennan, and Seiss (6) was chosen for use in evaluating the two material models. Characteristics of the beam and its loading are shown in Figure (5). A pneumatic loading machine was used to apply a dynamic loading with the time-history depicted in Figure (6). The finite element model of the beam was chosen so that comparisons with an earlier analysis attempt (7) would be facilitated. One version of this model used in SAMSON is shown in Figure (7). Note that the steel cover and interior concrete for this model can result in unrestrained node points if sufficient cracking occurs. A later SAMSON model, and the ANSR MODEL were devised without steel cover and with steel equivalent to the vertical reinforcement connecting the

nodes in the vertical plane, so that some restraint remains after cracking. The SAMSON model involved two-dimensional plate elements in plane stress. It was necessary to modify the linear elastic material model commonly used for SAMSON bar elements so that it would represent the steel reinforcement as elastic-perfectly plastic. The ANSR beam model was developed in such a fashion that a minimum number of elements were used, since the three-dimensional elements were expected to result in extremely long computer running times. The beam model was forced to undergo a plane strain type behavior to eliminate the requirement of modeling reinforcement through the thickness. Displacement of nodes on the rear side of the beam were forced to correspond to the displacements on the front side, eliminating the need for duplicating horizontal and vertical steel on the rear side. The reinforcing steel was modeled assuming an elastic-strain hardening material, with the strain hardening minimized so the steel behavior would be similar to that of the steel in the SAMSON model.

ANALYSIS OF RESULTS

An initial static check of the ANSR model produced incorrect results. Further checking of the ANSR elastic-plastic-strain hardening-fracture model using a much simpler structure revealed several areas where the subroutine seems to be inconsistent with the theory it represents. These apparent inconsistencies indicate that a considerable amount of reprogramming would be necessary to correct the ANSR material model. Because of the limited amount of time available for this study, it was decided to abandon the ANSR model and concentrate on the SAMSON analysis.

The SAMSON analysis was first run using an assumption of completely elastic behavior as a check of the finite element model. This solution was most conveniently effected with the smeared steel approach, rather than the discrete steel elements preferred for the nonlinear analysis. The model was then modified to accommodate the non-linear solution. In addition to the discrete steel elements, this change required rearranging the triangular concrete elements to meet the SAMSON restriction of no more than eight elements attached to a given node. Several errors were found in the endochronic material subroutine and were corrected. This finite element model was used only for the early portion of the beam response, since vertical steel was expected to be a factor in the later response, which would include inelastic behavior. Once the model appeared to give a consistent model of elastic behavior, the aforementioned SAMSON restriction on elements attached to a node required replacing the steel cover with quadrilaterial elements so that vertical steel could be added to the model. This model was run without vertical steel well into the region of inelastic response, where the cracking model apparently generated errors. Several errors were found but continued runs produced unrealistic values for stresses. This was possibly due to the lack of node point restraint which would be provided by the vertical steel, although the

possibility of additional errors or omissions in the sub-routine must also be considered as possible causes. A SAMSON model similar to the ANSR model in that all concrete elements are quadrilateral elements, steel cover is ignored, and vertical steel is included, was developed to determine whether the additional restraint provided by the vertical steel would be sufficient to prevent excessive deformation. At this writing, no data has been gathered using this model.

CONCLUSIONS AND RECOMMENDATIONS

Although no data has been gathered for the dynamically loaded beam, several conclusions can be drawn about the material models and the sub-routines which apply them.

1. The documentation of both material models presume a predominately compressive loading, leaving to the user any adaptation to major tensile effects.

2. The ANSR subroutine for the elastic-plastic strain hardening-fracture model appears to be presently insufficient to accurately model the variety of non-linear phenomena which may occur in the course of a general dynamic load.

3. The problems encountered in applying the tensile version of the SAMSON endochronic subroutine indicate that this subroutine requires further testing and study before it can be considered reliable for loadings other than uniaxial compression.

It is recommended that the endochronic subroutine be tested on a small scale until it is obvious that it can correctly handle all possible loading combinations. Once this has been done, the model should prove to be convenient for the analysis of dynamically loaded structural members.

The ANSR subroutine for the elastic-perfectly plastic-strain hardening material model should be analyzed and corrected so that it will be capable of handling a general dynamic loading. It is further recommended that this method be checked carefully using experimental data, and compared to the endochronic model. If the elastic-perfectly plastic-strain hardening model proves to be superior, it should be coded for SAMSON so that it could be used in conjunction with the existing SAMSON media interaction capability.

REFERENCES

1. PMB Systems Engineering, Inc., "Failure Criteria for Reinforced Concrete Structures", Vol. 1.

2. Chen, A. C. T., and Chen, W. F., "Constitutive Relations for Concrete", Vol. 101, No. EM4, Journal of Engineering Mechanics, August 1975.

3. Bazant, Z. P., and Bhat, P. D., "Endochronic Theory of Inelasticity and Failure of Concrete", Vol. 102, No. EM4, Journal of Engineering Mechanics, August 1976.

4. Belytschko, T., and Chiapetta, R. L., A Computer Code for Dynamic Stress Analysis of Media-Structure Problems With Nonlinearities (SAMSON), AFWL-TR-72-104, Vol. 1, Kirtland Air Force Base, New Mexico, February 1973.

5. Mondkar, D. P., and Powell, G. H., ANSR-I- General Purpose Program for Analysis of Nonlinear Structural Response, Report No. 75-37, Earthquake Engineering Research Center, University of California, Berkeley, California, December 1975.

6. Feldman, A., Keenan, W. A., and Siess, C. P., "Investigation of Resistance and Behavior of Reinforced Concrete Members Subjected to Dynamic Loading, Part III", Report No. DASA-1259, D74-174, Urbana, Illinois, University of Illinois, February 1962.

7. Adham, S., Bhaumik, A., Isenberg, J., Reinforced Concrete Constitutive Relations, AFWL-TR-74-72, Kirtland Air Force Base, New Mexico, February 1975.

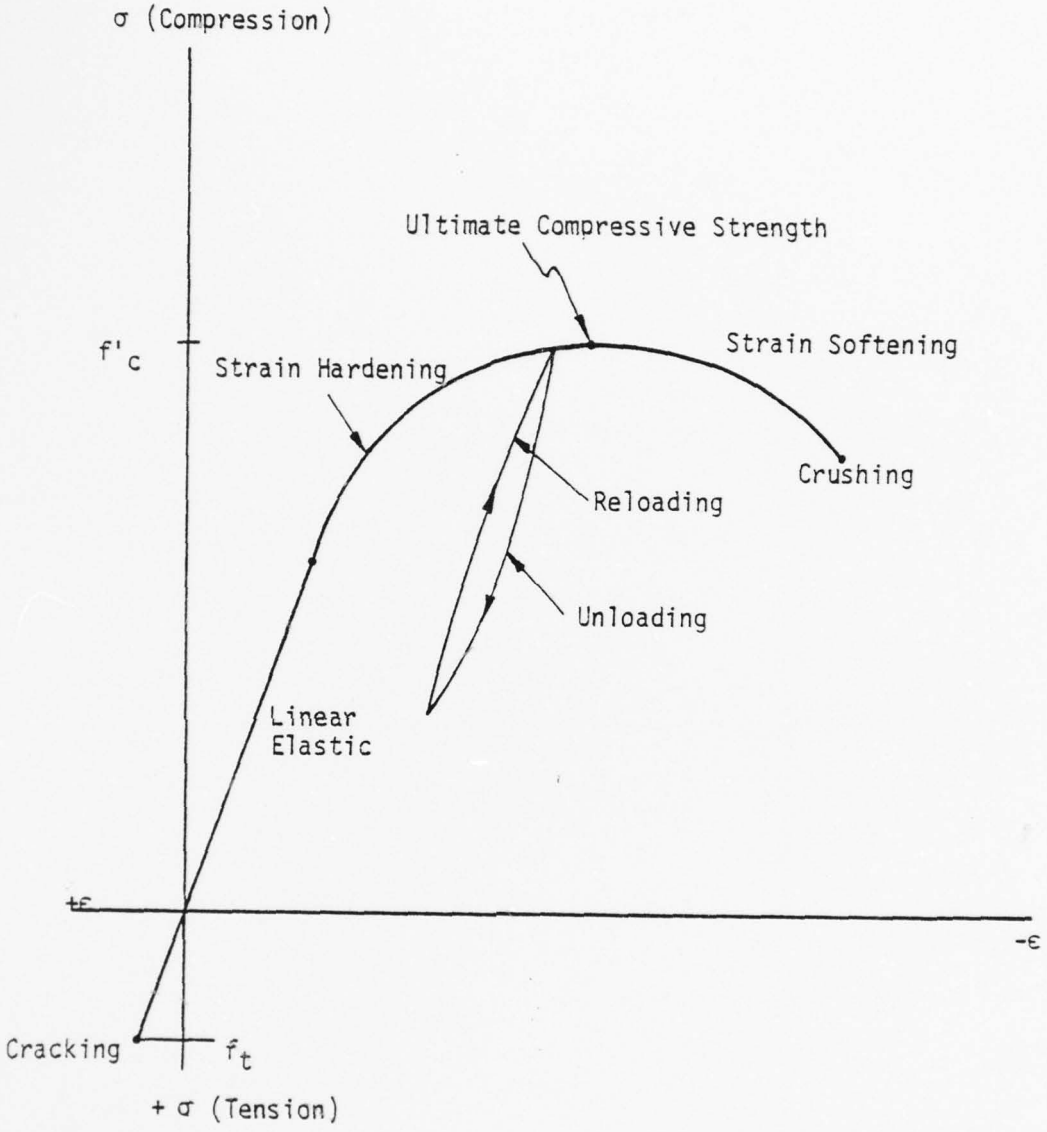

Figure (1). Typical Uniaxial Stress-Strain Relationship for Plain Concrete

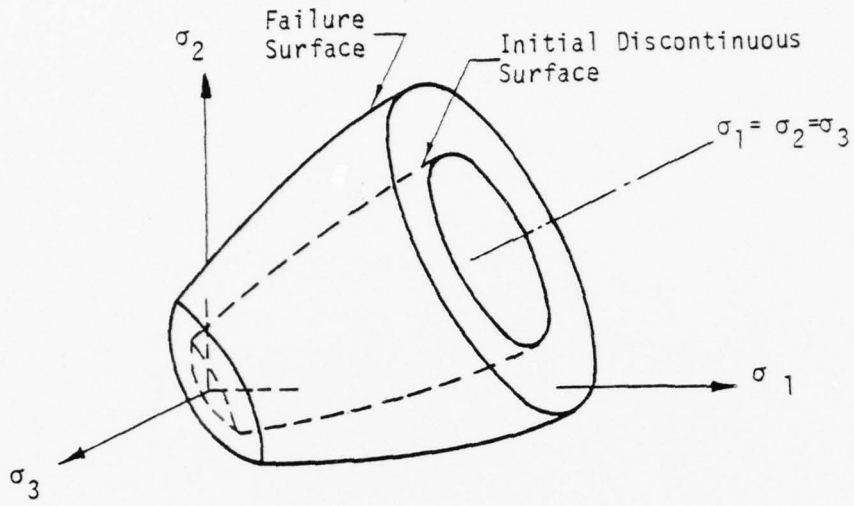

a) Triaxial Stress Space

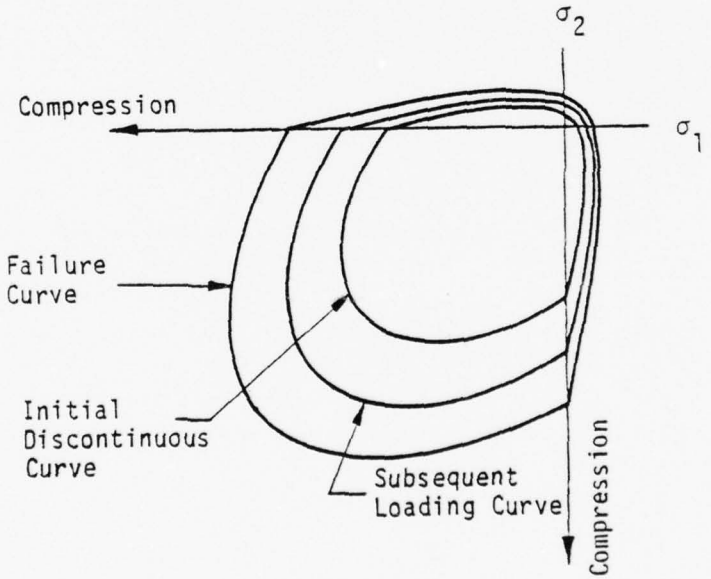

b) Biaxial Stress Space

Figure (2) Initial Discontinuous, Loading and Failure Surfaces

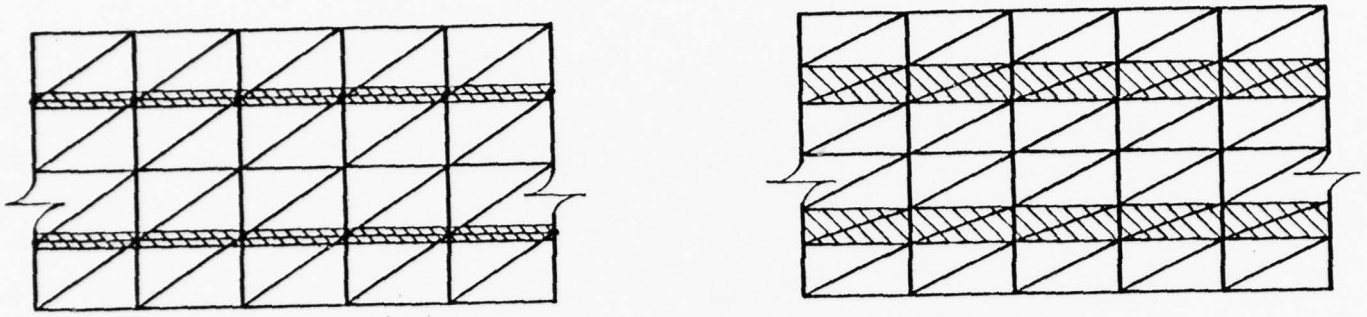

(a) DISCRETE ELEMENT MODEL

(b) COMPOSITE ELEMENT MODEL

Figure (3) Finite Element Reinforced Concrete Models

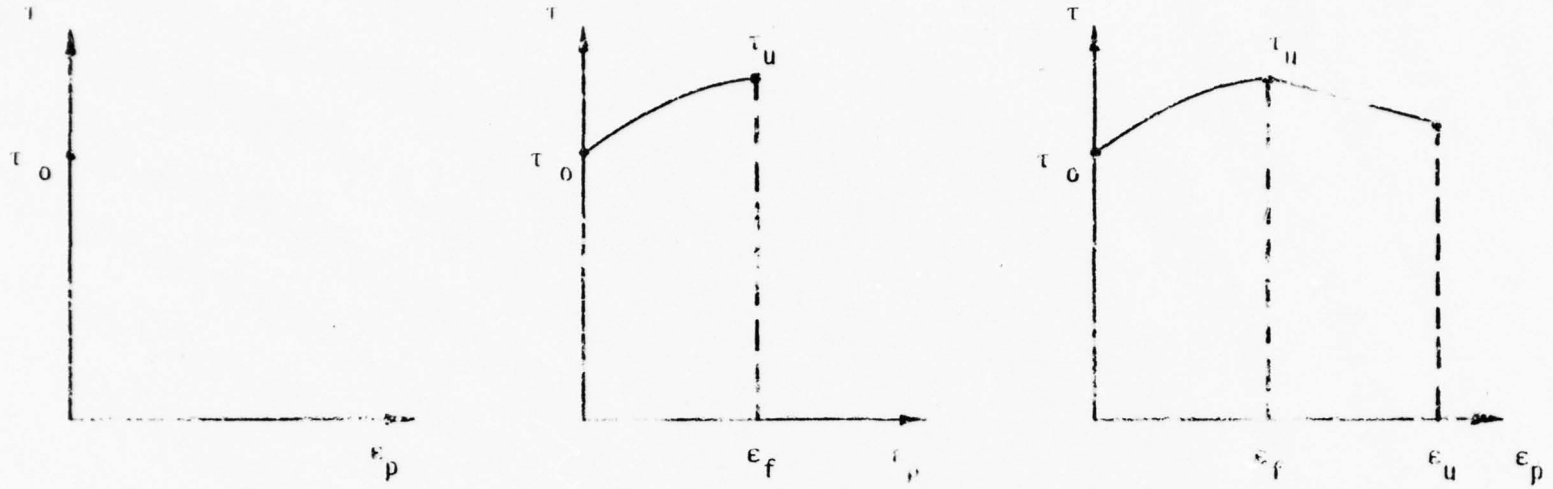

a) [illegible]
Stress State

b) [illegible]
Stress State

c) Compression-Compression
Stress State

(τ, term defined differently for each stress state)

Figure (A) Effective Stress vs. Equivalent Plastic Strain
for Three Possible Stress States

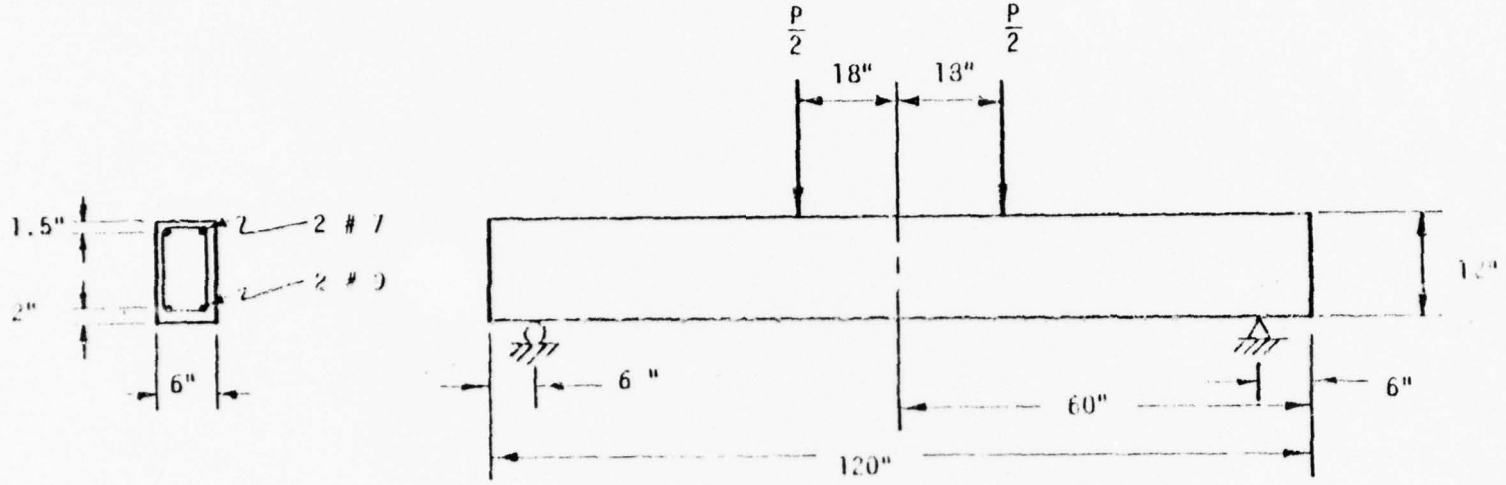

Figure (5) Characteristics of Test Beam

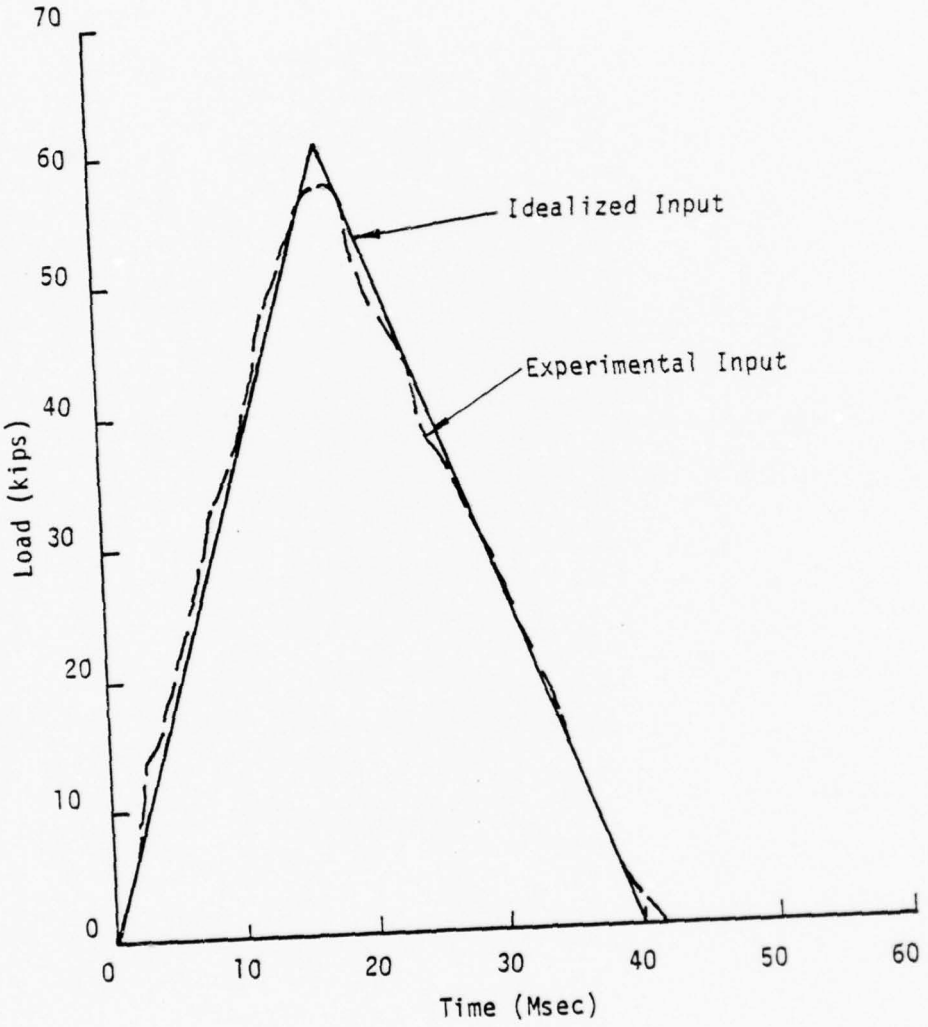

Figure (6) Load Time-History for Test Beam

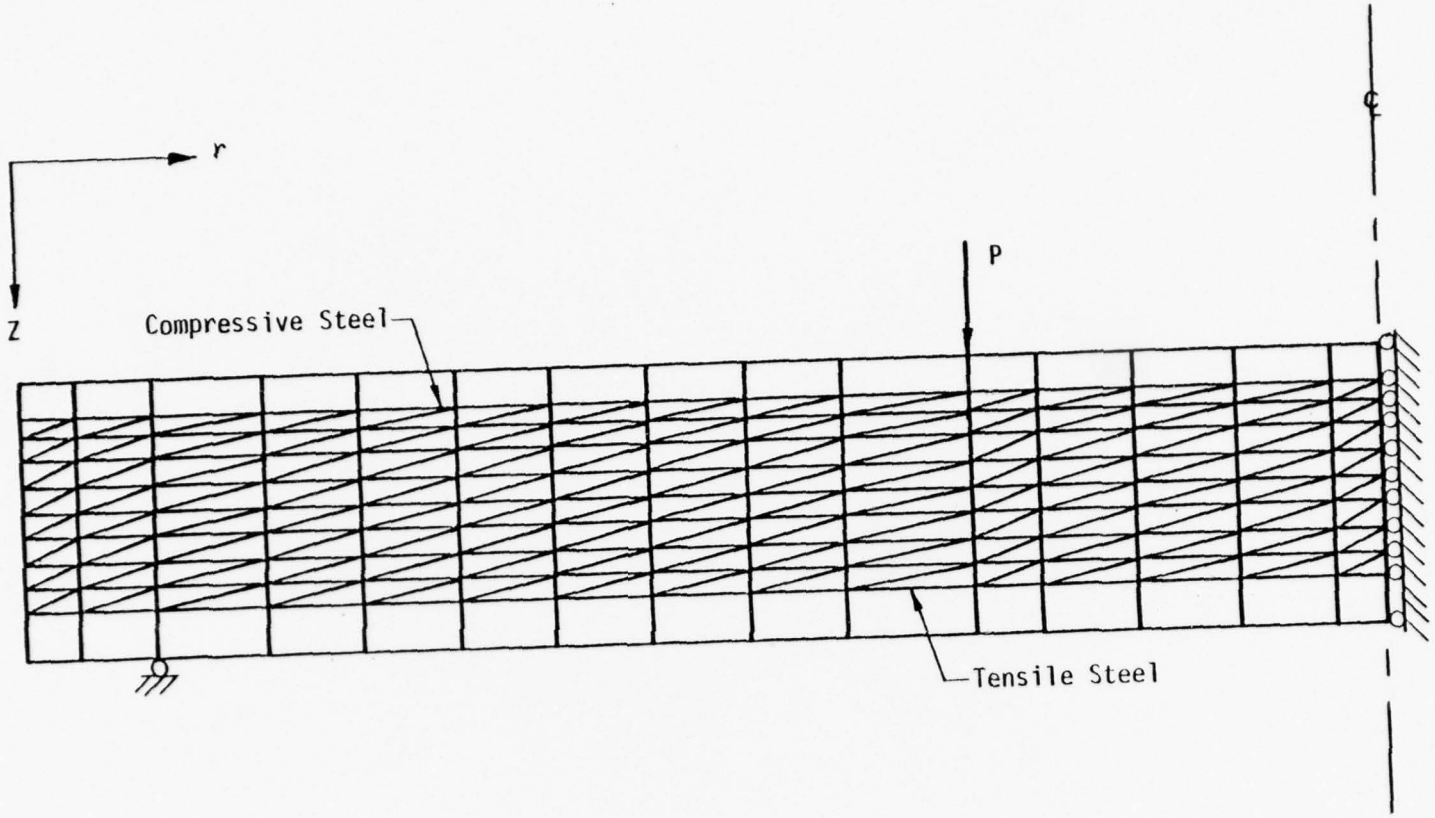

Figure (7). Finite Element Representation of Test Beam

1978 USAF-ASEE SUMMER FACULTY RESEARCH PROGRAM

sponsored by
THE AIR FORCE OFFICE SCIENTIFIC RESEARCH

conducted by
AUBURN UNIVERSITY AND OHIO STATE UNIVERSITY

PARTICIPANT'S FINAL REPORT

OPTIMIZED PROCEDURES FOR RADIATION TESTING OF LSI CIRCUIT TECHNOLOGY

Prepared by:	Thomas A. Williamson
Academic Rank:	Assistant Professor
Department and University:	College of Engineering and Technology Northern Arizona University
Assignment:	
(Air Force Base)	Kirtland Air Force Base
(Laboratory)	Air Force Weapons Laboratory
(Division)	Electromagnetics Division
(Branch)	Transient Radiation Effects Branch
USAF Research Colleague:	Lt Col Aaron B. Loggins
Date:	August 4, 1978
Contract No.:	F44620-75-C-0031

OPTIMIZED PROCEDURES FOR RADIATION TESTING OF LSI CIRCUIT TECHNOLOGY

by

T. A. Williamson

ABSTRACT

A brief review of radiation effects on electronic circuits is presented. Standard techniques are described for testing MSI and LSI circuits for permanent and transient radiation effects. It is suggested that it may not be necessary to run a complete series of transient effects tests for every member of a specially designed test set. Techniques for electrical testing of LSI circuits are presented in three categories: DC parametric testing, functional testing, and dynamic testing. It is suggested that DC parametric testing, while necessary for complete characterization of the device, yields relatively little information about functional damage, except possibly in CMOS circuits. In the section on functional testing, combinational circuits, random access memories, microprocessors, and implementation of functional tests are given separate discussions. Several types of circuit faults and fault-finding functional tests are described, and methods for designing such tests are discussed where practical. The section on dynamic testing discusses the possibility of substituting measurements of propagation delays and access times for more complete functional testing. It is suggested that the correlation, if one exists, between radiation-induced soft faults and radiation-induced changes in access times has not been established.

Introduction

Radiation effects in LSI (large scale integrated) circuits are difficult to evaluate. The problems are that a large amount of internal circuitry is involved, with very limited accessibility to the internal nodes from the external terminals, and the large number of functions that may have to be tested in a given device. Extensive study of the device under test is required in order to determine a test procedure that adequately characterizes the device before and after radiation exposure. Radiation-induced failure modes must be deduced and tests devised to detect them. The test procedures that finally result are complicated, long, and not easy to implement. Finally, there is no guarantee that the test procedures arrived at will, in fact, detect all of the radiation-induced faults.

Objectives

The objectives of this effort were, first, to review current LSI testing techniques to learn how to determine optimal test procedures for detailed functional testing of a given LSI device, and second, to investigate the possible existance of reasonable alternatives to this level of testing.

Background on Radiation Effects[1-4]

Radiation Effects in Bipolar Arrays

Bipolar junction transistors are subject to transient effects from ionizing radiation and to permanent effects from neutron radiation.

Photocurrents from ionizing radiation are in direct proportion to the dose rate. They are generated in the depletion regions of the pn junctions, and can be modeled as dose-rate dependent current sources in parallel with the pn junction whose photocurrent they represent. For a given dose rate, the sizes of the photocurrents obviously depend on many factors, but photocurrents in the range of several mA to several hundred mA at 10^8 rad(Si)/sec are typical in discrete transistors. In junction-isolated integrated circuits the dominant photocurrents may be those of the substrate junctions. In dielectrically-isolated arrays the dominant photocurrents are those of the transistor junctions.

As far as damage is concerned, the photocurrents can destroy the device by electrical overstress, or they can cause the circuit to temporarily malfunction even though no one element in the circuit was overstressed. A complicating factor in digital circuits is that in general the failure mode depends on the logical state the circuit is in during irradiation. This is because there is one set of photocurrent sources that is critical in upsetting the logic level, and another set that is critical in upsetting the other logic level. Experiments on commercial TTL gates have shown temporary malfunctions to occur at dose rates in the neighborhood of 10^9 rads(Si)/sec, the gates being somewhat more susceptible in the high-state than the low-state.

Permanent effects in bipolar circuits are of three kinds: (1) electrical overstresses due to excessive photocurrents are similar to, and generally treated in studies of, EMP damage. (2) Surface effects are in proportion to accumulated dose of ionizing radiation, but are relatively unimportant in bipolar circuits up to about 10^5 rads(Si) accumulated dose. (3) Displacement damage from neutron radiation, specifically the resulting degradation in transistor gain, is the primary mechanism for permanent damage in bipolar arrays.

The forward current gain, the beta, of a discrete bipolar junction transistor may typically be down to 30% of its pre-irradiation value at 10^{14} n/cm^2, and down to 40% at 10^{13} n/cm^2. In experiments on a bipolar microcomputer (Intel 8300) circuit, the unit failed completely and permanently at 3×10^{14} neutrons/cm^2 (14 MeV equivalent). Current interest in neutron effects is directed to the I^{2}L technology. The I^{2}L circuits appear to be about an order of magnitude more susceptible to neutron radiation than TTL circuits.

Radiation Effects in MOS Arrays

MOS circuits, while relatively immune to neutron radiation, are subject to both transient and permanent effects from ionizing radiation.

Transient effects are mainly the result of dose-rate dependent photocurrents in the substrate junctions in junction-isolated arrays. In SOS (silicon-on-sapphire) circuits, on the other hand, substrate junction photocurrents are virtually eliminated, and it is dielectric photoconduction that determines the transient failure threshold. Transient failure may occur at dose rates an order of magnitude higher than for junction-isolated MOS circuits.

The main problem with radiation effects in MOS circuits is and has always been permanent surface effects due to total accumulated dose of ionizing radiation. Subjected to ionizing radiation, the gate insulator, if it is silicon dioxide, tends to accumulate a positive charge within itself. This causes a shift in the operating characteristics of the transistor. The amount of shift depends on the gate bias during irradiation, being maximum when the gate bias is positive, and minimum when the gate bias is zero. Thus n-channel enhancement mode MOS-FET's in the "on" state are more susceptible than p-channel devices in the "on" state. Hence, the failure mode in a CMOS circuit is that the operating characteristics of the n-channel elements shift to the point where they can no longer be turned off. This may occur at accumulated doses of, typically, 10^4 rads(Si).

Testing for Radiation Effects[1-7]

Test Facilities

Pulsed gamma sources are simulated by flash X-ray (FXR) machines and linear accelerators. The larger FXR machines are characterized by very narrow pulse widths and very high dose rates. These machines produce a continuous spectrum of bremsstrahlung X-rays to 2 MeV at dose rates of 10^7 to 10^{11} rads(C)/sec, with a pulse width of 20 to 70 nsec. Wider and variable pulse widths of X-rays or electrons are obtained from linear accelerators. The FXR and the LINAC (linear accelerator) are used for studying transient effects of ionizing radiation. Co 60 sources are used for steady-state gamma radiation at relatively low dose rates, on the order of 10^5 rads(C)/sec and below. These are for studying permanent effects of accumulated doses of ionizing radiation. Studies of neutron damage require the use of a steady-state or pulsed neutron reactor, which is in fact a gamma-neutron source, as the neutrons are accompanied by significant doses of gamma radiation.

The use of a pulsed laser to simulate the effects of ionizing radiation has been described by Ellis and Kim (reference 18). The laser simulates the same type of environment as the FXR and the LINAC for transient radiation effects studies, but does not result in a build-up of total dose in the device under test.

Permanent Effects[3,4]

The main considerations in evaluating permanent radiation effects in MSI and LSI circuits are: (1) adequate pre-irradiation and post-irradiation characterization of the device under test, (2) selection of electrical bias conditions during irradiation, and (3) determination of the number of samples that must be characterized to insure adequate statistical representation.

Characterizing the electrical performance of the device under test before and after irradiation may require more complete testing than either the manufacturer or the normal user of the device is likely to be interested in. The problem is that the most sensitive and/or most critical indicator of radiation damage may be a parameter which in normal application is so noncritical as to go largely unspecified and untested. In general, radiation damage can affect the performance of the device in three ways: (1) as a change in the current-voltage characteristics of the device terminals, (2) as a functional failure, and (3) as a change in the switching times and propagation delays.

A radiation-induced change in the current-voltage characteristics of the device terminals will generally appear as a decrease in fan-out and noise margin at the output terminals, with only small effects at the input terminals. Increased leakage currents due to displacement and surface effects may show up as an increase in the power supply drain. Functional failure is usually the result of damage in the internal logic cells, and is therefore not related or only concidentally related to measurable degradation at the device terminals. In the third mode of performance degradation, having to do with switching times and propagation delays, the indication depends on whether the logic cells are saturating or non-saturating. In saturating cells the switching times and propagation delays may either increase or decrease with radiation damage. In non-saturating cells they will invariably increase.

Selection of electrical bias conditions during irradiation is more critical for MOS circuits than for bipolar circuits. In bipolar circuits, ionizing radiation effects depend strongly on bias during exposure, but in most cases the vulnerability of the device is determined by displacement effects. In MOS devices, on the other hand, performance degradation is always traceable to shifts in the MOS transistor threshold voltage, which depends in a complex manner on gate bias during exposure. Bias conditions for testing can be (a) static and (b) dynamic. A static test requires that a specific logic condition be selected. Careful study may be required in order to make an educated guess as to a worst-case logic condition, and several devices might be tested under different logic conditions, but there is never any guarantee that the actual worst-case condition was among those tested. Full dynamic operation of the device under test during exposure allows a broad and perhaps realistic coverage of logic conditions, and also allows evaluation of the device's performance during exposure. It is, however, far from a worst-case condition for MOS arrays.

The number of samples that need to be included in a radiation effects experiment to insure adequate statistical representation depends

inversely on the size of the chip. The array fails if one transistor on the chip fails, so the statistics are related to the number of transistors rather than the number of chips tested. The main reason for testing more than two or three chips is to allow for different bias conditions as discussed above.

The time interval between exposure and post-irradiation characterization should be documented because of annealing effects. Significant annealing of radiation effects in MOS circuits can occur at room temperature over a period of several hours.

Transient Effects[3-7]

In transient effects testing on LSI one seeks to find the conditions that lead to a radiation-induced error of the transient kind in the operation of the device under test. The error originates as a distortion in a logic signal to an undefined or erroneous voltage level. This type of logic failure occurs at fairly high dose rates, 10^7 to 10^{10} rads(Si)/sec. The radiation source used in these tests is of the narrow pulse type, partly in order to keep the accumulated dose low so as to insure negligible permanent effects, and partly because the narrow pulse is a better simulation of the nuclear burst environment. In any case, the fast pulse nature of these tests requires a wide-band, low noise instrumentation system to observe and record the effects.

A representative instrumentation system would consist of three main blocks: the test cassette, the cable system, and the monitoring and control system. The test cassette would be designed to minimize electrical and radiation-induced noise, and for convenient interchange of devices under test. The device under test plugs into a socket in the test cassette, whose pins are programmed by a logic circuit also in the test cassette. The logic circuit couples the device under test to wide-band output drivers, which drive the cables connecting the test cassette and remote instrumentation. Lead (Pb) shielding is used to minimize radiation-induced noise in the cable drivers. To monitor the timing and shape of the radiation pulse, a PIN diode is mounted behind the device under test. The cables bring the signals of interest out to a high speed oscilloscope for photographing.

Devices that are particularly hard to transient effects (CMOS/SOS devices, specifically) can be particularly difficult to instrument. Kjar et al., (reference 7) found the photoresponse of the CMOS/SOS devices under study to be pretty well masked by normally low level radiation induced noise sources such as air ionization and charge scattering. They were dealing with dose rates in excess of 10^{10}rads(Si)/sec. The solution they found by experiment was to maximize radiation in the device itself while shielding the rest of the circuitry, and to provide special grounding configurations. A special cap was designed and built to replace the standard cap that mounts over the FXR faceplate. The device under test was mounted in a double-chassis, and triaxial cables were used. The outer shield was connected to the outer box, and the inner shield was connected to the inner box and to earth ground.

Dosimetry is by means of thermoluminescent detectors (TLDs) attached to the device under test during one or more FXR shots. Radiation

energy absorbed by the TLD is measured and converted to rads(Si). For purposes of calculating a dose rate each FXR shot is considered to be 30 nsec wide, which is in fact its FWHM. The dosimetry probably does not have an error of more than 20 percent.

The dose rate at which a transient error will occur depends in general on the radiation pulse width. If the 2 MeV flash X-ray is used in all investigations, then the pulse width is eliminated as a variable. If a linear accelerator is used, the pulse width needs to be quoted as a variable.

The most critical aspect of transient effects testing in LSI circuits is often said to be the selection of internal signal conditions to be used during the test. The traditional approach to this question assumes the possible existance of a weakest logic cell, or a worst case logic condition. Various series of input signal patterns are devised which set up the internal logic cells in one way or another, so as to test for pattern sensitivity, or guarantee complete cell coverage, etc. Defining a minimized set of optimum internal logic conditions for the device under test can be an expensive and time-consuming process. Then each input pattern in the set requires a series of exposures of increasing intensity to determine the failure threshold. There is some question, however, as to whether these scientifically derived test conditions yield failure thresholds that are significantly different from those arrived at by either intuitively or randomly derived test conditions. For example, M. G. Krebs at Northrop Research and Technology Center, describing a logic cell coverage technique that involves a computer-generated set of test patterns, concludes that any single test from the set would have identified essentially the same failure threshold. He states, "It is the preponderance of characterization data in the general literature indicating similar findings that leads one to consider the very tempting conclusion that a few arbitrary tests are all that are necessary to identify a failure threshold for LSI circuits" (reference 6). It may be that the nature of the disturbances caused by the photo-response is that a single and perhaps therefore undetectable failure is simply not of high probability. That is, it may just be more likely for several upsets to occur at nearly equal dose rates in a localized group, with a correspondingly higher probability that at least one of the upsets will propagate to an output terminal.

It might be sufficiently accurate then, particularly in preliminary evaluations, to design the test on the basis of the expected manifestation of an internal failure whose manifestation is virtually guaranteed, rather than on the basis of which individual gates can propagate a transient failure under what specific input conditions. Now, an internal failure can manifest itself in only a few ways: as a transient logic error in the output terminals, as incorrectly stored information, as a change in stored information, or as a transient inhibit (inability to manipulate information). In a combinational array, only a transient logic error in the output terminals need be tested for, and a random input pattern containing both 1s and 0s might be quite sufficient as a test condition. In a memory or a microprocessor, all four error manifestations would have to be tested for. In testing a memory, for example, one might hit the device with the radiation pulse just prior to a write

operation. (One might even address the write to the part of the memory that is physically farthest from the data register, or that has the longest access time.) Then a series of read operations would indicate whether the write operation was actually carried out, whether the word was correctly stored, and whether there was a change in any previously stored information. In testing a microprocessor, one might trigger the radiation pulse just prior to a software-interrupt operation, thus attempting to manipulate and preserve large portions of the microprocessor within a few clock cycles of the radiation pulse.

When a circuit is hit with a pulse of ionizing radiation, the photocurrents will cause an electrical transient through the power supply line that could result in transient logic failure. Thus, the characteristics of the power supply became a factor in determining the vulnerability of the device being tested. A well-regulated supply is an absolute necessity in a transient effects test, and the power supply surge current should be monitored and documented as an essential part of the radiation characterization of the device under test.

The use of a pulsed laser to simulate transient effects of ionizing radiation is described in reference 18. The laser proves itself to be an excellent diagnostic tool for the analysis of basic transient upset failure mechanisms. Its usefulness is based on two factors. It does not cause a build-up of total accumulated dose in the device under test, as do the FXR and the LINAC. Thus, only the effects of the photoresponse are present. In addition, when a transient upset occurs, selected areas of the chip can be masked off from the laser until the upset disappears. Thus, the exact location of the weak point can be identified. A number of unknown factors make it necessary to follow up or verify the laser tests with FXR tests. For one thing, the upset level needs to be identified in terms of rads(Si)/sec, and the correlation between a given laser intensity and an equivalent dose rate will always have to be verified. In addition, the metallization strips on the chip tend to mask off parts of the chip from the laser, but not from the FXR. The effect of that difference too must be investigated for each chip.

LSI Testing Techniques

Three categories of testing techniques have been identified for evaluating radiation effects in LSI devices: DC parametric testing, functional testing, and dynamic testing. DC parametric testing is the measurement of whatever DC parameters one might feel contribute to the characterization of the device under test. Functional testing means verifying the logical correctness of the device in actual operation. Dynamic testing is basically to measure changes in the propagation delays along dynamic paths through the device under test.

DC Parametric Testing[3, 4, 8]

Among the parameters measured as indicators of radiation effects have been quiescent and dynamic power supply currents, minimum supply voltage at which the device continues to operate, output voltage and current, and transistor gain. DC parametric testing was sometimes considered to give sufficient characterization by itself for certain small

scale integrated circuits. For medium and large scale integrated circuits, however, this type of testing is considered to be inadequate. That is not to say that DC parametric testing isn't useful (some DC parameters are critical), just that it would not in general be a reliable alternative to more detailed testing.

In some cases the radiation effects on a given DC parameter may be indirectly related to the radiation-induced failure of the device under test. For example, surface and junction leakage currents are both increased by exposure to radiation, and these currents are definite factors in the power supply current drawn by the device under test. Circuits don't usually fail on account of excessive leakage current, but insofar as increases in leakage currents are an indication of the build-up of accumulated radiation dose they are coincidentally related to the eventual radiation-induced failure of the circuit.

Measuring the power supply current has been particularly useful in evaluating radiation effects in CMOS circuits. When a CMOS circuit is in a quiescent state, leakage current is the only supply current that flows. Its measurement, therefore, is a direct measurement of the accumulated radiation dose. Moreover, when the circuit fails there is a drastic increase in the supply current that is directly related to the failure. The radiation-induced permanent failure mode in CMOS circuits is that the gate threshold voltage of n-channel elements has shifted to the point that these elements in the circuit will no longer turn off. The condition causes both a functional failure and a drastic increase in supply current.

In applying this type of measurement to a CMOS MSI/LSI circuit, two rules need to be adhered to. One is that the circuit must be in a quiescent state. Otherwise, the measured current is predominantly due to charging and discharging of internal capacitances. The other rule is that the current needs to be measured at multiple logic states. Order-of-magnitude differences in supply current are easily noted in different logic states. It may not, of course, be practical to perform the measurement at all possible logic states, but measurements at just one or just a few states are probably useless.

The minimum supply voltage at which a CMOS array will operate has also been used as an indicator of radiation damage. Raymond, et al., (reference 3) performed this type of measurement in testing a series of CD 4024 CMOS counters, stating that the measurement inherently defines a failure level for whatever system supply voltage is to be used. Their results, however, are ambiguous. They state, on the one hand, that all the arrays that were exposed under static conditions "failed" at 20,000 rads(Si). Their data, on the other hand, shows the same arrays continuing to "operate" at increased minimum supply voltages well beyong the 20,000 rads(Si) dose.

A commonly used, but relatively insensitive, indicator of radiation damage in an MSI/LSI array has been the output voltage level in the "1" and "0" states, with some specified output load. This type of data is generally presented as a graph of volts vs. accumulated dose. However, digital arrays on the MSI and LSI level generally fail for internal

reasons before there appears any significant degradation in the output levels. This is partly because the internal elements simply outnumber the output elements by a large factor. Unless the output elements are particularly weak, the probabilities favor an internal failure. In addition, the internal circuitry may be operating at a reduced noise margin in the first place, and thus be inherently more susceptible to radiation damage. The measurement is not, however, useless insofar as these voltage levels affect the fan-out.

In general, DC parametric testing can be a useful shortcut in evaluating radiation effects providing the parameter being measured can be related directly (as opposed to coincidentally) to the mechanism by which the circuit actually fails. That seems to be the case with the quiescent supply current in CMOS devices, as long as the n-channel elements continue to be the initial failure point. In bipolar LSI circuits there is probably no externally measurable DC parameter that can be directly related to the expected failure mechanisms.

Functional Testing[8, 9]

Functional testing means verifying the logical correctness of the device in actual operation. This is the primary test technique used by the semiconductor industry for LSI circuits. A large variety of logic analyzers and microprocessor-based analyzers are available for this purpose. The idea is to exercise the device as thoroughly as possible while checking the response of the device for logical errors that would be indicative of internal faults. To maximize the effectiveness of an exercise, carefully contrived test patterns and algorithms are developed to detect specific types of faults in specific devices. This is what is meant by an optimum test procedure for functional characterization of the device.

Functional tests are often directed toward detecting the "stuck-at" type of faults. A stuck-at fault is one in which a certain line, input or output, is stuck at a logical 1 (SA1), or stuck at a logical 0 (SA0), or stuck at some indeterminate value (SAX). Other types of faults, having to do with voltage or current levels, pulse widths, risetimes, or circuit timing, might be detected by functional tests insofar as they might cause functional errors (and many functional tests are designed for this purpose), but in general they can be sought after in parametric and dynamic tests.

Stuck-at faults can be intermittent or permanent. Intermittent ("soft") faults can be transient, meaning they occur only under certain timing conditions, or pattern-sensitive, meaning they occur only when the circuit under test is in a certain logical state. As might be expected, intermittent faults are the most difficult to detect. One must, of course, stumble over the unique conditions under which they occur. Permanent ("hard") faults are relatively easy to detect. One simply exercises the circuit under test in such a way that each and every gate and memory element in the circuit must demonstrate its ability to be in either state. The problem with detecting the existance of permanent faults is not how to do it, but how to do it in a reasonable amount of time.

A relatively simple combinational circuit will be used to illustrate the basic problem of functional testing and the nature of the various solutions to it.

A	B	C	D	X	Y	F
0	0	0	0	0	0	1
0	0	0	1	0	0	1
0	0	1	0	0	0	1
0	0	1	1	0	1	0
0	1	0	0	0	0	1
0	1	0	1	0	0	1
0	1	1	0	0	0	1
0	1	1	1	0	1	0
1	0	0	0	0	0	1
1	0	0	1	0	0	1
1	0	1	0	0	0	1
1	0	1	1	0	1	0
1	1	0	0	1	0	0
1	1	0	1	1	0	0
1	1	1	0	1	0	0
1	1	1	1	1	1	0

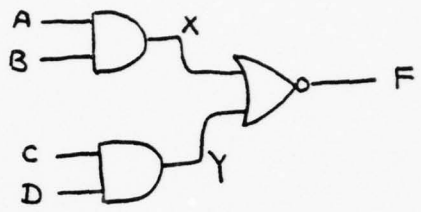

The circuit shown implements the AND-OR-INVERT function, $F = \overline{AB+CD}$. The object of functional testing is to verify the truth table shown above left. To accomplish this one can simply apply in sequence all possible combinations of 0's and 1's to the inputs, and check the output against the truth table for each input combination. This is called a full functional test. In this manner both permanent and pattern-sensitive faults will be detected. A shorter test is to apply the following sequence of inputs:

A	B	C	D	X	Y	F
0	0	0	0	0	0	1
0	0	1	1	0	1	0
1	1	0	0	1	0	0

The first input combination verifies that the output is not stuck at 0, and, under the assumption (to be verified with the second input combination) that the output is not stuck at 1 either, it also verifies that neither X nor Y is stuck at 1. The second input combination verifies that the output is not stuck at 1, and that Y is not stuck at 0. The third input combination verifies that X is not stuck at 0.

There are several things that should be noted about the shorter test sequence. First, it makes no particular attempt to detect pattern-sensitive faults. Second, it does not even detect all possible permanent faults. It verifies that X, Y, and F are free of stuck-at faults, and it verifies that no input is stuck at zero, and that neither AND gate

has both inputs stuck at 1, but if either AND gate has one input stuck at 1 and the other input free, this fault will not be detected. Third, if a fault is detected, it is not in general possible to determine what type of fault it is or where it lies. For example, if the response to the second input combination, 0011, had been 1 rather than the correct value of 0, one could not determine if the fault is that F is stuck at 1 or Y is stuck at 0. These then are the characteristics of a functional test that is not a full functional test: (1) Some types of stuck-at faults escape detection, and (2) an error indicates the existance of a fault, but not in general its type or location.

A full functional test to detect all permanent and pattern-sensitive faults is practical when the circuit under test has 4 inputs and therefore 16 combinations of input values. When the circuit has 24 inputs and therefore 16, 777, 216 combinations of input values, the full functional test is somewhat less practical. When memory elements and sequential operation are added, the number of individual exercises required for a full functional test becomes truly astronomical. Performing a full functional test on a microprocessor is not impractical, but impossible.

One is therefore faced with the problem of contriving a test sequence that is of a practical length and capable of detecting the types of faults that experience indicates are most characteristic of the circuit under test. The most convenient approach to generating an optimum test sequence, or test set, as it is also called, depends on the type of circuit to be tested. As follows are descriptions of useful approaches to the problem when the circuit under test is (a) a combinational array, (b) a random access memory, and (c) a microprocessor. The problem of implementing a test sequence once it is decided on is addressed after the discussion on microprocessors.

Functional Test Sets for Combinational Arrays[5,6,10-12]

The problem here is to determine a sequence of input combinations that will test the output of every gate in the circuit for permanent stuck-at faults. This amounts to driving the output of every gate to both of its logic levels in such a manner that a fault, if one exists, will cause a logical error in the output of the array. The number of combinations in the sequence should ideally be the minimum number that will do the job, but it is difficult to prove that a given test set is really of minimum size. A test set of "practical" size can either be computer-generated or manually developed.

A computer-generated test set is not necessarily of minimum size, as we shall see. The computer does, however, have a number of advantages. For one thing, its use gives the investigator some confidence that a test set of near minimum size, at least, will in fact be generated, and that the set will detect all permanent stuck-at faults in the outputs of all the gates in the array. The main advantage of the computer, however, does not seem to have been fully exploited, and that is that a good logic simulation program is not limited to combinational arrays nor permanent stuck-at faults. Krebs (references 5, 6, and 10) has used computer-generated test sets to detect hard faults in other than combinational arrays, but one gets the impression that the computer approach

may not be cost effective. What one buys with the computer time is a relatively direct approach to a test set of high confidence level, but not necessarily a superior test set.

Krebs calls his method a logic-cell-coverage (LCC) technique. He uses a Northrop in-house logic simulation program called LSP to generate a Fortran program which will in turn generate a test set by a technique called parallel fault simulation. Parallel fault simulation is the simulation in parallel of a number of faulted copies of the fault-free logic system. A satisfactory description of Krebs' LCC technique is well beyond the scope of this study and can not be attempted. It should be noted that Krebs was seeking radiation-induced faults that were transient effects in the sense that they were due to photoresponse, but were "permanent" faults in the sense that the test sets were not designed to detect pattern or timing sensitivities. In reference 6 the LCC technique is applied to an Intel 3003 Look-Ahead Carry Generator, shown in the figure below.

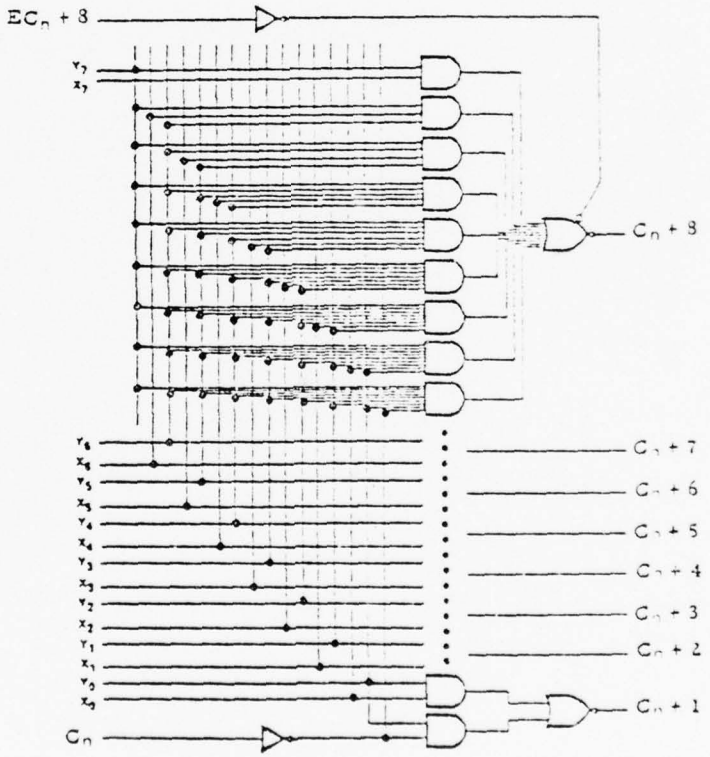

The device has two 8-bit input words, X and Y, and one 8-bit output word, C_{n+1}, ..., C_{n+8} . There is also a one-bit C_n input and an enable input, E, for the C_{n+8} output. The computer-generated test set, in hexadecimal digits, is as follows:

Test	X	Y	C_n	E	Output
1	00	FF	0	1	00
2	00	FF	1	1	FF
3	01	FF	1	1	00
4	02	FF	1	1	01
5	04	FF	1	1	03
6	08	FF	1	1	07
7	10	FF	1	1	0F
8	20	FF	1	1	1F
9	40	FF	1	1	3F
10	80	FF	1	1	7F
11	FF	00	0	1	FF
12	FF	FF	0	1	00
13	00	FF	1	0	(C_{n+8} open)

One will note that the circuit consists of eight NOR gates, and the inputs to each NOR gate is from a group of AND gates. There are 54 gates in all, and 13 steps in the test sequence. The first test checks all of the NOR gates for a stuck-at-one condition, and simultaneously checks the lowest AND gate in each of the 8 groups of AND gates for a stuck-at-zero fault. It also checks the C_n inverter for stuck-at-zero.

The second test checks all the NOR gates for a stuck-at-zero condition, and the C_n inverter for stuck-at-one, and all of the AND gates for stuck-at-zero fault. As each group of AND gates feeds a single NOR gate, only one AND gate of each group can be tested for stuck-at-zero at a time. Of course, one AND gate in each of several groups can be tested simultaneously, but since one of the groups contains nine AND gates, a minimum of nine separate tests are required to check them all. This is accomplished in tests 1, and 3 through 10. Test 11 checks all of the AND gates for a stuck-at-one fault. Test 12 checks all of the NOR gates for a stuck-at-one fault. The last test is just for the enable control on C_{n+8}.

The alternative to computer-generation of test sets is to develop them manually. This is not as impractical or difficult an approach as one might imagine. In fact, it's kind of fun, like working a puzzle. The disadvantages are obvious: There is no guarantee that a practical test set will not continue to elude the investigator after weeks of effort. There is the nagging suspicion that the computer would have generated a significantly shorter test set in a significantly shorter time. And there is a higher probability of an oversight. Nevertheless, the method should not be discounted.

There are a few simple rules that one needs to follow to check a gate for a stuck-at condition. For example, to check an AND gate for a stuck-at-zero fault one must drive the output to 1, which requires driving all of the gate's inputs to 1. To check the same gate for a stuck-at-one fault, at least one of its inputs must be driven to 0. These kinds of considerations lead to the following set of rules:

Gate Type	SA0	SA1
AND	All 1s	At least one 0
OR	At least one 1	All 0s
NAND	At least one 1	All 1s
NOR	All 0s	At least one 1
EX-OR	Odd number of 1s	Even number of 1s

A more efficient test vector is usually achieved if the "at-least-one" rules are interpreted as meaning one and only one. For example, if a 4-input NOR gate is to be checked for SA1, and its 4 inputs are from 4 AND gates, then driving only one of the AND gates to 1, while holding the other 3 at 0, accomplishes the SA1 test on the NOR gate while simultaneously testing the one AND gate for SA0. Three more separate tests will be required to test the other AND gates for SA0 faults.

To manually develop a test set it is absolutely essential to have an exact (as opposed to "equivalent") logic diagram of the array. It helps to have Boolean expressions for the outputs as functions of the inputs. The simple rules for checking the various gate types, plus a little common sense and patience, may sometimes result in the development of a practical test set in less time than it would take to even set the problem up for the computer. And it's definitely more fun. As an experiment an attempt was made to manually develop a test set for the Intel 3003, which was the object of Krebs' computer analysis. The development was done from scratch, that is, without reference to the computer-generated test set. It took about a half an hour to develop the following 11-vector set:

TEST	X	Y	C_n	E	OUTPUT
1	00	00	1	1	FF
2	00	FF	0	1	00
3	01	FF	1	1	00
4	02	FF	1	1	01
5	04	FF	1	1	03
6	08	FF	1	1	07
7	10	FF	1	1	0F
8	20	FF	1	1	1F
9	40	FF	1	1	3F
10	80	FF	1	1	7F
11	00	FF	1	0	(C_{n+8} open)

Another two hours were spent checking the manually developed set against the computer-generated set, in view of the fact that the computer-generated set defined 13 tests. It was not determined that the computer-generated set would be likely to detect any faults that the manually developed set would miss.

In the manually developed test set the first test checks all NOR gates for SA0, simultaneously checking all AND gates for SA1, and the C_n

inverter for SA1, simultaneously checking the C_n inverter for SA0 and one AND gate of each group for SA0. Tests 3 through 10 complete the SA0 checks on the other AND gates. The last test is just for the enable control on C_{n+8}.

The Intel 3003 is particularly easy to develop a test set for, owing to its regularity and the fact that it is only two gates deep. A somewhat more challenging array is the SN54181 Arithmetic Logic Unit. Several hours were spent trying to manually develop a test set for it, with no particular success. John Knaijuk, however, (reference 11 and 12) did not give up so easily, and manually developed a 14-vector test set for the SN 54181. He first developed a 21-vector test set for it, and subsequently reduced the set to 14. It is not known if he used a systematic approach in the original development (reference 11 was unfortunately not readily obtainable), but the reduction from 21 tests to 14 involved the use of no particular "method," just a closer look at the array.

In summary there is some question as to the cost effectiveness of the computer approach to defining a test set for a combinational array. The lack of a simple, fixed, cookbook procedure for manually developing test sets probably discourages the manual approach, and that is unfortunate.

Functional Test Sets for RAMs[13, 14]

Functional testing of RAMs is usually directed at detecting more than simple permanent stuck-at faults. Permanent stuck-at faults exist, and must be tested for in the memory cells, address decoders and data registers, but memories are prone to failures having to do with access times, recovery times, pattern-sensitivities, write/read transitions, etc. Testing the memory involves a sequence of writing and reading certain test patterns of data in the memory. Logical errors in the reads are checked for, and when found indicate one type of failure or another.

A large number of standard test patterns have evolved that are seen to be particularly effective at detecting particular types of faults. A test pattern that is highly useful for one circuit design or process technology can be practically worthless for a different design or process technology. The effectiveness of some of the patterns depends on the cell geometry. That is, it depends on whether a given 4 K-bit memory, for example, is laid out as a 64 X 64 cell array, or 32 X 128, or dual 16 X 128, etc., and on how the rows and columns are designated. Thus, one really needs to know the details of how a memory is laid out, in order to determine the true effect of a given test pattern. This information is not always available, and is in fact sometimes considered proprietary information. As follows are descriptions of some of the standard test patterns and the types of failures they are apt to catch.

In the walking one's pattern 1s are written into the first word and 0s into all the others. In an N-word memory, this initialization requires N writes. Then the entire memory is read (N reads) and checked for errors. This is followed by two writes: the word that was 1s is changed to 0s, and 1s are written into the second word. Then N reads

are executed, as the memory is again checked. Then two writes again: the word that was 1s is changed to 0s and 1s are written into the next word. Then N reads, 2 writes, etc., till the 1s have "walked" clear across the memory. Approximately N^2 memory accesses are required to complete the test, and this is considered excessive by many. (The exact number of accesses, including initialization, is $N^2 + 3N - 2$, which amounts to N^2 reads and 3N-2 writes.) The procedure is effective in verifying the functionality of the address decoder and detects slow sense-amplifier recovery. Slow sense-amplifier recovery would be indicated by a read sequence showing 1s in sequential words.

A shortened form of the walking one's pattern is the diagonal pattern. Here, one assumes the memory is laid out square. A 256-word memory, for example, would be liad out in an array 16 words wide and 16 words high. In a sequence of N writes, 1s are written into the words that lie along the main diagonal of the square and 0s into the other words. Then the entire memory is read and checked for errors (N reads). Each row is subjected to two writes: the word that was 1s is changed to 0s, and the word in the next column to the right is changed to 1s. In an N-word memory there would be N rows, so this write sequence involves 2 N accesses. Then the memory is read and checked again (N more reads). Each row is again subjected to two writes, as the all-1s word in each row is shifted one place to the right. As the all-1s word in each row arrives at the end of the row, its next shift is to the beginning of the row. The test is completed, after $N^{3/2} + 3N$ separate accesses, when the 1s are again in the main diagonal. This pattern, like the walking ones, is effective in detecting address decoder faults and recovery times, but is said to be less sensitive to certain other functionalities. It is considered to be a minimal functional test.

Another minimal test is the marching ones pattern. This begins by writing 1s in the first word and 0s in all the others. Only the word with 1s in it is read and checked. Thus, N writes and 1 read have been executed so far. Then 1s are written into the second word and the second word is read for verification (1 write, 1 read). Then 1s are written into the third word, and the third word is read (2 accesses), etc. This continues until the memory is filled with 1s. The complete sequence requires only 3N accesses. For a mere 2N more accesses it can be followed, and usually is, by its complement, the marching zeros pattern. The marching 1/0 pattern tests the functionality of the memory cells, but does not check write recoveries, multiple cell selections (a decoder fault), nor read/read nor write/write interactions.

The galloping ones pattern begins with 0s being written into all memory locations. The first word is read for verification, and replaced by ones. The second word is read (it should be 0s), and the first word is read (it should be 1s). The third word is read, and the first word is read again. The fourth is read, then the first, etc., until the Nth word is read and the first is verified one more time. Now the second word is read (it should still be 0s), and replaced by 1s. Then the first word is read (it should still be 1s). then the second is read again. The read-process continues: third and second, fourth and second, fifth and second, etc. Now the third word is read and replaced by 1s, after which the paired readings are repeated, pairing all readings

with the third word: first and third, second and third, fourth and third, fifth and third, etc. When all N words have been used as the second half of this paired reading process, then all possible read/read interactions will have been given a chance to occur and be checked for. It also examines the disturbance causes in other cells by writing in a given cell. It requires $2N^2 + N$ accesses.

There is a shorter version of the galloping ones pattern that requires definite knowledge of the cell geometry. The surround-disturb pattern assumes that if there are going to be any inter-cell disturbances they would be most likely to occur between adjacent cells, and so applies the galloping ones pattern to each cell, pairing it only with its eight adjacent neighbors.

While the galloping ones test checks for read/read interactions, write/read interactions are detected by a galloping write-recovery pattern. It requires approximately $12\ N^2$ accesses to the memory under test.

One will note that the more complete tests, namely, the walking ones, galloping ones, and galloping write-recovery tests, require on the order of N^2 memory accesses. The diagonal test has some characteristics similar to the walking ones, but reduces the required number of accesses by viewing the memory as being laid out in a square (which may or may not be factual--it probably doesn't matter), and driving the pattern down several rows of cells simultaneously. The reduction in accesses is from N^2 to $N^2/2$. The same technique is applied to other patterns to effect a reduction by N, that is, from N^2 to $N^2/2$. Hence we have these patterns, all requiring on the order of $N^2/2$ accesses: the galloping column, the galloping diagonal, walking columns, walking complementary columns, etc.

There are a good deal more test patterns that are used enough to have names, and an unnumbered quantity of unnamed user-written tests. It may be a fact that no memory chip will pass all the functional tests that currently exist. It is related in reference 13 that one investigator, testing "high reliability" memories, tried most of the popular patterns and collected the devices that passed, and then tested them with a modified galloping ones pattern, and obtained a 30% failure rate.

The implications of this for radiation effects testing is that the term "failure" should probably be recognized as a relative term rather than an absolute one, relative, that is, to the user's application. Thus, a radiation-induced "failure" can only be defined with respect to a specific test, and for any given level of radiation exposure, there probably exists a test which will show the device to have failed.

An interesting test pattern devised by Knaizuk and Hartmann (reference 14) is directed towards detecting all permanent stuck-at faults in the address decoder, memory cells, and data register of any RAM. The test is only 4N accesses long, and may therefore be useful in transient radiation effects studies. In this test the memory locations are divided into three groups in accordance with the addresses of the locations. Group zero, a_0, consists of locations whose addresses are

(in hexadecimal digits) 00, 03, 06, 09, 0C,... etc. Group one, G_1, consists of locations whose addresses are 01, 04, 07, 0A, 0D, ... etc. The last group, G_2, consists of locations whose addresses are 02, 05, 08, 0B,0E, ... etc. The algorithm is as follows:

1. Write 0s into G_1 and G_2.
2. Write 1s into G_0.
3. Read G_1. If all words in G_1 aren't 0s, a fault is indicated.
4. Write 1s into G_1.
5. Read G_2. If all words in G_2 aren't 0s, a fault is indicated.
6. Read G_0 and G_1. If all words in G_0 and G_1 aren't 1s, a fault is indicated.
7. Write 0s into G_0, then read G_0. If all words in G_0 aren't 0s, a fault is indicated.
8. Write 1s into G_2, then read G_2. If all words in G_2 aren't 1s, a fault is indicated.

Functional Test Sets for microprocessors[15, 16]

When testing a combinational array, one does not generally test the individual transistors, but rather groups them into gates and tests the gates. The same type of approach, under the name module sensorialization, can be used in testing a microprocessor. In module sensorialization individual gates are grouped into larger blocks and tested as individual subsystems. To apply this technique the investigator must be thoroughly familiar with the hardware architecture and software-response specifications of the microprocessor under test. This is not a trivial assignment. Semiconductor makers regularly change designs and masks slightly to improve yield, and these modifications often cause functional changes that may invalidate a given functional test set and its results. Naturally, there are sometimes important differences too between similar microprocessors from different manufacturers. If and when the test designer has attained a thorough familiarity with all of this particular microprocessor's idiosyncracies, he can then develop an ordered set of test sequences in the microprocessor's programming language for testing the subsystems or modules one by one.

The first step is to partition the microprocessor into modules, some of which may overlap. The inputs and outputs of each module need to be accessible directly or indirectly to the external terminals. The next step then is to devise an appropriate test sequence for each module. One must determine what types of faults he should be checking for in each module, and how comprehensive a test is required to uncover them. The design of the test proceeds from module to module, until the last one has been covered. Since some instructions may not have been used in testing any of the modules, a final sequence of commands must be

used to exercise any untested instructions. A final complication is the possible existence of pattern sensitivities, which in microprocessors show up in the form of sensitivities to certain instruction sequences. These may arise as a result of capacitive coupling paths between various points on the chip, or it may be that certain sequences don't allow enough time to complete charge transferrals in MOS devices. In any case their prediction is next to impossible, and they must simply be accidentally discovered for each device and, once discovered, included in the overall test sequence.

In reference 16 the module sensorialization technique is applied to the 8080 microprocessor. The unit was partitioned into the program counter, register files, stack pointer, arithmetic logic unit, accumulator, and timing and control. The 8080, being an MOS circuit, is subject to some pattern sensitivities. Tests for known sensitivities can be supplied by the manufacturer.

Designing an adequate test for a given microprocessor requires an intensive study of the microprocessor itself and careful consideration of the objectives of the test. A quick test, what one might call a minimal functional test, generally would require a series of test patterns about 1,000 clock cycles long. A more comprehensive test, tailored to a particular application so that specific requirements can be defined and exhaustively tested for, would be 10 to 20 times longer. In testing for permanent radiation effects it is not impractical to apply a fairly comprehensive test. In testing for transient radiation effects with the flash X-ray a much more abbreviated test is definitely called for. One could either take the approach of an extremely abbreviated test (just a few clock cycles long) on the microprocessor as a whole, or direct a somewhat less abbreviated test to a particular module of the device. Transient radiation effects studies using the pulsed laser technique offer some interesting possibilities in terms of testing the modules one by one. One can simply mask off the modules not currently under test. In that way, fairly complete studies of transient effects can be done using relatively comprehensive functional tests.

Implementation of Functional Test Sets[15, 16]

Implementing a functional test can be a problem in itself. It is a fairly simple problem when one is testing a combinational array for stuck-at faults. The test set is small and timing is probably not a factor. The test sequence can be stored in a memory and applied to the device under test by simply reading out the memory. The correct responses to each test vector can either be generated by a device of the same type as the one under test but known to be good, or stored in another memory and read out with the test vectors. In either case the correct responses are compared with the response from the device under test, and when the reponses being compared differ an indication is given and the test is discontinued. When the device under test is a memory or a microprocessor the sequence of tests, and the correct responses, may be too long to be conveniently stored in memory. The technique is, however, commonly used.

In the stored pattern approach the test vectors and responses are stored in a mass memory. They are transferred in batches to a high-speed RAM, and the test is implemented by transferring the bit patterns in a burst from the storage buffer to the unit under test. The main problem with this method is that it requires a lot of mass memory and a relatively large buffer memory. High-speed RAMs become quite expensive when any great amount of memory is needed. In reference [8] it is stated that the program counter test for the 8080 required 262,000 bit patterns and the register file test required another 50,000. The cost of the memory can become a major part of the total cost of the test system.

An alternate approach is algorithmic pattern generation. In this method the test patterns and responses are generated by a microcomputer. The method is fast and flexible where applicable, but not always practical. It depends on the nature of the bit patterns that need to be generated. In the 8080 tests cited above, the 262,000-pattern test set required for the program counter was generated by a 6-instruction microprogram. On the other hand, the register file test set was a more complex procedure. Generating the 50,000 patterns needed for that test required an 82-instruction program. Large commercial test systems can generally be operated in stored pattern, algorithmic, or combination of both modes.

In a technique called comparison testing, the correct responses to the test vectors are neither stored in memory nor algorithmically generated, but are, in fact, the responses from a reference device of the same type as the device under test. Obviously, the reference device must be known to be capable of passing all of the tests.

Dynamic Testing[8, 17]

The term dynamic testing as used here means measuring the propagation delays or access times along all dynamic paths through the device under test. As a means of evaluating radiation effects, this method of testing has much to offer. The measurements are made [illegible] during a functional test of the device. The functional test can be relatively simple. A functional test designed to detect nothing more than permanent stuck-at faults would be ideal, since that type of test is easy to design and requires relatively few test vectors. In addition, it exercises every gate in the circuit in both of its states in such a way that every gate's operation is propagated to an output terminal, and those are just the conditions under which the propagation delays need to be measured. Now, the propagation delays themselves are sensitive to many if not all of the same physical conditions that cause soft failures. Soft failures, that is, failures that occur only under certain logic and/or timing conditions, may be due to minor irregularities in the physical structure of the device resulting in variations in resistance values, transistor gains, and threshold voltages, as well as variations in the idiosyncracies of the internal capacitances. These are the very same factors that determine the propagation delays. Thus a relatively simple functional test during which propagation delays are measured might provide the same information as a series of much more sophisticated functional tests designed to detect various kinds of soft failures.

In evaluating radiation effects, one would be interested changes in the propagation delays, rather than in the propagation delays themselves.

Thus, the method is independent of circuit design and processing technology. It is also independent of the functional complexity of the circuit. It can provide a convenient basis of comparison of radiation effects in different types of RAMs, for example.

In reference 8, three types of RAMs were tested for total dose effects of ionizing radiation. The average change in access time for each device was measured as a function of total dose. Changes on the order of 10 to 20 percent were observed in the access times as the devices approached permanent failure. The devices were subjected to comprehensive functional testing at various accumulated doses, so that the results of the functional tests would be compared with the changes in the access times. It was concluded that changes in the access time are an accurate leading indicator of subsequent device failure with additional irradiation.

Unfortunately the particular functional tests used did not detect any soft failures prior to a permanent hard failure, so there was no opportunity to establish a correlation between radiation-induced soft failures and radiation-induced changes in the access times. This correlation would have to be established before one could with real confidence substitute dynamic measurements for the sophisticated functional testing required to ferret out soft failures. It might, therefore, be suggested that some effort be expended in establishing this correlation.

The main barrier to dynamic testing is the cost of the test equipment required to perform the measurements. The equipment must provide exceptionally good dynamic pulse fidelity, which probably requires that the signals be handled in a true transmission line environment. In reference 8 it is stated that computer controlled testers that have this capability for testing LSI devices have a base price in excess of $200,000. (Of course these are complete testers having extensive DC parametric and functional testing capabilities as well.) It is further stated that many manufacturers of functional test equipment claim a dynamic testing capability in their equipment on the basis of frequency and timing adjustments. However, this equipment often does not have sufficient pulse fidelity to make an accurate measurement unless many functional test passes are made with varying timing strobes.

Conclusions and Recommendations

Permanent Effects

Radiation-induced functional failure is usually not related, or is only coincidentally related to measurable degradation in the current-voltage characteristics of the device terminals. It is usually the result of damage in the internal circuitry. The only parameters that can be measured from the device terminals and then be directly related to the condition of the internal circuitry are the propagation delays.

Transient Effects

It may not be necessary to run a complete series of transient effects tests for every member of a specially designed test set. In

fact, a single and random test vector may be as effective as any other logical input condition for determining a failure threshold. Thus, it might be sufficiently accurate to design a series of transient effects tests on the basis of the expected manifestation of an internal failure whose manifestation is virtually guaranteed, rather than on the basis of which individual gates can propagate a transient failure under what specific input conditions.

LSI Testing in General

Functional tests to detect stuck-at faults are probably more conveniently and cheaply designed manually than with the aid of a computer.

It is probably true that for any given RAM there exists a functional test that will indicate a soft failure. As a corollary, it can be said that for any given level of radiation exposure there exists a functional test that will show the RAM under test to have "failed". The question is not so much whether a potential soft fault exists, but how many of them can be detected using what set of functional tests. It is possible that the measurement of access times in a RAM, during a functional test designed to detect only hard stuck-at faults, could reveal much about the existence and quantity of potential soft faults. Unfortunately, there does not seem to have been any work done to determine a correlation, if one really exists, between radiation-induced changes in access times and radiation-induced increases in the number of soft failures that can be detected using a given set of functional tests.

References

1. H. L. Olesen, Radiation Effects on Electronic Systems, Plenum Press, 1966.

2. L. W. Ricketts, Fundamentals of Nuclear Hardening of Electronic Equipment, Wiley Interscience, 1972.

3. J. P. Raymond, et al., Study of Radiation Effects in MSI/LSI Technologies, Report No. DNA 3517F, 26 March 1975.

4. J. P. Raymond, et al., Study of Radiation Effects in Bulk CMOS Microcircuits, I^2L/LSI Logic Cells and Optical Couplers, Report No. DNA NRTC 75-32R, June 1975.

[illegible]. G. Krebs, et al., Radiation Effects on MSI/LSI Devices, Report [illegible]o. NRTC 77-18R, 1 April 1977.

[illegible]. G. Krebs, "Logic-Cell-Coverage Technique for Transient Ionizing Radiation Characterization of Microcircuits," IEEE Transactions on Nuclear Science, Vol. NS-24, No. 6, December 1977.

7. R. A. Kjar, et al., Complementary-Symmetry/Metal Oxide Semiconductor (CMOS) Circuit Hardening, Vol. I, "Silicon-on-Sapphire (SOS) CMOS Circuit Fabrication and Characterization," Report No. AFWL-TR-74-243, Vol. I, July 1975.

8. G. F. Nelson and E. E. King, "Methods for Radiation Testing Random Access Memories and LSI Circuits," IEEE Transactions on Nuclear Science, Vol. NS-24, No. 6, December 1977.

9. D. E. White, Fault Detection Through Parallel Processing in Boolean Algebra, Report No. UCLA-ENG-7504, March 1975.

10. J. P. Raymond, et al., final report on Contract DNA001-73-C-0154 (period of performance: Jan. 1975 through Dec. 1975).

11. J. Knaizuk, Manual Testing Procedure for Detecting Single "Stuck-At" Faults. (This report was listed in reference 12 under an incorrect number. The correct number is not known. Garbled references have been a problem more than once during this study.)

12. J. Knaizuk, Manual Fault Detection Test Set Minimization, Report No. RADC-TR-77-149, May 1977.

13. M. Marshall, "Through the Memory Cells--further explorations of ICs in Testingland," EDN, February 20, 1976.

14. J. Knaizuk and C. R. P. Hartmann, An Optimal Algorithm for Testing Random Access Memories, Report No. RADC-TR-76-79, March 1976.

15. S. E. Scrupski, "Why and How Users Test Microprocessors," Electronics, March 2, 1978.

16. A. C. L. Chiang and R. McCaskill, "Two New Approaches Simplify Testing of Microprocessors," Electronics, January 22, 1976.

17. G. F. Nelson and W. F. Boggs, "Parametric Tests Meet the Challenge of High-Density IC's," Electronics, December 11, 1975.

18. T. D. Ellis and Y. D. Kim, "Use of a Pulsed Laser as an Aid to Transient Upset Testing of I^2L LSI Microcircuits," paper presented at 1978 IEEE Conference on Nuclear and Space Radiation Effects, Albuquerque, New Mexico, July 1978.

1978 USAF-ASEE SUMMER FACULTY RESEARCH PROGRAM
sponsored by
THE AIR FORCE OFFICE OF SCIENTIFIC RESEARCH
conducted by
AUBURN UNIVERSITY AND OHIO STATE UNIVERSITY

PARTICIPANT'S FINAL REPORT

RELATIONSHIP OF FIGHTER PILOT-OPERATOR AGE AND FLYING EXPERIENCE TO SELECTED UNSAFE ACTS AND PSYCHOPHYSIOLOGICAL AND ENVIRONMENTAL VARIABLES IN MAJOR/CLASS A MISHAPS

Prepared by:	Kenneth W. Wegner, Ed.D.
Academic Rank:	Associate Professor
Department and University:	Counseling Psychology Boston College
Assignment:	Norton AFB Air Force Inspection and Safety Center Directorate of Aerospace Safety Life Sciences Division
USAF Research Colleague:	Anchard F. Zeller, Ph.D.
Date:	August 11, 1978
Contract No.:	F44620-75-C-0031

RELATIONSHIP OF FIGHTER PILOT-OPERATOR AGE AND FLYING EXPERIENCE TO SELECTED UNSAFE ACTS AND PSYCHOPHYSIOLOGICAL AND ENVIRONMENTAL VARIABLES IN MAJOR/CLASS A MISHAPS

by
K. W. Wegner

ABSTRACT

Human factor involvement in aircraft mishaps remains an important concern to the Air Force, although the rate of mishaps per 100,000 flying hours is currently at a historically low level. Any improvement in prevention of human involvement in these mishaps depends on isolating those factors which occur most frequently and making recommendations toward reducing their rate of occurrence.

In this study, a variety of unsafe acts and psychophysiological and environmental variables were studied in relation to age, model hour, and total flying experience of fighter pilot-operators involved in major/Class A mishaps over a 6-year period (1972-77). The chi-square statistic was used to test these relationships.

With regard to age, the 24 to 25 and 30 to 31 year-old groups seem to have a higher frequency of occurrence of stall, spin, spiral, or dive-related unsafe acts; and the disorientation/vertigo, poor crew coordination, misjudged speed and distance, and selected wrong course of action psychophysiological variables. Those pilots with less than 500 flying hours in a particular model also appear to have the highest frequency of occurrence of the psychophysiological variables disorientation/vertigo, failure to use accepted procedures, distraction, selected wrong course of action, and delay in taking action. An important conclusion of this study is that all of the significant factors are amenable to prevention through improved emergency procedure training. It is recommended that the most practical, safe, and economical prevention program would include the increased use of simulator-type training as a supplement to in-flight training.

ACKNOWLEDGMENT

The writer is extremely grateful to the Air Force Office of Scientific Research for the opportunity to conduct this summer research. Mr. Fred O'Brien, representing ASEE and Auburn University, was most helpful in setting up the administrative procedures necessary for successful accomplishment.

The writer is indebted to the Air Force Inspection and Safety Center (AFISC) for providing a most receptive working environment; particularly to AFISC Commander Major General Robert W. Bazley; Director of Aerospace Safety Brigadier General Garry A. Willard, Jr.; and Deputy Director of Aerospace Safety Colonel Robert A. Owens. It also would have been impossible to conduct this study without the computer data bank output provided by Virginia Holley and Dean Thorpe. My sincere appreciation is expressed to them, and to Jim Marsh for his statistical consultation. A special note of thanks is also extended to Mary Razo who expedited the word processing of this report.

Last but not least, it has been enjoyable working directly with Dr. Anchard F. Zeller and Colonel William F. Belk, Life Sciences Division. Their advice and consultation on the conceptual and design elements of this study have been invaluable.

LIST OF TABLES

INTRODUCTION

Human factor involvement in aircraft mishaps* has been of concern to the Air Force for many years. However, focused study of human factors related to Air Force mishaps did not blossom until approximately 15 years ago. Historically, the Directorate of Flight Safety Research was established in 1943. In 1950 this service was moved to Norton AFB, California, and is presently known as the Directorate of Aerospace Safety (DAS), Air Force Inspection and Safety Center (AFISC). According to AFISC Regulation 23-1, 15 June 1977 (Ref. 3), part of the mission of DAS is to conduct safety studies and analyses to evaluate mishap prevention programs, and to develop policies and procedures to assist in the identification and correction of safety-related problems in all Air Force functional areas. Within DAS, part of the mission of the Life Sciences Division (LSD) is to analyze mishap data to determine methods of preventing mishaps caused by human factors. The efforts of the LSD in this area have produced approximately 140 studies and reports on the aeromedical, human factors, and bioenvironmental aspects of the Air Force Safety Program since 1962.

As a research laboratory, the DAS is unique in that it is the sole source of report data on all Air Force mishaps. The original input data are the individual mishap reports which are housed in the Center. In addition, these reports are analyzed and pertinent data abstracted for input to computer banks and later retrieval. The output information available for study includes the individual mishap report, a computer-produced individual mishap summary, and statistical summaries of data related to various mishaps. With this background, it is obvious that the DAS is the only focal point available for basic research in human factors related to aircraft mishaps, which is the general objective of this study.

This report documents efforts to determine whether selected human factors are related to the age and flying experience of pilots involved in aircraft accidents. In order to provide some common parameters, the study was limited to the pilot-operator involvement in major/Class A fighter mishaps during the 1972-77 calendar years. Prior to

---

*The terms "mishap" and "accident" are used interchangeably in this report. They mean the same thing but "accident" is used in some references cited. The current official Air Force term is "mishap."

1977, a major accident was defined as one in which an aircraft was destroyed or received substantial damage. Beginning 1 January 1977, mishap classification criteria were changed by the Department of Defense (DOD). Since then, a DOD Class A mishap is defined as one in which the resulting total cost of property damage, injury, and illness is $200,000 or greater; or an aircraft is destroyed; or a fatality occurs. For the calendar year 1977, the Class A mishaps were not identical in type with the major mishaps of previous years. However, the high degree of overlap in these two definitions and similarity of numbers suggested that the 1977 group could be validly included in this study.

OBJECTIVES

The general objectives of this study were to determine if any relationships existed between age and flying experience (taken separately), and the occurrence of selected unsafe acts and psychophysiological and environmental variables in fighter aircraft mishaps. The general null hypothesis is that these variables are not associated.

The background for selecting these variables is found in several previous studies. Zeller and Burke (Ref. 5) examined factors in jet pilot proficiency and arrived at several conclusions related to age and flying experience in jet aircraft. In their study, the highest mishap potential in jet fighter operations was experienced by pilots under 25 years or over 39 years of age, with those over 40 having an extremely high potential. In addition, jet fighter pilots with less than 500 hours of total jet and non-jet flying experience had an accident potential almost twice as high as those with more experience. Since this study was conducted during the early jet age (pre 1959) of the Air Force, data were not available to examine flying experience in different types and models of jet aircraft. Unfortunately, there has not been the opportunity to update and replicate this study.

Another related study by Ricketson et al. (Ref. 4) was focused on the analysis of pilot error accidents and various psychophysiological and environmental factors in U.S. Army aviation. Army field accident investigation board reports indicated that pilot error, alone or in combination with other factors, was the largest cause of Army aviation accidents. Ricketson et al. used the approach of factor analyzing 91 dichotomous psychophysiological and environmental variables contained in an accident form developed and used jointly by the Army, Navy, and Air Force. Their

purpose was to extract representative clusters (factors) that would approximate clusters of "human error events," which might explain malfunctions of the man-machine environment system that result in aircraft mishaps.

Ricketson et al. found that 29 of the 91 variables accounted for 96 percent of the 1,520 helicopter and 452 airplane pilot-error accidents. For airplane accidents, nine factors or clusters were identified as follows:

I. Disorientation
II. Overconfidence
III. Procedural Decisions
IV. Crew Coordination
V. Precise Multiple Control
VI. Limited Experience
VII. Task Oversaturation
VIII. Attention
IX. Inadequate Briefing

Factor IX was the only one not common to helicopter accidents. For helicopters, this factor was identified as "IX. Other Weather."

The results of the work of Ricketson et al. and Zeller and Burke suggested that it might be useful to extend and more deeply analyze the relationships between age, flying experience, and psychophysiological and environmental variables. For example, a specific question which arose was do the clusters found by Ricketson et al. also appear consistently in Air Force mishaps? Secondly, how do Zeller and Burke's results on age and flying experience relate to these same variables and clusters? If significant relationships could be found among these variables, it might suggest some recommendations regarding selection, retention, and/or changes in flight training procedures for aircraft pilots.

METHOD

An attempt to analyze all major/Class A aircraft mishaps over a period of time could lead to confusion or masking of significant information or trends. Different types of aircraft (fighters, bombers, cargo, etc.) have different missions and different crew functions. In order to keep some commonality in the variables analyzed, the sample for this study was limited to those variables associated with the pilot-operator only of fighter aircraft over a 6-year period. The

time period chosen was calendar years 1972-77. The data coding system for aircraft accident and incident classification elements and factors was changed beginning in January 1972, precluding the efficient use of that computer bank information for prior years. The independent variables for study were age, model hours, and total flying hours; and the dependent variables were selected unsafe acts and psychophysiological and environmental factors. Due to the suspected non-parametric occurrence of the dependent variables, the tool chosen for analysis was chi-square.

Samples and Variables. During calendar years 1972-77, there were 333 major/Class A mishaps involving fighter aircraft. Three models of fighter aircraft (F-5, F-15, and F-16) were at very low inventory level during this period, and the 14 mishaps involving those aircraft were deleted from the study. Of the remaining 319 mishaps, nine did not involve a pilot-operator and/or some necessary study data were not in the computer bank or individual mishap report. The resulting mishap sample was 310; however, 16 of these were mid-air collisions involving two pilot-operators. Thus, the total sample of pilot-operators was 326. Table I lists the above information by fighter type.

Within this sample of 326 pilot-operators, there were 170 individuals who were determined by the mishap investigation board to have committed a total of 257 unsafe acts. Table II lists these by frequency of occurrence within the major categories defined by AFISC Manual 127-1 (Ref. 1). Table III lists descriptive statistics by age for the sample of 326 pilot-operators, the sub-sample of 170 individuals committing unsafe acts, the total unsafe acts (257) committed by that sub-sample, and selected unsafe acts distributed by categories. The categories selected for study were determined by the following criteria: Only those unsafe acts related to the pilot-operator (incorrect operation of equipment, poor technique in-flight, and poor technique in landing or pattern) were selected. Two sub-categories of poor technique in-flight (collision related, air or ground; and stall, spin, spiral, or dive) also occurred with sufficient frequency to permit analysis. Tables IV and V list the same statistics by model flying hours and total flying hours, respectively.

In this same sample of 326 pilot-operators, there were 138 individuals who were determined by the mishap investigation board (specifically the flight surgeon and life support officer) to have played a primary or contributing (definite, probable, or possible) role in causing or contributing to the

mishap as defined by AFISC Manual 127-6 (Ref. 2). Tables VI, VII, and VIII list descriptive statistics by age, model hours, and total flying hours, respectively, for the sub-sample of 138 individuals. They also list psychophysiological and environmental variables related to those pilot-operators which were found to be of definite or suspected importance in the accident phase of the mishap. The psychophysiological and environmental variables were selected for study based on their frequency of occurrence and relevance as determined by the factors found in the Ricketson et al. study. Thus, variables disorientation/vertigo (615) and visual restrictions--weather, haze, or darkness (710) were related to Factor I: disorientation, excessive motivation to succeed (625) and overconfidence (626) were related to Factor II: overconfidence. Failure to use accepted procedures (304) and inadvertent operation, self-induced (814) were related to Factor III: procedural decisions. Poor crew coordination (103) and inattention (621) were related to Factor IV: crew coordination. Inadequate coordination and timing (808) and misjudged speed or distance (809) were related to Factor V: precise multiple control. Channelized attention (622) and distraction (623) were related to Factor VIII: attention. Finally, selected wrong course of action (810), delay in taking action (811), and violation of flight discipline (812) were related to Factor IX: inadequate briefing. The reader will note that not all of the variables used by Ricketson et al. were included in this study. Of their 29 variables, 12 did not occur with sufficient frequency for analysis in fighter pilot mishaps. In addition, two of the variables related to their Factor VI: limited experience were deleted because of their self-evident relationship to age and flying experience. None of the variables in their Factor VII: task oversaturation were cited with high enough frequency in fighter pilots. For informational purposes, Table IX lists the 15 psychophysiological and environmental variables chosen by the above criteria and shows their percentage of occurrence in the Ricketson et al. Army airplane sample and the present sample of fighter mishaps. No precise comparisons can be made between these two samples. Where major diferences occur, they are very possibly due to the different operational characteristics and missions of the two samples of aircraft.

Statistical Procedures. The first step in the statistical procedures was to determine whether there were differences in age, model flying hours, and total flying hours distributions for the total sample of fighter pilot-operators and those committing unsafe acts. A similar procedure was done comparing the total sample with those pilot-operators who caused or contributed to the cause of the mishap. The

purpose of these contrasts was to determine if the age and flying experience of the sub-sample groups were comparable to that of the total sample.

The second step in the statistical procedures was to compare distributions of the samples of unsafe acts and psychophysiological and environmental variables with appropriate base distributions. In the case of unsafe acts, the appropriate base distribution was the total unsafe acts committed by the sub-sample. The reason for this is that a member of the unsafe acts sub-sample could commit more than one unsafe act, and more than one unsafe act of the same general category could be committed by the same person. For example, one pilot-operator might have permitted the aircraft to stall, and also failed to recover from a spin, spiral or dive. These are separate unsafe acts but all are included in the category of poor technique in-flight and the specific category of stall, spin, spiral or dive used in this study. In the case of the psychophysiological and environmental variables, the appropriate comparison group was the 326 pilot-operators who played a primary or contributing role in the cause of the mishap. However, to provide some information on trends for these psychophysiological and environmental variables among all mishap-involved tighter pilot-operators, similar comparisons were made with the total sample of 326 as a base group. All of the above comparisons were made using the chi square technique.

RESULTS AND DISCUSSION

Total Sample Vs Sub-Sample Comparisons. Table X shows chi square significance levels by age, model hours, and total flying hours for the total sample (N=326) versus the unsafe acts sub-sample (N=170) and the contributing sub-sample (N=138). Referring back to Table III, those persons committing unsafe acts are significantly younger (by .87 years) than the total sample at the .05 level of confidence. Referring to Table V, they also have significantly less (255 hours) of total flying hours at the .10 level of confidence. Referring to Table VII, those contributing to the cause of the mishap have significantly fewer (90.5 hours) model flying hours at the .10 level of confidence.

Unsafe Acts Comparisons. The chi square significance levels for comparisons of total unsafe acts versus categories of unsafe acts are indicated in Table XI. Referring back to Table VII, it would appear that unsafe acts related to

stalls, spins, spirals, or dives occur more frequently in the age groups 24-25 and 30-31. Poor technique in landing or pattern appears to increase in frequency from age 24 through age 31. With regard to model hours of experience, Table IV indicates that collision-related unsafe acts are most prominent in the 201 to 400 hour range and again in the 701 to 800 hour range, dropping off dramatically after approximately 800 model hours of experience. Table V indicates that unsafe acts related to stalls, spins, spirals, or dives are very prominent in the 501 to 1,000 hour range of total flying hours.

Psychophysiological and Environmental Comparisons. Using the contributing sub-sample (N=138) as the base comparison group for frequency of occurrence of these variables produced only one significant value (.10 level). This was the variable excessive motivation to succeed in relation to total flying hours. This single .10 level value could have occurred by chance alone in the 15 total flying hours comparisons made. In order to determine if any possible trends for these variables might exist, a second set of comparisons were made using the total sample (N=396) of pilot-operators as a base group. The chi square significance values (.10 or above level of confidence) are presented in Table XII. Referring back to Table VI, these results suggest that poor crew coordination, disorientation/vertigo, misjudged speed or distance, and selected wrong course of action were most prominent in both the 24 to 25 and 30 to 31 year-old groups. Channelized attention was relatively constant from age 24 through age 31. With regard to model hours (see Table VII), failure to use accepted procedures and selected wrong course of action were prominent occurrences at the 1 to 100 and 301 to 500 hour levels of experience. Disorientation/vertigo and distraction tended to remain relatively constant through the first 500 model hours, then dropped off rapidly in frequency of occurrence. Delay in taking necessary action appeared to be most frequent in the 1 to 100 and 401 to 500 model hour ranges. The one significant value (.05) related to total flying hours could possibly have happened by chance in 15 similar comparisons. In Table VIII, the only possible trend that might be seen in the excessive motivation to succeed area was a decreasing frequency of occurrence after 1,500 total flying hours

CONCLUSION

A number of associations appear to remain consistent in the variables discussed above. First, the 24 to 25 and 30

to 31 year-old groups seemed to have the highest frequency of occurrence of the following:

Stall, spin, spiral, or dive
Disorientation/vertigo
Poor crew coordination
Misjudged speed or distance
Selected wrong course of action

Why the ages for these variables should be dichotomized in this way is difficult to explain. One possible rationale is that the 24 to 25 year olds were new to the aircraft and might be expected to be involved in these acts and factors. The 30 to 31 year olds might be instructor pilots, aircraft commanders, or flight leaders whose involvement is related to their in-flight leadership and supervision of the 24 to 25 year olds.

Secondly, poor technique in pattern or landing and channelized attention appeared to remain constant or increase from ages 24 through 31, and then drop off in frequency. No clear explanation for this association is apparent.

Thirdly, the following variables appeared to have the highest frequency of occurrence sometime during the first 500 model hours of experience:

Disorientation/vertigo
Failure to use accepted procedures
Distraction
Selected wrong course of action
Delay in taking necessary action

An association that might be made among these is that disorientation/vertigo and/or distraction resulted in occurrence of one or several of the other three variables, and that these are all associated with limited experience in a particular model of fighter or in performing the assigned mission.

RECOMMENDATIONS

How then is it possible to assist fighter pilots through the 24 to 31 year old and first 500 model hours of experience periods when they appear most likely to contribute to mishaps? Improved training seems a logical answer, but the type of training that might be most effective is not so clear. Thus, only general recommendations can be made from the data and conclusions of this study.

Within the constraints of economy and available aircraft, it is fairly obvious that increased supervised flight training would result in decreased accident potential for those fighter pilots under age 32 and with under 500 model hours of experience. Particular attention should be paid to recovery procedures from stall, spin, spiral, or dive situations, and to improving techniques in pattern or landing (especially under emergency conditions). The general theme of decision-making runs through the most frequently occurring (see Table IX) psychophysiological factors (selected wrong course of action, failure to use accepted procedures, delay in taking necessary action, misjudged speed or distance). Improved training in these areas appears important. The next most frequently occurring variables (disorientation/vertigo; visual restrictions--weather, haze, darkness; and distraction) suggest that there is a need for more intensive training in responding appropriately under these non-typical conditions. Finally, improvements in crew coordination training in two-place fighters also appear worthy of attention.

One could make the assumption that training is generally a matter of developing appropriate responses (or habits) and decision-making skills to signal or set off these responses. Some of this training must occur under actual real-life conditions. For pilot training, in-flight training appears to be an effective way of accomplishing this for normal flying procedures. However, it is not practical to conduct in-flight training under all or most of the non-typical or emergency conditions that might lead to a mishap. Thus, it would seem desirable to conduct most of the improved training suggested above in simulator/trainers. There are several advantages to this approach. First, the pilot could be trained to react to a variety of emergency conditions without any danger to personnel or aircraft. Secondly, the pilot may be trained in emergency decision-making skills under very real conditions, with the opportunity to make mistakes and repeat the decision-making process until it is done correctly.

The major thesis of the above recommendations is that, although the Air Force does an excellent job of training fighter pilots for normal flying procedures, some improved training under emergency conditions appears warranted. It has been suggested that increased simulator training as a supplement to in-flight is a most effective, safe, and economical approach to this problem.

REFERENCES

1. AFISC Manual 127-1, "Aircraft Accident and Incident Classification Elements and Factors." Air Force Inspection and Safety Center, Norton AFB, California, 1 January 1972.

2. AFISC Manual 127-6, "Life Sciences Accident and Incident Classification Elements and Factors." Air Force Inspection and Safety Center, Norton AFB, California, 1 December 1971.

3. AFISC Regulation 23-1, "Mission Directive of AFISC." Headquarters Air Force Inspection and Safety Center, Norton AFB, California, 15 June 1977.

4. Ricketson, D. S., S. A. Johnson, L. B. Branham, and R. K. Dean: "Incidence, Cost, and Factor Analysis of Pilot-Error Accidents in U.S. Army Aviation." Advisory Group for Aerospace Research and Development Conference Proceedings No. 132, Behavioral Aspects of Aircraft Accidents, K. G. G. Corkindale (Ed.). Technical Editing and Reproduction, Ltd., Hartford House, London, December 1973, C7-1 through C7-19.

5. Zeller, A. F., and J. M. Burke: "Factors in Jet Pilot Proficiency." Report No. 18-59. Aero Medical Safety Division, Directorate of Flight and Missile Safety Research, Norton AFB, California, December 1959.

TABLE I

SAMPLE OF PILOT-OPERATORS BY FIGHTER TYPE

	FIGHTER TYPE								
	F-5 F-15 F-16	F-4	F-100	F-101	F-102	F-104	F-105	F-106	F-111	Totals
Total Mishaps	(14)	145	34	17	10	15	30	29	39	319
+Mid-Air Collisions	(0)	9	1	1	0	1	1	2	1	+16
Total Aircraft	(14)	154	35	18	10	16	31	31	40	335
-Incomplete Data		6	0	0	0	0	1	1	1	-9
Total Sample Pilot-Operators		148	35	18	10	16	30	30	39	326

TABLE II

FREQUENCY OF OCCURRENCE OF UNSAFE ACTS RELATED TO FIGHTER PILOT-OPERATORS BY MAJOR CATEGORY

Major Categories of Unsafe Acts	N
01 - INADEQUATE FLIGHT PREPARATION	6
02 - MISCELLANEOUS UNSAFE ACTS CAUSING INJURY OR DAMAGE	16
03 - MISTREATED AIRFRAME	3
04 - INCORRECT OPERATION, POWER PLANT	2
05 - INCORRECT OPERATION, LANDING GEAR	4
06 - INCORRECT OPERATION, FLIGHT CONTROLS OR SPEED BRAKES	9
07 - INCORRECT OPERATION, FUEL SYSTEM	3
08 - INCORRECT OPERATION, ELECTRICAL SYSTEM	0
09 - INCORRECT OPERATION, OTHER EQUIPMENT	14
10 - CONFUSED TWO CONTROLS	0
11 - DEMONSTRATED POOR TECHNIQUE IN GROUND AND TAKEOFF OPERATION	6
12 - DEMONSTRATED POOR TECHNIQUE IN FLIGHT (EXCLUDES ACCIDENTS IN LANDING PATTERN)	143
16 - DEMONSTRATED POOR TECHNIQUE IN TRAFFIC PATTERN AND LANDINGS	51
TOTAL UNSAFE ACTS	257

TABLE III

DISTRIBUTIONS BY AGE OF THE TOTAL SAMPLE, INDIVIDUALS COMMITTING UNSAFE ACTS, TOTAL UNSAFE ACTS, AND SELECTED CATEGORIES OF UNSAFE ACTS

Age	Total Sample Pilot-Operators	Indiv. Committ. Unsafe Acts	Total Unsafe Acts	Incorrect Operation Equipment 04-09	Poor Technique Inflight 12	Collision Related Air or Ground (1201-1203)	Stall, Spin, Spiral or Dive (1213-1218)	Poor Technique, Pattern or Landing 16
24-25	49	29	39	4	22	5	9	6
26-27	42	27	37	8	18	8	6	7
28-29	43	25	39	3	21	5	4	9
30-31	53	32	56	4	35	4	11	13
32-33	35	14	18	3	10	4	1	3
34-35	32	12	17	1	11	3	0	4
36-37	18	10	17	6	9	1	1	0
38-39	15	7	7	0	4	2	1	3
40-41	17	7	13	1	7	1	3	4
42+	22	7	14	2	6	1	1	2
TOTALS	326	170	257	32	143	34	37	51
Mean	31.45	30.58						
Median	30.50	29.54						

TABLE IV

DISTRIBUTIONS BY MODEL HOURS OF THE TOTAL SAMPLE, INDIVIDUALS COMMITTING UNSAFE ACTS, TOTAL UNSAFE ACTS, AND SELECTED CATEGORIES OF UNSAFE ACTS

Model Flying Hours	Total Sample Pilot-Operators	Indiv. Committ. Unsafe Acts	Total Unsafe Acts	Incorrect Operation Equipment 04-09	Poor Technique Inflight 12	Collision Related, Air or Ground (1201-1203)	Stall, Spin, Spiral or Dive (1213-1218)	Poor Technique, Pattern or Landing 16
1-100	39	25	36	5	24	1	9	5
101-200	34	19	29	2	17	2	7	6
201-300	42	24	42	9	14	6	1	15
301-400	35	20	31	4	19	4	7	5
401-500	31	17	26	3	13	2	4	7
501-600	18	13	18	2	9	3	1	4
601-700	18	10	10	1	9	2	2	0
701-800	18	8	14	0	12	5	2	1
801-900	11	2	3	1	1	0	1	0
901-1000	15	7	10	0	3	1	0	2
1001-1500	38	14	22	2	15	6	2	1
1501-2000	16	8	12	2	5	2	1	5
2001+	11	3	4	1	2	0	0	0
TOTALS	326	170	257	32	143	34	37	51
Mean	630.36	555.88						
Median	441.90	405.00						

TABLE V

DISTRIBUTIONS BY TOTAL FLYING HOURS OF THE TOTAL SAMPLE, INDIVIDUALS COMMITTING UNSAFE ACTS, TOTAL UNSAFE ACTS, AND SELECTED CATEGORIES OF UNSAFE ACTS

Total Flying Hours	Total Sample Pilot-Operators	Indiv. Committ. Unsafe Acts	Total Unsafe Acts	Incorrect Operation Equipment 04-09	Poor Technique Inflight 12	Collision Related, Air or Ground (1201-1203)	Stall, Spin, Spiral, or Dive (1213-1218)	Poor Technique, Pattern or Landing 16
1-500	45	25	34	8	15	1	5	6
501-1000	62	41	57	3	37	13	12	12
1001-1500	42	22	35	4	18	4	8	6
1501-2000	30	19	33	5	16	5	2	9
2001-2500	46	29	41	5	25	4	3	8
2501-3000	25	6	16	1	8	1	1	6
3001-3500	26	10	15	1	9	1	3	3
3501-4000	10	5	5	1	3	1	0	1
4001+	40	13	21	4	12	4	3	0
TOTALS	326	170	257	32	143	34	37	51
Mean	1978.53	1723.53						
Median	1777.77	1463.41						

TABLE VI

DISTRIBUTIONS BY AGE OF TOTAL SAMPLE, INDIVIDUALS CONTRIBUTING TO MISHAP CAUSE, AND SELECTED PSYCHOPHYSIOLOGICAL AND ENVIRONMENTAL VARIABLES

Age	Total Sample Pilot-Operators	Indiv. Contrib. to Mishap Cause	Psychophysiological & Environmental Variables*														
			103	304	615	621	622	623	625	626	710	808	809	810	811	812	814
24-25	49	23	10	11	13	5	10	9	7	5	8	4	10	14	12	8	3
26-27	42	19	5	8	6	2	10	5	4	1	6	2	6	8	8	2	2
28-29	43	17	6	6	3	2	11	7	2	1	7	1	7	5	6	6	2
30-31	53	27	10	17	10	4	13	5	8	4	6	6	13	19	14	7	3
32-33	35	12	3	3	3	1	3	4	3	5	5	2	6	5	5	3	3
34-35	32	9	4	4	4	1	4	4	4	1	5	2	3	5	5	3	1
36-37	18	8	0	3	1	1	2	4	0	1	4	2	1	2	2	2	3
38-39	15	7	1	4	2	1	4	3	1	1	2	1	2	2	3	2	2
40-41	17	8	0	3	1	0	4	2	0	0	1	0	1	4	3	1	0
42+	22	8	2	4	0	2	1	2	1	1	1	1	1	3	2	1	1
TOTALS	326	138	41	63	43	19	61	45	30	20	45	21	50	67	60	35	20
Mean	31.45	31.19															
Median	30.50	30.24															

* Key to Psychophysiological and Environmental Variables:

103 - Poor Crew Coordination
304 - Failed to Use Accept. Proced.
615 - Disorientation/Vertigo
621 - Inattention
622 - Channelized Attention
623 - Distraction
625 - Excess. Motivation to Succeed
626 - Overconfidence
710 - Visual Restrict.--Wx, Haze, Darkness
808 - Inadeq. Coord. or Timing
809 - Misjudged Speed or Distance
810 - Select. Wrong Course of Action
811 - Delay in Taking Necessary Action
812 - Violation of Flight Discipline
814 - Inadvert. Oper., Self-Induced

TABLE VII

DISTRIBUTIONS BY MODEL HOURS OF TOTAL SAMPLE, INDIVIDUALS CONTRIBUTING TO MISHAP CAUSE, AND SELECTED PSYCHOPHYSIOLOGICAL AND ENVIRONMENTAL VARIABLES

Model Hours	Total Sample Pilot-Operators	Indiv. Contrib. to Mishap Cause	Psychophysiological & Environmental Variables*														
			103	304	615	621	622	623	625	626	710	808	809	810	811	812	814
1-100	39	21	7	13	8	3	6	7	4	2	6	2	5	12	10	2	1
101-200	34	14	5	8	6	3	6	6	3	3	5	3	4	7	7	7	2
201-300	42	17	3	5	4	1	5	6	3	1	8	0	8	6	8	2	2
301-400	35	19	6	12	8	2	7	7	5	4	8	6	5	12	5	3	3
401-500	31	17	5	6	4	2	8	7	5	4	2	1	6	9	11	5	3
501-600	18	8	2	2	2	0	5	2	1	0	4	0	3	1	1	1	0
601-700	18	7	2	3	2	0	3	3	1	0	2	1	2	4	4	2	1
701-800	18	8	1	2	2	1	5	2	2	3	1	2	6	5	4	4	2
801-900	11	2	0	1	0	0	1	1	1	0	0	0	1	1	0	0	0
901-1000	15	5	2	2	1	1	4	1	1	1	2	2	3	3	3	3	2
1001-1500	38	11	6	7	3	2	7	1	3	1	4	1	4	5	4	4	1
1501-2000	16	8	2	2	2	3	3	1	1	1	2	3	3	2	2	2	2
2001+	11	1	0	0	1	1	1	1	0	0	1	0	0	0	1	0	1
TOTALS	326	138	41	63	43	19	61	45	30	20	45	21	50	67	60	35	20
Mean	630.36	539.86															
Median	441.90	392.05															

* Key to Psychophysiological and Environmental Variables:

103 - Poor Crew Coordination
304 - Failed to Use Accept. Proced.
615 - Disorientation/Vertigo
621 - Inattention
622 - Channelized Attention
623 - Distraction
625 - Excess. Motivation to Succeed
626 - Overconfidence
710 - Visual Restrict.--Wx, Haze, Darkness
808 - Inadeq. Coord. or Timing
809 - Misjudged Speed or Distance
810 - Select. Wrong Course of Action
811 - Delay in Taking Necessary Action
812 - Violation of Flight Discipline
814 - Inadvert. Oper., Self-Induced

TABLE VIII

DISTRIBUTIONS BY TOTAL FLYING HOURS OF TOTAL SAMPLE, INDIVIDUALS CONTRIBUTING TO MISHAP CAUSE, AND SELECTED PSYCHOPHYSIOLOGICAL AND ENVIRONMENTAL VARIABLES

Total Flying Hours	Total Sample Pilot-Oper.	Indiv. Contrib. to Mishap Cause	Psychophysiological & Environmental Variables*														
			103	304	615	621	622	623	625	626	710	808	809	810	811	812	814
1-500	45	17	6	9	6	5	5	7	6	3	5	3	5	12	10	4	3
501-1000	62	33	9	14	14	4	18	10	9	5	13	6	13	16	16	10	4
1001-1500	42	15	6	9	5	2	10	6	5	2	5	3	9	9	6	4	3
1501-2000	30	18	5	9	5	1	7	6	3	4	6	1	7	9	5	5	1
2001-2500	46	18	7	8	4	4	8	2	3	2	3	2	8	9	9	4	2
2501-3000	25	7	2	1	3	1	3	2	1	1	2	0	2	5	3	2	2
3001-3500	26	10	2	4	4	0	4	5	1	0	5	3	1	3	2	2	2
3501-4000	10	5	1	2	2	1	2	3	1	2	2	1	2	0	2	1	1
4001+	40	15	3	7	0	1	4	4	1	1	4	2	3	4	7	3	2
TOTALS	326	138	41	63	43	19	61	45	30	20	45	21	50	67	60	35	20
Mean	1978.53	1862.32															
Median	1777.77	1575.75															

* Key to Psychophysiological and Environmental Variables:

103 - Poor Crew Coordination
304 - Failed to Use Accept. Proced.
615 - Disorientation/Vertigo
621 - Inattention
622 - Channelized Attention
623 - Distraction
625 - Excess. Motivation to Succeed
626 - Overconfidence
710 - Visual Restrict.--Wx, Haze, Darkness
808 - Inadeq. Coord. or Timing
809 - Misjudged Speed or Distance
810 - Select. Wrong Course of Action
811 - Delay in Taking Necessary Action
812 - Violation of Flight Discipline
814 - Inadvert. Oper., Self-Induced

TABLE IX

PERCENTAGE OF OCCURRENCE FOR SELECTED PSYCHOPHYSIOLOGICAL AND ENVIRONMENTAL VARIABLES IN ARMY AIRPLANE AND AIR FORCE FIGHTER MISHAPS

Army Factors & Associated Psychophysiological and Environmental Variables	Percentage of Occur. Army Airplanes	Air Force Fighters
I. Disorientation		
Disorientation/Vertigo	2	13
Visual Restrictions--Wx, Haze, Darkness	6	14
II. Overconfidence		
Excessive Motivation to Succeed	3	9
Overconfidence	13	6
III. Procedural Decisions		
Failure to Use Accepted Procedures	52	19
Inadvertent Operation, Self-Induced	21	6
IV. Crew Coordination		
Poor Crew Coordination	11	13
Inattention	19	6
V. Precise Multiple Control		
Inadequate Coordination or Timing	23	6
Misjudged Speed or Distance	31	15
VI. Limited Experience (not used in this study)		
VII. Task Oversaturation (occurred too infrequently for analysis)		
VIII. Attention		
Channelized Attention	7	8
Distraction	7	14
IX. Inadequate Briefing		
Selected Wrong Course of Action	46	21
Delay in Taking Necessary Action	44	18
Violation of Flight Discipline	10	11

TABLE X

CHI-SQUARE SIGNIFICANCE LEVELS
FOR COMPARISONS BY AGE, MODEL HOURS, AND TOTAL FLYING HOURS
BETWEEN THE TOTAL SAMPLE (N=326) OF PILOT-OPERATORS
VERSUS THE UNSAFE ACTS SUB-SAMPLE (N=178) AND THE
CONTRIBUTING SUB-SAMPLE (N=138)

	Total Versus Unsafe Acts	Total Versus Contributing
Age	.05	*
Model Hours	*	.10
Total Flying Hours	.10	*

*Not Significant

TABLE XI

CHI-SQUARE SIGNIFICANCE LEVELS FOR COMPARISONS BY
AGE, MODEL HOURS, AND TOTAL FLYING HOURS FOR DISTRIBUTIONS
OF TOTAL UNSAFE ACTS VERSUS SELECTED CATEGORIES OF UNSAFE ACTS

	Age	Model Hours	Total Flying Hours
Incorrect Operation of Equipment	*	*	*
Poor Technique In-Flight	*	*	*
Collision Related, Air or Ground	*	.10	*
Stall, Spin, Spiral, or Dive	.10	*	.005
Poor Technique, Pattern or Landing	.10	*	*

*Not Significant

TABLE XII

CHI-SQUARE SIGNIFICANCE LEVELS FOR COMPARISONS BY AGE, MODEL HOURS, AND TOTAL FLYING HOURS FOR DISTRIBUTIONS OF THE TOTAL SAMPLE VERSUS PSYCHOPHYSIOLOGICAL AND ENVIRONMENTAL VARIABLES

	Age	Model Hours	Total Flying Hours
103 - Poor Crew Coordination	.05	*	*
304 - Failure to Use Accepted Procedures	*	.05	*
615 - Disorientation/Vertigo	.05	.10	*
621 - Inattention	*	*	*
622 - Channelized Attention	.10	*	*
623 - Distraction	*	.05	*
625 - Excessive Motivation to Succeed	*	*	.05
626 - Overconfidence	*	*	*
710 - Visual Restrictions--Weather, Haze, Darkness	*	*	*
808 - Inadequate Coordination or Timing	*	*	*
809 - Misjudged Speed or Distance	.05	*	*
810 - Selected Wrong Course of Action	.10	.01	*
811 - Delay in Taking Necessary Action	*	.10	*
812 - Violation of Flight Discipline	*	*	*
814 - Inadvertent Operation, Self-Induced	*	*	*

*Not Significant

APPENDIX

RESEARCH REPORTS

1975 USAF/ASEE SUMMER FACULTY RESEARCH PROGRAM

RESEARCH REPORTS

1976 USAF/ASEE SUMMER FACULTY RESEARCH PROGRAM

Report No.	Title	Research Associates
1	A Near Field Model for Dissolved Oxygen and Other Water Quality Parameters	Dr. Barry A. Benedict
2	Ecological Considerations for Development of a Water Quality Assessment Model	Dr. Lloyd C. Fitzpatrick
3	Dynamic Responses of Aircraft Shelters	Dr. Fang-Hui-Chou
4	A Sensitivity Study of Noisemap Power Offset Profiles (DSELs)	Dr. D. K. Holger
5	Determination of Unloaded and Loaded Pavement Profiles Used for Prediction of Dynamic Response of Aircraft	Dr. William H. Highter
6	Wind Tunnel Experiment Program for Aerodynamics of Missiles at High Angle of Attack	Dr. William L. Oberkampf
7	Analysis of Millimeter Wave Signatures of Snow and Ice	Dr. Irene K. Petroff
8	Configuration Specifications for a Digital Guided Weapon Flight Control Module	Dr. C. W. Caldwell
9	Sensor and Navigation System Processing Requirements for Digital Guided Missiles	Dr. Robert A. Higgins
10	Interpretation of Laser Velocimeter Measurements in Transonic Turbulent Boundary Layers	Dr. William G. Tiederman
11	Methods to Quantify Constituents in Binary Component Cryodeposits	Dr. Kent F. Palmer
12	Engine Test Cell Acoustics	Dr. G. T. Patterson
13	High Angle of Attack Support Interference	Dr. Robert C. Nelson
14	Development of a Nested Virtual Machine, Data-Structure Oriented Software Design Methodology and Procedure for its Evaluation	Dr. M. M. Drossman
15	Real-World Limitations of Radar Signatures for Target Identification	Dr. Robert D. Strattan
16	Confidence Intervals for Life Cycle Cost Analysis	Dr. H. A. Wiebe

Report No.	Title	Research Associates
17	Computer Aided Decision of Special Monopole and Dipole Antennas	Dr. Shreedhar G. Lele
18	Satellite Based Remote Probing of Atmospheric Visibility: A Bibliography of Relevant Literature	Dr. George C. Sherman
19	Analysis of Spectroscopic Data for Trace Gases in the Earth's Atmosphere	Dr. Louise Gray Young
20	Potential Technology Breakthroughs in Next Generation Radars	Dr. John Spragins
21	Pilot Transfer Function Identification	Dr. Bruce K. Colburn
22	Modeling of Eye Level Blood Pressure and Flow as a Function of G_z	Dr. James J. Freeman
23	Effect of Radiofrequency Radiation (RFR) on Performance and Retention of a Delayed Response Task	Dr. Carole D. Hansult
24	Time-Resolved Fluorescence of the $a^3II_0^+$ State of BrCL	Dr. John J. Wright
25	Dynamic Response of an Aboveground Arch Subjected to a Blast Load	Dr. David Y. L. Wang
26	Optical Fiber Explosion-Initiation System	Dr. Donald A. Smith
27	Density and Temperature Dependence Studies of the Thallium Mercury Excimer System	Dr. P. W. Chan
28	Signal Processing for Optics Progress as of July 1, 1976	Dr. Craig S. Sims
29	Syntheses and Decomposition Mechanisms of New Nitroaliphatic and Polycyclic Triazoline Compounds	Dr. William D. Closson
30	Electrode Erosion in Pulsed Plasma Thrusters	Dr. D. D. Chesak
31	Preparation of Solid Propellant Burning Rate Modifiers	Dr. Amos J. Leffler
32	Electrochemical Studies in Anhydrous Liquid Hydrazine	Dr. John R. Dodd
33	The Transfer Effectiveness of Platform Motion and Field of View in Training Selected UPT Maneuvers	Dr. Edward D. McDowell

RESEARCH REPORTS

1977 USAF/ASEE SUMMER FACULTY RESEARCH PROGRAM

VOLUME I Report No.	Title	Research Associates
1	Livability as Applied to Air Force Bases	Dr. Harry H. Caldwell
2	Nondestructive Pavement Evaluations	Dr. Braja Mohan Das
3	Effect of Cooling Water Spray on Turbine Engine Test Cell Emissions	Dr. Charles Springer
4	A Study of Reliability of Deep Well Anodes for Cathodic Protection	Dr. John A. Stevens
5	Tactical Shelter Hardening	Dr. Alvin M. Strauss
6	The Status of Bishop Pine on Vandenberg Air Force Base and Recommendations for Its Management	Dr. Paul H. Zedler
7	Nonlinear Guidance for Air-to-Air Missiles	Dr. J. Frederick Andrus
8	Spread Spectrum ECCM Performance CW Jamming Signal Reduction in Spread Spectrum Receivers	Dr. Maurice J. Bouvier, Jr
9	An Analysis of Aerodynamic Force and Moment Models for Asymmetric Munitions	Dr. Robert W. Courter
10	Reducing the Volume of Computation in Monte Carlo Missile Flight Simulation	Dr. Carl G. Looney
11	Flush Mounted Aircraft Antennas for Satellite Communication. A Study of Multipath Performance	Dr. Vaughn P. Cable
12	A Multimode Fiber-Optic Coupler with Low Insertion Loss	Dr. Marvin M. Drake
13	Analysis of a Discrepancy in Trapped Proton Fluxes in the South Atlantic Anomaly	Dr. Thomas E. Morgan
14	A Study of the Particle Spectrum of the Continuous Aurora and Associated E-Region Ionization Before and After a Magnetic Storm	Dr. James R. Sharber

RESEARCH REPORTS (Continued)

Report No.	Title	Research Associates
15	Directionally Solidified Eutectic Materials for Electronic, Magnetic, and Optical Applications	Dr. Richard D. Sisson, Jr.
16	Synthesis and Characterization of Novel Nitroaliphatic Materials	Dr. Melvin L. Druelinger
17	Optimal Weapon Assignment in a Tiered Aimpoint System	Dr. Jerren Gould
18	Electrochemical and Luminescence Studies with Special Emphasis on Molten Salt Media	Dr. Csaba P. Keszthelyi
19	Test of Two Hypotheses Concerning the Optical Properties of Cryodeposited Gases	Dr. William B. Newbolt
20	Rocket Exhaust Gas Dynamics	Dr. Peter C. Sukanek
21	Simulation of Turbulent Flow Velocity	Dr. John W. Weatherly, III
VOLUME II		
22	Nitronium Salt Synthesis	Dr. Alton J. Banks
23	Synthesis of Fluorodinitroethylnitramines	Dr. Catherine H. Banks
24	Submicron Particle Size Measurements in Acetylene-Oxygen and Aluminum-Oxygen Flames	Dr. James F. Driscoll
25	Solid Teflon Propulsion Contamination Investigation	Dr. James K. Hartman
26	Infrared, Raman, Mass Spectroscopy and Gas Chromatography of Selected Fluorodinitro Plasticizers	Dr. Steven Riethmiller
27	Rotational and Mean Flow Effects on Motor Stability	Dr. Wm. K. Van Moorhem
28	Investigation of Raman Microwave Emission from Plasmas	Dr. Tse-Wen Hsu
29	Automatic Speech Processing-Speech Enhancement	Dr. Russell J. Niederjohn
30	Design of System Diagnostic and Fault Isolation Procedures	Dr. Theodore J. Sheskin

RESEARCH REPORTS (Continued)

Report No.	Title	Research Associates
31	Maximum Entrophy Spectral Demodulator Investigation	Dr. Robert G. Van Meter
32	Software Design Validation and Artificial Intelligence	Dr. Ralph M. Weischedel
33	Engineering Analysis of the Dynamics and Control of the Human Centrifuge	Dr. Thomas J. Jones
34	Investigation of Ultrashort 1060 NM Laser Pulse Induced Intensity Dependent Damage Processes and Development of an On-Line Pulse Width Measuring Technique	Dr. Demetrius D. Venable
35	Application of a Specialized Statistical Computer Program, Alphaf, To a Visual Evoked Response Data Analysis System	Dr. James M. Verlander
36	Fixed Capacity Measurement of Attentional Load Using Dual-Task Performance Operating Curves	Dr. Herbert A. Colle
37	Simulator for Air-to-Air Combat Platform Motion System Investigation	Dr. John A. Seevers
38	The Radiative Lifetime and Quenching Cross Sections of the $A^2\Sigma$ State of GeF	Dr. Richard A. Anderson
39	Transient Fields From a Vertically Polarized Dipole Radiator With a Ramp Function Input Voltage	Dr. Martin D. Bradshaw
40	Liquefaction Potential of Soils Under Blast Loads	Dr. Wayne A. Charlie
41	Double Resonance Apparatus for Relaxation Studies of HF in High Vibrational States	Dr. Richard L. Redington
42	Electron-Ion Recombination in Laser Gas Mixes	Dr. Harold D. Southward
43	The Nature and Prediction of Secondary Calcium Carbonate Cementation (Caliche) in Alluvial Basins of the Southwestern United States	Dr. Stephen G. Wells